

**The surface characterisation of
pharmaceutical mini-tablets using
thermal probe techniques**

Joanne Claire Peacock

School of Pharmacy
University of East Anglia



Thesis submitted for the degree of Doctor of Philosophy
February 2014

This copy of the thesis has been supplied on condition that anyone who consults it is understood to recognise that its copyright rests with the author and that use of any information derived there from must be in accordance with current UK Copyright Law. In addition, any quotation or extract must include full attribution.

ABSTRACT

This thesis assesses the ability of a range of novel thermo-analytical techniques to determine the spatial distribution of components across the surface of pharmaceutical mini-tablets. Such information is of use in formulation development, as the surface is the point at which a solid dosage form comes into contact with the environment, and where drug stability and excipient functionality are critical. Mini-tablets provide a good model system for surface characterisation, as they have much higher surface area to volume ratios than conventionally sized tablets.

Five excipients and two drugs, as powders and after compaction, were individually characterised by the following techniques: scanning electron microscopy (SEM), variable temperature infrared spectroscopy (VT-IR), differential scanning calorimetry (DSC), atomic force microscopy (AFM), micro-thermal analysis (micro-TA), nano-thermal analysis (nano-TA) and transition temperature microscopy (TTM). Compacts of mixed systems were tested using AFM, micro-TA, nano-TA and TTM, building up the complexity to 4-component systems for excipient-only mixtures and 5-component systems for drug-loaded mixtures. Micro-TA, nano-TA and TTM were able to detect each component in all of the multi-component compacts, but AFM could not differentiate between them in complex systems. The study was then repeated on realistic mini-tablet formulations, confirming these initial results. Additionally, Raman microspectroscopy was performed on the mini-tablets as a corroborative technique, this method being based on a different physical phenomenon.

In conclusion, the thermal probe techniques (micro-TA, nano-TA and TTM) were shown to be sufficiently discriminating to allow the spatial mapping of components across the surface of realistic mini-tablet formulations. Hence, these techniques could be used alongside spectroscopic techniques in the analysis of complex surfaces. However, some serious issues with the automated analysis and data display functions in the TTM software were identified, which could lead to misinterpretation of the results. Potential corrective measures were suggested to alleviate these concerns and improve experimental reliability.

Acknowledgements

I would like to convey my deep gratitude to Professor Duncan Craig and Dr Susan Barker for their encouragement, help and guidance they continued to give me though out. Their boundless patience in answering my many questions was appreciated. Professor Duncan Craig's Support and expertise in the subject was invaluable. Dr Susan Barker, who was most generous with her knowledge, time and advice. I am particularly grateful for the assistance of Dr Jonathan Moffat for all his practical assistance and knowledge in AFM and LTA.

I would like to thank Dr Juliette Guaquiere for supervising GlaxoSmithKline's support and technical advice. Thank you for giving me the opportunity to use GlaxoSmithKline laboratories to study Raman microscopy. The time I spent there was very valuable and furthered the project.

I would like to extend my thanks to my friends for all the support and understanding over this period. Their encouragement was greatly appreciated. Finally, my thanks go to my family for their support though out. Without my family's love and faith in me and all the help they have given me, none of this would be possible. The time donated was greatly appreciated and the endless trips to Norwich.

Contents page

	Page
Chapter 1 Introduction	1
1.1 Tablets	2
1.2 Mini-tablets	2
1.2.1 Oral use – general	2
1.2.2 Oral use - controlled-release and targeted-release	5
1.2.3 Ocular administration	7
1.3 Tablet formulation	8
1.4 Tablet manufacture	9
1.5 Formulation and manufacture of mini-tablets	13
1.6 Tablet characterisation	15
1.6.1 Bulk characterisation	15
1.6.2 Surface characterisation	16
1.7 Analytical techniques used in this work	17
1.7.1 Scanning Electron Microscopy (SEM)	17
1.7.2 Variable Temperature Infrared Spectroscopy (VT-IR)	18
1.7.3 Differential Scanning Calorimetry (DSC)	21
1.7.4 Atomic force Microscopy (AFM)	22
1.7.5 Localised Thermal Analysis (LTA)	26
1.7.6 Transition Temperature Microscopy (TTM)	29
1.7.7 Raman Microspectroscopy	30
1.7.8 Other techniques for tablet surface imaging	34
1.8 Aims and objectives of this project	35
Chapter 2 General methods and materials	37
2.1 Introduction	38
2.2 Materials	39

	Page
2.2.1 Microcrystalline cellulose	39
2.2.2 Pregelatinised Starch	40
2.2.3 Alpha- lactose monohydrate	42
2.2.4 Magnesium Stearate	43
2.2.5 Polyvinylpyrrolidone	43
2.2.6 Caffeine	44
2.2.7 Ibuprofen	45
2.2.8 Anhydrous Theophylline	46
2.2.9 Other drugs	47
2.3 Methods	48
2.3.1 Scanning electron microscope (SEM) procedures	48
2.3.2 Variable temperature infrared (VT-IR) procedures	48
2.3.3 Differential scanning calorimetry (DSC) procedures	49
2.3.4. Atomic force microscope (AFM) and Localised thermal Analysis (LTA) procedures	50
2.3.5 Transition temperature microscope (TTM) procedures	55
2.3.6 Raman microscope procedures	57
2.3.7 Production of compacts	58
2.3.8 Production of mini-tablets	58
2.3.8.1 Wet granulation procedures	58
2.3.8.2 Tableting procedures	60
2.2.9 Mini-tablet characterisation	61
2.2.9.1. Weight uniformity	61
2.2.9.2. Hardness	61
2.2.9.3. Thickness	62
2.2.9.4. Friability	62
2.2.9.5. Content uniformity assessment of the drug-loaded	

	Page
mini-tablets	64
Chapter 3 A physico-chemical profile of each excipient used in the formulations	65
3.1 Introduction	66
3.2 Materials and Methods	67
3.3 Results and Discussion	67
3.3.1 Microcrystalline Cellulose (MCC)	67
3.3.1.1 SEM	67
3.3.1.2 VT-IR	68
3.3.1.3 DSC	69
3.3.1.4 AFM	70
3.3.1.5 Micro-TA	72
3.3.1.6 Nano-TA	75
3.3.1.7 TTM	77
3.3.2 Pre-gelatinised starch (PGS)	78
3.3.2.1 SEM	78
3.3.2.2 VT-IR	79
3.3.2.3 DSC	81
3.3.2.4 AFM	82
3.3.2.5 Micro-TA	84
3.3.2.6 Nano-TA	87
3.3.2.7 TTM	88
3.3.3 Magnesium stearate (MS)	89
3.3.3.1 SEM	89

	Page
3.3.3.2 VT-IR	89
3.3.3.3 DSC	91
3.3.3.4 AFM	92
3.3.3.5 Micro-TA	93
3.3.3.6 Nano-TA	95
3.3.3.7 TTM	96
3.3.4 α -Lactose monohydrate (LM)	97
3.3.4.1 SEM	97
3.3.4.2 VT-IR	98
3.3.4.3 DSC	104
3.3.4.4 AFM	106
3.3.4.5 Micro-TA	111
3.3.4.6 Nano-TA	116
3.3.4.7 TTM	118
3.3.4.8 Mixed lactose systems	119
3.3.5 Polyvinyl pyrrolidone (PVP)	121
3.3.5.1 VT-IR	124
3.3.5.3 AFM	125
3.3.5.4 Micro-TA	128
3.3.5.5 Nano-TA	129
3.4 Conclusions	130

	Page
Chapter 4 A physico-chemical profile of the drugs used in the formulations	133
4.1 Introduction	134
4.2 Material and Methods	134
4.3 Results and Discussion	134
4.3.1 Caffeine	135
4.3.1.1 SEM	135
4.3.1.2 VT-IR	136
4.3.1.3 DSC	140
4.3.1.4 AFM	141
4.3.1.5 Micro- TA	145
4.3.1.6 Nano- TA	148
4.3.1.7 TTM	150
4.3.2 Ibuprofen	152
4.3.2.1 SEM	152
4.3.2.2 VT-IR	153
4.3.2.3 DSC	155
4.3.2.4 AFM	155
4.3.2.5 Micro- TA	158
4.3.2.6 Nano- TA	160
4.3.2.7 TTM	162
4.3.3 Theophylline (anhydrous)	162
4.3.3.1 SEM	162

	Page
4.3.3.2 VT-IR	163
4.3.3.3 DSC	166
4.3.3.4 AFM	166
4.3.3.5 Micro- TA	169
4.3.3.6 Nano- TA	170
4.3.3.7 TTM	171
4.4. Investigations into the micro-TA / nano-TA analysis of ibuprofen, caffeine and theophylline	172
4.5 Conclusions	177
Chapter 5 The analysis of multi-component samples	180
5.1 Introduction	181
5.2 Materials and Methods	181
5.3 Results and Discussion	183
5.31 Multi-component excipient compacts	183
5.3.1.1 AFM	183
5.3.1.2 Nano-TA	186
5.3.1.3 TTM	193
5.3.1.4 General discussion for the multi-component excipient compacts	199
5.3.2 Multi-component compacts containing caffeine	200
5.3.2.1 AFM	200
5.3.2.2 Nano-TA	205
5.3.2.3 TTM	214
5.3.2.4 General discussion for the multi-component	

	Page
6.3.3.1.5 DSC	259
6.3.3.1.6 Recommendation	260
6.3.3.2 Physical characterisation of the experimental mini-tablet batches	261
6.3.3.2.1 Weight uniformity	261
6.3.3.2.2 Thickness	261
6.3.3.2.3 Hardness	261
6.3.3.2.4 Friability	267
6.3.3.2.5 DSC	268
6.3.3.3 Content uniformity assessment of the drug-loaded experimental mini-tablet batches	270
6.3.3.4 Surface characterisation of the development mini-tablet batches	274
6.3.3.4.1 SEM	274
6.3.3.4.2 AFM	275
6.3.3.4.3 Nano-TA	276
6.3.3.4.4 TTM	278
6.3.3.5 Surface characterisation of the experimental mini-tablet batches	281
6.3.3.5.1 AFM	281
6.3.3.5.2 Nano-TA	282
6.3.3.5.3 TTM	284
6.4 Conclusions	292

	Page
Chapter 7 Raman microscopy	295
7.1 Introduction	296
7.2 Materials and Methods	296
7.3 Results and Discussion	296
7.3.1 Mono-component excipient compacts	296
7.3.2 Multi-component excipient compacts	298
7.3.3 Mini-tablets - "development" batches	304
7.3.4 Mini-tablets - "experimental" batches	307
7.4 Conclusions	318
Chapter 8 Overall discussion and conclusions	321
8.1 Summary of work performed	322
8.1.1 Individual components	322
8.1.2 Mixed systems	326
8.2 General discussion on the techniques used	328
8.2.1 AFM	328
8.2.2 Micro- TA and nano- TA	330
8.2.3 TTM	334
8.2.4 Raman microspectroscopy mapping	339
8.2.5 General discussion	340
8.3 Discussion on the mini-tablet formulations and results	345
8.4 Further work	346

	Page
Appendix	349
Abbreviation	350
References	352

Lists of figures

		Page
Figure 1.1	A mini- tablet in a pair of tweezers.	3
Figure 1.2	Schematic illustration of the wet granulation process	10
Figure 1.3	Schematic illustration of compression of a tablet	11
Figure 1.4	A diagrammatic representation of a mini-tablet (A) and a normal-sized tablet (B), both round and flat-faced.	14
Figure 1.5	Schematic of a scanning electron microscope.	18
Figure 1.6	Schematic of a scanning electron microscope.	20
Figure 1.7	Schematic diagram of the basic operational set-up of an AFM.	24
Figure 1.8	An explanation of nano-TA (also applicable to micro-TA) which shows probe movement with the resultant curve.	28
Figure 1.9	A simplified example of a TTM map.	29
Figure 1.10	Energy level diagram showing the concerted excitation relaxation phenomena responsible for scattering.	32
Figure 1.11	Schematic of a Raman microscope. Adapted from Smith and Clark (2004).	33
Figure 2.1	Structure of microcrystalline cellulose.	39
Figure 2.2	The chemical structure of unmodified starch. A) amylose. B) amylopectin.	41
Figure 2.3	Structure of α -LM.	42
Figure 2.4	Structure of magnesium stearate, $Mg (C_{18}H_{35}O_2)_2$.	43

	Page
Figure 2.5	Structure of PVP. 44
Figure 2.6	Structure of caffeine. 45
Figure 2.7	Structure of ibuprofen. 46
Figure 2.8	Structure of Theophylline. 47
Figure 2.9	An example of a Golden Gate ATR accessory with a thermal top plate. 49
Figure 2.10	An example of the calibration plot of the thermal probes. The blue curves show the actual results for the three standards used with the endpoints highlighted: 2) polycaprolactone, 3) polyethylene and 4) polyethylene terephthalate. Point 1 is the room temperature. The orange lines show the calibration values chosen for each endpoint. 51
Figure 2.11	An example of the topography map of a sample produced via AFM imaging 52
Figure 2.12	An example of the AFM and micro-TA results for an α -LM compact, showing the sites of the multiple micro-TA readings and the damage caused by the Wollaston wire probe. A) AFM scan of an α -LM compact before the micro-TA experiment. B) AFM scan of the same area on the α -LM compact after the micro-TA experiment. C) The results for the five micro-TA readings: dark blue - position 1, red - position 2, green - position 3, purple - position 4, light blue - position 5. The position numbers refer to the positions in image B. 54
Figure 2.13	The Vesta TTM (Anasys Instruments, USA). 55
Figure 2.14	An optical image of the TTM probe on the surface of a compact. The blue square is the region scanned and shows each reading in the grid pattern.  denotes the starting point for the scan. 56

	Page
Figure 2.15	An example of TTM mapping of a two-component compact. A) The discrete map and the corresponding nano-TA results for the two squares highlighted. B) The interpolated (smoothed) map for the same data generated by the software. 57
Figure 2.16	Photograph of a set of the 2 mm normal concave tooling used in this study. Top - upper punch, middle - die and bottom - lower punch. 60
Figure 2.17	The texture analyser set up used to measure the hardness of the mini-tablets. 62
Figure 2.18	Image of the friability tester (measurement parameters taken from the British Pharmacopoeia 2013).). 63
Figure 3.1	SEM image of MCC. A) magnification X250, B) magnification X1000. 67
Figure 3.2	FT-IR spectra for MCC between the temperatures of 30°C and 200°C. A) all scans at 10°C intervals, B) the results for 30°C (blue) and 200°C (red). 68
Figure 3.3	DSC trace of MCC powder (red) and MCC mini-tablet (Blue). 70
Figure 3.4	AFM scans showing the topography (as height) of the MCC compacts using a Wollaston wire (micro) probe. Column 1 - top of the compact, column 2 - bottom of the compact; position on the radius of the compact is given from A) edge to F) middle. 71
Figure 3.5	AFM scans showing the topography of the MCC compacts using a nano probe. Column 1 - height, column 2 - deflection of the probe; position on the radius of the compact is given from A) edge to C) middle. 72
Figure 3.6	Micro-TA results of MCC compacts, using a Wollaston wire probe. Column 1 - top of the compact, column 2 - bottom of the compact; position on the radius of the compact is given by A) edge

- to F) middle. Five micro-TA reading were taken at each position: dark blue - site 1, red - site 2, green - site 3, purple - site 4, light 73
- Figure 3.7 An example of micro-TA analysis of compact of MCC compressed at 10 tons, showing smoother traces than seen in Figure 3.6. 75
- Figure 3.8 Nano-TA results of MCC compacts using a nano probe, across the radius of the compact from A (edge) to C (middle). Five nano-TA reading were taken at each position: dark blue - site 1, red - site 2, green - site 3, purple - site 4, light blue - site 5. 76
- Figure 3.9 Nano-TA results for a MCC compact showing the probe lifting and going back in contact with the compact at the point of V- shape. 76
- Figure 3.10 TTM maps of MCC compacts. A) middle and B) edge of the compact. Column 1 is the interpolated (smoothed) map, Column 2 is the discrete map, and Column 3 shows the individual nano-thermal results. 78
- Figure 3.11 SEM image of PGS. A) magnification X250, B) magnification X1000. 78
- Figure 3.12 FT-IR spectra for PGS between the temperatures of 30°C and 200°C. A) all scans at 10°C intervals, B) the results for 30°C (blue) and 200°C (red). 80
- Figure 3.13 FT-IR "normal" and second derivative spectra for PGS at 30°C and 200°C. Blue - "normal" spectrum at 30°C, red - "normal" spectrum at 200°C, pale blue - second derivative spectrum at 30°C, pink - second derivative spectrun at 200°C. The arrows indicate peak of interest aligned for 200°C. 81
- Figure 3.14 DSC trace of PGS powder (red) and mini-tablet (blue). 82
- Figure 3.15 AFM scan showing the topography (as height) of the PGS compacts using a Wollaston wire (micro) probe. Column 1 - top of the compact, column 2 - bottom of the compact,

	Page
	83
Figure 3.16	84
Figure 3.17	85
Figure 3.18	87
Figure 3.19	88
Figure 3.20	89
Figure 3.21	90
Figure 3.22	92
Figure 3.23	92

- Figure 3.24 Micro-TA results of MS compacts, using a Wollaston wire micro probe. Column 1 - top of the compact, column 2 - bottom of the compact, position on the radius of the compact is given by A) outside to F) centre. Five readings were taken at each position: dark blue - site 1, red - site 2, green - site 3, purple - site 4, light blue - site 5. 94
- Figure 3.25 Nano-TA results of MS compacts using a nano probe across the radius of the compact from A (outside) to C (centre). Five nano-TA readings were taken at each position: dark blue - site 1, red - site 2, green - site 3, purple - site 4, light blue - site 5. 96
- Figure 3.26 TTM maps of MS compacts. A) centre and B) outside of the compact. Column 1 is the interpolated (smoothed) map, Column 2 is the discrete map, and Column 3 shows the individual nano-thermal results. 97
- Figure 3.27 SEM image of LM. A) magnification X250, B) magnification X1000. 98
- Figure 3.28 FT-IR spectra for α -LM between the temperatures of 30°C and 200°C. A) all scans; B) identification finger print region: blue 30°C, black 160°C, orange 170°C, green 180°C, pink 190°C, red 200°C; C) the results for 30°C (blue), 200°C (red), cooled back to 30°C (green); D) finger print region for 30°C (blue) and 200°C (red), cooled back to 30°C (green). 100
- Figure 3.29 The structures of α -lactose (A) and β -lactose (B) (images from www.sigma-aldrich.com). The red ring indicates the -OH group which dictates whether the structure is α or β . 102
- Figure 3.30 FT-IR spectra for anhydrous α -lactose between the temperatures of 30°C and 200°C: A) the results for 30°C (blue), 200°C (red), cooled back to 30°C (green); B) finger print region for 30°C (blue), 200°C (red), cooled back to 30°C (green). 102

	Page	
Figure 3.31	FT-IR spectra for β -lactose between the temperatures of 30°C and 200°C. A) the results for 30°C (blue), 200°C (red), cooled back to 30°C (green); B) finger print region for 30°C (blue) and 200°C (red), cooled back to 30°C (green).	103
Figure 3.32	DSC traces of α -LM powder (red) and mini-tablet (blue).	105
Figure 3.33	DSC traces of powder samples: anhydrous α -lactose (blue), α -lactose monohydrate (red) and beta lactose (green).	105
Figure 3.34	AFM scans showing the topography (as height) of the α -LM compacts using a Wollaston wire (micro) probe. Column 1 - top of the compact, column 2 - bottom of the compact; position on the radius of the compact is given from A) outside to F) centre.	107
Figure 3.35	AFM scan showing the topography (as height) of anhydrous α -lactose compacts using a Wollaston wire (micro) probe. Column 1 - top of the compact, column 2 - bottom of the compact; position on the radius of the compact is A) outside and F) centre.	108
Figure 3.36	AFM scan showing the topography (as height) of anhydrous β -lactose compacts using a Wollaston wire (micro) probe. Column 1 - top of the compact, column 2 - bottom of the compact; position on the radius of the compact is A) outside and F) centre.	108
Figure 3.37	The AFM scans using the nano probes showing the topography of the α -LM compacts. Column 1 - height of the scan, column 2 - deflection of the probe; position on the radius of the compact is given from A) outside to C) centre.	109
Figure 3.38	The AFM scans using the nano probes showing the topography of the anhydrous α -lactose compacts. Column 1 - height of the scan,	

	Page
	column 2 - deflection of the probe; position on the radius of the compact is given as A) outside and C) centre. 110
Figure 3.39	The AFM scans using the nano probes showing the topography of the β -lactose compacts. Column 1 - height of the scan, column 2 - deflection of the probe; position on the radius of the compact is given as A) outside and C) centre. 110
Figure 3.40	Micro-TA results of α -LM compacts, using a Wollaston wire (micro) probe. Column 1 - top of the compact, column 2 - bottom of the compact; position on the radius of the compact is given by A) outside to F) centre. Five readings were taken at each position: dark blue - site 1, red - site 2, green - site 3, purple - site 4, light blue - site 5. 113
Figure 3.41	Micro-TA results of anhydrous α -lactose compacts, using a Wollaston wire (micro) probe. Column 1 - top of the compact, column 2 - bottom of the compact; position on the radius of the compact is given by A) outside and F) centre. Five readings were taken at each position: dark blue - site 1, red - site 2, green - site 3, purple - site 4, light blue - site 5. 114
Figure 3.42	Micro-TA results of anhydrous β -lactose compacts, using a Wollaston wire (micro) probe. Column 1 - top of the compact, column 2 - bottom of the compact; position on the radius of the compact is given by A) outside and F) centre. Five readings were taken at each position: dark blue - site 1, red - site 2, green - site 3, purple - site 4, light blue - site 5. 114
Figure 3.43	Micro-TA results for compacts of α -LM (red) and anhydrous α -lactose (blue) compressed to 10 tons for 2 minutes. 115
Figure 3.44	Micro-TA results for compacts of α -LM (red), anhydrous α -lactose (blue) and β -lactose compressed to 2 tons for 30 seconds (all generated and performed on the same day). 115
Figure 3.45	Nano-TA results of α -LM compacts using a nano probe across the

- radius of the compact from A (outside) to C (centre). Five nano-TA readings were taken at each position: dark blue - site 1, red - site 2, green - site 3, purple - site 4, light blue - site 5. 116
- Figure 3.46 Nano-TA results of anhydrous α -lactose compacts using a nano probe across the radius of the compact from A (outside) to C (centre). Five nano-TA readings were taken at each position: dark blue - site 1, red - site 2, green - site 3, purple - site 4, light blue - site 5. 117
- Figure 3.47 Nano-TA results of β -lactose compacts using a nano probe across the radius of the compact from A (outside) to C (centre). Five nano-TA readings were taken at each position: dark blue - site 1, red - site 2, green - site 3, purple - site 4, light blue - site 5. 117
- Figure 3.48 Nano-TA results for compacts of α -LM (red), anhydrous α -lactose (blue) and β -lactose compressed to 2 tons for 30 seconds (all generated and performed on the same day). 118
- Figure 3.49 TTM maps of α -LM compacts. A) centre and B) outside of the compact. Column 1 is the interpolated (smoothed) map, Column 2 is the discrete map, and Column 3 shows the individual nano-thermal results. 119
- Figure 3.50 The AFM scan using the nano probe showing the topography of the mixed α -LM and β -lactose compacts. Column 1 - height of the scan, column 2 - deflection of the probe; position on the radius of the compact is given by A) outside and B) centre. 120
- Figure 3.51 Nano-TA results of the mixed α -LM and β -lactose compacts. Position on the radius of the compact is given by A (outside) and B (centre). Five nano-TA readings were taken at each position: dark blue - site 1, red - site 2, green - site 3, purple - site 4, light blue - site 5. 121

	Page	
Figure 3.52	TTM maps of the mixed α -LM and β -lactose compacts. Column 1 is the interpolated (smoothed) map, Column 2 is the discrete map, and Column 3 shows the individual nano-thermal results.	121
Figure 3.53	FT-IR spectra for the PVP gel form between the temperatures of 30°C and 200°C. A) all scans at 10°C intervals, B) the results for 30°C (blue) and 200°C (red).	123
Figure 3.54	FT-IR spectra for the three PVP forms at 30°C: 15 %w/v aqueous solution (blue), gel (red), solid (green).	124
Figure 3.55	DSC trace of PVP powder.	125
Figure 3.56	AFM scan showing the topography of the solid PVP compacts using a Wollaston wire (micro) probe. Column 1 - height, column 2 - deflection of the probe; position on the diameters of the compact is A) outside, B) centre and C) outside.	126
Figure 3.57	AFM scan showing the topography of the solid PVP compacts using a nano probe. Column 1 - height of the scan, column 2 - deflection of the probe; position on the diameters of the compact is A) outside, B) centre and C) outside.	126
Figure 3.58	Images of PVP in gel form using A) the Wollaston wire probe and B) the nano probe.	127
Figure 3.59	Micro-TA results of solid PVP compacts, using a Wollaston wire (micro) probe. Position on the diameter of the compact is given by A) outside, B) middle and C) outside. Five readings were taken at each position: dark blue - site 1, red - site 2, green - site 3, purple- site 4, light blue - site 5.	128
Figure 3.60	Micro-TA results of gel PVP compacts, using a Wollaston wire (micro) probe. Position on the diameter of the compact is given by A) outside, B) middle and C) outside. Five readings were taken at each position: dark blue - site 1, red - site 2, green - site 3, purple - site 4, light blue - site 5.	129

Figure 3.61	Nano-TA results of PVP (solid) compacts using a nano probe. Position on the diameter of the compact is given by A) outside, B) middle and C) outside. Five nano-TA readings were taken at each position: dark blue - site 1, red - site 2, green - site 3, purple - site 4, light blue - site 5.	130
Figure 3.62	A summary of the micro-TA results for the five excipients.	131
Figure 3.63	A summary of the nano-TA results for the four excipients.	132
Figure 4.1	SEM image of caffeine. A) Caffeine Form II magnification X250. B) Caffeine Form II magnification X1000. C) Caffeine Form I magnification X250. D) Caffeine Form I magnification X1000.	135
Figure 4.2	FT-IR spectra for caffeine (starting as Form II) between the temperatures of 30°C and 200°C. A) all scans at 10°C intervals. B) the results for 30°C (blue) and 200°C (red).C) the finger print region for 30°C (blue) and 200°C (red) scans.	137
Figure 4.3	FT-IR spectra for Form II (green) and Form I (orange) of caffeine at 30°C. A) full scan. B) the finger print region.	139
Figure 4.4	DSC trace of caffeine Form II (red) and Form I (blue).	140
Figure 4.5	The DSC trace of caffeine Form II at different heating rates: 5°C/minute (green), 10°C/minute (blue), 15°C/minute (pink), 20°C/minute (red).	141
Figure 4.6	AFM scans showing the topography of the top of the caffeine Form II compacts using a Wollaston wire (micro) probe. Column 1 - height, column 2 - deflection; position on the radius of the compact is given from A) edge to F) middle.	142

	Page
Figure 4.7	AFM scans showing the topography of the top of the caffeine Form I compacts using a Wollaston wire (micro) probe. Column 1 - height, column 2 - deflection; position on the radius of the compact is given by A) edge and B) middle. 143
Figure 4.8	AFM scan showing the topography of the top of caffeine Form II compacts using a nano probe. Column 1 - height, column 2 - deflection of the probe; position on the radius of the compact is given from A) edge to C) middle. 144
Figure 4.9	AFM scan showing the topography of the top of caffeine Form I compacts using a nano probe. Column 1 - height, column 2 - deflection of the probe; position on the radius of the compact is given by A) edge and B) middle. 145
Figure 4.10	Micro-TA results of caffeine Form II compacts using a Wollaston wire probe, across the radius of the compact from A (outside) to F (edge). Five micro-TA readings were taken at each position: dark blue - site 1, red - site 2, green - site 3, purple - site 4, light blue - site 5. 147
Figure 4.11	An example of the micro-TA of caffeine Form II compacts: the arrow highlights the small peak ascribed to the transition of Form II to Form I. 147
Figure 4.12	Micro-TA results of compacts of caffeine Form I (A) and Form II (B) compacts using a Wollaston wire probe, across the radius of the compact: i) outside and ii) edge. The heating rate was 25°C/second. Five micro-TA readings were taken at each position: dark blue - site 1, red - site 2, green - site 3, purple - site 4, light blue - site 5. 148
Figure 4.13	Nano-TA results of caffeine Form II compacts using a nano probe, across the radius of the compact from A (edge) to C (middle). Five nano-TA readings were taken at each position: dark blue - site 1, red

	Page
- site 2, green - site 3, purple - site 4, light blue - site 5.	149
Figure 4.14 Nano-TA results of compacts of caffeine Form I (A) and Form II (B) using a nano probe, across the radius of the compact: i) outside and ii) edge. The heating rate was 25°C/second. Five nano-TA readings were taken at each position: dark blue - site 1, red - site 2, green - site 3, purple - site 4, light blue - site 5.	150
Figure 4.15 TTM maps of caffeine compacts. A) middle and B) edge of the compact. Column 1 is the interpolated (smoothed) map, Column 2 is the discrete map, and Column 3 shows the individual nano-thermal results.	151
Figure 4.16 SEM image of ibuprofen. A) magnification X250. B) magnification X1000.	152
Figure 4.17 FT-IR spectra for ibuprofen between the temperatures of 30°C and 100°C. A) All scans at 10°C intervals, B) The full spectra for selected temperatures, C) The finger print region for selected temperatures - 30°C (blue), 70°C (green), 80°C (orange) and 100°C (red).	154
Figure 4.18 DSC traces of ibuprofen. Red - the batch used for the compacts work; blue -the batch used for the mini-tablets work.	155
Figure 4.19 AFM scans showing the topography (as height) of the top of an ibuprofen compact using a Wollaston wire (micro) probe. The position on the radius of the compact is given from A) edge to F) middle.	156
Figure 4.20 AFM scan showing the topography of the top of an ibuprofen compact using a nano probe. Column 1 - height, column 2 - deflection of the probe; position on the radius of the compact is given from A) edge to C) middle.	157

- Figure 4.21 AFM scan using a nano-probe showing the topography of the top of the ibuprofen compact prepared using the "new" batch of drug. Column 1 - height, column 2 - deflection; the position on the radius of the compact is given from A) edge to C) middle. 158
- Figure 4.22 Micro-TA results across the top of an ibuprofen compact, using a Wollaston wire probe. Position on the radius of the compact is given by A) edge to F) middle. Five micro-TA readings were taken at each position: dark blue - site 1, red - site 2, green - site 3, purple - site 4, light blue - site 5. 159
- Figure 4.23 Nano-TA results of the top of the ibuprofen compacts, using a nano probe. Position across the radius of the compact is given by A (edge) to C (middle). Five nano-TA readings were taken at each position: dark blue - site 1, red - site 2, green - site 3, purple - site 4, light blue - site 5. 160
- Figure 4.24 Nano-TA results of the top of the heat-treated ibuprofen compacts, using a nano probe. Five nano-TA readings were taken: dark blue - site 1, red - site 2, green - site 3, purple - site 4, light blue - site 5. 161
- Figure 4.25 Nano-TA results of the top of the ibuprofen compacts (lot number 1B1T1575, batch used to prepare mini-tablets) using a nano probe. Position across the radius of the compact is given by A (edge) and B (middle). Five nano-TA readings were taken at each position: dark blue - site 1, red - site 2, green - site 3, purple - site 4, light blue - site 5. 161
- Figure 4.26 TTM maps of ibuprofen compacts. A) middle and B) edge of the compact. Column 1 is the interpolated (smoothed) map, Column 2 is the discrete map, and Column 3 shows the individual nano-thermal results. 162

- Figure 4.27 SEM images of anhydrous theophylline. A) magnification X250. B) magnification X1000. 163
- Figure 4.28 FT-IR spectra for anhydrous theophylline between the temperatures of 30°C and 200°C. A) All scans at 10°C intervals, B) the results for 30°C (blue) and 200°C (red), C) the fingerprint region for 30°C (blue) and 200°C (red). 164
- Figure 4.29 DSC traces of anhydrous theophylline. 166
- Figure 4.30 AFM scan showing the topography of the top of the theophylline compacts using a Wollaston wire (micro) probe. Column 1 - height, column 2 - deflection; position on the radius of the compact is given from A) outside to B) centre to C) outside. 167
- Figure 4.31 AFM scan showing the topography of the top of the theophylline compacts using a nano probe. Column 1 - height, column 2 - deflection; position on the radius of the compact is given from A) outside to B) centre to C) outside. 168
- Figure 4.32 Micro-TA results of theophylline compacts, using a Wollaston wire (micro) probe; position across the diameter of the compact is given by: A (outside), B (centre), C (outside). Five readings were taken at each position: dark blue - site 1, red - site 2, green - site 3, purple - site 4, light blue - site 5. 169
- Figure 4.33 Nano-TA results of the theophylline compact, using a nano probe; position across the diameter of the compact is given by: A (outside), B (centre), C (outside). Five readings were taken at each position: dark blue - site 1, red - site 2, green - site 3, purple - site 4, light blue - site 5. 170

- Figure 4.34 Nano-TA results of the theophylline compact, using a nano probe, after the compact had been dried in an oven for 4 hours at 160°C. Five nano-TA readings were taken at the same position: dark blue - site 1, red - site 2, green - site 3, purple - site 4, light blue - site 5. 171
- Figure 4.35 TTM maps of theophylline compacts. A) centre and B) outside of the compact. Column 1 is the interpolated (smoothed) map, Column 2 is the discrete map, and Column 3 shows the individual nano-thermal results. 171
- Figure 4.36 A summary of the nano-TA results for four excipients plus caffeine. 178
- Figure 4.37 A summary of the nano-TA results for four excipients plus Ibuprofen. 179
- Figure 5.1 Summary of the nano-TA profile of the four excipients (α -LM, MCC, PGS and MS) and two drugs (caffeine and ibuprofen) used in this study. 182
- Figure 5.2 AFM images of 2-excipient compacts, using a nano probe. A) 99% α -LM / 1% MS. B) 99% MCC / 1% MS. C) 99% PGS / 1% MS. D) 50% α -LM / 50% MCC. E) 50% α -LM / 50% PGS. F) 50% MCC / 50% PGS. Position on the compact is given by i) centre, ii) outside. Column 1 - height, Column 2 - deflection. 183
- Figure 5.3 AFM images of 3-excipient compacts, using a nano probe. A) 49.5% α -LM / 49.5% PGS / 1% MS. B) 49.5% α -LM / 49.5% MCC / 1% MS. C) 49.5% MCC / 49.5% PGS / 1% MS. D) 33.3% α -LM / 33.3% PGS / 33.3% MCC. Position on the compact is given by i) centre, ii) outside. Column 1 - height, Column 2 - deflection. 185
- Figure 5.4 AFM images of 4-excipient compacts using a nano probe. A) 33% α -LM / 33% PGS / 33% MCC / 1% MS. B) 25% α -LM / 25% PGS / 25% MCC / 25% MS. Position on the compact is given by i) centre, ii) outside. Column 1 - height, Column 2 deflection. 186

- Figure 5.5 Nano-TA results for the 2-excipient compacts, using a nano probe. A) 99% α -LM / 1% MS. B) 99% MCC / 1% MS. C) 99% PGS / 1% MS. D) 50% α -LM / 50% PGS. E) 50% α -LM / 50% MCC. F) 50% MCC / 50% PGS. Position on the compact is given by i) centre, ii) outside. Five readings were taken at each position: dark blue - site 1, red - site 2, green - site 3, purple - site 4, light blue - site 5. 187
- Figure 5.6 Nano-TA results for the 3-excipient compacts, using a nano probe. A) 49.5% α -LM / 49.5% PGS / 1% MS. B) 49.5% α -LM / 49.5% MCC / 1% MS. C) 49.5% MCC / 49.5% PGS / 1% MS (inset is the temperature range 200 to 300°C expanded). D) 33.3% α -LM / 33.3% PGS / 33.3% MCC. Position on the compact is given by i) centre, ii) outside. Five readings were taken at each position: dark blue - site 1, red - site 2, green - site 3, purple - site 4, light blue - site 5. 189
- Figure 5.7 Nano-TA results for the 4-excipient compacts, using a nano probe. A) 33% α -LM / 33% PGS / 33% MCC / 1% MS. B) 25% α -LM / 25% PGS / 25% MCC / 25% MS. Position on the compact is given by i) centre, ii) outside. Five readings were taken at each position: dark blue - site 1, red - site 2, green - site 3, purple - site 4, light blue - site 5. 191
- Figure 5.8 TTM maps for 2-excipient compacts, with representative colours. A) 99% α -LM (red / yellow / pink) / 1% MS (blue / purple). B) 99% MCC (orange / yellow) / 1% MS (not detected). C) 99% PGS (orange / yellow) / 1% MS (not detected). D) 50% α -LM (pink) / 50% MCC (yellow). E) 50% α -LM (pink) / 50% PGS (yellow). F) 50% MCC (yellow) / 50% PGS (yellow / bright yellow / pink). The dark blue colour is noise. Position on the compact is given by i) centre, ii) outside. Column 1 is the interpolated (smoothed) map, Column 2 is the discrete map, and Column 3 shows the individual nano-thermal results taken at the crossed points (+) on the discrete map. 194

- Figure 5.9 TTM maps for 3-excipient compacts, with representative colours. A) 49.5% α -LM (pink / purple) / 49.5% PGS (yellow / orange) / 1% MS (blue). B) 49.5% α -LM (pink) / 49.5% MCC (yellow) / 1% MS (blue). C) 49.5% MCC (yellow) / 49.5% PGS (pink / yellow) / 1% MS (blue). D) 33.3% α -LM (purple) / 33.3% PGS (pink / yellow) / 33.3% MCC (yellow). The dark blue colour is noise. Position on the compact is given by i) centre, ii) outside. Column 1 is the interpolated (smoothed) map, Column 2 is the discrete map, and Column 3 shows the individual nano-thermal results taken at the crossed points (+) on the discrete map. 196
- Figure 5.10 TTM maps for 4-excipient compacts, with representative colours. A) 33% α -LM (pink / purple) / 33% PGS (yellow / orange) / 33% MCC (yellow / orange) / 1% MS (blue). B) 25% α -LM (pink / purple) / 25% PGS (yellow / orange) / 25% MCC (orange) / 25% MS (blue). The dark blue colour is noise. Position on the compact is given by i) centre, ii) outside. Column 1 is the interpolated (smoothed) map, Column 2 is the discrete map, and Column 3 shows the individual nano-thermal results taken at the crossed points (+) on the discrete map. 198
- Figure 5.11 AFM images of the 2-component compacts based on caffeine, using a nano probe. A) 99% CAF / 1% MS. B) 50% CAF / 50% α -LM. C) 50% CAF / 50% MCC. D) 50% CAF / 50% PGS. Position on the compact is given by i) centre, ii) outside. Column 1 - height, Column 2 - deflection. 202
- Figure 5.12 AFM images of the 3-component compacts based on caffeine, using a nano probe. A) 49.5% CAF / 49.5% α -LM / 1% MS. B) 49.5% CAF / 49.5% MCC / 1% MS. C) 49.5% CAF / 49.5% PGS / 1% MS. D) 33.3% CAF / 33.3% α -LM / 33.3% PGS. E) 33.3% CAF / 33.3% α -LM / 33.3% MCC. F) 33.3% CAF / 33.3% MCC / 33.3% PGS. Position on the compact is given by i) centre, ii) outside. Column 1 - height, Column 2 - deflection. 202

- Figure 5.13 AFM images of the 4-component compacts based on caffeine, using a nano probe. A) 33% CAF / 33% α -LM / 33% MCC / 1% MS. B) 33% CAF / 33% MCC / 33% PGS / 1% MS. C) 33% CAF / 33% α -LM / 33% PGS / 1% MS. D) 25% CAF / 25% α -LM / 25% PGS / 25% MCC. Position on the compact is given by i) centre, ii) outside. Column 1 - height, Column 2 - deflection. 203
- Figure 5.14 AFM images of the 5-component compacts based on caffeine, using a nano probe. A) 24.75% CAF / 24.75% α -LM / 24.75% MCC / 24.75% PGS / 1% MS. B) 20% CAF / 20% α -LM / 20% MCC / 20% PGS / 20% MS. Position on the compact is given by i) centre, ii) outside. Column 1 - height, Column 2 - deflection. 204
- Figure 5.15 Nano-TA results for the 2-component compacts based on caffeine, using a nano probe. A) 99% CAF / 1% MS. B) 50% CAF / 50% α -LM. C) 50% CAF / 50% MCC. D) 50% CAF / 50% PGS. Position on the compact is given by i) centre, ii) outside. Five readings were taken at each position: dark blue - site 1, red - site 2, green - site 3, purple - site 4, light blue - site 5. 206
- Figure 5.16 Nano-TA results for the 3-component compacts based on caffeine, using a nano probe. A) 49.5% CAF / 49.5% α -LM / 1% MS. B) 49.5% CAF / 49.5% MCC / 1% MS. C) 49.5% CAF / 49.5% PGS / 1% MS. D) 33.3% CAF / 33.3% α -LM / 33.3% PGS. E) 33.3% CAF / 33.3% α -LM / 33.3% MCC. F) 33.3% CAF / 33.3% MCC / 33.3% PGS. Position on the compact is given by i) centre, ii) outside. Five readings were taken at each position: dark blue - site 1, red - site 2, green - site 3, purple - site 4, light blue -site 5. 208
- Figure 5.17 Nano-TA results for the 4-component compacts based on caffeine, using a nano probe. A) 33% CAF / 33% α -LM / 33% MCC / 1% MS. B) 33% CAF / 33% MCC / 33% PGS / 1% MS. C) 33% CAF / 33% α -LM / 33% PGS / 1% MS. D) 25% CAF / 25% α -LM / 25% PGS / 25% MCC. Position on the compact is given by i) centre, ii) outside. Five readings were taken at each position:

- dark blue - site 1, red - site 2, green - site 3, purple - site 4, light blue - site 5. 210
- Figure 5.18 Nano-TA results for the 5-component compacts based on caffeine, using a nano probe. A) 24.75% CAF / 24.75% α -LM / 24.75% MCC / 24.75% PGS / 1% MS. B) 20% CAF / 20% α -LM / 20% MCC / 20% PGS / 20% MS. Position on the compact is given by i) centre, ii) outside. Five readings were taken at each position: dark blue - site 1, red - site 2, green - site 3, purple - site 4, light blue - site 5. 212
- Figure 5.19 TTM maps for 2-component compacts based on caffeine, with representative colours. A) 99% CAF (blue / pink / purple) / 1% MS (not detected). B) 50% CAF (blue, pink / purple) / 50% α -LMH (pink). C) 50% CAF (blue / pink / purple) / 50% MCC (yellow). D) 50% CAF (blue / pink / purple) / 50% PGS (yellow). Position on the compact is given by i) centre, ii) outside. Column 1 is the interpolated (smoothed) map, Column 2 is the discrete map, and Column 3 shows the individual nano-thermal results taken at the crossed points (+) on the discrete map. 215
- Figure 5.20 TTM maps for 3-component compacts based on caffeine, with representative colours. A) 49.5% CAF (blue) / 49.5% α -LM (pink / yellow) / 1% MS (not detected). B) 49.5% CAF (blue) / 49.5% MCC (yellow) / 1% MS (purple). C) 49.5% CAF (blue) / 49.5% PGS (yellow / pink) / 1% MS (not detected). D) 33.3% CAF (blue) / 33.3% α -LM (pink) / 33.3% PGS (yellow). E) 33.3% CAF (blue / purple) / 33.3% α -LM (pink) / 33.3% MCC (yellow). F) 33.3% CAF (blue) / 33.3% MCC (yellow) / 33.3% PGS (yellow / pink). Position on the compact is given by i) centre, ii) outside. Column 1 is the interpolated (smoothed) map, Column 2 is the discrete map, and Column 3 shows the individual nano-thermal results taken at the crossed points (+) on the discrete map. 216

- Figure 5.21 TTM maps for 4-component compacts based on caffeine, with representative colours. A) 33% CAF (blue) / 33% α -LM (pink) / 33% MCC (yellow) / 1% MS (purple). B) 33% CAF (blue / purple) / 33% MCC (yellow) / 33% PGS (yellow / pink) / 1% MS (not detected). C) 33% CAF (blue) / 33% α -LM (pink / purple) / 33% PGS (yellow) / 1% MS (not detected). D) 25% CAF (blue) / 25% α -LM (pink) / 25% PGS (yellow) / 25% MCC (yellow). Position on the compact is given by i) centre, ii) outside. Column 1 is the interpolated (smoothed) map, Column 2 is the discrete map, and Column 3 shows the individual nano-thermal results taken at the crossed points (+) on the discrete map. 219
- Figure 5.22 TTM maps for 5-component compacts based on caffeine, with representative colours. A) 24.75% CAF (blue) / 24.75% α -LM (pink) / 24.75% MCC (yellow) / 24.75% PGS (yellow) / 1% MS (purple). B) 20% CAF (blue) / 20% α -LM (pink) / 20% MCC (yellow) / 20% PGS (yellow) / 20% MS (purple). Position on the compact is given by i) centre, ii) outside. Column 1 is the interpolated (smoothed) map, Column 2 is the discrete map, and Column 3 shows the individual nano-thermal results taken at the crossed points (+) on the discrete map. 220
- Figure 5.23 AFM images of the 2-component compacts based on ibuprofen, using a nano probe. A) 99% IBU / 1% MS. B) 50% IBU / 50% α -LM. C) 50% IBU / 50% MCC. D) 50% IBU / 50% PGS. Position on the compact is given by i) centre, ii) outside. Column 1 - height, Column 2 - deflection. 222
- Figure 5.24 AFM images of the 3-component compacts based on ibuprofen, using a nano probe. A) 49.5% IBU / 49.5% α -LM / 1% MS. B) 49.5% IBU / 49.5% MCC / 1% MS. C) 49.5% IBU / 49.5% PGS / 1% MS. D) 33.3% IBU / 33.3% α -LM / 33.3% PGS. E) 33.3% IBU / 33.3% α -LM / 33.3% MCC. F) 33.3% IBU / 33.3% MCC / 33.3% PGS. Position on the compact is given by i) centre, ii) outside. Column 1 - height, Column 2 - deflection. 223

- Figure 5.25 AFM images of the 4-component compacts based on ibuprofen, using a nano probe. A) 33% IBU / 33% α -LM / 33% MCC / 1% MS. B) 33% IBU / 33% MCC / 33% PGS / 1% MS. C) 33% IBU / 33% α -LM / 33% PGS / 1% MS. D) 25% IBU / 25% α -LM / 25% PGS / 25% MCC. Position on the compact is given by i) centre, ii) outside. Column 1 - height, Column 2 - deflection. 224
- Figure 5.26 AFM images of the 5-component compacts based on ibuprofen, using a nano probe. A) 24.75% IBU / 24.75% α -LM / 24.75% MCC / 24.75% PGS / 1% MS. B) 20% IBU / 20% α -LM / 20% MCC / 20% PGS / 20% MS. Position on the compact is given by i) centre, ii) outside. Column 1 - height, Column 2 - deflection. 225
- Figure 5.27 Nano-TA results for the 2-component compacts based on ibuprofen, using a nano probe. A) 99% IBU / 1% MS. B) 50% IBU / 50% α -LM. C) 50% IBU / 50% MCC. D) 50% IBU / 50% PGS. Position on the compact is given by i) centre, ii) outside. Five readings were taken at each position: dark blue - site 1, red - site 2, green - site 3, purple - site 4, light blue - site 5. 227
- Figure 5.28 Nano-TA results for the 3-component compacts based on caffeine, using a nano probe. A) 49.5% IBU/ 49.5% α -LM / 1% MS. B) 49.5% IBU/ 49.5% MCC / 1% MS. C) 49.5% IBU/ 49.5% PGS / 1% MS. D) 33.3% IBU/ 33.3% α -LM / 33.3% PGS. E) 33.3% IBU/ 33.3% α -LM / 33.3% MCC. F) 33.3% IBU/ 33.3% MCC / 33.3% PGS. Position on the compact is given by i) centre, ii) outside. Five readings were taken at each position: dark blue - site 1, red - site 2, green - site 3, purple - site 4, light blue - site 5. 229
- Figure 5.29 Nano-TA results for the 4-component compacts based on ibuprofen, using a nano probe. A) 33% IBU / 33% α -LM / 33% MCC / 1% MS. B) 33% IBU / 33% MCC / 33% PGS / 1% MS. C) 33% IBU / 33% α -LM / 33% PGS / 1% MS. D) 25% IBU / 25% α -LM / 25% PGS / 25% MCC. Position on the compact is given by i) centre, ii) outside. Five readings were taken at each

- position: dark blue - site 1, red - site 2, green - site 3, purple – site 4, light blue - site 5. 231
- Figure 5.30 Nano-TA results for the 5-component compacts based on ibuprofen, using a nano probe. A) 24.75% IBU / 24.75% α -LM / 24.75% MCC / 24.75% PGS / 1% MS. B) 20% IBU / 20% α -LM / 20% MCC / 20% PGS / 20% MS. Position on the compact is given by i) centre, ii) outside. Five readings were taken at each position: dark blue - site 1, red - site 2, green - site 3, purple - site 4, light blue - site 5. 233
- Figure 5.31 TTM maps for 2-component compacts based on ibuprofen, with representative colours. A) 99% IBU (blue) / 1% MS (not detected). B) 50% IBU (blue) / 50% α -LMH (yellow / pink). C) 50% IBU (blue) / 50% MCC (yellow / pink). D) 50% IBU (blue) / 50% PGS (yellow / pink). Position on the compact is given by i) centre, ii) outside. Column 1 is the interpolated (smoothed) map, Column 2 is the discrete map, and Column 3 shows the individual nano-thermal results taken at the crossed points (+) on the discrete map. 236
- Figure 5.32 TTM maps for 3-component compacts based on ibuprofen, with representative colours. A) 49.5% IBU (blue) / 49.5% α -LM (pink / orange) / 1% MS (purple). B) 49.5% IBU (blue) / 49.5% MCC (yellow) / 1% MS (not detected). C) 49.5% IBU (blue) / 49.5% PGS (yellow) / 1% MS (purple). D) 33.3% IBU (blue) / 33.3% α -LM (pink) / 33.3% PGS (yellow). E) 33.3% IBU (blue) / 33.3% α -LM (pink) / 33.3% MCC (yellow). F) 33.3% IBU (blue) / 33.3% MCC (yellow) / 33.3% PGS (yellow). Position on the compact is given by i) centre, ii) outside. Column 1 is the interpolated (smoothed) map, Column 2 is the discrete map, and Column 3 shows the individual nano-thermal results taken at the crossed points (+) on the discrete map. 237
- Figure 5.33 TTM maps for 4-component compacts based on ibuprofen, with representative colours. A) 33% IBU (blue) / 33% α -LM (pink) /

- 33% MCC (yellow) / 1% MS (purple). B) 33% IBU (blue) / 33% MCC (yellow) / 33% PGS (yellow) / 1% MS (purple). C) 33% IBU (blue) / 33% α -LM (pink) / 33% PGS (yellow) / 1% MS (purple). D) 25% IBU (blue) / 25% α -LM (pink) / 25% PGS (yellow) / 25% MCC (yellow). Position on the compact is given by i) centre, ii) outside. Column 1 is the interpolated (smoothed) map, Column 2 is the discrete map, and Column 3 shows the individual nano-thermal results taken at the crossed points (+) on the discrete map. 240
- Figure 5.34 TTM maps for 5-component compacts based on ibuprofen, with representative colours. A) 24.75% IBU (blue) / 24.75% α -LM (pink) / 24.75% MCC (yellow) / 24.75% PGS (yellow) / 1% MS (purple). B) 20% IBU (blue) / 20% α -LM (pink) / 20% MCC (yellow) / 20% PGS (yellow) / 20% MS (purple). Position on the compact is given by i) centre, ii) outside. Column 1 is the interpolated (smoothed) map, Column 2 is the discrete map, and Column 3 shows the individual nano-thermal results taken at the crossed points (+) on the discrete map. 241
- Figure 6.1 SEM images of powders and granules. A) Powder mix for the direct compression batch, magnification X250. B) Wet granulated granules, magnification X250. C) Wet granulated granules, magnification X90. 250
- Figure 6.2 A typical example of the force exerted by the upper punch during a compression cycle for a mini-tablet. 254
- Figure 6.3 The compression loading profile for an example of the wet granulated tablets (red) and the direct compression tablets (blue). 256
- Figure 6.4 The optical microscopy image (magnification X10) of the development mini-tablets batches. A) Wet granulated mini-tablets. B) Direct compression mini-tablets. 257

	Page
Figure 6.5	DSC spectra for the development batches. A) Wet granulated mini-tablets (red), wet granulated granules (blue). B) Direct compression mini-tablets (green), direct compression mixed powders (pink). 260
Figure 6.6	The optical microscopy image (magnification X10) of the experimental mini-tablets batches. A) Excipient-only mini-tablets. B) Ibuprofen-loaded. C) Caffeine-loaded mini-tablets. 266
Figure 6.7	The compression loading profile for an example of the excipients-only mini-tablets (blue), ibuprofen-loaded mini-tablets (green) and caffeine-loaded mini-tablets (red). 267
Figure 6.8	DSC spectra for the experimental batches. A) Excipient-only granules (blue) and mini-tablets (red). B) Ibuprofen-loaded granules (blue) and mini-tablets (red). C) Caffeine-loaded granules (blue) and mini-tablets (red). 268
Figure 6.9	SEM images of the development batches of mini-tablets. A) Direct compression batch. B) Wet granulated batch. i) Magnification X100. ii) Magnification X250. 274
Figure 6.10	AFM scan of the development batches of mini-tablets using a nano probe. A) Direct compression batch. B) Wet granulated batch. Column 1 - height, Column 2 - deflection. Position on the radius of the compact is given by i) centre and ii) outside. 275
Figure 6.11	Nano-TA results of the development batches of mini-tablets using a nano probe. A) Direct compression mini-tablets. B) Wet granulated mini-tablets. Position on the radius of the compact is given by i) centre and ii) outside. Five nano-TA readings were taken at each position: dark blue - site 1, red - site 2, green - site 3, purple - site 4, light blue - site 5. 277
Figure 6.12:	TTM maps for the development batches of mini-tablets. A) Direct compression mini-tablets. B) Wet granulated mini-tablets. Position on the radius of the compact is given by i) centre and ii)

outside. Column 1 is the interpolated (smoothed) map, Column 2 is the discrete map, and Column 3 shows the individual nano-thermal results taken at the crossed points (+) on the discrete map. The colours represent the components: MCC (orange), PGS (orange/yellow), α -LM (pink/yellow), MS (blue/purple); the dark blue colour is noise.

279

Figure 6.13: AFM scan of the experimental batches of mini-tablets using a nano probe. A) Excipients-only batch. B) Ibuprofen-loaded batch. C) Caffeine-loaded batch. Column 1 - height, Column 2 - deflection. Position on the radius of the compact is given by i) centre and ii) outside.

281

Figure 6.14 Nano-TA results of the experimental batches of mini-tablets using a nano probe. A) Excipients-only batch. B) Ibuprofen-loaded batch C) Caffeine-loaded batch. Position on the radius of the compact is given by i) centre and ii) outside. Five nano-TA readings were taken at each position: dark blue - site 1, red - site 2, green - site 3, purple - site 4, light blue - site 5.

283

Figure 6.15 TTM maps for the experimental batches of mini-tablets. A) Excipients-only batch. B) Caffeine-loaded batch. C) Ibuprofen-loaded batch. Column 1 is the interpolated (smoothed) map, Column 2 is the discrete map, and Column 3 shows the individual nano-thermal results taken at the crossed points (+) on the discrete map. The colours represent the components: MCC (orange), PGS (orange/yellow), α -LM (pink/purple), MS (light blue), Ibuprofen (blue), Caffeine (pink/blue); the dark blue colour is noise.

286

Figure 6.16 Detailed TTM maps for the experimental batches of mini-tablets. A) Excipients-only batch. B) Caffeine-loaded batch. C) Ibuprofen-loaded batch. Column 1 is the interpolated (smoothed) map, Column 2 is the discrete map, and Column 3 shows the individual nano-thermal results taken at the crossed points (+) on the discrete map. The colours represent the components: MCC (orange),

- PGS (orange/yellow), α -LM (pink/purple), MS (light blue), Ibuprofen (blue), Caffeine (pink/blue); the dark blue colour is noise. 287
- Figure 6.17 A TTM map of a mini-tablet where the probe has not made contact with the surface (column 1) and the individual nano-TA traces generated for the whole area (column 2). 289
- Figure 6.18 The TTM map of an excipient-only mini-tablet shown in Figure 6.16 A (column 1) and the individual nano-TA traces for the blue (noise) squares (column 2). 290
- Figure 6.19 The corrected detailed TTM maps for the experimental batches of mini-tablets. A) Excipients-only batch. B) Caffeine-loaded batch. C) Ibuprofen-loaded batch. The colours represent the components: MCC (orange), PGS (orange/yellow), α -LM (pink/purple), MS (light blue), Ibuprofen (blue), Caffeine (pink/blue). 291
- Figure 7.1 The reference Raman spectra for the finger print region for the excipients used in the formulation. α -LM (red), MCC (green), MS (blue) and PGS (pink). 297
- Figure 7.2 The raw Raman spectral data (the "global spectrum") for the multi-excipient compact (25 %w/w each of α -LM, MCC, PGS and MS). 298
- Figure 7.3 Examples of the analysis of the individual spectra and assignment of components. The test sample is the multi-excipient compact (25 %w/w each of α -LM, MCC, PGS and MS). For each location (A to D), the sample spectrum is dark blue and the reference spectrum is the alternate colour. A) α -LM (red). B) MCC (green). C) MS (green). D) PGS (pink). 300
- Figure 7.4 An example of the data processing and map generation. The test sample is the multi-excipient compact (25 %w/w each of α -LM, MCC, PGS and MS). A) The processed multi-component map.

- B) The processed maps of the individual components. The components are shown in the colours allocated in Figure 7.1: α -LM (red), MCC (green), MS (light blue), PGS (pink). 302
- Figure 7.5 The The multi-component map from Figure 7.4 of the multi-excipient compact (25 %w/w each of α -LM, MCC, PGS and MS). A) The "unknown" areas are highlighted. B) The assigned spectra for "unknown brown". C) The assigned spectra for "unknown orange". For each location (B and C), the sample spectrum is dark blue and the reference spectra are as follows: α -LM - red, MCC - bright green, MS - dark green, PGS - pink. 303
- Figure 7.6 An example of the Raman microspectroscopy results for the direct compression mini-tablet development batch. A) The global spectrum of the scanned area. B) The processed multi-component map. C) The processed maps of the individual components. The components are shown in the following colours: α -LM - red, MCC -green, MS - blue, PGS - pink. 305
- Figure 7.7 An example of the Raman microspectroscopy results for the wet granulated mini-tablet development batch. A) The global spectrum of the scanned area. B) The processed multi-component map. C) The processed maps of the individual components. The components are shown in the following colours: α -LM - red, MCC -green, MS - blue, PGS - pink. 306
- Figure 7.8 An example of the Raman microspectroscopy results for the excipient-only experimental batch of mini-tablets. A) The global spectrum of the scanned area. B) The processed multi-component map. C) The processed maps of the individual components. The components are shown in the following colours: α -LM - red, MCC -green, MS - blue, PGS - pink. 308

- Figure 7.9 An example of the high resolution Raman microspectroscopy results for the excipient-only experimental batch of mini-tablets. A) The global spectrum of the scanned area. B) The processed multi-component map. C) The processed maps of the individual components. The components are shown in the following colours: α -LM - red, MCC -green, MS - blue, PGS - pink. 309
- Figure 7.10 The reference Raman spectra for the excipients used in the formulation and caffeine. α -LM (red), MCC (green), MS (dark blue), PGS (pink) and caffeine (pale blue). 310
- Figure 7.11 A sample spectrum of a caffeine-rich region on a caffeine-loaded compact. The sample spectrum is dark blue, caffeine's reference spectrum is pale blue and PGS is show in pink. 311
- Figure 7.12 An example of the Raman microspectroscopy results for the caffeine-loaded experimental batch of mini-tablets. A) The global spectrum of the scanned area. B) The processed multi-component map. C) The processed maps of the individual components. The components are shown in the following colours: α -LM - red, MCC -green, MS - blue, PGS - pink, caffeine - pale blue. 312
- Figure 7.13 An example of the high resolution Raman microspectroscopy results for the caffeine-loaded experimental batch of mini-tablets. A) The global spectrum of the scanned area. B) The processed multi-component map. C) The processed maps of the individual components. The components are shown in the following colours: α -LM - red, MCC -green, MS - blue, PGS - pink, caffeine - pale blue. 313

- Figure 7.14 The reference Raman spectra for the excipients used in the formulation and ibuprofen. α -LM (dark blue), MCC (red), MS (green), PGS (light blue) and IBU (pink). 314
- Figure 7.15 A sample spectrum of an ibuprofen-rich region on an ibuprofen-loaded compact. The sample spectrum is dark blue, ibuprofen's reference spectrum is pink, α -LM is shown in blue, MCC is shown in red, MS is shown in green and PGS is shown in pale blue. 315
- Figure 7.16 An example of the Raman microspectroscopy results for the ibuprofen-loaded experimental batch of mini-tablets. A) The global spectrum of the scanned area. B) The processed multi-component map. C) The processed maps of the individual components. The components are shown in the following colours: α -LM (blue), MCC (red), MS (green), PGS (light blue) and ibuprofen (pink). 316
- Figure 7.17 An example of the high resolution Raman microspectroscopy results for the ibuprofen-loaded experimental batch of mini-tablets. A) The global spectrum of the scanned area. B) The processed multi-component map. C) The processed maps of the individual components. The components are shown in the following colours: α -LM (blue), MCC (red), MS (green), PGS (light blue) and ibuprofen (pink). 317
- Figure 7.18 The raw results for a high resolution scan of a wet granulated mini-tablet (100 μ m x 100 μ m area and readings taken every 2 μ m). 319
- Figure 8.1 A summary of the micro-TA profile of the excipients (α -LM, MCC, PGS, MS and PVP) and drugs (caffeine and ibuprofen) used in this study. 325

- Figure 8.2 A summary of the nano-TA profile of the excipients (α -LM, MCC, PGS and MS) and drugs (caffeine and ibuprofen) used in this study. 326
- Figure 8.3 An example of the thermal colour banding which would be ideal for this study. 335
- Figure 8.4 TTM maps for a compact of 50:50 %w/w MCC and α -LM compact. A) The maps generated automatically by the instrument software. B) The maps generated by manual processing. Column 1 is the discrete map and Column 2 is the interpolated (smoothed) map. The colours represent the components: MCC (orange), α -LM (pink); the blue colour is noise. 337

List of tables

		Page
Table 1.1	The geometry of the tablets in figure 1.1, with calculations surface area, volume and surface area: volume ratio.	15
Table 2.1	Details of the additional drugs used for the micro-TA and nano-TA investigations	47
Table 2.2	The wet granulation process used here	59
Table 2.3	The instrument parameters for testing the hardness of the mini-tablets	62
Table 4.1	Summary of results obtained by DSC, micro-TA and nano-TA (heating rate 25°C/second). Two DSC temperatures means two thermal events were detected: a probable polymorphic transition and melting. The * indicates that the measured temperature changes with heating rate. Line = minimum (V shape) was not recorded.	176
Table 4.2	Summary of results obtained by DSC, micro-TA and nano-TA (heating rates 10 and 25°C/second). Two DSC temperatures means two thermal events were detected: a probable polymorphic transition and melting. The * indicates that the measured temperature changes with heating rate. Line = minimum (V-shape) was not recorded.	177
Table 5.1:	A summary of the most probable components identified from the nano-TA scans of the 2-excipient compacts shown in Figure 5.5. The number indicates the number of scans assigned to a particular component. X indicates that this component is not present in the compact.	189
Table 5.2	A summary of the most probable components identified from the nano-TA scans of the 3-excipient compacts shown in Figure 5.6.	

	The number indicates the number of scans assigned to a particular component. X indicates that this component is not present in the compact.	191
Table 5.3	A summary of the most probable components identified from the nano-TA scans of the 4-exipient compacts shown in Figure 5.7. The number indicates the number of scans assigned to a particular component. X indicates that this component is not present in the compact.	192
Table 5.4	A summary of the most probable components identified from the nano-TA scans of the 2-component compacts based on caffeine shown in Figure 5.15. The number indicates the number of scans assigned to a particular component. X indicates that this component is not present in the compact.	207
Table 5.5	A summary of the most probable components identified from the nano-TA scans of the 3-component compacts based on caffeine shown in Figure 5.16. The number indicates the number of scans assigned to a particular component. X indicates that this component is not present in the compact.	210
Table 5.6	A summary of the most probable components identified from the nano-TA scans of the 4-component compacts based on caffeine shown in Figure 5.17. The number indicates the number of scans assigned to a particular component. X indicates that this component is not present in the compact.	212
Table 5.7	A summary of the most probable components identified from the nano-TA scans of the 5-component compacts based on caffeine shown in Figure 5.18. The number indicates the number of scans assigned to a particular component. X indicates that this component is not present in the compact.	213

Table 5.8	A summary of the most probable components identified from the nano-TA scans of the 2-component compacts based on ibuprofen shown in Figure 5.27. The number indicates the number of scans assigned to a particular component. X indicates that this component is not present in the compact.	228
Table 5.9	A summary of the most probable components identified from the nano-TA scans of the 3-component compacts based on ibuprofen shown in Figure 5.28. The number indicates the number of scans assigned to a particular component. X indicates that this component is not present in the compact.	231
Table 5.10	A summary of the most probable components identified from the nano-TA scans of the 4-component compacts based on ibuprofen shown in Figure 5.29. The number indicates the number of scans assigned to a particular component. X indicates that this component is not present in the compact.	233
Table 5.11	A summary of the most probable components identified from the nano-TA scans of the 5-component compacts based on ibuprofen shown in Figure 5.30. The number indicates the number of scans assigned to a particular component. X indicates that this component is not present in the compact.	234
Table 6.1:	Formulation of the mini-tablets	248
Table 6.2	The weight and crushing strength results for the development batches (SD = standard deviation; RSD = relative standard deviation).	256
Table 6.3	The thickness results for the development batches (SD = standard deviation; RSD = relative standard deviation).	258
Table 6.4	The friability results for the development batches.	259

		Page
Table 6.5	The weight, thickness and crushing strength results and the calculated tensile strength for the excipients-only experimental mini-tablet batch (SD = standard deviation; RSD = relative standard deviation).	264
Table 6.6	The weight, thickness and crushing strength results and the calculated tensile strength for the ibuprofen-loaded experimental mini-tablet batch (SD = standard deviation; RSD = relative standard deviation).	264
Table 6.7	The weight, thickness and crushing strength results and the calculated tensile strength for the caffeineloaded experimental mini-tablet batch (SD = standard deviation; RSD = relative standard deviation).	265
Table 6.8	The friability results for the experimental batches, using both methods (50 mini-tablets and 6.5 g of mini-tablets).	268
Table 6.9	Analytical data for the ibuprofen standard solutions. Diluent used = 0.1 M NaOH, $\lambda = 224$ nm.	272
Table 6.10	The content uniformity results for the ibuprofen-loaded mini- tablets.	272
Table 6.11	Analytical data for the caffeine standard solutions. Diluent used = 0.1 M HCl, $\lambda = 272$ nm.	273
Table 6.12	The content uniformity results for the ibuprofen-loaded mini- tablets.	273
Table 6.13	A summary of the most probable components identified from the nano-TA scans of the development batches of mini-tablets shown in Figure 6.11. The number indicates the number of scans assigned to a particular component.	278

Table 6.14	A summary of the most probable components identified from the nano-TA scans of the experimental batches of mini-tablets shown in Figure 6.14. The number indicates the number of scans assigned to a particular component. X indicates that this component is not present in the mini-tablet.	284
Table 7.1	The Raman shift value and bond assignment of the representative peak used in the modelling.	297
Table 7.2	Calculation of the % components in the scans shown in Figure 7.2	299
Table 8.1	A summary of the advantages and disadvantages of AFM.	342
Table 8.2	A summary of the advantages and disadvantages of micro/nano TA	343
Table 8.3	A summary of the advantages and disadvantages of TTM.	344

List of equations and calculations

		Page
Equation 1.1	The wavenumber of the absorbed light in FT-IR.	19
Equation 1.2	Reduced mass of the bond (FT-IR).	19
Equation 1.3	Heat flow rate for a heat flux DSC.	21
Equation 1.4	Hooke's law.	24
Calculation 6.1	Pressure used to prepare the compacts used in previous chapters.	251
Calculation 6.2	Pressure used to prepare the mini-tablets.	251
Calculation 6.3	The tensile strength calculation using the standard tensile strength equation.	263
Calculation 6.4	The tensile strength calculation using the Pitt equation.	263

Chapter 1
Introduction

CHAPTER 1

Introduction

1.1 Tablets

Tablets are solid oral dosage forms, prepared by the compression of powders into a solid mass. Although the general public often refer to all solid oral preparations as "pills", this is technically wrong, as pills are based on a wet massing and rolling technique, rather than powder compression used in tablet manufacture. Tablets can be designed to be "immediate release", whereby the drug is released from the tablet within a few minutes of swallowing, or "modified release", where the drug is released at a specific site in the gastro-intestinal tract or in a controlled, continuous fashion. For ease of manipulation most tablets are greater than 200 mg in weight and have a diameter of 7 mm or more (assuming a round shape) but there is an upper limit of about 1 g weight, above which patients perceive difficulties in swallowing. This may lead to issues with patient compliance. For example, Overgaard et al (2001) found that in Norway every one in three women and every one in six men reported trouble in swallowing tablets.

1.2 Mini-tablets

1.2.1. Oral use - general

Recently, mini-tablets have received interest as a potential oral dosage form for paediatric and geriatric patients (Thomson et al (2009)). There is no official definition of the size of a mini-tablet, but it is generally accepted that mini-tablets are round and have a diameter in the order of 2 to 5 mm (Lennartz and Mielck (1998)). The weight of a mini-tablet is generally between 8 and 60 mg, depending on the size of the mini-tablet. A mini-tablet held by a pair of tweezers is shown in Figure 1.1.

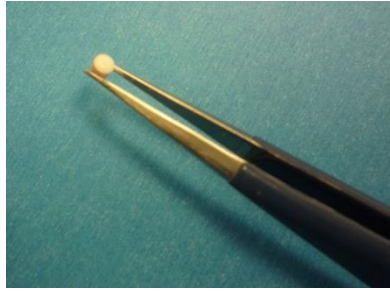


Figure 1.1: A mini-tablet held by a pair of tweezers.

This interest in the use of mini-tablets followed an EU regulation that encourages development and clinical research for products specifically intended for paediatric patients. The World Health Organisation (WHO) also ran a campaign to encourage development in this field (Spooner et al (2012)). Historically, there have been very few drugs and / or formulations which were designed specifically for children (Succliffe (1999)). One particular problem with paediatric clinical research is recruiting subjects into trials. Parents want age appropriate medication designed for children but are reluctant to allow their own children to be enrolled on a trial (Succliffe (1999)).

Ernest et al (2007) state "There is a clear need for paediatric medicine". They reminded readers that children are not small adults, they have different pharmacokinetic and pharmacodynamic profiles to adults and also that children are not a homogeneous patient group with varying dose requirements for different age groups. For example, the dose difference between a six month old baby and a ten year old child is sizeable. Recent studies have found that it is a common procedure in UK hospitals to manipulate dosage forms to achieve the correct doses for babies and children (Nunn et al (2013)). However, dosage form manipulation has the potential for calculation errors, which may result in the plasma drug levels not falling within the required therapeutic window, by either overdosing or under dosing (Nunn et al (2013)).

At present oral solutions tend to be prescribed to children aged between 0 and 6 years old (Schrim et al (2003)). They are easy to administer, easily absorbed by the body to give a fast response (there is no dissolution / disintegration stage as with tablets or capsules) and the dose can be easily varied by varying the dosing volume. However, even given these advantages of oral liquids, the WHO encourage the development of a solid dosage form for

children. There are several reasons for this. Compared to liquids, solid dosage forms show an improved reproducibility of dosing. It is possible to control the rate of drug release from solid dosage forms using a range of mechanisms, which is not possible with liquids. Transportation is easier and solid dosage forms are less bulky than liquids. Solid dosage forms generally have better physical, chemical and microbial stability than liquids. Finally, there is an issue of taste in liquid dosage forms (most drugs are bitter), which has the potential to reduce patient compliance. All dosage forms need child-friendly excipients whether for a liquid dosage form (e.g. preservatives, sweeteners or flavours) or solid dosage forms (e.g. binders, diluents or lubricants).

A principal concern of the European Medicines Agency (EMA) and the Committee for Medicinal Products for Human Use (CHMP) was the acceptability of a solid dosage form for children. Those younger than six years old may have difficulties swallowing large solid dosage forms and children under two years old should be given only powders, multiparticulates and orodispersibles to avoid choking. Nunn and Williams (2005) found that it was perceived to be safe for children of school age or above to take tablets without the risk of inhalation or choking, but not younger children. However, they concluded that there was no evidence for the perceived risk and that children as young as three years old could swallow a full size tablet.

One possible solution to these issues is to use mini-tablets in paediatric patients. As they are a solid unit-dose formulation, mini-tablets should give more accurate and reproducible dosing than liquids. As these are smaller than conventionally sized tablets, they should be easier to swallow, which will be an advantage for those patients at risk of choking, such as small children and dysphagic patients. However, EMA was concerned about the possible risk of inhalation of small solid particles such as mini-tablets. Spooner et al (2012) found that most children could swallow and accepted 2 mm diameter mini-tablets equally or better than liquid dosage forms and Thompson et al (2010) also found that mini-tablets were well tolerated.

Mini-tablets can be encapsulated in an ordinary gelatin capsule shell to provide containment and dose control, and then sprinkled over soft food, such as yoghurt, for administration. Dose control is maintained simply by varying the number of mini-tablets contained within each capsule. Encapsulation also allows the possibility of mixed dosing, i.e. a capsule may contain two populations of mini-tablets, each with a different drug, or

the same drug with a different release profile. Although not specifically (or only) for children, this simpler dosage regimen can then lead to improved patient compliance and steadier blood levels (Goole et al (2007)) and in the future may allow more individualised medication profiles.

1.2.2 Oral use - controlled-release and targetted-release

Mini-tablets may also be developed as controlled-release systems. For example, De Brabander et al (2000a and 2000b) developed a mini-tablet formulation based on a hydrophobic microcrystalline wax with a hydrophilic starch derivative. The drug release profile was due in part to the starch swelling and in part due to drug diffusion through and erosion of the mini-tablet matrix. The authors found that this approach provided a flexible system where the composition could be changed to achieve the desired drug release profile and this could be related to physico-chemical properties of the excipients. For example, the melting point of the wax affected the drug release profile. De Brabander et al (2000b) used ibuprofen as an example drug in their work, as this is both rapidly absorbed and is rapidly excreted, leading to a multiple time per day dosage schedule, so potentially patient compliance should be improved by a sustained release formulation. They showed that better plasma levels could be maintained via the use of these mini-tablets. Similar work has been done by Tomuta and Leucuta (2007) and Mohamed et al (2013) using a hydrophilic polymer (hydroxypropylmethylcellulose) to make matrix mini-tablets for extended released.

"Dose dumping" is a major concern for large monolithic oral controlled-release preparations. This occurs when the drug is released from the dosage form abruptly, rather than in the intended manner. It is generally believed in the literature that this is less of a problem with multi-particulate formulations as they have a larger total surface area for release than a monolithic product, which gives them a more reliable and reproducible release. Additionally, failure of one unit of the multi-particulate formulation will not cause such an immense release of drug as failure of the monolithic formulations, so multiparticulate formulations may be considered to be inherently safer. Multi-particulate preparations will spread out along the digestive tract, unlike monolithic preparations which can only be in one place at one time. The EMA Guidance on Quality of Modified Release Products at present states that "The development of single unit non-disintegrating dosage forms is discouraged since their residence time in the stomach is unpredictable and in

general longer than disintegrating dosage forms with multiple units of pellets" (Podczeck et al (2007)). Mini-tablets contained within a capsule fall into the definition of multi-particulate formulations, so may have a role to play in controlled-release dosing.

Another way to control the drug release from mini-tablets is to coat them. Mini-tablets have several advantages over granules and pellet, such as a more consistent shape and size and therefore a more uniform coat can be achieved with a more reproducible drug release (Munday et al (1994)). The drug release profile of mini-tablets may be manipulated in the same way as larger tablets, but it is also possible to combine multiple mini-tablets of different release profiles into one capsule formulation, allowing a specific overall release profile to be obtained (Ishida et al (2008)) e.g. immediate release mini-tablets and sustained release mini-tablets are administered together in one capsule.

Floating mini-tablets are designed to remain in the stomach for as long as possible. This is advantageous if the drug is locally active in the stomach as the drug will remain at its site of action for longer. If the drug has low solubility in the higher pH regions of the gastrointestinal tract, a narrow absorption window in the upper intestine or a short therapeutic half life (fast elimination), it may be beneficial to prolong the delivery of the drug to the intestine by retaining the dosage form in the stomach and allowing a sustained release of drug. Within the core matrix formulation of these floating tablets is a gas-generating compound, which will produce carbon dioxide upon reaction with the acid conditions of the stomach. The carbon dioxide is then trapped between the core matrix formulation and the insoluble (but water permeable) film coat, allowing the product to float on the stomach contents (Goole et al (2007) and (Meka et al (2009))). Drug is released at a pre-determined rate from the core formulation due to the swelling of the matrix and diffuses through the film coat into the stomach contents. Floating mini-tablets will have the advantages of multi-particulate formulations compared to monolithic formulations, as discussed above.

The colon is a good target for drug delivery, as it has reasonable exposure to the systemic circulation and a comparatively gentle environment in terms of pH and digestive enzymes. It also has a large bacterial population which release characteristic enzymes (existing almost exclusive in the colon) which can be utilised in developing colonic drug delivery systems. A major challenge in colonic drug targetting is that, after being taken orally, the drug and formulation has to survive the low pH conditions in the stomach, the higher pH conditions found in the intestine and exposure to other digestive enzymes before reaching

its colonic target. Various formulation solutions to the challenge of transit to the colon have been proposed, including some based on mini-tablets. Fernández-Hervás and Fell (1998) designed a system that protected and reduced drug release in the upper intestine by using chitosan and pectin as a coating for mini-tablets. The bacteria in the colon then degraded the coating and released the drug. Park et al (2002) used a similar approach but their mini-tablets were coated with an enteric coating and then a polysaccharide coating. The mini-tablets were designed to remain intact when in the stomach with the enteric coat being removed in the small intestine. Finally, in the colon the bacterial enzymes would remove the polysaccharide coat which then releases the drug. The high total surface area of the multiple mini-tablets composing the dosage form provides a large surface area for attack by the bacterial enzymes and should promote reproducibility of effect.

1.2.3 Ocular administration

Ocular administration of drugs is a challenge. Surface administration of eye drops usually results in poor ocular bioavailability due to the blink reflex, rapid draining and lacrimation. Ocularly-administered mini-tablets make a good alternative dosing strategy, as they are small enough to be inserted into the eye pocket and will be retained there, resulting in prolonged drug delivery. The use of ocular mini-tablets should not only improve patient compliance but also reduce the amount of drug that needs to be given in order to obtain a suitable effect. For example, Saettone et al (1995) designed ophthalmic mini-tablets of 3.5 mm diameter, 1.5 mm height and 13 to 16 mg weight. Mini-tablets can be used as implants when sutured in place, with residence times of a month to a year (Weyenberg et al (2004)). Alternatively, the mini-tablets may be soluble tablets giving drug release for just a few hours. One concern over the use of ocular mini-tablets was whether the tablet would cause irritation and a grainy feeling in the eye pocket as it disintegrated, but this did not seem to be a large issue in studies by Weyenberg et al (2004). Their mini-tablets consisted of matrix drug / polymer system which gave controlled release drug delivery and a bioadhesive holding the mini-tablet in place in the eye socket. Due to the water-absorbing nature of the material, the mini-tablets had to be dry granulated and it was noted that the granulation process and compression process greatly affected the properties and effectiveness of the mini-tablets (Weyenberg et al (2005)).

1.3 Tablet formulation

All tablet formulations are based on the same principles. The most important component is the active ingredient (the drug) and all others must be chemically and physically compatible with the drug (Jivraj et al (2000)). The first excipient to be considered is the diluent, which is added to the formulation to bulk it out so that the final tablet is a suitable size for handling. Typical diluents are α -lactose monohydrate (α -LM) and di-calcium phosphate (DCP), both of which provide mechanical strength to the tablet. The second excipient to be considered is a compression aid such as microcrystalline cellulose (MCC). α -LM and DCP both undergo brittle fracture on compression, which is the basis of the tablet's high mechanical strength, but this high strength can also result in retarded drug dissolution. MCC, on the other hand, undergoes plastic deformation, so the tablets are not as tough, but will allow a faster drug dissolution rate. The relative content of the diluent and the compression aid is adjusted so that a balance is struck between the opposing requirements of mechanical strength and fast dissolution. The compression behaviour of the drug, i.e. does it undergo brittle fracture or plastic deformation, is also taken into account in adjusting the ratio of these two excipients, becoming more significant as the drug loading in the tablet is increased. The third main excipient in a tablet formulation is a disintegrant, the role of which is to aid the fragmentation of the tablet once swallowed into the stomach, providing an increased surface area for drug dissolution. A typical example of a disintegrant is pre-gelatinised starch (PGS), which works by drawing in water from the surroundings (i.e. the stomach), dissolving and swelling, eventually overcoming the forces holding the tablet together and allowing fragmentation to occur. The final excipient in all tablet formulations is a lubricant, such as magnesium stearate (MS). The role of the lubricant is to prevent sticking of the powder components of the tablet formulation to the metal surfaces of the equipment used to manufacture the tablets (Miller and York (1988)). Care must be taken in the levels of the lubricant, which tend to be hydrophobic and can result in impeded tablet disintegration and drug dissolution. Additionally, only a thin layer on the surface of the powder is required, otherwise the contact and binding between the different components during compression is reduced, leading to weaker tablets. Further excipients are added as required. For example, a binder may be used in wet granulation formulations (see below) and stabilisers such as anti-oxidants may be required if the drug is chemically sensitive. The general background to tablet formulation is described comprehensively in Aulton (2007).

1.4 Tablet manufacture

The first stage of tablet manufacture is to prepare the powder mix. Two main techniques are used. "Direct compression" takes its name from the fact that there is no intermediate granulation step and the powders are simply mixed, lubricated and then compressed. Direct compression is a simple and straightforward process and does not require heat or moisture, which reduces stability issues (Grund et al (2014)). However, it depends heavily on the properties of the drug and excipients. The powders must be mixed so that the correct drug distribution is obtained, then the mix must be maintained during the compression process so that the content uniformity of the product is maintained. Mixing is difficult if the materials are non-spherical and segregation is likely if the powders have different particle sizes and shapes, both of which lead to non-uniformity of the product. The excipients used for a direct compression process are spray-dried to make them (roughly) spherical, but the drug is not usually. Very low and very high drug concentrations will be difficult to prepare as direct compression mixtures: low concentrations lead to mixing and segregation issues, and high concentrations lead to potential compression issues.

"Wet granulation" is the other most common technique used. Here, the drug and excipients are mixed to obtain good distribution, then it is granulated by the application of a solution during mixing. During granulation, individual powder particles are combined into larger granules, fixing the pattern of the mixture. The granulation solution is generally an aqueous solution of a binder such as polyvinylpyrrolidone (PVP), with the solvent being removed after the granulation process is complete. Wet granulation will reduce the segregation issues seen with direct compression mixtures (Aulton (2007)), so is especially useful for low dose formulations. The granules formed are roughly spherical, so will flow much better than direct compression formulations, leading to greater reproducibility of the final product. Finally, the presence of the binder, which essentially acts as a glue to hold the granule together, gives added mechanical strength to the tablet, making wet granulated tablets much more suitable to further processing, such as the application of a film coat, than direct compression tablets.

The process of wet granulation is illustrated schematically in Figure 1.2. The dry powders are mixed together to form a homogeneous mix, then granulation fluid is added to bind individual particles together to form a granule. The wet granules are then dried to remove

the granulation solvent, leading the structure of the granule in place, and then milled to remove large particles. Wet milling is not conventionally used.

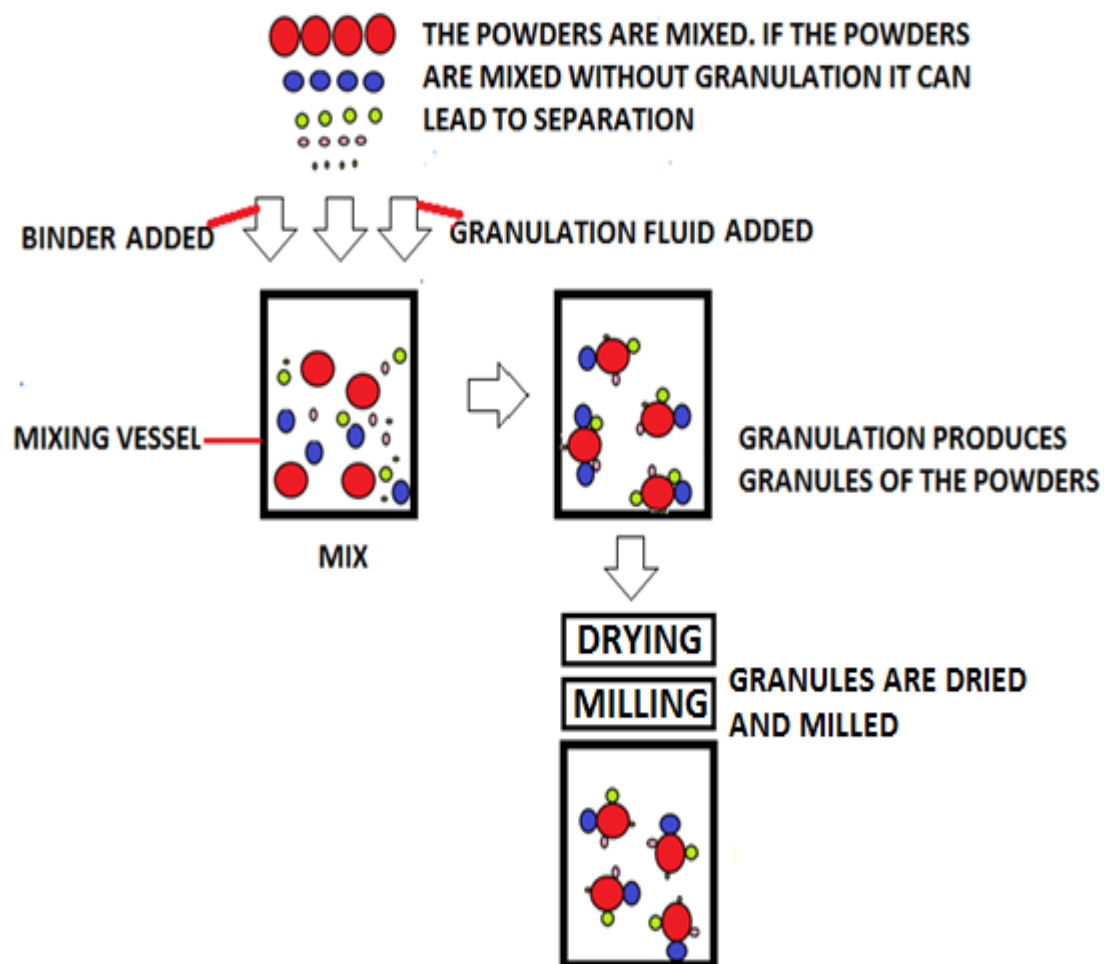


Figure 1.2: Schematic illustration of the wet granulation process.

However, there are some disadvantages of wet granulation, due to the need for a solvent as a processing aid and the removal of the solvent after the process has finished. This makes it less suitable as a preparation method if the drug is water-sensitive or heat-sensitive. Additionally, it is possible for the drug to undergo polymorphic changes or hydrate status changes during this process, so care must be taken to ensure that this has been taken account of. Aulton (2007) provides a detailed introduction to this topic.

The second stage of tablet manufacture is to compress the powder mix or granule into tablets. Tableting (or compression) is the process of turning powder or granules into tablets and is shown diagrammatically in a very simplified form in Figure 1.3. The powder or granules flows from a holding hopper to a feed frame (or feed shoe), from where it is dispensed into a die. Pressure is applied by two punches, one each at the top and bottom of

the die. Initially, air is removed from the powder / granule mix by the particles rearranging to reduce the void space, then the pressure is continued to be applied until the particles have been compressed into a tablet. The tablet is then ejected from the die and the process begins again. Compression occurs for each tablet individually, although it can be considered to be a continuous process, as the powder or granule flows continually from the hopper to the compression zone. The tablet weight is controlled by the volume of powder or granule flowing into the empty space in the die, hence uniformity of particle size and flow is critical for obtaining reproducible tablets. The volume of empty space in the die is controlled by the lowest position of the lower punch. Tablet hardness and thickness are controlled by the forces exerted by the punches.

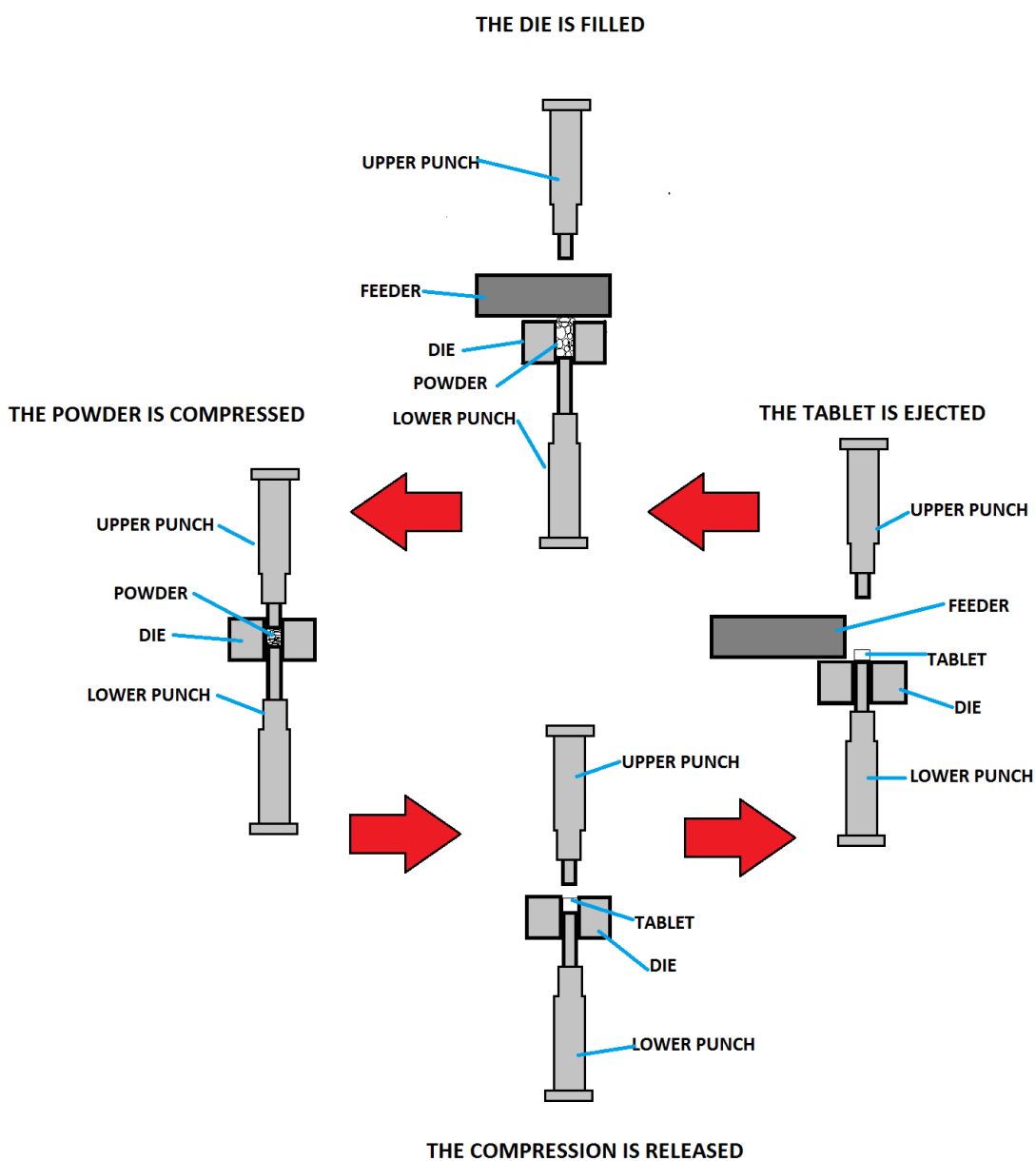


Figure 1.3: Schematic illustration of compression of a tablet.

Tabletting takes place on a tablet press. There are two types of press used commonly - a single station (eccentric) and a rotary press. A single station press has one compression station only, so has one set of tooling - a set being defined as a die, an upper punch and a lower punch. At the start of the compression cycle, the upper punch is pulled up out of the compression zone, the lower punch moves to its lowest position and the feed shoe moves over the die, dispensing powder or granule by gravity into the die. The feed shoe then moves out of the compression zone and the upper punch is lowered, providing the force to compress the powder or granule into a tablet. The lower punch does not move during this stage, so the compressive force is administered by the upper punch only. After compression, both punches move up to allow the tablet to be ejected from the die and removed from the press, and the process starts again. Single station presses run at a maximum of about 80 tablets/minute and require a minimum of only about 30 g of powder, so are ideal for small batches, e.g. during product formulation and development or for the manufacture of clinical trials materials.

The second type of tablet press is a rotary tablet press. Here, a number of tooling stations (each consisting of a die, an upper punch and a lower punch) are arranged in a circle on a die table held horizontally in a turret. At various points around the turret, there are the feed frame, dispensing powder or granule into the die, a compression station and an ejection station. The die table rotates during the compression process so that each tooling station is sequentially situated at each of these points, filling the die, compressing the powder or granule into tablets and ejecting the tablets. Powder or granule flow into the die may be under gravity or may be assisted by rotating paddles within the feed frame. Both the upper and lower punches move to compress the powder or granule into tablets, which is different to the single station press described above. During the compression cycle, the die remains fixed within the die table and movement of punches is controlled by a series of cams so that they are always at the correct position in the cycle. Rotary press can have as few as 4 or as many as 70 stations, which can produce in the orders of 100,000 to 500,000 tablets per hour (Jackson et al (2007)), so are ideal for large scale production and scale up exercises.

Compaction of powders or granules into tablets occurs in a number of stages. Initially, air is forced out of the powder or granule bed in the die by the pressure exerted by the punches. At the same time, the powder or granule particles rearrange to occupy the smallest possible volume. As pressure continues to be exerted by the punches, the powder

or granule particles will deform, possibly fragment and will bind to their neighbours. It is the strength of these bonds that will determine the strength of the final tablet. At the end of this process, all of the powder or granule has been incorporated into the tablet. Materials such as α -LM will deform by brittle fracture, creating new surfaces for bonding and will lead to strong tablets (Karehill et al (1990)). Other materials, such as MCC, will deform plastically, meaning that the particle retains its overall volume, but its shape has changed and the change is maintained after the pressure has been removed. These particles do not fragment. This results in tablets which are not so strong, but will disintegrate more easily. Some materials will deform elastically, i.e. once the pressure has been removed the particle returns to its original size and shape. Excessive elastic recovery leads to capping and lamination of tablets, i.e. the top and bottom surfaces of the tablet (generally curved) fall off (capping) and the central waist area is broken into layers (lamination) (Akseli et al (2013)). If the granulation process is poor and the granules are friable, they can undergo erosion and attrition during compaction, losing the benefit of granulation. The compaction process will be dependent on the pressure exerted by the punches, the time frame over which the pressure is applied, temperature and humidity, as well as the material properties of the formulation itself. Lubricant must be added to the formulation to prevent sticking of the formulation to the metal components of the tablet press.

1.5 Formulation and manufacture of mini-tablets

Mini-tablets are essentially small tablets and the same fundamental formulation and processing considerations apply to mini-tablets as to normal-sized tablets. The initial powder processing stage may be either direct compression or wet granulation. Due to the intended use of the mini-tablets, direct compression or dry granulation has been the most utilised method of production for mini-tablets in the literature (Weyenberg (2004), Angyal (2007), Lennartz and Mielck (1998)). One issue with mini-tablets is that they are very much more dependent on the particle size distribution (see below) and flow characteristics of the powder mix than larger tablets, so wet granulation may be a better approach, to ensure that the particle size distribution is maintained within narrow boundaries, ensuring better flow and more uniform die filling, leading to more reproducible tablets. Direct compression has the advantage of not requiring water or heat in the process, so is good for heat-sensitive or water-sensitive compounds, but does have the disadvantage that segregation is more likely than with wet granulation, leading to non-uniformity of product (Martinello et al (2006)). Wet granulation has the advantage of producing stronger tablets,

more resilient to further treatment and packaging than direct compression tablets (Šantl et al (2011)). A case-by-case decision should be made, taking into account all relevant factors. In this project, wet granulation was used because of the improvement in product uniformity.

Mini-tablets will be compacted in exactly the same fashion as larger tablets. However there are a few extra considerations for mini-tablets, which do not apply as severely to larger sized tablets. As the die is only 2 mm in diameter, the particle size of the powder or granule has to be controlled within very narrow limits to ensure that a sufficient number of individual particles flow into the die in order to give a reproducible tablet product. At the other end of the size scale, fines need to be controlled as they would be for any batch of tablets. Powder or granule flow from the hopper and feed frame is obviously critical to give a reproducible tablet product. The punches are very delicate and easily bent or broken, so the maximum compression force possible is very low, so this has implications for the formulation, so that a robust tablet can actually be made. As the surface to volume ratio is much greater for mini-tablets than larger tablets, there is more contact between the formulation and the tooling for the mini-tablets, which will lead to differing force profiles within the tablets and potentially different behaviour of the final tablet product.

Importantly for processing, a mini-tablet has a much greater surface area to volume ratio than a normal-sized tablet, as illustrated in Figure 1.4 and Table 1.1, below. During compression of a mini-tablet, a greater number of particles are in contact with the die wall and punches are more likely to be subjected to deformation and fragmentation than is the case with a normal sized tablet. This therefore means that the overall compaction and post-compaction behaviour of the tablets will vary with size.

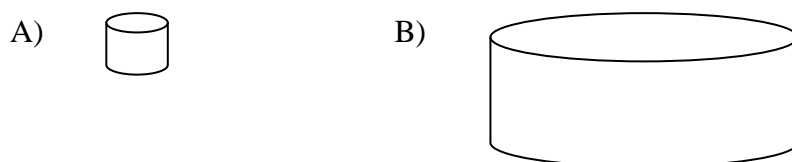


Figure 1.4: A diagrammatic representation of a mini-tablet (A) and a normal-sized tablet (B), both round and flat-faced.

	Mini-tablet	Normal-sized tablet
Radius = r	1 mm	5 mm
Height = h	2 mm	5 mm
Surface area = $2\pi r(r+h)$	18.84 mm ²	314.00 mm ²
Volume = $\pi r^2 h$	6.28 mm ³	392.50 mm ³
Ratio	3.0	0.8

Table 1.1: The geometry of the two tablets in Figure 1.4, with calculations of surface area, volume and the surface area: volume ratio.

1.6 Tablet characterisation

1.6.1 Bulk characterisation

All tablets must meet the requirements of the British Pharmacopoeia before use, if they are to be used within the UK. The tablets should contain the correct drug at the correct level. All tablets within a batch should be uniform in appearance and drug content, and should behave uniformly in terms of drug dissolution. Finally, the tablets should be stable over an extended period of time (the "shelf-life"), both in terms of drug content and drug dissolution profiles. The tests that are carried out on a batch of tablets at release (i.e. just after manufacture) are:

- Weight uniformity
- Content uniformity
- Hardness (resistance to crushing)
- Thickness
- Friability
- Disintegration
- Dissolution

Where possible, pharmacopoeial methods were used for these measurements and full details of all techniques are given in Chapter 2.

1.6.2 Surface characterisation

The tablet surface is a complex interface between the components of the tablet and the external environment and, as seen above, may behave differently in mini-tablets and larger tablets. The surface is the first part of the tablet to meet the dissolution medium (e.g. gastric fluid) and is the point of contact between the tablet components and potential reactants, such as oxygen or moisture vapour in the air. Knowledge of the distribution of materials through a tablet and specifically on the surface of the tablet may help explain observed behaviour. For example, if it is known that two components are preferentially located at the surface and in close proximity, this may help to explain instability if these components are likely to interact (Dai et al (2012)), although such chemical interaction should really have been detected at the pre-formulation stage. If the distribution of materials across a tablet surface can be manipulated, it may help improve formulation performance, for example by ensuring that the disintegrant is at the tablet surface not the core.

There is currently limited understanding of the spatial distribution of materials across a tablet surface, with a general assumption being made that it is the same as the bulk distribution of materials throughout the whole tablet. For example, if a component is present at 10 % w/w of the total tablet formulation, then it will cover 10 % of the surface of the tablet. The one exception to this will be the lubricant, which is added just before compression and needs to be on the surface of the powder or granule to prevent sticking to the metal surfaces of the die, punches and tablet press.

This project will examine the spatial distribution of materials across the surface of mini-tablets using a range of techniques. Mini-tablets are ideal for this work because of the greater proportion of the surface area to volume ratio than for larger tablets, meaning that more of the tablet can be examined. Many of the techniques used can only analyse a small area per run, so a greater proportion of the surface of the mini-tablets can be analysed than for larger tablets.

1.7 Analytical techniques used in this work

The analytical techniques used in this work fall into one of two broad categories: the first being the analysis of the powder and the second being the analysis of the compacted surfaces. For the powder analysis scanning electron microscopy (SEM), variable temperature infrared spectroscopy (VT-IR) and differential scanning calorimetry (DSC) was used. For the compacted surfaces atomic force microscopy (AFM), local thermal analysis (LTA), transition temperature microscope mapping (TTM mapping) and Raman microspectroscopy were used. The powder analysis was used to support the data from the compacted surface which is of interest in this project.

1.7.1 Scanning Electron Microscopy (SEM)

SEM is a microscopic technique used to obtain information about the size, shape and surface appearance of materials. It is used extensively in the development and optimisation of nano-scale drug delivery systems (Klang et al (2013)).

The basic operating principle of SEM is that a beam of accelerated, and therefore highly energetic, electrons is shone onto a small area of the surface of a sample. Upon hitting the sample, some of the energy of this electron beam is dissipated through a range of electron-sample interactions, such as the production of secondary electrons, backscattered electrons, diffracted backscattered electrons, photons, visible light and heat. Secondary electrons are most commonly detected and used in conventional SEM image generation, such as was used in this study. As the secondary electrons scatter more from an oblique (angled) surface than from a flat surface, a detailed three dimensional image may be obtained from a two-dimensional rastering pattern of the incident electron beam.

Experimentally, an electron beam is generated by a thermionic electron gun, accelerated and then focussed through a series of lenses onto the sample surface. The condenser lens is used to control the strength of the beam and the objective lens is used to focus the beam. Any secondary electrons produced from the interaction of the sample with the electron beam are then detected via scintillation counting - the detector is coated with a material which produces light when hit by the secondary electrons. This impulse is then magnified by a photo-multiplier tube system to allow images to be generated. Figure 1.5 illustrates this diagrammatically.

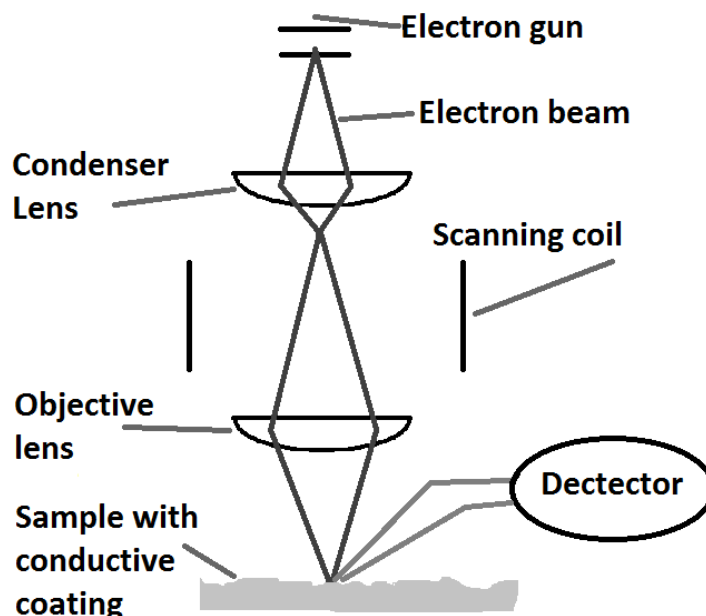


Figure 1.5: Schematic of a scanning electron microscope.

SEM can give very highly resolved images of a sample surface, but there are a few disadvantages to the technique. Generally speaking it has to be conducted in a vacuum so there are sample limitations, e.g. wet samples cannot usually be studied by SEM, although there are some environmental SEMs or low vacuum SEMs which can cope with these samples. Additionally, the sample needs to be electrically conductive. If not, it must be coated with a thin layer of conductive material. In this case, SEM becomes a destructive technique.

1.7.2 Variable Temperature Infrared Spectroscopy (VT-IR)

Most molecules will absorb light with wavelengths in the IR region and it is the measure of this absorption that forms the basis of IR spectroscopy. Bonds within a molecule will vibrate, with the frequency of the vibration being dependent on a number of factors such as the relative size of the two atoms in the bond and the dipole moment across the bond, which is related to the charge difference between the two atoms. There are a number of possible modes of vibration, such as stretching, bending, wagging and rocking. If the frequency of the applied light is the same as the resonant frequency of the bond, it will be

absorbed. The wavenumber of the absorbed light can be estimated as follows:

$$\nu = \frac{1}{2\pi c} \cdot \sqrt{k/\mu} \quad \text{Equation 1.1}$$

where ν is the wavenumber of the absorbed light, c is the speed of light, k is the spring constant for the bond under study and μ is the reduced mass of the bond, defined as:

$$\mu = \frac{m_1 \cdot m_2}{m_1 + m_2} \quad \text{Equation 1.2}$$

where m_1 and m_2 are the masses of the two atoms in the bond (Akins (1996)).

Typically light with wavenumbers of 4000 to 400 cm^{-1} is used in IR spectroscopy (wavenumber = 1 / wavelength). Absorption in the region 4000 to 1000 cm^{-1} is generally due to functional groups and can be used to assign probable chemical groups to an unknown material. The region from 1500 cm^{-1} downwards is known as the "fingerprint" region and is usually considered to be specific to an individual molecule (Williams and Fleming (1997)). The vibrational energy of the bonds will be dependent on the surrounding chemical structure, and this is seen more dramatically in this region.

In the first generation IR spectrometers, light was fractionated into individual wavelengths for experimental measurement, which resulted in long experimental times. Fourier Transform (FT) IR speeds up the experimental time by applying light of multiple wavelengths to the sample and performing a mathematical deconvolution process (FT) in order to obtain the absorption pattern. Most modern IR spectrometers work on this basis. In standard transmission mode FT-IR instruments the light beam is split into two, with one beam penetrating the sample and the other not. Recombination of the two beams post-sample will generate an interference pattern (an interferogram), which will give information on the extent of any absorption by the sample. An advance on this process is the use of the "Attenuated Total Reflectance" (ATR) process. Here, the sample is placed on top of a reflective crystal, for example diamond. Following beam splitting, the "sample" beam is directed through the reflective crystal towards the sample at a particular angle, known as the angle of incidence. It is then reflected back into the crystal and then at least once more towards the sample, in a process known as total internal reflectance. At

the point of contact between the crystal and the sample, the reflected beam will form an evanescent wave which will penetrate into the sample up to a distance of a few μm , but this will occur only if the crystal has a higher refractive index than the sample (Chan et al (2003)). The penetration distance is dependent on the wavelength of the light, the angle of incidence and the refractive indices of the sample and the crystal. After exiting the ATR crystal, the "sample" beam is then recombined with the "non-sample" beam and processed as normal to assess which wavelengths have been absorbed and to what extent. Figure 1.6 shows this ATR effect schematically.

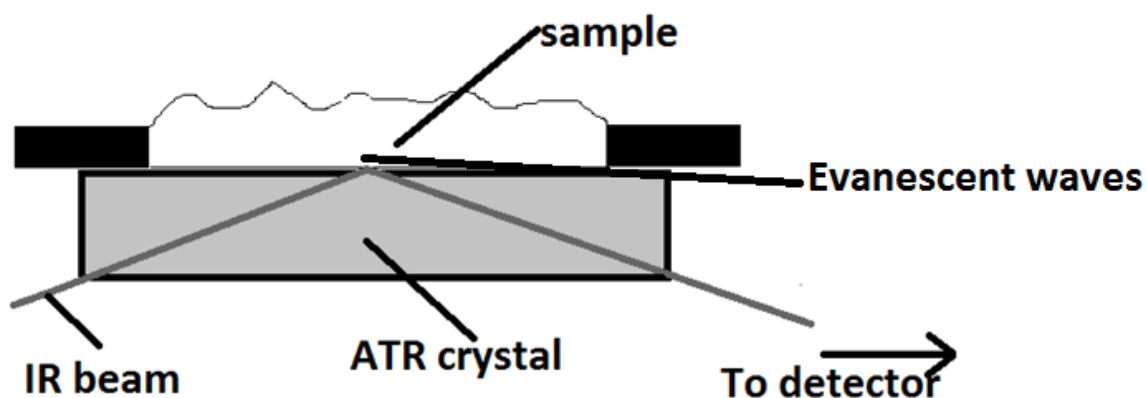


Figure 1.6: The path of the incident IR light in an ATR experiment.

The use of the ATR has many advantages over conventional transmission FT-IR spectroscopy, because it requires a smaller amount of sample and the sample may be used in any state (liquid or solid) with no prior modification or preparation. The number of times the beam is reflected through the ATR crystal is critical in obtaining a good sample-to-noise ratio and hence a good spectrum. A longer path length, i.e. a greater number of reflections, will decrease the intensity of the beam, but a greater number of interactions with the sample will give greater sensitivity. It is thus a balancing act between these two parameters to obtain the best experimental result.

In the ATR configuration, it is possible to apply heat to the sample via the crystal. In this case, the FT-IR spectra of the same sample at a different temperature can be easily obtained. This technique is known as Variable Temperature FT-IR, or VT-IR.

1.7.3 Differential Scanning Calorimetry (DSC)

DSC is widely used in the pharmaceutical and chemical industries and is performed to characterise thermal transitions in materials, such as melting (e.g. ibuprofen (Moreno-Piraja et al (2011))), glass transition (e.g. HPMC (McPhilips et al (1999))), or a polymorphic transition (e.g. famotidine (Cheng et al (2008))). DSC works by measuring the changes in heat flow to a sample compared to a reference over a pre-determined programme of temperature and / or time. When a thermal transition happens, the sample either absorbs extra energy compared to the reference (e.g. if melting) and shows an endotherm, or it can release energy (e.g. if re-crystallising) and shows an exotherm. A DSC trace allows interpretation of the temperature of the thermal event, the energy of a transition such as melting obtained by integration (area) of the peak, and the change in underlying heat capacity of a material after a glass transition.

There are two types of DSC instrument: heat flux and power compensation. In a power compensation instrument, the reference and sample pans are heated in two separate chambers. During the experimental run, the temperature of the two pans is kept the same and the difference in power input required to maintain them at the same temperature is measured. In a heat flux instrument, the sample and reference pans are heated in the same chamber, with separate thermocouples monitoring the temperature of the two pans, i.e. there is only one heat input signal. Due to the heat capacity of the sample, the sample and reference pans will be at a slightly different temperature and there will be heat flow between them (Craig and Reading (2007)). This can be quantified using the Equation 1.3:

$$q = \frac{T_r - T_s}{R_{(T)}} \quad \text{Equation 1.3}$$

where q = heat flow rate, T_r = temperature of reference, T_s = temperature of sample, $R_{(T)}$ = temperature-dependent thermal resistance of the heating disk (Rady (2009)).

This equation is simplified compared to the true experimental situation, because a number of assumptions have been made: the heat flow rates are constant throughout the run; any thermal resistances between the pans and the furnace have been ignored (but these should be equal for both the sample and reference if balanced pans are used); the heat capacities of the pans and the instrument itself have been ignored (again, this is probably reasonable

in the case of the pans as both the sample and reference pans will have the same specific heat capacity); the measured sample temperature is the actual sample temperature; and there is no heat exchange between the instrument and the environment (Rady (2009)). The main experimental issue with the heat flux technique is that the thermocouple is outside the sample, so there may be some discrepancy between the temperature recorded and the actual sample temperature.

1.7.4 Atomic Force Microscopy (AFM)

AFM is a type of scanning probe microscopy and operates at a very high resolution to generate a topographical image of the surface of a sample, so gives more detailed information than conventional light microscopes. This is obtained by the use of a probe, which moves across the surface of a sample in a pre-determined x-y pattern. The probe will also move in the z direction, monitoring bumps, valleys or ridges in a material and allowing a topographical map to be generated.

AFM was developed first reported in 1986 (Binnig et al (1986)). The instrument was developed to overcome some of the challenges of optical and SEM microscopes and to improve the magnification which could be achieved by these methods. AFM has a range of uses in several area of science from physics to biology to material science. According to Wallace (2012), development of this new type of microscope started in 1929 when Shmalz used the concept of dragging a sharp tip on a small bar (or profiler) across the surface of a sample. The profiler had a mirror on the top; a light source was shone on the mirror and then reflected onto photographic film. A magnification of 1000X was generally achieved. The profiler was attached to the instrument by a spring, designed to allow movement across the surface of the sample. However, one issue with the early set-up was that the profilers still suffered from damage and bending when they hit a high feature in the sample's topography. In 1955 Becker submitted a patent for an instrument which solved this issue of the bending profiler and suggested that the profiler should oscillate from just above the surface of the sample, which then produced high resolution images (Becker et al (1955)).

The instrument was further developed by Young who developed a non-contact stylus profiler (topografiner) (Young et al (1972)). The topografiner was mounted on three piezoelectric elements which controlled the x, y and z movements. The principle is that

the electron field emission current between the sample and the sharp metal probe is dependent on the distance between them. A feedback circuit was developed to keep the distance between the probe and the sample fixed by monitoring the electron emission. The up and down movement of the probe is controlled by the z piezoelectric element. The major limitation to this was the instrument's vibrations which limited the resolution of the 3D image that could be achieved.

In 1982, Binnig and Rohrer developed scanning tunnel microscopy (STM) which was the predecessor to the AFM (Binnig et al (1982)). Rather than using electronic field emission they found that by electron tunnelling greater sensitivity could be achieved. They also found that levitating the whole instrument reduced the vibrations. This solved some of the earlier problems seen. In this instrument the tunnelling current is monitored via a feedback loop so the probe can be kept very close to the surface. A 3D map can be generated down to atomic level. The invention of this instrument led to Binnig and Rohrer sharing the Nobel Prize for physics in 1986 (Wallace (2012)).

One serious problem still existed for this technique, in that it relied on the sample being conductive and solving this issue gave birth to AFM as it is known today. In 1986 Binnig, Quate and Gerber (Binnig et al (1986)) replaced the probe of the STM with a spring gold strip with a tiny diamond glued to it. AFM probes have greatly improved today with the use of Si and the range of experiment that can be performed has expanded greatly.

Figure 1.7 shows a schematic diagram of the operation of the AFM. The probe is gently lowered towards the surface of the sample until the forces between the probe and the surface pull the cantilever towards the surface. A laser beam is shone onto the mirror on top of the probe, reflecting light back to the detector. Any movement of the probe is therefore monitored by the laser-mirror-detector arrangement. The probe is moved across the sample in a pre-determined pattern in the x-y plane, maintaining contact with the surface of the sample. When it reaches a topographical feature, e.g. a bump or a valley, the force measured will change. Based on this reading, the probe is then moved upwards or downwards (the z plane) in order to maintain the force at its initial reading. This is then recorded as the topographical image of the sample.

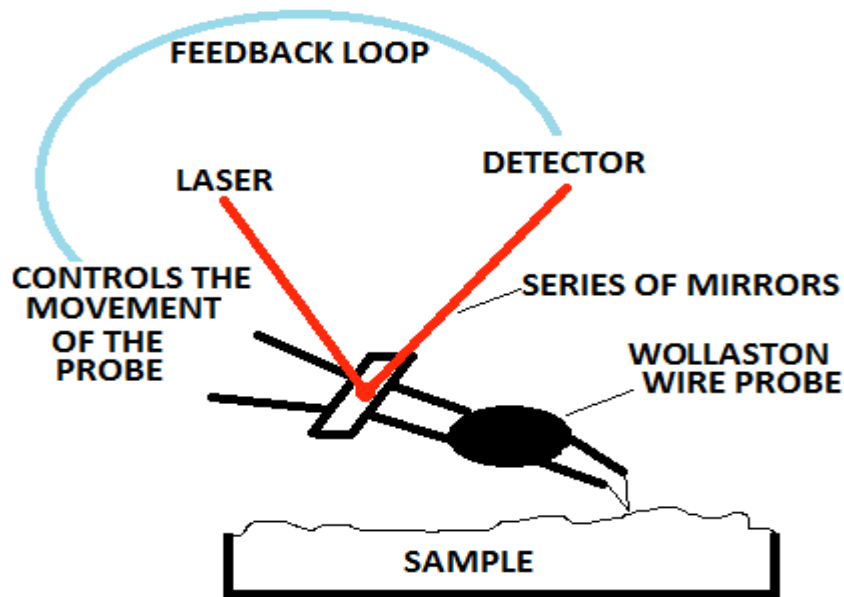


Figure 1.7: Schematic diagram of the basic operational set-up of an AFM.

There are thus a number of major parts of an AFM instrument that are involved in the generation of a topographical image. The first is the piezoelectric transducer which controls the movement of the probe tip over the surface. The piezoelectric transducer is supplied by a voltage and converts electrical potential into mechanical motion via a change in its geometry, allowing probe movement (Wallace (2012)).

The second is the force transducer which measures the force between the probe tip and the sample. In most cases, this is the cantilever. The cantilever will respond to the forces detected at the surface of the sample in accordance with Hooke's law (Equation 1.4 below).

$$F = -k \cdot d \quad \text{Equation 1.4}$$

where F = force measured, k = force constant (i.e. the spring constant quoted by the probe manufacturer) and d = distance moved by the probe (Giuliodori et al (2009)).

Thirdly, the detector system is extremely important in enabling responses to be monitored. The laser beam shines onto the mirror at the back of the probe and is reflected onto a photo-diode. Any movement of the probe will result in a change in detection at the photo-diode. The primary response of the photo-diode is electrical, so the movement of the probe is recorded in volts, rather than more conventional distance units such as μm . The starting point for the deflection is set individually for each experimental run by the user when setting up the laser on the AFM instrument, so it will vary between analyses and probes. Hence, it is the relative change in deflection (volts) which is important, rather than the actual numerical value recorded.

The final significant factor is the feedback control loop that ensures a constant force is maintained between the probe and the sample, which in turn allows reliable topographical images to be obtained. This is achieved by measuring the change in the force at the tip and changing the voltage at the piezoelectric transducer to compensate (Binnig et al (1986)).

There are many ways AFM may be used, but there are three main operating methods: contact, tapping and non-contact modes. In contact mode the probe tip is in physical contact with the sample surface throughout the experimental run. This mode is good for solid state materials, but there will be a limit to the surface roughness that can be accommodated, due to the need for the probe to move in the z direction. Additionally, there is more chance of probe damage and contamination than in the other modes. In non-contact mode, the probe does not touch the sample, but rather is oscillated (moved up and down) at or just above its resonant frequency. The difference in the force between tip and sample with distance (the force gradient) is measured, as is the oscillation amplitude and phase of the vibrating cantilever. These measurements will allow image of the surface of the sample to be obtained. Non-contact mode is useful if the sample is delicate or soft, such as biological samples (Dai et al (2012)). Tapping mode is very similar to the non-contact mode, as the probe oscillates at a resonant frequency but during an oscillation it briefly comes in contact with the surface. This operating method is really designed to give the best of the other two techniques, so there is not the instability of the probe being in the air as in the non-contact mode and lateral forces are almost eliminated compared to contact mode.

Royall et al (1999) used contact mode AFM for the characterisation of the surface of a tablet formation composed of ibuprofen and hydroxypropylmethylcellulose (HPMC).

They used AFM to generate a topographical image and were able to visually distinguish the two components. Seitavavuopio et al (2003) compared various imaging techniques such as optical microscopy SEM, laser profilometry and AFM to assess the surface roughness of compacts composed of potassium chloride and sodium chloride, which were compressed under different pressures. They found that AFM could give quantitative results for the roughness to a much higher resolution than some other techniques, but that AFM had the disadvantages that only a small area of the sample could be measured per experiment, the experimental time was long, and a reasonably flat sample surface was required. Non-contact mode AFM is used for soft materials, such as biological systems and the probe oscillates above the surface of the sample. Intermittent contact mode AFM is essentially a mixture of the other two modes. The probe does come into contact with the surface but only intermittently, i.e. it "taps" the surface to generate the topographical map. This mode is also known as "tapping" mode and has been used to study polymeric systems (Zhang et al (2009)) and amorphous systems (Ward et al (2005)).

1.7.5 Localised Thermal Analysis (LTA)

LTA involves replacing an AFM tip with a miniaturised thermistor, which will heat up the small amount of the surface that it is in contact with. Power is supplied to the probe, which then heats up in a fast linear ramp. Heat is quickly transferred from the probe to the sample. As the sample heats up, any thermal transitions within that region of the sample will result in a softening or flowing of the material, leading to downward probe movement, i.e. the probe will penetrate through the sample surface. Essentially, this technique is performing a DSC experiment on a very small sample, hence the name "localised thermal analysis". LTA is a generic term and is further sub-divided into micro-TA and nano-TA depending on the size of the probe and the area of scrutiny. It allows investigation of surface distribution of materials in a sample, unlike in conventional DSC whereby the whole of the sample is tested and a global result is recorded

A thermal probe with a resistive sensor that was used in scanning thermal microscope was originally developed by Dinwiddle and co workers (Buzin et al (2002)). Reading and colleagues then performed some of the critical initial development work on the concept of LTA (Murray et al (1998)). The initial experiments allowed exploration on a micron scale, so the technique became known as "micro-thermal analysis" or "micro-TA". The micro-TA instrument was commercially launched in 1998 and micro-TA has been used to study a

wide range of materials, including pharmaceuticals, foods, biological materials, electronic materials and polymers (Pollock and Hammiche (2001)).

For micro-TA, the thermistor is a Wollaston wire probe, which is a thin silver coated platinum wire, with the tip etched away by acid to reveal the platinum core. Hence, when an electric current is passed through the Wollaston wire probe all the electrical resistance is in the uncoated tip, and therefore only the tip heats up (Craig et al (2002)). The temperature of the tip can be controlled, hence it can be used as a thermal probe allowing localised heating at specific points on the surface of a sample. A reference probe suspended in air, i.e. with no contact between it and the sample, is used as a reference and the difference in the signals between the two probes is taken as the experimental result.

More recently, a smaller probe has been developed, which will examine a much smaller region and the use of this probe results in "nano-thermal analysis" or "nano-TA". In nano-TA, the AFM probe is replaced with a very small doped silicon probe tip attached to the cantilever. Otherwise, the principle is the same as for micro-TA. The main advantage of nano-TA is that a much smaller area can be imaged than with micro-TA - the spatial resolution for nano-TA is quoted as 20 nm and for micro-TA it is $\sim 1 \mu\text{m}$ (Zhang et al (2009)). Additionally, a control probe is not required.

Figure 1.8 illustrates the experimental response which is seen during a nano-TA experiment (NB the same process is seen for micro-TA). The first point shows the probe just in contact with the sample, so no response is seen. The second point is when the probe starts to heat up and transfer heat to the sample. The baseline is not flat, but increases in a roughly linear fashion with temperature due to thermal expansion of the surface as it is heated. At the third point, the sample is starting to soften and the probe is starting to move but no sharp transition is seen until point four when the sample has just reached its thermal transition point and the probe has penetrated into the sample. The endpoint is usually taken as the temperature at which the probe begins to penetrate into the sample and the deflection is seen on the graph. The probe is then taken from the sample which is illustrated in point five.

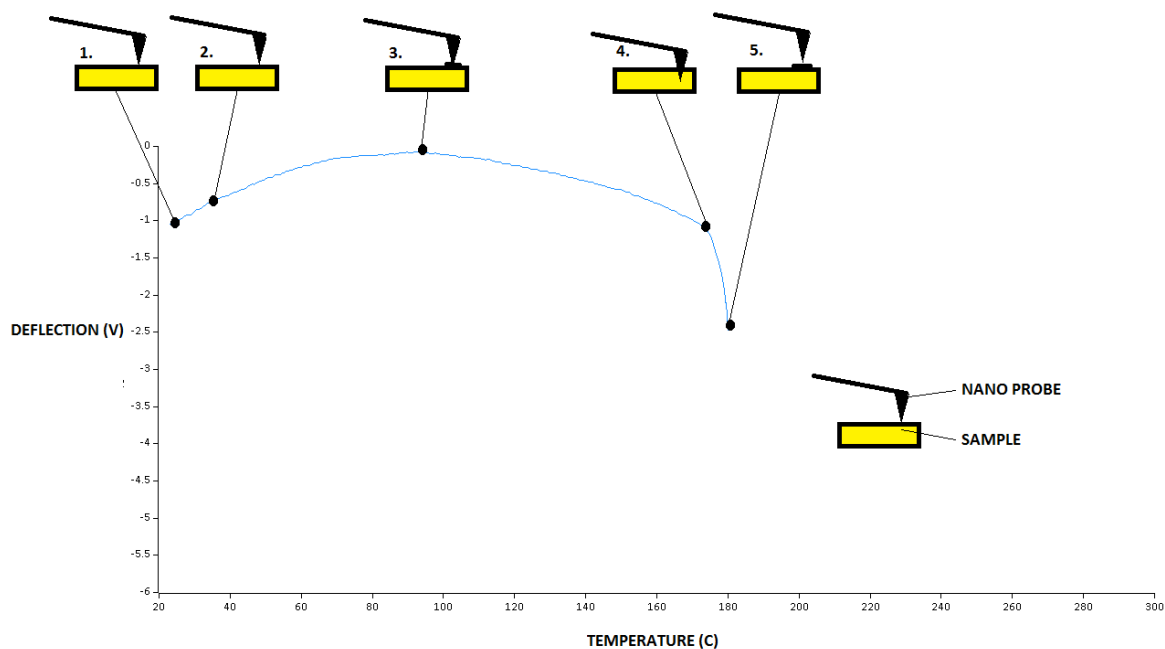


Figure 1.8: An explanation of nano-TA (also applicable to micro-TA) which shows probe movement with the resultant curve.

Micro-TA was used by Saunders et al (2000) to analyse the polymorphic forms of cimetidine on the surface of a compact. They had found that it was difficult to distinguish these polymorphs using bulk differential scanning calorimetry (DSC) or thermomicroscopy, but micro-TA was sensitive enough to show the differences between the two polymorphs on the surface of the compacts. A modified version of the LTA technique, whereby the probe is heated to a set temperature and then the power required to maintain it at that temperature was used by both Royall et al (1999) and Saunders et al (2000). In both cases, identification of the different components in the sample was possible. Harding et al (2007) showed that micro-TA was able to distinguish between amorphous and crystalline indometacin on the surface of a compact, because the two forms have distinct thermal behaviour. As part of this study "pull off" forces were measured. The pull off force is the force required to detach the probe from the sample surface and is likely to be different below, at and above a thermal transition such as the glass transition or melting. Additionally, it will vary between different materials. Using the pull off force technique, Harding et al (2007) were able to investigate the glass transition behaviour of indometacin and show some subtle behaviour not seen in bulk DSC measurements. Subsequently, Dai et al (2009) used this pulsed force mapping technique to map the amorphous and crystalline regions on the surface of a lactose compact.

1.7.6 Transition Temperature Microscopy (TTM)

It is possible to use micro-TA and nano-TA to generate a map of the distribution of materials over the surface of a sample by performing localised thermal analysis on specific areas on the surface of a sample and then plotting the response, but this requires a lot of operator input in terms of sample positioning and is unlikely to be reproducible in terms of distance between the sample points. Transition temperature microscopy (TTM) is essentially an automated version of nano-TA, which allows a more detailed image to be generated in the form of a map of the transition temperatures measured in a predetermined grid pattern, hence the name "transition temperature mapping". The automated nature of the TTM means that it speeds up data acquisition compared to the manual approach of nano-TA. The TTM equipment measures the temperature at which the probe penetrates the sample (i.e. the "transition temperature") at each location and automatically assigns that temperature a colour. This is repeated until all the points are covered and a coloured map is then generated, reflecting all the transitions measured.

The basic principle of operation of TTM is the same as described above for the micro-TA and nano-TA experiments with one major difference. The Vesta TTM (Anasys Instruments, USA) is built around an optical microscope not an AFM, hence a topographical image cannot be obtained. As the topographical images can help in the interpretation of the thermal responses, this is a potential drawback to the technique. The Vesta TTM uses the same nano probes as discussed previously for nano-TA. Both the probe and the laser are mounted in the Vesta head. Once the operator has initially positioned the head over the area of interest on the surface of the sample, the software will then perform a series of automated experiments, moving the probe from one position to another in a predefined grid pattern. During this operation, the probe is removed from contact with the surface at the end of one test, then moved to the new site and repositioned on the surface of the sample ready to start the next test.

Data analysis is performed by the software. The transition temperature is registered automatically and assigned a colour. Ultimately, each site in the grid is assigned a colour and a map generated showing the distribution of transition temperatures. Figure 1.9 shows a simplified TTM map of a sample with two components which show distinctly different transition temperatures. The component which shows the transition at the lower temperature is coloured yellow and the component with the higher temperature transition is

coloured blue. A temperature bar shows the colour-temperature relationship. The data output is therefore initially in the form of a pixellated map, but an in-built software procedure will "smooth" the pixellation and will produce an interpolated map.

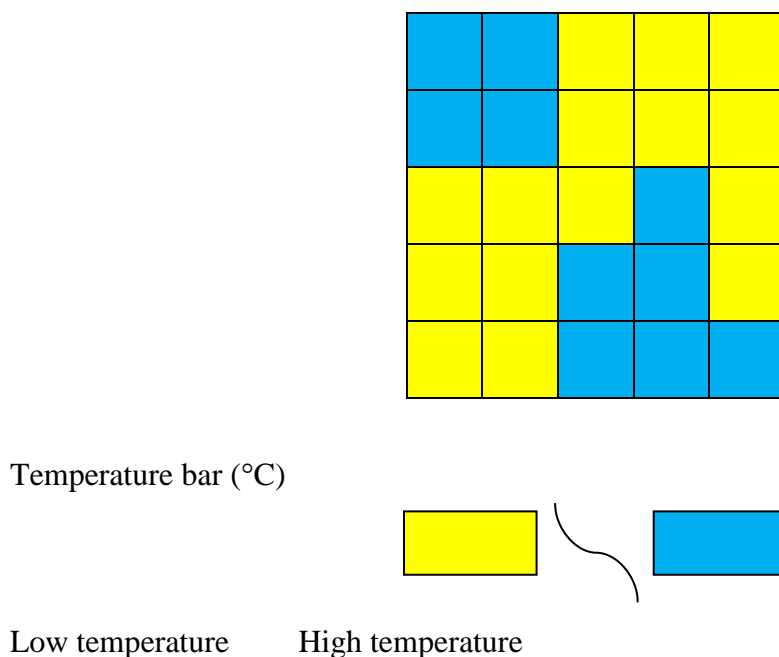


Figure 1.9: A simplified example of a TTM map.

TTM has been used to characterise the thermal properties of nano-fibres for drug delivery and biomedical systems (Raimi-Abraham et al (2014)) and the mapping of felodipine-PVP solid film dispersion films (Qi et al (2013)). Dai et al (2012) demonstrated the mapping of the surface of paracetamol-HPMC compacts.

1.7.7 Raman Microspectroscopy

Raman radiation was first documented by Raman and Krishnan (1928). In the 1990s with the development of the supporting technology, Raman spectroscopy became a useful analytical tool because generally samples need no preparation, it is non invasive, it is good for aqueous solutions, it is easy to perform and is quick (Vankeirsbilck et al (2002)). Raman spectroscopy uses the scattering of light as an analytical technique to determine molecular structure and to allow chemical identification. Raman microscopy (or microspectroscopy) is the use of Raman spectroscopy in combination with an optical microscope, in order to perform localised chemical analysis and identification on a

millimetre scale (Smith and Clark (2004)). It is an effective analytical tool which has the ability to analyse the spatial distribution of, for example, components of a tablet or constituents within archaeological samples.

The fundamental physical process underpinning Raman spectroscopy is the scattering of light. When incident light of a specific wavelength interacts with the electron cloud of a bond within a molecule, the electron cloud is polarised and promoted to a virtual higher energy state. This virtual higher energy state is unstable, decay is almost instantaneous and the excess energy is released as a photon of light, which can be in any direction. In most cases, the energy released is the same as that absorbed, so the wavelength of the light emitted is unchanged from that absorbed. This is described as "elastic scattering" or "Rayleigh scattering". Much less frequently observed is "inelastic scattering", where the wavelength of the emitted light has a different frequency to that of the absorbed light and it is this inelastic scattering that forms the basis of Raman spectroscopy. Two types of inelastic scattering are possible: "Stokes" and "anti-Stokes" scattering. In Stokes scattering the molecule retains some of the absorbed energy, returning it a higher vibrational state rather than its ground state, and the light emitted has a longer wavelength than the incident light. In the case of anti-Stokes scattering the molecule loses more energy than it originally absorbed and the light emitted has a shorter wavelength than the incident light. Anti-Stokes scattering is possible only if the molecule was initially in a higher vibrational state than its ground state and it returns to its ground state, rather than its higher vibrational state. As the chance of the molecule being in this higher vibrational state is much lower than that of being in the ground state, anti-Stoke's scattering is much less common than Stoke's scattering. As the energy difference between Stoke's and anti-Stoke's scattering is the same, they form symmetrical peaks around the Rayleigh peak and it is this shift that is the Raman effect. Raman spectroscopy usually uses just the Stoke's scattering, because it is more common than the anti-Stoke's scattering (Turrell and Corset (1996)). Figure 1.10 illustrates the energy levels observed in Rayleigh and Raman scattering. It is important to note that the scattering discussed here is not the same as the absorption of light in, for example, ultra-violet spectroscopy, as the molecule is promoted to a virtual state in Rayleigh and Raman scattering and a "real" higher energy state in the other techniques.

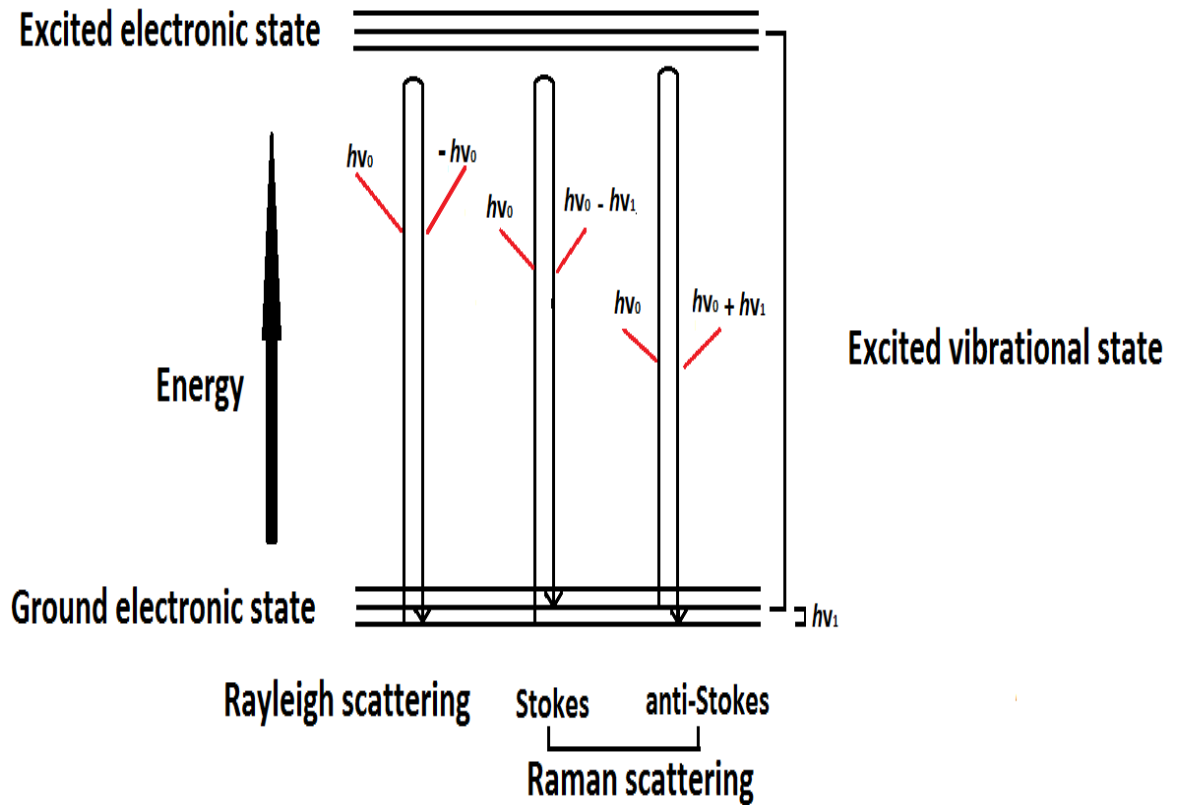


Figure 1.10: Energy level diagram showing the concerted excitation- relaxation phenomena responsible for scattering.

A Raman microspectrophotometer works by using the light microscope component to identify an area of interest to be studied. The microscope then directs the laser on to this specific region and the light is scattered. Holographic notch filters are used to filter out the intense Rayleigh scattering and allow the weaker Raman signal to be picked up. A diffraction grating is used to diffract the filtered beam and can be rotated to select different wavelengths into the detector. Charge coupled devices (CCDs) are commonly used as detectors because they allow the whole spectrum to be collected at once. Figure 1.11 shows a schematic diagram of a Raman microspectrophotometer.

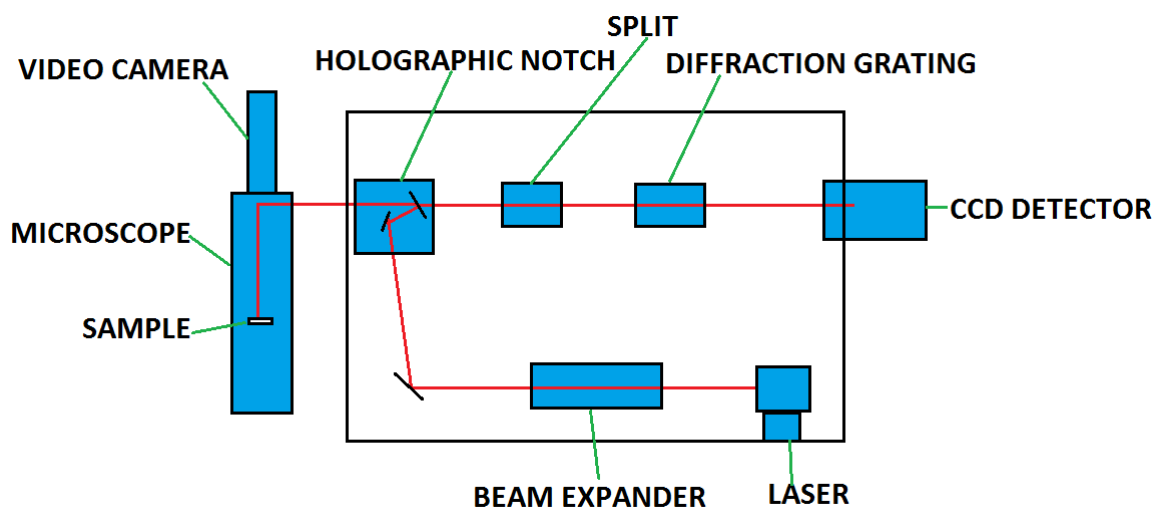


Figure 1.11: Schematic of a Raman microscope. Adapted from Smith and Clark (2004).

Although Raman spectroscopy has mainly been used for chemical identification, it can also be used as a mapping technique, e.g. Vajna et al (2010), Mazurek and Szostak (2011) and Bugay (2001). Ward et al (2005) used Raman microspectroscopy to map different forms of a crystalline material across a surface and Taylor and Langkide (2000) used it to examine the distribution of a low concentration of a drug in a formulation. These authors also estimated that Raman microspectroscopy is more sensitive to low quantities of materials than other techniques and quoted figures of 0.7 %w/w for Raman microspectroscopy, 1 %w/w for IR mapping, 5 %w/w for solid state NMR and an even higher value for X-ray powder diffraction. Widjaja and Seah (2008) performed Raman analysis on a pharmaceutical tablet. By using multivariate data analysis they were able to identify all four ingredients in these tablets, even the ingredients that were in low concentration.

"Spatially offset" Raman spectroscopy has been used to perform Raman spectroscopy on tablets within blister packs and other packing. This has the potential to be used in on-line analysis of production processes. Ricci et al (2007) examined anti-malarial tablets using FT-IR imaging, conventional Raman spectroscopy and spatially offset Raman spectroscopy. The combination of all three analytical techniques allowed the authors to fully identify all relevant components.

1.7.8 Other techniques for tablet surface imaging

Various other techniques could be employed to image tablets, but as this project is interested in the spatial distribution of component across the surface of a tablet, techniques that penetrate the whole sample would be unsuitable here e.g. magnetic resonance imaging, X-ray computed tomography and far-IR (Terahertz spectroscopy). A technique with a limited penetration depth is required which suggests that near-IR spectroscopy (NIR), FT-IR spectroscopy and mass spectrometry (time of flight secondary ion) could be suitable techniques (Pivonka et al (2007)). All the mapping spectroscopic techniques work on similar principles where a reading is taken at allotted distance apart and a map is developed just as seen in Raman microspectroscopy and TTM mapping. None of the other techniques use the thermal properties of the sample which LTA and TTM exploit.

NIR and mid-IR spectroscopy measure the absorbance of molecules bonds in these regions of the electro-magnetic spectrum. The spatial resolution for NIR is greater than for mid-IR, but mid-IR is the more popular technique because the sample has to be thicker in order to obtain an adequate intensity with NIR. These techniques are very similar to Raman spectroscopy and may also be used in conjunction with a microscope. There are several references to mid-IR mapping in tablets such as Chan et al (2003), Elkhider et al (2006), Lee and Lin (2005) and Chan et al (2005). Chan et al (2003) analysed tablets composed of two to four components and were able to identify each component separately and produce a distribution map of each individual component.

NIR mapping has also been successfully used to map pharmaceutical solid dosage forms (Cruz and Blanco (2011), Clarke et al (2001) and Zhao et al (2010)). Clarke et al (2001) used NIR and Raman spectroscopy to map the surface of pharmaceutical dosage forms. The two techniques produced very similar maps. Zhao et al (2010) used NIR mapping to examine the results of splitting tablets by comparing whole and tablets split in half. Cruz and Blanco (2011) examined tablet content uniformity and drug distribution throughout the tablet using the same technique. Romero-Torres et al (2011) used Raman microscopy and NIR chemical imaging to examine tablets produced by different production process. The results showed the technique used to produce the tablets induced the drug to change its solid state form. NIR chemical imaging was able to analyse the whole tablet. The real benefit of these techniques is that they are non destructive so can be used to assess real-time production process to assess changes in production process (Lee and Lin (2005)).

Mass spectrometry has been used to examine the surface of solids. Huang et al (2007) characterised a solid surface using electrospray assisted laser desorption ionisation mass spectrometry. They examined six drugs in tablets and were able to generate spectra for all the drugs present in the tablets without any sample preparation at ambient conditions. They did not map the tablets but able to recognise the drug particles on the surface of the tablets.

Time of flight secondary ion mass spectrometry (TOF- SIMS) has been used for a range of applications from coatings to mineral processing (Barns et al (2011)). It can also be used to examine the surface of pharmaceutical tablets, with a penetration depth of about 1 nm (Barns et al (2011)). It is highly sensitive, with no significant damage being caused to the sample surface. TOF-SIMS has been used by Belu et al (2000) and Edge et al (2002) for pharmaceutical applications. Belu and colleagues examined three different drugs in a controlled release system consisting of a central core containing the drug and two excipients and a coating. A cross section was taken of the tablet which covered the core and coating. A "global" map of 250 μm x 250 μm was produced by overlaying each of the maps for each of the components which were identified by their mass. A disadvantage of this technique is it identifies a component by its mass so polymorphic form will not be distinguished (Bugay (2001)).

1.8 Aims and objectives of this project

The overall aim of this project is to investigate the utility of novel thermal surface analytical techniques to characterise surfaces and in particular to determine the distribution of components across the surface. Mini-tablets are used here as an example of a pharmaceutical product for which this information is likely to be useful.

The specific objectives of this project are:

- To characterise the behaviour of a range of commonly used tablet excipients (α -LM, MCC, PGS, MS and PVP) using the following techniques: scanning electron microscopy (SEM), differential scanning calorimetry (DSC), variable temperature Fourier Transform infra-red spectroscopy (VT-IR), atomic force microscopy (AFM), microthermal analysis (micro-TA), nano-thermal analysis (nano-TA) and transition temperature mapping (TTM). This is presented in Chapter 3.
- To characterise the behaviour of a range of commonly used drugs (caffeine, ibuprofen and theophylline) using the following techniques: SEM, DSC, VT-IR, AFM, micro-TA, nano-TA and TTM. This is presented in Chapter 4.
- To prepare mixed compacts of the excipients and the drugs, building up the complexity from the mono-component compacts studied in Chapters 3 and 4 to 2-, 3-, 4- and 5-component compacts, and to assess these using the following techniques: AFM, nano-TA and TTM. This is presented in Chapter 5.
- To prepare mini-tablet formulations containing caffeine or ibuprofen, to characterise them using standard pharmacopoeial and industry techniques and to assess these using the following techniques: AFM, nano-TA and TTM. This is presented in Chapter 6.
- To use a more established technique such as Raman microspectroscopy to confirm the results as the novel techniques. This is presented in Chapter 7.
- To perform a critical appraisal of the advantages and disadvantages of the novel thermal surface analytical techniques. This is presented in Chapter 8.

Chapter 2
Materials and methods

CHAPTER 2

Materials and methods

2.1 Introduction

The aim of this work was to investigate the utility of novel techniques for the analysis of the spatial distribution of materials across the surface of a pharmaceutical mini-tablet. The approach taken was to separately assess the individual components, then build up the complexity of materials within the sample until the complete mini-tablet formulation was present.

The investigation broadly fell into two categories, which were an analysis of the powder material and analysis on a compacted material surface. Powders were analysed by scanning electron microscopy (SEM) for an indication of particle size, shape and surface roughness; variable temperature infra-red spectroscopy (VT-IR) to assess the effect of temperature on the material; and differential scanning calorimetry (DSC) to assess the thermal properties (e.g. melting point) of the material. The surface techniques used were atomic force microscopy (AFM) to examine the topography of the sample; micro-thermal analysis (micro-TA) and nano-thermal analysis (nano-TA) to determine the thermal behaviour of the material on a surface; transition temperature mapping (TTM) to provide a visual map of the components' distribution on the surface; and Raman microspectroscopy, also to provide a visual map of the components' distribution on the surface.

For the initial surface analysis, compacts of the materials were prepared containing one or more components in defined ratios and tested using all analytical methods. Finally, mini-tablets were produced and analysed using the range of methods described above.

In this Chapter, the materials used throughout this study are detailed, the experimental details of analytical methods are described, the production methods used to prepare the mini-tablets are described and finally the analytical methods used to characterise the mini-tablets are detailed.

2.2 Materials

In this project, five commonly used excipients and three drugs were studied. The excipients used were microcrystalline cellulose (MCC), pregelatinised starch (PGS), α -lactose monohydrate (α -LM), magnesium stearate (MS) and polyvinylpyrrolidone (PVP). The drugs used for the main study were ibuprofen, caffeine and anhydrous theophylline, with a smaller study being performed on a range of other drugs. The materials were used as received, unless otherwise stated.

2.2.1 Microcrystalline cellulose (MCC)

This off-white powder is widely used in the food, cosmetic and pharmaceutical industries. Chemically, MCC is a glucose polymer, with β -(1 \rightarrow 4) glycosidic bonds between the glucose residues, as shown in Figure 2.1, with a generic chemical formula of $C_{6n} H_{10n+2} O_{5n+1}$.

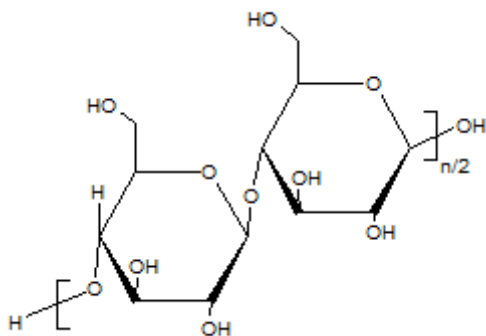


Figure 2.1: Structure of microcrystalline cellulose.

MCC is produced by treating α -cellulose from the pulp of fibrous plant material with mineral acid. The α -cellulose is purified and partly depolymerised. The acid treatment results in the formation of MCC, which has both amorphous and small crystalline regions (hence the name MCC) within a single particle, depending on the relative positions of the cellulose chains within the solid. The degree of crystallinity in the final MCC product depends on the extent of the treatment of the α -cellulose and it will affect its physical and manufacturing properties, e.g. compactibility and hygroscopicity (Terinte et al (2011)).

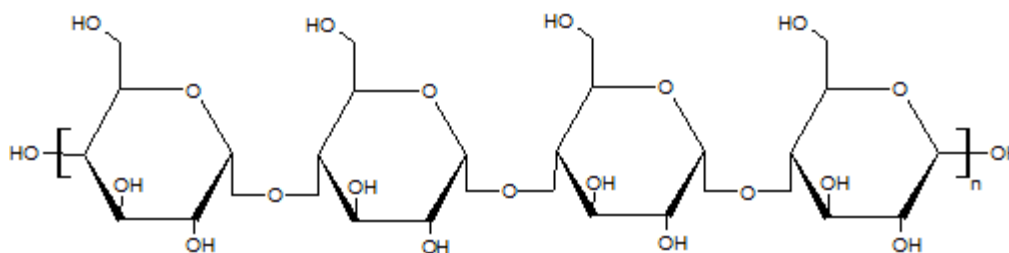
MCC has relatively low reactivity, both chemical and thermal, which makes it a good excipient for pharmaceutical use and it has been used as a diluent, binder, disintegrant and anti-adherent in a range of formulations (Uesu et al (2000)). It has good compatibility properties, deforming by plastic deformation, and is usually used with α -LM in balanced tablet formulations.

In this study, the grade of MCC used was Avicel PH101 manufactured by FMC Biopolymer and supplied by MSD. Avicel PH101 is a grade specifically designed for wet granulation. The batch of MCC used was lot 1420550115.

2.2.2 Pregelatinised Starch (PGS)

PGS is also a glucose polymer. It is off-white in colour and used widely in the food and pharmaceutical industries. Unmodified starch composes of two polysaccharides - amylose and amylopectin. The main difference between the two molecules is that amylose is held together with α -(1 \rightarrow 4) glycosidic linkages and forms long chain (there is some branched chain bonding), but amylopectin is held together with the same backbone of α -(1 \rightarrow 4) glycosidic bonds, but with branch chain bonding which serve as branch points (Kizill et al (2002)) as shown in Figure 2.2.

A)



B)

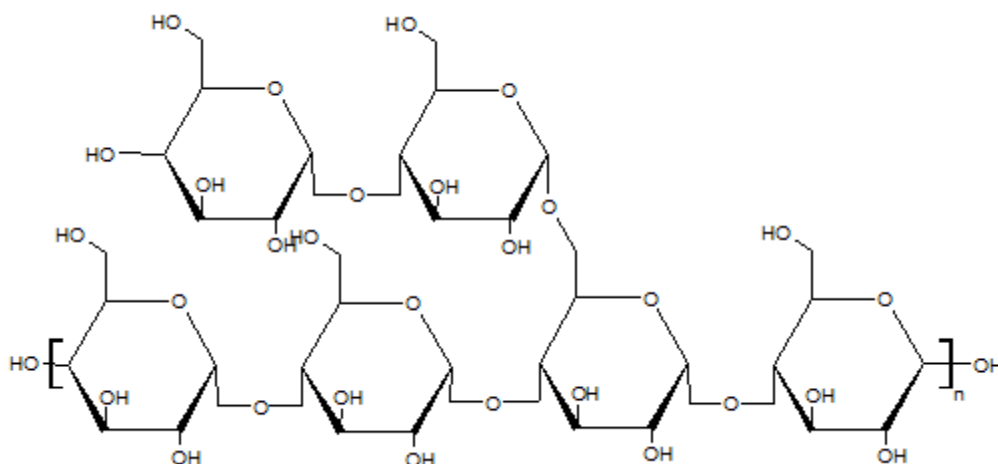


Figure 2.2: The chemical structure of unmodified starch. A) amylose. B) amylopectin.

PGS is manufactured from unmodified maize starch. The maize starch is gelatinised in water by heat, forming a thick semi-solid substance, and during this gelatinisation process the intermolecular bonds between the starch molecules, i.e. the crystalline structure, are broken and hydrogen bonds are formed between the starch molecules with the water. This changes the structure of the product permanently and greatly improves its aqueous solubility. When added to cold water, pregelatinised starch will dissolve and produce a viscous solution (Bulut and Schick (2012)).

PGS used in pharmaceutical formulations is only partially pre-gelatinised. The amylopectin component will dissolve in cold water, so it may be used as a binder in wet granulation tablet formulations. The amylose portion will swell in water, thus acting as a disintegrant in compressed tablets. The tablet will fragment, which then increases the surface area for drug dissolution.

In this study, the grade of PGS used was Starch 1500 manufactured and supplied by Colorcon (UK). The batch of PGS used was lot 1N521375.

2.2.3 α -Lactose Monohydrate (α -LM)

Lactose is a white to off-white solid. Chemically, it is a disaccharide consisting of glucose and galactose which are bonded by a β -(1 \rightarrow 4) glycosidic linkage, shown in Figure 2.3. There are two possible orientations of the -OH group on the glucopyranose ring (highlighted in Figure 2.3), giving rise to the α -pyranose form and the β -pyranose form. The galactose residue is always in the β -form, so the anomeric form of lactose is dictated solely by the glucopyranose ring. Lactose may exist in either the anhydrous or monohydrate forms.

The chemical name of α -LM is β -D-galactopyranosyl-(1 \rightarrow 4)- α -D-glucose monohydrate, with the chemical formula $C_{12}H_{22}O_{11} \cdot H_2O$ and a molecular weight of 360.3 gmol^{-1} .

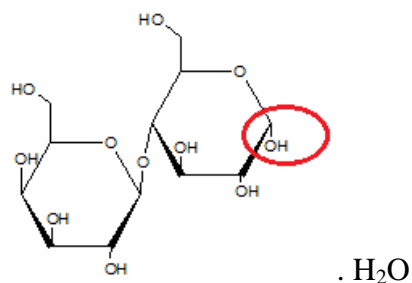


Figure 2.3: Structure of α -LM.

Lactose has many uses in the food and pharmaceutical industries: for example, it is used in tablets and capsules as a diluent (filler, bulking agent) and in dry powder inhalers as a carrier particle. In tablet formulations, it will deform by brittle fracture, making very strong tablets. It is usually used in combination with MCC in balanced formulations. α -LM is generally provided in the crystalline state, suitable for wet granulation formulations, but α -lactose is also available in an amorphous spray-dried form, suitable for direct compression formulations. Although it is widely used pharmaceutically, there are a few issues with the use of lactose: some patients are lactose-intolerant, and drugs which are primary or secondary amines will undergo the Maillard reaction with lactose, leading to degradation and discolouration (brown spots on the tablets) (Flemming and Picker-Freyer (2008).

In this study, crystalline α -LM supplied by Fisher Scientific, UK (lot 1012543) was used. Where α -lactose was required, this was prepared immediately before use by heating α -LM in an oven at 190°C for a minimum of four hours to remove the water of crystallisation.

This temperature was chosen based on the DSC traces for α -LM. DSC was performed on the sample after drying to confirm the removal of the water but retention of the α -structure. β -Lactose was purchased from Acros (UK), lot 412985000, as a stated 80:20 % mixture of β -lactose and α -lactose, as pure β -lactose was unavailable commercially. However, DSC experiments conducted here indicated that this commercial sample was effectively 100% β -lactose as no evidence of α -lactose was seen by DSC (see Chapter 3).

2.2.4 Magnesium stearate (MS)

MS is a white solid, which can come from either animal or vegetable sources. MS is not a pure substance, but rather it is a mixture of magnesium salts of a range of organic acids. The most common organic component in MS is stearate (with a C_{18} chain), as shown in Figure 2.4, but palmitate (with a C_{16} chain), is also found in large quantities (Bracconia et al (2003)).

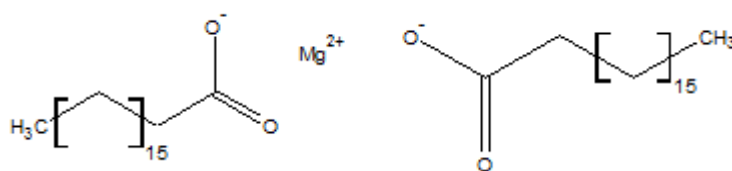


Figure 2.4: Structure of magnesium stearate, $Mg(C_{18}H_{35}O_2)_2$.

MS has wide applicability as a lubricant in the pharmaceutical and other industries and the fact that it is a mixture does not seem to affect its lubricant properties (Sharpe et al (1997)). In tablet formulations MS is added to the powder mix or granule as the last step before tableting. It forms a thin layer on the surface of the particles, preventing adhesion to the metal surfaces of the tableting equipment and tooling. MS is used at a low level, typically 1 %w/w, because of its hydrophobic properties - a too thick layer may retard the dissolution and disintegration of the tablets.

In this work, the MS used was lot U13596 from Aldrich, UK.

2.2.5 Polyvinylpyrrolidone (PVP)

PVP, also known as povidone, is an off-white powder. It is a polymer of N-vinylpyrrolidone, as shown in Figure 2.5. PVP has the general chemical formula of

$(C_6H_9NO)_n$ and different grades are available, with molecular weights ranging from about 10,000 $g\text{mol}^{-1}$ to about 700,000 $g\text{mol}^{-1}$, allowing a range of applications.

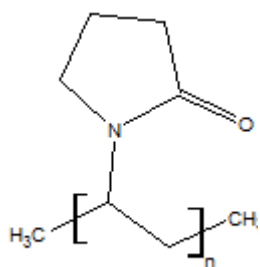


Figure 2.5: Structure of PVP.

PVP has a range of uses in a wide variety of industries, including the pharmaceutical, food and cosmetics industries (Haaf et al (1985)). In tablet formulations, it is used as a wet granulation binder in order to strengthen the granules and ultimately to produce strong, resilient tablets. It is usually added to the dry powder mix as part of the granulation fluid (Rowe et al (2009)).

In this work, the PVP used was lot MKB6069V from Aldrich, UK.

2.2.6 Caffeine

Caffeine is a white, bitter tasting crystalline solid, which is sparingly soluble in cold water, freely soluble in boiling water and slightly soluble in 96 % aqueous ethanol (British Pharmacopoeia (2013)). It is most commonly found in coffee, tea and "energy" drinks. Pharmacologically, it is a central nervous system stimulant and is used to stimulate breathing in pre-term infants (BNF (2013)). It is used widely in compound analgesic preparations with paracetamol and/or aspirin.

The chemical structure of caffeine is shown in Figure 2.6. Its chemical name is 1,3,7-trimethyl-3,7-dihydro-1*H*-purine-2,6-dione (British Pharmacopoeia (2013)) with formula $C_8H_{10}N_4O_2$ and molecular weight 194.2 $g\text{mol}^{-1}$.

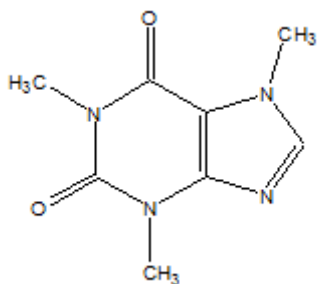


Figure 2.6: Structure of caffeine.

Caffeine has two polymorphs which exist in an enantiotropic relationship. Form II is the low-temperature stable form and Form I is the high-temperature stable form. On heating, Form II will convert to Form I via a sublimation stage (Pinto and Diogo (2006)).

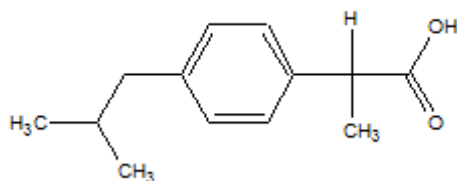
In this work, caffeine Form II was purchased from Acros (UK), lot A0283756, and used as received unless otherwise stated. When Form I was required, a sample of Form II was placed in a covered Petri dish and maintained at 180°C for four hours to allow the conversion to occur following the method of Manduva et al (2008). DSC was performed to check the polymorphic transformation had been achieved.

2.2.7 Ibuprofen

Ibuprofen is a white crystalline solid which is practically insoluble in water but freely soluble in acetone, methanol and methylene chloride. It dissolves in dilute solutions of alkali hydroxides and carbonates (British Pharmacopoeia (2013)). Flowability and compression properties are poor, so ibuprofen usually needs to be granulated (Rasenack and Müller (2002)).

Ibuprofen is a cyclo-oxygenase inhibitor and is used clinically as an analgesic and anti-inflammatory drug (BNF, 2013). It has one chiral carbon which allows two enantiomers to be formed. Ibuprofen is usually formulated as the racemic mixture, but (S)-ibuprofen is the active form. However, *in vivo* an isomerase enzyme can re-arrange the structure of (R)-ibuprofen to form the active (S)-enantiomer (Thomason et al (1998)).

The chemical structure of ibuprofen is shown in Figure 2.16. Its chemical name is (2*RS*)-2-[4-(2-Methylpropyl)phenyl] propanoic acid (British Pharmacopoeia (2013)) with formula C₁₃H₁₈O₂ and molecular weight 206.3 gmol⁻¹.



And enantiomer.

Figure 2.7: Structure of ibuprofen.

In this study, racemic ibuprofen was purchased from BASF (UK). Lot 1B1M687 was used for all the primary analyses and lot 1B1T1575 was used in the mini-tablet production. The two batches were shown to behave identically on DSC and nano-TA.

2.2.8 Anhydrous Theophylline

Theophylline is a white crystalline solid which is slightly soluble in water and sparingly soluble in 96 % aqueous ethanol. It dissolves in solutions of alkali hydroxides, in ammonia and in mineral acids (British Pharmacopoeia (2013)).

Theophylline is a non-selective phosphodiesterase inhibitor used in the treatment of reversible airways obstruction (BNF, 2013). The drug relaxes bronchial smooth muscle and increases heart rate, increasing heart muscle contractility and efficiency. It also increases blood pressure, increases renal blood flow, has anti-inflammatory effects, and has stimulatory effects on the central nervous system. It is derived from xanthine and belongs to the same family of drugs as caffeine and theobromine (Oprea et al (2012)).

The chemical structure of anhydrous theophylline is shown in Figure 2.8. Its chemical name is 1,3-dimethyl-3,7-dihydro-1*H*-purine-2,6-dione (British Pharmacopoeia (2013)) with formula C₇H₈N₄O₂ and molecular weight 180.2 gmol⁻¹. Theophylline can exist in either the anhydrous or monohydrate state, but was used here exclusively in the anhydrous state.

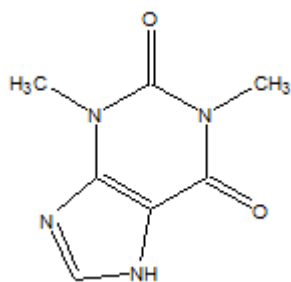


Figure 2.8: Structure of Theophylline.

In this work, theophylline purchased from Sigma (UK), lot 048K0709, was used.

2.2.9 Other drugs

A small study was performed on a range of small molecular weight compounds to investigate some anomalous micro-TA and nano-TA results seen in Chapter 4. The compounds used are detailed in Table 2.1 below.

Compound	Supplier	Lot Number
Ciprofloxacin	Fluka (UK)	0001437014
Phenytoin	Sigma (UK)	121K1518
Piroxicam	Gattefosse (France)	109105A01
Naproxen	Sigma (UK)	078K1629
Tetracycline HCl	Sigma (UK)	0001428858
Flurbiprofen	Sigma (UK)	035K1245
Diclofenac (sodium salt)	Sigma (UK)	96H0737
Tolfenamic acid	Sigma (UK)	047K1628
Fenbufen	Sigma (UK)	048F0508
Sulindac	Sigma (UK)	087K0069
Indometacin	Sigma (UK)	115K0689
Mefenamic acid	Sigma (UK)	090M1623V

Table 2.1: Details of the additional drugs used for the micro-TA and nano-TA investigations.

2.3 Methods

2.3.1 Scanning electron microscopy (SEM) procedures

The SEM used here was a JMS 5900LV (Jeol, Japan). All samples were used in the powder form. A small amount of the sample powder was attached to a sample stub with double-sided adhesive (Agar Scientific, UK). As none of the samples were conductive they had to be coated with a thin layer of conductive material in order to obtain good scans. The sample stubs were placed in a Polaron CC7640 gold sputter coater (Quorum technologies, UK). The average distance of the sample was 50 mm, the plasma current was 20 mA, the voltage applied was 2.1 kV and the samples were coated for 30 seconds. Once coated, the sample was placed in the vacuum chamber of the SEM for the experiment. The experimental conditions were: vacuum of 6×10^{-2} mbar pressure in an argon environment; beam acceleration voltage 20 kV; working distance from sample to detector 10 mm; magnification X 150 to X 3500.

2.3.2 Variable temperature infra-red spectroscopy (VT-IR) procedures

In this study, all samples were analysed on an IFS/66/S FT-IR spectrometer from Bruker Optics (UK) which was equipped with a Golden Gate (ATR) accessory (Specac, UK) (shown in Figure 2.9). In this instrument, there is one reflection of the beam only, but this is compensated for by the beam having a short path length. The samples were placed on the ATR crystal and clamped securely in place to improve contact with the ATR crystal and to remove any trapped air that would distort the results.

The samples were run in a nitrogen environment to reduce interference from the background atmospheric gases. FT-IR spectra were acquired between 4000 cm^{-1} and 550 cm^{-1} with a resolution of 4 cm^{-1} . For each run 32 scans were acquired and co-added for analysis. FT-IR spectra were acquired every 10°C from 30°C to 200°C , which is the temperature limit of this instrument, unless otherwise stated. At each temperature, the sample was allowed to equilibrate for 2 minutes before the scan was taken.

Background scans were performed as for the sample scans, but with an empty sample chamber. It was not possible to take a background scan at elevated temperatures before running the sample at that temperature, as this would have meant opening and closing the

instrument multiple times and the temperature would not have been maintained. Hence, a general "empty cell" background reading was taken at all temperatures in a single run and was subtracted from the sample readings at the appropriate temperatures.



Figure 2.9: An example of a Golden Gate ATR accessory with a thermal top plate.

2.3.3 Differential scanning calorimetry (DSC) procedures

In this study, a Thermal Analysis Q1000 DSC (a heat flux instrument), fitted with a refrigerated cooling system, was used to analyse all samples. The instrument was fully calibrated before use following the manufacturer's recommendations. The Tzero baseline calibrations were performed using an empty cell run then a run with sapphire disks. Temperature calibration was performed using indium (melting point 156.6°C and heat of fusion 28.57 J/g), tin (melting point 231.93°C and heat of fusion 60.6 J/g) and n-octadecane (melting temperature 28.24°C and heat of fusion 238.76 J/g) (values supplied by TA instruments (USA)). The cell constant was calculated using indium.

The experimental procedure was the same for all samples. Aluminium pans were used throughout as they are light, inexpensive and non-reactive so ideal for this type of work. The pans (both sample and reference) were pin-holed in order to allow the release and removal of evaporated gases as the sample was heated. This was particularly important with the samples purporting to be monohydrate, as water vapour would be released as the temperature is increased above 100°C. Nitrogen was used as both the carrier gas to improve thermal transfer between the furnace and the pans, and as the purge gas to remove

evaporated water, oxygen and other materials which could interfere with the detection of sample transitions. The nitrogen flow rates were maintained at 150 mL/minute and 45 mL/minute, respectively. The heating rate was 10°C/minute (unless otherwise stated). No modulation was used in any of the experiments. The start and end temperatures varied dependent on the individual materials and their thermal transitions.

2.3.4 Atomic force microscopy (AFM) and localised thermal analysis (LTA) procedures

Atomic force microscopy (AFM) and localised thermal analysis (LTA) are treated together as related techniques, as LTA is performed using a modified version of the AFM probe.

For this study, two AFM instruments were used: a diCaliber AFM head (Veeco, USA) and an Explorer AFM head (Veeco, USA). Micro-TA analysis was performed on the Explorer (unless stated) and the nano-TA analysis was performed on the diCaliber. Each AFM had a thermal analyser (Anasys Instruments, USA) connected for thermal analysis. The diCaliber was fitted with a Wollaston wire micro-probe (Bruker, UK) and the Explorer with a Thermal leverTM probe mounted on a cantilever 200 µm in length (Anasys Instruments, USA). For the Explorer instrument, the AFM images are presented in terms of deflection and for the diCaliber instrument both the deflection and height were obtained. Micro-TA and nano-TA results are presented as temperature against probe deflection.

The probes were calibrated before use following the manufacturer's recommendations. Polymer discs of materials with well-known melting behaviour were used as the calibrants. As the probes are heated via application of electricity, the primary endpoint, i.e. probe deflection, is recorded as a voltage. The voltage recordings for the melting of the calibrants are then converted to a temperature scale via knowledge of their melting points. This calibration then allows the estimation of the temperature of transition of unknown materials from the voltage readings. The calibrants used were polyethylene terephthalate, polyethylene and polycaprolactone (discs supplied by Anasys Instruments, USA) with an additional reading of the ambient room temperature via a glass thermometer being used as a low temperature calibration point. Figure 2.10 below shows an example of the calibration runs.

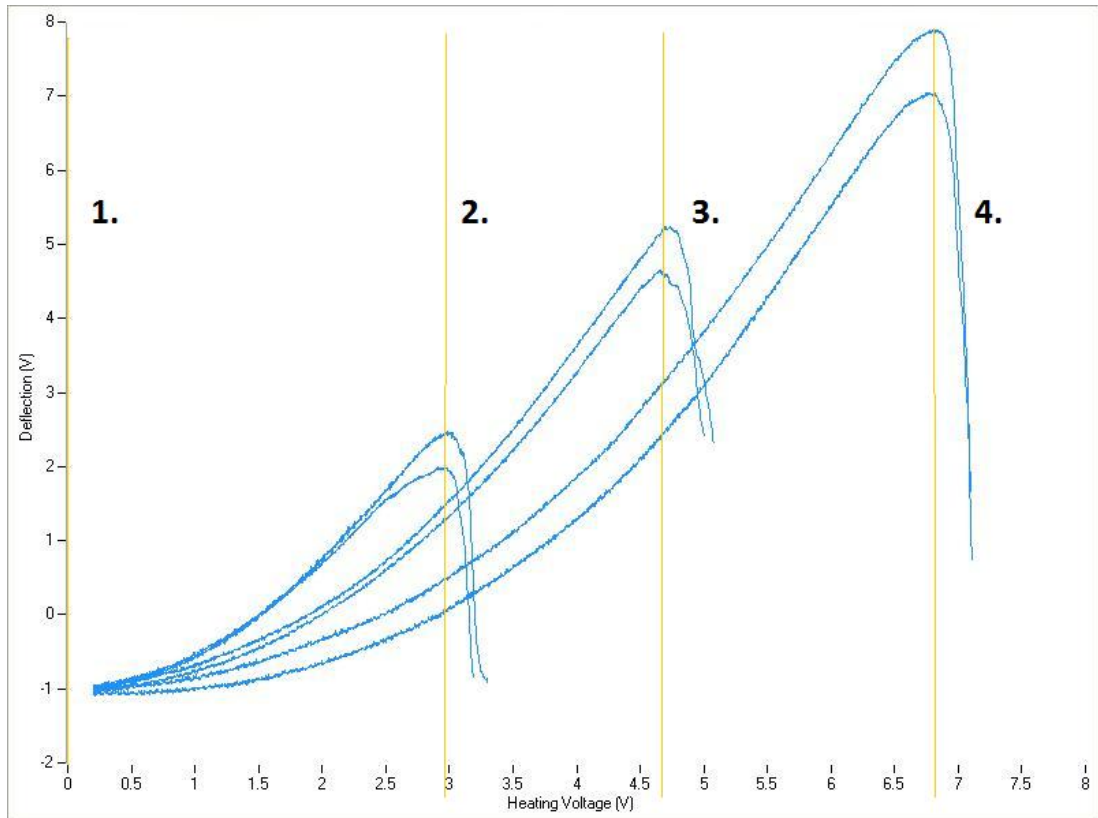


Figure 2.10: An example of the calibration plot of the thermal probes. The blue curves show the actual results for the three standards used with the endpoints highlighted: 2) polycaprolactone, 3) polyethylene and 4) polyethylene terephthalate. Point 1 is the room temperature. The orange lines show the calibration values chosen for each endpoint.

For all samples, an AFM image was generated before micro-TA or nano-TA was conducted. At the start of the experiment, the probe was brought into contact with the sample and the integral parameter of the AFM, which controls the response time of the piezo material to change, was set to 0, enabling the probe to move in the Z direction. The probe was programmed to start heating at room temperature and to stop heating at the maximum temperature of 300°C, unless the experimental endpoint had already been reached (obviously this is dependent on the material under study), at a heating rate of 10°C/second (unless otherwise stated) and a cooling rate of 100°C/second (unless otherwise stated). The rapid heating rate reduced the diffusion of heat to the surrounding sample, ensuring that only the area under the probe is being heated and examined. After each run, the micro-TA probes were heated to 400°C for cleaning and to burn off any

sample residue, but the nano-TA probes were not, as per the manufacturer's recommendations, as they are very delicate and hence easily damaged.

Throughout this work, contact mode was used, as the samples are solid and it was thought that contact mode would be better than tapping mode for the variety of samples and topographies likely to be seen. AFM images are usually presented in terms of "height", reflecting the movement of the scanner in the z plane (up and down) from its set point. An additional recording of the bending of the cantilever may be obtained with some instruments and this is recorded as "deflection".

The topography of the sample is shown by the colour of the map and the bar beside the map shows the colour - height / deflection scale. Low regions in the topography are shown to be dark in colour and high regions are shown to have a lighter colour. The topography bars are scaled by the instrument for each experimental run, so it is important to note that when comparing between different scans, the same colour does not mean the same height or deflection. Figure 2.11 shows an example of an AFM topography map and bar.

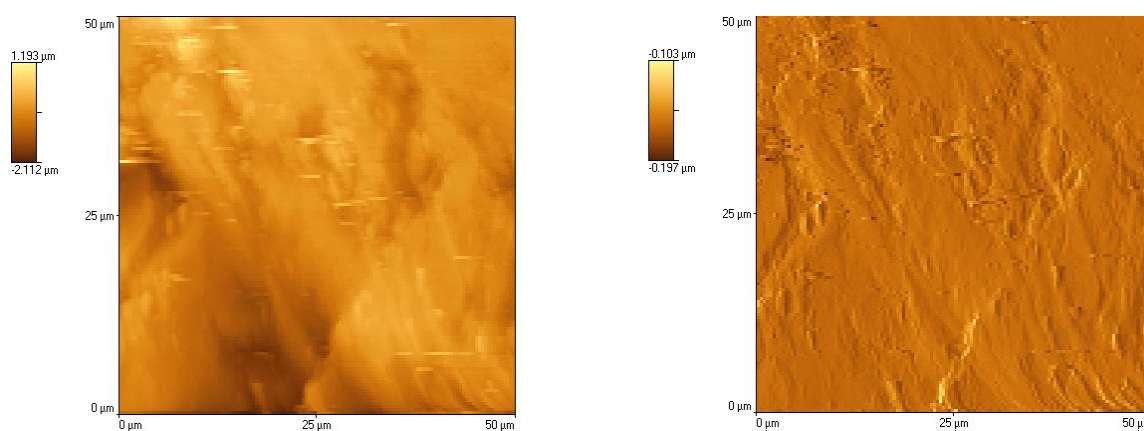


Figure 2.11: An example of the topography map of a sample produced via AFM imaging.

Both micro-TA and nano-TA were performed on all samples. The areas analysed depended on the probes, with regions of 100 μm x 100 μm being examined for the micro probe and 50 μm x 50 μm being investigated with the nano probes. The area scanned is only a very small representation of the whole surface of the sample, so a number of scans were taken across the surface of the sample (the exact number was dependent on the

experiment) to assess the variability of the response. The distance between the repeat scans could not be accurately controlled by the instrument, but was approximately controlled by manually moving the sample on the stage so that a new area was placed under the measurement zone.

Within each scanned area, five micro-TA or nano-TA readings were taken at the four corners and centre of an imaginary square. Some damage to the surface of the sample is always seen in this type of analysis, so these readings had to be far enough away from each other so as not to affect each other by, for example, thermal diffusion from one site to the next. This pattern of five readings seemed to give the best compromise between a set of readings close enough to be regarded as one site, but far enough apart so as not to be mutually interfering. Figure 2.12 shows an example of an AFM scan of an α -lactose monohydrate (α -LM) compact before (A) and after (B) the 5 micro-TA readings were taken, showing the damage caused by the probe. Figure 2.12 C shows the results of the repeated micro-TA results, with the colours of the individual traces being related to the position of the test site shown in Figure 2.12 B. For all micro-TA and nano-TA results, the position numbering and the colour allocated were kept constant, e.g. dark blue was always position 1 in the top left hand corner of the square. The temperature of transition for the LTA is always taken as the top highest point of the curve before the curve has fallen away e.g. for Figure 2.12 C the value would be circa 180°C. The probe has heated the sample enough for a thermal event to happen on the surface which causes the probe to move and sink into the sample. The starting point for the LTA curve is analyst-controlled and varies thought out the project. This is due to the laser alignment in the AFM set up so is not reflective of the materials analysed and does not affect the results. For ease of comparison, the results have been normalised, i.e. moved up or down the y axis, so that each trace starts at the same point.

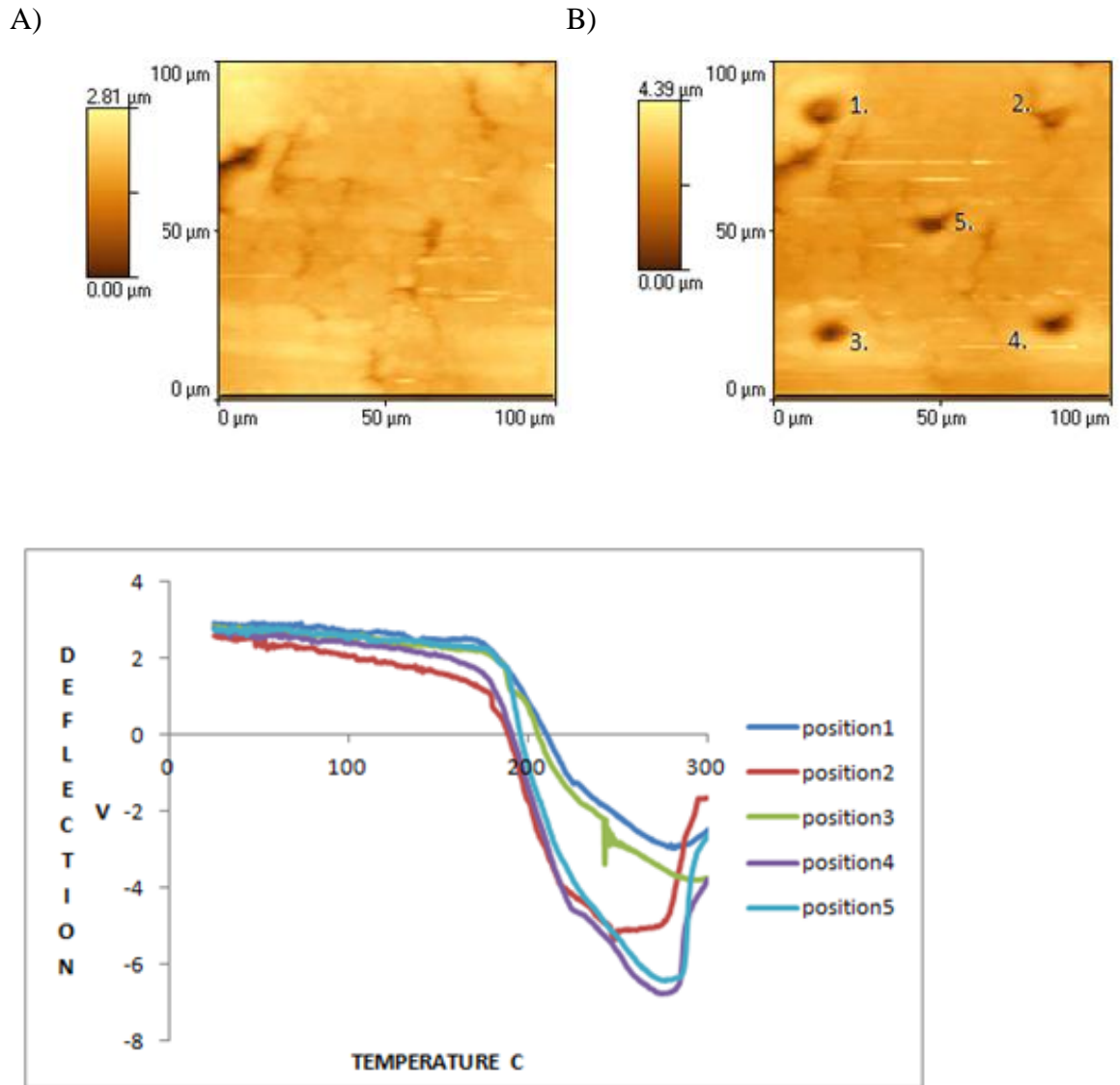


Figure 2.12: An example of the AFM and micro-TA results for an α -LM compact, showing the sites of the multiple micro-TA readings and the damage caused by the Wollaston wire probe. A) AFM scan of an α -LM compact before the micro-TA experiment. B) AFM scan of the same area on the α -LM compact after the micro-TA experiment. C) The results for the five micro-TA readings: dark blue - position 1, red - position 2, green - position 3, purple - position 4, light blue - position 5. The position numbers refer to the positions in image B.

2.3.5 Transition temperature microscopy (TTM) procedures

A Vesta TTM (Anasys Instruments, USA), shown in Figure 2.13, was used for all TTM measurements. A nano probe was used for all the TTM mapping, calibrated as described above for the nano-TA system.



Figure 2.13: The Vesta TTM (Anasys Instruments, USA).

Figure 2.14 shows the optical microscope image of the probe in contact with the sample and the experimental grid to be followed. The blue square is made up of blue crosses, each of which represents a reading which is going to be performed. The readings are started in the top left hand side of the blue square. For most samples (unless otherwise specified), the pattern studied was an 11 x 11 grid, giving 121 readings overall. The individual readings were taken 10 μm apart, leading to an area of interest of 100 μm x 100 μm .

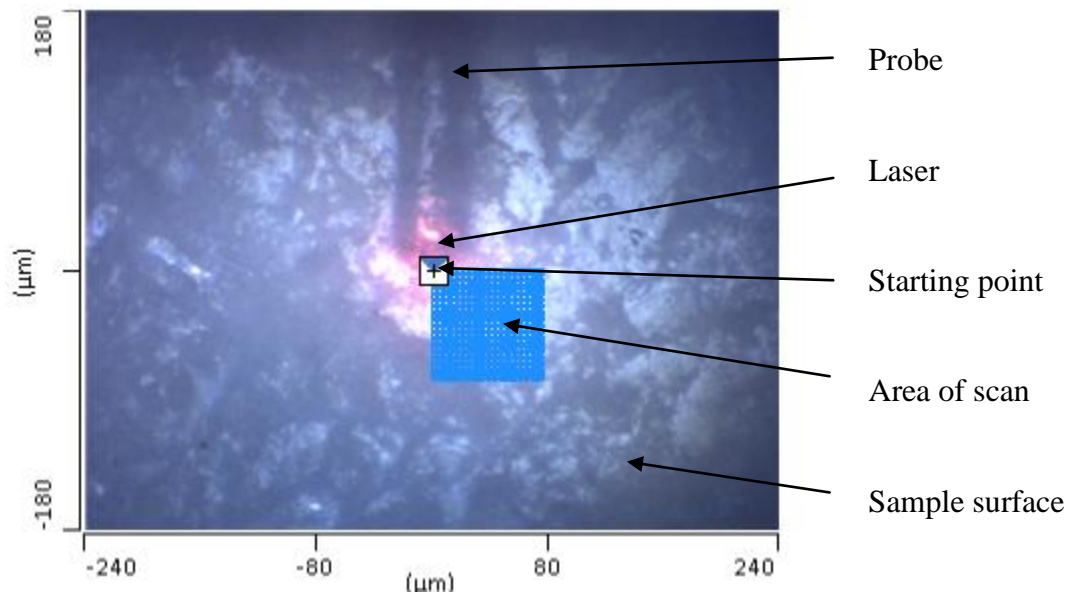


Figure 2.14: An optical image of the TTM probe on the surface of a compact. The blue square is the region scanned and shows each reading in the grid pattern.  denotes the starting point for the scan.

The thermal data were automatically interpreted by the software, unless otherwise stated. Figure 2.15 is an example of a TTM map produced from the analysis of a two-component compact. Each square represents one reading from the grid pattern discussed above. In Figure 2.15 two points are highlighted by crosses on the map, representing the two different components. The corresponding nano-TA results for these two points are also shown illustrating their different responses. The pink square shows a nano-TA response of circa 150°C which is then read off the temperature-colour scale bar beside the map, giving the square its pink colour. The orange square has a nano-TA response of circa 220°C which is then read off the temperature-colour scale bar and the orange colour is allocated. The process is repeated where the temperature of each of the TA results is allocated a colour and a coloured map is produced, with discrete pixels relating to each point of measurement. The software then blends the colours to give an interpolated map (Figure 2.15 C).

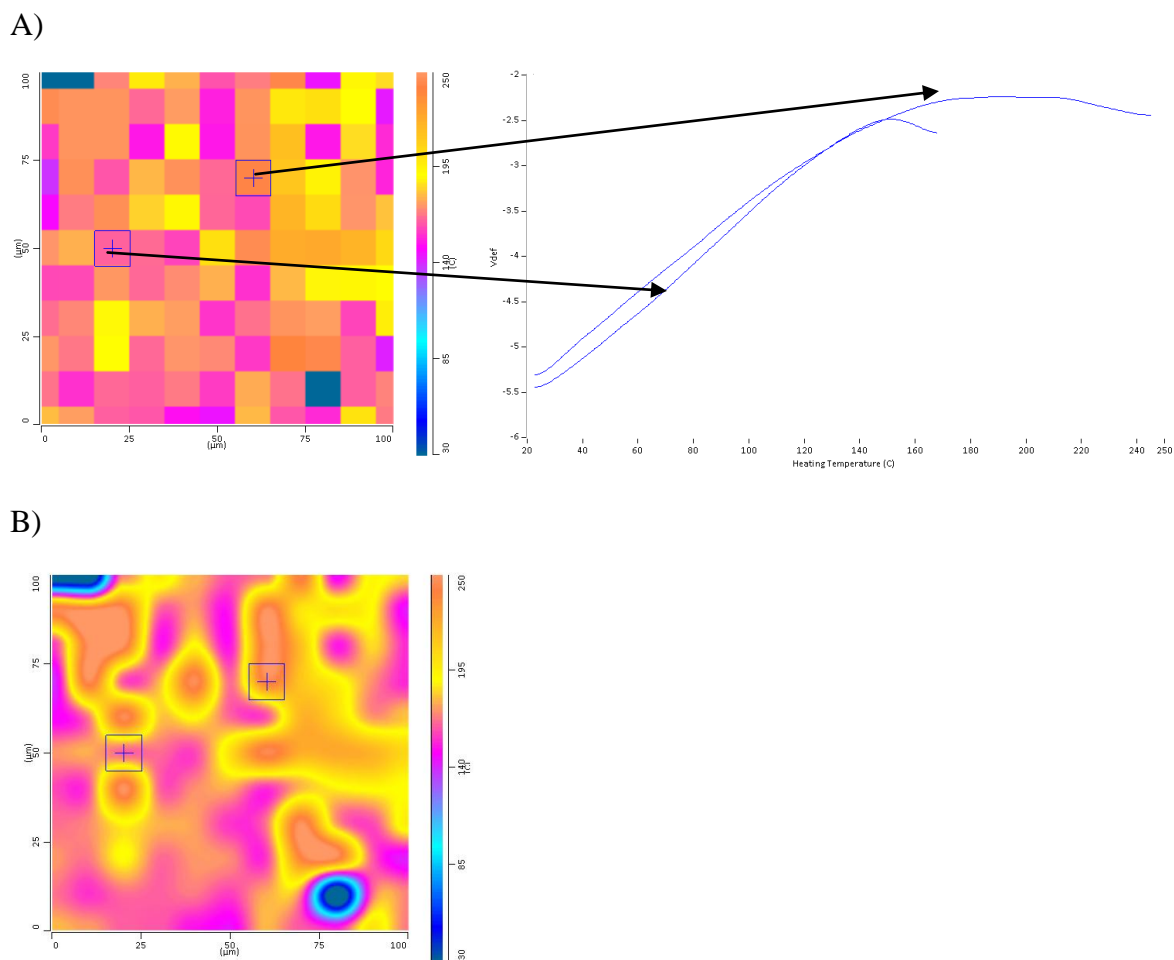


Figure 2.15: An example of TTM mapping of a two-component compact. A) The discrete map and the corresponding nano-TA results for the two squares highlighted. B) The interpolated (smoothed) map for the same data generated by the software.

2.3.6 Raman microspectroscopy procedures

In this project a Horiba Jobin Yvon LabRam Aramis Raman microscope was employed to analyse the samples. The instrument parameters were kept the same throughout, described as follows. A 785 nm diode laser was used with no filter. The confocal hole was selected as 400 μm and the slit as 100 μm. The spectrometer grating was selected as 999.946 cm⁻¹. The microscope objective lens was selected as X50 Fluorescence. Each reading was taken over 5 seconds in order to obtain a good spectrum. Two spectra were taken at each point and averaged. The instrument was calibrated by sucrose. From a reference spectrum of each component, a peak was selected to represent each component and overlap was kept to a minimum when selecting a peak which lead to degree of error which is discussed in chapter 7.

2.3.7 Production of compacts

For the surface analysis, flat compacts of the individual and mixed components were required. If necessary, powders were mixed in the appropriate ratios using a mortar and pestle. Samples were then compacted using an IR press (Specac, UK): 400 mg of powder was compacted at 2 tons pressure for 30 seconds to give a 13 mm flat compact. Some samples were additionally compacted at 10 tons pressure, as indicated in the text.

2.3.8 Production of mini-tablets

2.3.8.1 Wet granulation procedures

The formulations used here were based on a standard recipe used within the research group. A relatively low level of drug (10 %w/w) was used to ensure that the mini-tablets studied here had a wide range of components and to challenge the techniques maximally. α -Lactose monohydrate (α -LM) was used as a diluent and to provide strength to the tablets, microcrystalline cellulose (MCC) was used as a compression aid, pre-gelatinised starch (PGS) was used as a binder and disintegrant, polyvinylpyrrolidone (PVP) was used as a binder, water was used to produce the granulation solvent and magnesium stearate was used as a lubricant. PVP was dissolved in water to give a 15 %w/v solution, with a defined volume being used for each run to ensure that the same amount of PVP was added to each batch. Additional water was used as necessary to ensure that the granulation endpoint was reached. The exact formulations are detailed in Chapter 6. The manufacturing process used for the wet granulation stage is detailed in Table 2.2 below. For the development batches the total batch size was 750 g and for the experimental batches it was 100 g. The mixer used was a domestic Kenwood chef (UK), fitted with a K blade.

Method stage	Time (minutes)	Mixing speed
<p>Powder loading into the mixer.</p> <p>Half the α-LM, MCC and PGS, followed by the drug (if used), then the remaining half of the α-LM, MCC and PGS, i.e. the drug is sandwiched between the other ingredients.</p>		
Dry mixing (1).	1	Low
Dry mixing (2).	2	Medium
<p>Addition of granulation fluid whilst mixing.</p> <p>This was a 15 % w/v PVP aqueous solution.</p>	1	Low
Granulation.	2	Medium
Addition of extra water as required.	1	Medium
Granulation.	1	Medium
<p>Wet sieving.</p> <p>Through a 500 μm sieve.</p>		
<p>Drying.</p> <p>Tray drying at 40°C in the oven.</p>	Overnight	
<p>Loss on drying test to assess residual moisture content.</p> <p>1g of sample at 105°C for 15 minutes.</p>	15	
<p>Dry sieving.</p> <p>Through a 500 μm sieve.</p>		
<p>Lubrication.</p> <p>Magnesium stearate was added.</p>	1	Low
<p>Final sieving.</p> <p>Through 500 μm and 150 μm sieves. Granules between these two sizes were used.</p>		

Table 2.2: The wet granulation process used here.

2.3.8.2 Tableting procedures

A Piccola rotary tablet press (Riva, Argentina) was used to compress the tablets in this study. This is fitted with four B and four D stations, although the D stations were blanked off and only the B stations were used. The tooling used was 2 mm normal concave plain punches supplied by Adamus (Poland). Figure 2.16 shows a photograph of this tooling.

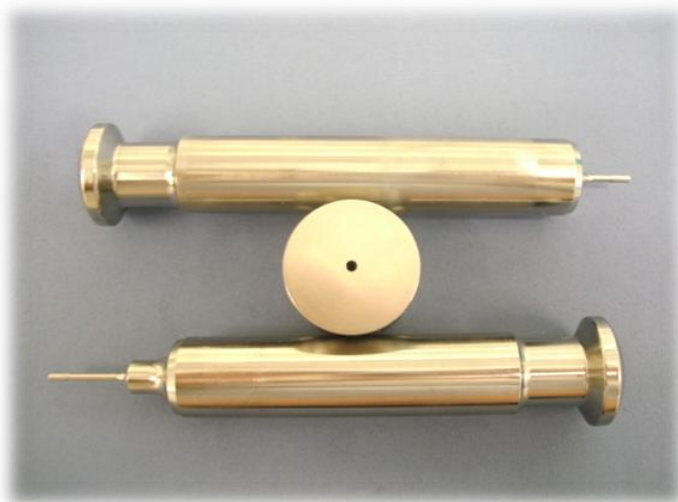


Figure 2.16: Photograph of a set of the 2 mm normal concave tooling used in this study. Top - upper punch, middle - die and bottom - lower punch.

In this study, either two or three tooling stations were used. The Piccola press was set with a 6 mm cam, allowing a fill depth of approximately 5 mm. Usually on the Piccola, after the die is filled, the lower punch is pulled down slightly to allow the powder or granule within the die to settle before compression. This wasn't possible here, as the small size of the punch and the design of the die meant that this was cause the material in the die to fall out, leading to issues of tablet reproducibility and machine seizure. This feature was therefore disabled. The feeder speed was maintained at circa 30 rpm. The turret speed was varied between 12 rpm for the initial batches and 30 rpm for the later batches. A small amount of pre-compression was applied to all batches. The main compaction pressure was maintained at approximately 1.2 kN. Details for the individual batches are given in Chapter 6.

To avoid effects of external factors such as temperature and humidity (Augsburger and Hoag (2008)), the main tablet batches used in Chapter 6 were produced on the same day, one immediately after the other.

2.3.9 Mini-tablet characterisation

2.3.9.1 Weight uniformity

The weight of the mini-tablets is circa 10 mg, so falls below the BP 2013 limit for the requirement of assessment of weight uniformity - content uniformity is recommended instead. However, weight uniformity was performed in accordance with the BP 2013 process for larger tablets.

For each batch, 20 tablets were individually weighed on a Mettler Toledo XS205 5-figure balance (Switzerland). The mean weight, standard deviation, and relative standard deviation, maximum and minimum were calculated and the results compared to the pharmacopoeial specification. For uncoated tablets of less than 80 mg weight, the BP 2013 specification is that the weight of no more than two of the tablets deviates by more than 10 % of the mean value and none of the tablets deviate by more than 20 % of the mean weight.

2.3.9.2 Hardness

Hardness is the (wrong) colloquial term used in the pharmaceutical industry to denote resistance to diametral crushing of tablets and has been used here as it is the term that most people are familiar with. Harder tablets will be more resistant to handling and further processing, but excess hardness will lead to extended dissolution times, so there is a balance to be struck for each formulation between these competing requirements. As mini-tablets are so small, the forces required to crush them are correspondingly small and are below the recording / detection limit of the tablet hardness equipment conventionally used to assess larger tablets. Here, a texture analyser was used to measure the crushing strength of the mini-tablets, following the general method described by Choonara et al (2006). In this case, the mini-tablet is placed on a fixed platform and a probe descends vertically to the tablet, making contact and continuing to move downwards. The force required to break the mini-tablet is then recorded. A TA.XT plus Texture Analyzer (Stable Micro Systems, UK) was used with a 11.6 mm diameter Perspex cylinder probe and the experimental parameters listed in Table 2.3. The mini-tablets were placed on their side during the test in order to mimic as closely as possible the standard BP method of diametral compression. The experimental set-up is shown in Figure 2.17.

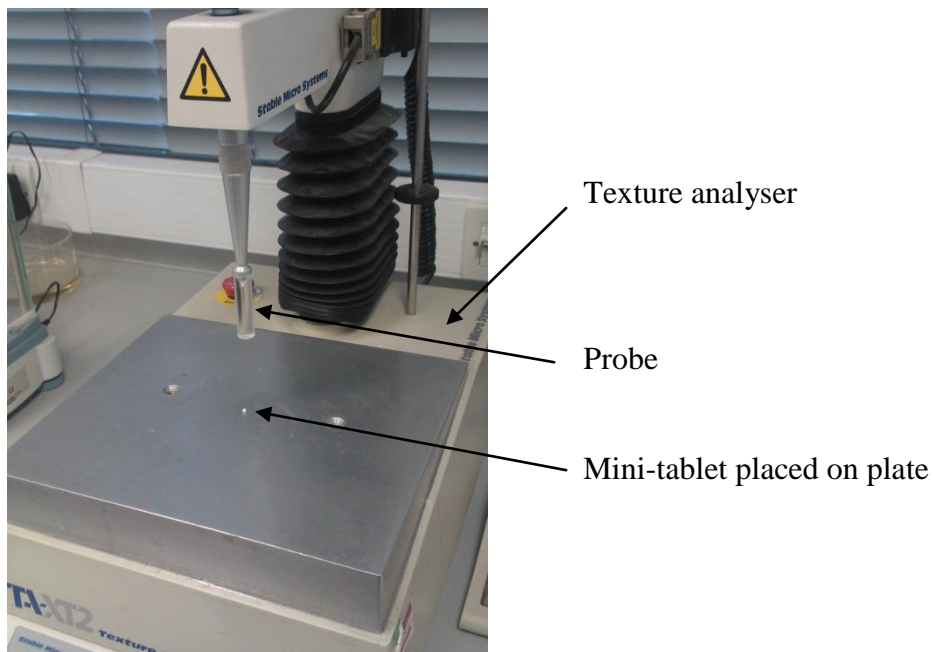


Figure 2.17: The texture analyser set up used to measure the hardness of the mini-tablets.

Test Parameters	Settings
Pre-test speed (mm/s)	1.000
Test speed (mm/s)	0.100
Post-test speed (mm/s)	1.000
Compressive distance (mm)	1.000
Trigger force (N)	0.050

Table 2.3: The instrument parameters for testing the hardness of the mini-tablets.

The hardness results were then used to calculate the tensile strength of the tablets. Hardness is dependent on the geometry of the sample as well as its material composition, whereas tensile strength calculations take this into account and therefore enables easier comparison between batches. Details and example calculations are given in Chapter 6.

2.3.9.3 Thickness

The thickness of tablets is generally measured manually using callipers. However, due to the small size and handling issues of the mini-tablets, an optical microscopy process was used, whereby images of the mini-tablets were recorded and analysed via the inbuilt software. The microscope used was a Leica MZ7.5 microscope (Leica, Germany).

2.3.9.4 Friability

Friability is a measure of the robustness of tablet formulations. Tablets are subjected to mechanical trauma, by being rotated in a drum, and the weight loss during this process measured. A low (or zero) friability value is desired, although the BP 2013 specification at a maximum of 1 % weight loss is very high.

Figure 2.18 shows the schematic diagram of the BP 2013 friability apparatus. The BP 2013 does not specifically consider mini-tablets, so a range of experimental conditions were used. Tablets were dusted, weighed, rotated in the drum of the Erweka tarA friability instrument for 4 minutes at 25 revolutions per minute rpm, then de-dusted, re-weighed and the weight loss calculated. The results and the limitations of this approach are discussed in Chapter 6.

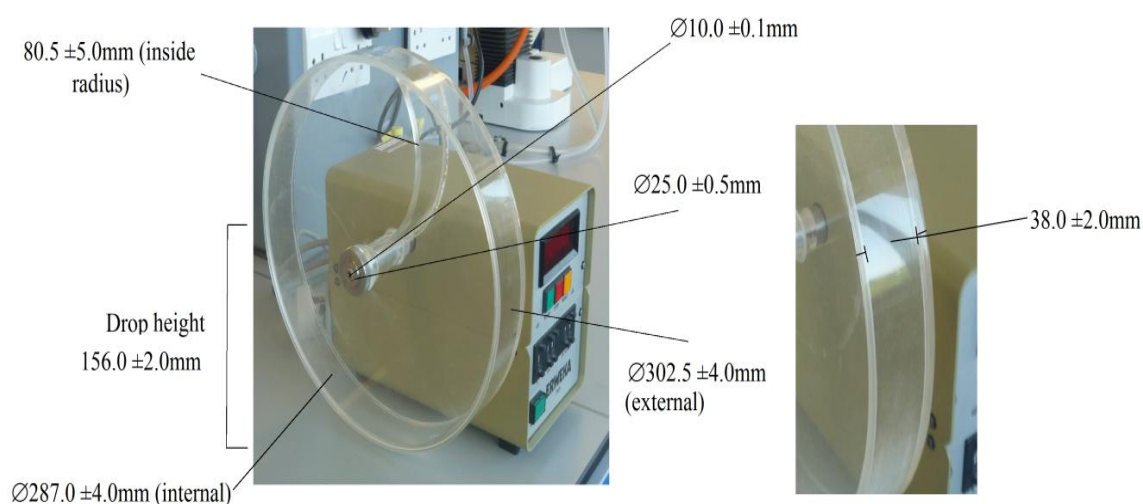


Figure 2.18: Image of the friability tester (measurement parameters taken from the British Pharmacopoeia 2013).

2.3.9.5 Content uniformity assessment of the drug-loaded mini-tablets

A simple UV-visible spectrophotometric method of analysis was developed to assess the content uniformity of the drug-loaded mini-tablets. For each batch of mini-tablets, 10 individual mini-tablets were tested. Each tablet was dispersed in the relevant solvent to extract the drug (0.1 M NaOH for ibuprofen and 0.1 M HCl for caffeine). The sample was filtered, made up to a 200 mL and then assayed in duplicate at $\lambda = 224$ nm for ibuprofen and $\lambda = 272$ nm for caffeine. For each drug, two standard solutions were prepared at the target concentration of the drug in the test solutions. Both of the standard solutions were tested to confirm reliability of the data. During the actual analysis, the standard solution bracketed every five test solutions. Test solutions from two excipients-only mini-tablets were prepared and tested to ascertain whether there was any interference from the excipients in the assay.

The batches of ibuprofen (BASF, lot 1B1T1575) and caffeine (Acros, UK, lot A0283756) used here for the content uniformity analysis were the same as used to produce the mini-tablets. Sodium hydroxide and hydrochloric acid were supplied by Fisher (UK) - lots 1225332 and 0946938, respectively.

The content of drug in the test solutions was determined by reference to the control solutions and used to calculate the content of drug in the mini-tablets.

Chapter 3

**A physico-chemical profile of each excipient used
in the formulations**

CHAPTER 3

A physico-chemical profile of each excipient used in the formulations

3.1 Introduction

The main aim of this thesis was to examine the use of a range of conventional and novel analytical techniques in the characterisation of mini-tablets. In particular, the spatial separation of the ingredients across the surface of the mini-tablets was of interest. Prior to studying a full mini-tablet formulation, the five excipients that were used in the formulation were examined individually to establish an analytical profile which could then be used as a basis for the analysis of the mini-tablet formulations. The same techniques were used for all samples, so that the results of the individual components could be used to assess the ability of the techniques to distinguish between materials in the more complicated, multi-component systems. Scanning electron microscopy (SEM), variable temperature infra-red spectroscopy (VT-IR), differential scanning calorimetry (DSC), atomic force microscopy (AFM), micro-thermal analysis (micro-TA), nano-thermal analysis (nano-TA) and transition temperature mapping (TTM) were performed on each excipient, using the methodology described in Chapter 2. SEM was conducted to examine the particle shape and to estimate the particle size of the powders, because of the potential effect that these parameters may have on the granulation process and on the flow properties and the compression behaviour of the formulated powders. VT-IR was performed to examine the effect of temperature on the compound and to help interpret other experimental results. Any thermal events, such as dehydration, melting or a solid-state transition, were examined by DSC. The DSC data were used to support the understanding of micro-TA and nano-TA results. An image of the topography was gained by AFM to examine any distinguishing features for each compound. Micro-TA and nano-TA were performed to gain a thermal profile of each component, which should in more complicated systems allow identification of individual components. TTM was also conducted on each individual component to build up a multi-point map and to compare the technique to nano-TA.

3.2 Materials and Methods

The five excipients studied in this chapter were microcrystalline cellulose (MCC, Avicel PH101), pre-gelatinised starch (PGS, Starch 1500), magnesium stearate (MS), α -lactose monohydrate (α -LM), and polyvinylpyrrolidone (PVP). Details of their chemical and physical properties are given in Chapter 2. Background explanations of the theory of each analytical technique are given in Chapter 1, with the standard experimental protocols used throughout this work being detailed in Chapter 2.

3.3 Results and Discussion

3.3.1 Microcrystalline Cellulose (MCC)

3.3.1.1 SEM

Figure 3.1 A and B shows SEM images of MCC at magnifications of 250 and 1000. The particles are irregular in size and shape, but are generally elongated and have an estimated size range (longest axis) of 25 to 250 μm . This is in broad agreement with the stated mean particle size of 50 μm (Rowe et al (2009) and www.fmcbiopolymer.com). Figure 3.1 B shows that the surface is very rough with a flaky appearance.

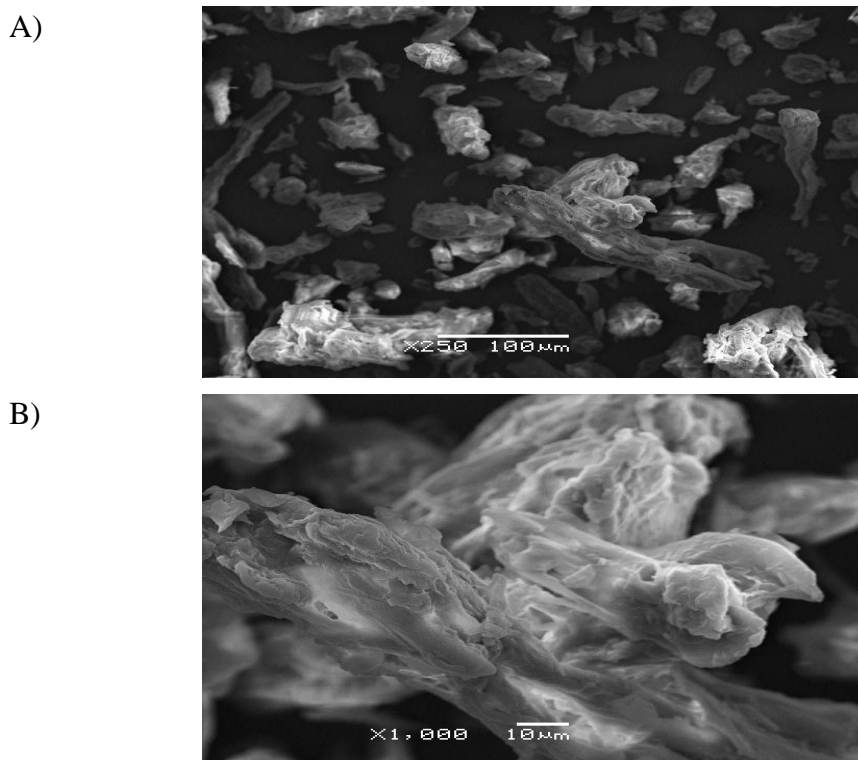
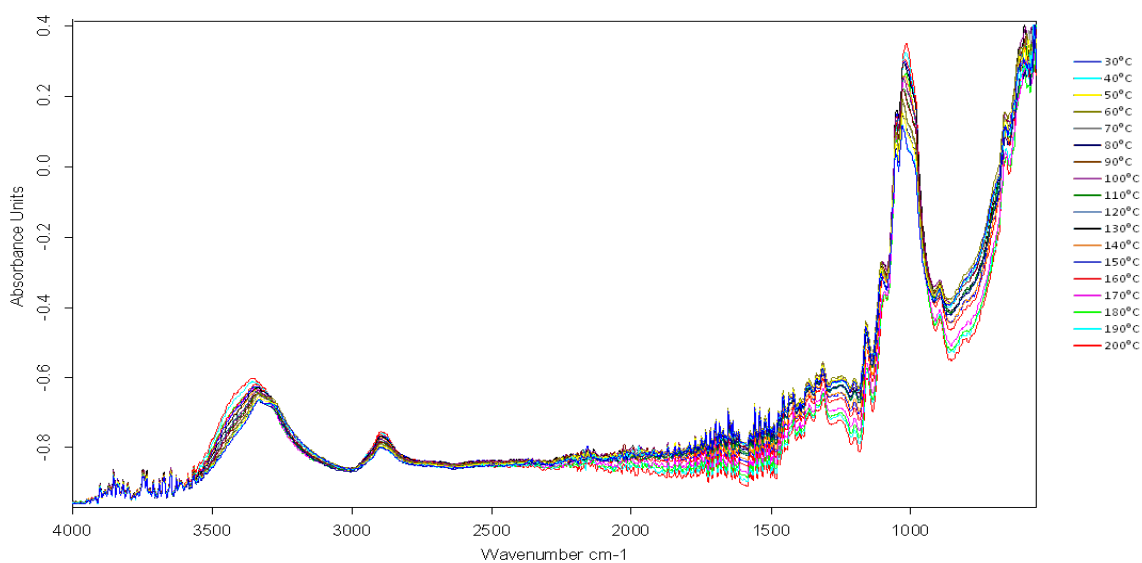


Figure 3.1: SEM image of MCC. A) magnification X250, B) magnification X1000.

3.3.1.2 VT-IR

An IR scan was taken at 10°C intervals from 30°C to 200°C. Figure 3.2 A and B shows a superimposition of all temperature scans (A) and a summary of the lowest and highest temperatures studied (B). It can be seen that any changes with temperature are very gradual, i.e. there are no major thermal transitions. A clear broad large peak is observed at 3300 to 3400 cm^{-1} ascribed to H-bonded stretching of the -OH group. This is expected as MCC contains numerous hydroxyl groups in the cellulose backbone and also has approximately 5 % loosely adhered water (Watanabe et al (2006)). This peak broadens as the temperature increases, which may be explained by the loss of the loosely adhered water above 100°C, changes in the hydrogen-bonding arrangements of the cellulosic hydroxyl groups at higher temperatures, and the general increased molecular mobility to be expected at higher temperatures. The peak at approximately 2900 cm^{-1} , assigned to C-H stretching along the cellulosic backbone, appears to become smoother as the temperature increases and loses its fine structure, which may be a consequence of the increased molecular mobility at higher temperatures. A similar observation can be made for the band at 1300 to 1400 cm^{-1} due to C-H bending and wagging. The expected peak at circa 1700 cm^{-1} due to C-O stretching was not observed; however, this is within the region of noise ascribed to the effects of atmospheric gases within the experimental system. Finally, the O-C-O band at 1030 cm^{-1} shows only limited change with temperature.

A)



B)

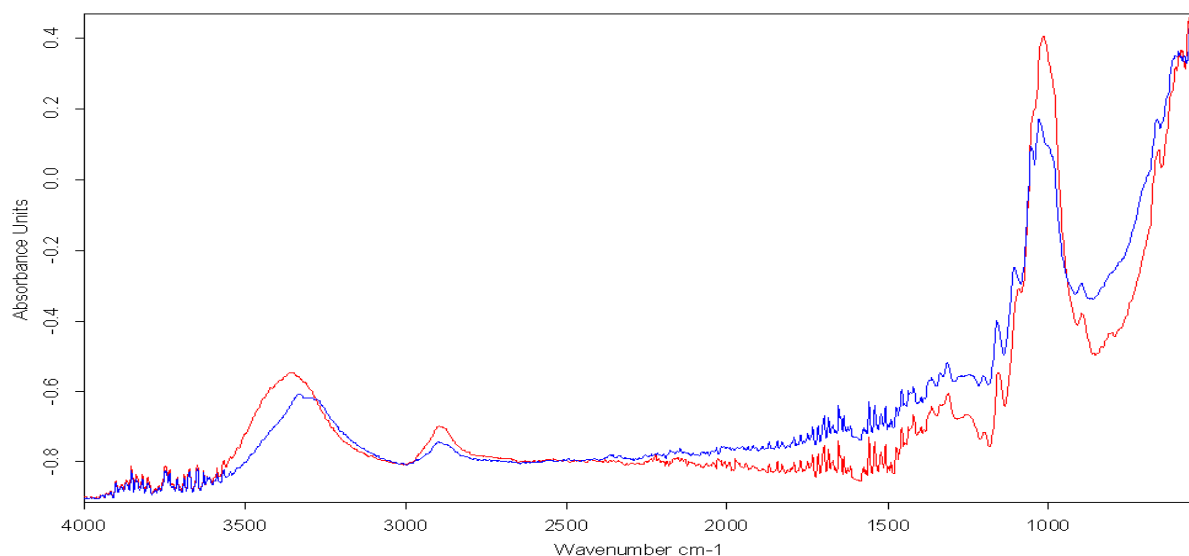


Figure 3.2: FT-IR spectra for MCC between the temperatures of 30°C and 200°C. A) all scans at 10°C intervals, B) the results for 30°C (blue) and 200°C (red).

3.3.1.3 DSC

The DSC traces for MCC as loose powder and mini-tablets are shown in Figure 3.3 in red and blue, respectively. A similar profile is observed for the two samples, with a broad loosely-adhered water loss peak being observed, centred at circa 89°C and 102°C, respectively. Interestingly, the water loss for the compacted MCC occurred at a higher temperature and appeared to require greater energy input than was observed with the powdered MCC. This is most probably explained by the slower penetration of heat into the sample and slower escape of water vapour out of the sample. At temperatures greater than 300°C, both endothermic and exothermic processes are observed in the powder sample, which are assigned to sample degradation. To prevent damage to the DSC furnace, further studies on pure MCC were terminated at 250°C. These results suggest that compaction had no effect on the thermal behaviour of MCC.

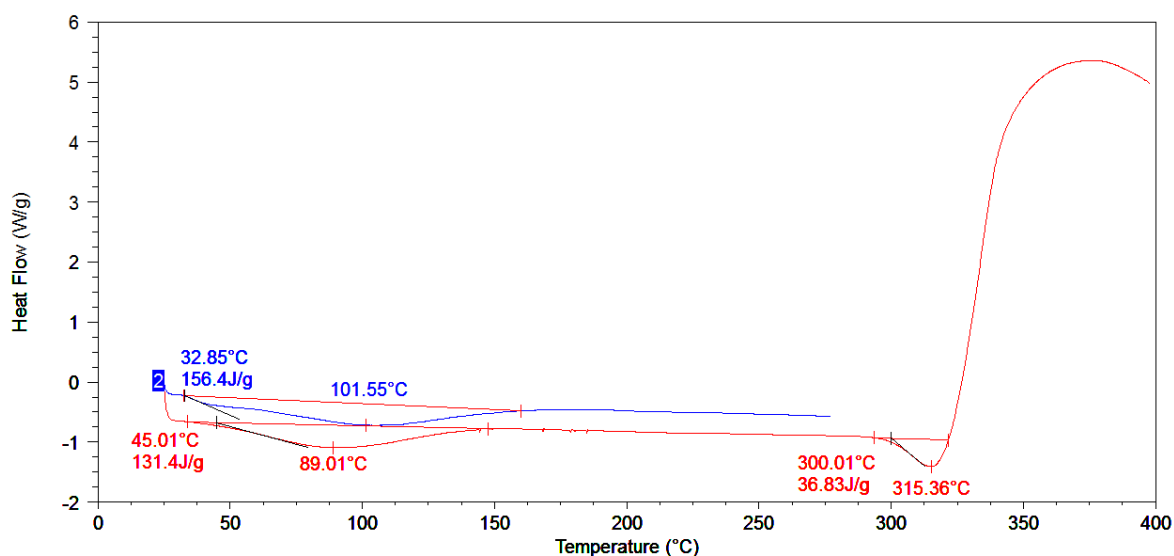


Figure 3.3: DSC trace of MCC powder (red) and MCC mini-tablet (Blue).

3.3.1.4 AFM

In this part of the work, only surface topography was investigated. The topographical AFM images of areas of 100 μm x 100 μm generated using a Wollaston wire probe (the "micro" probe) are shown in Figure 3.4. Column 1 shows the top surface of a representative compact, with six images (A to F) from sites across the radius of the compact, from the outside to the centre. Column 2 shows a similar set of images from the bottom of a representative compact. There were no obvious topographical features in any of the MCC compacts studied and the surface is relatively smooth. The only differences between the top and bottom surfaces of the compacts is the slight imprint from the punches which can be seen on the top of the compact. There was no difference across the surface from the edge to the middle.

The micro probe is relatively large and robust, so can withstand reasonably rough surfaces; it was therefore ideal for generating a preliminary profile of the excipient, but for a greater resolution a similar exercise was performed using a nano probe. Figure 3.5 shows the topographical images of a 50 μm x 50 μm region using a nano-probe across the top of an MCC compact and the three images are representative of positions across the radius of the compact from the outside to the centre. There were no obvious features of the compacts or across the surface from the edge to the middle.

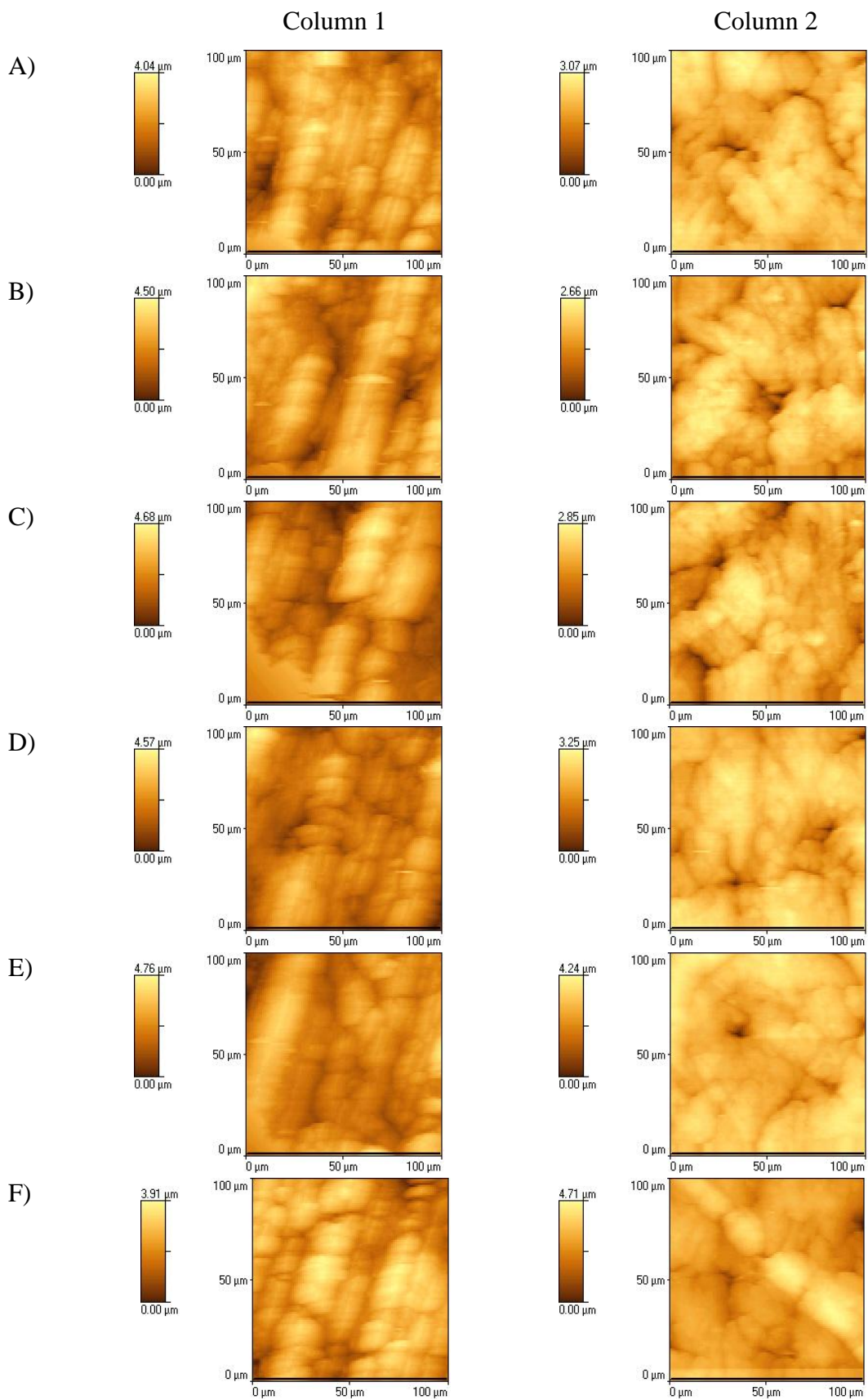


Figure 3.4: AFM scans showing the topography (as height) of the MCC compacts using a Wollaston wire (micro) probe. Column 1 - top of the compact, column 2 - bottom of the compact; position on the radius of the compact is given from A) edge to F) middle.

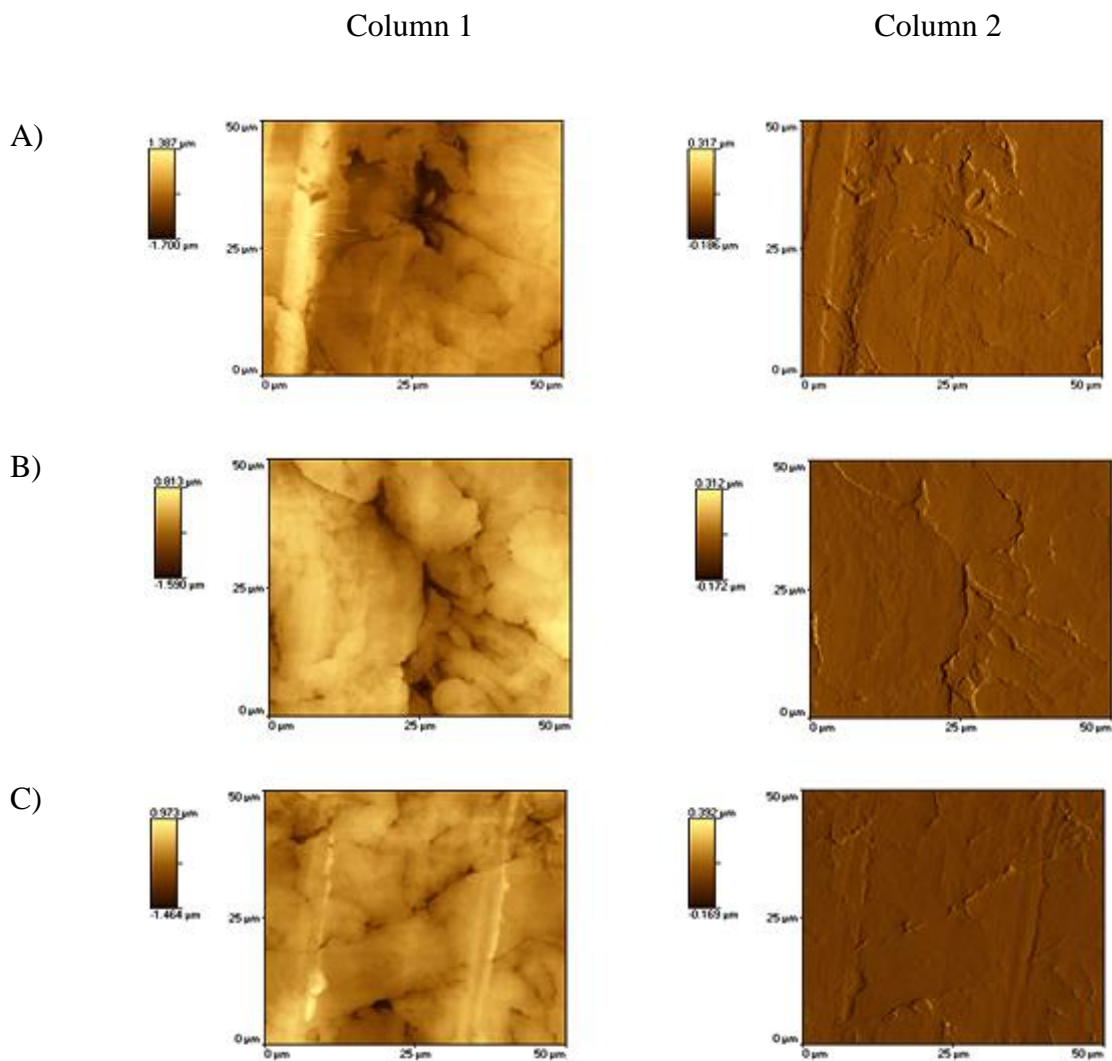


Figure 3.5: AFM scans showing the topography of the MCC compacts using a nano probe. Column 1 - height, column 2 - deflection of the probe; position on the radius of the compact is given from A) edge to C) middle.

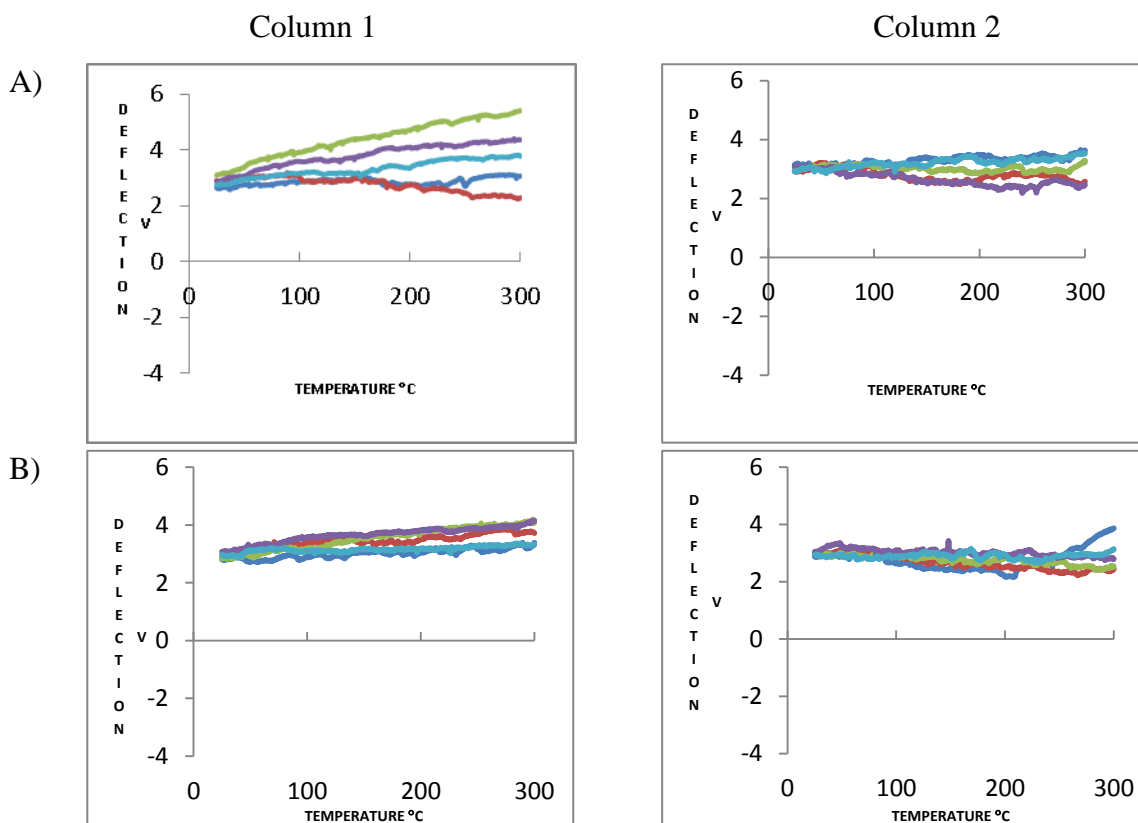
3.3.1.5 Micro-TA

Micro-TA was performed in the same manner as the AFM experiments, i.e. across the radius of both the top and bottom surfaces of the compacts. The results are shown in Figure 3.6. Column 1 shows the top surface of a representative compact, with six images (A to F) from positions across the radius of the compact, from the outside to the centre. Column 2 shows a similar set of images from the bottom of a representative compact.

There were no obvious thermal features in any of the MCC compacts studied and no differences between the top and bottom surfaces of the compacts or across the surface from

the edge to the middle. This lack of thermal events is compatible with the DSC results whereby the only transition observed was a water loss peak. The most plausible explanation of the inability of the micro-TA technique to observe the water loss peak is that it is not sensitive enough to detect such a small transition, given the relatively noisy background.

Experimentally, the micro-TA results are presented as a diagram of the position (deflection) of the probe against temperature and any thermal events which cause softening of the surface, e.g. melting or glass transitions, will result in a deflection of the probe at that temperature. In addition, there will be generalised thermal expansion of the surface, so the probe position will change slightly even in the absence of any detectable thermal transitions. This can be seen as either a positive or slightly negative incline. Some baseline noise was observed, which is probably a reflection of the limit of detection of probe movement in this technique: effectively, all that is being observed for this sample is background noise. As the sample is so thermally stable, no transitions are observed and the probe movement due to thermal expansion or background noise is not "hidden" by obvious thermal events, hence the baseline appears rougher. Interestingly, the background noise was reduced when a compact of MCC was produced using a pressure of 10 tons, presumably attributable to the slightly smoother surface resulting from the higher compaction force (see Figure 3.7).



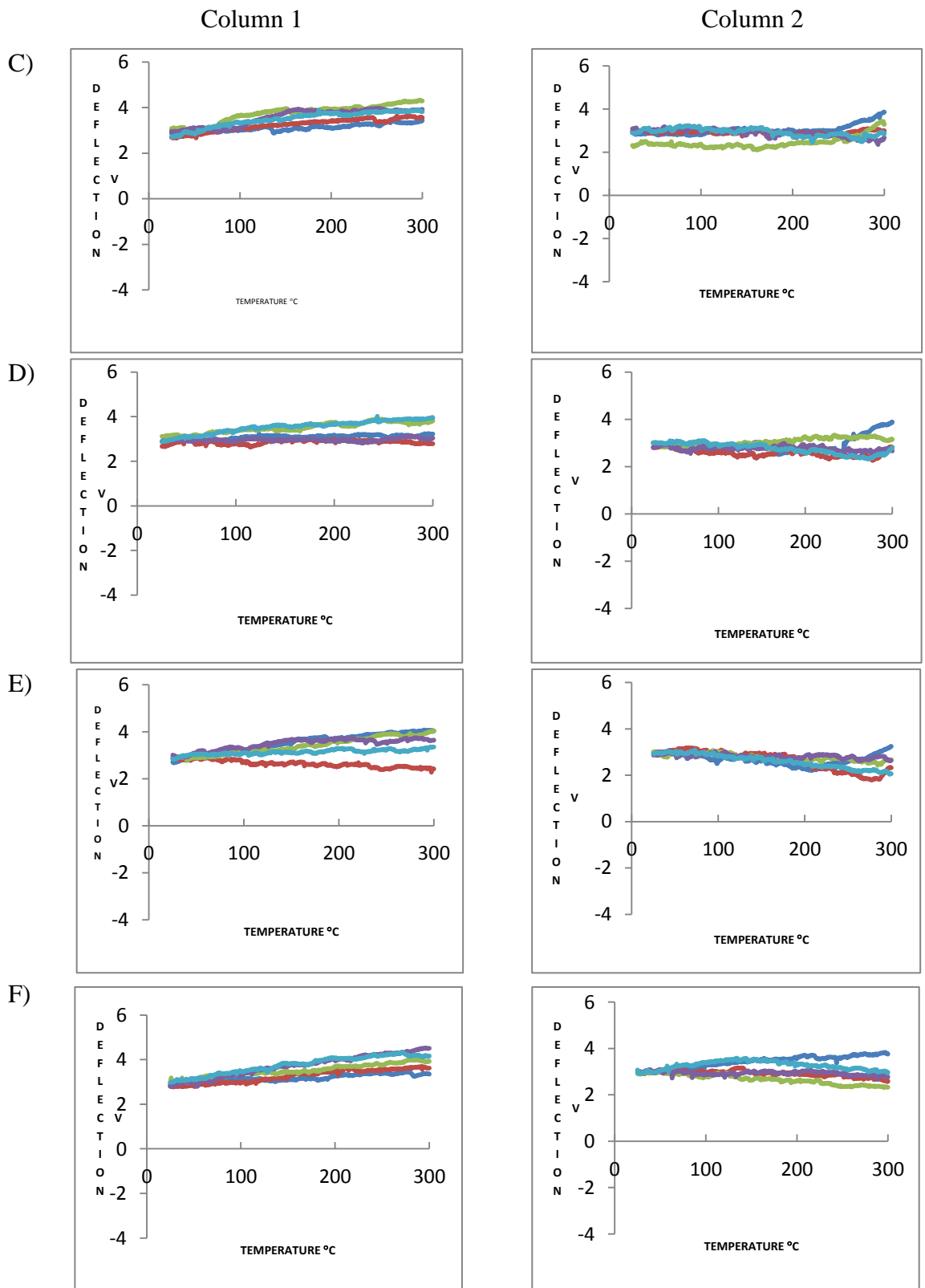


Figure 3.6: Micro-TA results of MCC compacts (compressed to 2 tons for 30 seconds), using a Wollaston wire probe. Column 1 - top of the compact, column 2 - bottom of the compact; position on the radius of the compact is given by A) edge to F) middle. Five micro-TA readings were taken at each position: dark blue - site 1, red - site 2, green - site 3, purple - site 4, light blue - site 5.

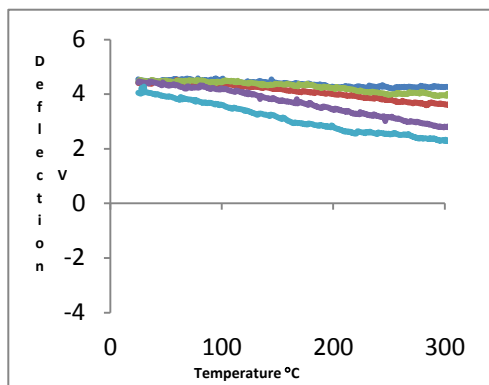


Figure 3.7: An example of micro-TA analysis of compact of MCC compressed at 10 tons, showing smoother traces than seen in Figure 3.6.

3.3.1.6 Nano-TA

Nano-TA was performed in the same manner as the AFM experiments, i.e. across the radius of the surfaces of the compacts. The results are shown in Figure 3.8 for three scans across the radius of the compact.

There were no obvious thermal features in any of the MCC compacts studied and no differences across the surface from the edge to the middle. This lack of thermal events is compatible with both the DSC results, whereby the only transition observed was a water loss peak, and the micro-TA results, where again no obvious thermal features were observed. As with micro-TA, it can be assumed that the nano-TA technique is not sensitive enough to detect such a small transition as the water loss.

Again like the micro-TA results, the nano-TA results show both a positive and negative deflection, probably due to the same reason, i.e. the probe moves slightly on the surface due to generalised thermal expansion, but because the sample is so thermally stable, no transitions are observed and the probe movement due to thermal expansion is not "hidden" by obvious thermal events. In some scans for the MCC compacts, a distinct V shape (Figure 3.9) was observed. As MCC is so thermally stable, as indicated by the other techniques, this is most likely not a reflection of a true thermal event, but more an indication of probe movement. As the probe increases in temperature it bends slightly and lifts from the surface and then it makes contact again at the point of the V-shape.

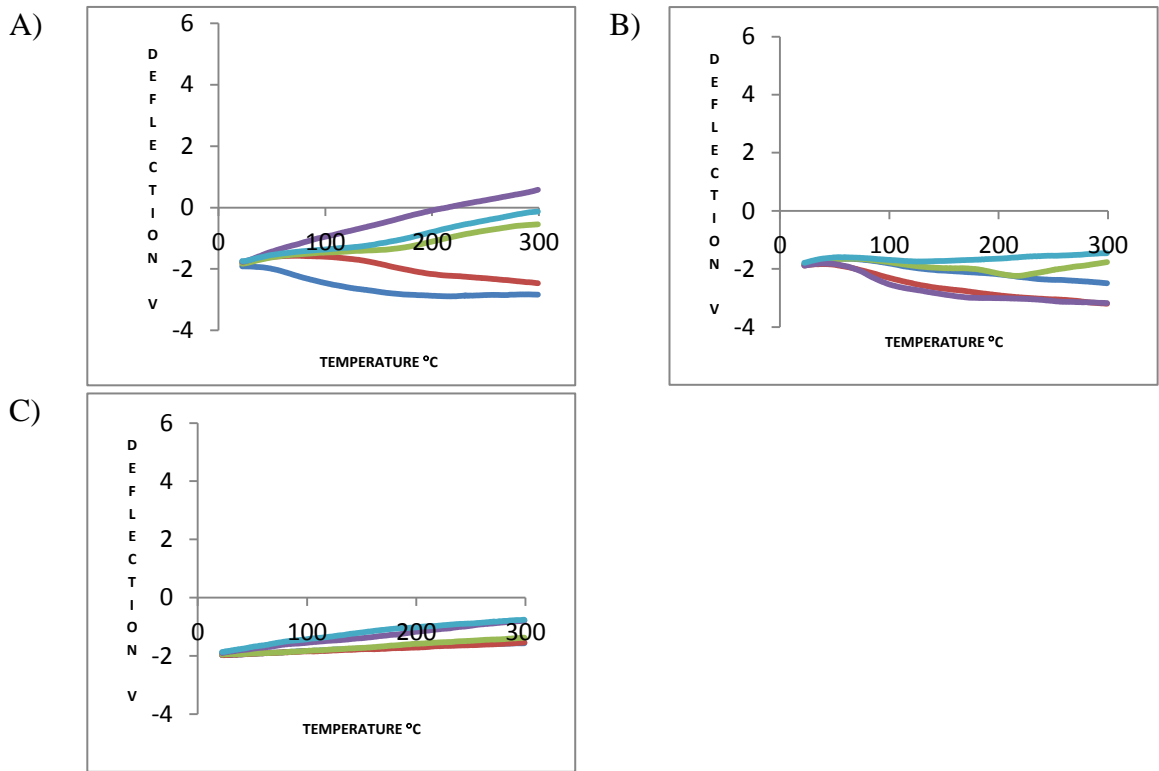


Figure 3.8: Nano-TA results of MCC compacts using a nano probe, across the radius of the compact from A (edge) to C (middle). Five nano-TA readings were taken at each position: dark blue - site 1, red - site 2, green - site 3, purple - site 4, light blue - site 5.

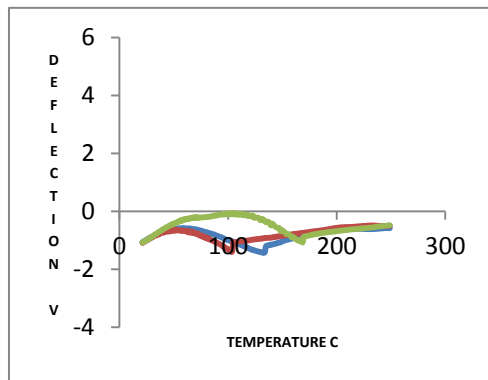


Figure 3.9: Nano-TA results for a MCC compact showing the probe lifting and going back in contact with the compact at the point of V- shape.

3.3.1.7 TTM

TTM was performed on the MCC compacts using a nano probe. Three scans were taken across the diameter of the compact (i.e. the two edges and the centre were scanned), with the results being shown in Figure 3.10.

TTM results are expressed in three ways: the individual results at each point (analogous to the nano-TA results) are shown as thermal deflection graphs, with all points superimposed on one graph (column 1 in Figure 3.10). From these, a colour is assigned to each point by the software reflecting the temperature of any observed transition. This is then expressed as a "discrete" pixel map across the scanned area, in this case an 11 x 11 grid (column 2 in Figure 3.10). Finally, a "smoothed" or "interpolated" graph is produced from the discrete pixellated map showing possible transition regions between one "colour" and the next (column 3 in Figure 3.10).

For the scans taken at the centre of the MCC compacts, there is no obvious thermal event detected, with all pixels being coloured the same, which is supported by the nano-TA and micro-TA results, discussed above. Interestingly, all the results show a positive deflection, which is different from the previous micro-TA and nano-TA results, where the incline for the deflection varied.

For the scans taken at the edge of the MCC compacts, the results are more variable, particularly round the extremities of the area of observation, shown as blue pixels in Figure 3.10, representing low temperature transitions. As MCC was shown to be thermally stable by all other techniques, it is thought that this observation is unlikely to represent a true thermal transition, but is more likely to be attributed to a variety of other factors such as environmental noise and the topography of the sample. Due to the delicate nature of the technique, the instrument is very sensitive, so any vibration or lab noise is detected and recorded as an endpoint. The technique is also influenced by the topography of the sample because the probe has to make good contact with the surface for a measurement to be made. In TTM, the topography cannot be recorded as the instrument is based around an optical microscope rather than an AFM. The data processing is also performed automatically because the instrument generates a high number of results so small changes of incline of the deflection may be recorded as a transition when it is in fact not a true thermal event.

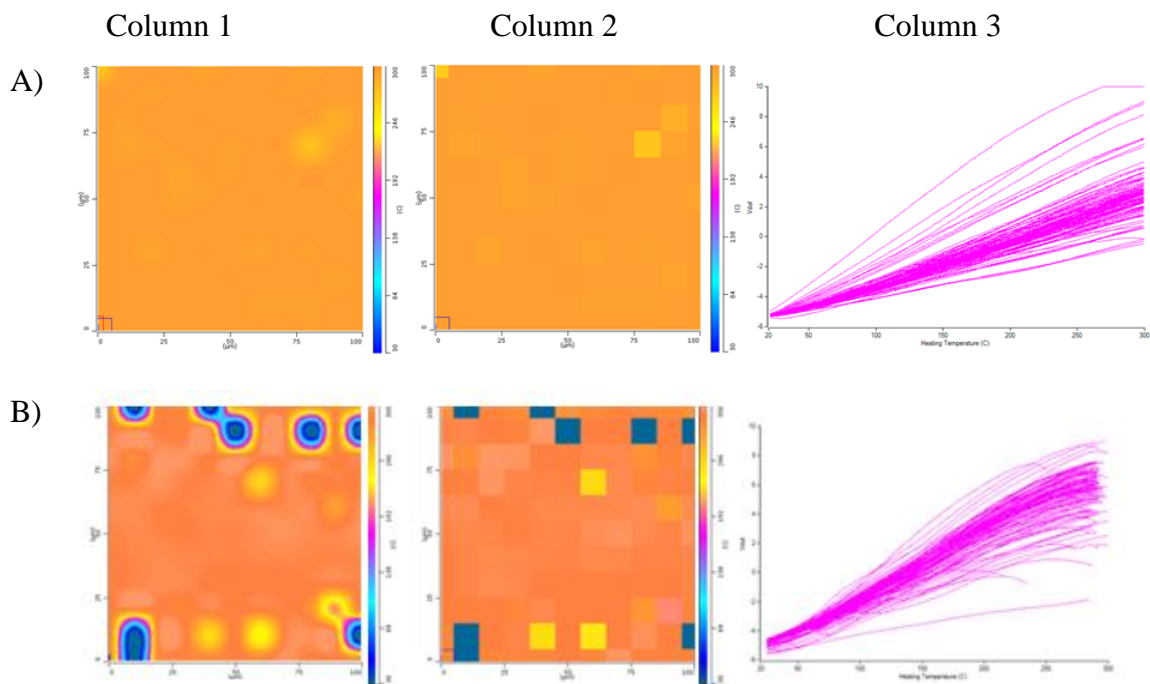
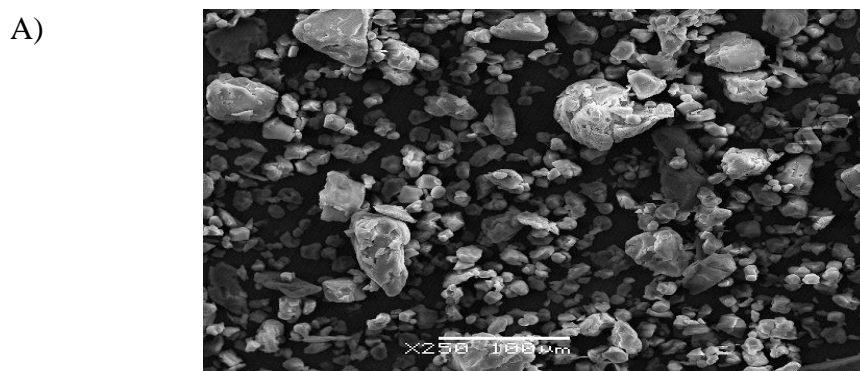


Figure 3.10: TTM maps of MCC compacts. A) middle and B) edge of the compact. Column 1 is the interpolated (smoothed) map, Column 2 is the discrete map, and Column 3 shows the individual nano-thermal results.

3.3.2 Pre-gelatinised starch (PGS)

3.3.2.1 SEM

Figure 3.11 A and B shows SEM images of PGS at magnifications of 250 and 1000. The particles are irregular in shape and the size varies greatly with most particles being much smaller than 100 μm . The specification for PGS is that more than 90 % of particles must be smaller than 149 μm and less than 0.5 % of particles are larger than 420 μm (Rowe et al (2009) and www.colorcon.com). The image in Figure 3.11 A is in general agreement with this specification. Figure 3.11 B highlights the texture of the sample, which has a very rough and flaky surface.



B)

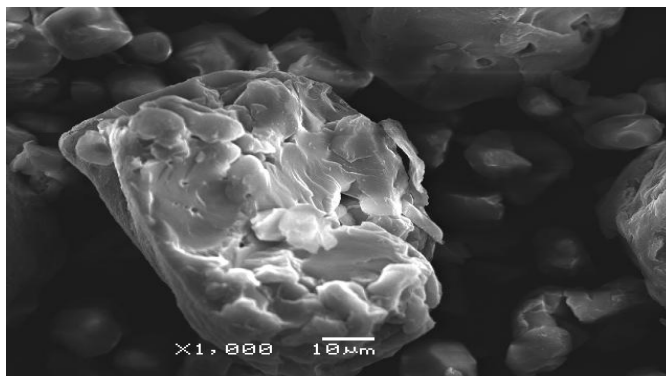


Figure 3.11: SEM image of PGS. A) magnification X250, B) magnification X1000.

3.3.2.2 VT-IR

Figure 3.12 A and B shows a superimposition of all temperature scans (A) and a summary of the lowest and highest temperatures studied (B). It can be seen that any changes with temperature are very gradual, i.e. there are no major thermal transitions. The spectra show a large peak in the region of 3300 cm^{-1} which is assigned to the H-bonded -OH bond. The sample contains a certain amount of loosely adhered water (8 to 10 % w/w according to the manufacturer's specification, www.colorcon.com) as well as -OH groups in the chemical structure of the PGS, both of which probably contribute to this peak. The peak is quite broad, and reduces in size and shifts slightly as the sample is heated, which may be explained by the loss of the loosely adhered water and changes in the hydrogen-bonding arrangements of the hydroxyl groups in the structure at higher temperatures, and the general increased molecular mobility to be expected at higher temperatures. The peak at 2980 cm^{-1} has been attributed to C-H stretch and this peak is not influenced by heat. A sharp peak occurs at 1724 cm^{-1} which could be assigned to C-O stretch; again this is unaffected by temperature. The range of peaks that appear in the region centred on 1370 cm^{-1} could be attributed to O-CH, C-CH and C-OH bonds. In the region of 1150 cm^{-1} and 1080 cm^{-1} the peaks are due to C-O, C-C, OH and the C-O-C glycosidic bridge asymmetric stretch. C-OH deformation gives rise to the peak at 1016 cm^{-1} . The region of 930 cm^{-1} to 860 cm^{-1} is due to CH bending. The effect of heat appeared to be limited and many of the peaks are unchanged; the exception being the -OH peak at 3300 cm^{-1} .

PGS is partly amorphous and partly crystalline. It has been documented in the literature that the degree of crystallinity can be followed by X-ray diffraction (Xie et al (2006) and van Soest et al (1995)), but FT-IR is also sensitive to physical structure. In particular, the region around $1000\text{ to }1050\text{ cm}^{-1}$ in the "normal" spectrum will give information as to the

relative content of amorphous and crystalline regions (Xie et al (2006) and van Soest et al (1995)). In the second derivative plot for the scan taken at 30°C, this is more easily seen as a peak at 1046 cm⁻¹ reflecting crystalline content and a peak at 1016 cm⁻¹ reflecting amorphous content. At 200°C, these peaks are seen at 1042 cm⁻¹ and 1015 cm⁻¹. Figure 3.13 shows the "normal" and second derivative IR scans taken at 30°C and 200°C. From the heights of these two second derivative peaks, the ratio of crystalline content to amorphous content can be calculated. A ratio of 0.84, leading to a calculation of the crystalline content of 46 %, is obtained for the sample at both 30°C and 200°C, indicating that there is no change with increased temperature.

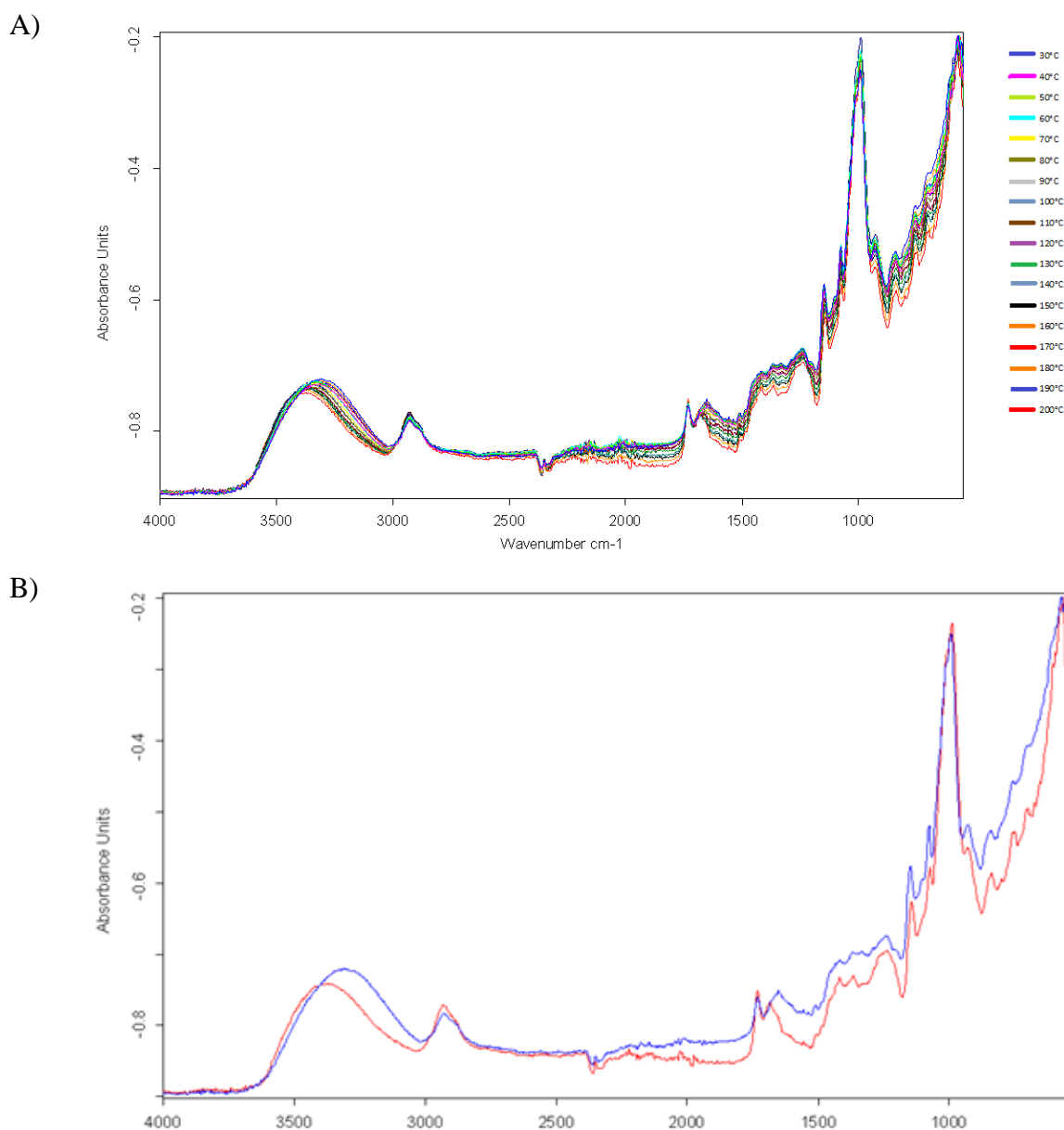


Figure 3.12: FT-IR spectra for PGS between the temperatures of 30°C and 200°C. A) all scans at 10°C intervals, B) the results for 30°C (blue) and 200°C (red).

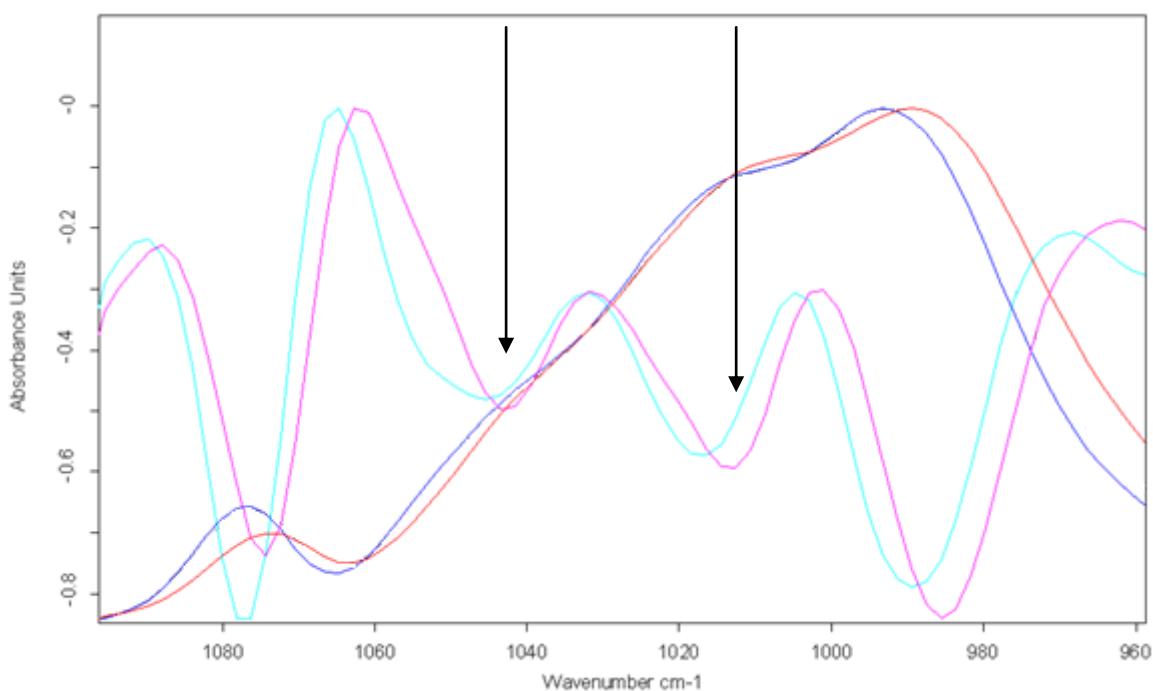


Figure 3.13: FT-IR "normal" and second derivative spectra for PGS at 30°C and 200°C. Blue - "normal" spectrum at 30°C, red - "normal" spectrum at 200°C, pale blue - second derivative spectrum at 30°C, pink - second derivative spectrum at 200°C. The arrows indicate the peaks of interest (aligned for 200°C).

3.3.2.3 DSC

The DSC traces for PGS (Figure 3.14) show one very broad endotherm centred at $\sim 128^\circ\text{C}$ for both the mini-tablet (displayed in blue) and the loose powder (displayed in red). This is probably due to the loosely adhered water in the sample. A slight increase in the values for energy and temperature of this transition is observed for the mini-tablets compared to the loose powder. As discussed earlier for the MCC powder and mini-tablets, it would be expected the heat would take longer to disperse into and for the water to be released from the mini-tablet structure, but this was not observed for PGS to the same extent as for MCC. A small endotherm is seen at 270°C followed by various other peaks, which collectively can be assigned to sample degradation. To prevent any damage to the furnace in future experiments, further PGS runs were terminated at 250°C . Overall, compaction appeared to have no effect on the thermal behaviour of PGS.

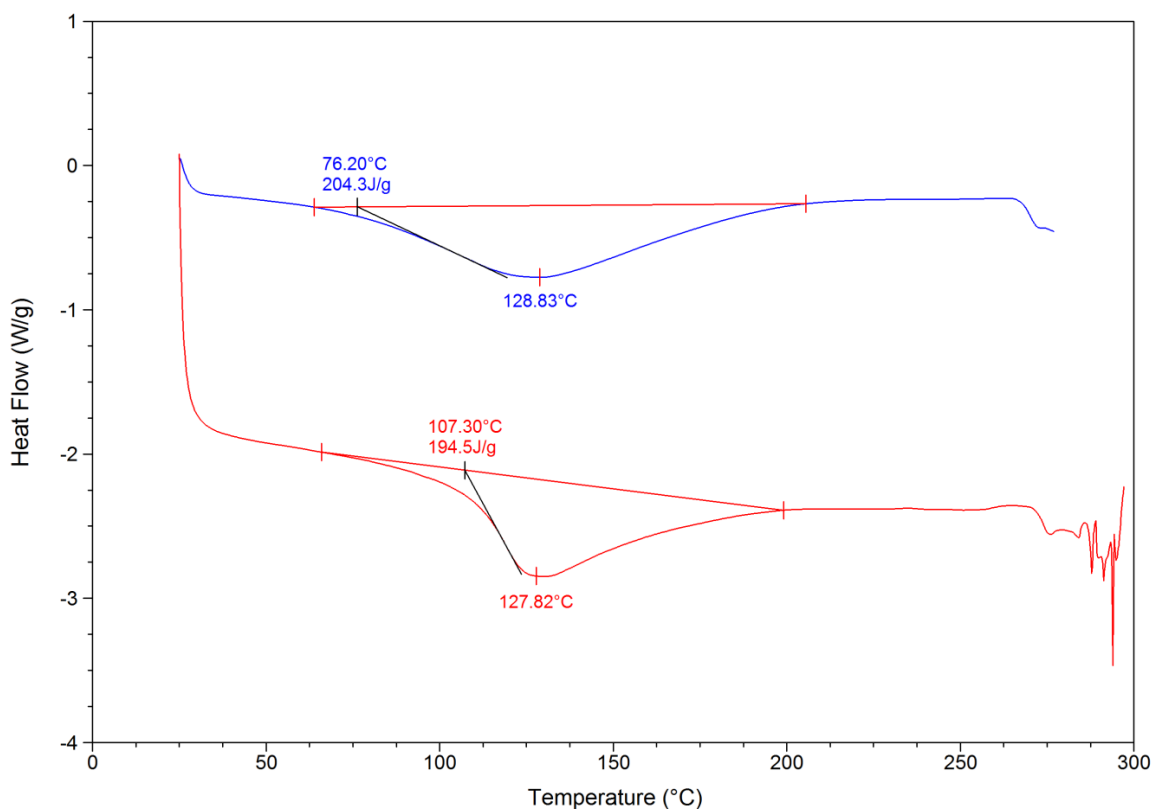


Figure 3.14: DSC trace of PGS powder (red) and mini-tablet (blue).

3.3.2.4 AFM

The surface topography of PGS was investigated using AFM. AFM images of areas of 100 μm x 100 μm generated using a Wollaston wire probe (micro probe) are shown in Figure 3.15. Column 1 shows the top surface of a representative compact, with six images (A to F) from positions across the radius of the compact, from the outside to the centre. Column 2 shows a similar set of images from the bottom of a representative compact. There is a distinct patterning on both the top and bottom surfaces of the compact of small circular shapes. However, there is no observed difference between the top and bottom surfaces and there is no difference across the surface from the outside to the centre.

After the preliminary profile using the Wollaston wire micro probe, a similar exercise was performed using a nano probe for greater resolution. Figure 3.16 shows the topographical images using a nano probe where three 50 μm x 50 μm regions across the radius of the PGS compact was scanned (A - outside to C - centre). The same small circular shapes were observed as for the micro probe images and again no difference was seen for the centre and the outside of the compact.

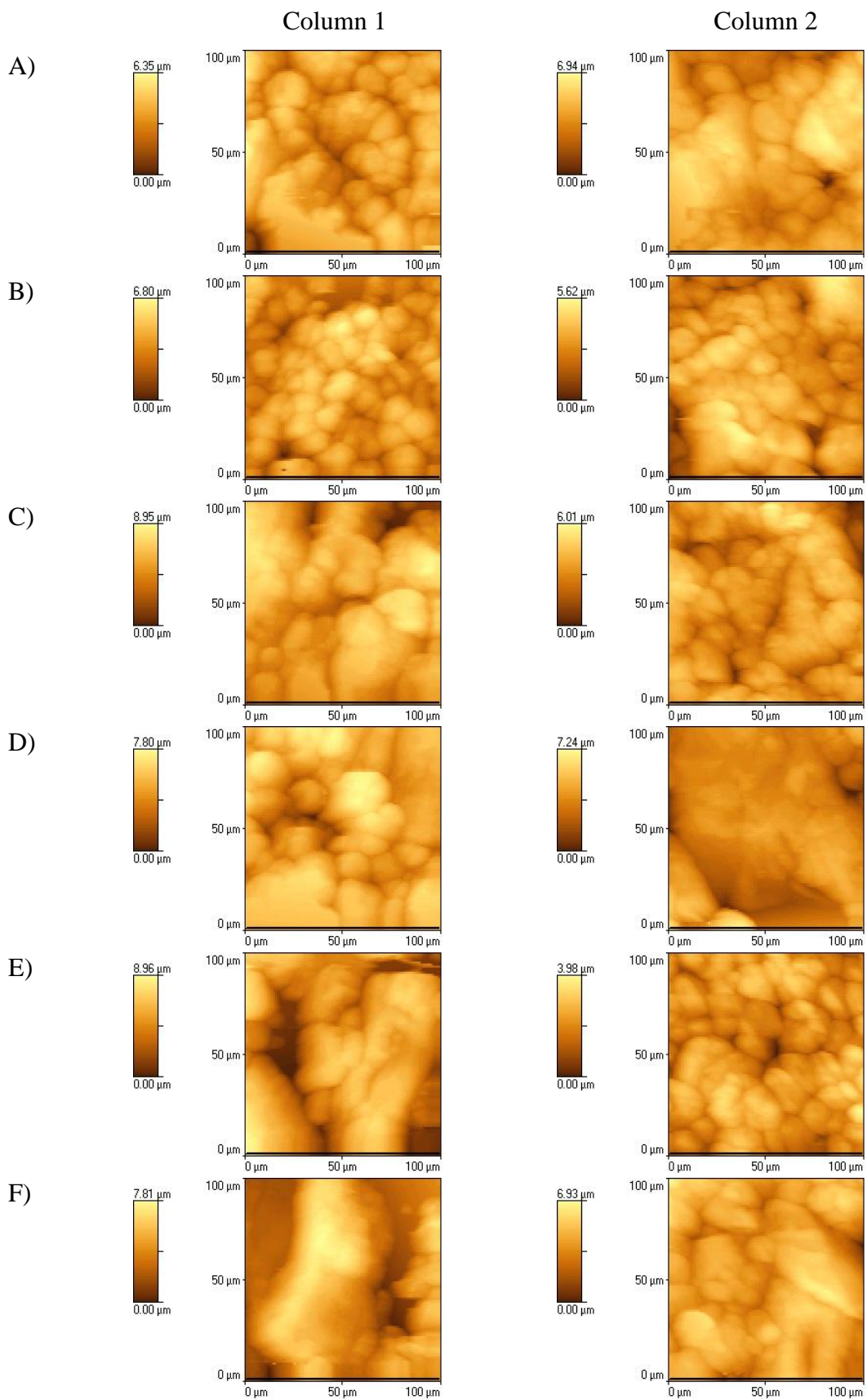


Figure 3.15: AFM scan showing the topography (as height) of the PGS compacts using a Wollaston wire (micro) probe. Column 1 - top of the compact, column 2 - bottom of the compact, position on the radius of the compact is given from A) outside to F) centre.

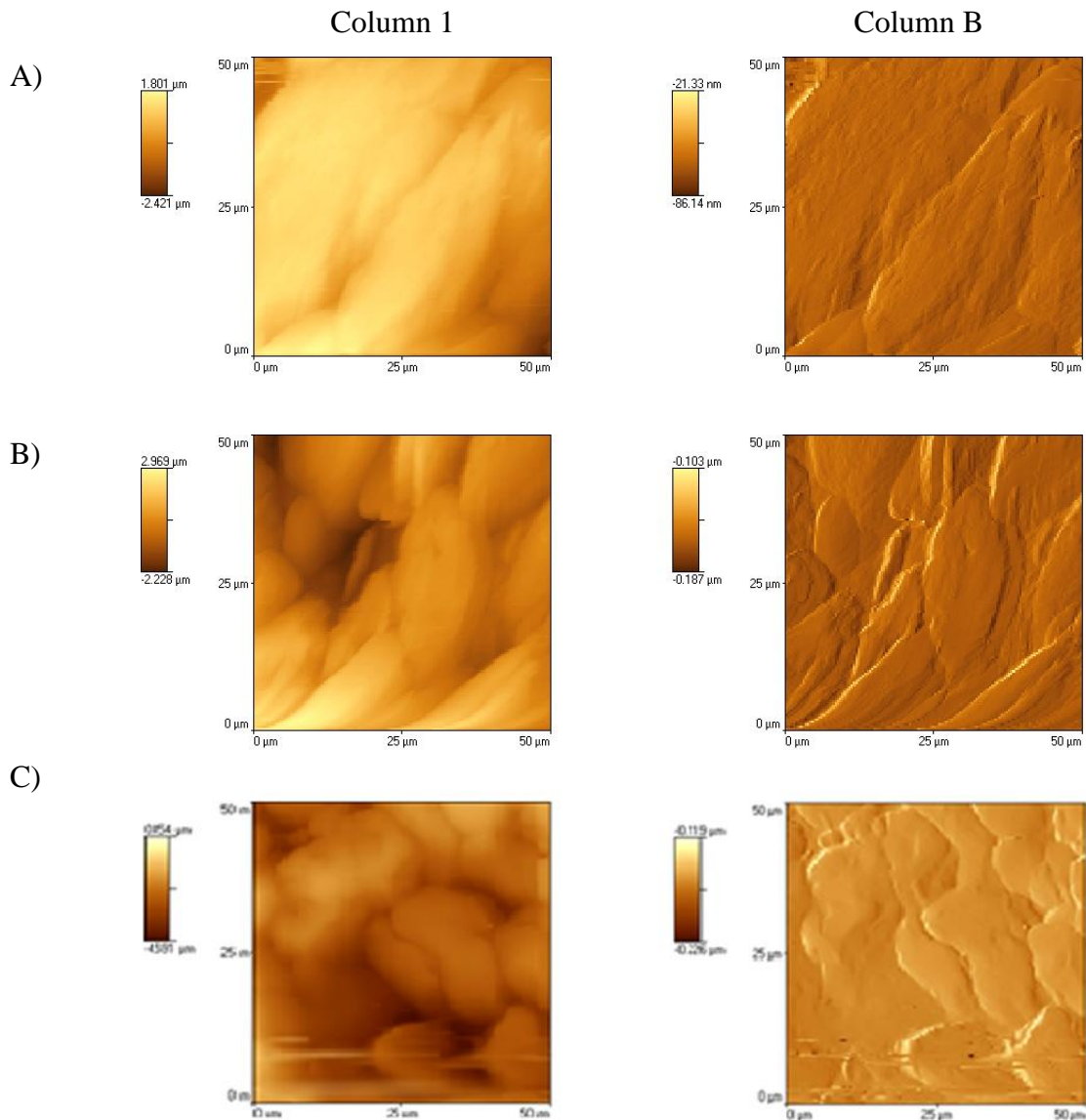
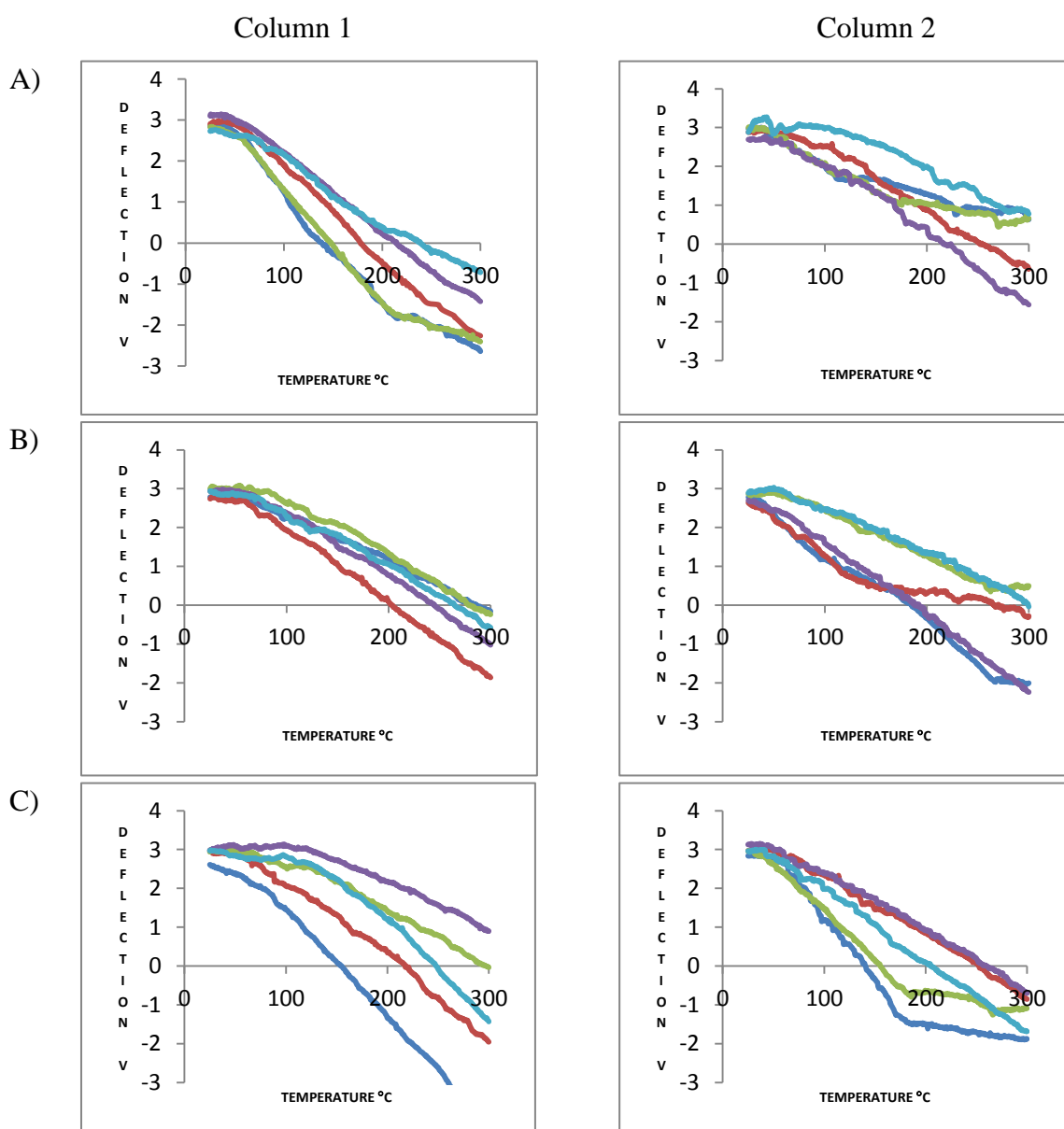


Figure 3.16: The AFM scan using nano probes showing the topography of the PGS compacts. Column 1 - height of the scan, Column 2 - deflection of the probe, position on the radius of the compact is given from A) outside to C) centre.

3.3.2.5 Micro-TA

Micro-TA was performed in the same manner as the AFM experiments, i.e. across the radius of both the top and bottom surfaces of the compacts. The results are shown in Figure 3.17. Column 1 shows the top surface of a representative compact, with six images (A to F) from sites across the radius of the compact, from the outside to the centre. Column 2 shows a similar set of images from the bottom of a representative compact.

When studying PGS compacts, there was no obvious thermal event observed and no differences were seen when examining the top / bottom or the outside / centre of the compacts. This is supported by the DSC results where only a broad peak for the loss of loosely-bound water was observed. This peak was not detected by micro-TA for PGS and earlier it was demonstrated not to be observed for MCC either. In both cases, this is probably due to the technique not being sensitive enough to detect such a transition occurring over a wide temperature range. The only feature observed in the micro-TA scan was a change in the background slope - in this case it was predominantly negative. Although the micro-TA results for PGS and MCC are very similar, in that no obvious thermal event was observed for either, the difference in the background slope on heating may provide a means of distinguishing between the two components in the mixed samples.



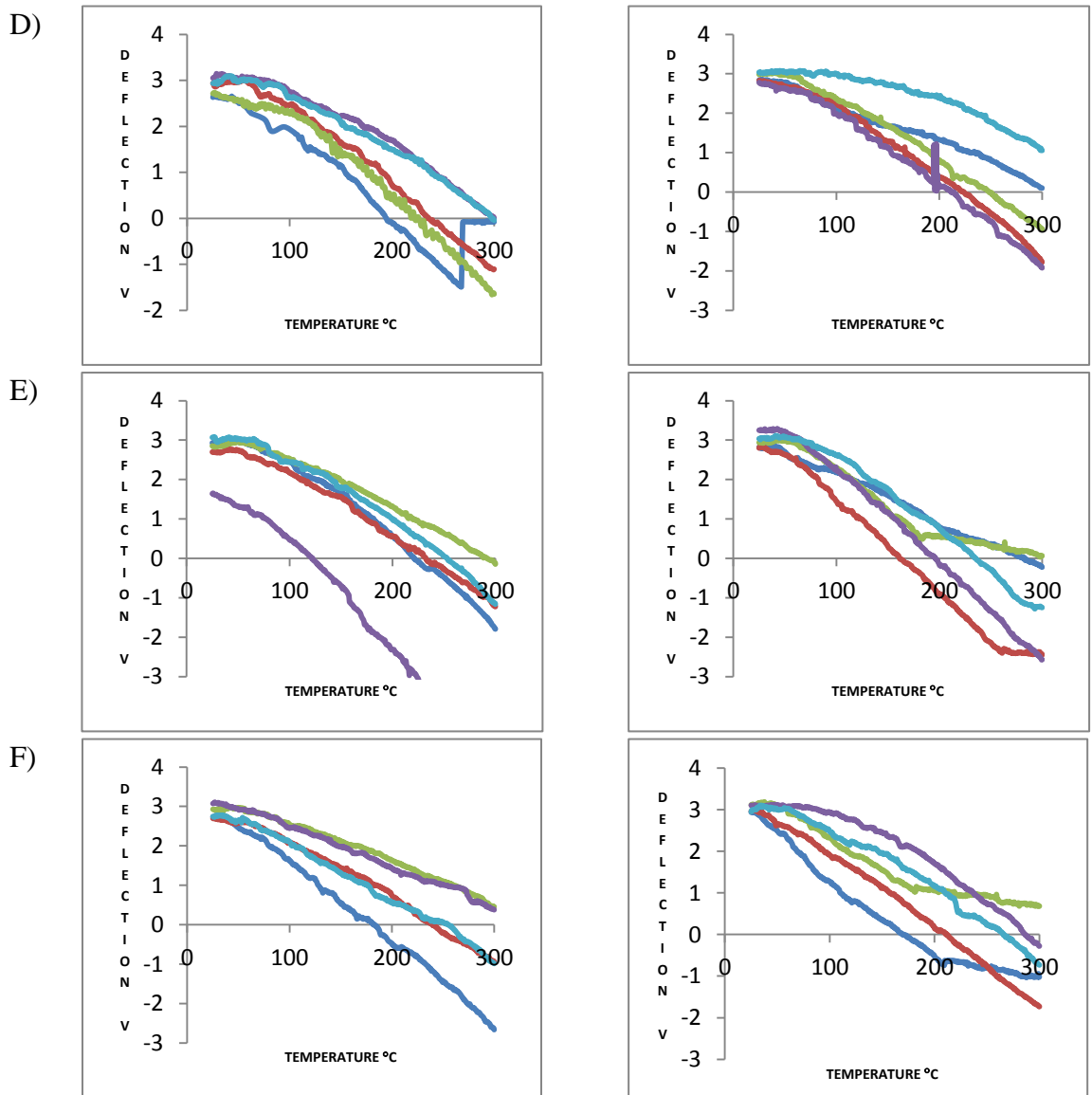


Figure 3.17: Micro-TA results of PGS compacts, using a Wollaston wire micro probe. Column 1 - top of the compact, column 2 - bottom of the compact, position on the radius of the compact is given by A) outside to F) centre. Five micro-TA readings were taken at each position: dark blue - site 1, red - site 2, green - site 3, purple - site 4, light blue - site 5.

3.3.2.6 Nano-TA

Nano-TA was performed in the same manner as the AFM experiments, i.e. across the radius of the surfaces of the compacts. The results are shown in Figure 3.18 for three scans across the radius of the compact.

There was no obvious thermal feature except for a slight curvature in the deflection at the end of the temperature range. This was not detected with the Wollaston wire (micro) probe, but in the DSC trace there is an endotherm at circa 270°C as the sample starts to degrade. Hence, the curvature seen in the nano-TA trace could be attributed to the start of the degradation process of the PGS. The dehydration of the sample is not detected by this technique. An explanation of this could be the nano-TA technique is still not sensitive enough to detect this small transition. In contrast to the micro-TA results, all the results have a positive deflection, which is probably due to the probe being lighter and having a higher sensitivity.

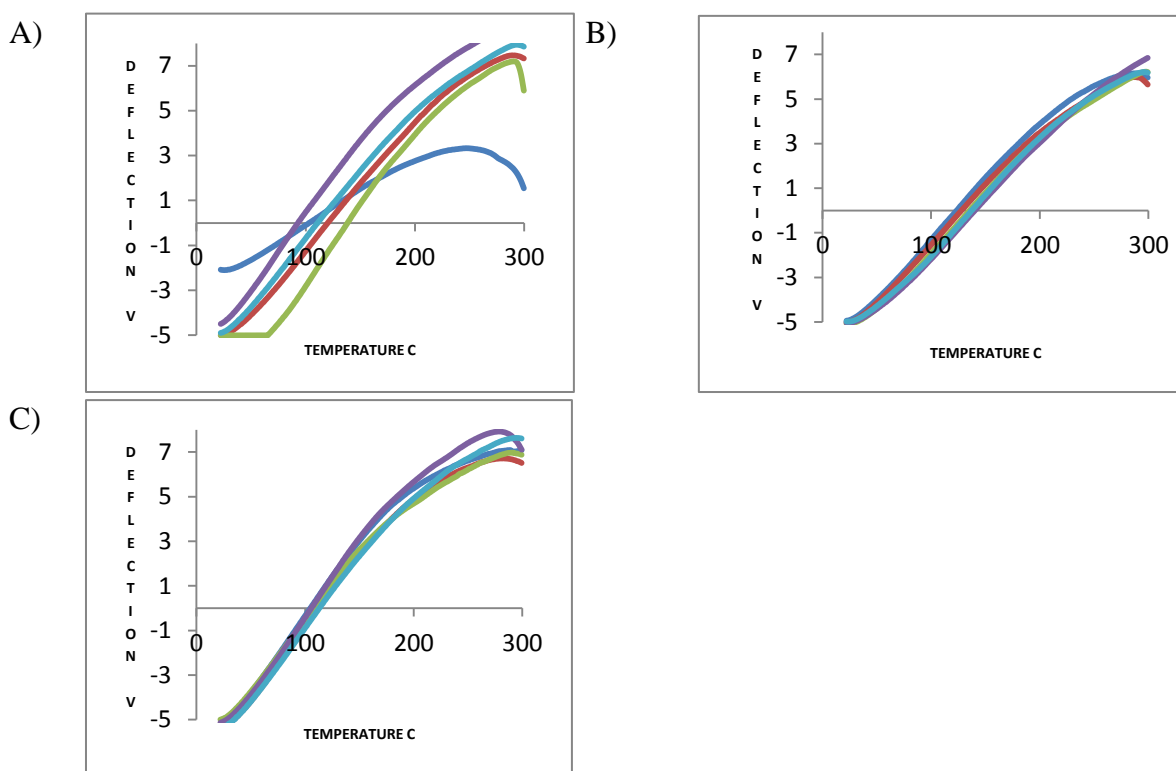


Figure 3.18: Nano-TA results of PGS compacts using a nano probe across the radius of the compact from A (outside) to C (centre). Five readings were taken at each position: dark blue - site 1, red - site 2, green - site 3, purple - site 4, light blue - site 5.

3.3.2.7 TTM

Three TTM maps were generated across the diameter of the compact (i.e. the two outside edges and the centre were scanned) and the results are shown in Figure 3.19. A small curvature of the deflection is observed at higher temperatures, but no true thermal transition was noted - this is similar to the nano-TA results.

The pixellated map for the scan at the centre of the compact shows a single colour, whereas that for the edge scans shows a greater range of colour, suggesting a range of thermal processes. However, as discussed for MCC above, this could be attributed to sample topography, vibrations or lab noise rather than the position of the probe on the compact. In addition, the curving of the deflection as the sample starts to degrade could be incorrectly interpreted by the instrument as a true endpoint and be assigned a colour. This latter point may also be variable because of the steepness of the curvature when the deflection is recorded. This explanation of experimental artefacts is preferred as no other technique suggested that PGS exhibited any thermal transitions.

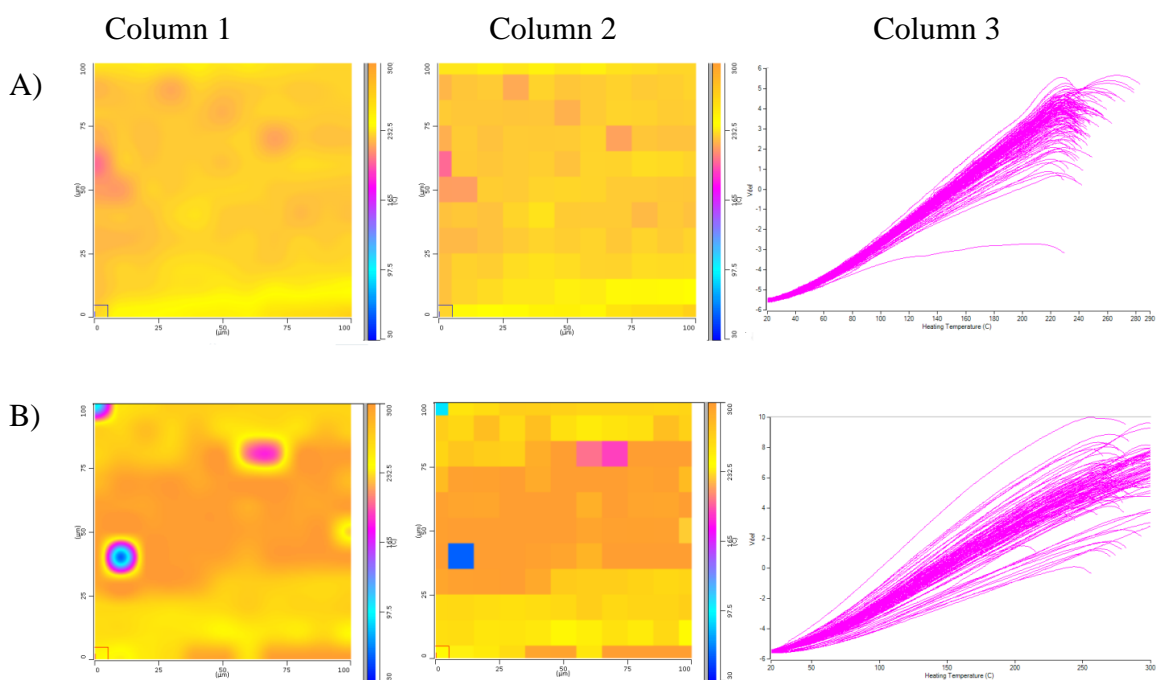


Figure 3.19: TTM maps of PGS compacts. A) middle and B) edge of the compact. Column 1 is the interpolated (smoothed) map, Column 2 is the discrete map, and Column 3 shows the individual nano-thermal results.

3.3.3 Magnesium stearate (MS)

3.3.3.1 SEM

Figure 3.20 A and B displays SEM images of magnesium stearate at magnifications of 250 and 1000. The particles are irregular in shape; the size varies greatly and is estimated to range between 10 and 50 μm . Figure 3.20 B is a higher magnification image of one of the larger particles seen in Figure 3.20 A. It highlights the texture of the sample, which is very rough with a very flaky surface.

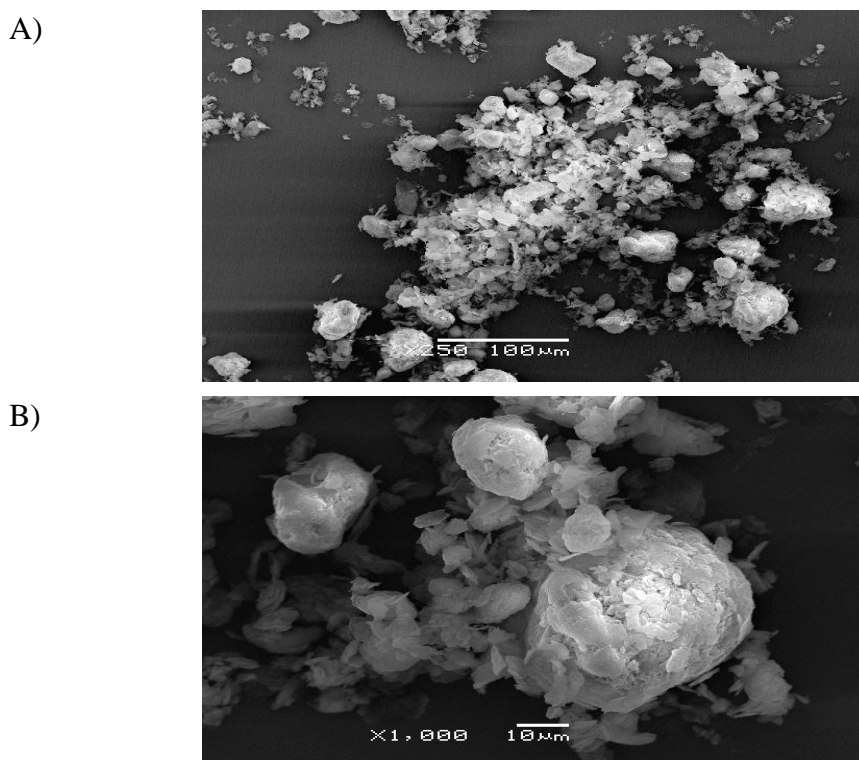


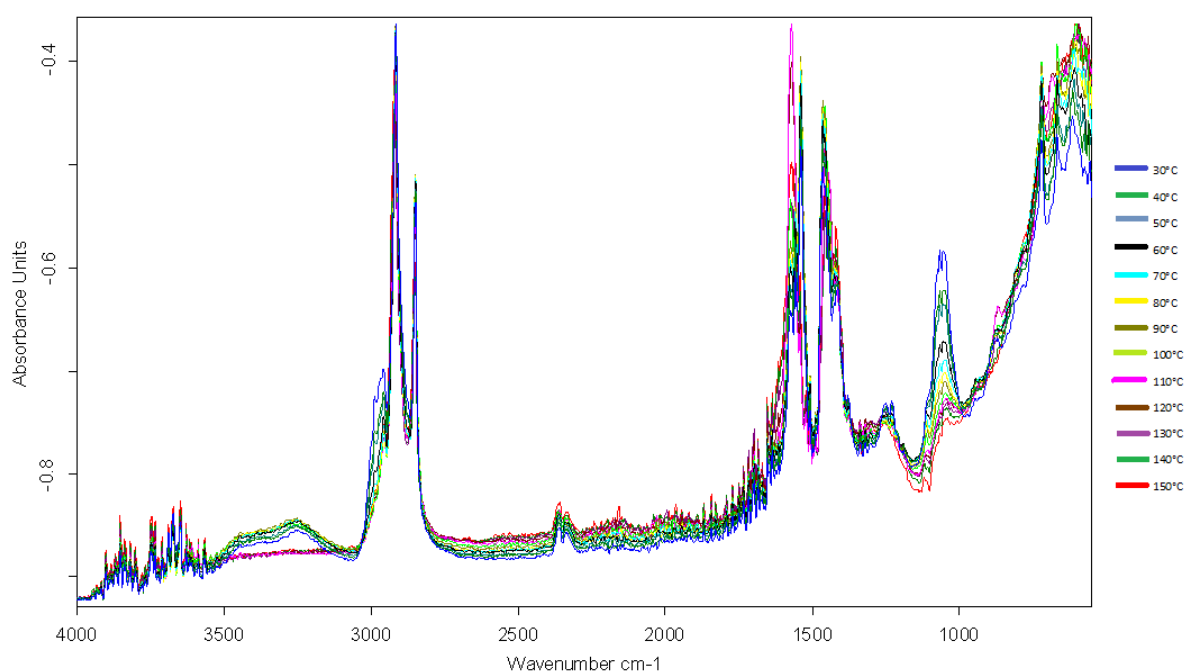
Figure 3.20: SEM image of magnesium stearate. A) magnification X250, B) magnification X1000.

3.3.3.2 VT-IR

All the spectra taken across the temperature range studied (30°C to 150°C; the lower endpoint compared to the other materials being due to lower melting point of magnesium stearate) have been superimposed in Figure 3.21 A and a summary of the results at significant temperatures is shown in Figure 3.21 B. From Figure 3.21 A, it can be seen that all temperature-related changes are small and gradual until the temperature reaches

110°C, at which point there is evidence of major change. The peak at 3500 cm⁻¹ is assigned to water, either water of crystallisation or loosely adhered water: as the temperature is increased the peak gradually reduces in size and by 110°C this peak disappears as the water is removed completely from the sample. The peaks at 3000 cm⁻¹ and 2800 cm⁻¹ can be attributed to C-H stretch in methyl (-CH₃) and methylene (-CH₂-) groups. The bands in the range 1580 cm⁻¹ to 1465 cm⁻¹ correspond to stretching of the carboxyl anion (-COO⁻) (Ertel and Carstensen (1988)). The peaks in the circa 700 cm⁻¹ to 600 cm⁻¹ range are due to various C-H bonds and movements. As the temperature is increased, the peaks tend to merge.

A)



B)

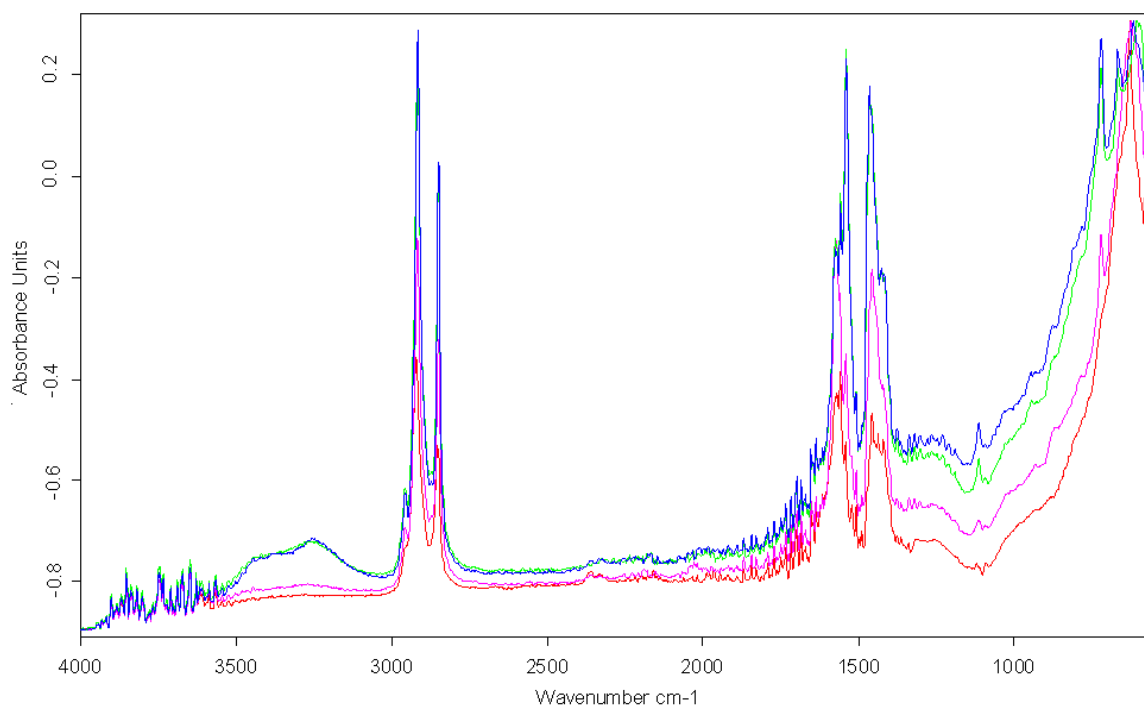


Figure 3.21: FT-IR spectra for MS between the temperatures of 30°C and 150°C. A) All scans at 10°C intervals, B) the results for 30°C (blue), 100°C (green), 110°C (pink) and 150°C (red).

3.3.3.3 DSC

The DSC traces for MS as loose powder and mini-tablets are shown in Figure 3.22 in red and blue, respectively. "Magnesium stearate" as purchased is not a pure material, but rather consists of a range of components and hydrate states, which could help explain the DSC results. For the loose powder, three main broad endotherms are seen. The endotherm centred at circa 67°C may be assigned to the water of crystallisation being lost from magnesium stearate trihydrate, where the water is not bound so tightly in the crystal lattice as it is in the other forms (Sharpe et al (1997)). The endotherm centred at circa 92°C can be assigned to the water lost from the dihydrate form. The final endotherm centred at circa 115°C is attributed to the melting of anhydrous magnesium stearate. The DSC trace for the MS mini-tablets was not as clear as for the loose powder and only the melting peak was clearly defined. This peak appeared at a higher temperature and with a higher energy of transition in the mini-tablets than in the loose powder. The other peaks appeared to be merged for the mini-tablets. This is most probably explained by the slower penetration of heat into the mini-tablets than the loose powder, and similarly a slower escape of water

vapour out of the sample, so the broad dehydration peaks are merging as the temperature range of all the thermal events is close.

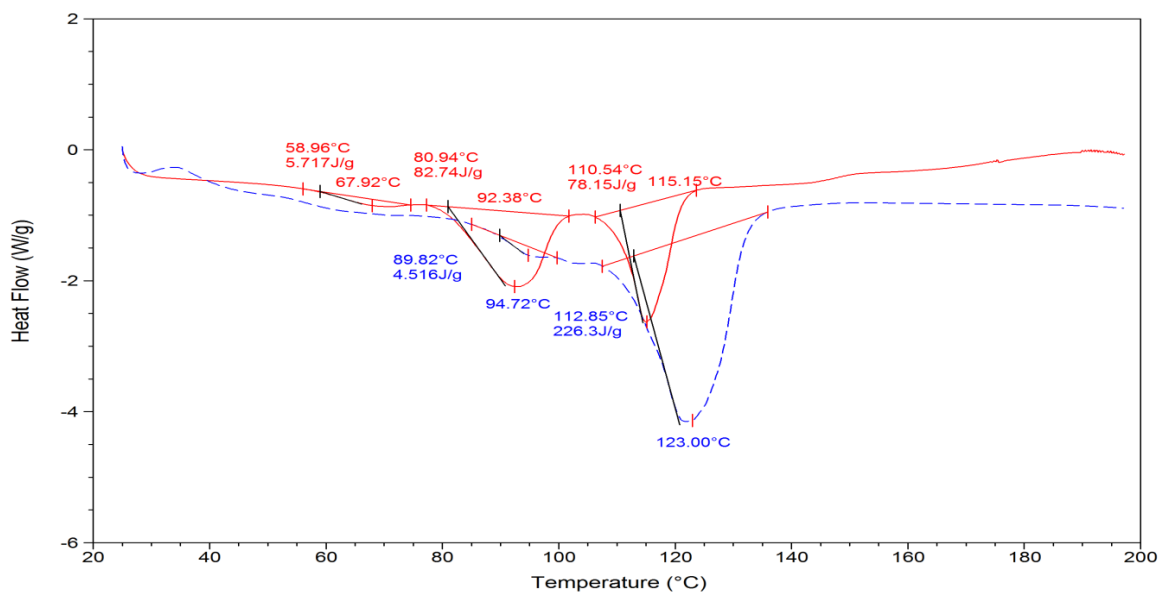
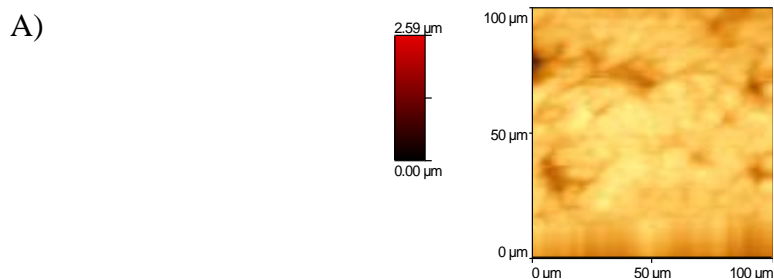


Figure 3.22: DSC traces of MS powder (red) and mini-tablet (blue).

3.3.3.4 AFM

It is difficult to make compacts of MS and they tend to be brittle and rough. Due to the surface roughness being greater than that usually compatible with the AFM technique, it was impossible to get a full range of images across the surface using either the Wollaston probe or a nano probe. Figure 3.23 A is an example of a scan with the micro probe of an MS compact in one of the flatter regions and B is a similar image generated using a nano-probe. No distinct features were observed on the surface.



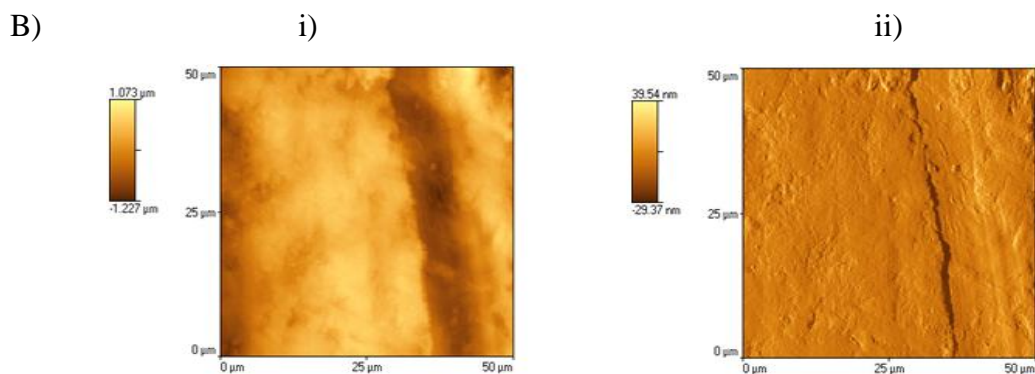


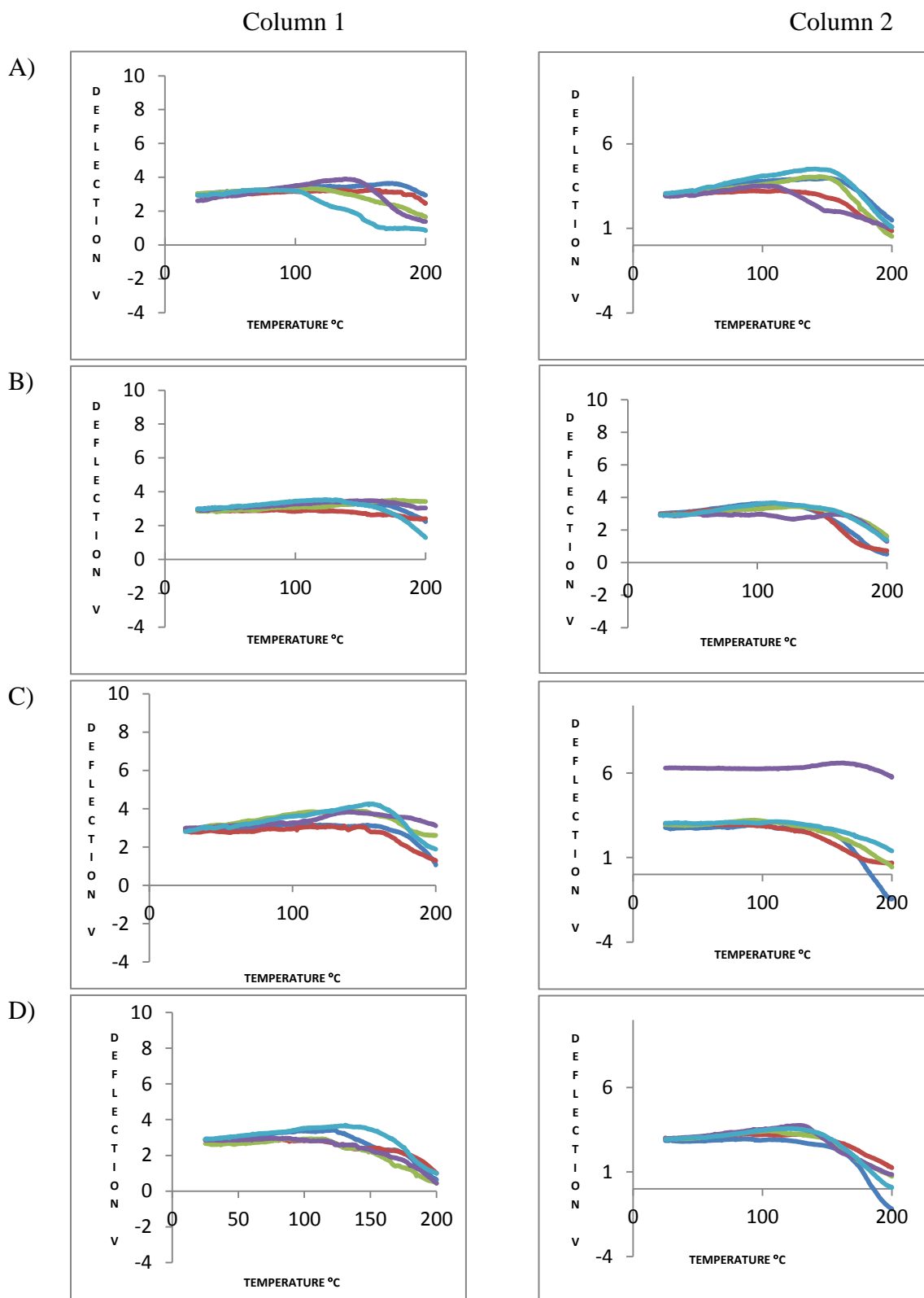
Figure 3.23: The AFM scan showing the topography of the magnesium stearate compacts. A - height of the scan using a Wollaston wire probe, B i) height scan, ii) a scan of deflection of the probe using a nano probe.

3.3.3.5 Micro-TA

In a similar manner to the other single component compacts, micro-TA was performed across the radius and on the top and bottom surfaces, even though the topography was too rough to perform an AFM scan. Figure 3.24 show the results with column 1 indicating the top of the compact and column 2 the bottom of the compact. A to F represent the readings across the radius from the outside to the centre. A thermal event is detected at circa 110°C to 150°C, which from the DSC data is best assigned to melting of the dehydrated magnesium stearate, although the temperatures observed here are higher than in the DSC experiments. The variability in the data could possibly be attributed to the rough surface of the compact and the probe not achieving good contact with the surface. In Figure 3.24 column 1 scans E and F and column 2 Scan F, one of the five results did not record a clear transition, which again can be explained by the topography of the sample. The height difference in the deflection result was due to the set point being changed to achieve contact.

The micro-TA technique appears to be not sensitive enough to detect the dehydration processes that were observed in the DSC trace for the loose MS powder. However, these peaks were not as clear on the DSC trace for the mini-tablets as the loose powder, and as the compacts used for the micro-TA analysis more closely resemble the mini-tablets, this apparent lack of sensitivity may not be particularly surprising. The micro-TA technique did not detect any obvious difference between the top and bottom of the compact or across

the radius of the compact. This could be explained by the inherent variability in results due to the surface roughness, the noise that is seen and the lack of sensitivity of the technique.



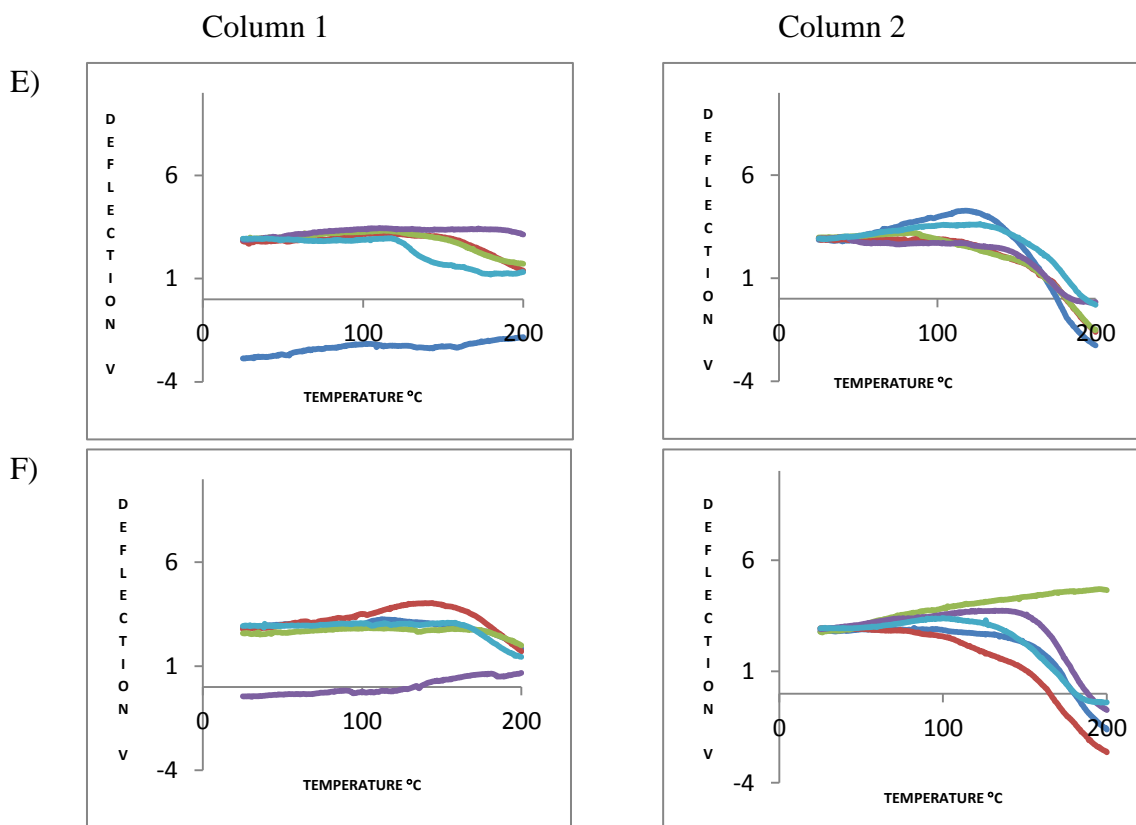


Figure 3.24: Micro-TA results of MS compacts, using a Wollaston wire micro probe. Column 1 - top of the compact, column 2 - bottom of the compact, position on the radius of the compact is given by A) outside to F) centre. Five readings were taken at each position: dark blue - site 1, red - site 2, green - site 3, purple - site 4, light blue - site 5.

3.3.3.6 Nano-TA

Nano-TA was performed across the radius of the surfaces of the compacts. The results are shown in Figure 3.25 for three scans across the radius of the compact. A thermal event was detected at circa 110°C to 180°C, but was quite variable in its onset temperature. Again the variability could possibly be explained by the surface roughness of the sample and the ability (or lack of) the probe to make appropriate contact with the surface of the compact. The main peak could be assigned to the melting of dehydrated magnesium stearate, although as was seen for the micro-TA results, the temperature of the event is much higher than was observed on the DSC traces. Several scans have a small secondary peak before the main peak and this could possibly be attributed to the dehydration of magnesium stearate dihydrate as observed in the DSC trace. If so, this indicates that the nano-TA technique was sensitive enough to detect this process which was not seen by

micro-TA. However, further work is needed to fully investigate this and to exclude the possibility that these secondary peaks are due to random fluctuations in the sample surface. Again, no difference was observed across the compact but any differences may have been lost in the baseline noise.

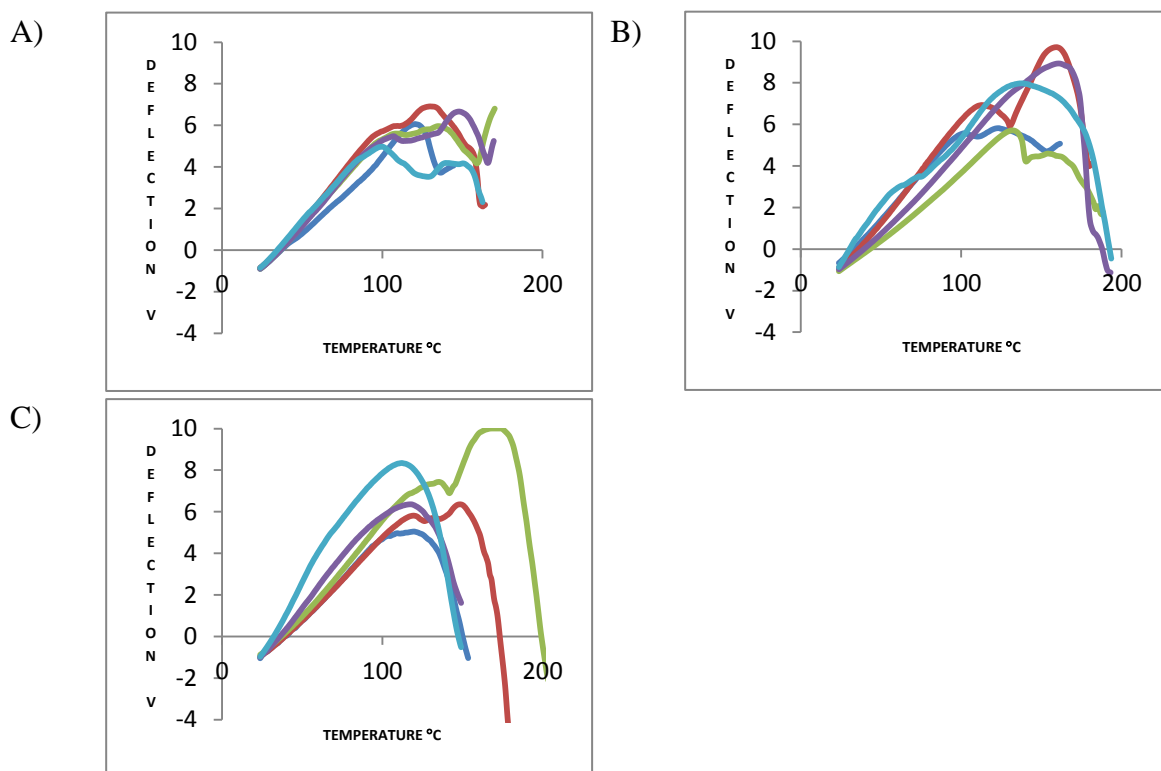


Figure 3.25: Nano-TA results of MS compacts using a nano probe across the radius of the compact from A (outside) to C (centre). Five nano-TA readings were taken at each position: dark blue - site 1, red - site 2, green - site 3, purple - site 4, light blue - site 5.

3.3.3.7 TTM

Three TTM maps were generated across the diameter of the magnesium stearate compacts (i.e. the two outsides and the centre were scanned). Both the pixellated and smoothed TTM maps displayed a mixture of colours indicating a wide range of thermal events detected (Figure 3.26). These varied in temperature from 80°C to 170°C, with the majority occurring at temperatures less than 140°C. This can be explained by the complicated dehydration processes of MS and the subsequent melting of the dehydrated solid. This is supported by the DSC data for the MS compacts, where dehydration is seen as a broad peak centred at circa 95°C and the compound has a broad melting peak centred at circa 123°C. The higher values seen in the TTM results could possibly be explained by the

rough topography and poor contact between the probe and the compact. Additionally, some of the variability may be attributed to vibration and general lab movement and noise as discussed earlier

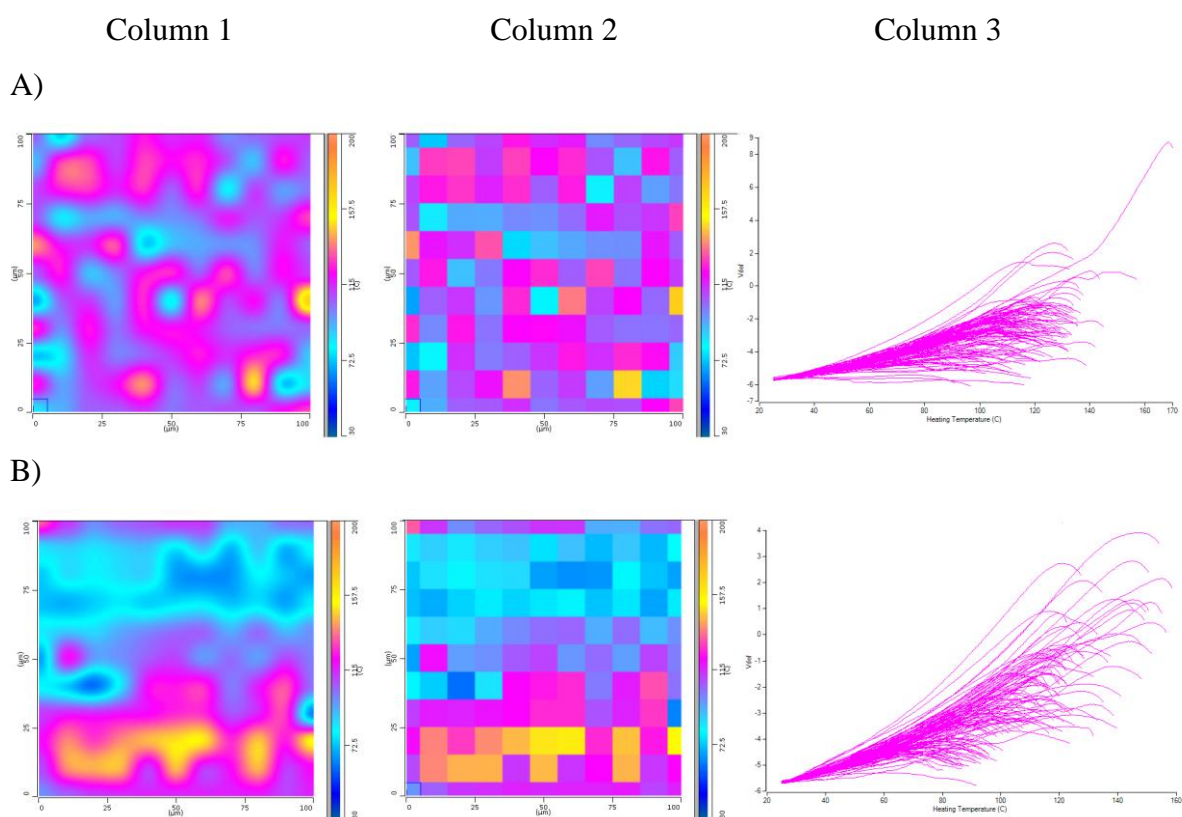


Figure 3.26: TTM maps of MS compacts. A) centre and B) outside of the compact. Column 1 is the interpolated (smoothed) map, Column 2 is the discrete map, and Column 3 shows the individual nano-thermal results.

3.3.4 α -Lactose monohydrate (α -LM)

3.3.4.1 SEM

The SEM images for α -LM are displayed in Figure 3.27 A and B at magnifications of 250 and 1000. The particles are irregular in both size and shape, but broadly speaking a cuboidal shape is observed. The estimated size range is 10 μm to 100 μm over the longest dimension. Figure 3.27 B indicates that the larger particles have some very fine particles adhered to their surfaces, leading to an overall rougher appearance.

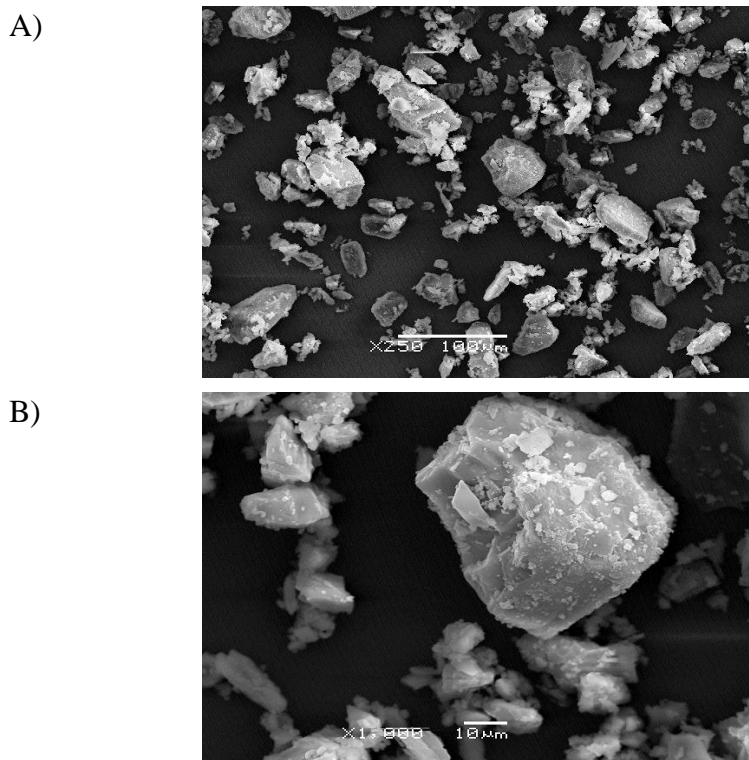


Figure 3.27: SEM image of α -LM. A) magnification X250, B) magnification X1000.

3.3.4.2 VT-IR

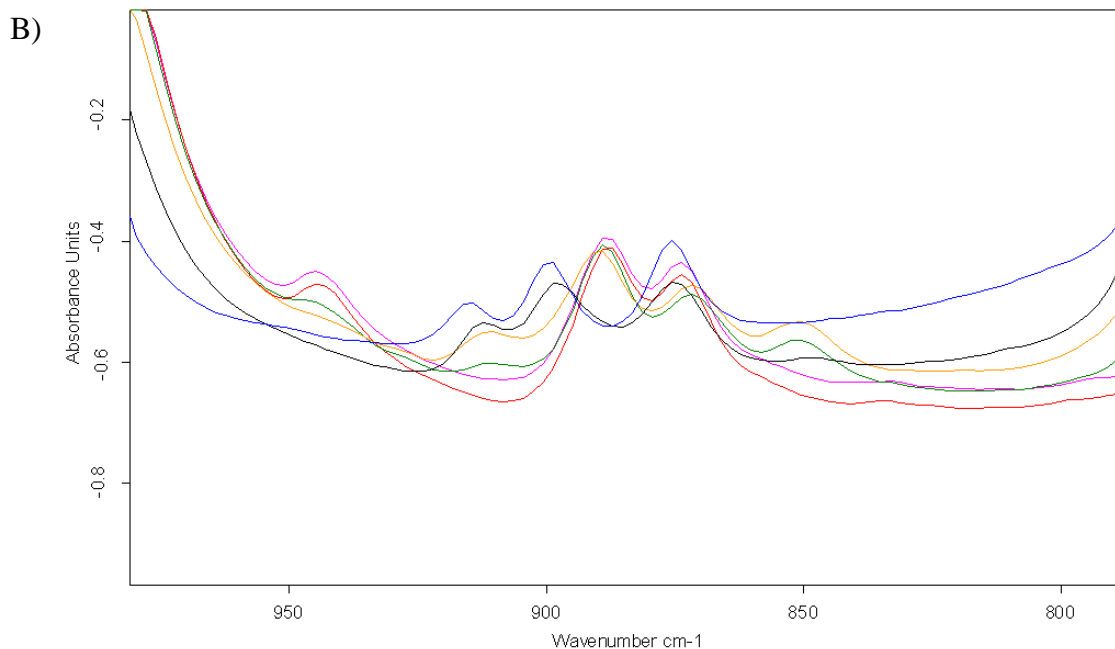
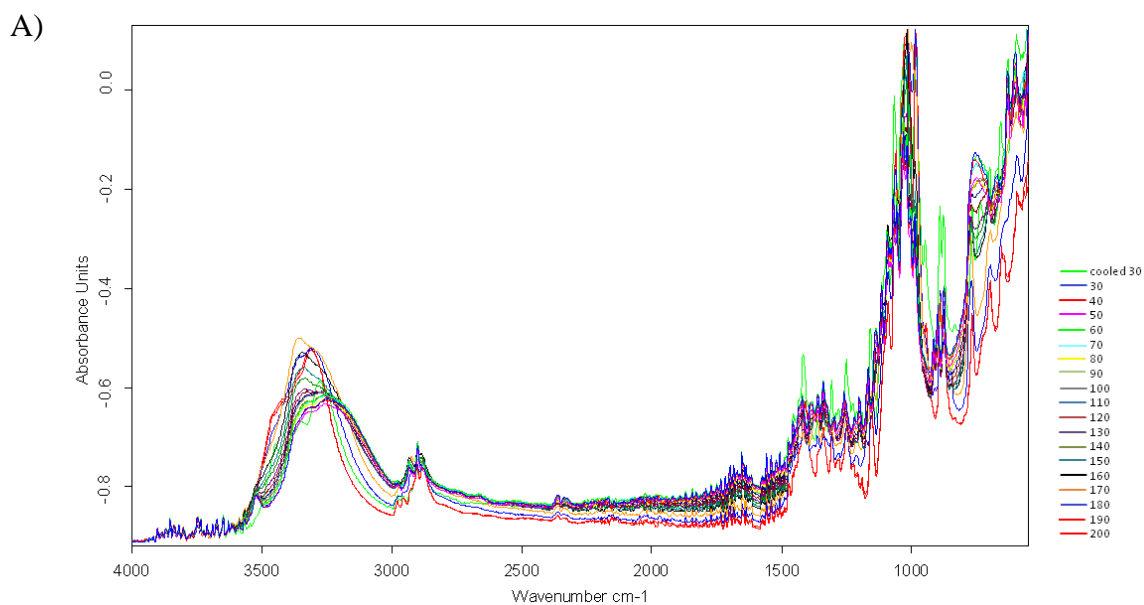
Figure 3.28 A shows a superimposition of all temperature scans for α -LM generated on the heating cycle, with an additional scan run at 30°C after cooling. It can be seen that any spectral changes on heating are very gradual until the temperature reaches about 170°C, at which point the spectrum starts to change. A small peak is seen circa 3500 cm^{-1} and this can be assigned to the O-H stretch of loosely adhered water in the sample. This peak gradually disappears from the spectrum as the temperature is increased. A clear broad large peak is observed at 3300 to 3200 cm^{-1} ascribed to H-bonded stretching of the -OH group. The compound contains many -OH groups attached to its ring structure. As the temperature increases the peak becomes larger, sharper and shifts slightly as the hydrogen bond structure rearranges. The frequency of the peak observed here is at the lower end of the range generally seen for an -OH bond, and suggests there is a strong hydrogen bond network in this sample, which is supported by inspection of its chemical structure (shown in Figure 3.29). The next range of peaks are in the 2900 cm^{-1} region and may be assigned to C-H bond stretch. These peaks shift, change shape and develop with increased temperature. Between 1400 cm^{-1} and 1200 cm^{-1} there is a range of peaks that also change with temperature. The peak at 1060 cm^{-1} may be assigned to C-O stretch in the C-OH bond and the large peak at 1029 cm^{-1} is due to O-C-O bond (Lei et al (2010)) where an

apparent doublet peak become one sharper peak with increasing temperature. At 767 cm^{-1} the peaks may be assigned to C-H bond movement. The changes in the spectra observed at temperatures greater than 170°C are maintained after cooling back to 30°C , suggesting that there is a fundamental, non-reversible change to the α -LM on heating. Figure 3.28 B shows the fingerprint region of the spectrum (990 to 830 cm^{-1}) at selected temperatures on the heating cycle. Again, the peak pattern alters when the α -LM is heated above about 170°C . A peak at 945 cm^{-1} develops and the 916 cm^{-1} peak slowly disappears. The two peaks at 891 cm^{-1} and 873 cm^{-1} shift and grow and finally another peak develops at 833 cm^{-1} . Figures 3.28 C and D, respectively, show the full and fingerprint spectra of α -LM at 30°C (before heating), 200°C and 30°C (after cooling), indicating more clearly the permanent nature of the change to the sample.

One possible explanation of these results is that the experimental VT-IR protocol used produces a structural change in the α -LM, and indeed FT-IR in the fingerprint region of 990 to 830 cm^{-1} has been used to identify the presence of the different lactose anomers (stereoisomers) by analysis of the peak pattern for the out of phase ring stretching and twisting of C-H bonds (Kirk et al (2007)). Figure 3.29 shows the structures of α - and β -lactose, indicating the position of the -OH group on the anomeric carbon.

To confirm this hypothesis, anhydrous α -lactose was produced from α -LM by oven heating in an open pan and an authentic sample of β -lactose was purchased from Sigma (UK). The nature of both materials was confirmed by DSC and then VT-IR data were collected following the experimental method used for α -LM. Figure 3.30 A and B show the full and fingerprint spectra, respectively, of anhydrous α -lactose at 30°C (before heating), 200°C and 30°C (after cooling). Figure 3.31 shows the equivalent results for β -lactose. Neither anhydrous α -lactose nor β -lactose showed significant changes in their FT-IR spectra on heating and subsequent cooling. However, the spectrum of α -LM at 30°C prior to heating has a similar peak pattern to that of anhydrous α -lactose, but at 200°C and after cooling the α -LM spectra match those of β -lactose, suggesting that the α -LM converts to β -lactose upon heating in the VT-IR equipment. This is interesting as it is known that the anomerisation process will occur preferentially in the solution or liquid phase rather than the crystalline phase (Kirk et al (2007)), indicating that the liberated water of crystallisation from the heated α -LM is retained within the VT-IR sample cell for a sufficient period of time to allow interaction with at least some of the newly dehydrated α -lactose and subsequent conversion to the β form. The VT-IR sample cell is a relatively

confined area, as contact must be maintained between sample and detector, hence removal of evaporated solvent is likely to be slow because of physical constraints and hence the anomerisation process may be observed. Unconfined heating, such as was used in the drying oven, will lead to simple dehydration with no change to the fundamental crystal lattice. This result is of significance for the interpretation of the other analytical data discussed below.



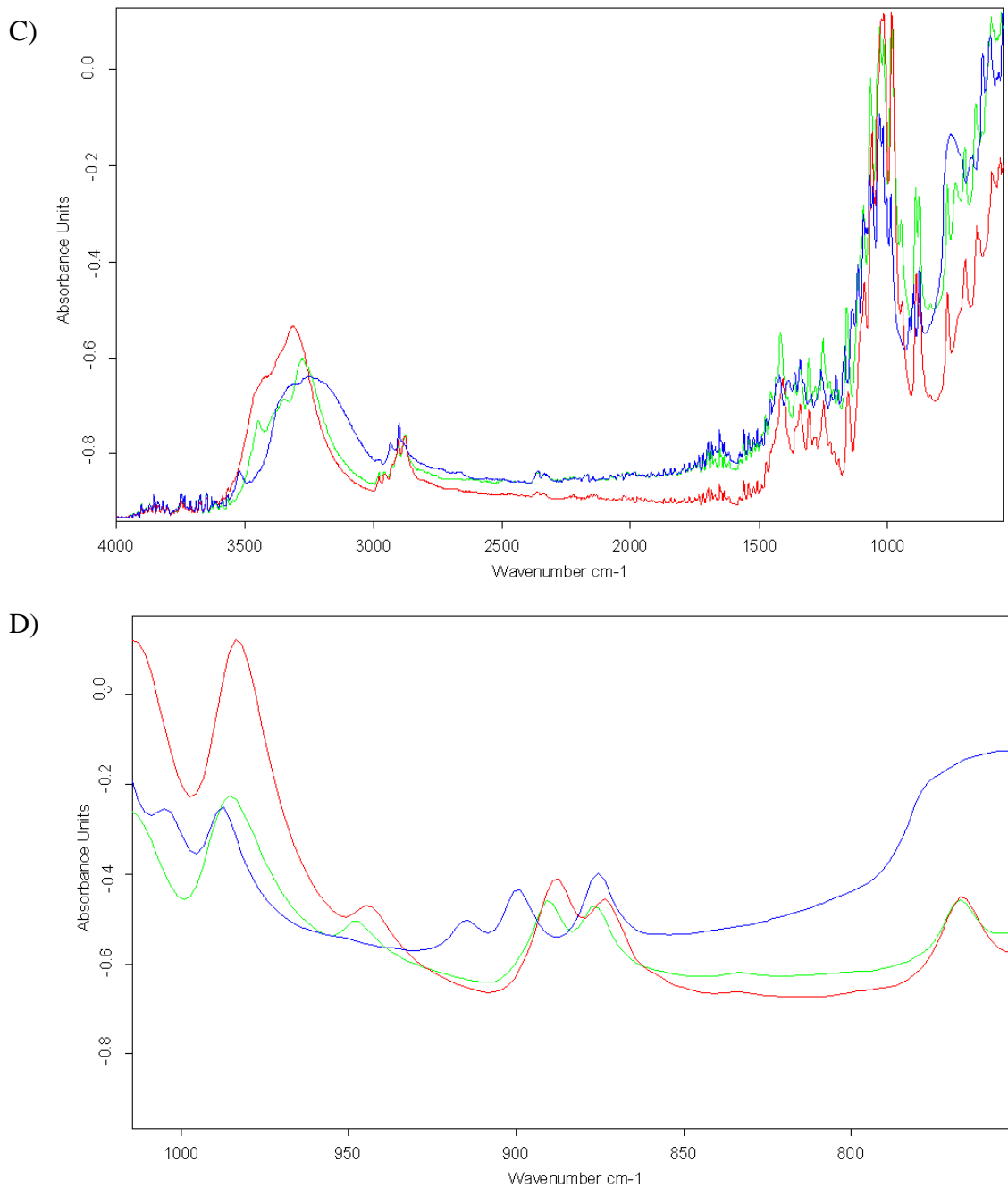


Figure 3.28. FT-IR spectra for α -LM between the temperatures of 30°C and 200°C. A) all scans; B) identification finger print region: blue 30°C, black 160°C, orange 170°C, green 180°C, pink 190°C, red 200°C; C) the results for 30°C (blue), 200°C (red), cooled back to 30°C (green); D) finger print region for 30°C (blue) and 200°C (red), cooled back to 30°C (green)

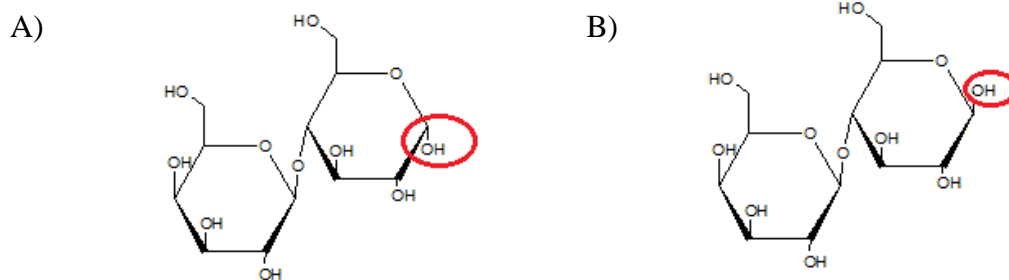


Figure 3.29: The structures of α -lactose (A) and β -lactose (B). The red ring indicates the -OH group which dictates whether the structure is α or β .

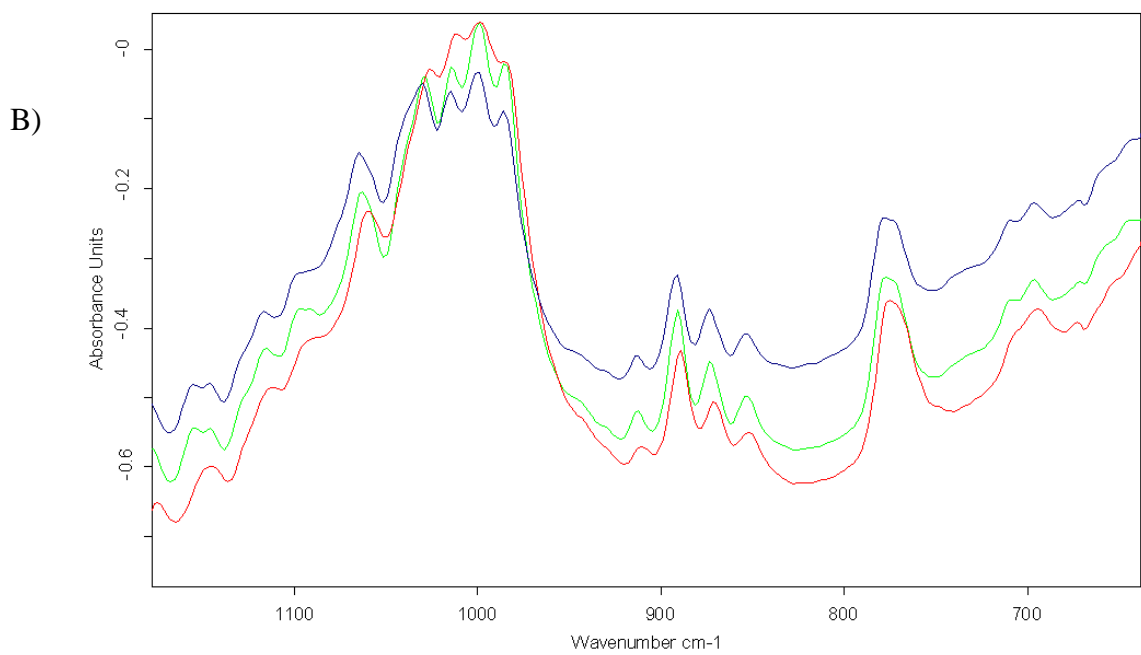
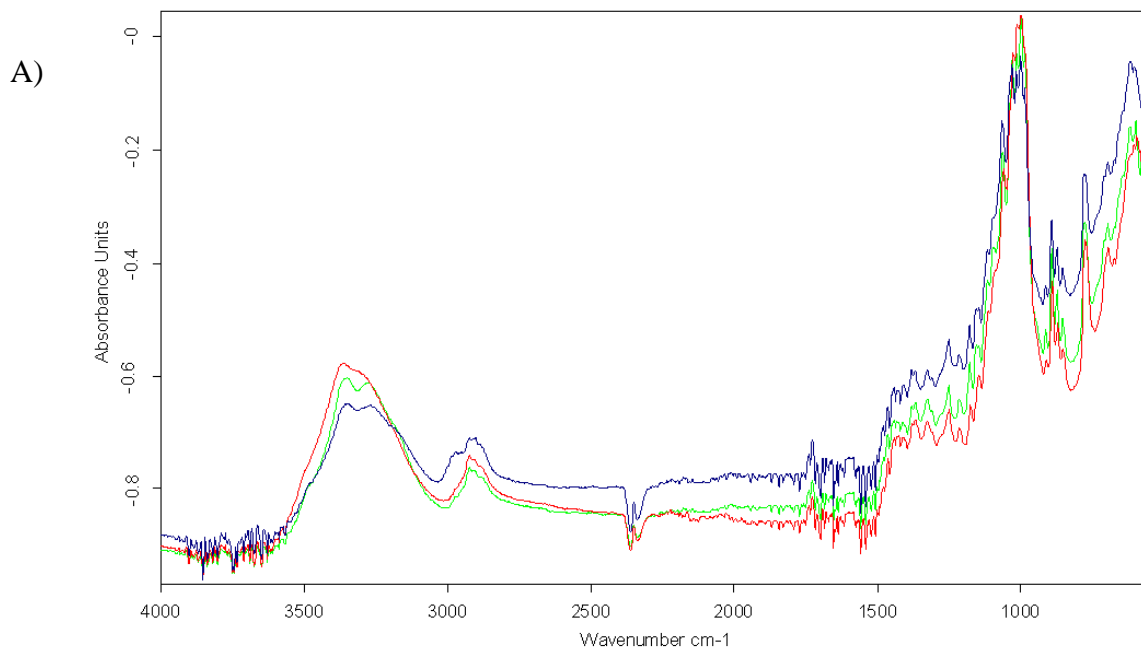


Figure 3.30: FT-IR spectra for α -lactose between the temperatures of 30°C and 200°C: A) the results for 30°C (blue), 200°C (red), cooled back to 30°C (green); B) finger print region for 30°C (blue), 200°C (red), cooled back to 30°C (green).

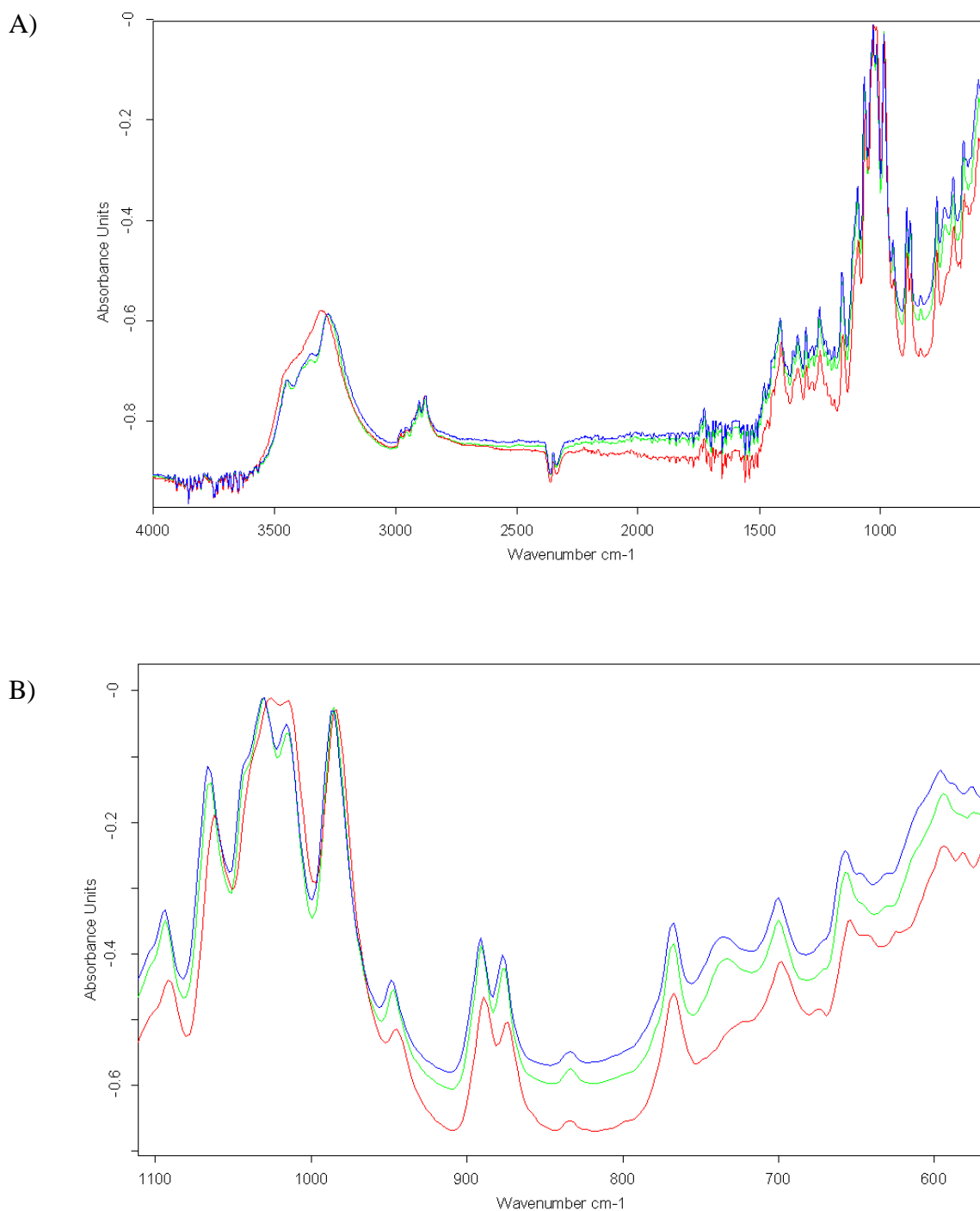


Figure 3.31: FT-IR spectra for β -lactose between the temperatures of 30°C and 200°C. A) the results for 30°C (blue), 200°C (red), cooled back to 30°C (green); B) finger print region for 30°C (blue) and 200°C (red), cooled back to 30°C (green).

3.3.4.3 DSC

Figure 3.32 show the DSC trace for α -LM as loose powder and mini-tablets (in red and blue respectively). The results show a similar profile for both samples, which was not the case for some of the other excipients studied here. Two main endotherms were observed. The first is a broad peak and occurs at circa 140°C, which can be attributed to the dehydration of the water of crystallisation from the crystal lattice. The second endotherm at circa 210°C can be assigned to melting of the newly dehydrated α -lactose (Huang et al (2013)). A small endotherm was observed at circa 235°C for the mini-tablets but not the loose powder, which can be ascribed to the melting of β -lactose.

The VT-IR results showed α -LM undergoes anomerisation to β -lactose on heating and that the presence of water is required for this process to occur. The conversion is more likely to occur in the VT-IR experiments as the sample is held within a constrained environment, whereas the DSC experiments were conducted in pin-holed pans, expressly to allow the removal of evaporated water. However, removal of evaporated water from the core of the mini-tablet is likely to be a slower process than from a powdered sample, hence a small amount of conversion may be expected for the α -LM mini-tablets.

For comparison, the two other forms of lactose (anhydrous α -lactose and β -lactose) were also analysed by DSC and the results are displayed in Figure 3.33. As expected, neither of the DSC traces show a peak associated with dehydration. Anhydrous α -lactose showed a single melting endotherm with onset at circa 210°C, similar to that of the main melting endotherm observed for the α -LM, whereas β -lactose showed a single melting endotherm with onset at circa 235°C, similar to the minor melting endotherm observed for the α -LM mini-tablets. All lactose forms showed decomposition peaks at higher temperatures.

These results indicate that a small amount of conversion is seen from the α - to the β - form of lactose during the DSC experiments and that a more constrained environment (mini-tablets rather than loose powder), which retains some evaporated water, is required for this to happen. A simplistic comparison of the size of the melting endotherms at circa 235°C for the pure β -lactose and the heated α -LM suggests that approximately 5% conversion occurs during the DSC experiment under the conditions used here.

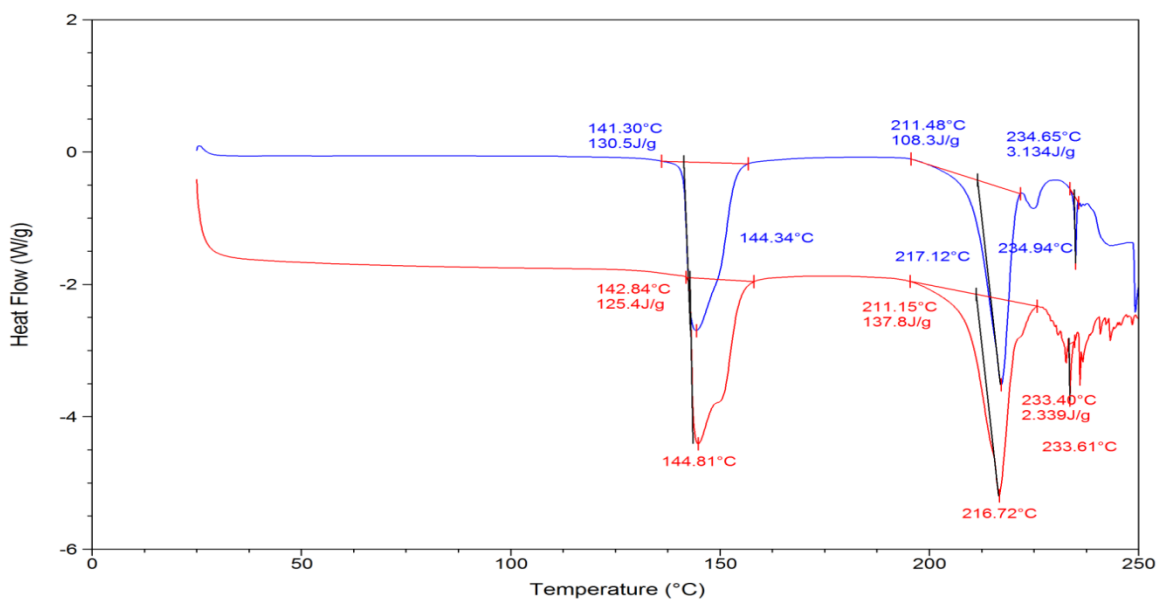


Figure 3.32: DSC traces of α -LM powder (red) and mini-tablet (blue).

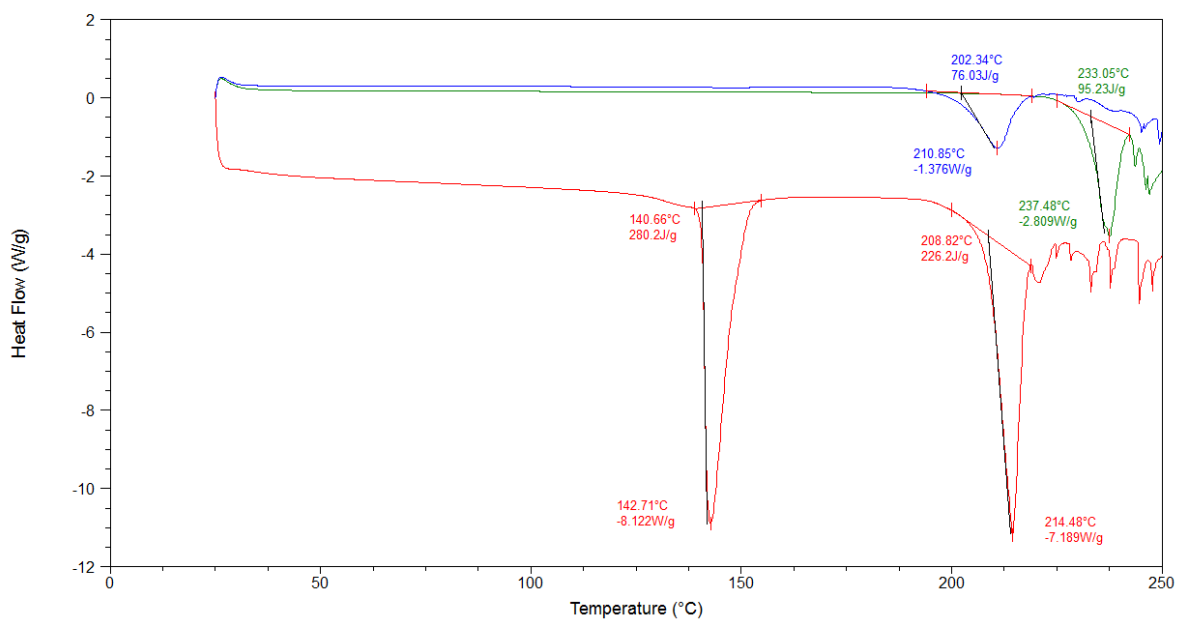


Figure 3.33: DSC traces of powder samples: anhydrous α -lactose (blue), α -lactose monohydrate (red) and beta lactose (green).

The results shown here for β -lactose are somewhat unexpected and contradictory to the those shown by Kirk et al (2007), who suggested that an "authentic sample" of β -lactose was in fact a mixture of α -lactose and β -lactose mixture in an approximate ratio of 40:60. This was ascribed to difficulties in manufacture of β -lactose. The Certificate of Analysis for the sample of β -lactose used in this study states that it is approximately 80 % β -lactose and 20 % α -lactose. However, the DSC trace clearly shows one melting endotherm only (circa 233°C onset) for the β -lactose sample, corresponding to the melting of the β -form and no transitions at the melting point of the α -form (circa 205°C onset). In the fingerprint region of the IR spectrum, the peak at approximately 900 cm^{-1} appears to be characteristic of α -lactose and does not appear in the scans of β -lactose. The peak at approximately 880 cm^{-1} seems to be characteristic of β -lactose and does not appear in the low temperature (i.e. prior to anomerisation) scans of α -lactose. This suggests that the sample of β -lactose was in fact purer than the manufacturer claimed.

3.3.4.4 AFM

The topographical AFM images of 100 μm x 100 μm using a Wollaston wire probe (micro probe) are shown in Figure 3.34. Column 1 shows the top surface of a representative compact, with six images (A to F) from sites across the radius of the compact, from the outside to the centre. Column 2 shows a similar set of images from the bottom of a representative compact. There were no obvious features in any of the α -LM compacts studied, with the only differences between the top and bottom surfaces of the compacts being the slight imprint from the punches which can be seen on the top of the compact. There was no difference across the surface from the edge to the middle. The same AFM analysis was performed on compacts of anhydrous α -lactose and β -lactose, with the resultant images being shown in Figures 3.35 and 3.36, respectively. No obvious features was observed for these samples.

To achieve a higher resolution image a nano probe was then used to scan the topography of a region of 50 μm x 50 μm . Figure 3.37 shows three topographical images taken across the surface of an α -LM compact. Figures 3.38 and 3.39 show similar images for compacts of anhydrous α -lactose and β -lactose, respectively. No obvious features were seen for any sample.

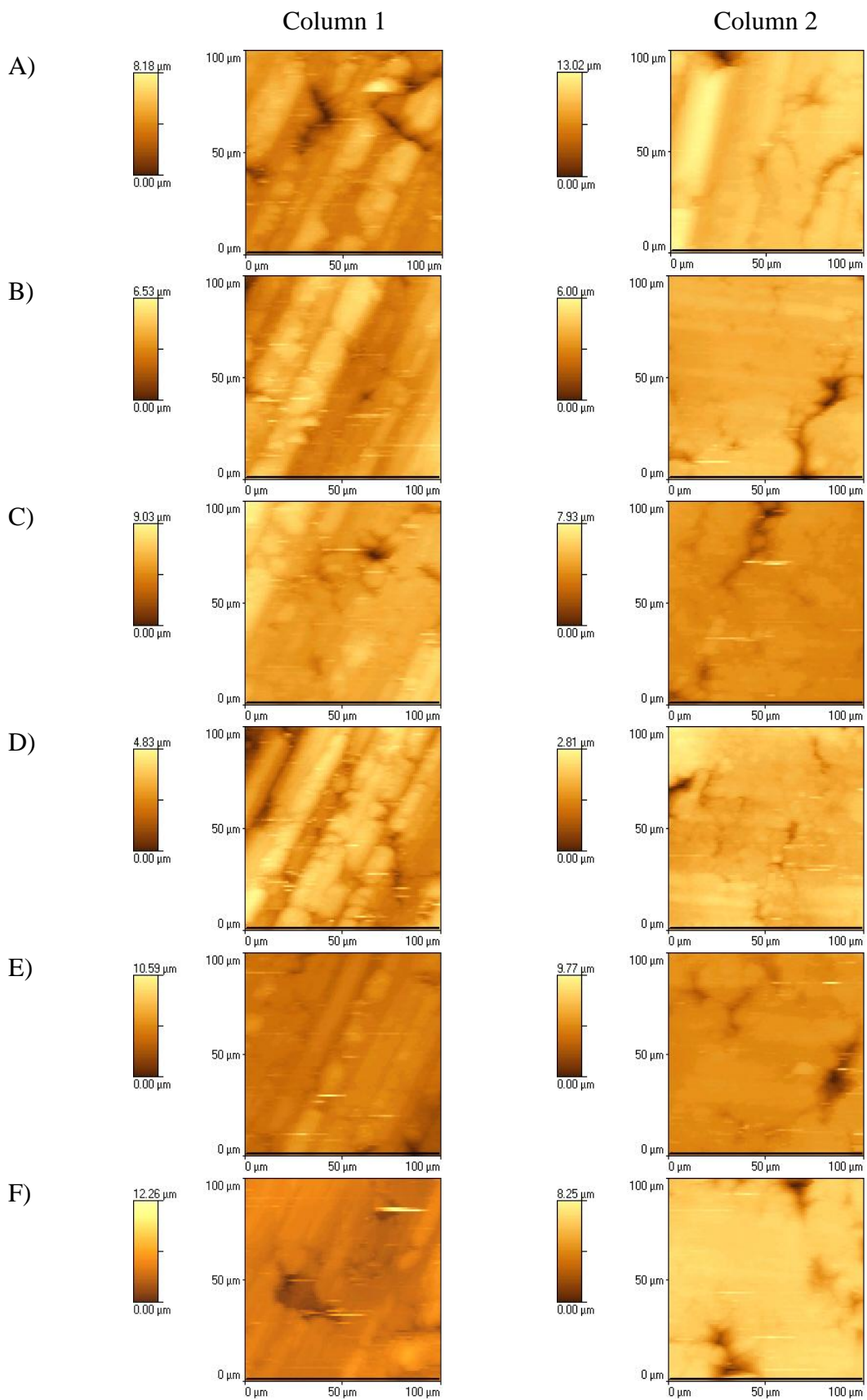


Figure 3.34: AFM scans showing the topography (as height) of the α -LM compacts using a Wollaston wire (micro) probe. Column 1 - top of the compact, column 2 - bottom of the compact; position on the radius of the compact is given from A) outside to F) centre.

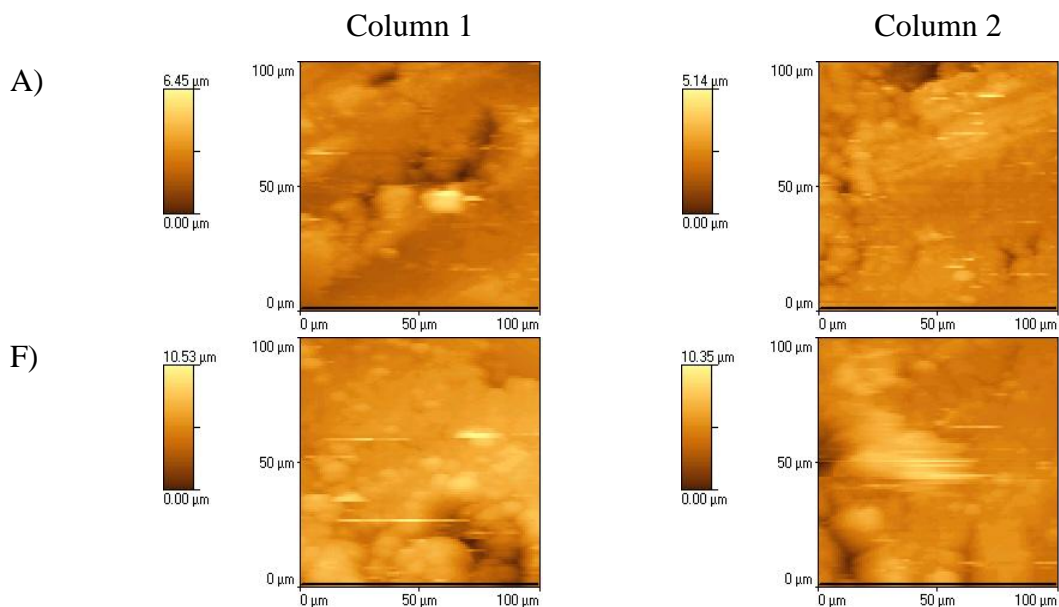


Figure 3.35: AFM scans showing the topography (as height) of anhydrous α -lactose compacts using a Wollaston wire (micro) probe. Column 1 - top of the compact, column 2 - bottom of the compact; position on the radius of the compact is A) outside and F) centre.

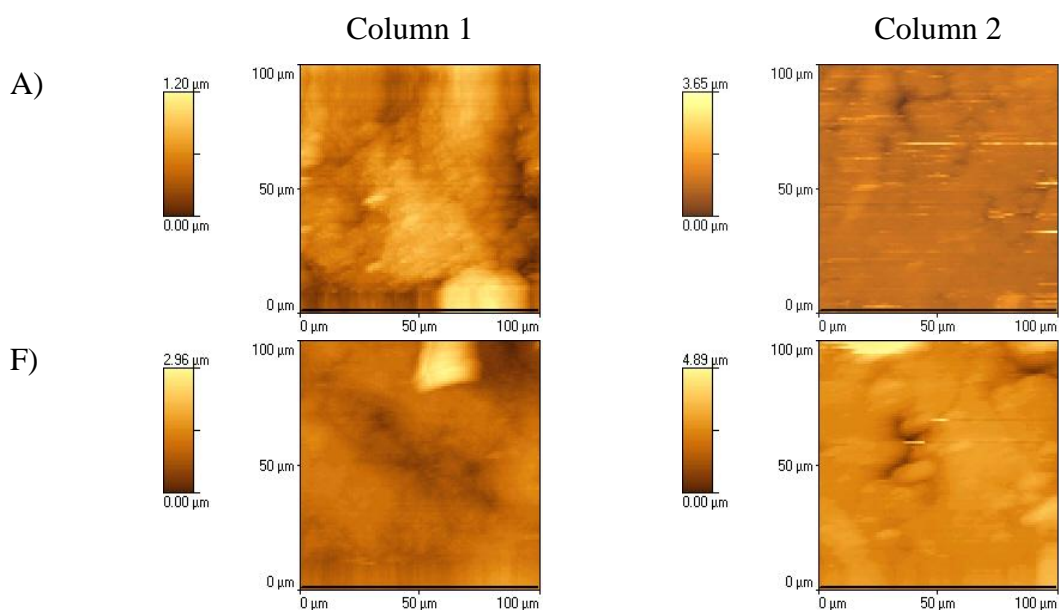


Figure 3.36: AFM scans showing the topography (as height) of β -lactose compacts using a Wollaston wire (micro) probe. Column 1 - top of the compact, column 2 - bottom of the compact; position on the radius of the compact is A) outside and F) centre.

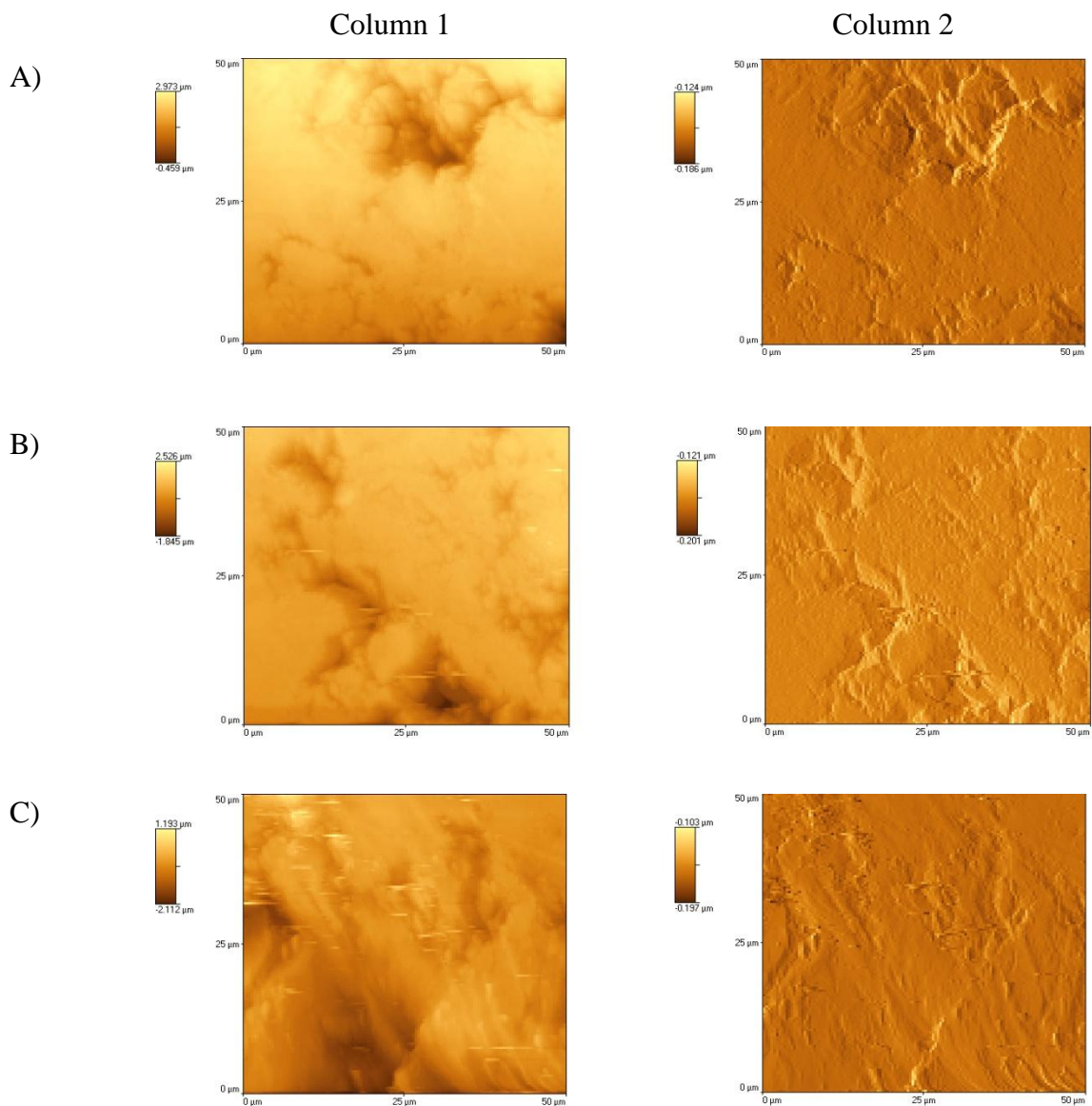


Figure 3.37: The AFM scans using the nano probes showing the topography of the α -LM compacts. Column 1 - height of the scan, column 2 - deflection of the probe; position on the radius of the compact is given from A) outside to C) centre.

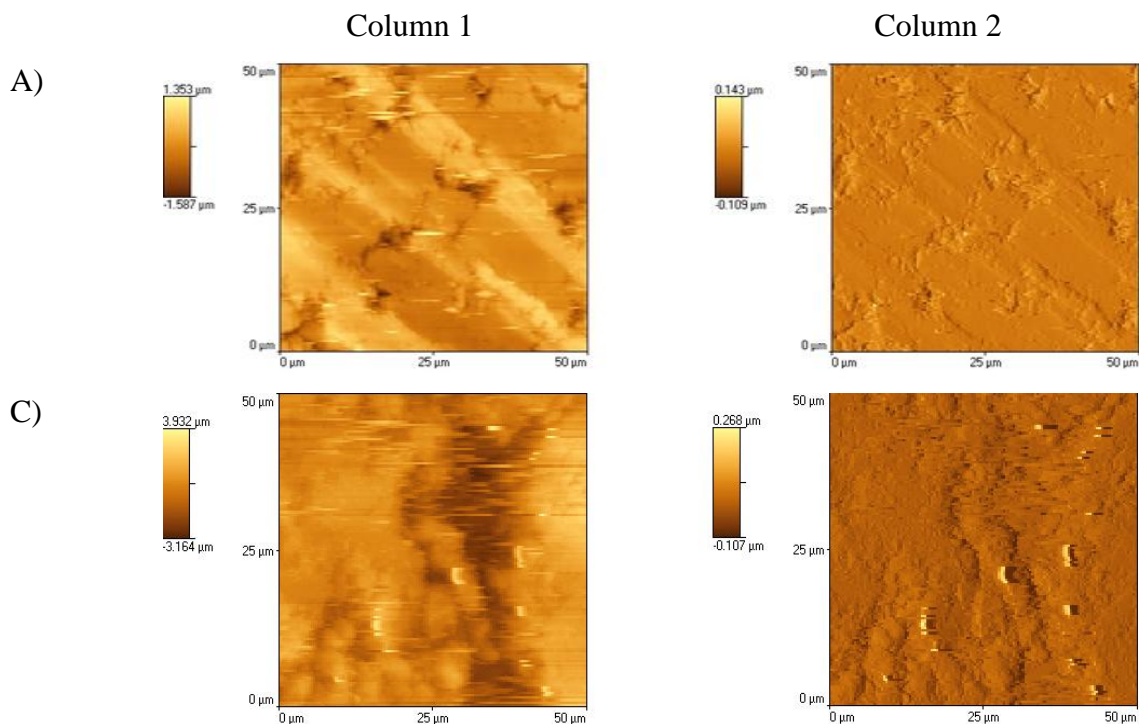


Figure 3.38: The AFM scans using the nano probes showing the topography of the anhydrous α -lactose compacts. Column 1 - height of the scan, column 2 - deflection of the probe; position on the radius of the compact is given as A) outside and C) centre.

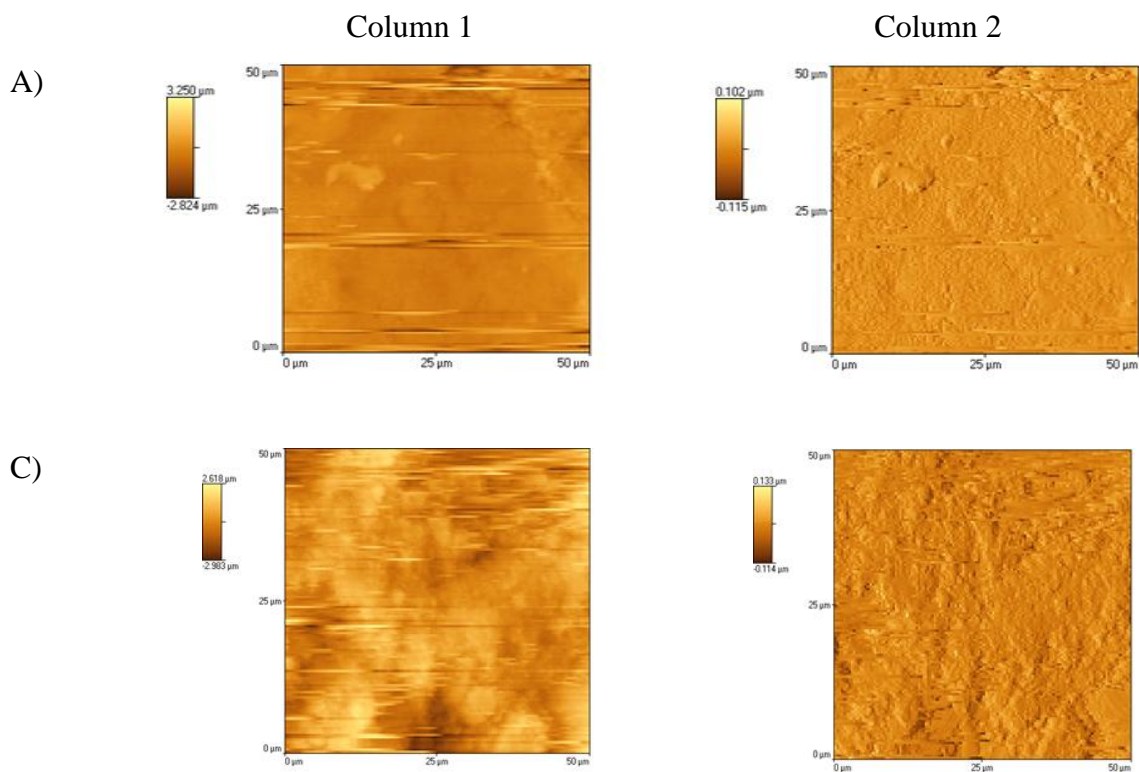


Figure 3.39: The AFM scans using the nano probes showing the topography of the β -lactose compacts. Column 1 - height of the scan, column 2 - deflection of the probe; position on the radius of the compact is given as A) outside and C) centre.

3.3.4.5 Micro-TA

Micro-thermal analysis was performed in the same manner as the AFM experiments, i.e. across the radius of both the top and bottom surfaces of the compacts. The results are shown in Figure 3.40. Column 1 shows the top surface of a representative compact, with six images (A to F) from sites across the radius of the compact, from the outside to the centre. Column 2 shows a similar set of images from the bottom of a representative compact. No substantial differences were detected between the top and bottom surfaces of the compact or across the surface from the edge to the middle. A thermal event is seen in all scans at circa 180°C, but this value varies between runs and occasionally a two step process can be observed. These results were unexpected, so were investigated further.

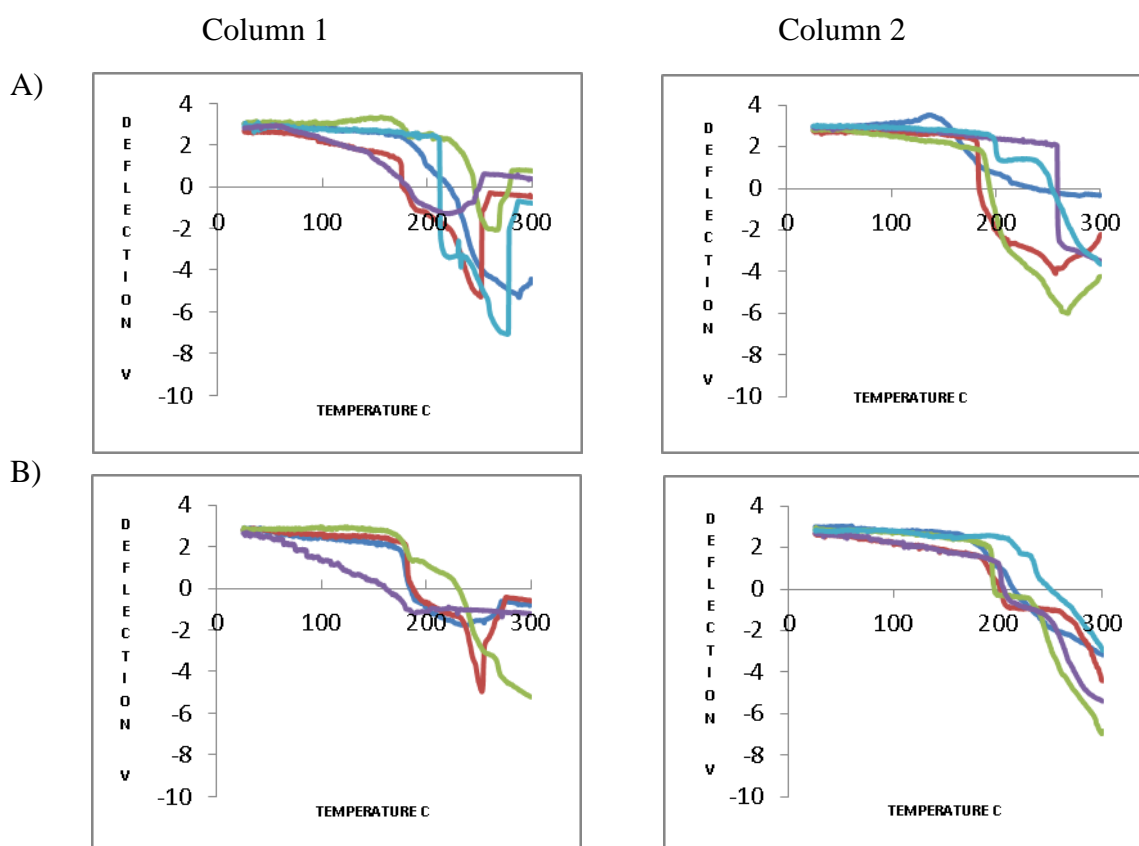
The DSC traces shows two main endotherms, at circa 140°C (dehydration of the α -LM) and circa 210°C (melting of the newly anhydrous α -lactose) and a minor endotherm at circa 235°C (melting of the formed β -lactose). However, the thermal events observed for α -LM with micro-TA do not correspond directly to any of these temperatures. Separate compacts of anhydrous α -lactose and β -lactose were produced and analysed in the same manner as the α -LM compacts. The results are shown in Figures 3.41 and 3.42, respectively. Thermal events were seen at circa 200°C and 240°C for the two samples, respectively, which more closely resemble the DSC data for these materials. Again, no differences were observed for the top and bottom or across the radius. Interestingly, both anhydrous α -lactose and β -lactose gave more reproducible results than the α -LM.

Micro-TA was then performed on compacts which had undergone a more strenuous compaction process (compacted to 10 tons and held for 2 minutes, rather than 2 tons for 30 seconds, as was normal), to ascertain whether the results were due to surface irregularities. Figure 3.43 shows the micro-TA results for separate compacts of α -LM and anhydrous α -lactose. The α -LM compacts showed more clearly a two-step process, with the first step being at circa 180°C and the second step being at circa 240°C. The anhydrous α -lactose compact showed a single deflection at circa 240°C. These results suggest that surface roughness may have an effect on the results, as the probe needs to make good contact with the sample for any transitions to be observed.

A possible explanation for the two step process seen for α -LM is that the first step is dehydration and the second step is melting, even though the temperatures of processes are

different to those indicated by the DSC experiments. An alternative explanation is that the α -LM is undergoing in situ anomerisation to the β -form, as was observed in the VT-IR experiments. This is supported by the fact that the first thermal event seen in the micro-TA results is at circa 180°C, similar to the temperature at which conversion began in the VT-IR experiments, so could possibly relate to the onset of the conversion process, with the second thermal event being the melting of the formed β -lactose. However, the anomerisation process requires water to be present and, although the compacts will have a reduced rate of removal of evaporated water compared to loose powder, the micro-TA experiments are conducted in an open environment, so retention of large quantities of water is unlikely.

Finally, compacts of all three materials were produced on the same day (compressed to 2 tons for 30 seconds), to limit the effects of day-to-day variability, with the results shown in Figure 3.44. The results indicate that distinguishing between anhydrous α -lactose and β -lactose is difficult by this technique, even though by DSC they have different melting points. However, the α -LM showed the thermal event at circa 180°C, which was not seen for the other two samples, so may be assigned to dehydration of the α -LM.



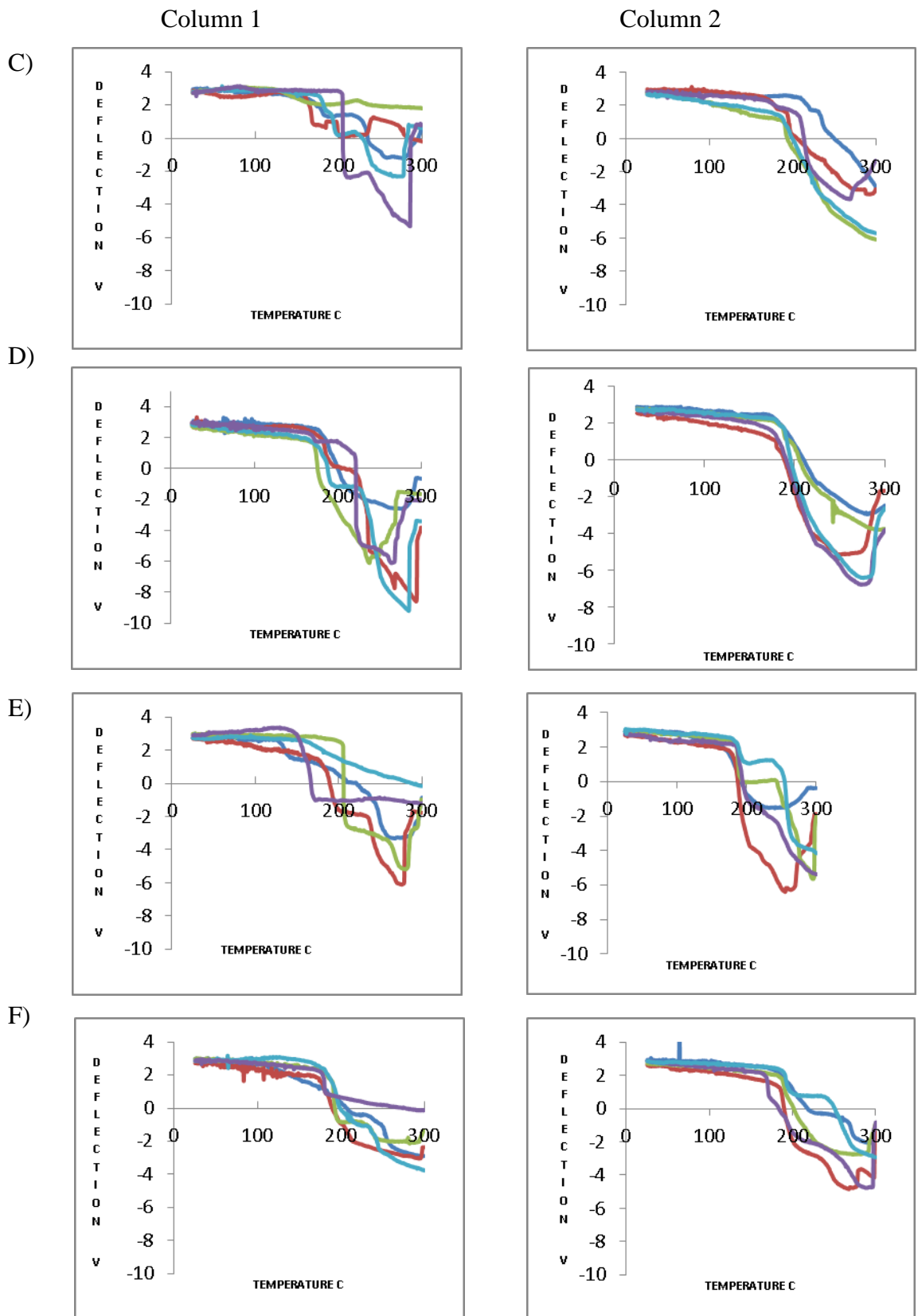


Figure 3.40: Micro-TA results of α -LM compacts, using a Wollaston wire (micro) probe. Column 1 - top of the compact, column 2 - bottom of the compact; position on the radius of the compact is given by A) outside to F) centre. Five readings were taken at each position: dark blue - site 1, red - site 2, green - site 3, purple - site 4, light blue - site 5.

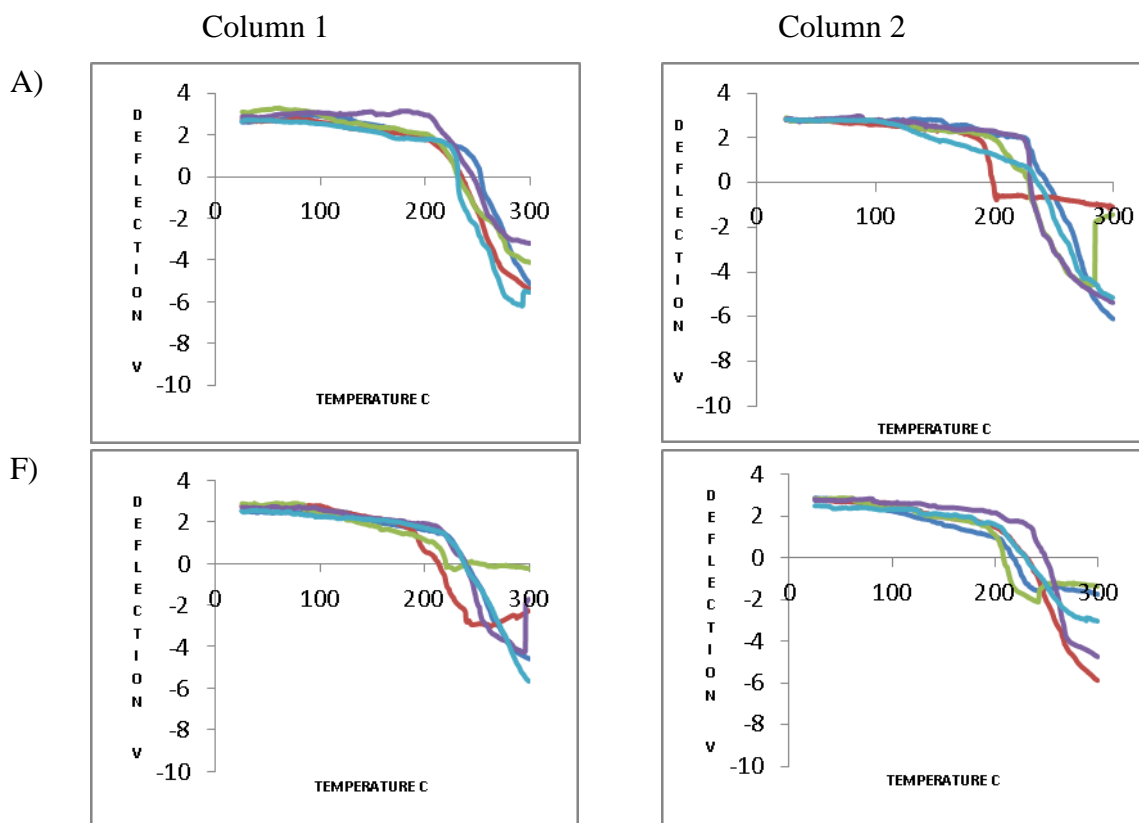
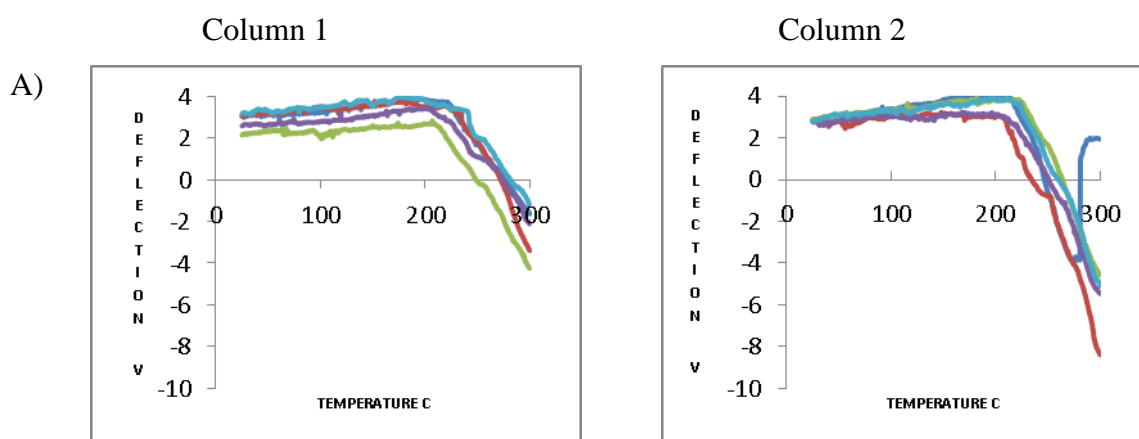


Figure 3.41: Micro-TA results of anhydrous α -lactose compacts, using a Wollaston wire (micro) probe. Column 1 - top of the compact, column 2 - bottom of the compact; position on the radius of the compact is given by A) outside and F) centre. Five readings were taken at each position: dark blue - site 1, red - site 2, green - site 3, purple - site 4, light blue - site 5.



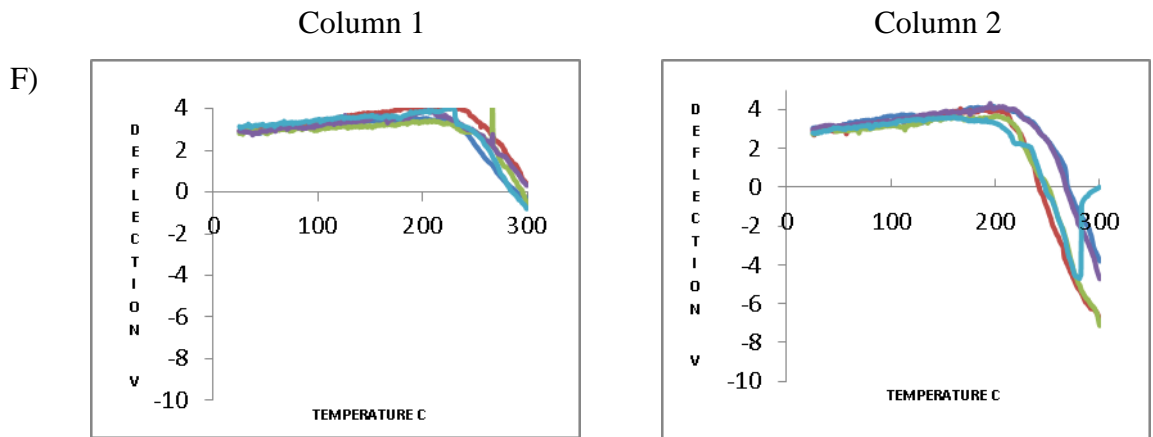


Figure 3.42: Micro-TA results of β -lactose compacts, using a Wollaston wire (micro) probe. Column 1 - top of the compact, column 2 - bottom of the compact; position on the radius of the compact is given by A) outside and F) centre. Five readings were taken at each position: dark blue - site 1, red - site 2, green - site 3, purple - site 4, light blue - site 5.

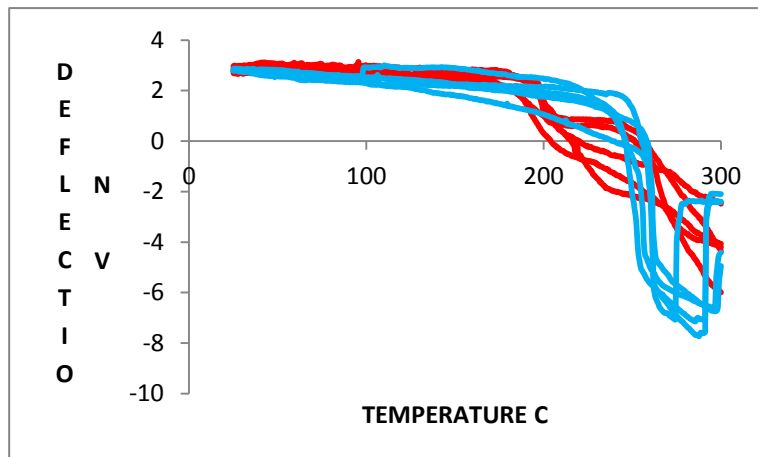


Figure 3.43: Micro-TA results for compacts of α -LM (red) and anhydrous α -lactose (blue) compressed to 10 tons for 2 minutes.

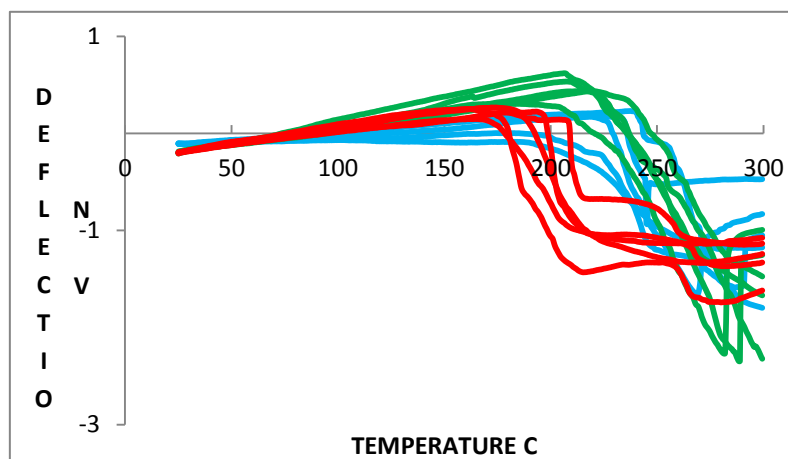


Figure 3.44: Micro-TA results for compacts of α -LM (red), anhydrous α -lactose (blue) and β -lactose compressed to 2 tons for 30 seconds (all generated and performed on the same day).

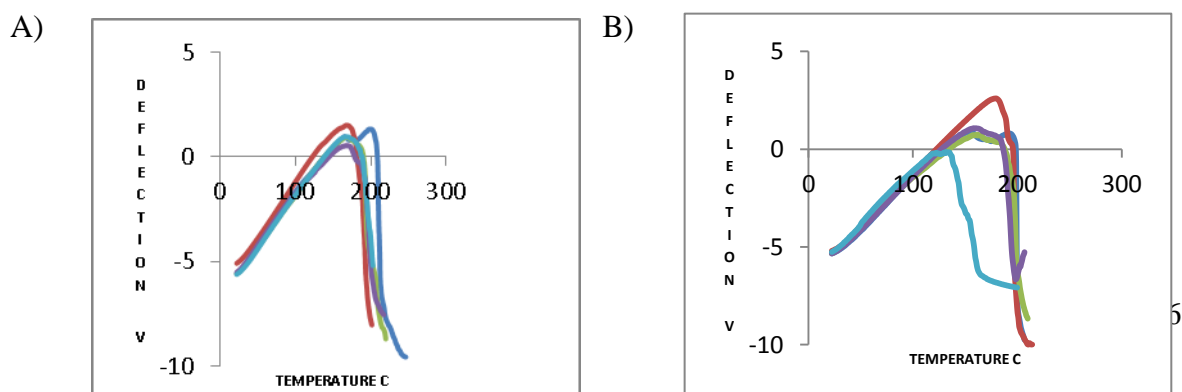
3.3.4.6 Nano-TA

Nano-thermal analysis was performed in the same manner as the AFM experiments, i.e. across the radius of the surfaces of the compacts. The results are shown in Figure 3.45 for three scans across the radius of the α -LM compact.

No differences were observed across the surface of the compact from the edge to the middle. As has been seen with other excipients, the nano-TA showed a positive baseline movement. A thermal event was observed for all samples at circa 180°C but there was a degree of variability of the actual temperature for some samples. This is probably the dehydration of the α -LM, based on the micro-TA and DC results. Only one thermal event was recorded for each sample, as the run was stopped after the first probe deflection in order to protect the probe.

Separate compacts of anhydrous α -lactose and β -lactose were also analysed and the results are shown in Figures 3.46 and 3.47, respectively. Again, there is no difference detected between the two positions on the compacts. Similarly to the micro-TA results, the temperatures of the thermal events seen in the nano-TA analysis vary from those observed in the DSC traces.

Finally, the three lactose samples were compared using the same compacts examined in Figure 3.44 (micro-TA analysis), with the results of the nano-TA analysis being shown in Figure 3.48. Similarly to the micro-TA results, the anhydrous α -lactose and the β -lactose could not be easily distinguished, although there was a slight trend towards a higher temperature for the event for the β -lactose. A lower temperature thermal event was observed for the α -LM, which is ascribed to the dehydration process.



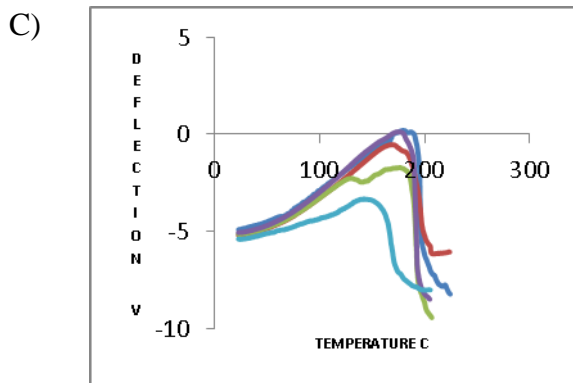


Figure 3.45: Nano-TA results of α -LM compacts using a nano probe across the radius of the compact from A (outside) to C (centre). Five nano-TA readings were taken at each position: dark blue - site 1, red - site 2, green - site 3, purple - site 4, light blue - site 5.

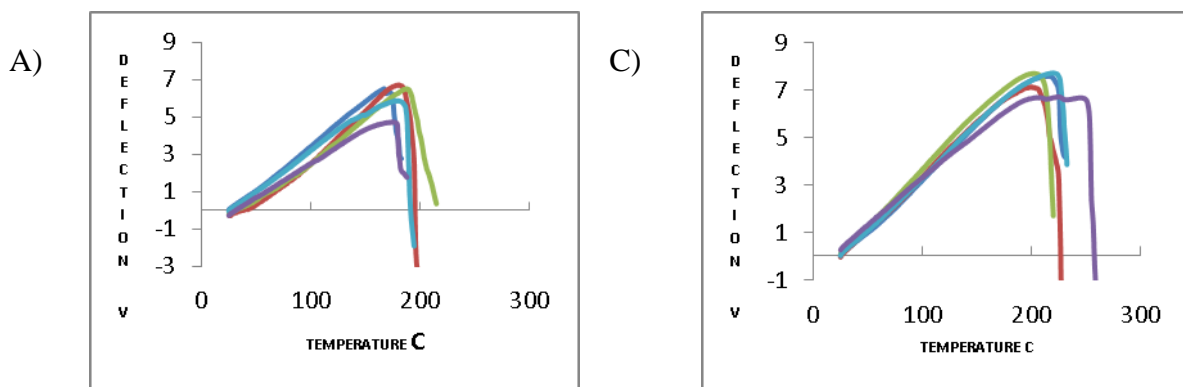


Figure 3.46: Nano-TA results of anhydrous α -lactose compacts using a nano probe across the radius of the compact from A (outside) to C (centre). Five nano-TA readings were taken at each position: dark blue - site 1, red - site 2, green - site 3, purple - site 4, light blue - site 5.

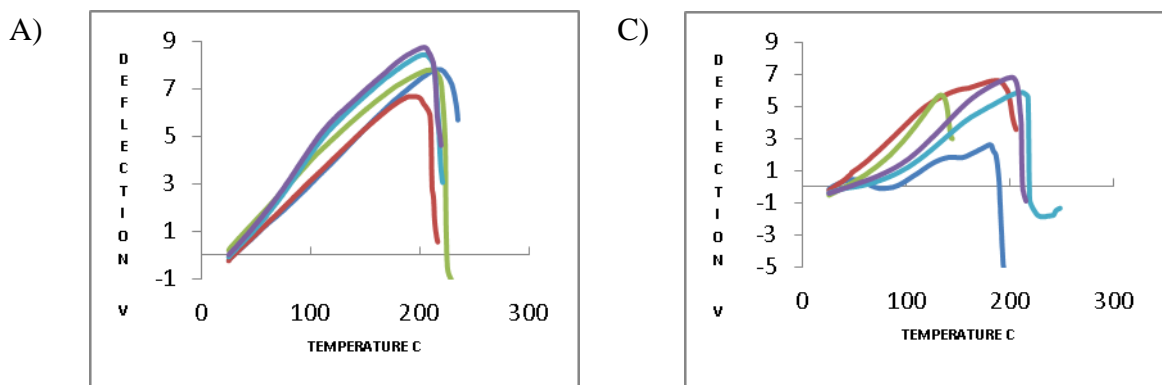


Figure 3.47: Nano-TA results of β -lactose compacts using a nano probe across the radius of the compact from A (outside) to C (centre). Five nano-TA readings were taken at each position: dark blue - site 1, red - site 2, green - site 3, purple - site 4, light blue - site 5.

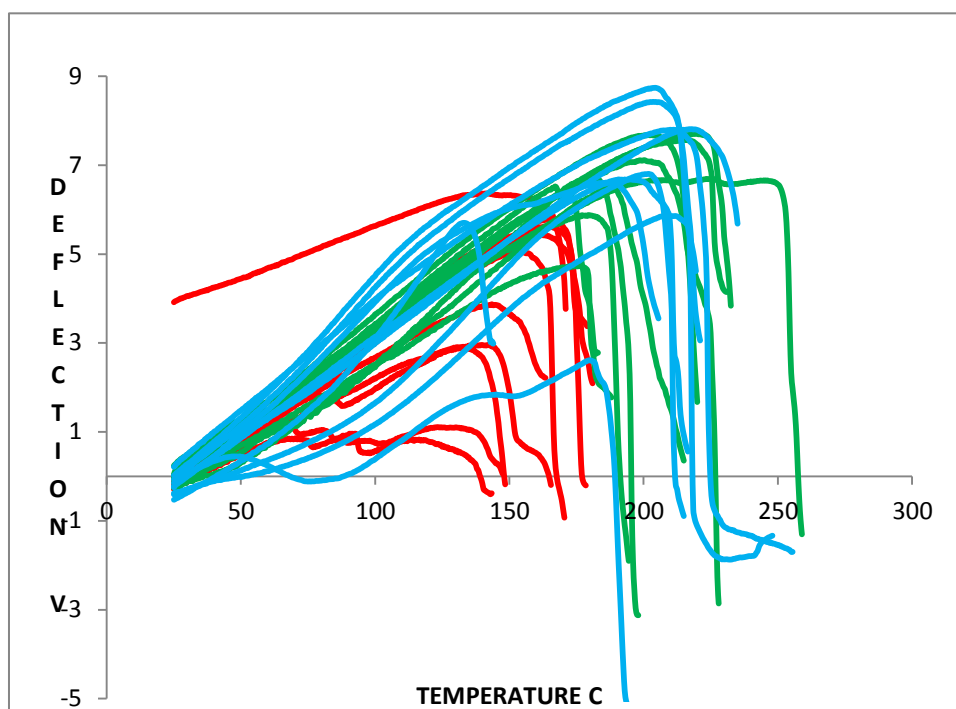


Figure 3.48: Nano-TA results for compacts of α -LM (red), anhydrous α -lactose (blue) and β -lactose compressed to 2 tons for 30 seconds (all generated and performed on the same day).

3.3.4.7 TTM

TTM was performed on the α -LM compacts. Three scans were analysed across the diameter of the compact (i.e. the two edges and the centre was scanned) and an example of the results is shown in Figure 3.49. There is generally a thermal event detected circa 180°C which is similar to the results obtained in the nano-TA and micro-TA scans. Generally, a single coloured pixellated map was produced.

The results show some variability, but as previously stated this may be influenced by the surface topography and the quality of contact between the probe and the sample. Additionally, environmental factors (e.g. lab noise and vibrations) can affect the results, but as most of the results here are in a similar range to that observed with the nano-TA, this

is unlikely to be a major factor in this case. The use of interpolation smoothes the discrete data, taking them through the colour temperature scale.

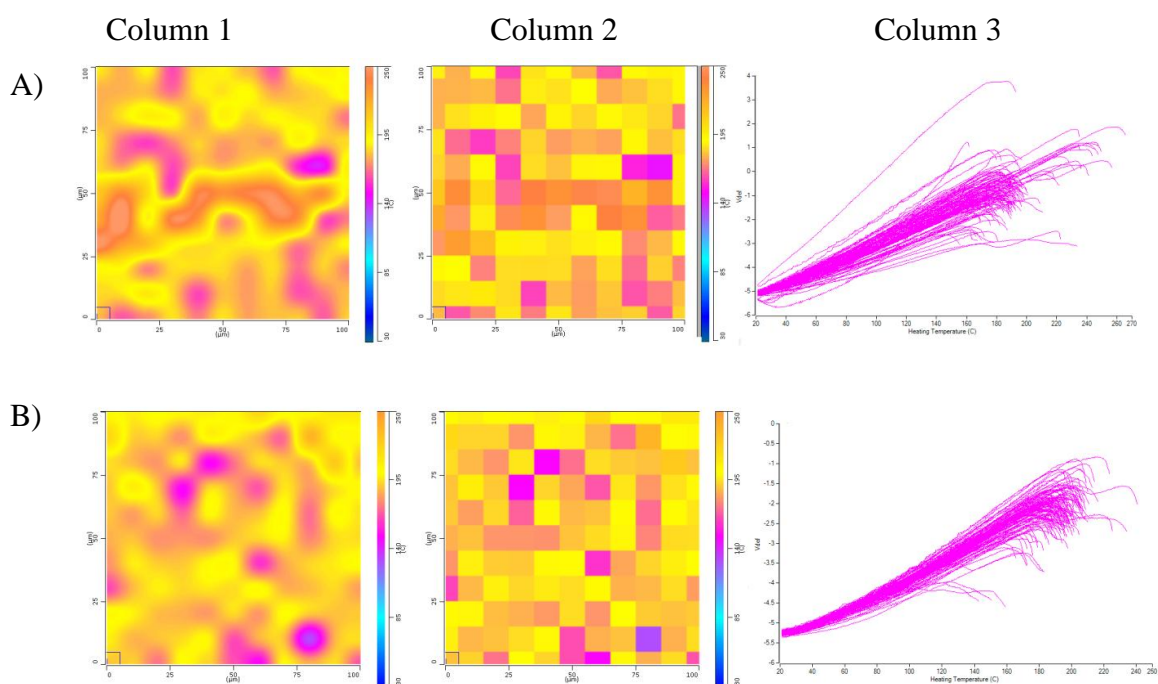


Figure 3.49: TTM maps of α -LM compacts. A) centre and B) outside of the compact. Column 1 is the interpolated (smoothed) map, Column 2 is the discrete map, and Column 3 shows the individual nano-thermal results.

3.3.4.8 Mixed lactose systems

The results discussed above suggested that the α -LM can undergo anomersation to the β form at high temperatures during some of the experimental procedures, if sufficient evaporated water is still present within the system. It would therefore be useful to be able to detect one form of lactose in the presence of another. To investigate this possibility, mixed compacts of 50 %w/w α -LM and 50 %w/w β -lactose were prepared and tested using AFM, nano-TA and TTM.

Figure 3.50 shows the AFM scans for these compacts: the two components could not be distinguished from each other. Figure 3.51 shows the nano-TA results for the mixed compacts. As the nano-TA response is different for the two forms of lactose (see earlier), it can be hypothesised that the lower temperature events are the responses of α -LM and the higher temperature events those of β -lactose. In Figure 3.51 A, two scans probably

represent α -LM and three β -lactose. In Figure 3.51 B, four scans probably represent α -LM and one β -lactose. Interestingly, the red result in Figure 3.51 A shows two peaks i.e. two thermal events. The first event is small in magnitude and the temperature corresponds with the thermal event for α -LM, with the second event being greater in magnitude and corresponding to β -lactose. As the magnitude of the two events are so different, it is unlikely to be due to complete local conversion of the α -LM to β -lactose. Hence, it is hypothesised that there is a small layer of α -LM on top of the β -lactose. On contact with the surface of the compact, the probe heats the α -LM layer and penetrates it, subsequently meeting the β -lactose layer, where a second thermal event occurs and is recorded.

TTM mapping of the mixed compacts is shown in Figure 3.52. The colour scale of the map in Figure 3.52 has been altered compared to the previous TTM results, in order to try and highlight the relatively small differences in the temperature of the thermal events of the different forms of lactose. Some differences were observed between measurement sites, but it is unclear whether these are truly a result of detecting the different components or the inherent variability of the technique, particularly given the sensitivity to surface roughness. In this case, it is probably better to position the probe manually (as is the case in the micro-TA and nano-TA experiments) on a visually flat surface, rather than perform the operation automatically (as is the case with the TTM) in order to maximise contact of the probe with the sample.

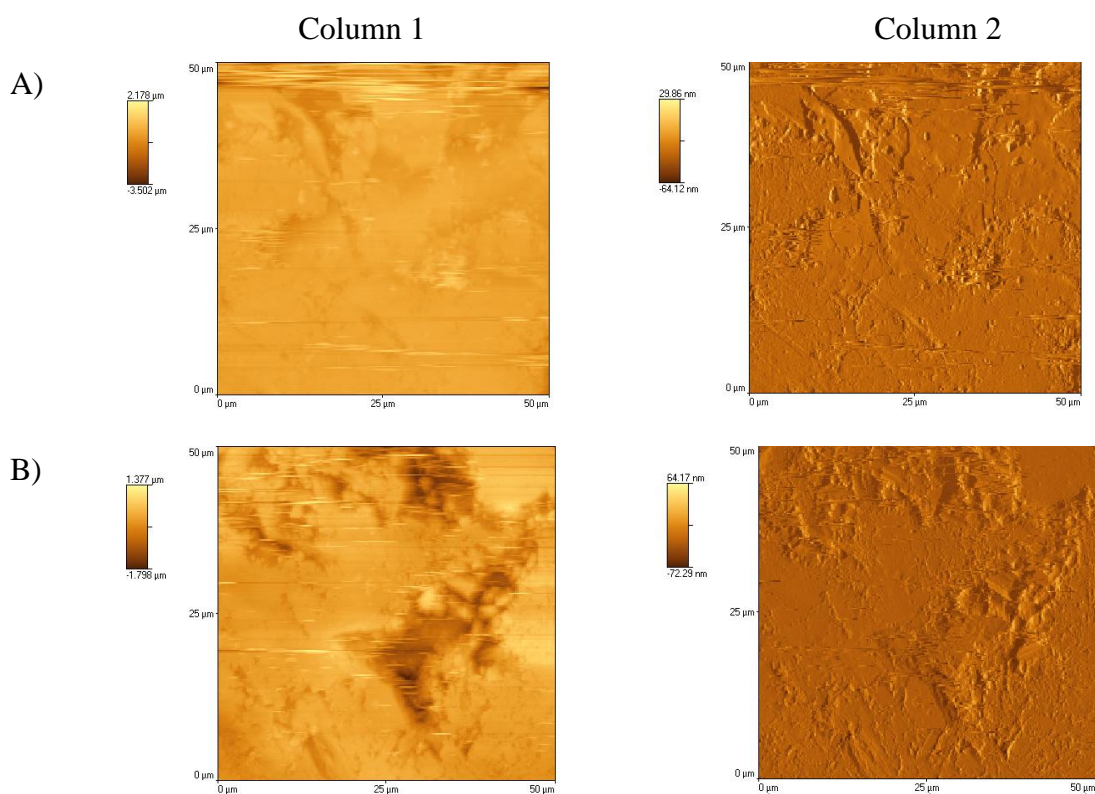


Figure 3.50: The AFM scan using the nano probe showing the topography of the mixed α -LM and β -lactose compacts. Column 1 - height of the scan, column 2 - deflection of the probe; position on the radius of the compact is given by A) outside and B) centre.

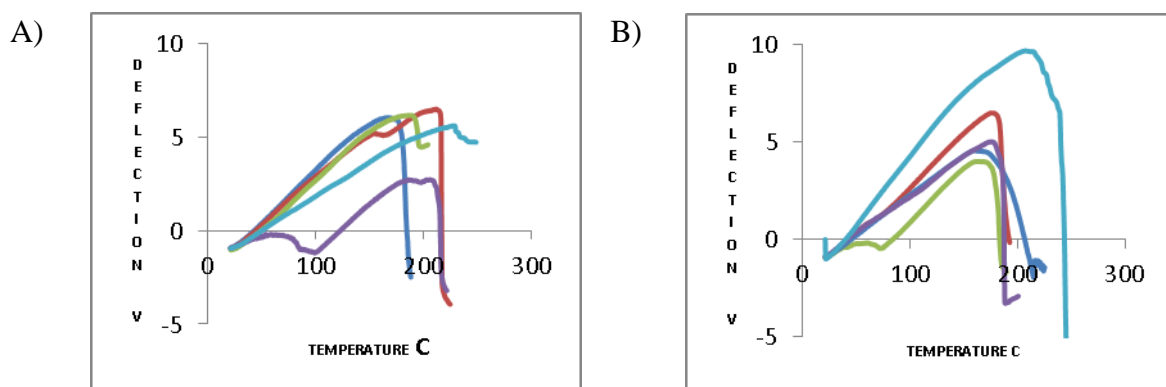


Figure 3.51: Nano-TA results of the mixed α -LM and β -lactose compacts. Position on the radius of the compact is given by A (outside) and B (centre). Five nano-TA readings were taken at each position: dark blue - site 1, red - site 2, green - site 3, purple - site 4, light blue - site 5.

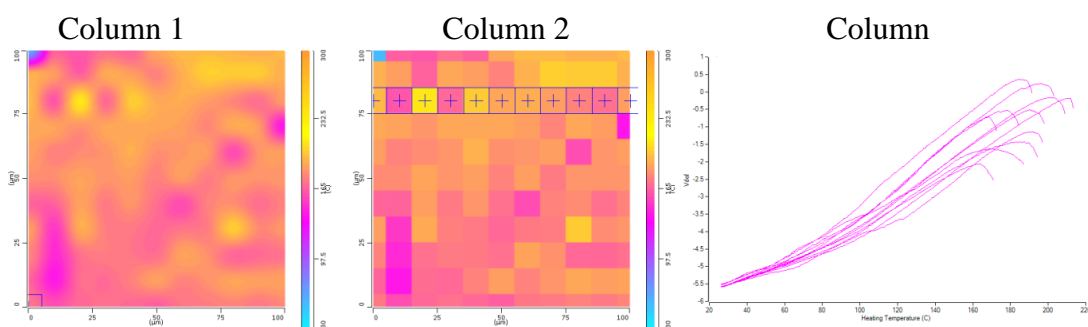


Figure 3.52: TTM maps of the mixed α -LM and β -lactose compacts. Column 1 is the interpolated (smoothed) map, Column 2 is the discrete map, and Column 3 shows the individual nano-thermal results for the line of crosses (+).

3.3.5 Polyvinyl pyrrolidone (PVP)

PVP is used in wet granulated tablet formulations as a binder, i.e. to act as an adhesive to hold the components together within the granule. It is not usually used in direct compression, but may be added as a dry binder. PVP is present in low concentrations in the final tablet (approximately 2 %w/w), so it could be argued that as the concentration used is so low, the chance of detecting any is very small. However, it is still necessary to

characterise its analytical behaviour. The question arises as to what physical form(s) PVP takes in the tablets and is there any differences in response between the forms. As PVP maybe added to a formulation as a solid (direct compression tablets) or in solution (wet granulated tablets), it was examined here in three forms: a solution (15 % w/v in water), a "dried gel" (the solution dropped onto a glass slide and dried over night in oven at 40°C (to mimic the production of the granules) and a solid (powder compressed into a compact). Some of the techniques used were unsuitable for all the forms, e.g. AFM can not be conducted on an aqueous solution, so PVP was not investigated in as much detail as the other materials and it not used in the mixed compacts.

3.3.5.1 VT-IR

An FT-IR scan was taken at 10°C intervals from 30°C to 200°C on the dried gel form of PVP, which was removed from the glass slide to allow good contact in the FT-IR. Figure 3.53 (A and B) shows a superimposition of all temperature scans for the dried gel form (A) and a summary of the lowest and highest temperatures studied (B). It can be seen that any changes with temperature are very gradual, i.e. there are no major thermal transitions. A clear broad large peak is observed at 3300 to 3400 cm^{-1} ascribed to H-bonded stretching of -OH groups and is probably due to the water remaining as part of the dried gel formation process. This peak decreases and become broader when the sample is heated as the water is evaporated and removed from the sample environment. The peaks at approximately 2900 cm^{-1} and 1400 cm^{-1} may be assigned to C-H stretching and deformation respectively. The peak at 1600 cm^{-1} can be attributed to the C=O group on a 5 member ring (Kazarian and Martirosyan (2002)) and the peak at 1300 cm^{-1} can be assigned to C-N stretch. The group of peaks observed at 2349 cm^{-1} are due to carbon dioxide being detected in the system.

Figure 3.54 displays the FT-IR spectra at 30°C for the three forms of PVP: aqueous solution, dried gel and solid. The solid and the dried gel gave very similar spectra and, predictably, the greatest difference in the spectrum of the solution was in the magnitude of the -OH peak (3400 cm^{-1}), reflecting the quantity of water present in the solution. The solution phase also showed some slight changes in the finger print region (1200 cm^{-1} to 1000 cm^{-1}), which may be as a result of greater molecular mobility in a solution and hence possible conformational changes compared to the more static solid phases.

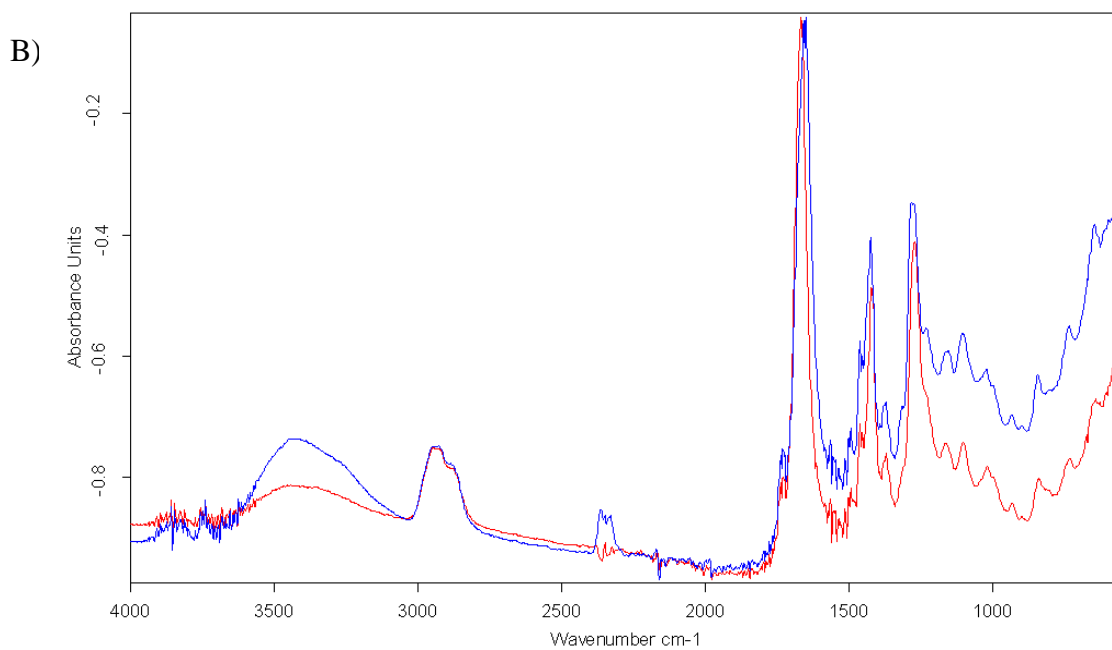
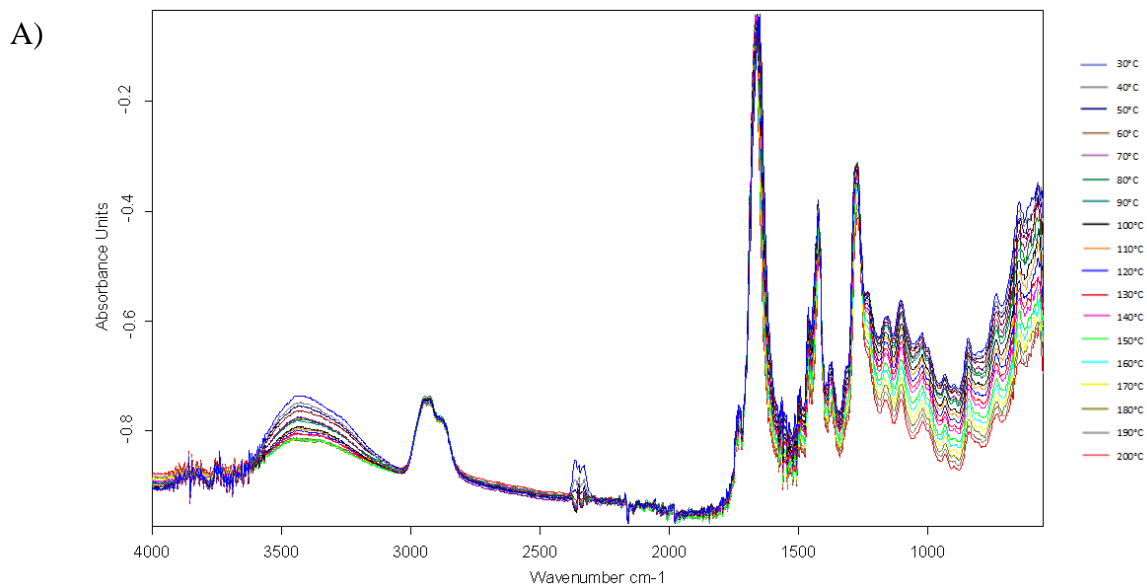


Figure 3.53: FT-IR spectra for the PVP dried gel form between the temperatures of 30°C and 200°C. A) all scans at 10°C intervals, B) the results for 30°C (blue) and 200°C (red).

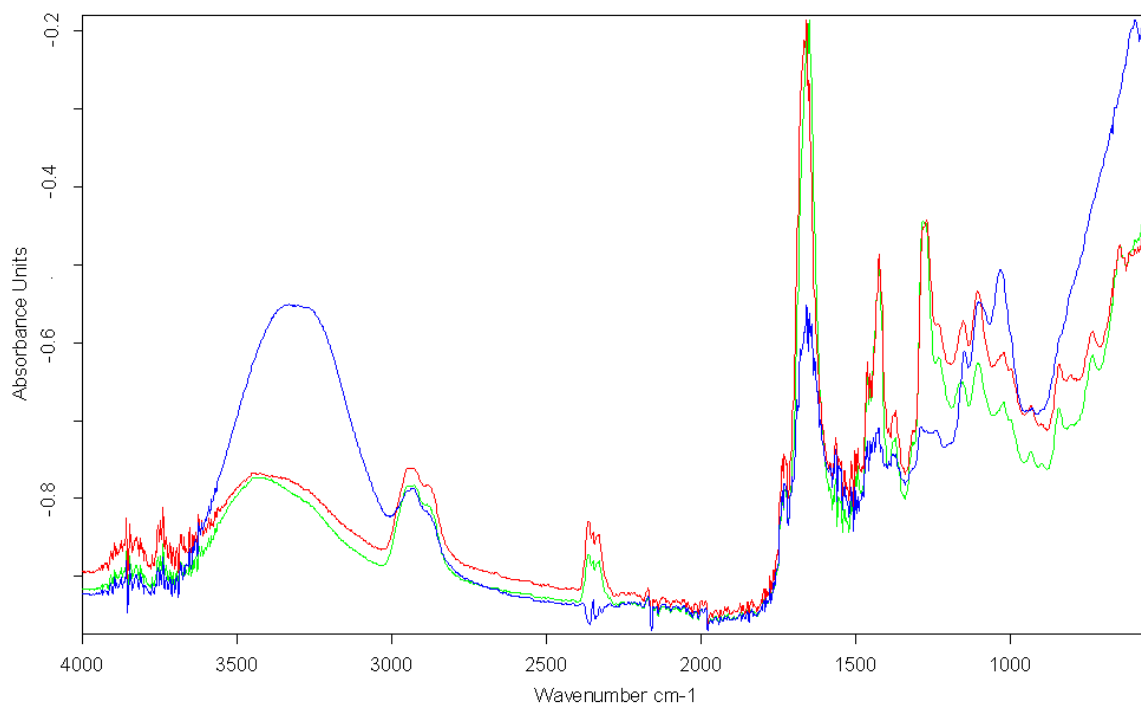


Figure 3.54: FT-IR spectra for the three PVP forms at 30°C: 15 %w/v aqueous solution (blue), dried gel (red), solid (green).

3.3.5.2 DSC

Figure 3.55 displays the DSC trace for PVP loose powder (the dried gel and the solution were not run due to concerns of conducting DSC experiments at elevated temperatures on samples with high water contents). A broad endotherm centred at circa 98°C may be assigned to the dehydration of the sample. The manufacturer's literature indicates that the sample is supplied with a residual moisture content of less than 5 %, but PVP is hygroscopic and is likely to pick up some more moisture on storage. A small thermal event is seen at circa 156°C, which can be interpreted as a glass transition and is probably related to the reported softening of PVP (Rowe et al (2009)).

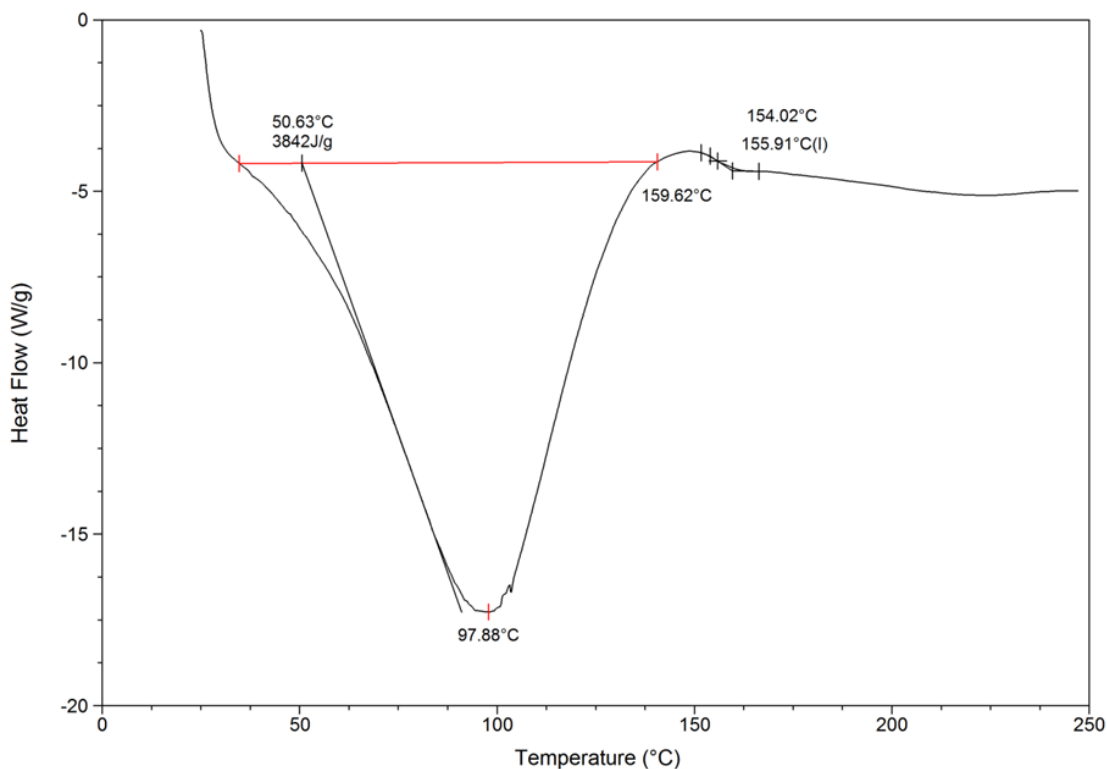


Figure 3.55: DSC trace of PVP powder.

3.3.5.3 AFM

The topographical AFM images of areas of 100 μm x 100 μm generated using a Wollaston wire probe (the "micro" probe) on solid compacts are shown in Figure 3.56. Column 1 shows the height of the surface of a representative compact, with three images (A to C) from sites across the diameter of the compact, from the outside, centre and outside. Column 2 shows a set of images for the height of the compact. The surface of the compacts is rough, with a circular patterning being observed. There is no difference across the surface between the outside and the centre.

After the preliminary work, a nano probe was employed to scan the surface and the topographical images of 50 μm x 50 μm region are displayed in Figure 3.57. The three images are representative of positions across the diameter of the compact from the outside, centre and outside. There were no obvious features of the compacts or across the surface between the outside and the centre.

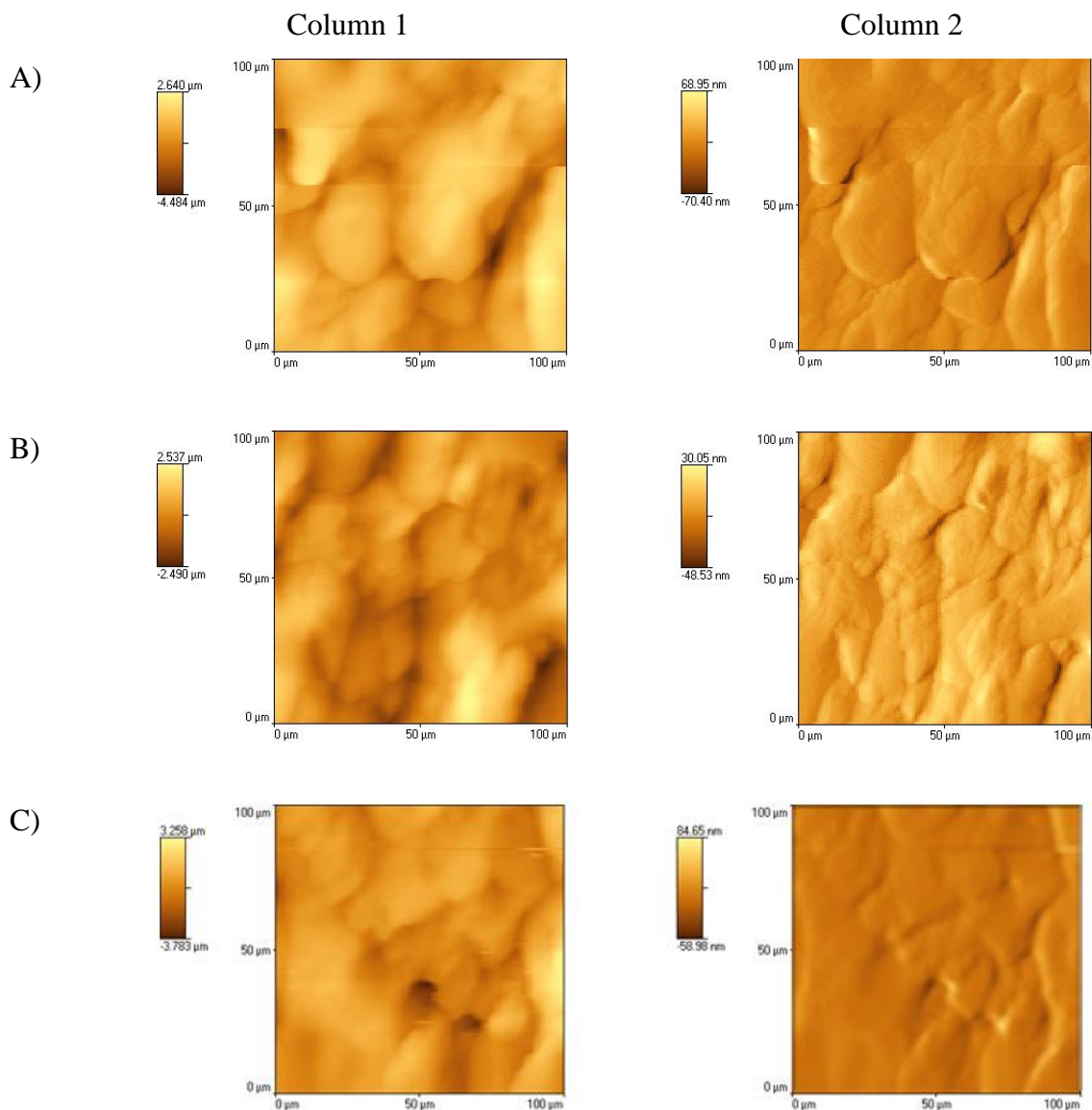
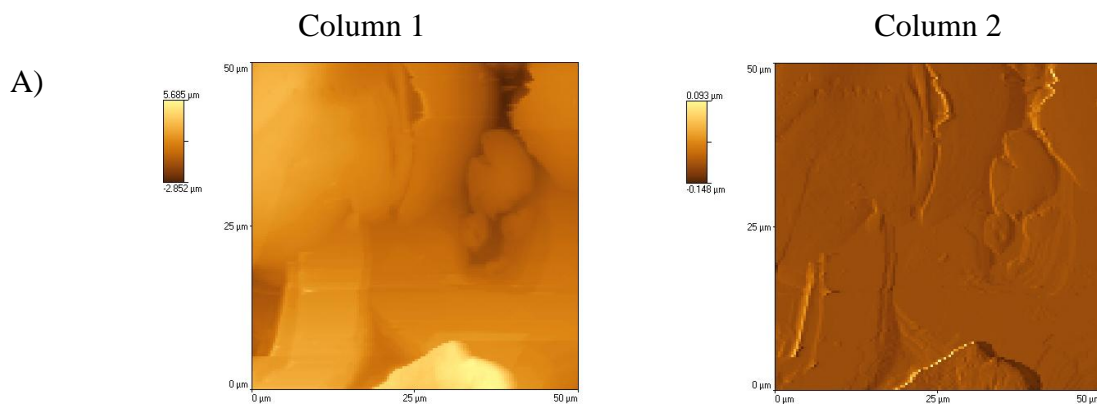


Figure 3.56: AFM scan showing the topography of the solid PVP compacts using a Wollaston wire (micro) probe. Column 1 - height of the scan, column 2 - deflection of the probe; position on the diameters of the compact is A) outside, B) centre and C) outside.



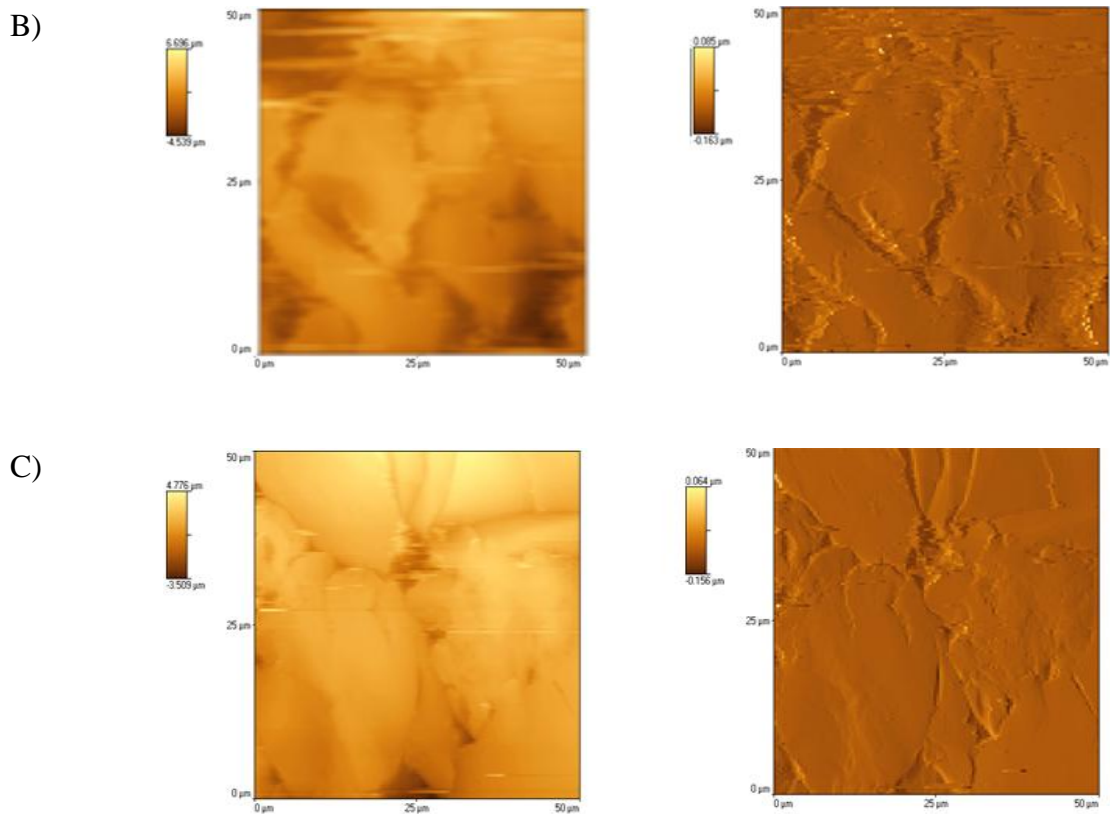


Figure 3.57: AFM scan showing the topography of the solid PVP compacts using a nano probe. Column 1 - height of the scan, column 2 - deflection of the probe; position on the diameters of the compact is A) outside, B) centre and C) outside.

It was not possible to obtain an AFM image of the dried gel phase of PVP. As the solution dried on the glass slide to form the dried gel, it formed ridges which were too high for the probe to cope with. Figure 3.58. shows a photomicrograph of the sample surface and probe indicating the ridges.

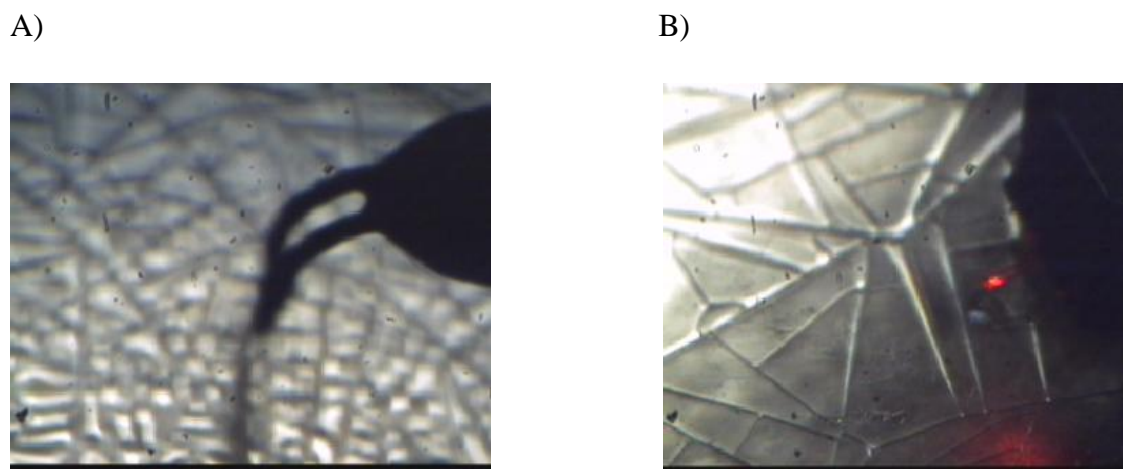


Figure 3.58: Images of PVP in dried gel form using A) the Wollaston wire probe and B) the nano probe.

3.3.5.4 Micro-TA

Micro-TA was performed on compacts made from solid PVP as described previously. Three regions were analysed across the diameter, which are represented by A and C (outsides) and B (centre) and in Figure 3.59. Micro-TA scans were also performed on the dried gel form by manual positioning the probe at a relatively smooth site between the ridges and the results are shown in Figure 3.60. The main thermal event occurs at approximately 200°C, which is most likely related to the softening process seen in the DSC trace, albeit at a higher temperature. Some of the curves exhibit an additional peak at lower temperatures, which may be associated with dehydration of the sample. No differences were observed across the diameter of the compacts or between the two forms of PVP.

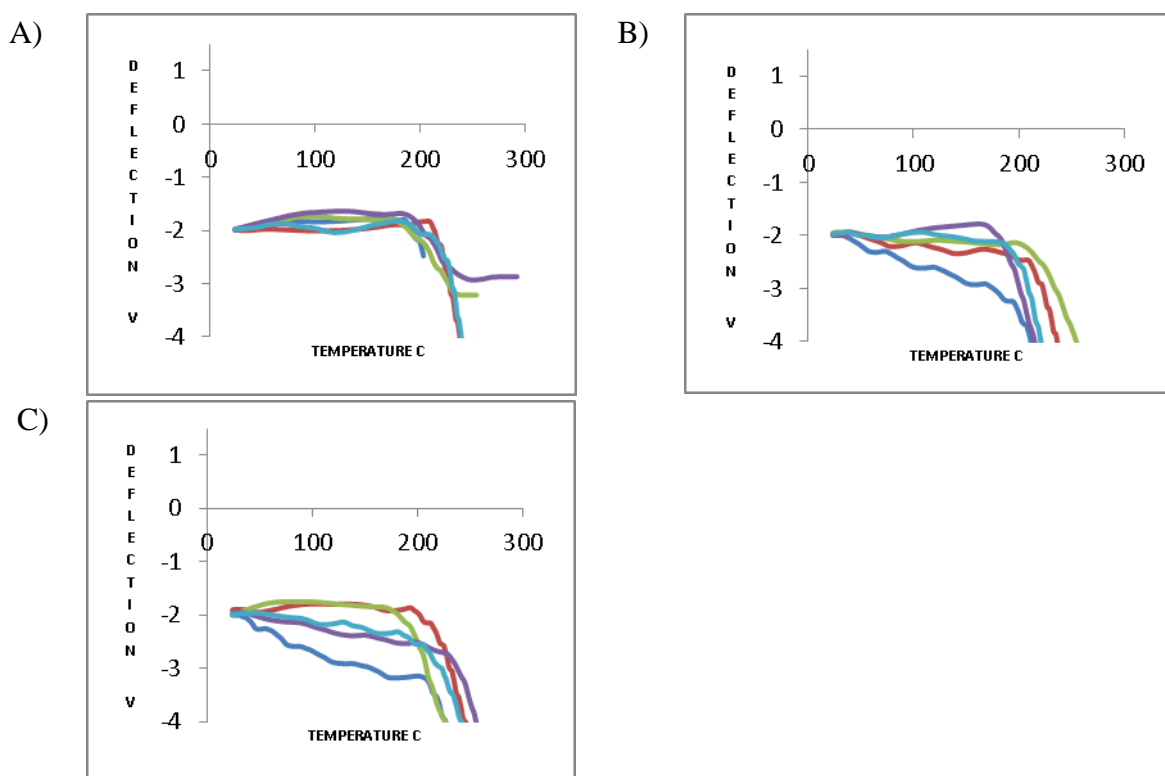


Figure 3.59: Micro-TA results of compacts of solid PVP, using a Wollaston wire (micro) probe. Position on the diameter of the compact is given by A) outside, B) middle and C) outside. Five readings were taken at each position: dark blue - site 1, red - site 2, green - site 3, purple - site 4, light blue - site 5.

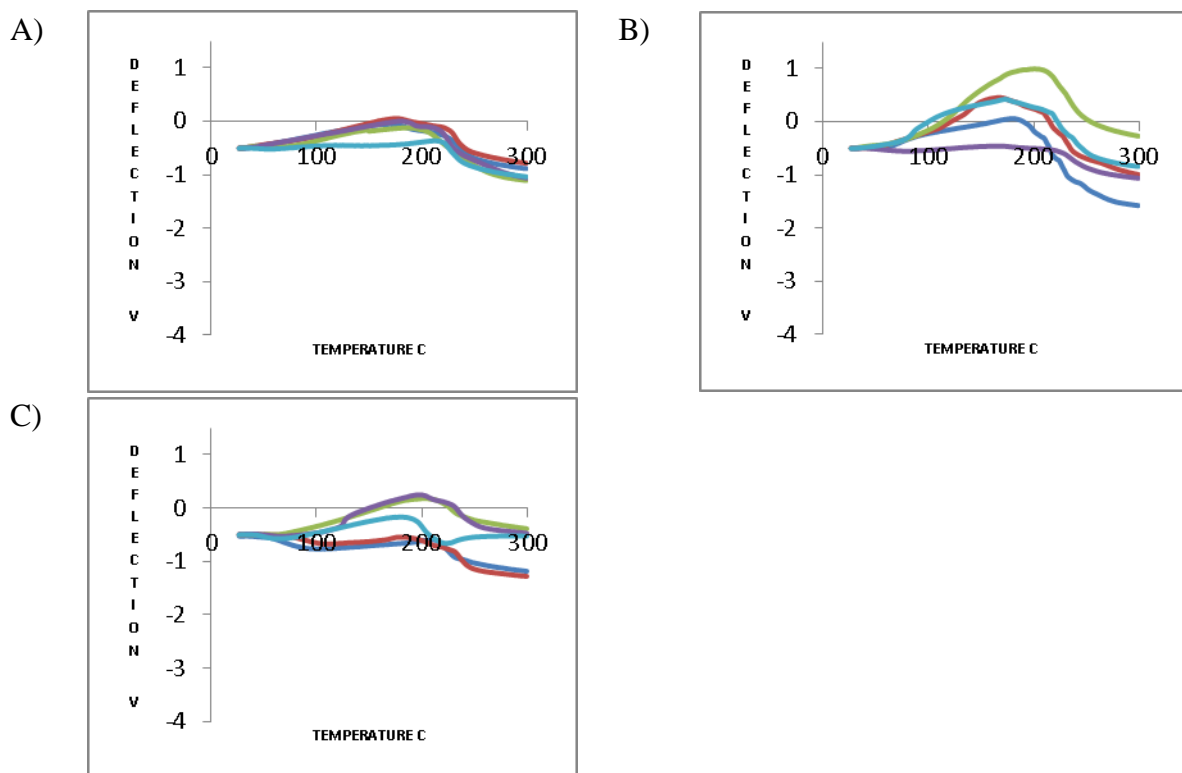


Figure 3.60: Micro-TA results of dried gel-form PVP using a Wollaston wire (micro) probe. Position on the diameter of the compact is given by A) outside, B) middle and C) outside. Five readings were taken at each position: dark blue - site 1, red - site 2, green - site 3, purple - site 4, light blue - site 5.

3.3.5.5 Nano-TA

Nano-TA was performed on the compacts of solid PVP in a similar manner to the micro-TA with scans being taken across the diameter of the compact. The results are shown in Figure 3.61. A thermal event was detected at circa 175°C which could be attributed to the softening of the PVP. Interestingly, the nano-TA data are much closer in temperature to the DSC results than the micro-TA data. Some of the nano-TA traces show a double peak, similar to the micro-TA, and the lower temperature peak is probably associated with the dehydration event. As with the micro-TA, no differences were observed across the diameter of the compact. It was not possible to obtain nano-TA scans on the dried gel form of PVP.

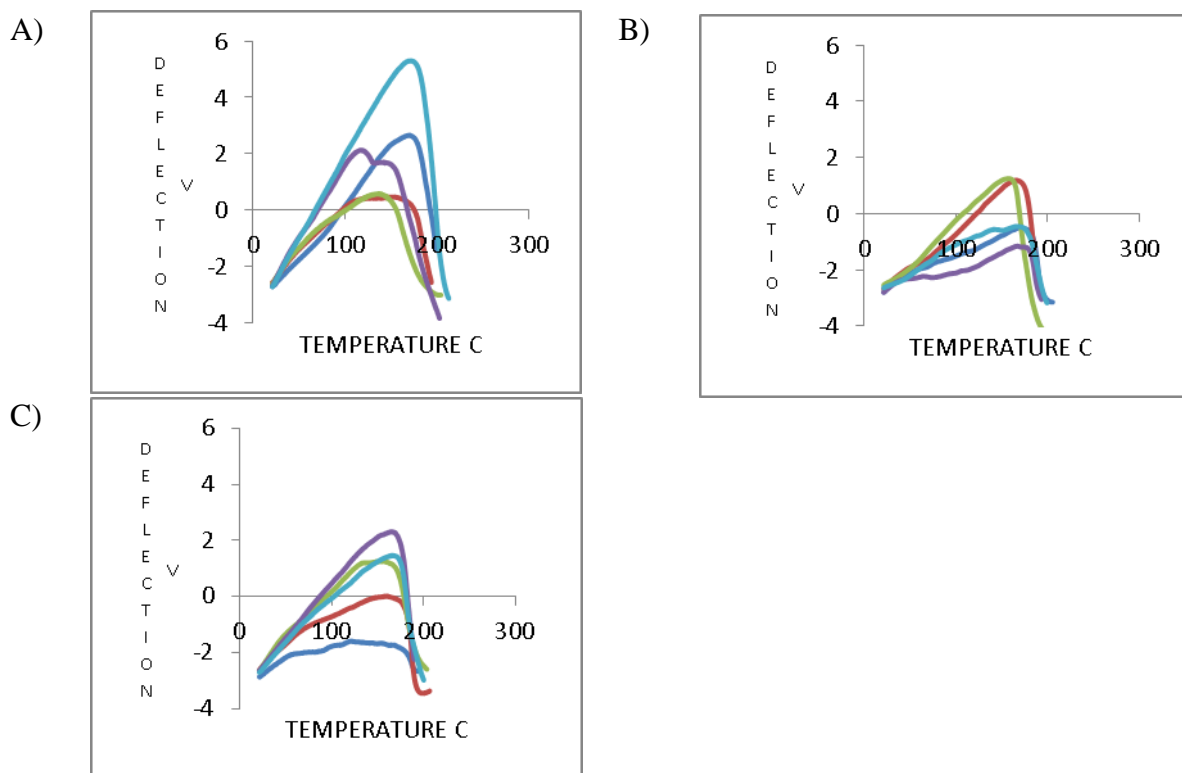


Figure 3.61: Nano-TA results of compacts of solid PVP using a nano probe. Position on the diameter of the compact is given by A) outside, B) middle and C) outside. Five nano-TA readings were taken at each position: dark blue - site 1, red - site 2, green - site 3, purple - site 4, light blue - site 5.

3.4 Conclusions

In this chapter, five excipients were profiled individually using a range of physical analytical techniques in order to provide a baseline set of data for use in subsequent work. SEM showed that the materials varied greatly in their particle morphology. VT-IR indicated that, with the exception of α -LM, the materials were stable to heating, showing only dehydration and melting responses. Unexpectedly, the α -LM sample demonstrated anomerisation to the β - form during the VT-IR experiment. This is explained by the slow rate of removal of evaporated water from the VT-IR sample cell, allowing interaction of the water with the newly-anhydrous α -lactose and permitting the anomerisation process. Free water is required for this process to occur, as demonstrated by the lack of transformation when anhydrous α -lactose was used as the starting material. The conversion of α -LM to β -lactose was also seen, but to a lesser extent, in the DSC experiments. In this case, most of the evaporated water was removed swiftly through the pin holes in the pan lids.

DSC was used to establish the thermal behaviour of the individual components to aid in the interpretation of micro-TA and nano-TA data. Before the micro-TA and nano-TA experiments were conducted, AFM scans were performed on the same region of the surface of the compacts to establish whether there were any topographical details which might affect interpretation of the micro-TA and nano-TA results. No distinguishing features were seen for any of the individual materials, except for PGS and solid PVP where a circular pattern was observed. Figure 3.62 shows a summary of the micro-TA results for the five excipients, with PVP added as the dried gel form as it is the most representative of the form it is likely to be in within the mini-tablets. In this case, the responses were scaled so that they all start at the same point. PGS and MCC show no thermal response over the temperature range studied, which could be a potential problem in differentiating materials in a mixed system. However, the baseline incline change is steeply negative for PGS and generally slightly positive for MCC, so this may be used as a means of distinguishing between these two components. The other components have distinct responses. A summary of the nano-TA results is shown in Figure 3.63: all of the materials give a distinct response. Again, the responses were scaled so that they all start at the same point. In this case, PVP is not included, as solid PVP is not likely to be the form it is in within the final mini-tablet formulation.

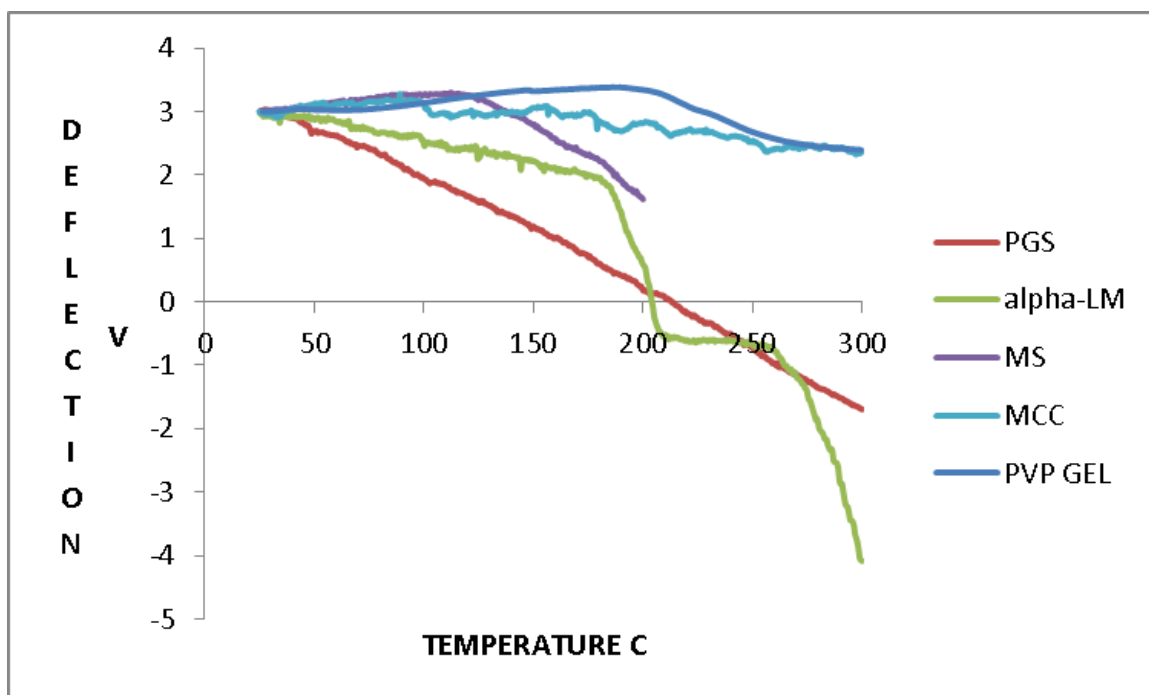


Figure 3.62: A summary of the micro-TA results for the five excipients.

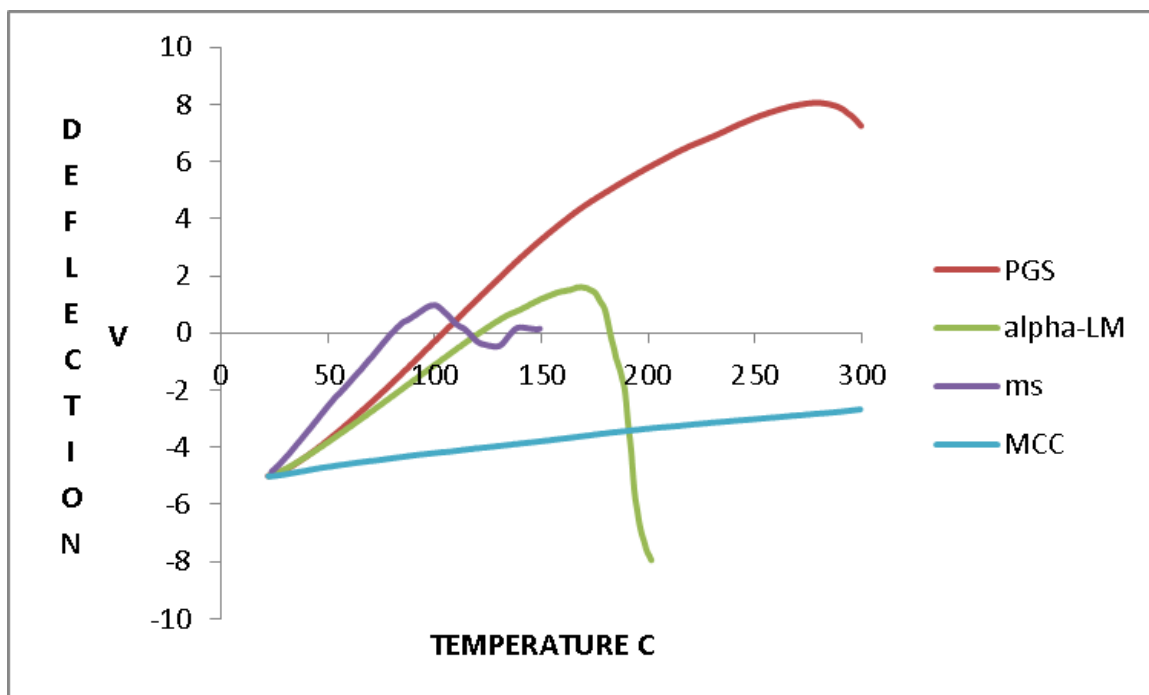


Figure 3.63: A summary of the nano-TA results for four excipients.

TTM is an expansion of the nano-TA procedure, whereby multiple nano-TA measurements are performed in an automated process in a grid-like scheme and the results used to generate a distribution map of the various components. Based on the data shown in Figure 3.63, it should be possible to identify these components in a mixed system such as a mini-tablet.

Generally, the transition temperatures measured by the nano-TA are similar to those observed using the micro-TA data. However, these temperatures can be different to those obtained by DSC, so a degree of interpretation is required when looking at the nano-TA or micro-TA scans. Additionally, the nano-TA instrument is subject to noise and vibration from its environment, which may lead to spurious results. Finally, it does not show the topography of the sample, hence it is more difficult to establish whether good contact has been made between the probe and the sample surface than with the micro-TA.

Chapter 4

A physico-chemical profile of the drugs used in the formulations

CHAPTER 4

A physico-chemical profile of the drugs used in the formulations

4.1 Introduction

In this Chapter, the analytical profiles of three model drugs - caffeine, ibuprofen and anhydrous theophylline - were generated, using the same techniques as for the model excipients described in Chapter 3, i.e. SEM, VT-IR, DSC, AFM, micro-TA, nano-TA and TTM. The same techniques were used for all samples, so that the results of the individual components could be used to assess the ability of the techniques to distinguish between materials in the more complicated, multi-component systems. Following the main studies, twelve further compounds were studied by DSC, micro-TA and nano-TA in an attempt to resolve some experimental issues identified in the main study.

4.2 Materials and Methods

The three drugs studied extensively in this chapter were caffeine, ibuprofen and anhydrous theophylline. Details of their chemical and physical properties are given in Chapter 2.

The twelve additional drugs studied were ciprofloxacin, phenytoin, piroxicam, naproxen, tetracycline HCl, flurbiprofen, diclofenac sodium, tolfenamic acid, fenbufen, sulindac, indometacin and mefenamic acid.

Background explanations of the theory of each analytical technique are given in Chapter 2, along with the standard experimental protocols used throughout this work.

4.3 Results and Discussion

4.3.1 Caffeine

Caffeine exists as two polymorphs and both polymorphs were examined here. It exists at room temperature mainly as Form II, with Form I being present in very small quantities; Form I is the predominant form at higher temperatures. Form II converts to Form I with

increased pressure and temperature and the transformation appears to proceed via a vapour phase intermediate (Manduva et al (2008)). In this work, Form II was used as received and Form I was produced as required by sublimation of Form II. Crystals of Form II were held at 180°C for four hours in a glass Petri dish, allowing sublimation of the Form II and recondensation of Form I on the inside surface of the Petri dish lid. DSC was used to confirm polymorphic conversion.

4.3.1.1 SEM

Both forms of caffeine were examined at magnifications of 250 and 1000 as shown in Figure 4.1. The two forms are distinctly different visually, with caffeine Form II being more granular and Form I exhibiting larger, thinner, needle shape crystals. This is seen in more detail in the higher magnification images. The particle size also varies between the two forms: for form II the particle size is estimated to be around 50 μm or less whereas for Form I the longest dimension is in excess of 100 μm .

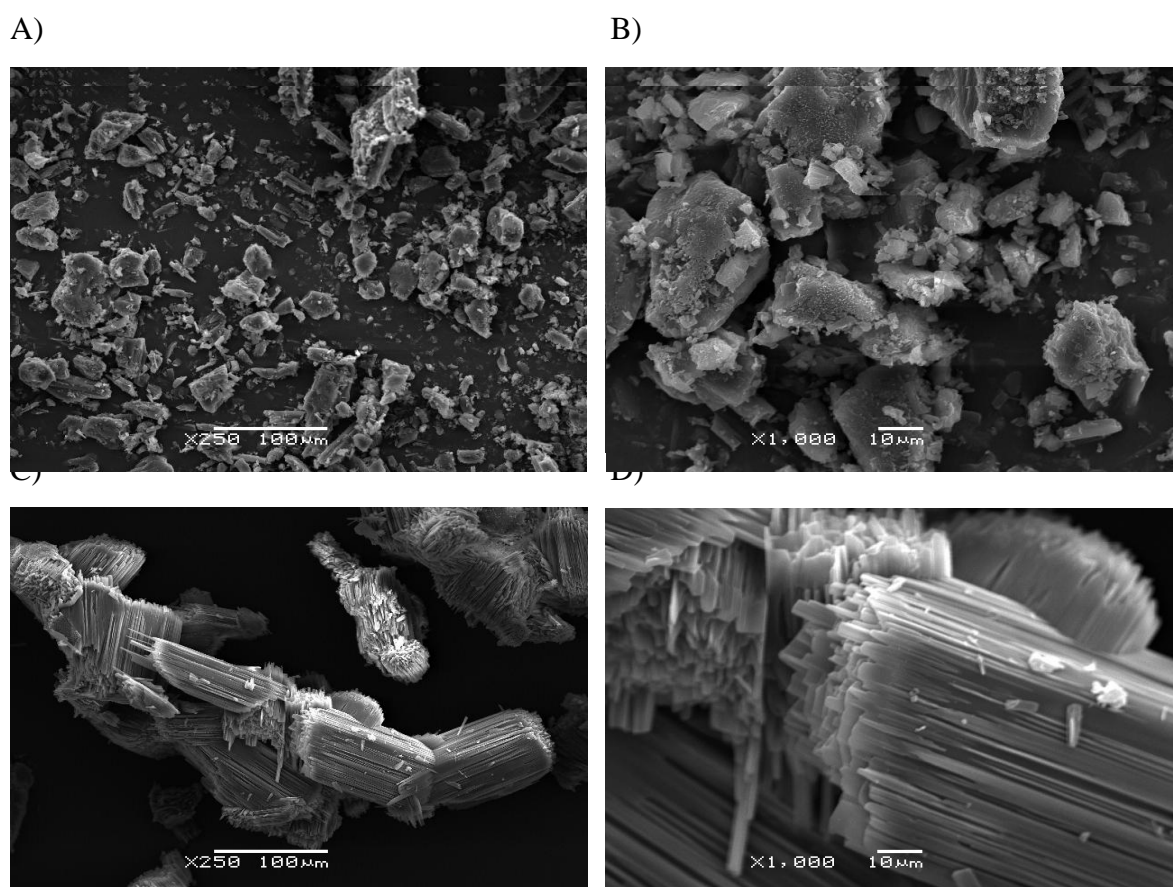


Figure 4.1: SEM image of caffeine. A) Caffeine Form II magnification X250. B) Caffeine Form II magnification X1000. C) Caffeine Form I magnification X250. D) Caffeine Form I magnification X1000.

4.3.1.2 VT-IR

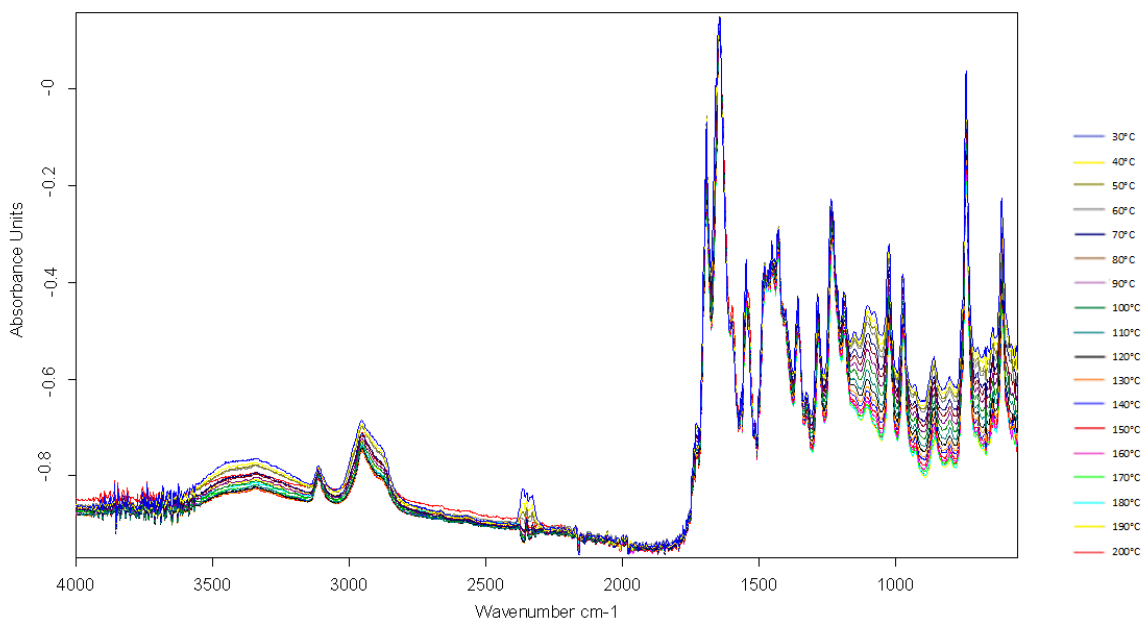
VT-IR was performed on caffeine Form II (the low temperature stable form) and a scan was taken at 10°C intervals from 30°C to 200°C. Figure 4.2 shows a superimposition of all temperature scans (A) and a summary of the lowest and highest temperatures studied (B). The fingerprint region at 30°C and 200°C is highlighted in Figure 4.2 C.

There is a large broad peak circa 3400 cm^{-1} which could be assigned to O-H stretch, arising from water. This peak was not seen in the initial caffeine runs where the equipment was located in the original laboratory, but was seen in all runs on all samples after the equipment was moved to the second laboratory. A possible explanation is that this is due to residual moisture in the nitrogen used as the carrier gas, which may have been of different grades in the two labs. The fact that this peak does not change in size with temperature may be explained by the fact that the nitrogen itself does not get heated during the run and therefore the water will not be evaporated.

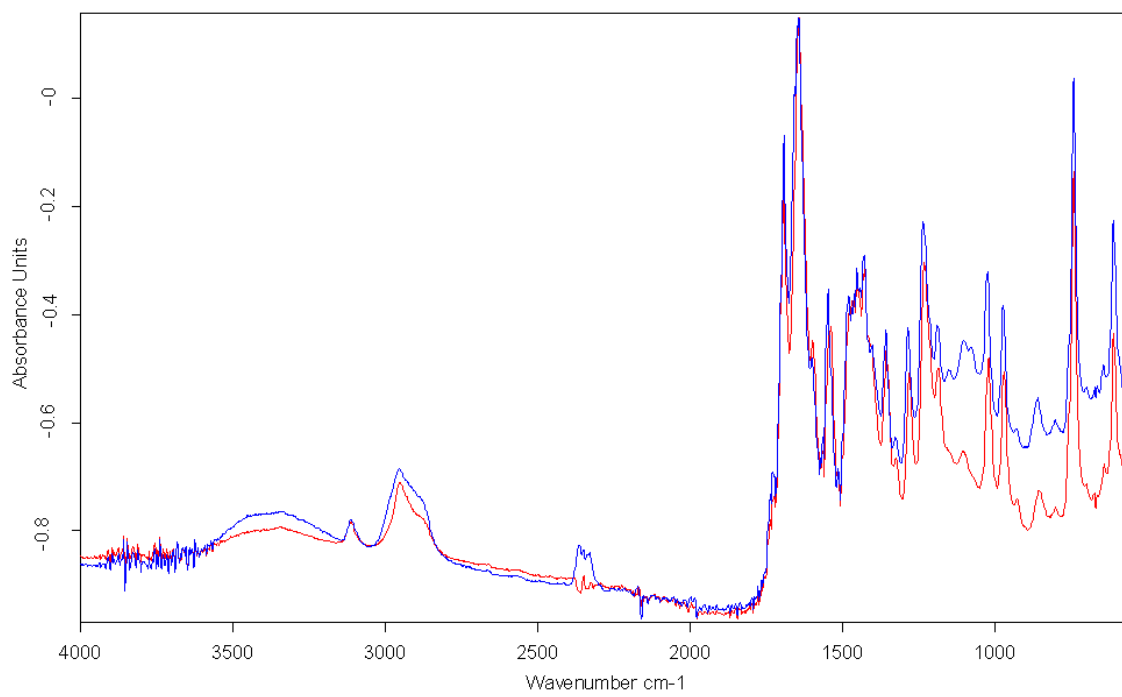
The two peaks either side of 3000 cm^{-1} can be assigned to C-H stretch from the nitro heterocyclic ring and the $-\text{CH}_2$ and $-\text{CH}_3$ groups respectively. In the finger print region for the compound a peak at circa 1750 cm^{-1} is due to C=N stretching. The peaks at 1650 cm^{-1} and 1500 cm^{-1} can be assigned to C=O stretching. The group of peaks in 1400 cm^{-1} region can be explained as C-H deformation. The peaks appearing at circa 1380 cm^{-1} , 1270 cm^{-1} , and 1150 cm^{-1} can be attributed to C-N stretching. The peak in the region of 1050 cm^{-1} can be explained by N- CH_3 stretch and that at circa 850 cm^{-1} can be assigned to N-CH deformation (Gunasekaran et al (2005)). The final peaks, from 720 cm^{-1} onwards, can be assigned to C-H₂ rocking.

Increasing the temperature had only subtle effects on the FT-IR spectrum. The most noticeable effect was the reduction in the baseline transmission in the very low wavenumber region. Two peaks at circa 1050 cm^{-1} and 1150 cm^{-1} reduce in size until at circa 170°C they are negligible.

A)



B)



C)

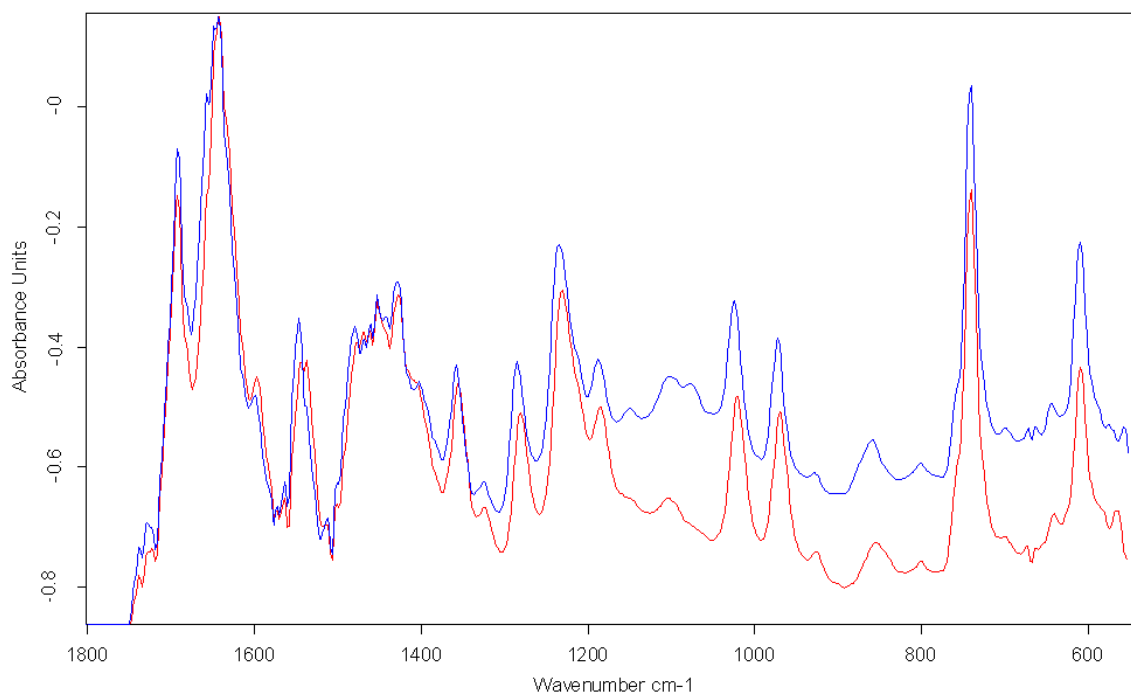
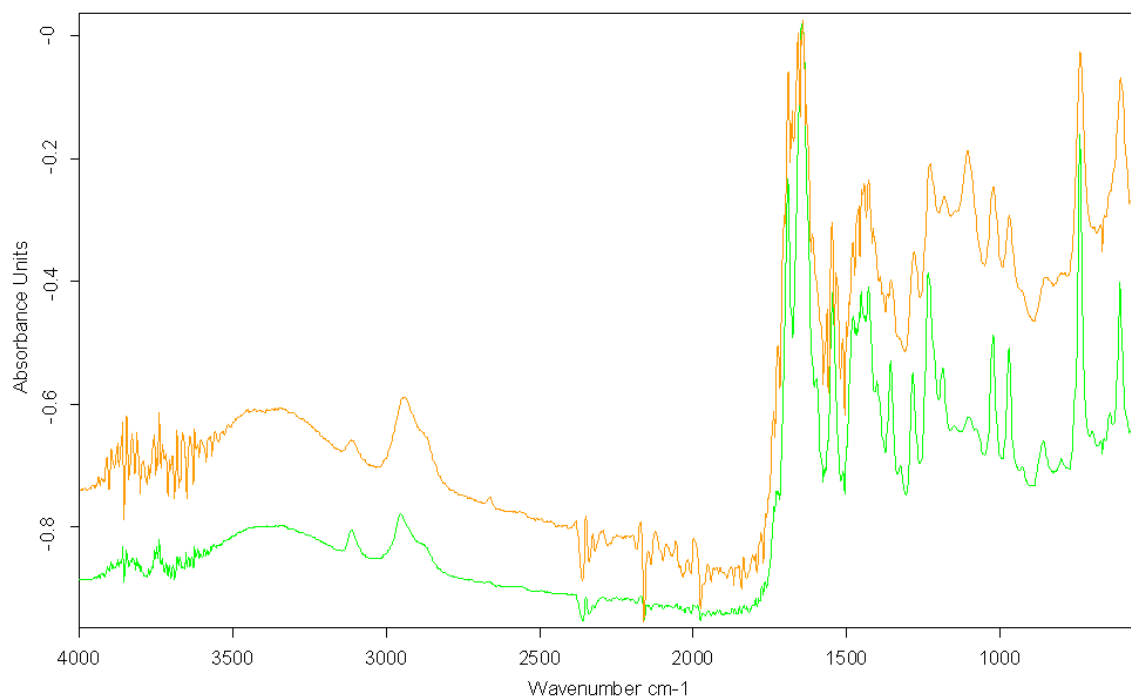


Figure 4.2: FT-IR spectra for caffeine (starting as Form II) between the temperatures of 30°C and 200°C. A) all scans at 10°C intervals. B) the results for 30°C (blue) and 200°C (red). C) the finger print region for 30°C (blue) and 200°C (red) scans.

Figure 4.3 shows the superimposed spectra of caffeine Form I and Form II at 30°C: A is the full wavenumber scan and B is the fingerprint region. Subtle differences only are seen between the two spectra. The peaks at circa 1750 cm^{-1} have a slightly different pattern in the two forms of caffeine; there is peak at circa 1500 cm^{-1} which is slightly sharper for Form I than Form II; and the peak cluster between 1000 cm^{-1} and 1200 cm^{-1} show slight differences.

A)



B)

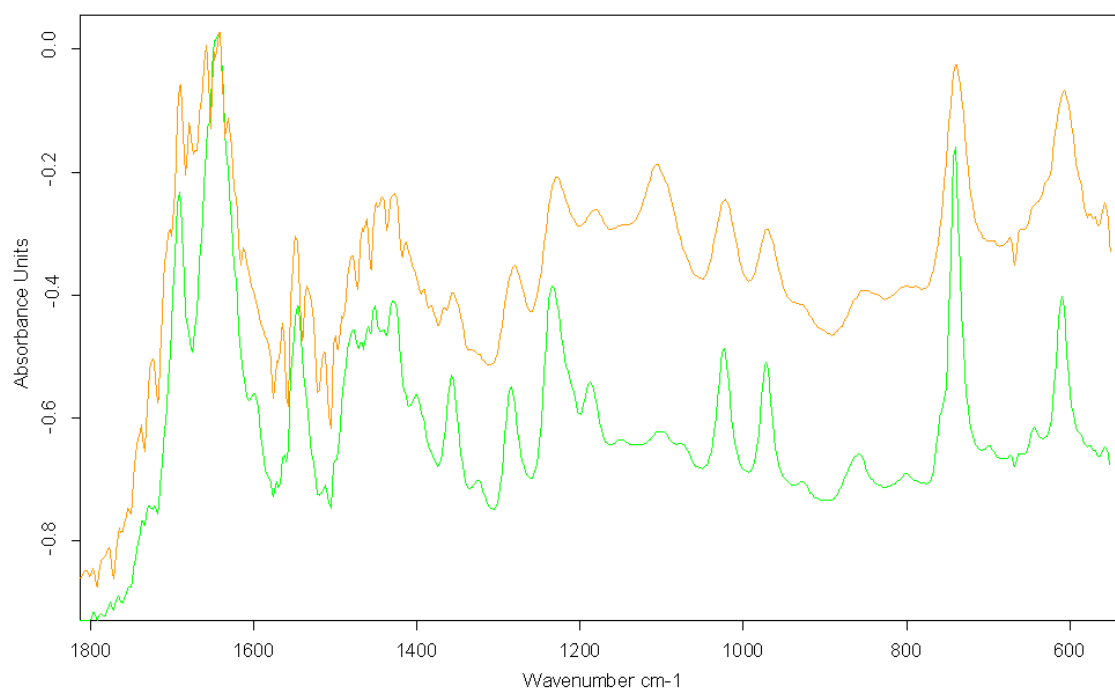


Figure 4.3: FT-IR spectra for Form II (green) and Form I (orange) of caffeine at 30°C. A) full scan. B) the finger print region.

4.3.1.3 DSC

DSC was performed on powdered caffeine, both Form I and Form II. The results are shown in Figure 4.4 with Form II being shown in red and Form I in blue. Form II shows two endotherms. The first endotherm is at 147°C and is attributed to the polymorphic change from Form II to Form I. This is assigned because the peak was not observed in the DSC trace for Form I and it agrees with literature results of about 143°C (Lehto and Laine (1998)). Both scans show an endotherm at 234°C which can be assigned to the melting of caffeine Form I.

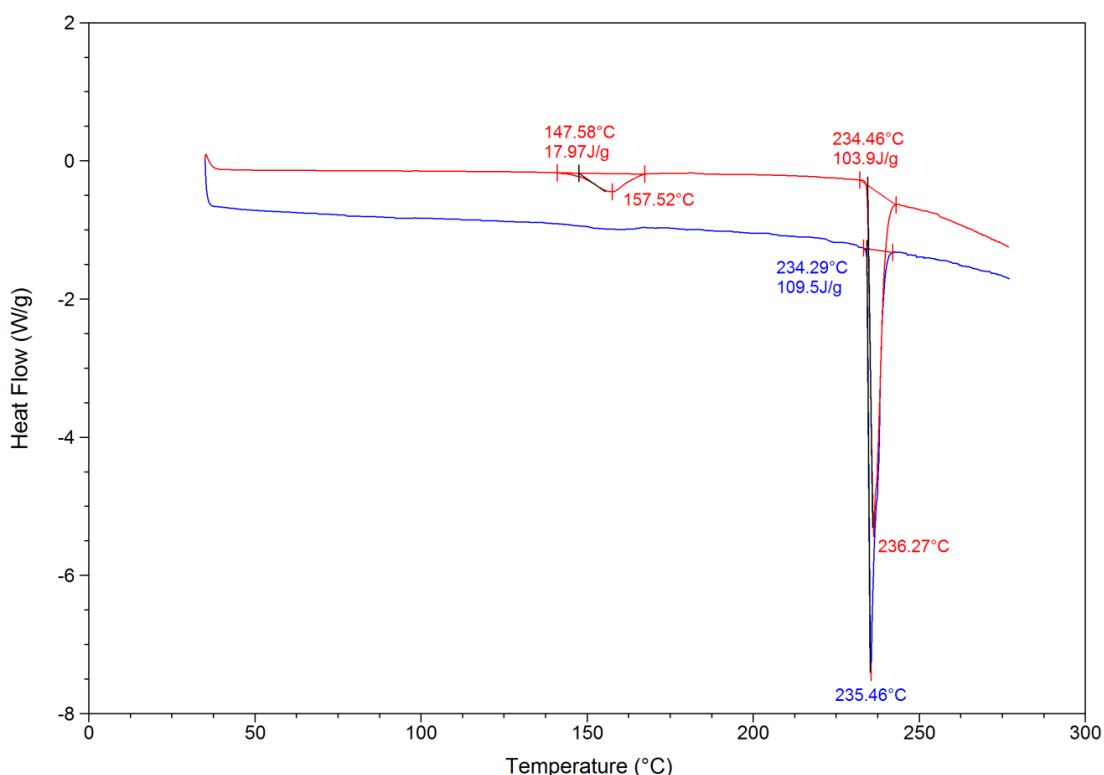


Figure 4.4: DSC trace of caffeine Form II (red) and Form I (blue).

Caffeine's polymorphic transition temperature has been reported to vary with heating rate, with values ranging between 144°C for a heating rate of 10°C/minute and 137°C for an effectively zero heating rate seen in a quasi-isothermal experiment (Manduva et al (2008)). This was briefly investigated here, to enable easier interpretation of data from other techniques. Figure 4.5 shows the DSC data generated on caffeine Form II at heating rates of 5, 10, 15 and 20 °C/minute. It can be seen that the polymorphic transition temperature increases with increasing heating rate and becomes more energetic, in line with the previous reports. As expected, the melting point remains unchanged with heating rate.

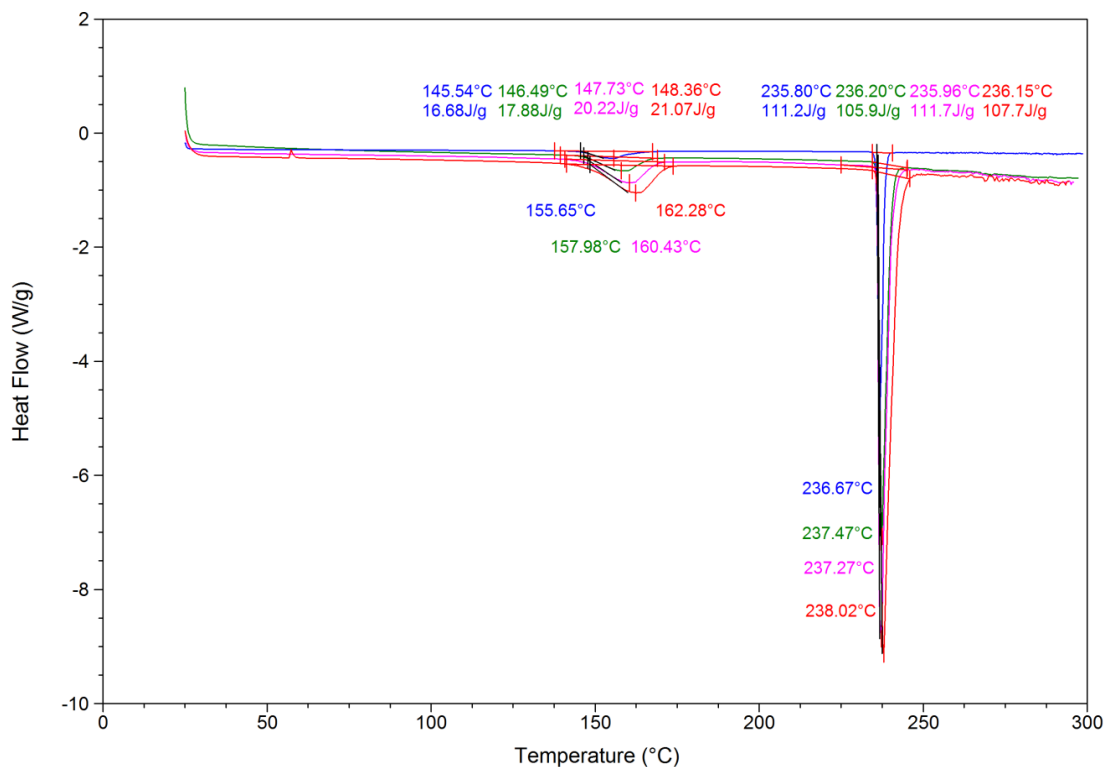


Figure 4.5: The DSC trace of caffeine Form II at different heating rates: 5°C/minute (green), 10°C/minute (blue), 15°C/minute (pink), 20°C/minute (red).

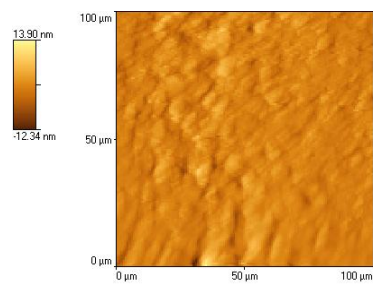
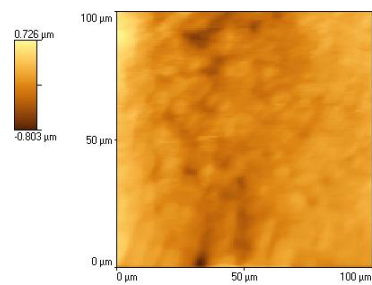
4.3.1.4 AFM

A Wollaston wire (micro) probe was used to investigate the surface topography of the caffeine Form II compacts in the same manner as was used for the excipients discussed in Chapter 3. As the scans of the excipient compacts showed no difference between the top and bottom surfaces of the compacts, only the top of the compact was scanned here. Six scans, each of area 100 μm x 100 μm , were performed across the radius of the compact, represented by A (outside) to F (centre) on Figure 4.6. In Figure 4.6, Column 1 represents the height and column 2 represents the probe deflection. No obvious distinctive topographical features were observed for the caffeine compacts and the compacts showed a smooth surface in the area scanned. There are no observed differences between the outside and the centre imaging sites. A similar set of results was obtained for compacts of caffeine Form I, shown in Figure 4.7. There were no obvious differences between Form I and Form II compacts.

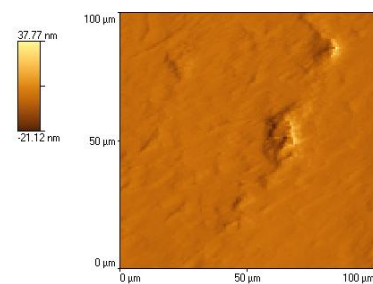
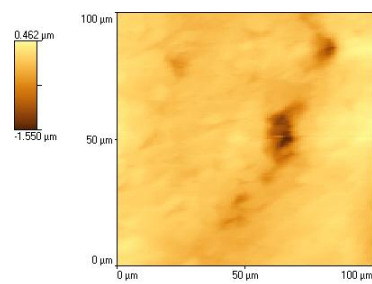
Column 1

Column 2

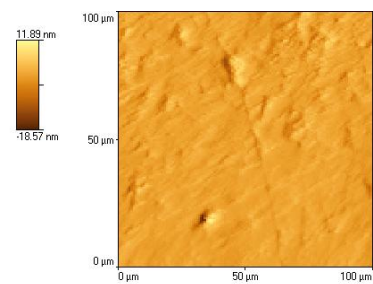
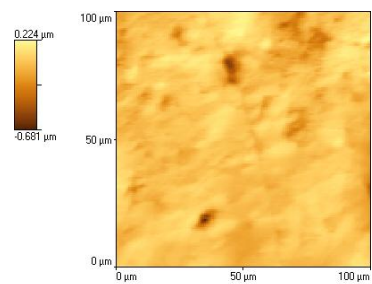
A)



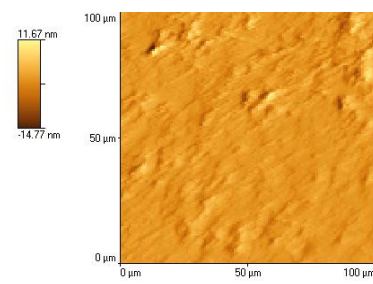
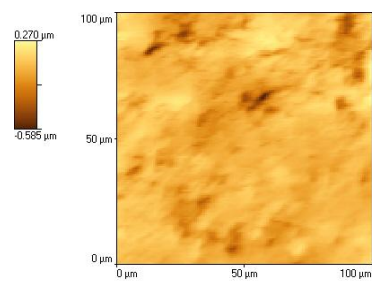
B)



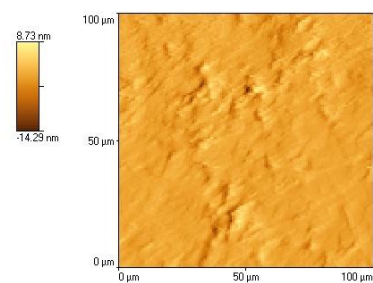
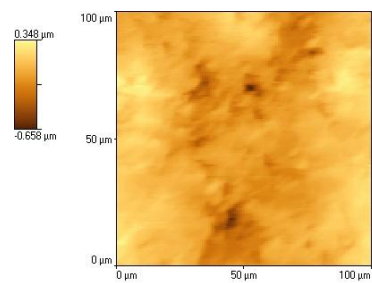
C)



D)



E)



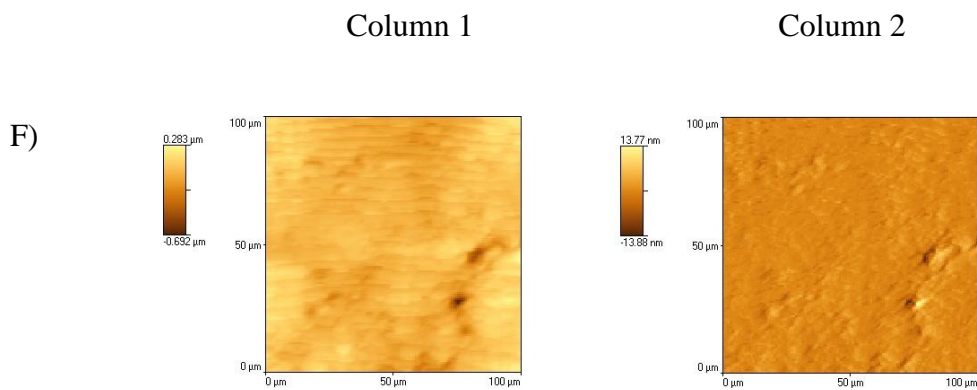


Figure 4.6: AFM scans showing the topography of the top of the caffeine Form II compacts using a Wollaston wire (micro) probe. Column 1 - height, column 2 - deflection; position on the radius of the compact is given from A) edge to F) middle.

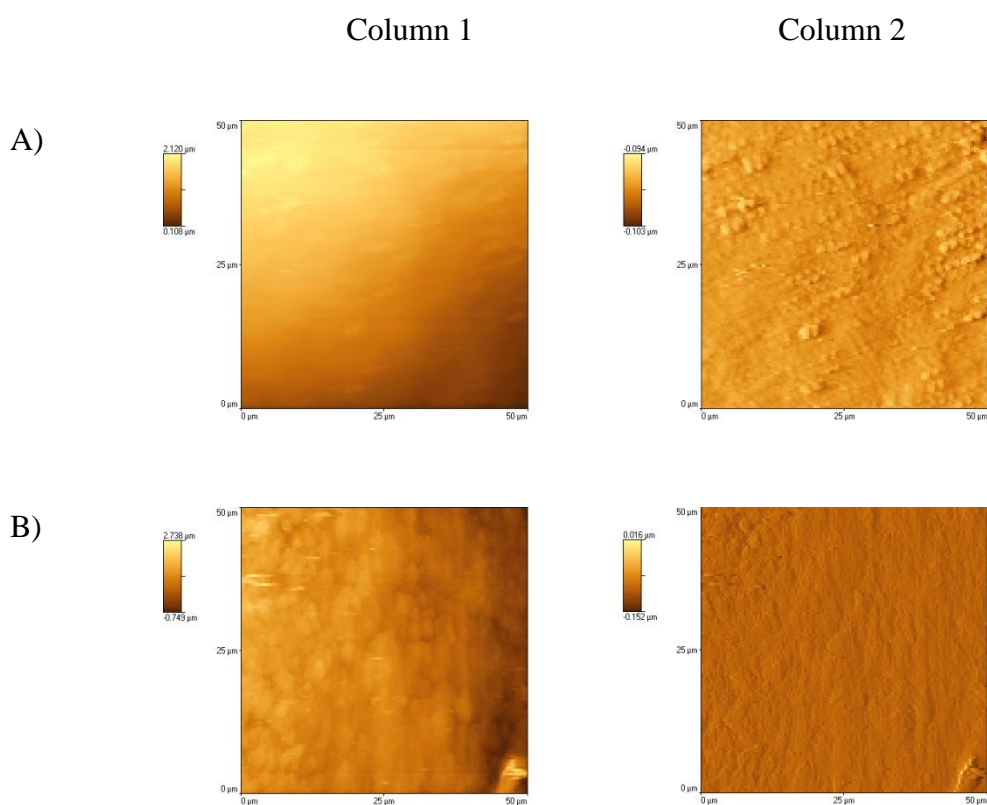


Figure 4.7: AFM scans showing the topography of the top of the caffeine Form I compacts using a Wollaston wire (micro) probe. Column 1 - height, column 2 - deflection; position on the radius of the compact is given by A) edge and B) middle.

For compacts of both forms of caffeine, a similar AFM exercise was performed on scanning with the nano probe. A 50 μm x 50 μm region was imaged on three sites across the radius of the compact, with the results displayed in Figures 4.8 and 4.9 for Form II and Form I compacts, respectively. Again, there are no distinguishing features seen in the images, no differences were observed between the different sites across the radius of the compacts and no difference was seen between the two forms of caffeine.

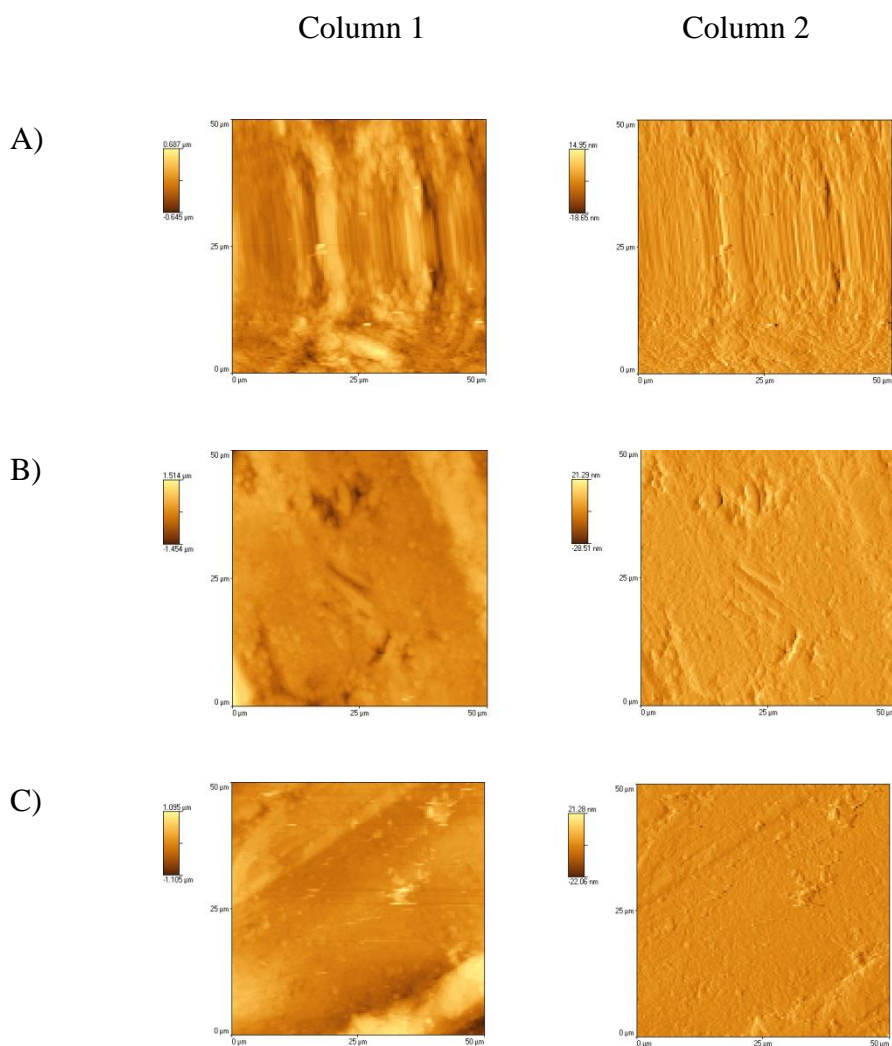


Figure 4.8: AFM scan showing the topography of the top of caffeine Form II compacts using a nano probe. Column 1 - height, column 2 - deflection of the probe; position on the radius of the compact is given from A) edge to C) middle.

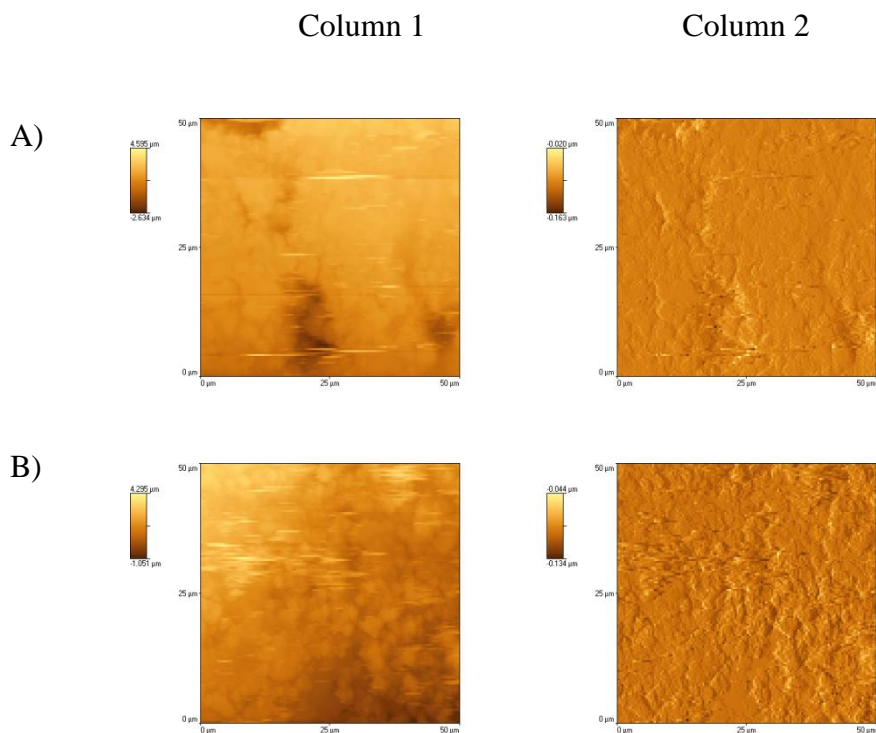


Figure 4.9: AFM scan showing the topography of the top of caffeine Form I compacts using a nano probe. Column 1 - height, column 2 - deflection of the probe; position on the radius of the compact is given by A) edge and B) middle.

4.3.1.5 Micro-TA

Micro-TA measurements were performed across the top surface of compacts of caffeine Form II, imaging at six locations across the radius. Figure 4.10 shows the results from a representative compact, with A to F indicating the position across the radius from outside to middle.

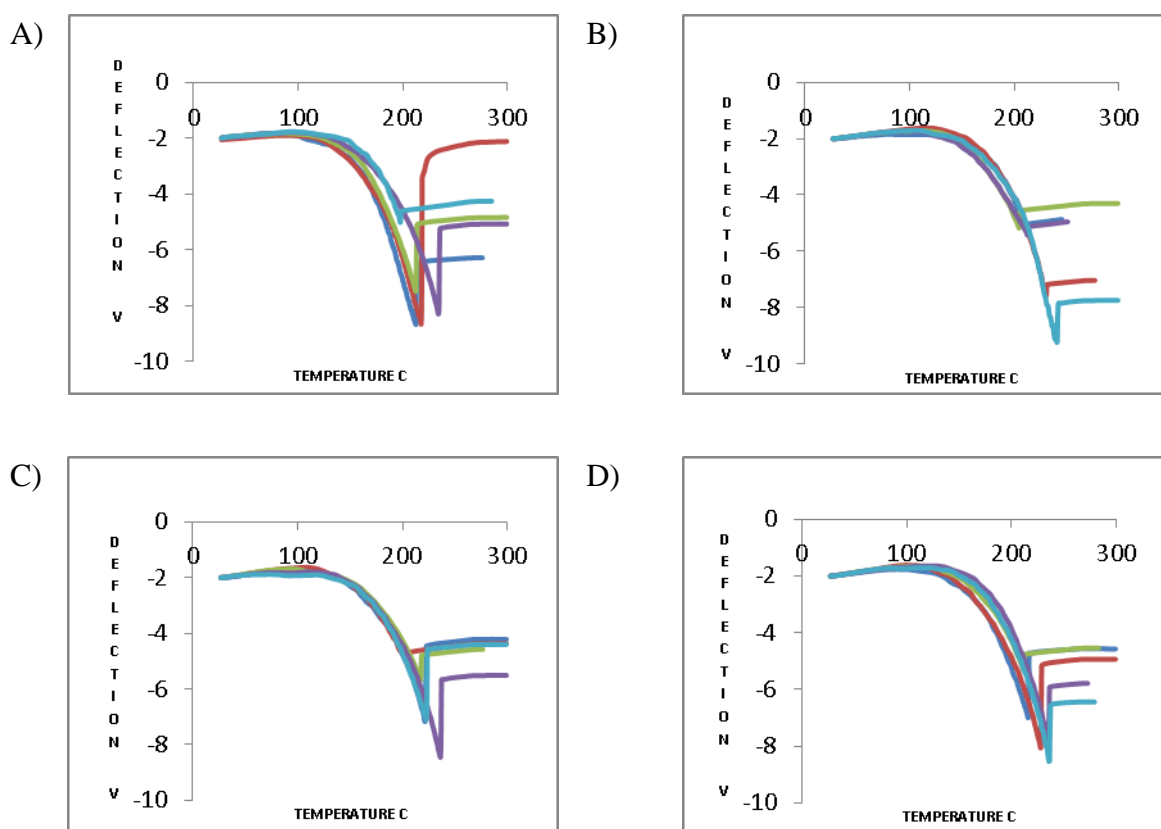
A thermal event was observed with an onset at circa 180°C, which is much lower than the melting point recorded in the DSC trace as 235°C and the literature value of 234°C to 239°C (British Pharmacopoeia (2013)). The minimum point of the V shape of the micro-TA profile is circa 220°C, which is closer to, but still lower than, the DSC melting point.

However, the usual interpretation of micro-TA results is that the temperature of the thermal event is the onset temperature, whereby the material softens and the probe starts to penetrate into the sample (Dai et al (2012)); this is how the equipment undergoes temperature calibration. The results observed here for caffeine Form II are quite different

to this usual interpretation and will be investigated further later in this chapter. However, for the purposes of this analysis, the onset temperature determined here will be taken as the characteristic temperature for caffeine.

The micro-TA results occasionally showed a small peak on the top of the main peak, illustrated in Figure 4.11. It is not seen in every scan, but as it is so small it may have been lost in the baseline noise. This small peak may be explained by the polymorphic transition of caffeine from Form II to Form I. In this example, the rate of heating was 10°C/second and temperature of this transition was circa 147°C.

Figure 4.12 shows the micro-TA results generated on compacts of both forms of caffeine at a higher heating rate of 25°C/second (rather than 10°C/second as was the normal heating rate). The micro-TA profiles for both forms are very similar at this heating rate.



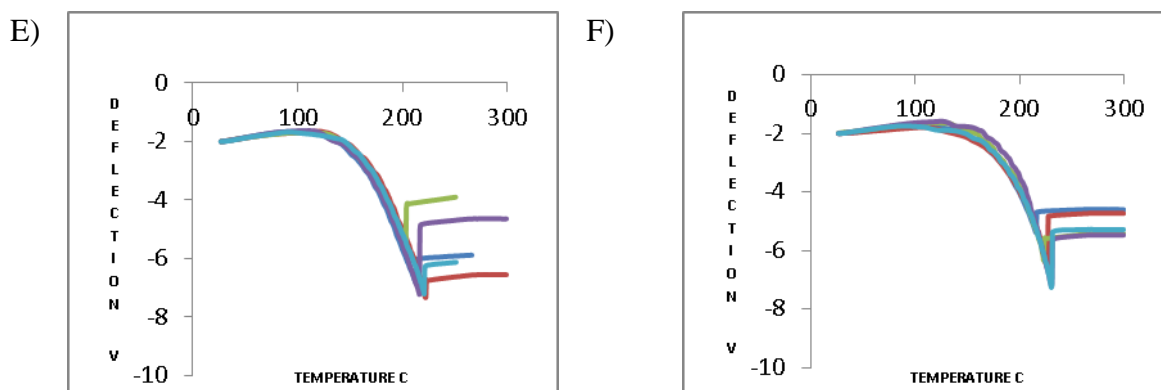


Figure 4.10: Micro-TA results of caffeine Form II compacts using a Wollaston wire probe, across the radius of the compact from A (outside) to F (edge). Five micro-TA readings were taken at each position: dark blue - site 1, red - site 2, green - site 3, purple - site 4, light blue - site 5.

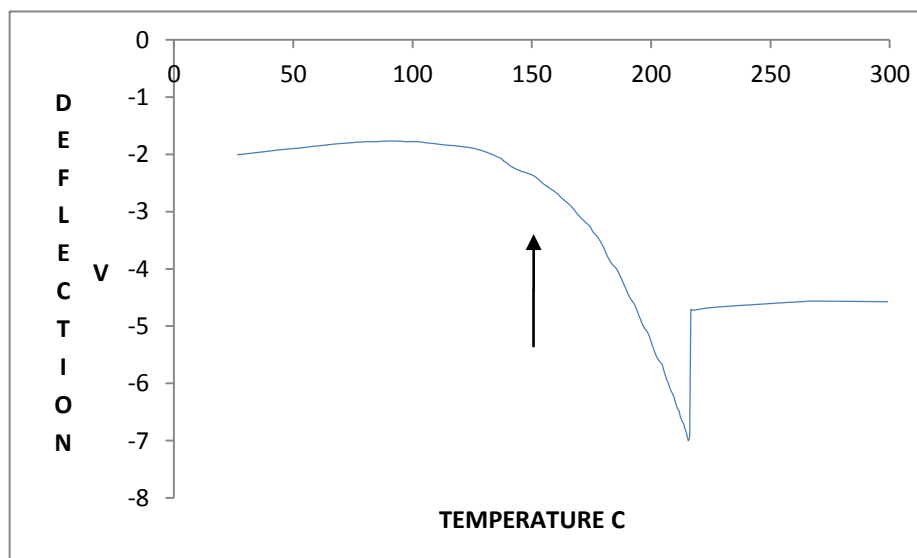
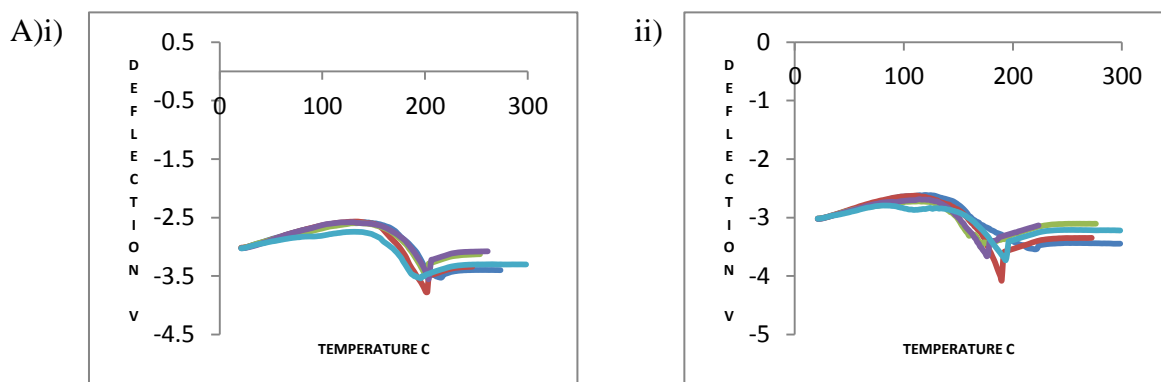


Figure 4.11: An example of the micro-TA of caffeine Form II compacts: the arrow highlights the small peak ascribed to the transition of Form II to Form I.



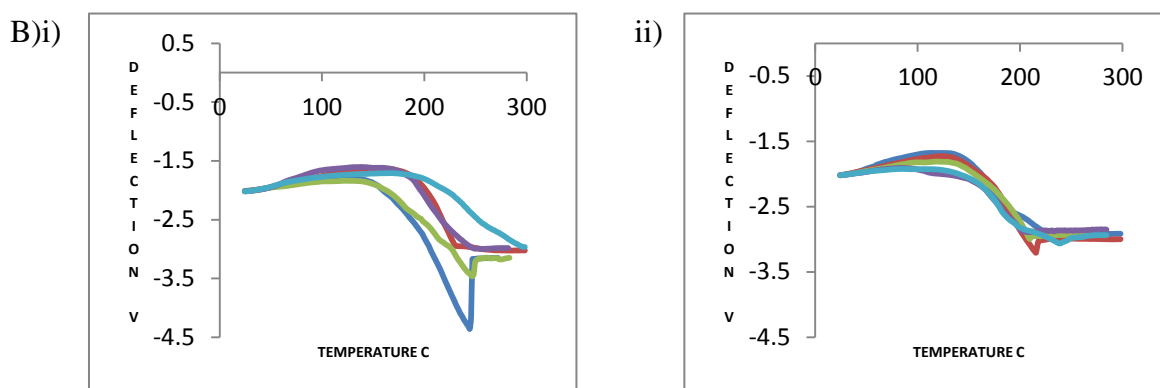


Figure 4.12: Micro-TA results of compacts of caffeine Form I (A) and Form II (B) compacts using a Wollaston wire probe, across the radius of the compact: i) outside and ii) edge. The heating rate was 25°C/second. Five micro-TA readings were taken at each position: dark blue - site 1, red - site 2, green - site 3, purple - site 4, light blue - site 5.

4.3.1.6 Nano-TA of caffeine

Figures 4.13 illustrates the nano-TA results for caffeine Form II compacts. The experiments were performed in the same manner as the AFM experiment i.e. at three areas across the radius of the compact surface. No differences were observed across the radius of the compact.

One thermal event was detected with an onset at circa 100°C. It is unlikely that this can be ascribed to either the melting or the polymorphic transition from Form II to Form I as the temperature of transition is so much lower than that seen by DSC or micro-TA. Possible explanations of this event are discussed later in this thesis, but for now, this thermal event will be accepted as the nano-TA profile of caffeine.

As described earlier for micro-TA, nano-TA scans were performed on both Form I and Form II compacts, using the higher heating rate of 25°C/second. The results are shown in Figure 4.14. A difference between the results can be seen with Form I showing an onset at circa 130°C and a minimum point of 180 to 190°C, whereas Form II had an onset at circa 115°C and a minimum value of 150°C. It is possible that this difference is due to the polymorphic phase transition from Form II to Form I. Alternatively, it may just be the same effect seen at the 10°C/minute heating rate but occurring at slightly higher temperatures due to the faster heating rate. Interestingly, the probe profiles for the two

forms of caffeine were different. Form II compacts showed a similar profile to previous micro-TA and nano-TA scans, whereas the Form I compacts showed a steeper initial expansion and deeper penetration of the probe into the sample at the transition point. This is possibly related to the differences in particle morphology between the two forms.

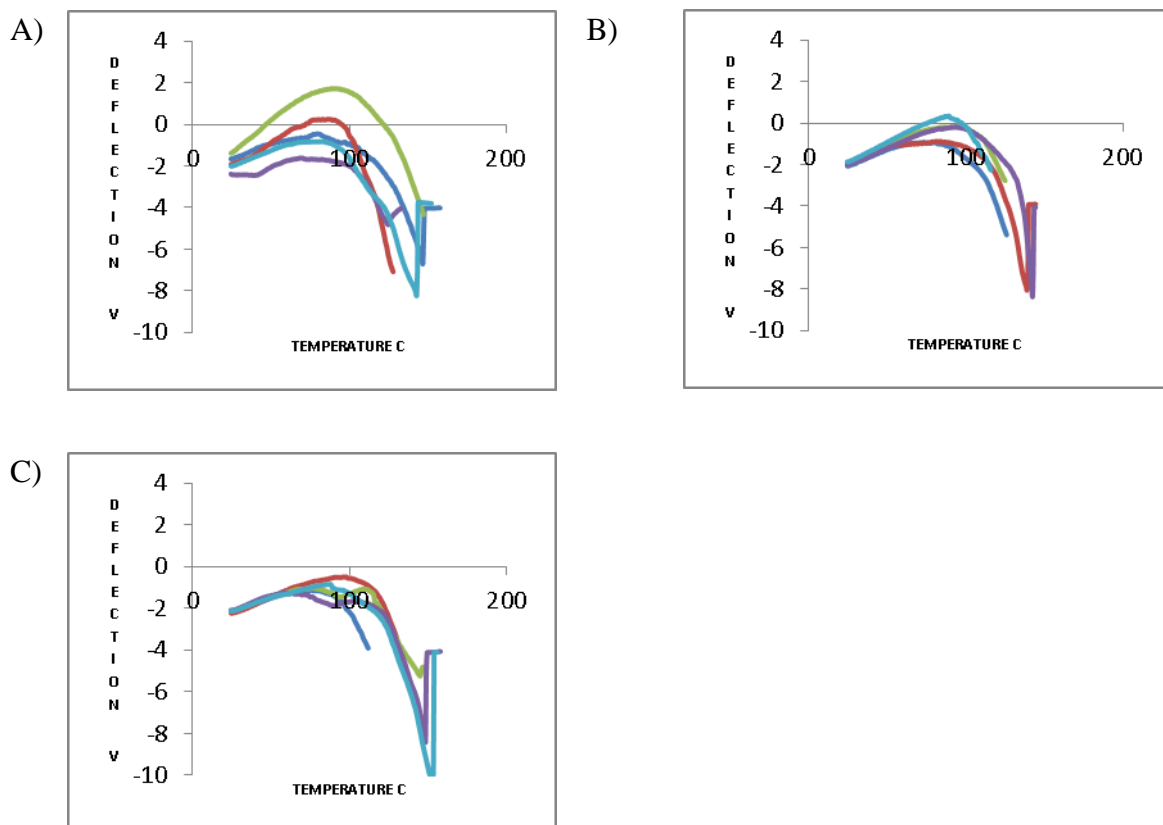


Figure 4.13: Nano-TA results of caffeine Form II compacts using a nano probe, across the radius of the compact from A (edge) to C (middle). Five nano-TA readings were taken at each position: dark blue - site 1, red - site 2, green - site 3, purple - site 4, light blue - site 5.

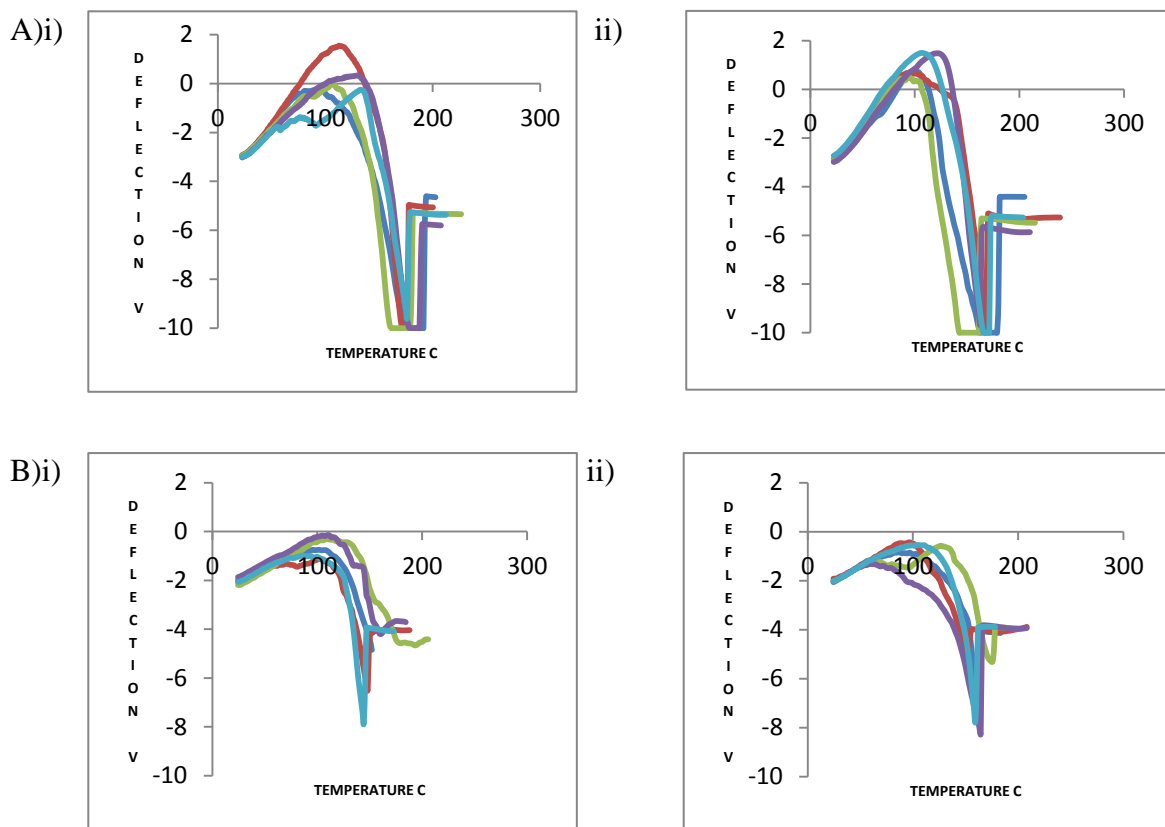


Figure 4.14: Nano-TA results of compacts of caffeine Form I (A) and Form II (B) using a nano probe, across the radius of the compact: i) outside and ii) edge. The heating rate was 25°C/second. Five nano-TA readings were taken at each position: dark blue - site 1, red - site 2, green - site 3, purple - site 4, light blue - site 5.

4.3.1.7 TTM

TTM was performed on three sites across the diameter of a caffeine Form II compact, with the results being shown in Figure 4.15. A thermal event is detected between 80°C and 150°C. As discussed above, this is unlikely to be either the melting or the polymorphic transition of caffeine, as the observed temperature is so much lower than that seen with other techniques, such as DSC.

No real difference was observed between the outside and the middle of the compacts, but the TTM results are variable, as suggested by the colouration of the TTM maps, reflecting the different temperatures at which the probe moves through the sample. Such variability is usually explained by rough sample topography; however, in this case the sample surface

was smooth and the nano-TA results were reproducible. As it is such a sensitive technique, TTM is prone to environmental problems such as lab noise and vibrations, which can cause artefacts. In this case, outlier responses would be expected to be seen, which is not the case here, so this is probably not the explanation of the variation in the current results. Possible explanations are discussed later, but for now, this is taken to be the TTM signature of caffeine Form II. TTM was not performed on caffeine Form I compacts.

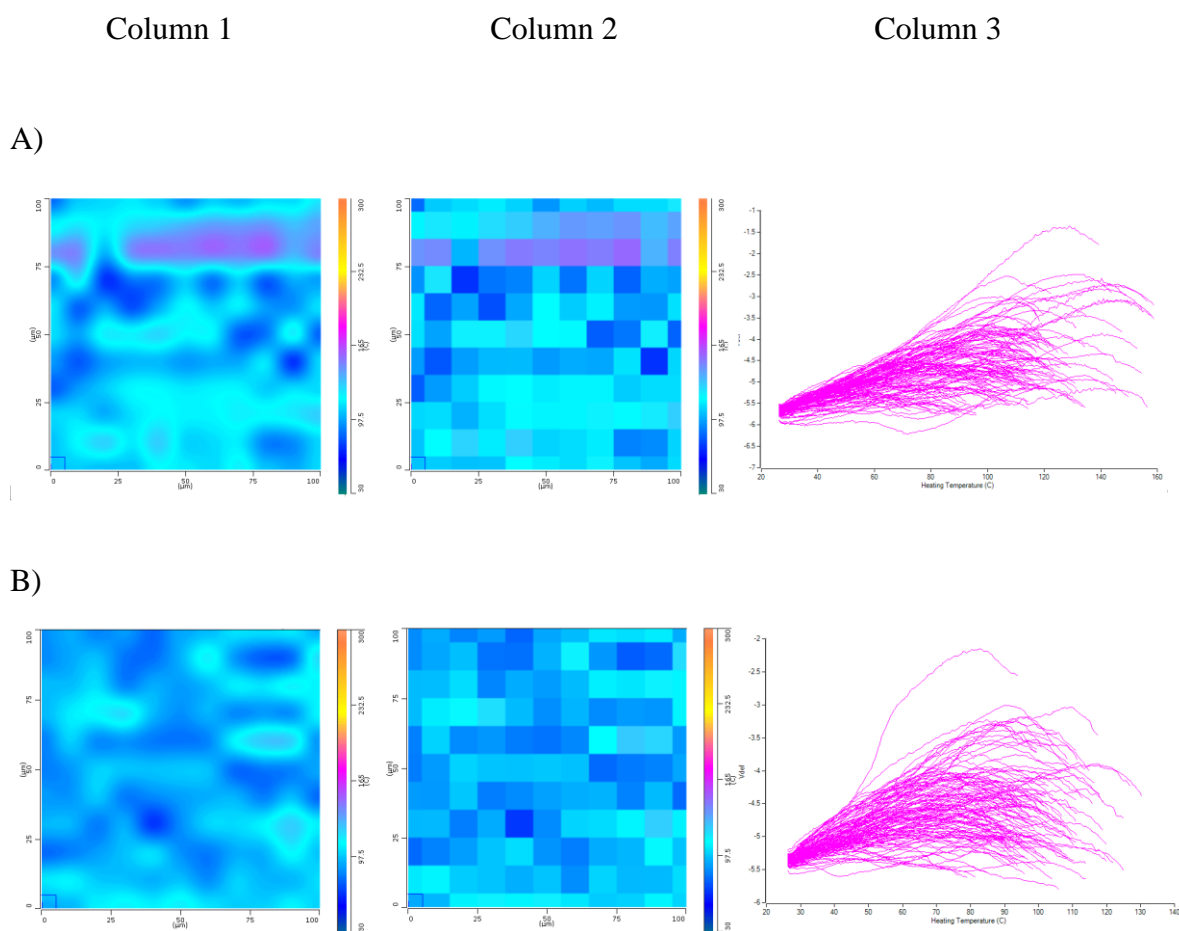


Figure 4.15: TTM maps of caffeine compacts. A) middle and B) edge of the compact. Column 1 is the interpolated (smoothed) map, Column 2 is the discrete map, and Column 3 shows the individual nano-thermal results.

4.3.2 Ibuprofen

Ibuprofen has one chiral carbon atom and hence can exist as two enantiomers. The sample tested is a mixture of the two forms. Due to drug availability at the time of the experiments, two batches of ibuprofen powder were used: the compact work was performed using the first batch (lot no. 1B1M687 BASF (UK)) and the mini-tablet work (Chapter 6) was performed using the second batch (lot no. 1B1T1575 BASF (UK)). DSC and nano-TA were additionally performed on the second batch of ibuprofen to confirm that comparable results would be obtained with both batches.

4.3.2.1 SEM

Figure 4.16 (A and B) illustrates SEM images of ibuprofen at magnifications of 250 and 1000. The particles are long and thin, with width approximately 10 μm and length generally less than 100 μm . Figure X B shows the smooth surface of the particles and that individual particles appear to be fused together to form larger agglomerates.

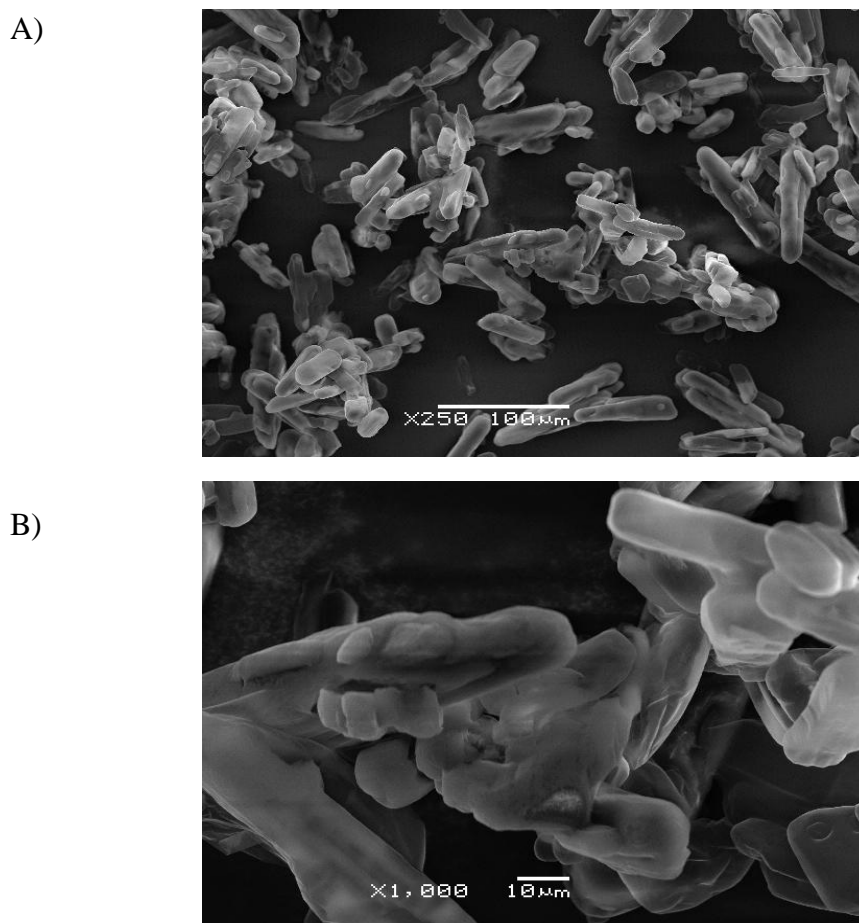


Figure 4.16: SEM image of ibuprofen. A) magnification X250. B) magnification X1000.

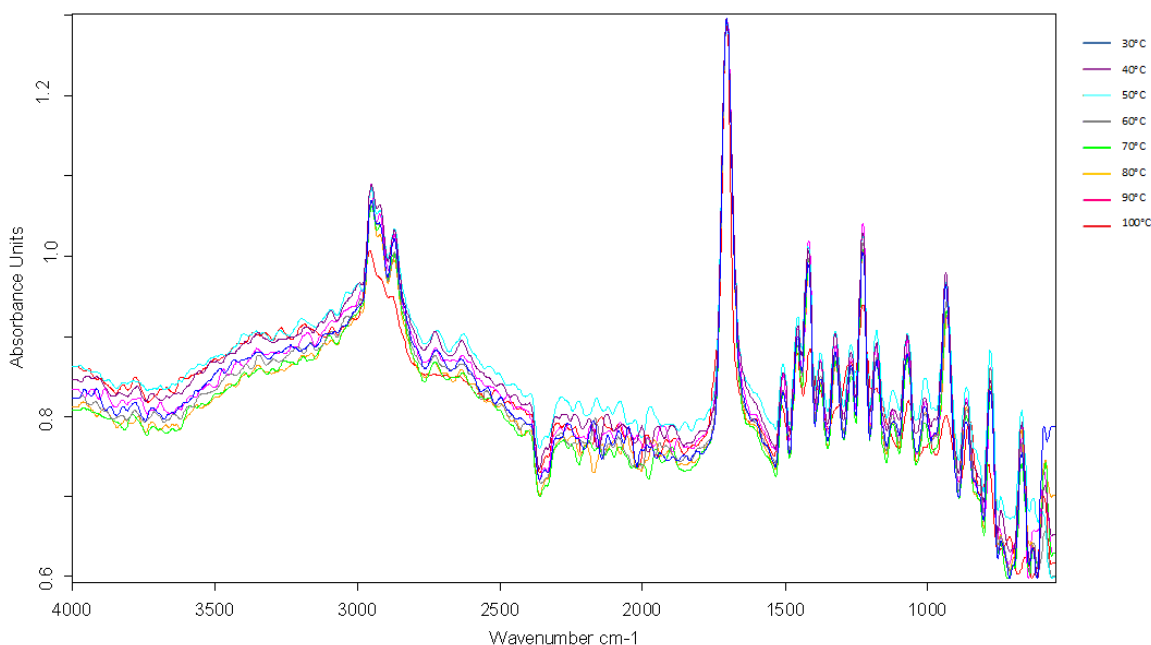
4.3.2.2 VT-IR

Figure 4.17 (A) shows the superimposition of all the FT-IR scans taken at the various temperatures. Figure 4.17 (B) and (C) show the results at selected temperatures across the full wavenumber range and in the fingerprint region, respectively.

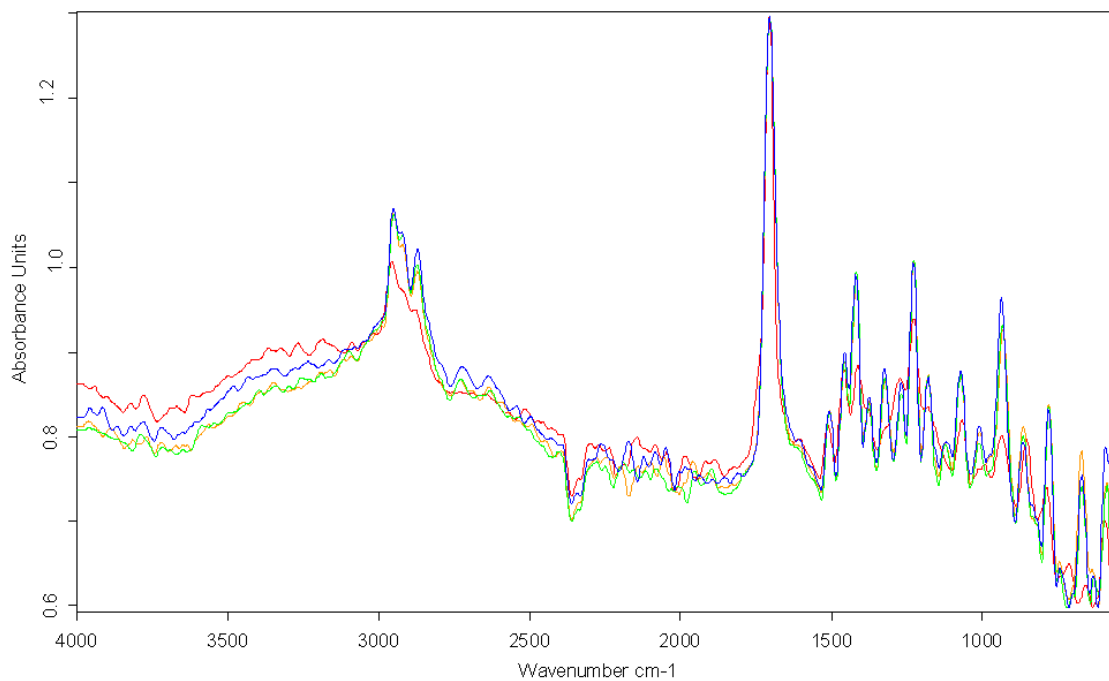
The spectra show only a gradual change with increasing temperature until 90°C and 100°C, above the melting point of ibuprofen (76°C by DSC - see section 4.4.3 below). It is not until these temperatures that the spectrum starts to lose its fine structure.

The spectra show two peaks at circa 2900 cm^{-1} and 2800 cm^{-1} which could be attributed to C-H stretch in the CH_2 and CH_3 stretch. The peaks at circa 2400 cm^{-1} are probably due to carbon dioxide in the atmosphere. A large peak is observed at 1700 cm^{-1} which could be due to the C=O bond stretch in the carboxylic acid group. In the fingerprint region there are many small peaks. The peaks at 1500 cm^{-1} , 1400 cm^{-1} and 1200 cm^{-1} may be explained by C-C stretch. The CO-H bend could be attributed to the peaks at 1400 cm^{-1} , 1325 cm^{-1} , 1230 cm^{-1} and 935 cm^{-1} . The peak at 1130 cm^{-1} could be assigned to C-O stretch. Peaks at 1460 cm^{-1} and 1390 cm^{-1} can be attributed to C-H deformation and $-\text{CH}_3$ deformation, respectively. C-H bend and twist can be assigned to the peaks at 1260 cm^{-1} and 1080 cm^{-1} . Peaks at 870 cm^{-1} and 790 cm^{-1} are explained by $-\text{CH}_3$ rocking (Vueba et al (2008)).

a)



b)



c)

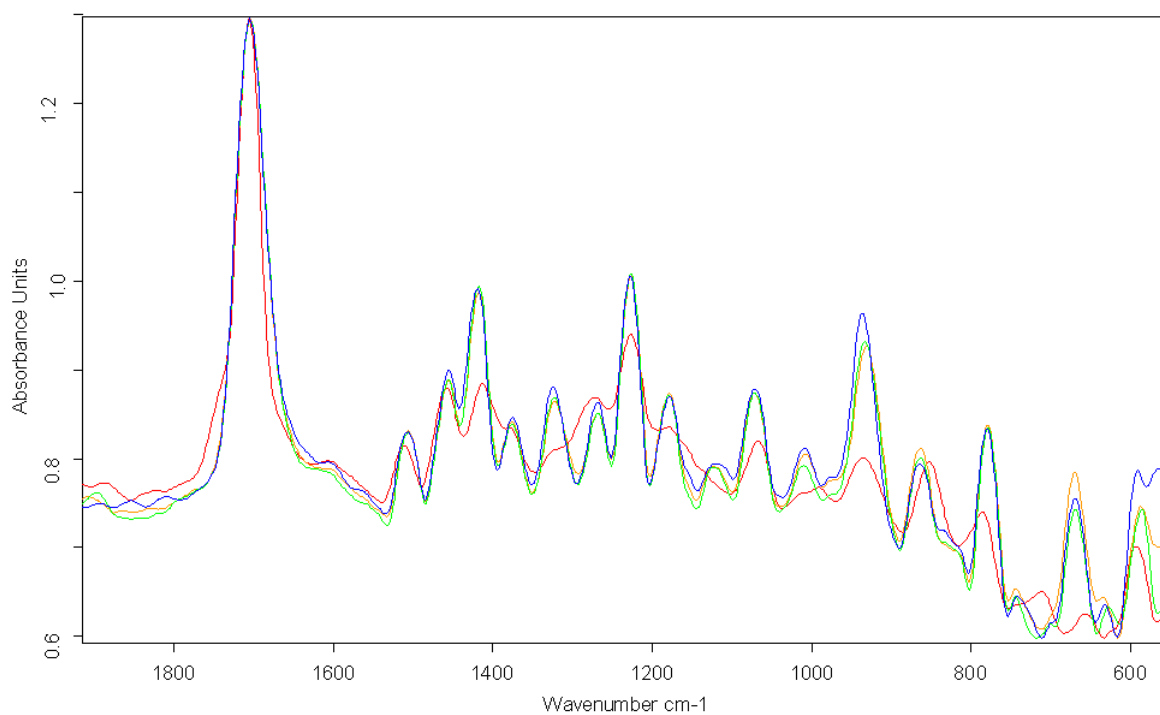


Figure 4.17: FT-IR spectra for ibuprofen between the temperatures of 30°C and 100°C. A) All scans at 10°C intervals, B) The full spectra for selected temperatures, C) The finger print region for selected temperatures - 30°C (blue), 70°C (green), 80°C (orange) and 100°C (red).

4.3.2.3 DSC

Figure 4.18 shows the DSC trace for ibuprofen. Two batches of ibuprofen were used: one for the initial compacts work and one for the later mini-tablets work. These are represented by red and blue, respectively, in the DSC trace. As can be seen, the results for the two batches are very similar. One thermal transition only was observed: an endotherm with onset at 75.2 to 75.7 °C, which is attributed to the melting of the ibuprofen (British Pharmacopoeia (2013)).

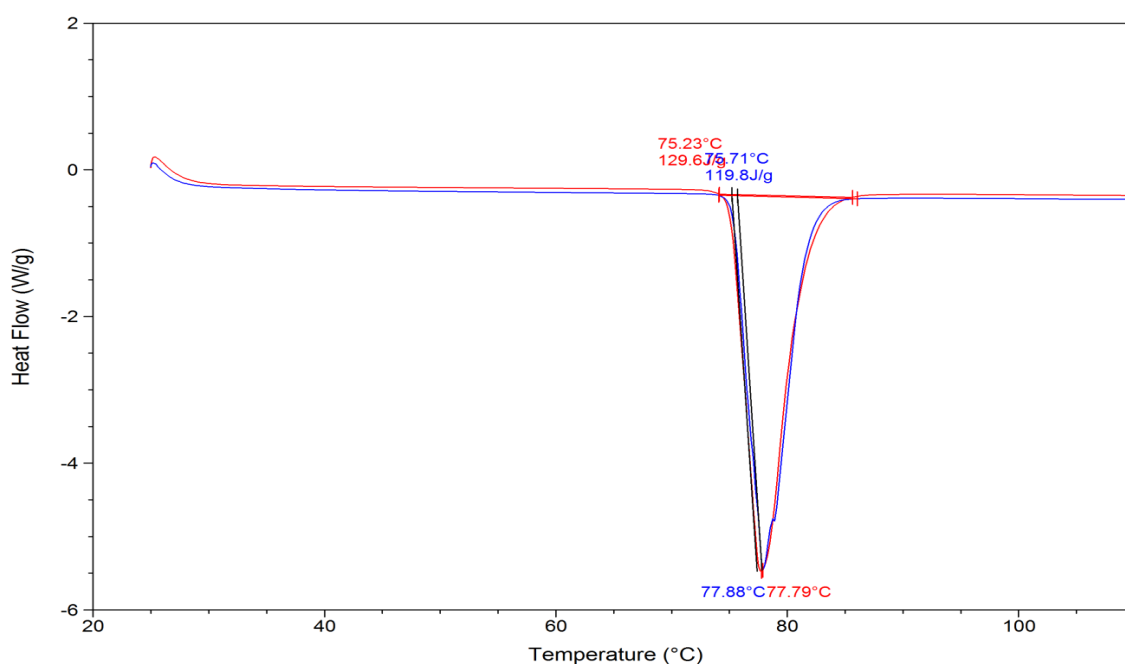


Figure 4.18: DSC traces of ibuprofen. Red - the batch used for the compacts work; blue - the batch used for the mini-tablets work.

4.3.2.4 AFM

Figure 4.19 shows the topographical AFM images of the top surface of an ibuprofen compact generated using a Wollaston wire (micro) probe and the initial batch of ibuprofen powder. A (outside) to F (centre) represent the scanned areas (100 µm x 100 µm) across the radius of the compact. No distinguishing features were observed which could assist with the identification of ibuprofen in a multi-component system and there was no observed differences between the outside and the centre of the compact's surface.

Figure 4.20 shows the AFM scans performed with a nano-probe on the same sample. Three 50 μm x 50 μm areas were scanned across the diameter of the compact. As with the micro-probe, the scans showed no distinguishing features and no difference was seen across the compact. As a new batch of ibuprofen powder was used for mini-tablet work, the AFM scan using the nano-probe was repeated on compacts made from this new batch - these results are shown in Figure 4.21. Minor differences only were observed between the compacts made from the two batches of drug.

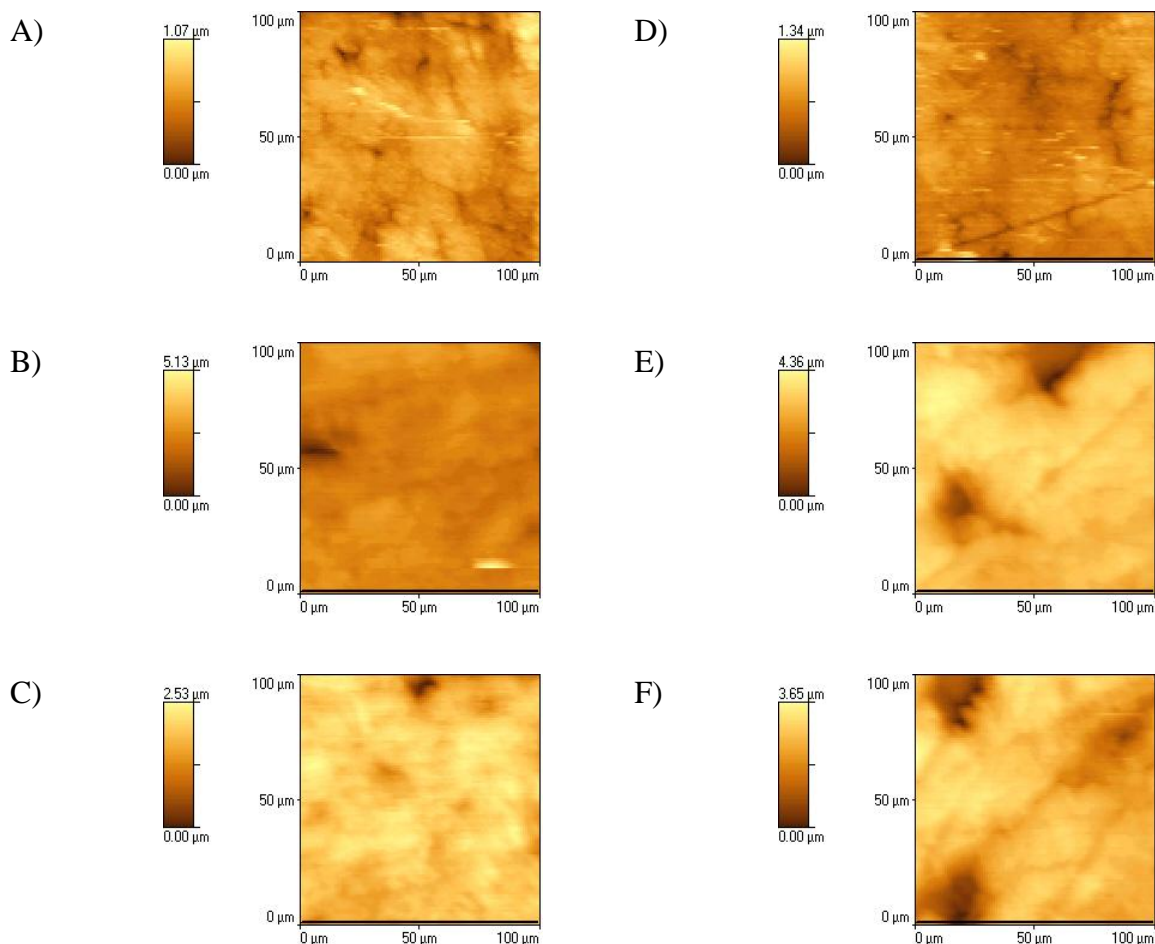


Figure 4.19: AFM scans showing the topography (as height) of the top of an ibuprofen compact using a Wollaston wire (micro) probe. The position on the radius of the compact is given from A) edge to F) middle.

Column 1

Column 2

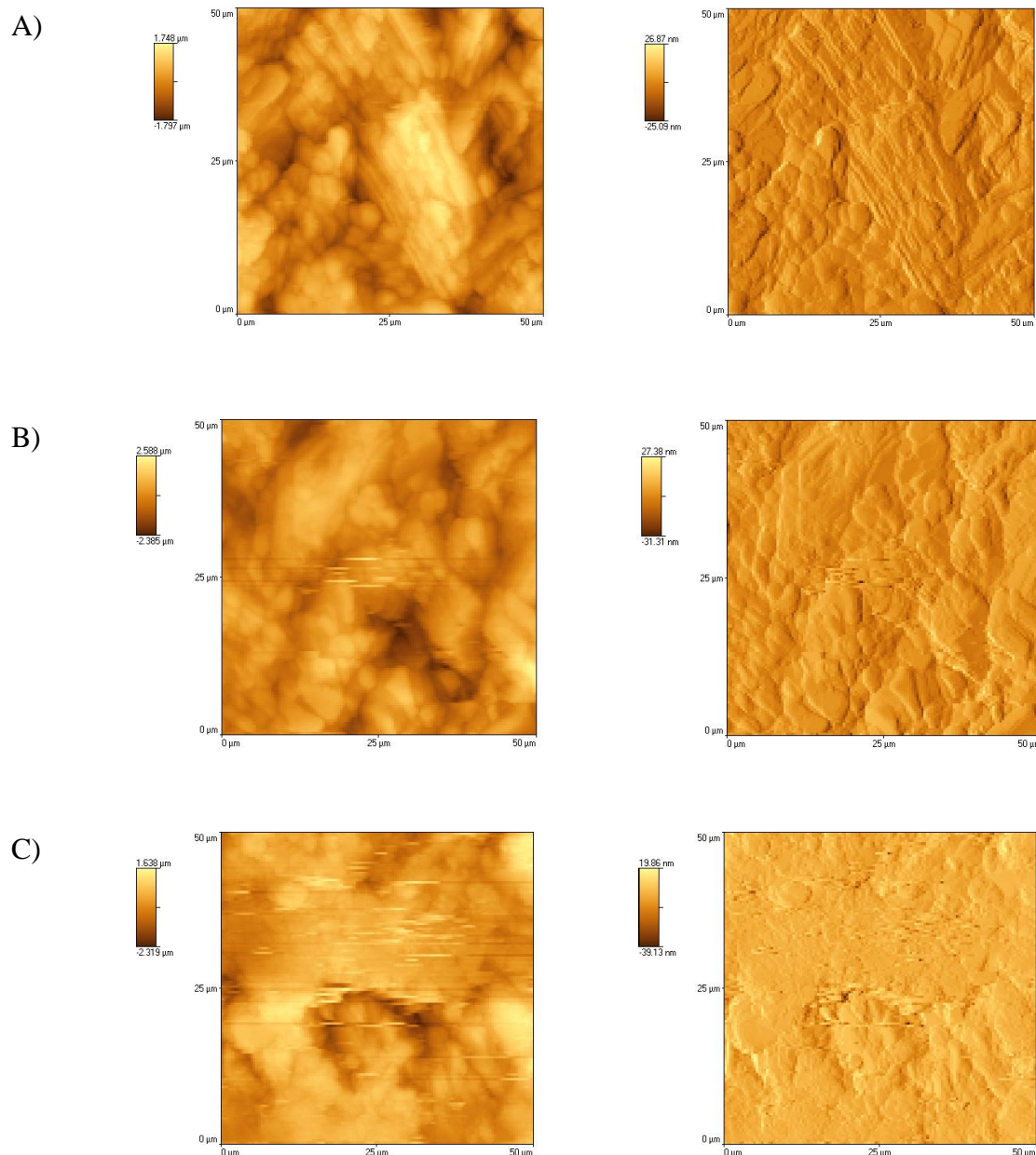


Figure 4.20: AFM scan showing the topography of the top of an ibuprofen compact using a nano probe. Column 1 - height, column 2 - deflection of the probe; position on the radius of the compact is given from A) edge to C) middle.

Column 1

Column 2

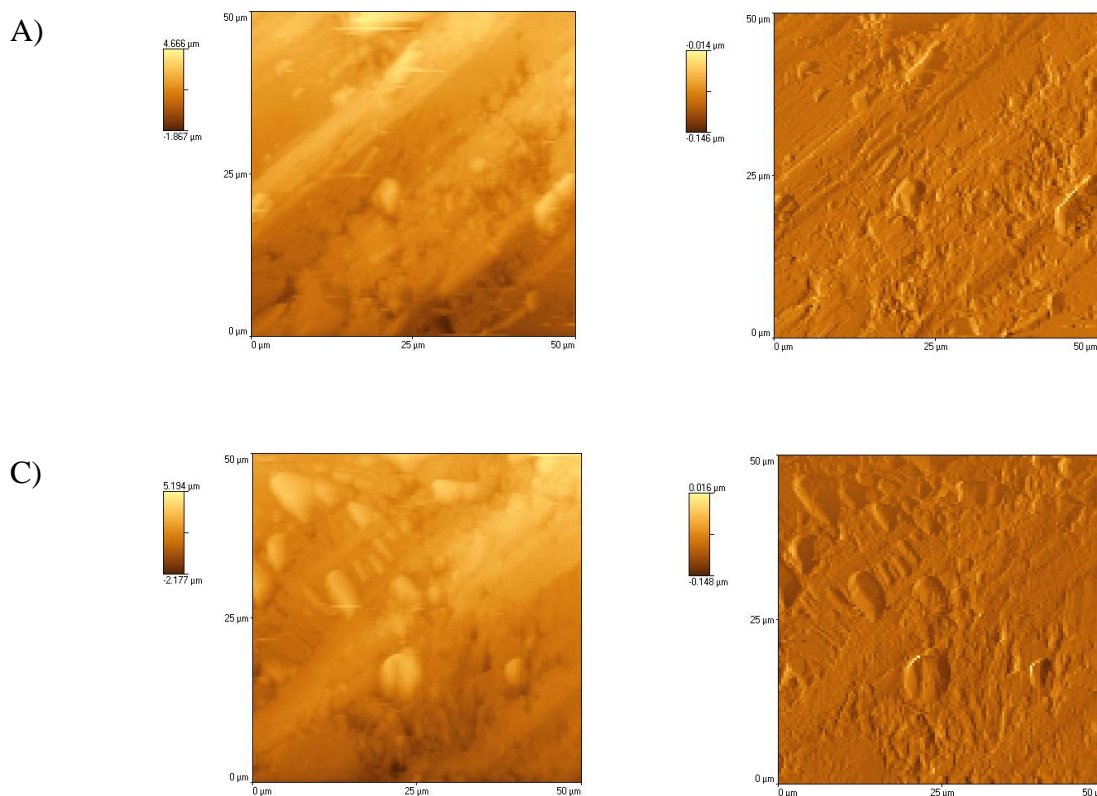


Figure 4.21: AFM scan using a nano-probe showing the topography of the top of the ibuprofen compact prepared using the "new" batch of drug. Column 1 - height, column 2 - deflection; the position on the radius of the compact is given from A) edge to C) middle.

4.3.2.5 Micro-TA

Figure 4.22 illustrates the micro-TA results generated across the top surface of an ibuprofen compact. A (outside) to F (centre) are representative of the different positions on the radius of the compact. A thermal event is detected at circa 75°C which can be explained by the melting of the solid as the temperature of transition seen here is very similar to result obtained by the DSC analysis. The results are extremely consistent across the radius of the compacts.

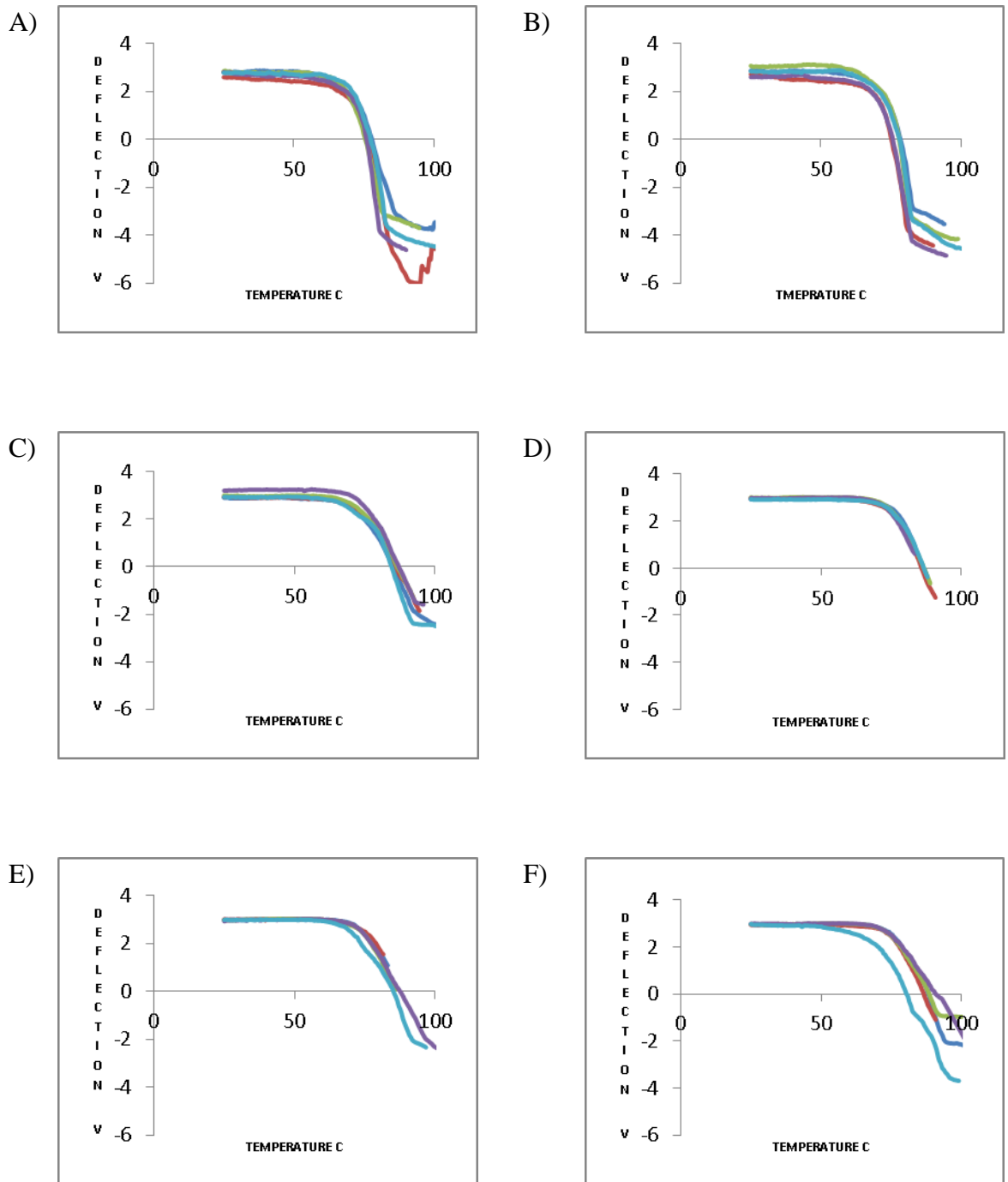


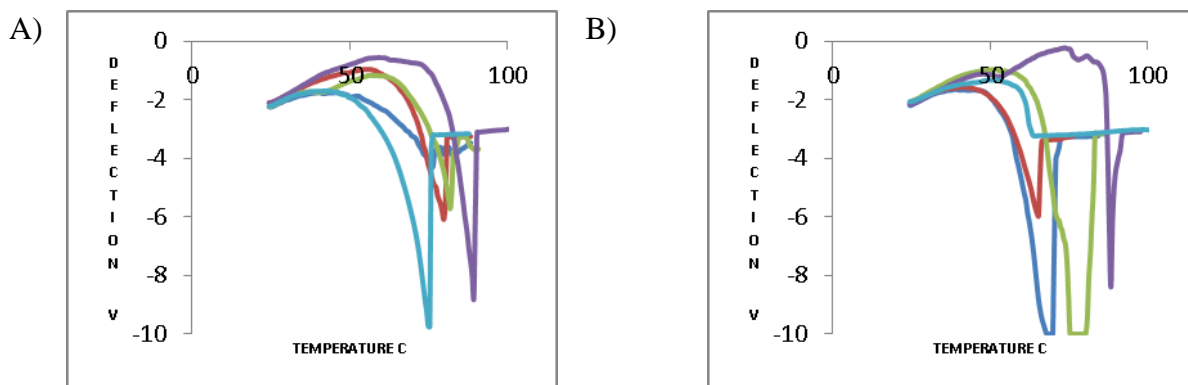
Figure 4.22: Micro-TA results across the top of an ibuprofen compact, using a Wollaston wire probe. Position on the radius of the compact is given by A) edge to F) middle. Five micro-TA readings were taken at each position: dark blue - site 1, red - site 2, green - site 3, purple - site 4, light blue - site 5.

4.3.2.6 Nano-TA

Nano-TA was performed at three locations across the surface of the compacts, with the results being shown in Figure 4.23. No difference was observed between the positions across the radius of the compact, but the results were very variable at each location. Several scans showed a transition with onset at circa 50°C, although some scans showed the onset temperature to be much higher. No thermal transitions were observed around 50°C for ibuprofen in the DSC or micro-TA experiments, so it is unlikely that the nano-TA transitions seen here reflect true thermally-related events.

Although no water had been detected in the ibuprofen sample by DSC, the compacts were dried in an oven for 4 hours at 60°C and re-tested to eliminate the possibility that surface water, and hence surface dissolution of the drug, was responsible for the probe movement. No differences, however, were seen before and after drying, as can be seen by comparison of Figure 4.23 (before drying) and Figure 4.24 (after drying).

The batch of ibuprofen used for the mini-tablets was also analysed by nano-TA (without drying) and showed similar results to the original batch as shown in Figure 4.25. These results gave confidence that the profiles for the compacts and the mini-tablets would be comparable.



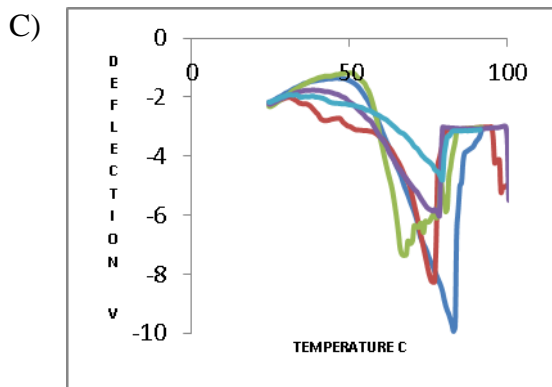


Figure 4.23: Nano-TA results of the top of the ibuprofen compacts, using a nano probe. Position across the radius of the compact is given by A (edge) to C (middle). Five nano-TA readings were taken at each position: dark blue - site 1, red - site 2, green - site 3, purple - site 4, light blue - site 5.

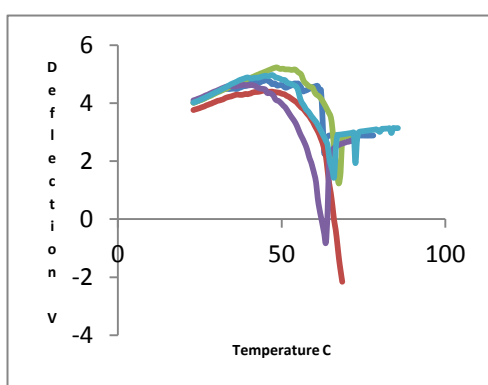


Figure 4.24: Nano-TA results of the top of the heat-treated ibuprofen compacts, using a nano probe. Five nano-TA readings were taken: dark blue - site 1, red - site 2, green - site 3, purple - site 4, light blue - site 5.

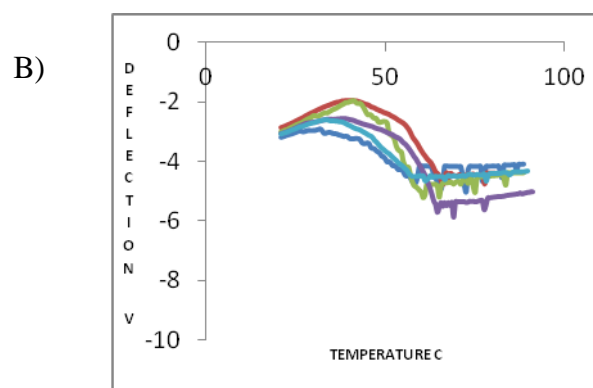
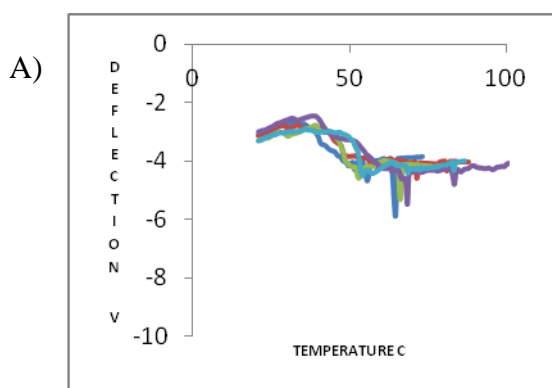


Figure 4.25: Nano-TA results of the top of the ibuprofen compacts (lot number 1B1T1575, batch used to prepare mini-tablets) using a nano probe. Position across the radius of the compact is given by A (edge) and B (middle). Five nano-TA readings were taken at each position: dark blue - site 1, red - site 2, green - site 3, purple - site 4, light blue - site 5.

4.3.2.7 TTM

A TTM map was generated at three locations across the surface of the ibuprofen compact and the results are shown in Figure 4.26. As with the nano-TA results, a thermal event was detected circa 50°C, but the results are variable. As the TTM is based on the individual nano-TA technique, the same explanations as to the data would apply.

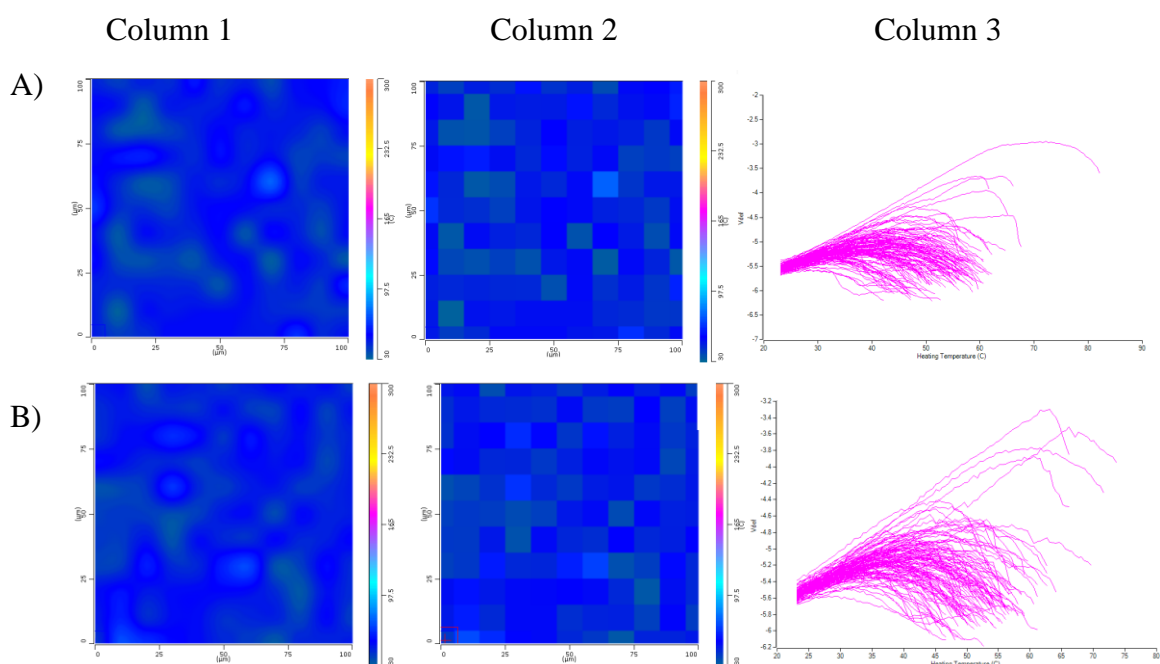


Figure 4.26: TTM maps of ibuprofen compacts. A) middle and B) edge of the compact. Column 1 is the interpolated (smoothed) map, Column 2 is the discrete map, and Column 3 shows the individual nano-thermal results.

4.3.3 Theophylline (anhydrous)

Theophylline is a member of the same family of drugs as caffeine and the structures differ only in that a N-CH₃ group on the 5 membered ring in caffeine is replaced by a N-H group in theophylline. Theophylline exists in both an anhydrous and monohydrate form. However, only the anhydrous form was used here.

4.3.3.1 SEM

Anhydrous theophylline was examined by SEM at magnifications of 250 and 1000, with the results being shown in Figure 4.27. The particles are large, with an elongated, cylindrical shape. The estimated size is approximately 100 μm over the shorter dimension

and greater than 200 μm over the longer dimension. Figure 4.27 B illustrates that the large elongated structures are made up of smaller, long thin crystals adhered together.

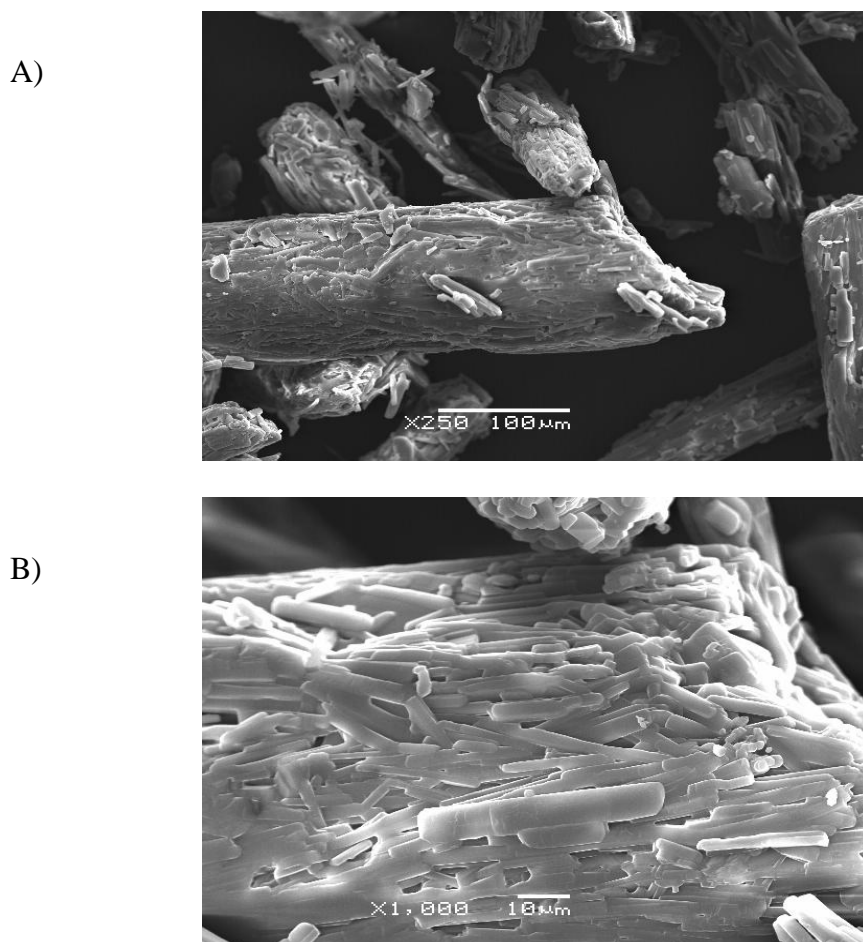


Figure 4.27: SEM images of anhydrous theophylline. A) magnification X250. B) magnification X1000.

4.3.3.2 VT-IR

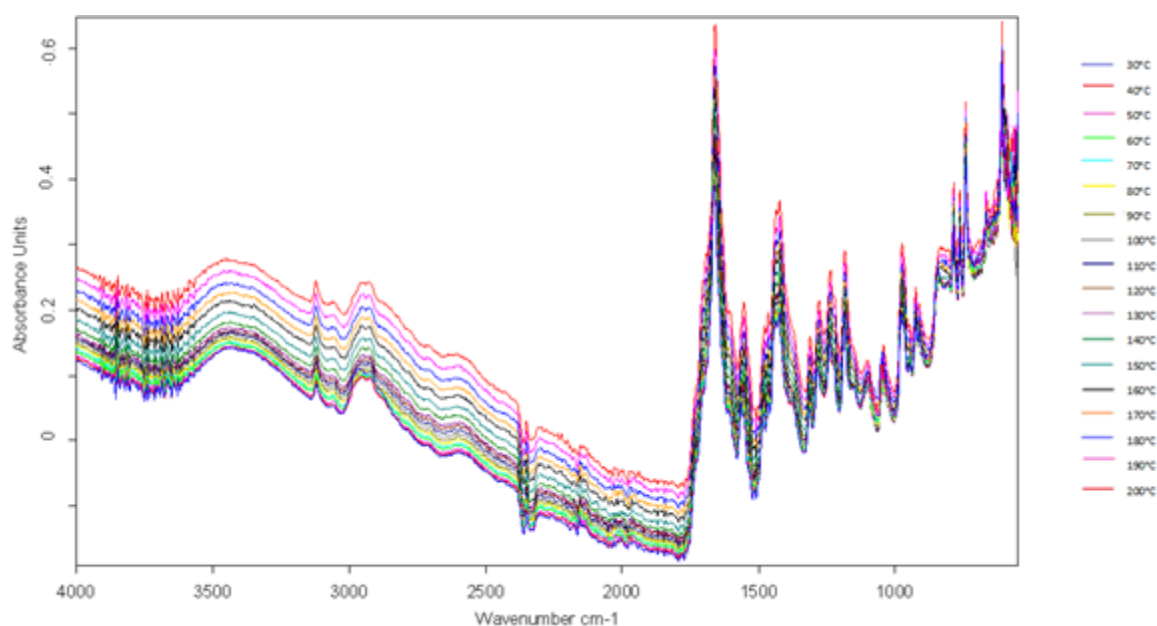
FT-IR scans were obtained on anhydrous theophylline at 10°C intervals between 30°C and 200°C. The results are shown in Figure 4.28: (A) shows the full scan across all temperatures, (B) shows the full scan at the highest and lowest temperatures studied, and (C) shows the fingerprint region at the extremes of temperature.

As the structure of theophylline is very similar to caffeine, varying only by the N-H group (theophylline) and N-CH₃ (caffeine) in the 5 membered ring, their spectra would be expected to be similar, with differences mainly being seen in the fingerprint region.

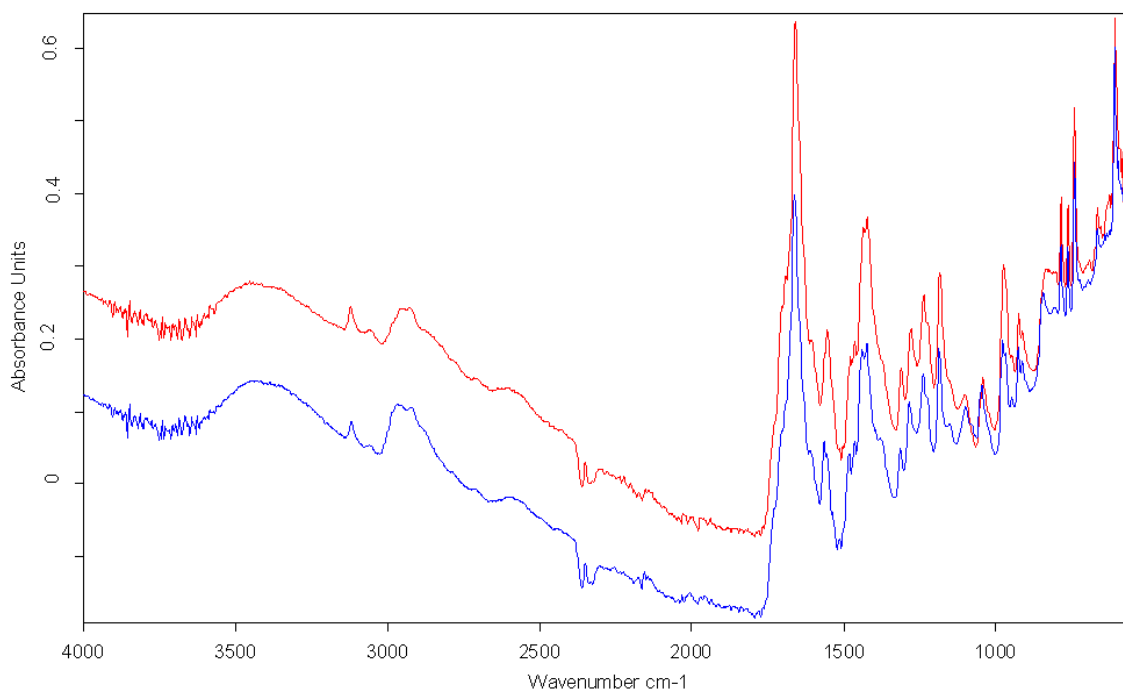
The large, broad peak at circa 3400 cm^{-1} is attributed to -OH stretch in water and is most likely explained by residual moisture in the system rather than in the sample, as the theophylline used here is anhydrous and no dehydration peak was seen on the DSC (discussed in section 4.5.3 below). The next group of peaks can be assigned to the C-H stretch from various positions in the structure; the sharp peak at circa 3100 cm^{-1} may be due to C-H in the ring structure and the peak at circa 2900 cm^{-1} may be attributed to C-H in a side-chain. There is a small peak at 2470 cm^{-1} which could be explained by C-N-C stretch. There is then a group of peaks at circa 2400 cm^{-1} which are due to the carbon dioxide in the atmosphere, as discussed earlier.

In the fingerprint region the spectrum of theophylline is different to that of caffeine. The peak at 1717 cm^{-1} could be assigned to CO-N(R)-CO bond stretch (Oprea et al (2012)). The small peaks at 1650 and 1500 cm^{-1} could be assigned to C=O stretch. The next group of peaks at circa 1400 cm^{-1} can be explained as C-H deformation. The group of peaks appearing at circa 1380 cm^{-1} to 1150 cm^{-1} could be assigned to C-N stretch. The peaks in the region of 1050 cm^{-1} can be explained by the N-CH₃ stretch. The peak at circa 850 cm^{-1} can be assigned to N=CH. The final peaks can be attributed to CH₂ rocking. Increasing temperature had very little effect on the FT-IR spectrum, suggesting no thermal transitions in this range, but it must be remembered that the melting point of this compound is higher than the temperatures studied here.

A)



B)



C)

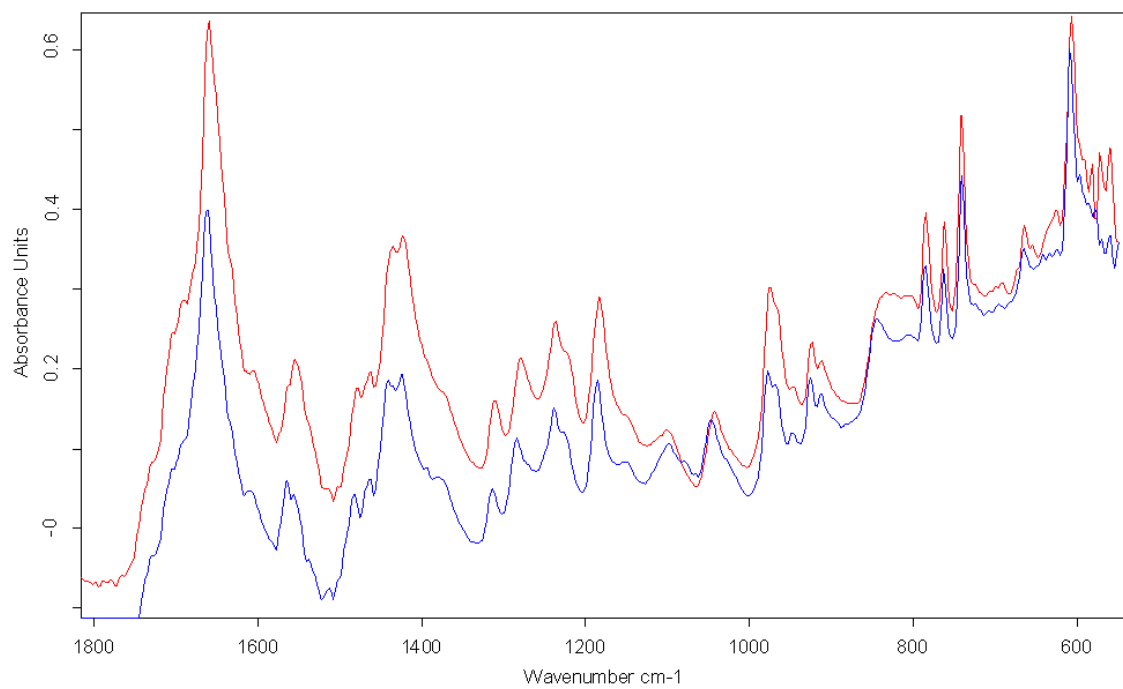


Figure 4.28: FT-IR spectra for anhydrous theophylline between the temperatures of 30°C and 200°C. A) All scans at 10°C intervals, B) the results for 30°C (blue) and 200°C (red), C) the fingerprint region for 30°C (blue) and 200°C (red).

4.3.3.3 DSC

Figure 4.29 shows the DSC data for anhydrous theophylline powder. One endotherm is observed with onset at 270.5°C and midpoint 272.4°C, which corresponds to the melting point of theophylline (melting point 270 to 274°C, BP 2013). In this temperature range no other thermal events were detected. No water loss peak was observed, confirming that the sample of theophylline was anhydrous.

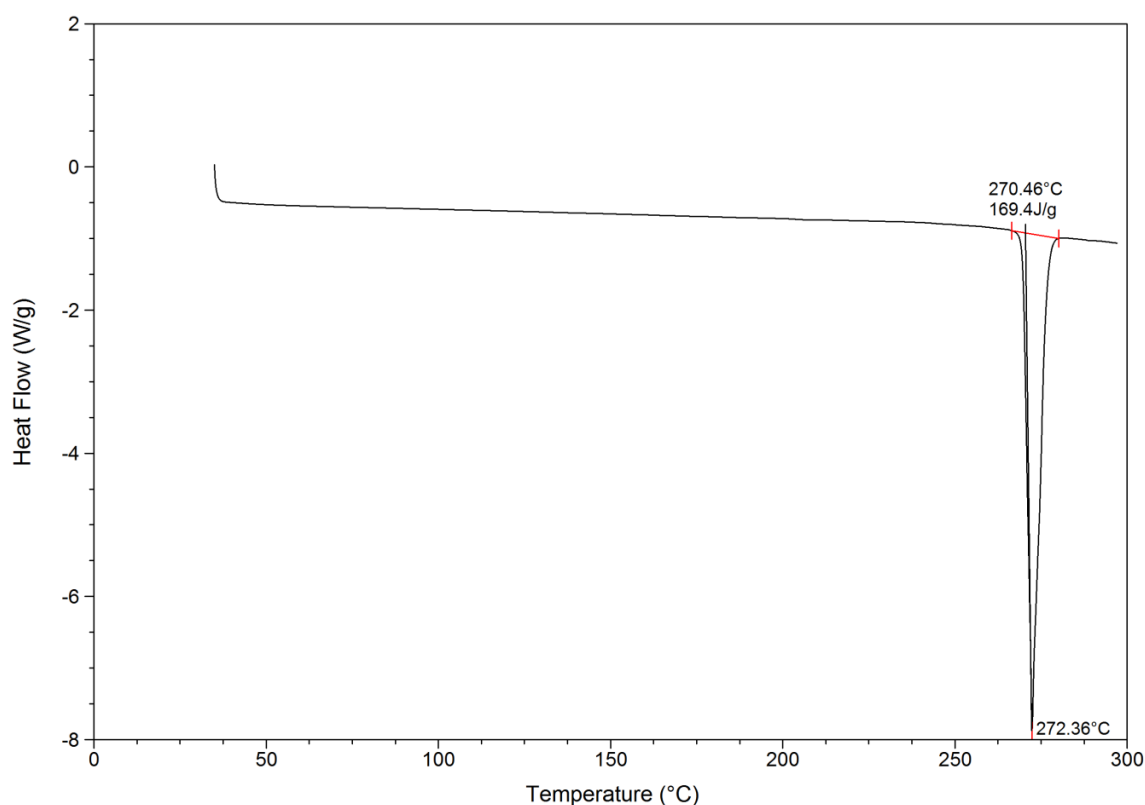


Figure 4.29: DSC traces of anhydrous theophylline.

4.3.3.4 AFM

Figure 4.30 shows the topographical AFM images of the theophylline compact. Three areas of 50 μm x 50 μm across the diameter of the compact were scanned using a Wollaston wire (micro) probe (this was a smaller region than for the other samples because it was intended only as exploratory testing). Apart from the slight indentation of the punches, there were no distinct topographical features on the theophylline compacts, with no differences between the different locations.

Column 1 Column 2

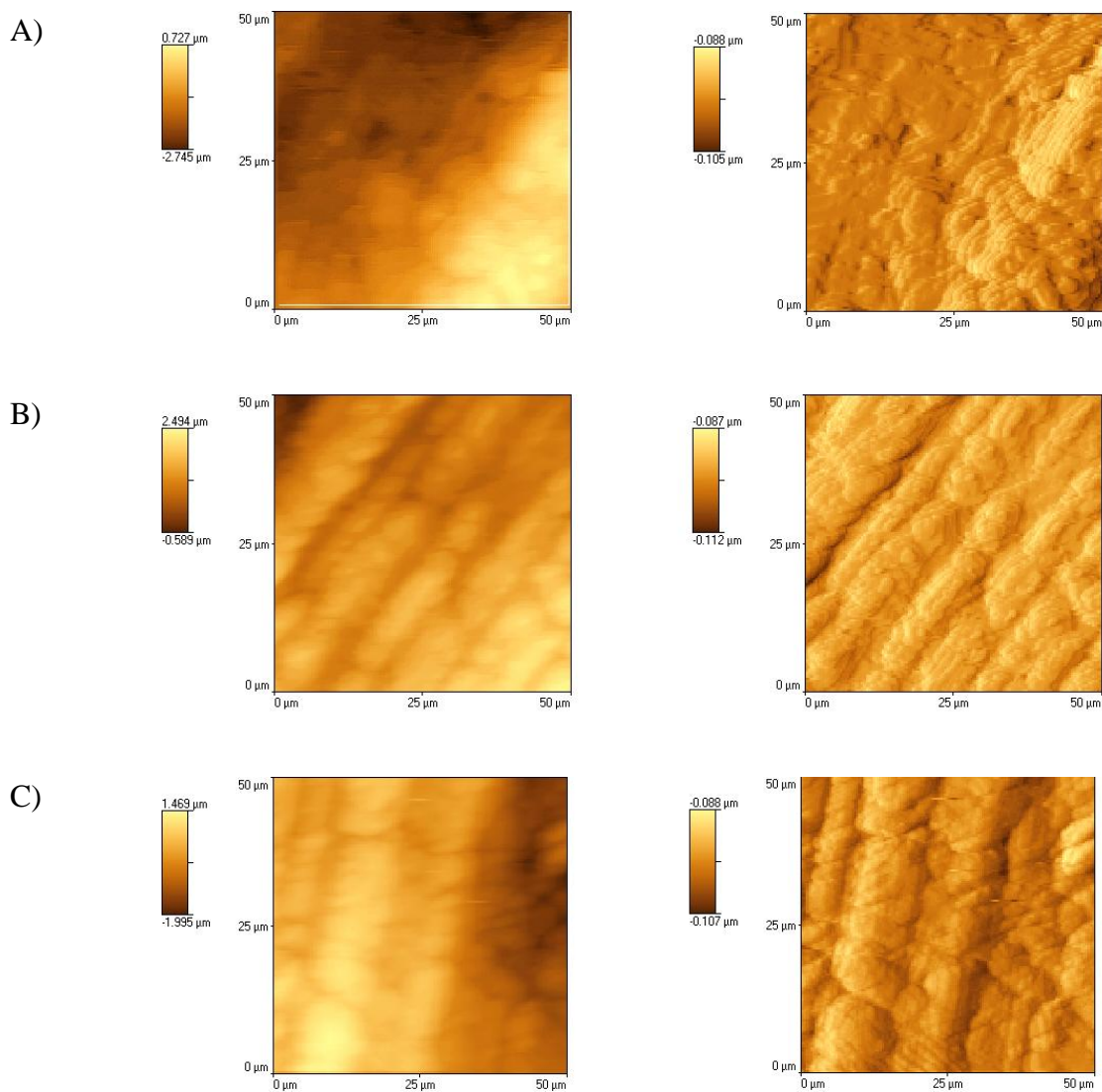


Figure 4.30: AFM scan showing the topography of the top of the theophylline compacts using a Wollaston wire (micro) probe. Column 1 - height, column 2 - deflection; position on the radius of the compact is given from A) outside to B) centre to C) outside.

The exercise was repeated using a nano probe, with the results shown in Figure 4.31. Again, no differences were observed between the different sites and no distinguishing features were seen.

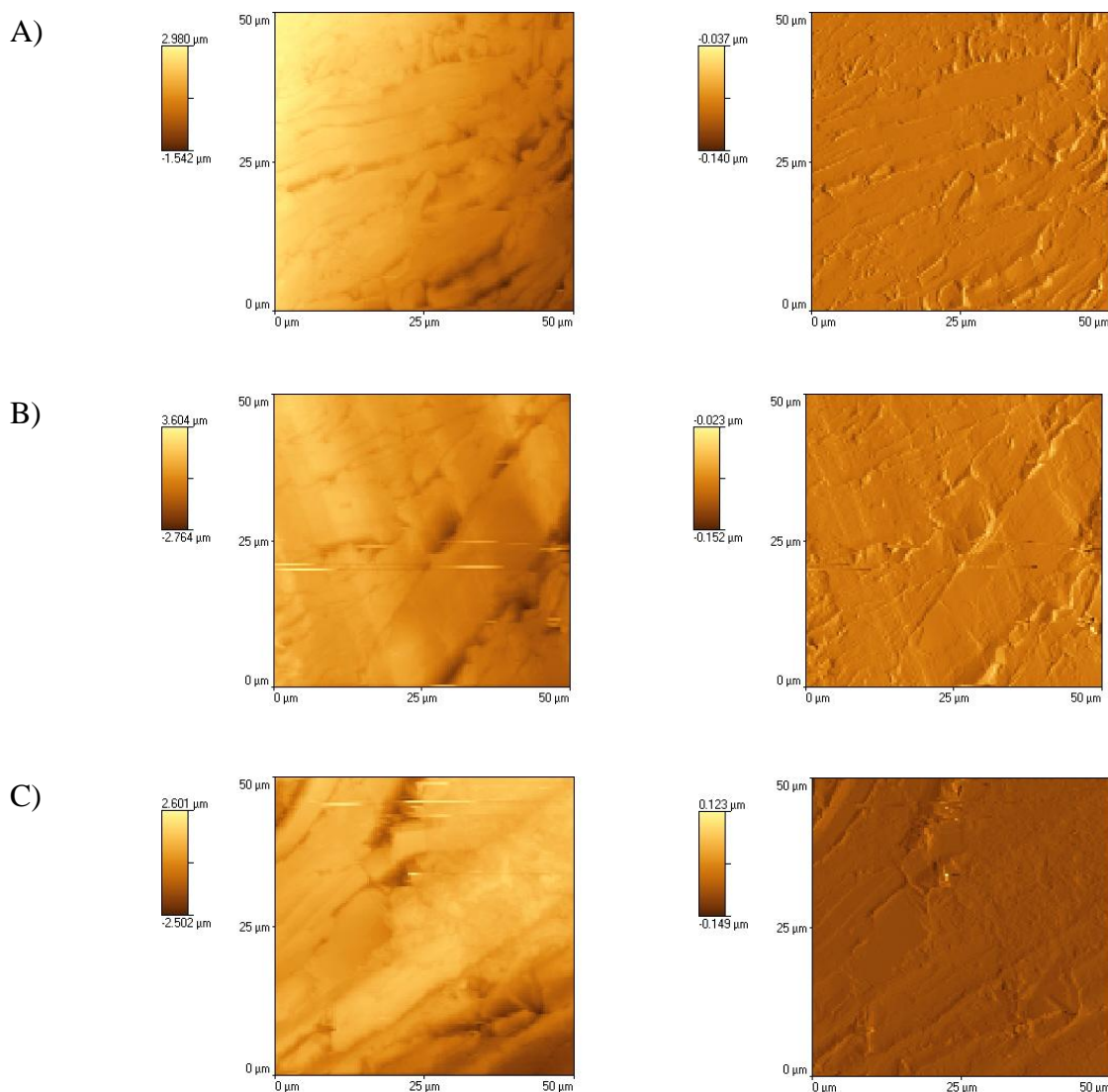


Figure 4.31: AFM scan showing the topography of the top of the theophylline compacts using a nano probe. Column 1 - height, column 2 - deflection; position on the radius of the compact is given from A) outside to B) centre to C) outside.

4.3.3.5 Micro-TA

Micro-TA measurements were performed in the same regions that had been scanned by AFM. Across the top of the surface of the compact three regions were analysed and this is represented by A (outside), B (centre) and C (outside) in Figure 4.32.

The results were somewhat variable, but in most cases a thermal event was observed with onset at circa 200°C. This is unlikely to be the melting of the theophylline, as its melting point by DSC is 270.5°C (onset) and no other thermal transitions were detected by DSC. The same observation was made for caffeine (a similar compound), i.e. an apparent thermal event at a temperature significantly lower than any known thermal transition, but caffeine also showed a distinct V shape on the micro-TA trace, with the minimum value closer to its true melting point. However, this V-shaped profile was not observed here for theophylline.

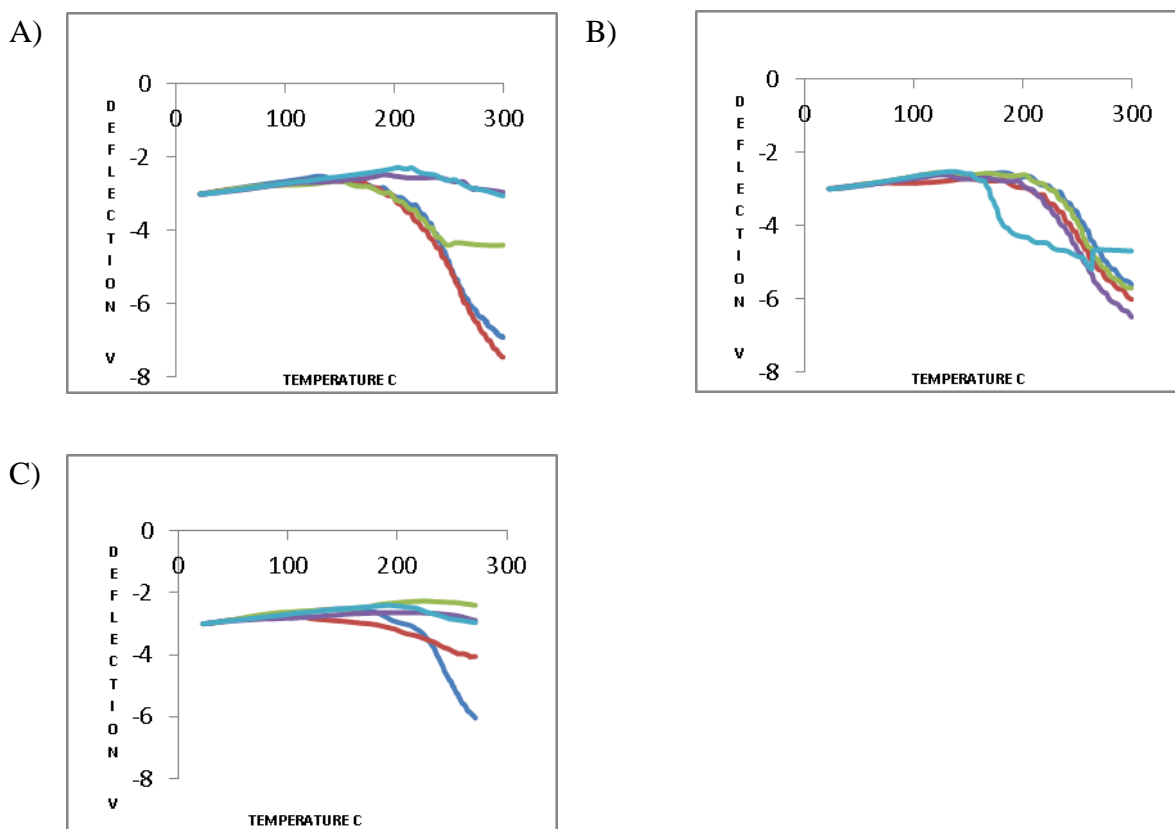


Figure 4.32: Micro-TA results of theophylline compacts, using a Wollaston wire (micro) probe; position across the diameter of the compact is given by: A (outside), B (centre), C (outside). Five readings were taken at each position: dark blue - site 1, red - site 2, green - site 3, purple - site 4, light blue - site 5.

4.3.3.6 Nano-TA

Three regions were scanned across the diameter in the same fashion as for the AFM images. A thermal event was detected with onset at circa 150°C. This value is even lower than that recorded in the micro-TA profiles and is certainly not representative of the melting point seen by DSC (onset 270.5°C). Although no water had been detected in the theophylline sample by DSC, the compacts were dried in an oven for 4 hours at 160°C and re-tested to eliminate the possibility that surface water, and hence surface dissolution of the drug, was responsible for the probe movement. No differences, however, were seen before and after drying, as can be seen by comparison of Figure 4.33 (before drying) and Figure 4.34 (after drying).

Overall, the nano-TA results of theophylline follow the same pattern as those of caffeine and ibuprofen, which suggest that there may be an issue relating to the technique itself.

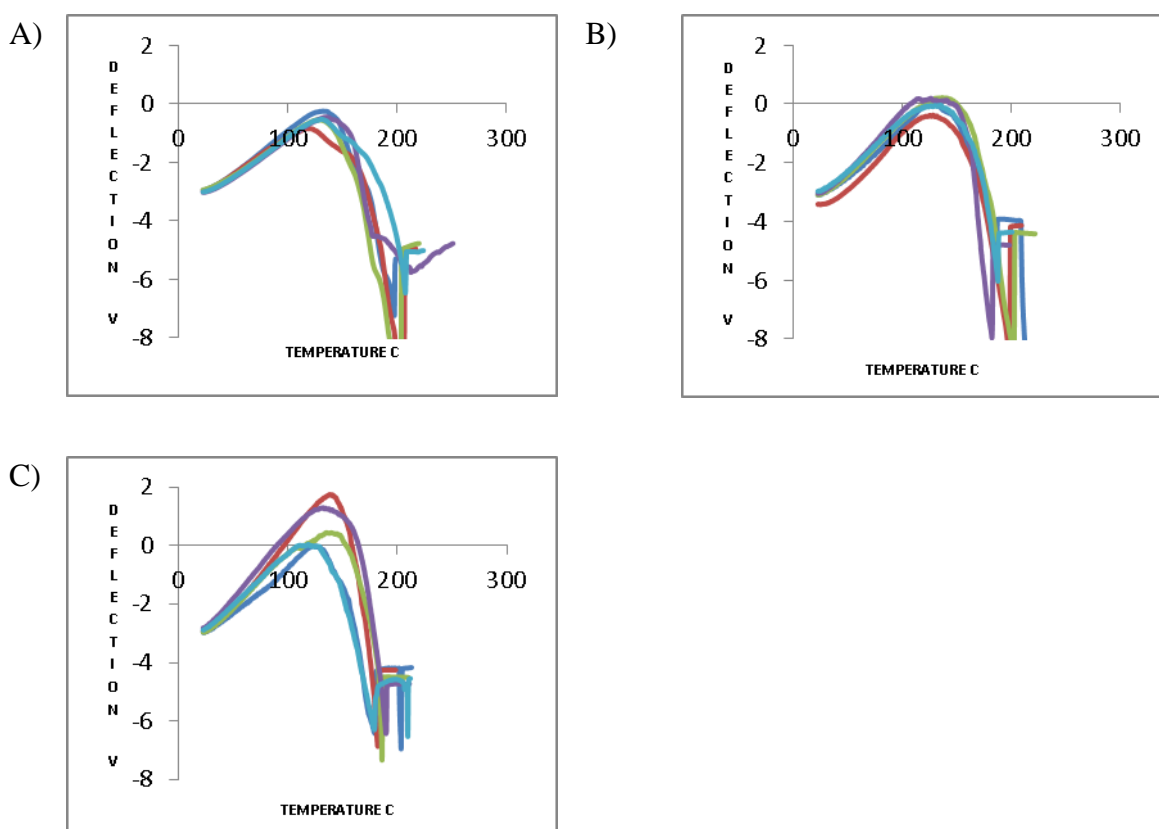


Figure 4.33: Nano-TA results of the theophylline compact, using a nano probe; position across the diameter of the compact is given by: A (outside), B (centre), C (outside). Five readings were taken at each position: dark blue - site 1, red - site 2, green - site 3, purple - site 4, light blue - site 5.

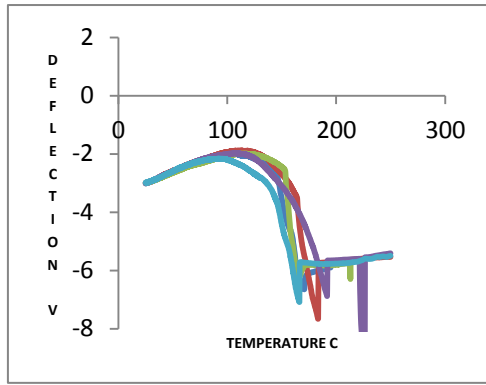


Figure 4.34: Nano-TA results of the theophylline compact, using a nano probe, after the compact had been dried in an oven for 4 hours at 160°C. Five nano-TA readings were taken at the same position: dark blue - site 1, red - site 2, green - site 3, purple - site 4, light blue - site 5.

4.3.3.7 TTM

A TTM map was generated at three locations across the surface of the theophylline compact and the results are shown in Figure 4.35. As with the nano-TA results, a thermal event was detected circa 150°C but the results are somewhat variable. As the TTM is based on the individual nano-TA technique, the same explanations as to the data would apply.

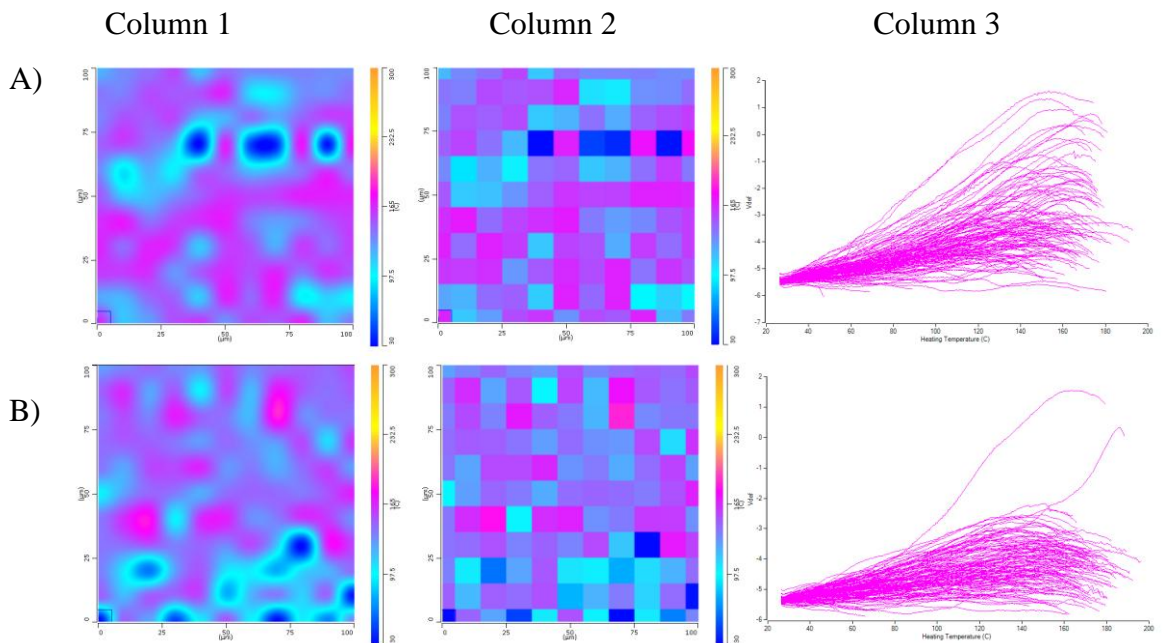


Figure 4.35: TTM maps of theophylline compacts. A) centre and B) outside of the compact. Column 1 is the interpolated (smoothed) map, Column 2 is the discrete map, and Column 3 shows the individual nano-thermal results.

4.4 Investigations into the micro-TA / nano-TA analysis of ibuprofen, caffeine and theophylline

Consistently low temperatures for the thermal events were observed when the drug samples were analysed by micro-TA and nano-TA as compared to the temperatures of thermal events obtained by DSC. Only the ibuprofen micro-TA results were consistent with the complementary DSC data. Hence, it was considered that further analysis was required to explain these discrepancies.

An initial consideration was that there was a thin layer of surface water on the compacts, which could potentially have resulted in the probe sinking into a solution of the drug, leading to artefactual results. However, it has already been established that this is unlikely, as the results generated after the compacts had been dried in an oven were the same as those generated prior to this step.

A group of twelve further drugs were selected for investigation. DSC was performed on the loose powder as before. Powder samples of each were compacted at 2 tons for 30 seconds and the compacts analysed by both micro-TA and nano-TA. For these experiments, the run was not terminated after the onset of the thermal event, but allowed to continue until the minimum point had been reached (the V-shape discussed earlier). Estimates of the transition temperatures were made at both points; however, given the variability in the results, these are "best estimates" only. A heating rate of 25°C/second was used for these analyses in order to generate comparable results for indometacin to those in the literature (Harding et al (2008)). Four of the compounds were also analysed at the standard rate of 10°C/second to ascertain whether the heating rate had any effect on the temperature of thermal events.

Table 4.1 summarises the temperatures of the thermal events, as estimated from the three techniques, for all sixteen compounds studied. Twelve compounds showed a micro-TA onset value lower than the DSC melting point temperature, for three compounds it was higher and for one compound (ibuprofen) the two values were the same. For eight compounds, the minimum value (bottom of the V-shape) on the micro-TA trace gave a result more comparable to the DSC melting point than the onset value. For five compounds the thermal event temperature recorded by DSC was closer to the micro-TA onset values than the minimum values. Three compounds showed no minimum value on

their profiles. However, as their melting points recorded by DSC are close to or above 300°C, which was the highest temperature reached in the micro-TA experiment, it is likely that micro-TA would not show these transitions. Fifteen out of the sixteen compounds showed a nano-TA onset temperature which was lower than the DSC melting point, with only tetracycline hydrochloride showing a higher value. The difference between the onset values and the DSC melting points was generally greater for the nano-TA than the micro-TA. Table 4.2 shows the data for the different heating rates in the micro-TA and nano-TA experiments. Overall, there was very little difference observed between the two heating rates.

The phenomenon of low transition temperatures seen in micro-TA and nano-TA compared to DSC has been previously reported in the literature (e.g. Manduva et al (2008) and Zhang et al (2009)). One explanation is based on the fact that DSC and micro-TA / nano-TA examine different facets of the sample, so may be expected to generate different results: DSC measures the bulk properties of the component, but micro-TA / nano-TA measure the surface properties of the compact. The melting behaviour of the bulk and surface may also be different (Dash et al (2007)). With increasing temperature the crystalline structure first begins to break down in the surface layer and there are an increased number of defects in the surface which allows more molecular diffusion. Before the melting point of the bulk material is reached, the surface displays an increase in disorder and mobility increases which spreads inwardly, so a film of melted component is formed but the bulk retains its solid order underneath. The melted layer is referred to as a quasi-liquid as there is some order from the crystal layer below (Pluis et al (1987)).

If this is extended to the micro-TA / nano-TA situation, as the probe heats the surface of the compact a small local area of increased disorder is formed, resembling a thin surface liquid film. The probe will sink through this when it is soft and mobile enough - this is the onset temperature. The probe will then reach the bulk core of the compact, which will melt at the "correct" temperature (i.e. as recorded by DSC) - this is the minimum value (base of the V-shaped deflection). Harding et al (2008) performed a micro-TA study which measured the "pull-off" force required to separate the probe from the surface of the sample at specific temperatures. They found that the change in probe behaviour occurred at temperatures below those expected from other studies. Their work and the current study are complementary in that their work measured pull-off forces, whereas the current study was looking at penetration. Both studies show that the surface of the sample is behaving

differently to the bulk and that the temperatures of the thermal events are lower at the surface than in the bulk.

The issue seems to be related to low molecular weight compounds rather than polymers and may be related to the local viscosity of the molten surface layer - a polymer layer may be expected to be more viscous than one composed of a low molecular weight drug, and hence the probe will not penetrate it as much and the observed melting will be much closer to the "true" value. Supporting this suggestion is the fact that the temperature calibration of the micro-TA and nano-TA equipment is via the use of polymer discs, indicating that they behave as expected. Alternative calibration methods may be required for low molecular weight compounds.

In the literature, this issue of discrepancies between DSC data and micro-TA and nano-TA data has been "solved" by either quoting the minimum value or simply noting the discrepancy. Neither approach is particularly satisfactory, especially when a mixed system of polymer(s) and low molecular weight compound(s) is studied. Further complications of interpretation arise when a compound is known to undergo phase transitions prior to melting, as it is tempting to assign the low temperature events seen with micro-TA or nano-TA to these transitions. It may be possible to use a different method of temperature calibration rather than polymer discs when studying low molecular weight compounds, but again this will be a problem when studying mixed systems.

Another contribution to the issues discussed above and, in particular, to the differences between the micro-TA and nano-TA results is the relative sizes of the probe. The nano-probe is so small that it is effectively probing the surface of compact in a topographical manner. On heating, the expansion of the compact surface may be sufficient to allow the probe to move downwards if the surface is not completely smooth, as may be the case between neighbouring curved particles. As the technique assumes that any deflection of the probe is related to thermal processes, e.g. softening or melting, this would lead to experimental artefacts and transitions being wrongly ascribed. This "topographical" hypothesis would explain the variability of the nano-TA results, as they would be very dependent on the precise location of the probe, i.e. on the centre of the surface of a particle or at a junction. Additionally, the increased consistency of the micro-TA results compared to the nano-TA results can be explained simply by the size of the two probes: the micro-probe is relatively so large that it is unlikely to penetrate between two neighbouring

particles and hence will give a "truer" result.

A final consideration is that TTM, used to assess spatial distribution of material across a surface, is based on the nano-TA technique. It is an automated process, whereby the probe deflection at each location in a grid is measured. Once probe deflection has been measured, the software immediately moves the probe to the next location in the grid. Hence, the temperature measured will be that of the initial surface response, i.e. the onset value, rather than that of the bulk material, which may then lead to incorrect assignments.

Compound name	RMM (g mol ⁻¹)	Temperature of thermal event (°C)				
		DSC	Micro-TA		Nano-TA	
			Onset	Minimum	Onset	Minimum
Ciprofloxacin	331.4	267.72 / 315.06	263	_____	237	263
Phenytoin	252.3	294.83	232	296	186	218
Piroxicam	331.3	200.21 / 243.18	185	193	142	181
Naproxen	230.3	145.55 / 153.77	141	156	91	128
Tetracycline HCl	480.9	71.64 / 156.00	163	203	199	206
Flurbiprofen	244.3	115.09	108	128	93	116
Diclofenac (Na salt)	318.1	282.83	241	_____	243	265
Tolfenamic acid	261.7	184.58	201	242	101	160
Fenbufen	254.3	185.04	174	206	91	155
Sulindac	356.4	184.58	188	206	152	167
Indometacin	357.8	159.79	146	159	133	147
Mefenamic acid	241.3	160.91 / 228.57	190	236	148	176
Caffeine (Form II)	194.2	146.80* / 234.40	190	243	114	145
Caffeine (Form I)	194.2	234.44	170	214	130	188
Ibuprofen	206.3	75.87	75	80	46	59
Theophylline anhydrous	180.2	270.43	212	_____	196	208

Table 4.1: Summary of results obtained by DSC, micro-TA and nano-TA (heating rate 25°C/second). Two DSC temperatures means two thermal events were detected: a probable polymorphic transition and melting. The * indicates that the measured temperature changes with heating rate. Line = minimum (V shape) was not recorded.

Compound name	RMM (g mol^{-1})	Temperature of thermal event ($^{\circ}\text{C}$)								
		DSC	Micro-TA				Nano-TA			
			Onset		Minimum		Onset		Minimum	
			10 $^{\circ}\text{C}/\text{s}$	25 $^{\circ}\text{C}/\text{s}$	10 $^{\circ}\text{C}/\text{s}$	25 $^{\circ}\text{C}/\text{s}$	10 $^{\circ}\text{C}/\text{s}$	25 $^{\circ}\text{C}/\text{s}$	10 $^{\circ}\text{C}/\text{s}$	25 $^{\circ}\text{C}/\text{s}$
Indometacin	357.8	159.79	137	146	166	159	133	133	143	147
Caffeine (Form II)	194.2	146.80* / 234.40	180	190	235	214	100	114	141	145
Ibuprofen	206.3	75.87	75	75	80	80	50	46	79	59
Theophylline anhydrous	180.2	270.43	204	212	—	—	150	196	203	208

Table 4.2: Summary of results obtained by DSC, micro-TA and nano-TA (heating rates 10 and 25 $^{\circ}\text{C}/\text{second}$). Two DSC temperatures means two thermal events were detected: a probable polymorphic transition and melting. The * indicates that the measured temperature changes with heating rate. Line = minimum (V shape) was not recorded.

4.5 Conclusions

In this chapter, three drugs were profiled individually using a range of physical analytical techniques in order to provide a baseline set of data for use in subsequent work, in the same way that in Chapter 3 the excipients were profiled. SEM was performed on powder samples of each compound, highlighting the morphological differences between them, and in particular, the differences between the two polymorphs of caffeine. Each compound as analysed by VT-IR, with very little change being observed on heating, except for the melting of ibuprofen. Unfortunately, the two polymorphs of caffeine could not be easily distinguished by VT-IR. DSC was used to establish the thermal behaviour of the individual components to aid in the interpretation of micro-TA and nano-TA data. For ibuprofen and theophylline, a single clear peak attributed to melting was observed. Caffeine Form II (the low temperature stable form) showed an endotherm associated with polymorphic conversion to Form I (the high temperature stable form) and a single melting peak thereafter.

AFM did not show any distinguishing feature for compacts of any drug and, in common with the excipient compacts, no difference was seen across the radius of the surface. Micro-TA and nano-TA were performed on separate compacts of all three drugs. The measured temperatures of the thermal events for caffeine and theophylline were variable and significantly different to and lower than those observed on DSC, with the nano-TA results being even more dissimilar to the DSC results than the micro-TA results. The micro-TA results for ibuprofen matched the DSC data reasonably closely, but the nano-TA results showed the general trend of lower temperatures. As this effect was not seen with the excipients, it was investigated in more detail using an additional range of small molecular weight drugs. The results for these additional drugs confirmed those of the earlier studies. It is suggested that the surface of the compact is behaving differently to the bulk material and that the probe movement is reflective of surface softening rather than "true" bulk melting. This issue will make the interpretation of the TTM maps of mixed samples more challenging. However, the onset of probe movement is characteristic for each compound, so will be used to establish a profile for each compound and form the basis of TTM. The nano-TA results for the four excipients plus caffeine and the four excipients plus ibuprofen are summarised in Figures 4.36 and 4.37, respectively.

The results presented in this Chapter, together with those shown in Chapter 3, will be used to assess the mixed systems in Chapters 5 and 6.

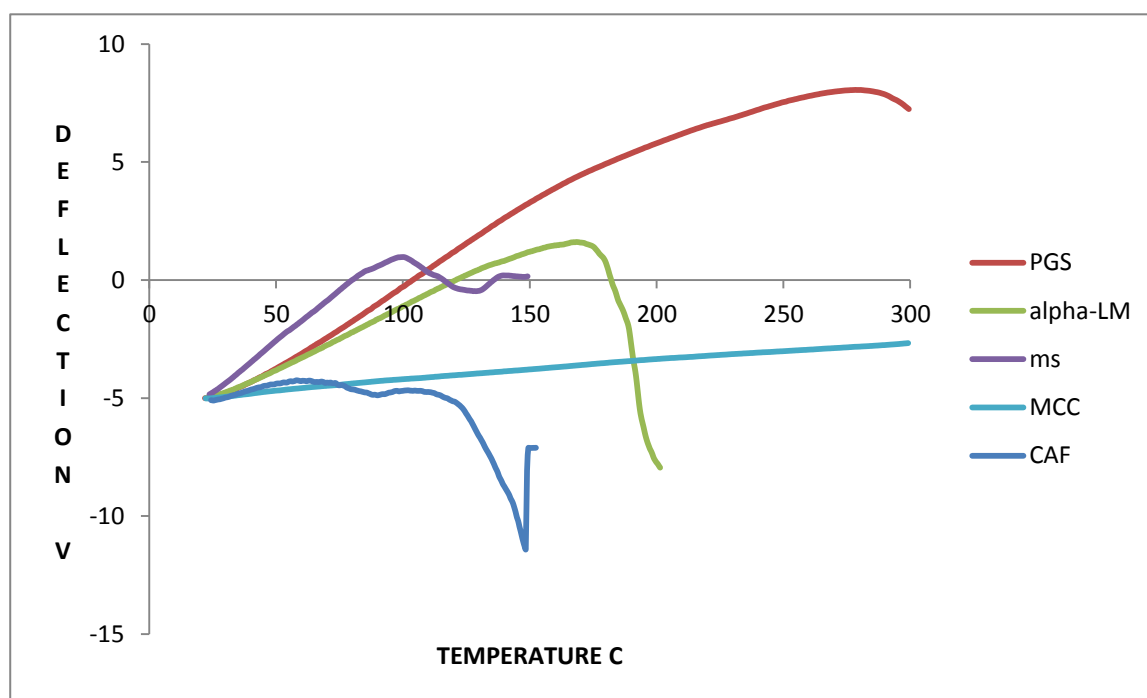


Figure 4.36: A summary of the nano-TA results for four excipients plus caffeine.

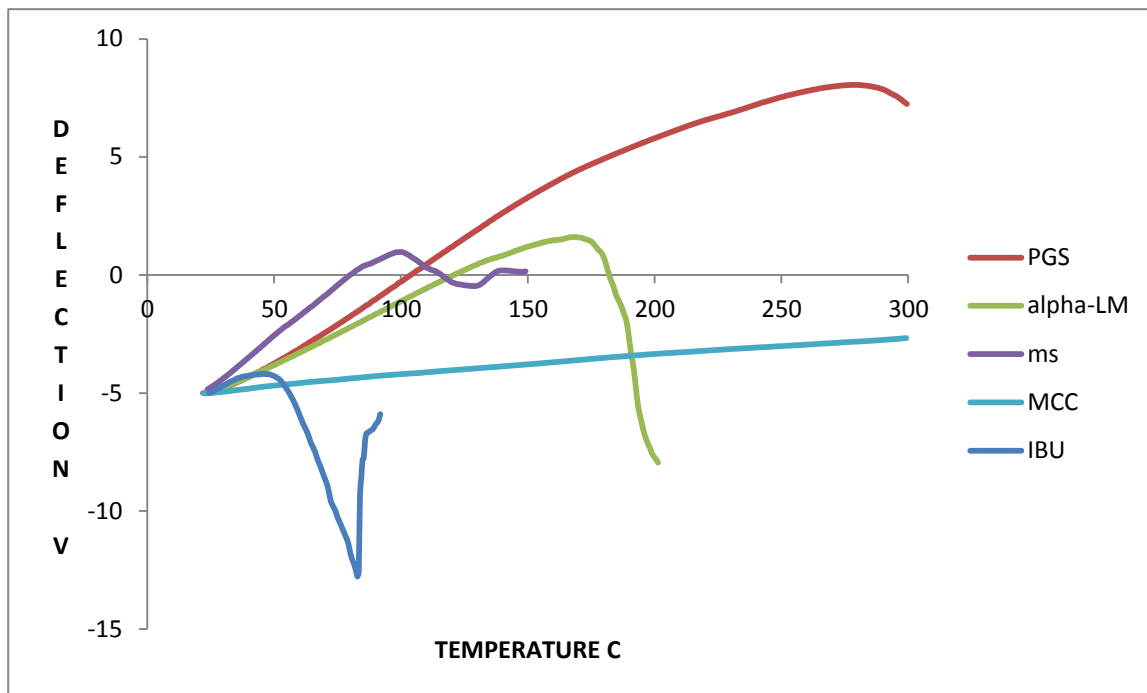


Figure 4.37: A summary of the nano-TA results for four excipients plus ibuprofen.

Chapter 5

The analysis of multi-component samples

CHAPTER 5

The analysis of multi-component samples

5.1 Introduction

The individual excipients and drugs were profiled by a range of analytical techniques in Chapters 3 and 4, respectively. The aim of this Chapter is to establish the potential of the novel analytical techniques (nano-TA and TTM) to analyse complicated multi-component samples. Using a standard tablet formulation as a reference (i.e. drug, α -LM, MCC, PGS and MS), compacts of all combinations of two, three, four and five components were produced and examined by AFM, nano-TA and TTM. The results of this Chapter will be used to assess the spatial distribution of components across the surface of "real" mini-tablets in Chapter 6.

5.2 Materials and Methods

Chapter 2 gives details of the analytical methods employed here. The excipients used here were described in Chapter 2 in terms of their chemical and physical properties and were profiled analytically in Chapter 3. α -LM, MCC, PGS and MS were used as they form the basis of most tablet formulations. PVP was not included in this part of the study due to the lack of thermal events detected when PVP was tested in a gel form in Chapter 3 - the gel form representing the form it is likely to take in a tablet formulation when it is added as part of the granulation fluid. Caffeine and ibuprofen were used as model drugs in separate formulations. Their chemical and physical properties and analytical profiles are described in Chapters 2 and 3, respectively.

In order to establish the ability of the techniques to detect the various components in a mixed sample, the concentration of the different components in the compact was kept equal (by weight), unlike in a normal tablet formulation where the relative concentrations vary according to the requirements of the formulation and the physical properties of the drug. The one exception to this was MS. This is added to tablet formulations as a lubricant and its role is to cover the outside surface of the powder / granule particles to stop the punch and dies sticking to the tablet during compression. Hence, there was a

possibility that, after mixing, MS would cover the surface of the powder particles and block the detection of the other components. For most formulations, the concentration of MS was kept to 1%, resembling that in most "real" tablet formulations; however, a higher concentration was also studied, to establish whether MS could be detected in the mixed samples.

Compacts were analysed by AFM, nano-TA and TTM, following the process used for the mono-component compacts. Images were taken at two positions across the radius of the compact, i.e. the outside and the centre. AFM was used to obtain a visual image of the topography of the compact and to aid in the interpretation of the nano-TA results. TTM was used to give a larger number of results over a greater surface area and hence to provide a more in-depth profile of the mixed compacts. Nano-TA is therefore at the heart of this study and Figure 5.1 summarises the nano-TA profiles of the four excipients and two drugs studied, indicating that it should be possible to separate out their profiles in a mixed system.

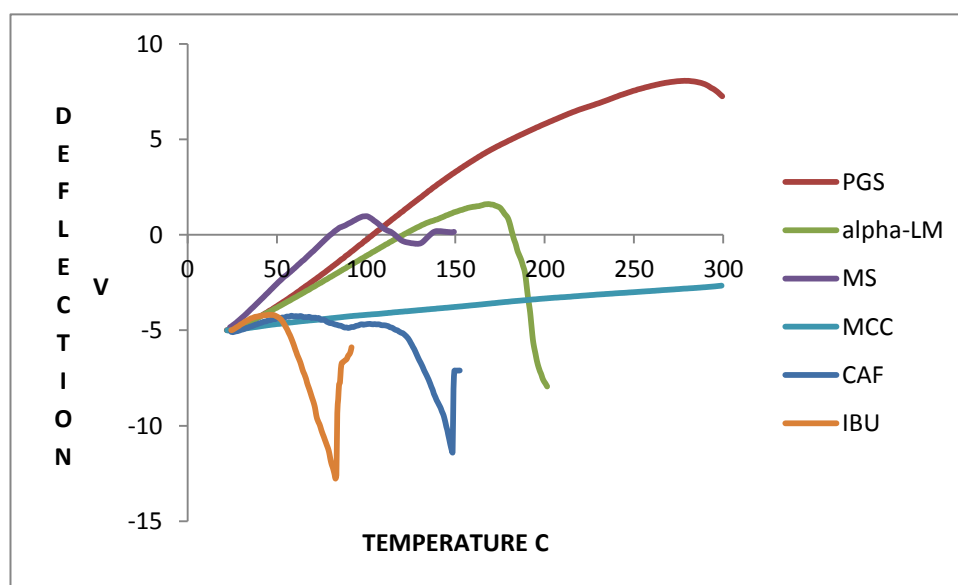


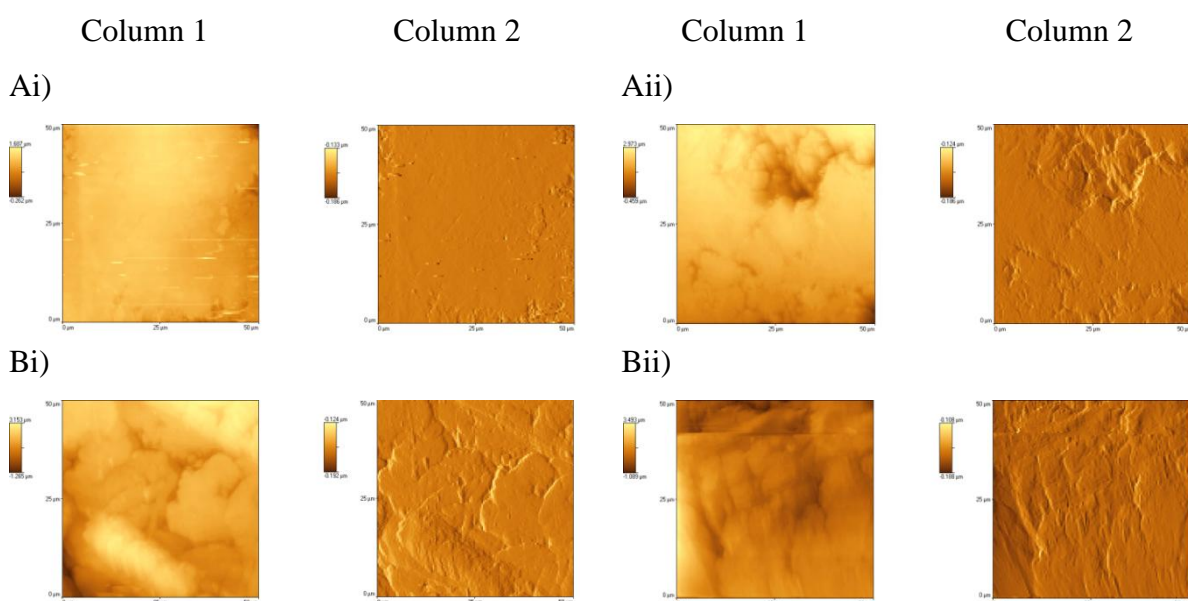
Figure 5.1: Summary of the nano-TA profile of the four excipients (α -LM, MCC, PGS and MS) and two drugs (caffeine and ibuprofen) used in this study.

5.3 Results and Discussion

5.3.1 Multi-component excipient compacts

5.3.1.1 AFM

Compacts were made of all combinations of two, three and four excipients. Representative AFM scans are shown in Figures 5.2, 5.3 and 5.4 for the two-, three- and four- excipient compacts, respectively. For mono-component compacts, it is reasonably easy to distinguish between materials via visual examination of the smoothness or roughness of the surface, as shown in Chapter 3. However, for multi-component samples, this becomes progressively more difficult as the number of components increases. PGS is the most distinctive of the excipients, with a circular structure on the AFM images, and can easily be distinguished in the two- and three- component systems. MCC and α -LM, being less distinctive, are more difficult to identify in the multi-component systems. Where MS was included at 1% loading, reflecting its concentration in a tablet formulation, it proved hard to detect, so for example Figure 5.2 A, B and C show only the features of α -LM, MCC and PGS, respectively. This is most likely just a concentration effect and reflects the probability of the probe landing on a site containing MS. Images taken at the centre and the outside of the compact showed some differences, but it is more likely that this is a reflection of the mixture of excipients present in the different locations rather than a limitation of the technique, given that the mono-component compacts showed no differences at different locations.



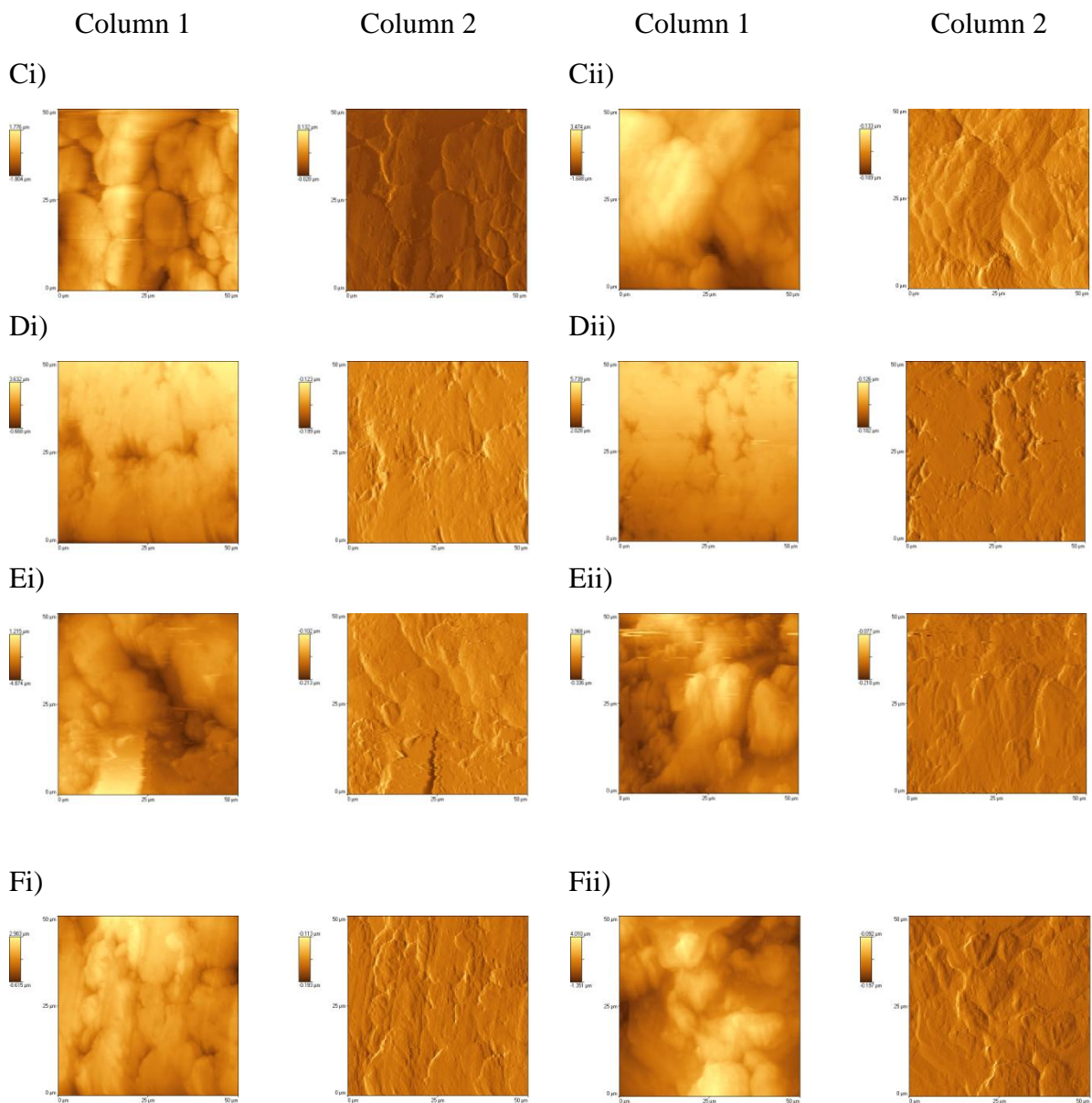


Figure 5.2: AFM images of 2-excipient compacts, using a nano probe. A) 99% α -LM / 1% MS. B) 99% MCC / 1% MS. C) 99% PGS / 1% MS. D) 50% α -LM / 50% MCC. E) 50% α -LM / 50% PGS. F) 50% MCC / 50% PGS. Position on the compact is given by i) centre, ii) outside. Column 1 - height, Column 2 - deflection.

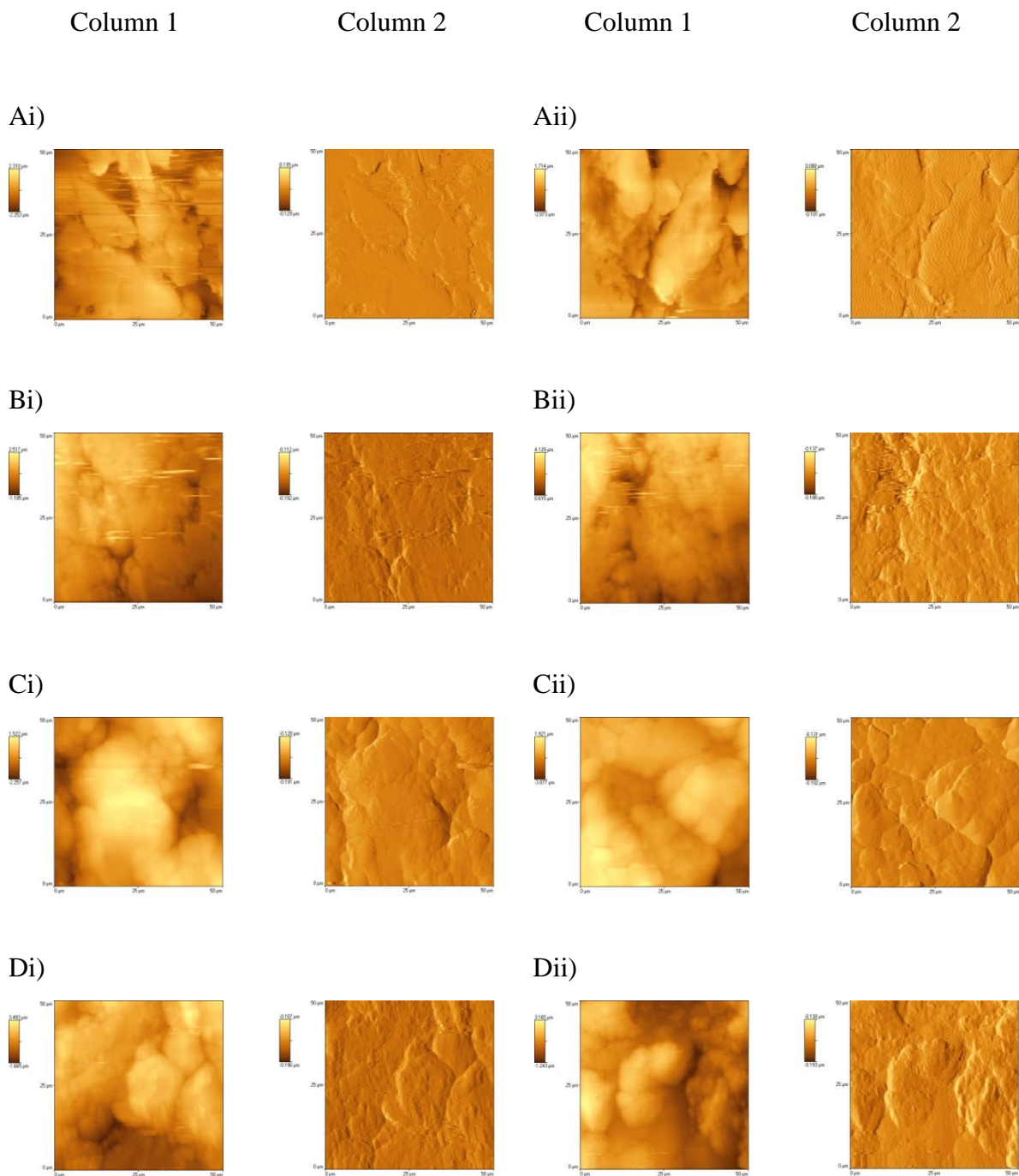


Figure 5.3: AFM images of 3-ingredient compacts, using a nano probe. A) 49.5% α -LM / 49.5% PGS / 1% MS. B) 49.5% α -LM / 49.5% MCC / 1% MS. C) 49.5% MCC / 49.5% PGS / 1% MS. D) 33.3% α -LM / 33.3% PGS / 33.3% MCC. Position on the compact is given by i) centre, ii) outside. Column 1 - height, Column 2 - deflection.

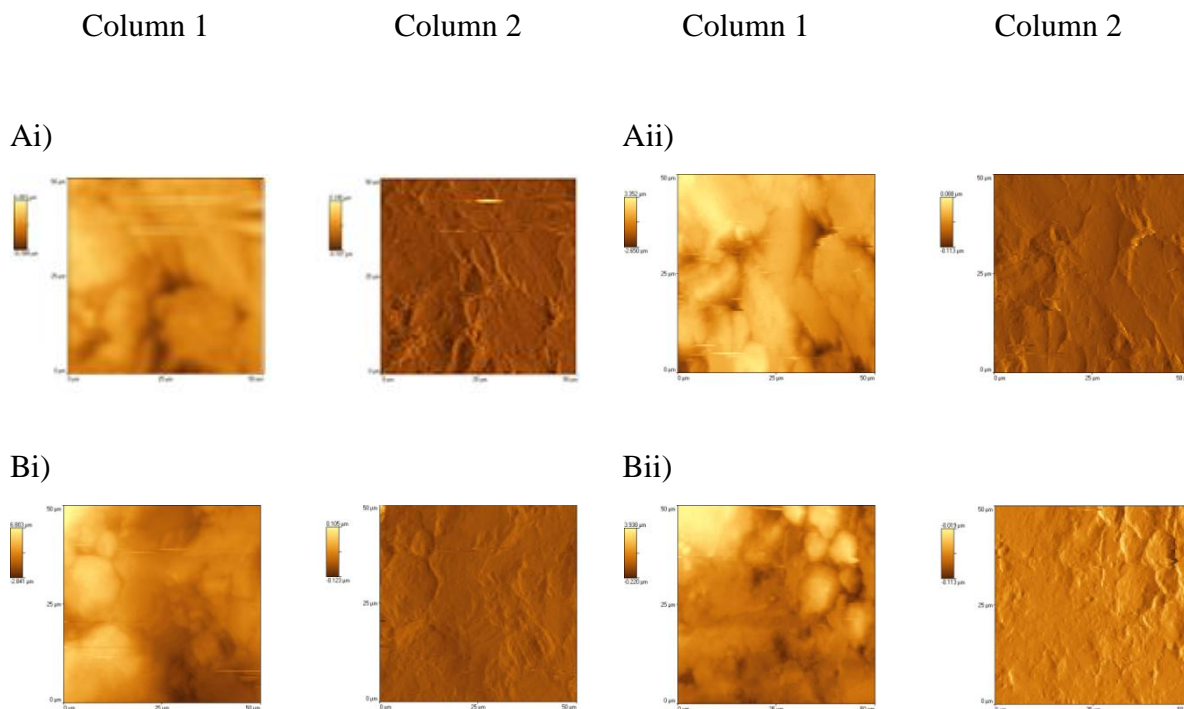


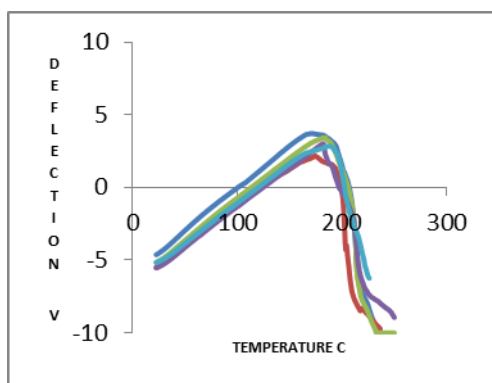
Figure 5.4: AFM images of 4-excipient compacts using a nano probe. A) 33% α -LM / 33% PGS / 33% MCC / 1% MS. B) 25% α -LM / 25% PGS / 25% MCC / 25% MS. Position on the compact is given by i) centre, ii) outside. Column 1 - height, Column 2 - deflection.

5.3.1.2 Nano-TA

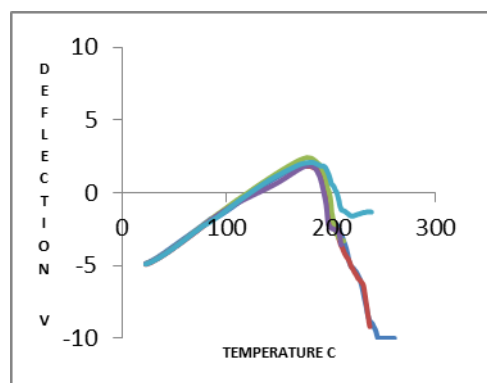
Nano-TA was performed on each of the multi-excipient compacts after the AFM images were generated and representative scans are shown in Figures 5.5, 5.6 and 5.7 for the two-, three- and four- excipient compacts, respectively. Comparison of these scans with those of the compacts of the individual components shown in Chapter 3 allowed identification of the most likely component(s) present. This is summarised in Tables 5.1, 5.2 and 5.3, respectively. As was seen with the AFM images, where MS was present at 1% (a normal concentration for a real tablet formulation), it was not detected, which is most likely due to the low probability of the probe landing on a part of the surface containing MS. In all the compacts with 1% MS, the other components were clearly seen and distinguishable. When MS was added at 25% to the 4-excipient compacts, all materials could be identified, again suggesting that the probability of identification is related to concentration. The temperature of the thermal event associated with α -LM in the mixed systems was slightly higher than for the single component compacts. The reason for this is unclear, but this

effect was consistent for the mixed systems and allowed identification of this component. MCC alone showed only an expansion in the baseline, so could be identified in mixed systems by an absence of thermal events. PGS alone showed either an expansion in the baseline with some curvature, different to MCC where a straighter baseline was observed, or a definite thermal event near the high end of the temperature range. This subtle difference in the profiles was used to identify both PGS and MCC when they were both in a formulation, as is shown in Figure 5.5 F (2 excipients) and Figure 5.6 D (3 excipients).

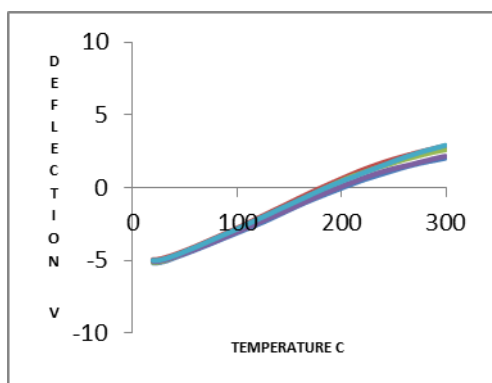
Ai)



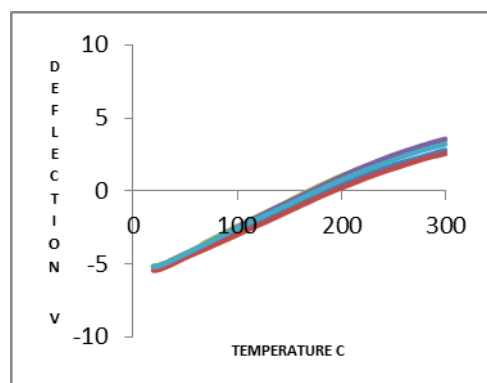
Aii)



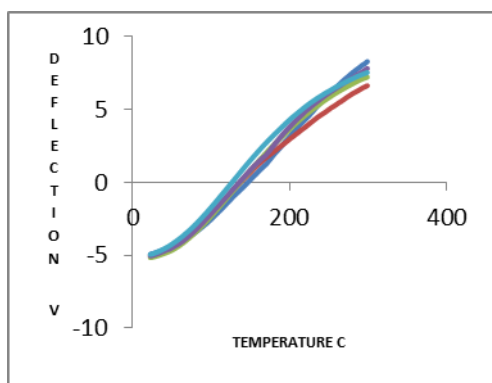
Bi)



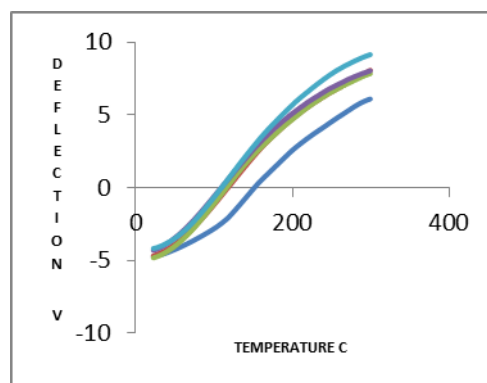
Bii)



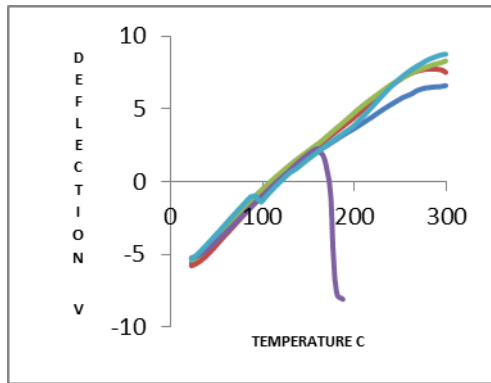
Ci)



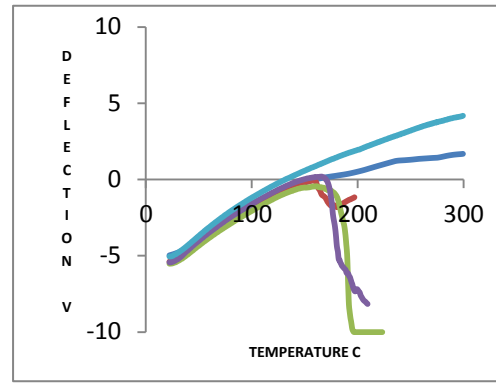
Cii)



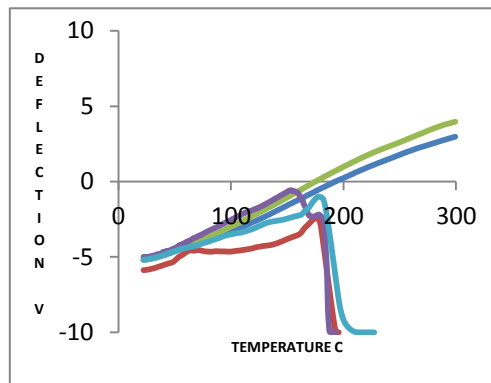
Di)



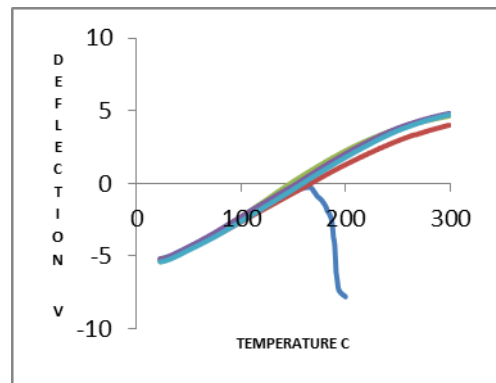
Dii)



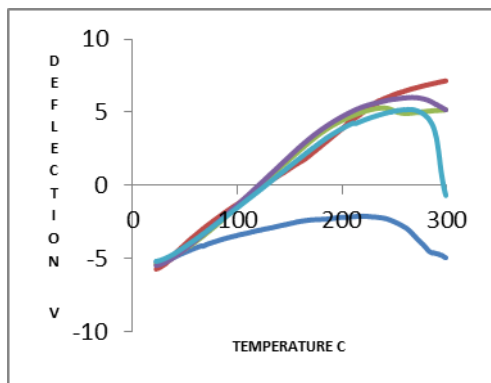
Ei)



Eii)



Fi)



Fii)

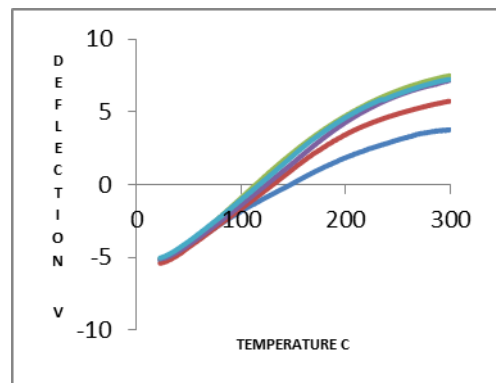
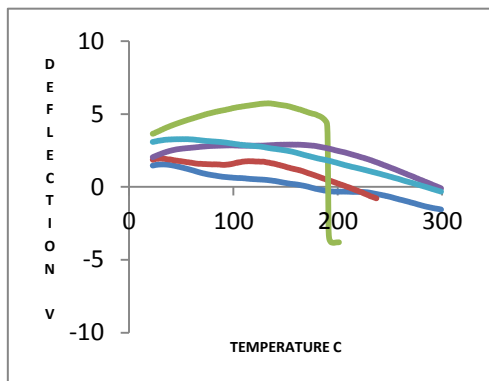


Figure 5.5: Nano-TA results for the 2-excipient compacts, using a nano probe. A) 99% α -LM / 1% MS. B) 99% MCC / 1% MS. C) 99% PGS / 1% MS. D) 50% α -LM / 50% PGS. E) 50% α -LM / 50% MCC. F) 50% MCC / 50% PGS. Position on the compact is given by i) centre, ii) outside. Five readings were taken at each position: dark blue - site 1, red - site 2, green - site 3, purple - site 4, light blue - site 5.

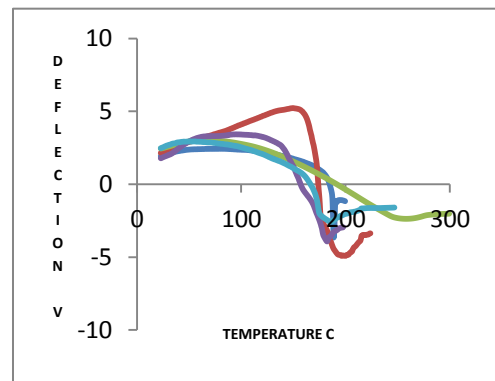
Formulation	Compact	Components identified (number of sites; maximum = 5)			
		α -LM	MS	MCC	PGS
99% α -LM / 1% MS	A i	5	0	X	X
	A ii	5	0	X	X
99% MCC / 1% MS	B i	X	0	5	X
	B ii	X	0	5	X
99% PGS / 1% MS	C i	X	0	X	5
	C ii	X	0	X	5
50% α -LM / 50% PGS	D i	1	X	X	4
	D ii	3	X	X	2
50% α -LM / 50% MCC	E i	3	X	2	X
	E ii	1	X	4	X
50% MCC / 50% PGS	F i	X	X	1	4
	F ii	X	X	5	0

Table 5.1: A summary of the most probable components identified from the nano-TA scans of the 2-excipient compacts shown in Figure 5.5. The number indicates the number of scans assigned to a particular component. X indicates that this component is not present in the compact.

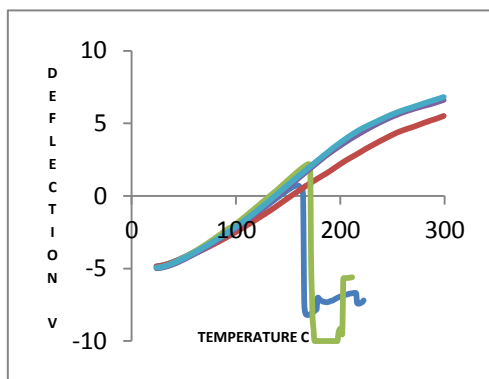
Ai)



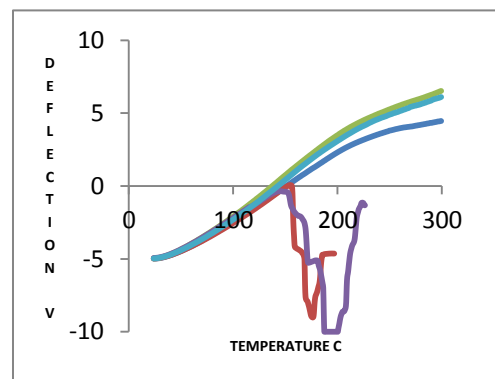
Aii)



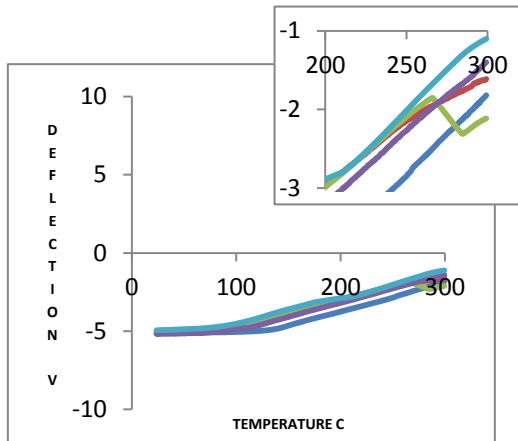
Bi)



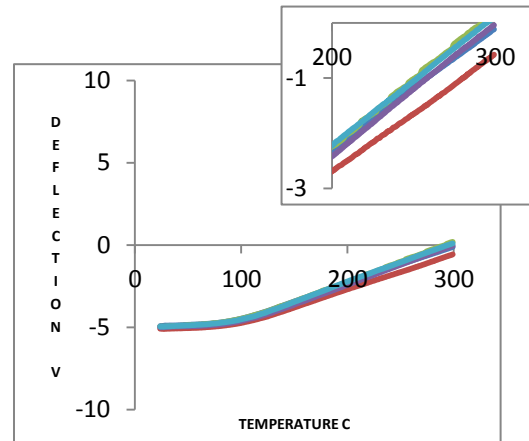
Bii)



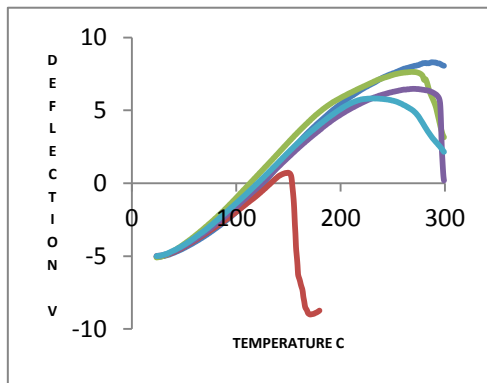
Ci)



Cii)



Di)



Dii)

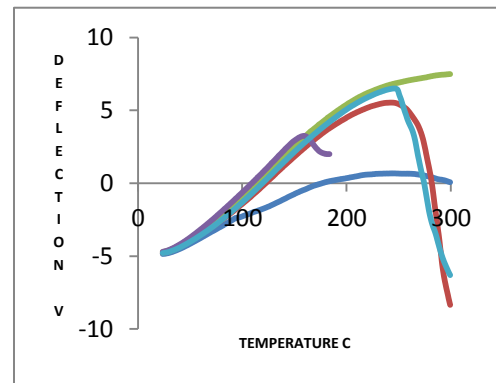
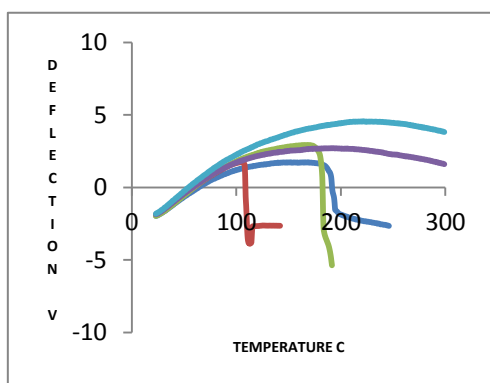


Figure 5.6: Nano-TA results for the 3-excipient compacts, using a nano probe. A) 49.5% α -LM / 49.5% PGS / 1% MS. B) 49.5% α -LM / 49.5% MCC / 1% MS. C) 49.5% MCC / 49.5% PGS / 1% MS (inset is the temperature range 200 to 300°C expanded). D) 33.3% α -LM / 33.3% PGS / 33.3% MCC. Position on the compact is given by i) centre, ii) outside. Five readings were taken at each position: dark blue - site 1, red - site 2, green - site 3, purple - site 4, light blue - site 5.

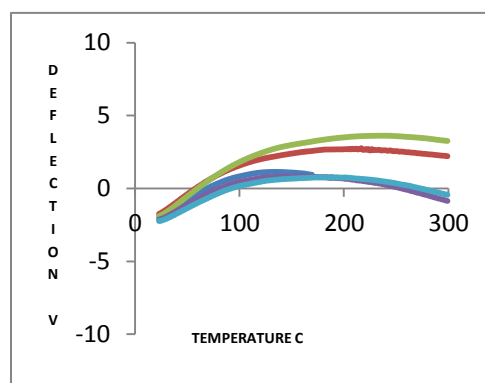
Formulation	Compact	Components identified (number of sites; maximum = 5)			
		α -LM	MS	MCC	PGS
49.5% α -LM / 49.5% PGS / 1% MS	A i	1	0	X	4
	A ii	4	0	X	1
49.5% α -LM / 49.5% MCC / 1% MS	B i	2	0	3	X
	B ii	2	0	3	X
49.5% MCC / 49.5% PGS / 1% MS	C i	X	0	4	1
	C ii	X	0	5	0
33.3% α -LM /	D i	1	X	1	3
33.3% PGS /	D ii	1	X	2	2
33.3% MCC					

Table 5.2: A summary of the most probable components identified from the nano-TA scans of the 3-excipient compacts shown in Figure 5.6. The number indicates the number of scans assigned to a particular component. X indicates that this component is not present in the compact.

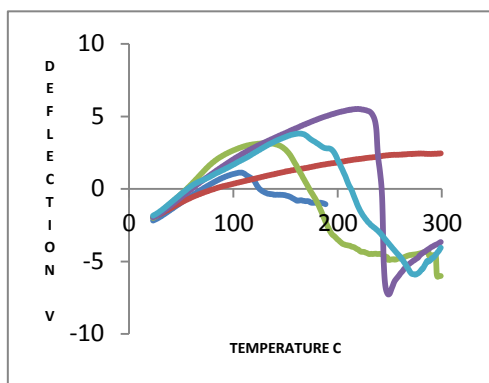
Ai)



Aii)



Bi)



Bii)

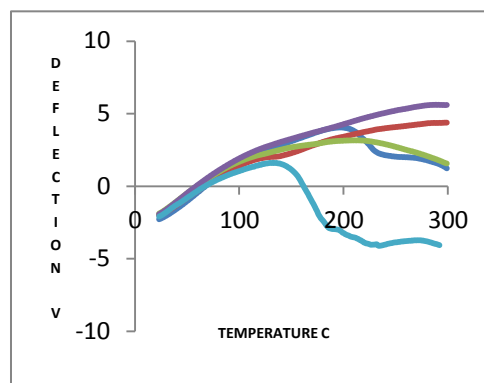


Figure 5.7: Nano-TA results for the 4-excipient compacts, using a nano probe. A) 33% α -LM / 33% PGS / 33% MCC / 1% MS. B) 25% α -LM / 25% PGS / 25% MCC / 25% MS. Position on the compact is given by i) centre, ii) outside. Five readings were taken at each position: dark blue - site 1, red - site 2, green - site 3, purple - site 4, light blue - site 5.

Formulation	Compact	Components identified (number of sites; maximum = 5)			
		α -LM	MS	MCC	PGS
33% α -LM / 33% PGS / 33% MCC/ 1% MS	A i	2	1	0	2
	A ii	0	0	0	5
25% α -LM / 25% PGS / 25% MCC / 25% MS	B i	2	1	1	1
	B ii	1	0	2	2

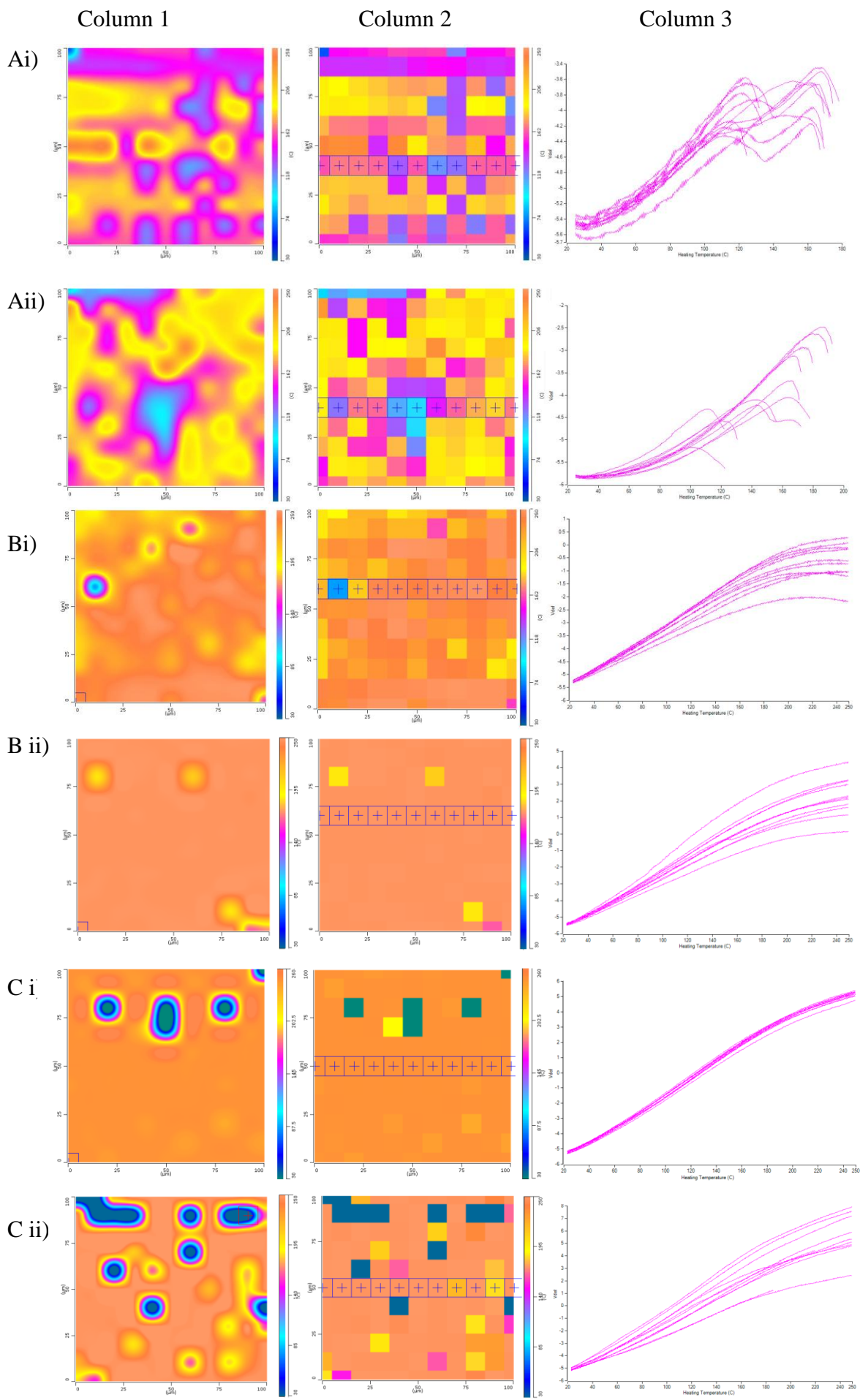
Table 5.3: A summary of the most probable components identified from the nano-TA scans of the 4-excipient compacts shown in Figure 5.7. The number indicates the number of scans assigned to a particular component. X indicates that this component is not present in the compact.

5.3.1.3 TTM

TTM was performed on the same mixed compacts as AFM and nano-TA. The results are shown in Figures 5.8, 5.9 and 5.10 for the two-, three- and four- excipient compacts, respectively. Column 1 is the interpolated (smoothed) map, Column 2 is the discrete map, and Column 3 shows the individual nano-thermal results taken at the crossed points (+) on the discrete map - a line through the centre of the imaged area. The colour is automatically allocated by the software depending on the temperature of the thermal event detected. The dark blue colouration is thought to be detection noise due to vibration in the laboratory or inadequate contact of the probe with the compact's surface, as it represents a very low temperature of transition, below that identified for any of the compounds studied here.

In the binary compacts of α -LM and MS, two thermal events are detected, assigned to MS (circa 100°C) and α -LM (higher temperatures). A range of colours was seen to represent the α -LM. None of the nano-TA results showed above suggested the presence of MS in these compacts, but with TTM 121 readings are performed in each 100 μm x 100 μm region, rather than 5 readings over a 50 μm x 50 μm region in nano-TA, so the likelihood of detecting a low concentration component is increased. However, MS was not detected in the binary compacts with either PGS or MCC when it was present only at 1 %. The images generated for the compacts of either PGS or MCC with 1% MS were more consistent than those for α -LM, probably reflecting the lack of thermal response of these materials. These two materials were assigned the same colour (yellow) by the software reflecting the fact that neither had shown a definite thermal event by the time the experiment was terminated. In the binary compacts of α -LM with either MCC or PGS, where each component was present at 50 %, α -LM was clearly identified by the pink colouration. However, the TTM technique could not easily distinguish between PGS and MCC in the binary compacts consisting of these two materials.

As before, α -LM was most easily identified in the three-excipient and four-excipient compacts and, again, the technique had difficulty differentiating between PGS and MCC. MS was most easily identified when it was present at 25 % loading. Several scans for the three-excipient compacts gave profiles which could be misleading and require interpretation by the operator in light of the overall composition of the compact. The colour was assigned automatically by the software based on a presumed transition.

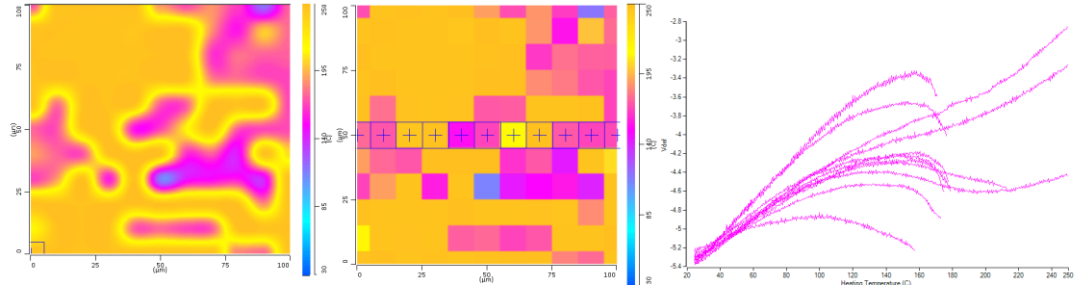


Column 1

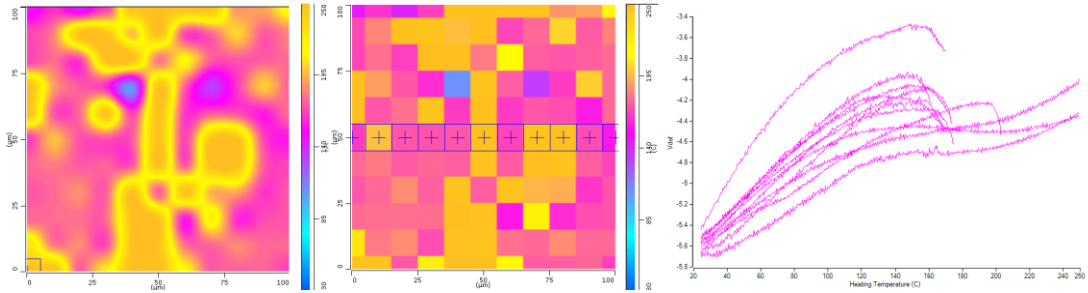
Column 2

Column 3

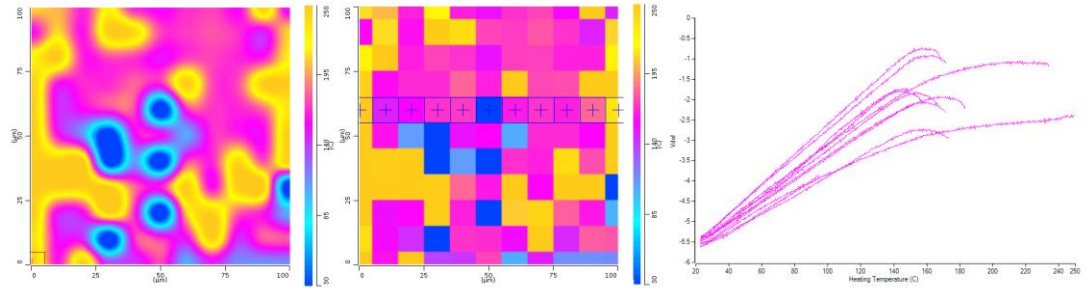
Di)



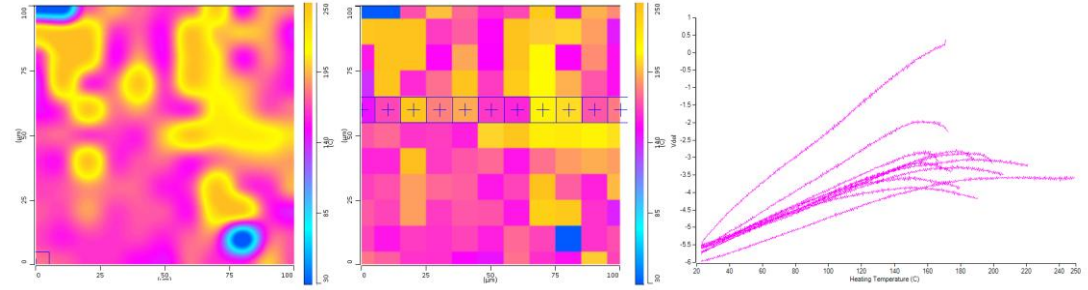
Dii)



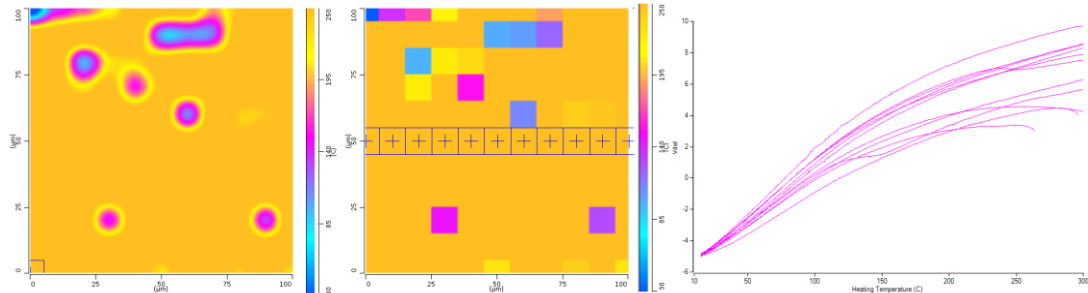
Ei)



Eii)



Fi) i



Fii)

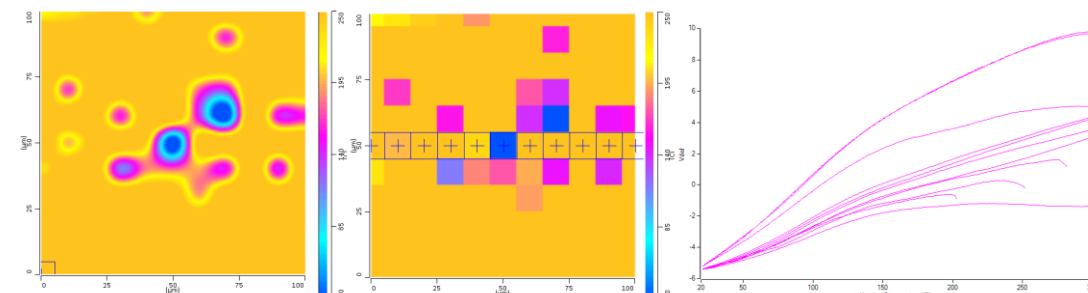
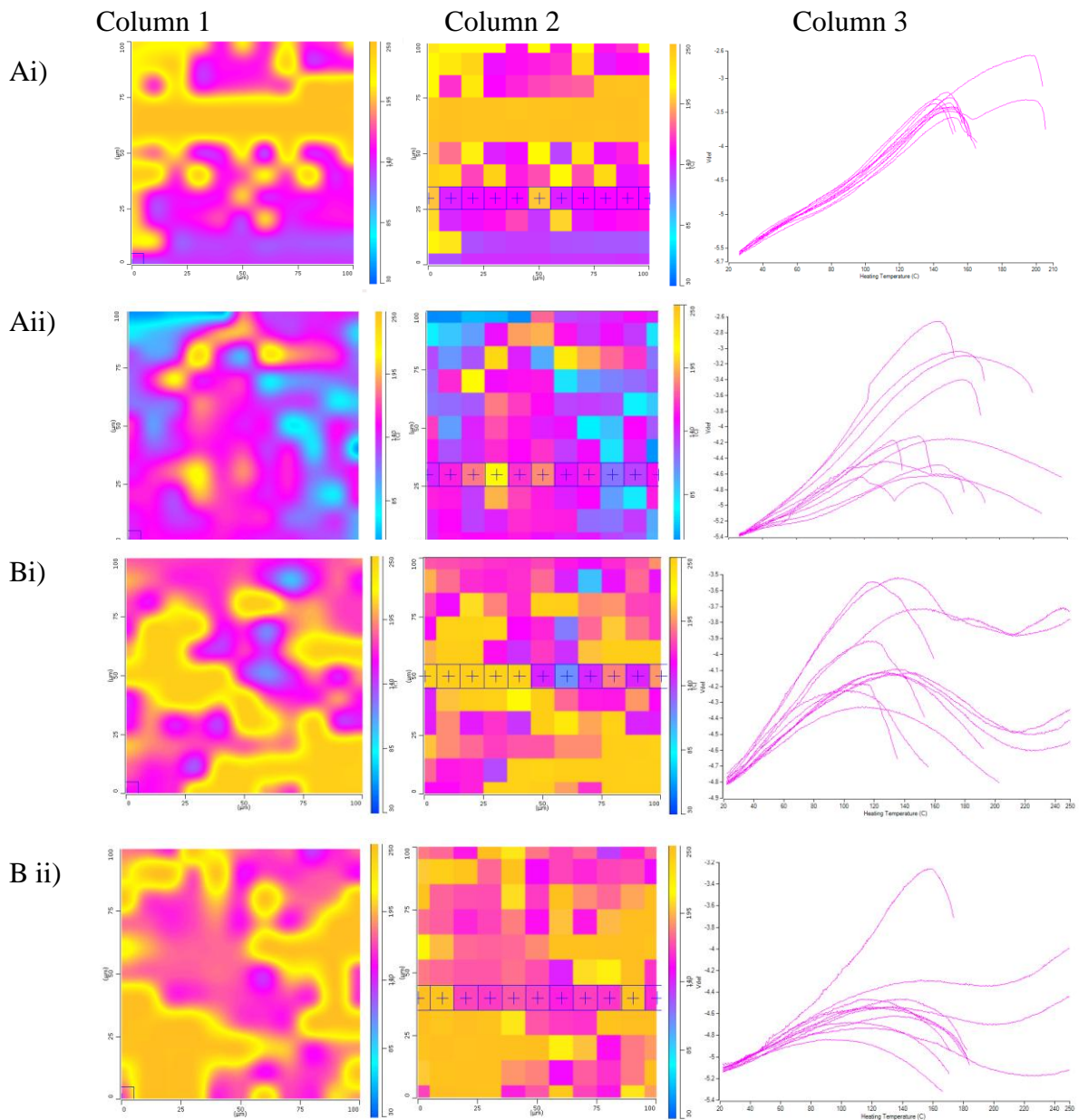


Figure 5.8: TTM maps for 2-excipient compacts, with representative colours. A) 99% α -LM (red / yellow / pink) / 1% MS (blue / purple). B) 99% MCC (orange / yellow) / 1% MS (not detected). C) 99% PGS (orange / yellow) / 1 % MS (not detected). D) 50% α -LM (pink) / 50% MCC (yellow). E) 50% α -LM (pink) / 50% PGS (yellow). F) 50% MCC (yellow) / 50 % PGS (yellow / bright yellow / pink). The dark blue colour is noise. Position on the compact is given by i) centre, ii) outside. Column 1 is the interpolated (smoothed) map, Column 2 is the discrete map, and Column 3 shows the individual nano-thermal results taken at the crossed points (+) on the discrete map.



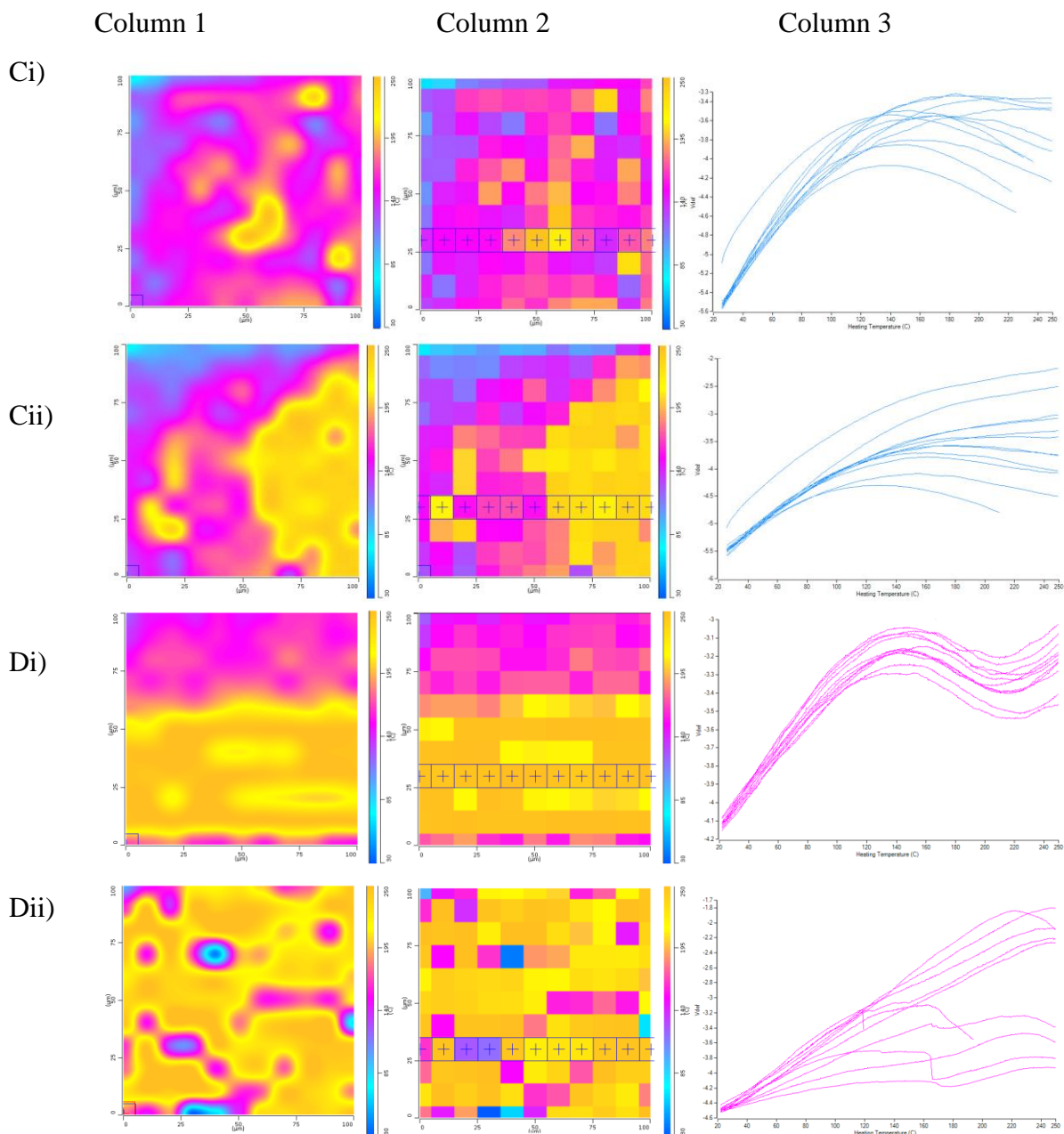


Figure 5.9: TTM maps for 3-*excipient* compacts, with representative colours. A) 49.5% α -LM (pink / purple) /49.5% PGS (yellow / orange) /1% MS (blue). B) 49.5% α -LM (pink) /49.5% MCC (yellow) /1% MS (blue). C) 49.5% MCC (yellow) /49.5 % PGS (pink /yellow) /1% MS (blue). D) 33.3% α -LM (purple) /33.3% PGS (pink /yellow) / 33.3% MCC (yellow). The dark blue colour is noise. Position on the compact is given by i) centre, ii) outside. Column 1 is the interpolated (smoothed) map, Column 2 is the discrete map, and Column 3 shows the individual nano-thermal results taken at the crossed points (+) on the discrete map.

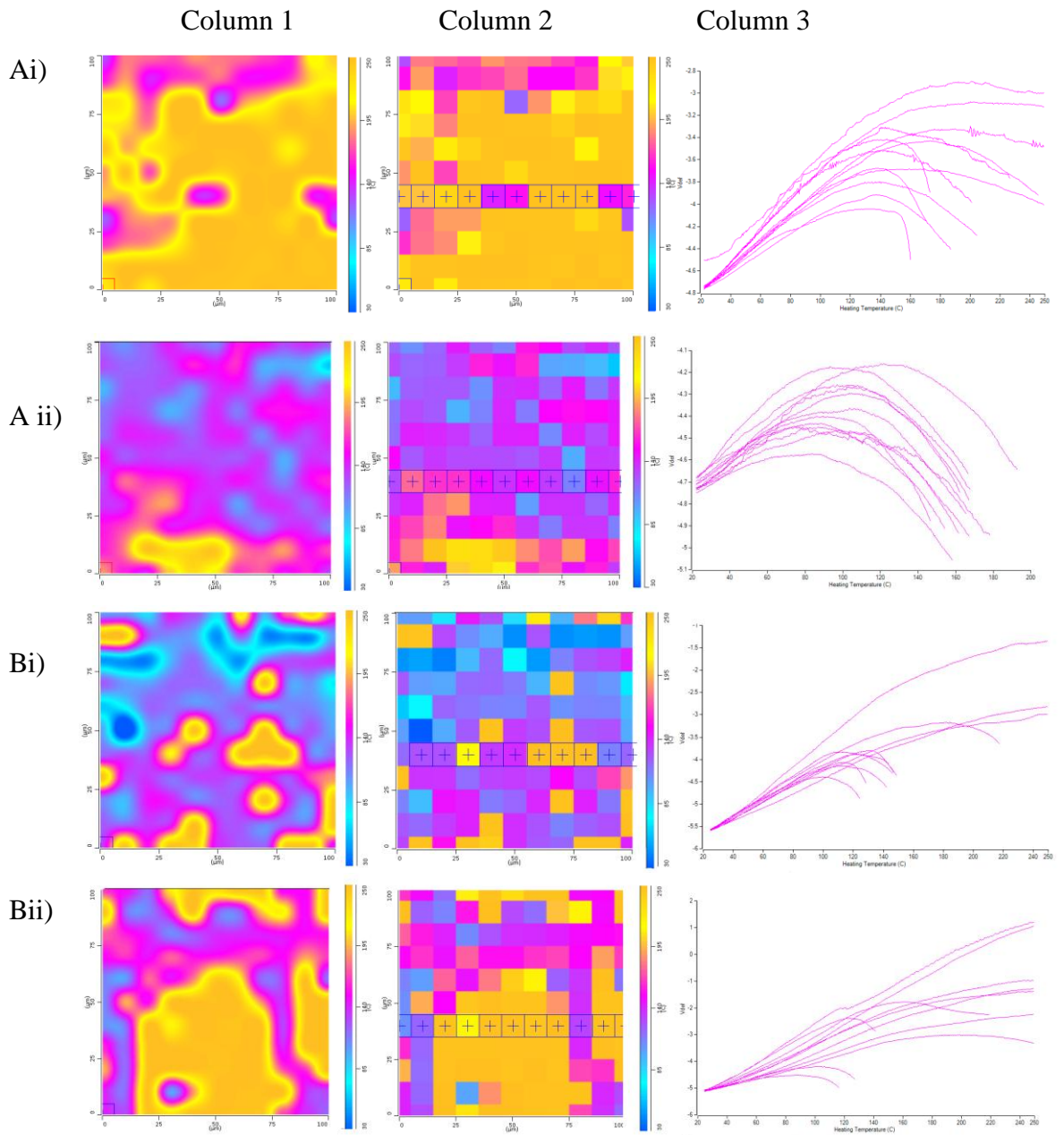


Figure 5.10: TTM maps for 4-excipt compact, with representative colours. A) 33% α -LM (pink / purple) / 33% PGS (yellow / orange) / 33% MCC (yellow / orange) / 1% MS (blue). B) 25% α -LM (pink / purple) / 25% PGS (yellow / orange) / 25% MCC (orange) / 25% MS (blue). The dark blue colour is noise. Position on the compact is given by i) centre, ii) outside. Column 1 is the interpolated (smoothed) map, Column 2 is the discrete map, and Column 3 shows the individual nano-thermal results taken at the crossed points (+) on the discrete map.

5.3.1.4 General discussion for the multi-component excipient compacts

The results shown here demonstrate that it is feasible to detect different components on the surface of a multi-component compact by their thermal behaviour. However, there are a few potential issues, experimentally.

All the AFM scans were performed in contact mode at room temperature to examine the region of the surface over which the nano-TA was performed. In terms of information gained about the distribution of the components these scans were poor, but the main reason for performing the scans was to aid the interpretation of the nano-TA results if any unusual or anomalous results were observed. Such anomalies may arise if the surface is very rough and the probe lands in a large valley or top of a large mound. A more accurate and detailed determination of the distribution of components may be obtained by using different AFM modes, e.g. tapping mode with a heated probe just below the melting point of a component. As the components have a different thermal profile, the forces required to lift the probe from the surface will be different and should allow differentiation between components. This approach has previously been used (Dai et al (2009)), but was not explored in detail here because the surface of these compacts is too rough. Additionally, heating the compact's surface, as required in this technique, would then affect the nano-TA results if the same locations were studied, as is required. Performing the nano-TA before obtaining AFM scans would damage the surface also and render the AFM scans invalid.

The nano-TA results were encouraging, in that it was possible to assign each scan to a particular component and to demonstrate that the components can be distinguished from each other. However, this assignment was made manually with knowledge of the formulation of the compacts and in some cases the differences in the scans were subtle, such as MCC and PGS. The area being scanned in these studies is still a statistically small region of the total tablet surface, so this must be kept in mind when interpreting the data and is a possible disadvantage of the technique.

TTM is effectively an automated version of nano-TA, taking multiple scans over a pre-defined area with accurate spacing between the readings. The equipment software then allocates a colour to each reading, depending on the temperature of the thermal event observed, i.e. at what temperature the probe moved. This means that one component may be represented by several colours depending on the precise temperature of transition

detected by the equipment and the colour-temperature scale used, as was seen most clearly here for α -LM. It then follows that if two components show thermal events in the same temperature range, they will be allocated a similar colour by the software, which may then lead to difficulties in interpretation. The colour-temperature scale used by the software is automatically selected for each map to maximise visually the differences between pixels, so this may be misleading when comparing maps. It is recommended to ensure that all maps use the same colour-temperature scale. It was seen in Chapters 3 and 4 that many factors affect TTM imaging, such as the topography of the sample, lab noise etc, so not every reading is a "true" reading and some evaluation of the images is required.

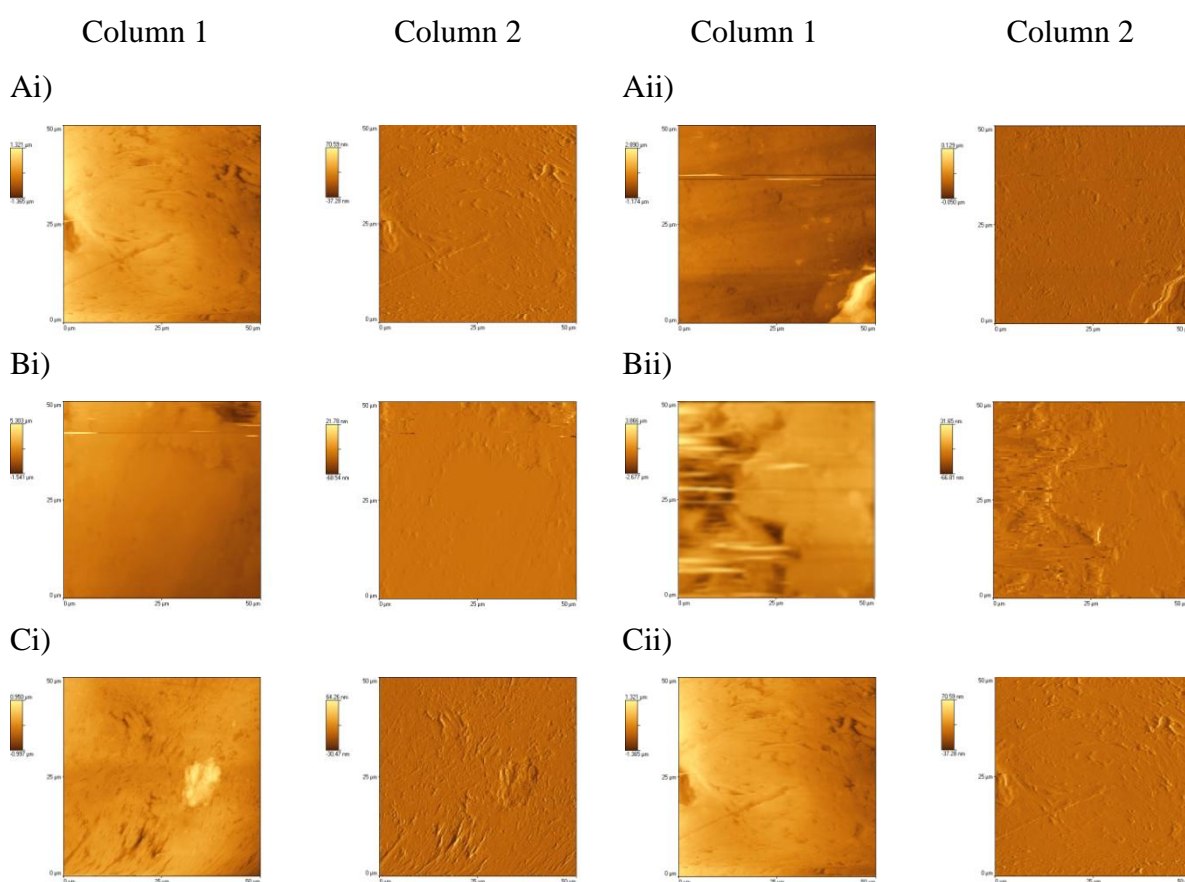
A second serious issue arises when the software processes the pixellated images into smoothed images. If neighbouring pixels are due to different components and therefore show different colours, the software blends the interface by travelling through the colour-temperature scale, resulting in an intermediate colour being allocated to the interface. This gives the impression that there are three components in this area rather than two, as is shown by the pixellated map, and that the intermediate component always has a transition temperature between those of the other two components. Use of the pixellated images is therefore recommended to avoid this issue.

5.3.2 Multi-component compacts containing caffeine

5.3.2.1 AFM

Compacts were made of all combinations of caffeine (Form II, used as received) and one, two, three and four excipients. Representative AFM scans are shown in Figures 5.11, 5.12, 5.13 and 5.14 for the two-, three- four- and five- component compacts, respectively. As discussed earlier for the mixed excipient compacts, it is difficult to identify materials in mixed systems from the AFM images alone. PGS has the most distinctive AFM profile and could be identified in most of the mixed systems where it was present. However, topographical variations do not necessarily mean the presence of a different material and this needs to be confirmed by the nano-TA analysis. For example, in Figure 5.11 Bii there is a slightly rougher region down the left hand side of the AFM image which could suggest the presence of a different material to that on the right hand side. However, the nano-TA scan for that area (Figure 5.15 Bii) suggests otherwise. Two of the five sites were in the left hand column, but these gave profiles belonging to two different materials. Hence, the

rough region in the AFM image represents a local difference in the compact's topography rather than the distribution of components across its surface. Similarly, in Figure 5.11 Ci a raised area is seen, which may be a speck of powder that has adhered to the surface. Unfortunately, nano-TA could not be performed in this area as making and maintaining contact between the probe and the surface is challenging on such a raised point. Generally, the analysis of the caffeine-based compacts is the same as for the excipient-only compacts: as the complexity of the formulation increases, it becomes more difficult to identify the individual components by AFM imaging alone. The concentration of the component in the formulation will also play a part in the probability of its detection and any differences in the images generated at the centre and the outside of the compact probably reflect the local distribution of the component materials.



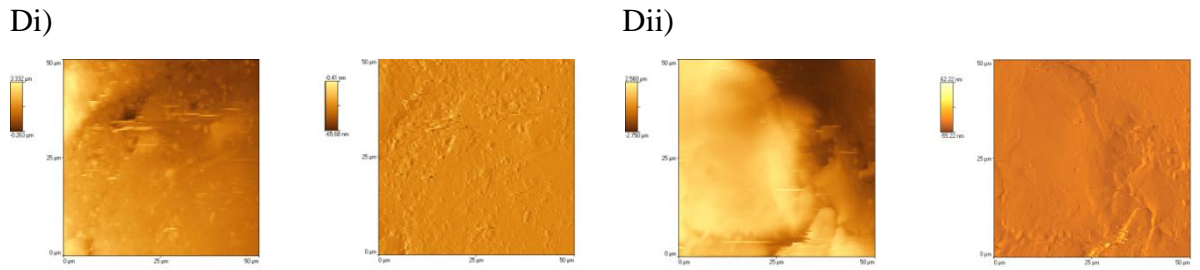
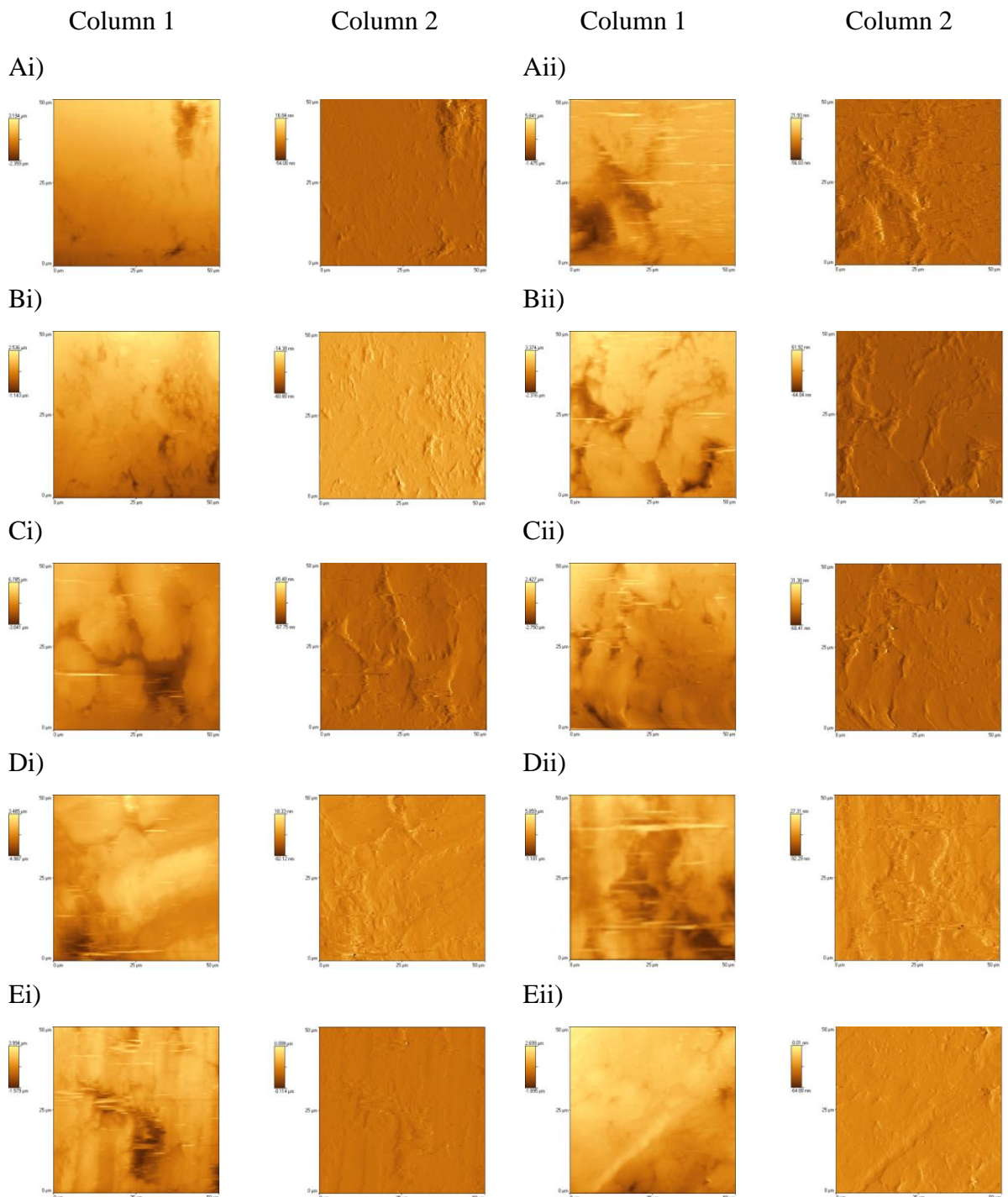


Figure 5.11: AFM images of the 2-component compacts based on caffeine, using a nano probe. A) 99% CAF / 1% MS. B) 50% CAF / 50% α -LM. C) 50% CAF / 50% MCC. D) 50% CAF / 50% PGS. Position on the compact is given by i) centre, ii) outside. Column 1 - height, Column 2 - deflection.



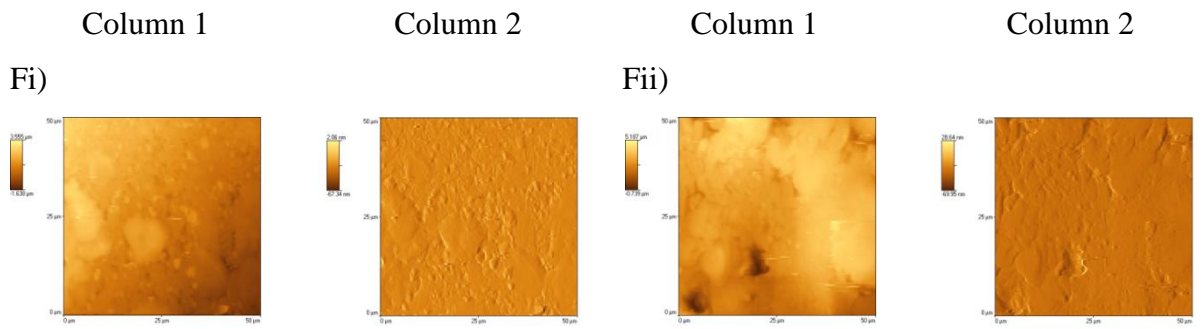
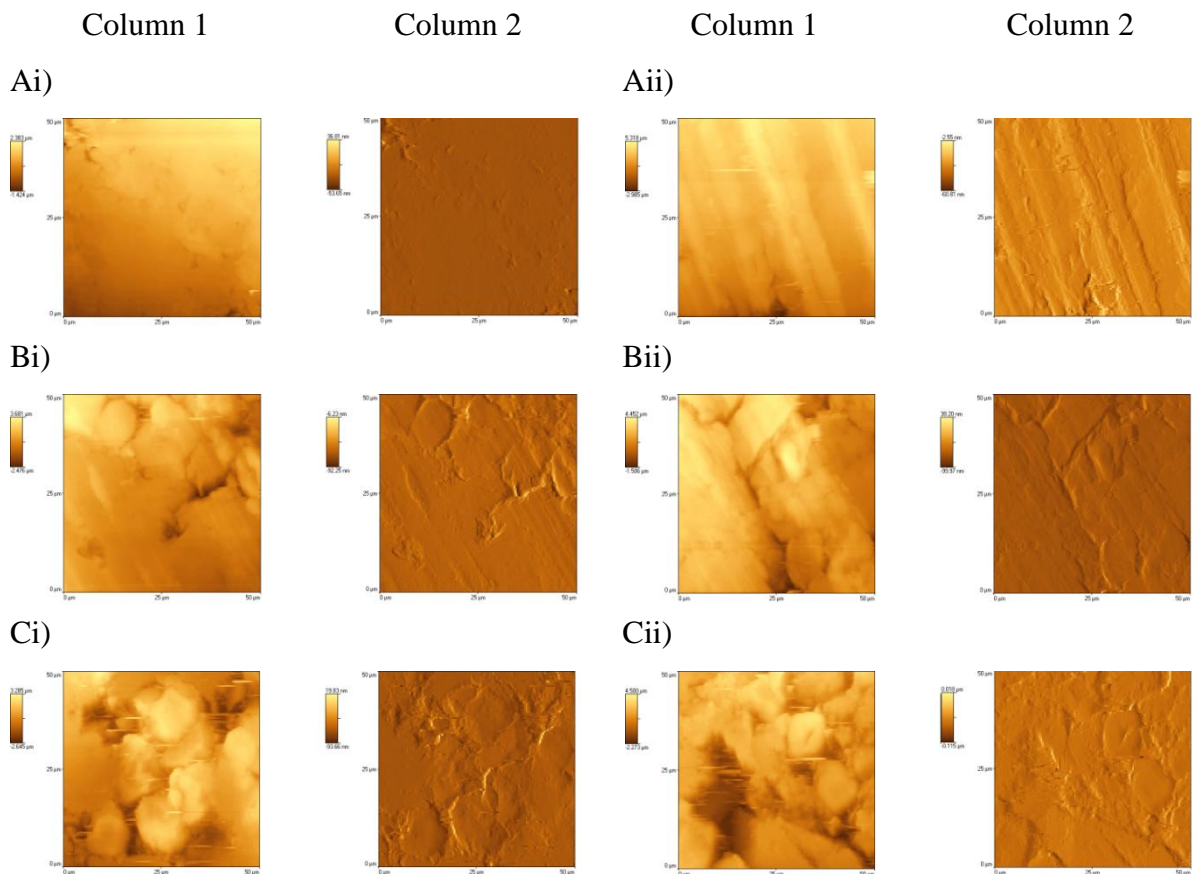


Figure 5.12: AFM images of the 3-component compacts based on caffeine, using a nano probe. A) 49.5% CAF / 49.5% α -LM / 1% MS. B) 49.5% CAF / 49.5% MCC / 1% MS. C) 49.5% CAF / 49.5% PGS / 1% MS. D) 33.3% CAF / 33.3% α -LM / 33.3% PGS. E) 33.3% CAF / 33.3% α -LM / 33.3% MCC. F) 33.3% CAF / 33.3% MCC / 33.3% PGS. Position on the compact is given by i) centre, ii) outside. Column 1 - height, Column 2 - deflection.



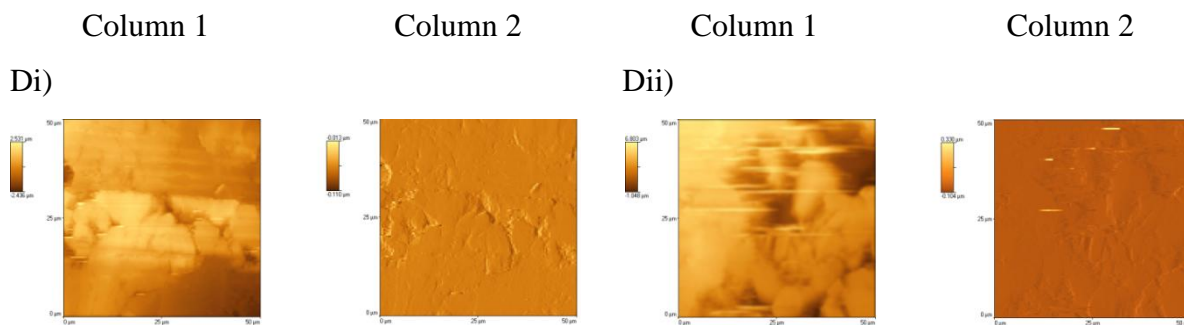


Figure 5.13: AFM images of the 4-component compacts based on caffeine, using a nano probe. A) 33% CAF / 33% α -LM / 33% MCC / 1% MS. B) 33% CAF / 33% MCC / 33% PGS / 1% MS. C) 33% CAF / 33% α -LM / 33% PGS / 1% MS. D) 25% CAF / 25% α -LM / 25% PGS / 25% MCC. Position on the compact is given by i) centre, ii) outside. Column 1 - height, Column 2 - deflection.

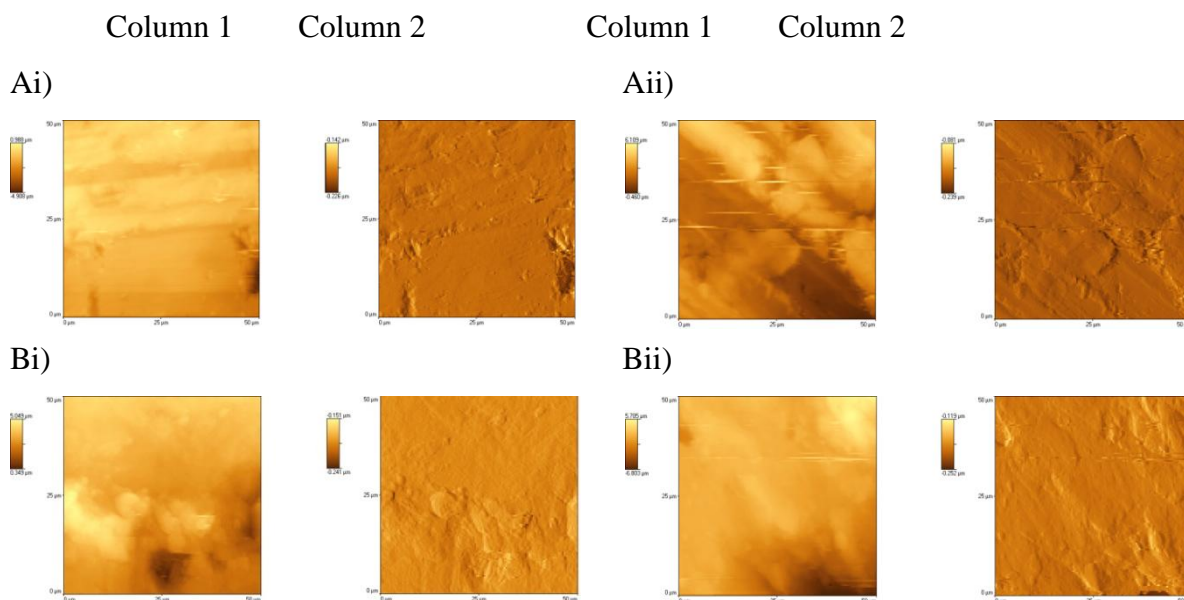


Figure 5.14: AFM images of the 5-component compacts based on caffeine, using a nano probe. A) 24.75% CAF / 24.75% α -LM / 24.75% MCC / 24.75% PGS / 1% MS. B) 20% CAF / 20% α -LM / 20% MCC / 20% PGS / 20% MS. Position on the compact is given by i) centre, ii) outside. Column 1 - height, Column 2 - deflection.

5.3.2.2. Nano-TA

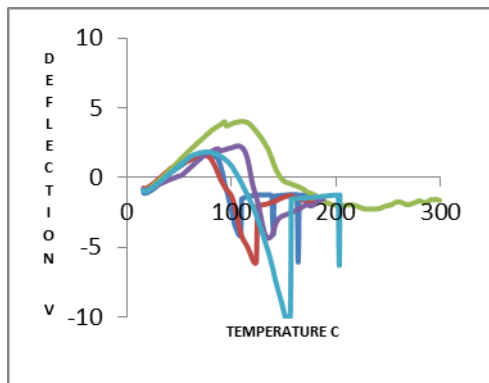
Nano-TA was performed on each of the multi-component compacts based on caffeine after the AFM images were generated. Representative scans are shown in Figures 5.15, 5.16, 5.17 and 5.18 for the two-, three-, four- and five- component compacts, respectively. Comparison of these scans with those of the compacts of the individual components shown in Chapters 3 and 4 allowed identification of the most likely component(s) present. This is summarised in Tables 5.4, 5.5, 5.6 and 5.7, respectively. All five components could be identified by their thermal profiles, although MS was identified the least frequently, reflecting its low concentration in the compacts.

The thermal event attributed to caffeine in the mixed compacts occurs at a slightly lower temperature than previously seen when examining caffeine as a single component. This effect was consistent and allowed identification of caffeine in the samples. As discussed in Chapter 4, the nano-TA thermal event for caffeine occurs at a lower temperature than would be expected from the DSC melting point, and it is possible that this is accentuated in mixed samples.

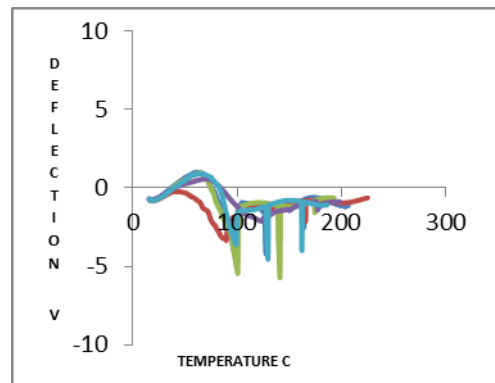
Several of the nano-TA traces show evidence of two transitions. For example, in Figure 5.15 Dii the light blue and dark blue lines (representing two of the five nano-TA results taken at different sites) appear to show a dip at circa 100°C, then continue to show a response at higher temperatures attributable to PGS. This could possibly be explained by the presence of a very thin layer of caffeine on the surface of a region of PGS. The probe would penetrate through the caffeine layer at the lower temperature but quickly meet the underlying PGS layer which would stop the probe penetrating any further. Hence, an endpoint would not be registered and the experiment would continue until a "true" endpoint had been reached.

A similar two-transition process is seen in Figure 5.17 Ci (light blue line), where a small thermal event is detected in the caffeine temperature range and then a larger response in the α -LM region, suggesting that in this case there is a thin layer of caffeine on top of the bulk α -LM region. In the five-component compacts, there was evidence of a thin layer of MS on top of a bulk region of α -LM and a thin layer of caffeine on a bulk region of MS (Figure 5.18 Bi dark blue and red lines, respectively).

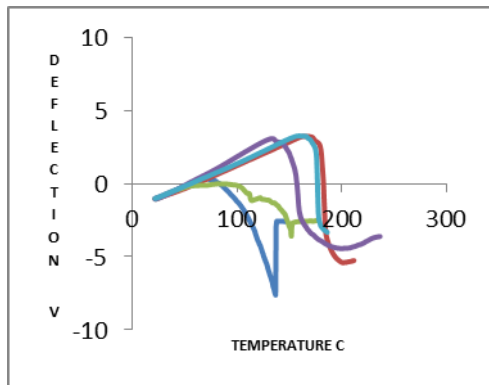
Ai)



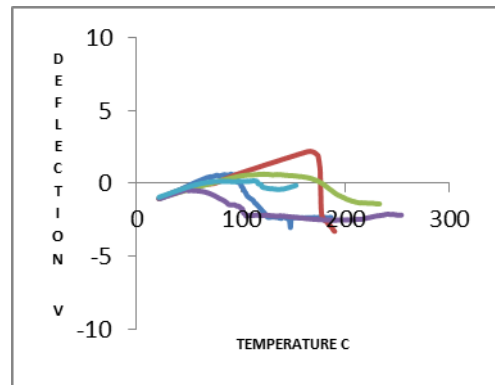
Aii)



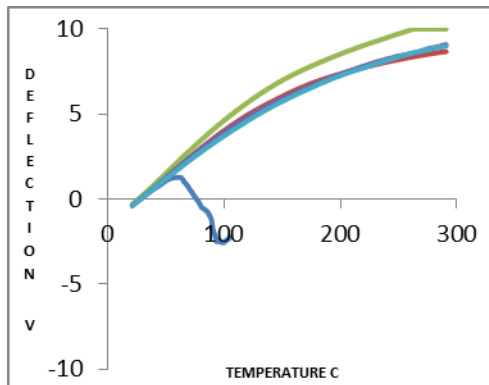
Bi)



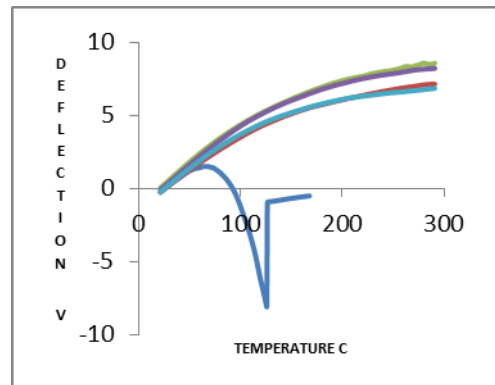
Bii)



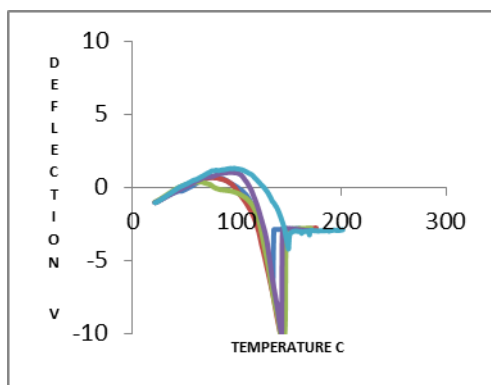
Ci)



Cii)



Di)



Dii)

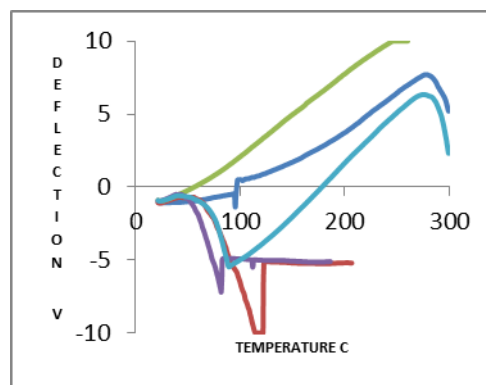


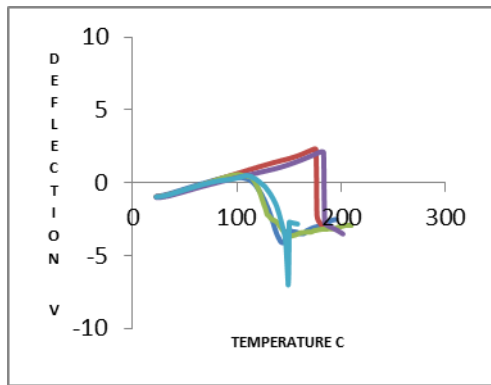
Figure 5.15: Nano-TA results for the 2-component compacts based on caffeine, using a nano probe. A) 99% CAF / 1% MS. B) 50% CAF / 50% α -LM. C) 50% CAF / 50% MCC. D) 50% CAF / 50% PGS. Position on the compact is given by i) centre, ii) outside. Five readings were taken at each position: dark blue - site 1, red - site 2, green - site 3, purple - site 4, light blue - site 5.

Formulation	Compact	Components identified (number of sites; maximum = 5)				
		CAF	α -LM	MS	MCC	PGS
99% CAF / 1% MS	A i	4	X	1	X	X
	A ii	5	X	0	X	X
50% CAF / 50% α -LM	B i	2	3	X	X	X
	B ii	3	2	X	X	X
50% CAF / 50% MCC	C i	1	X	X	4	X
	C ii	1	X	X	4	X
50% CAF / 50% PGS	D i	5	X	X	X	0
	D ii	2	X	X	X	1 and 2*

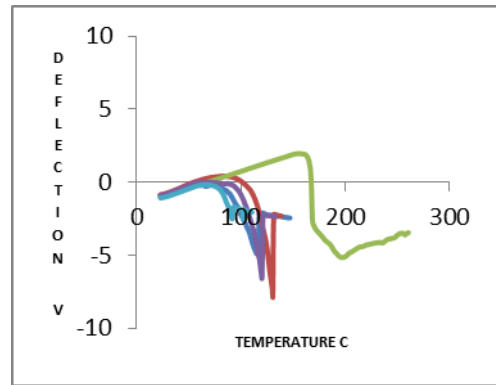
Table 5.4: A summary of the most probable components identified from the nano-TA scans of the 2-component compacts based on caffeine shown in Figure 5.15. The number indicates the number of scans assigned to a particular component. X indicates that this component is not present in the compact.

* These two results suggest a thin layer of caffeine on top of a bulk layer of PGS.

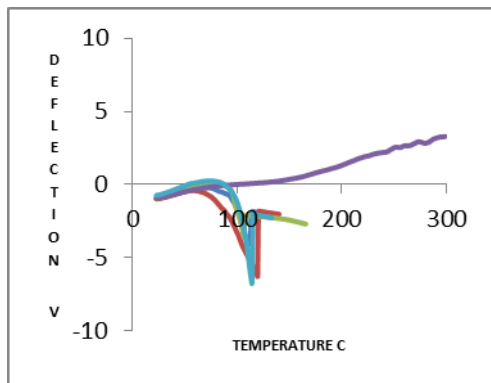
Ai)



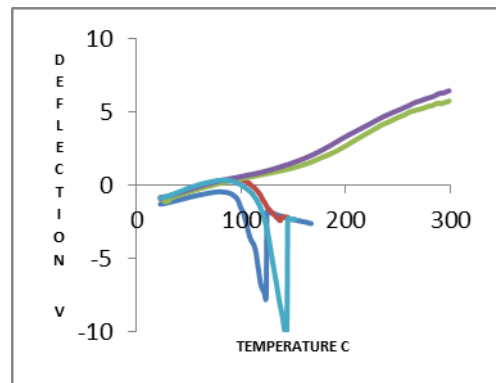
Aii)



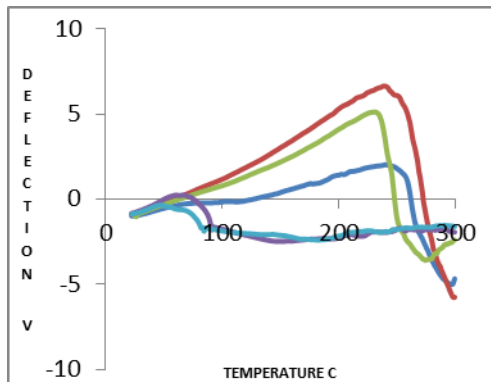
Bi)



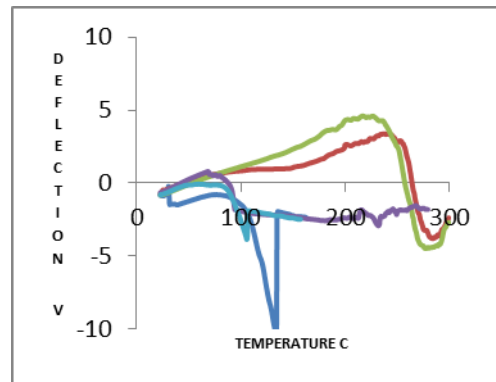
Bii)



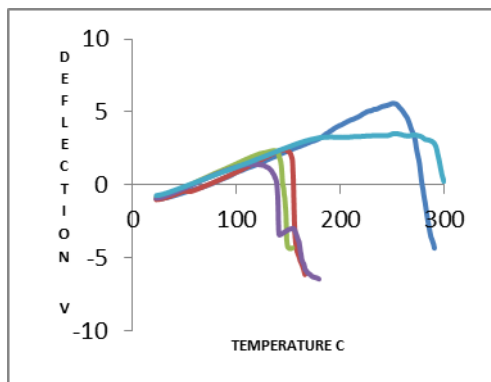
Ci)



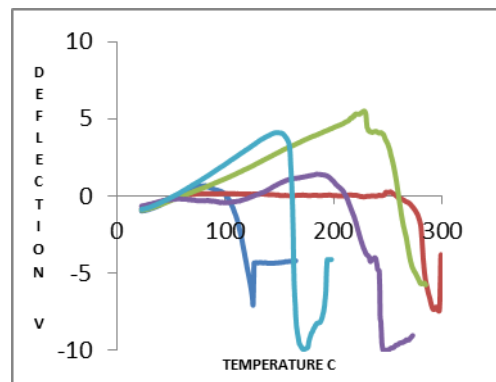
Cii)



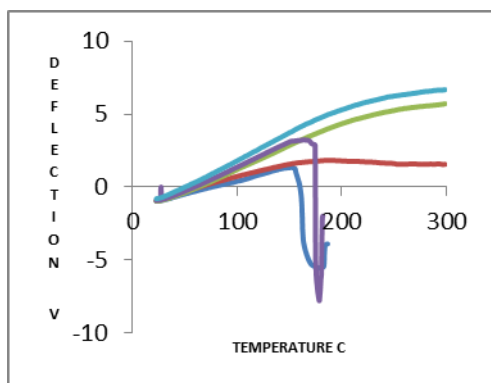
Di)



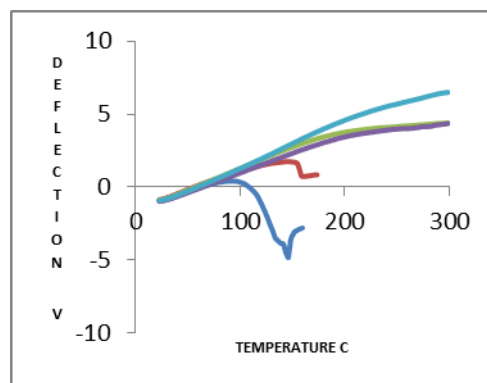
Dii)



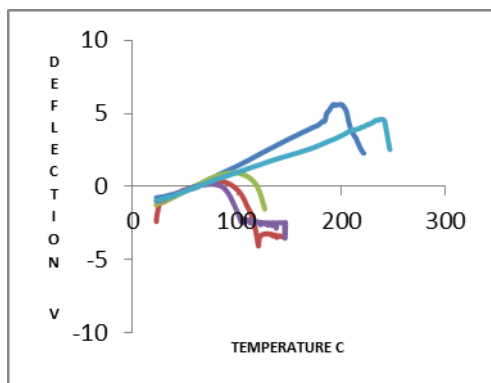
Ei)



Eii)



Fi)



Fii)

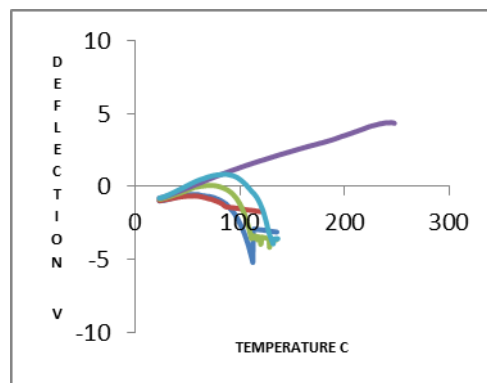
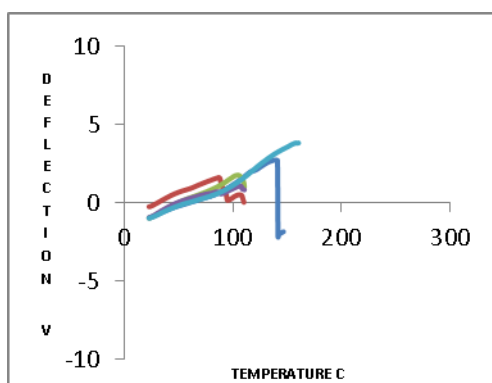


Figure 5.16: Nano-TA results for the 3-component compacts based on caffeine, using a nano probe. A) 49.5% CAF / 49.5% α -LM / 1% MS. B) 49.5% CAF / 49.5% MCC / 1% MS. C) 49.5% CAF / 49.5% PGS / 1% MS. D) 33.3% CAF / 33.3% α -LM / 33.3% PGS. E) 33.3% CAF / 33.3% α -LM / 33.3% MCC. F) 33.3% CAF / 33.3% MCC / 33.3% PGS. Position on the compact is given by i) centre, ii) outside. Five readings were taken at each position: dark blue - site 1, red - site 2, green - site 3, purple - site 4, light blue - site 5.

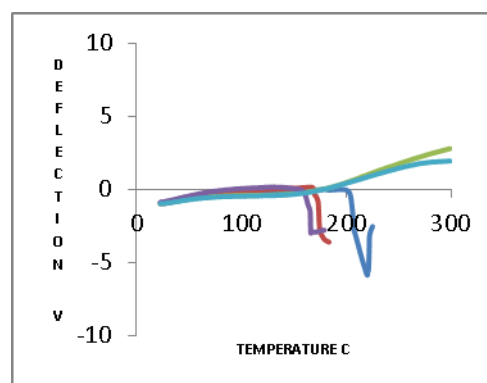
Formulation	Compact	Components identified (number of sites; maximum = 5)				
		CAF	α -LM	MS	MCC	PGS
49.5% CAF / 49.5% α -LM / 1% MS	A i	3	2	0	X	X
	A ii	4	1	0	X	X
49.5% CAF / 49.5% MCC / 1% MS	B i	4	X	0	1	X
	B ii	3	X	0	2	X
49.5% CAF / 49.5% PGS 1% MS	C i	2	X	0	X	3
	C ii	3	X	0	X	2
33.3% CAF / 33.3% α -LM / 33.3% PGS	D i	0	3	X	X	2
	D ii	1	2	X	X	2
33.3% CAF / 33.3% α -LM / 33.3% MCC	Ei	0	2	X	3	X
	Eii	1	1	X	3	X
33.3% CAF / 33.3% MCC / 33.3% PGS	Fi	3	X	X	2	0
	Fii	4	X	X	0	1

Table 5.5: A summary of the most probable components identified from the nano-TA scans of the 3-component compacts based on caffeine shown in Figure 5.16. The number indicates the number of scans assigned to a particular component. X indicates that this component is not present in the compact.

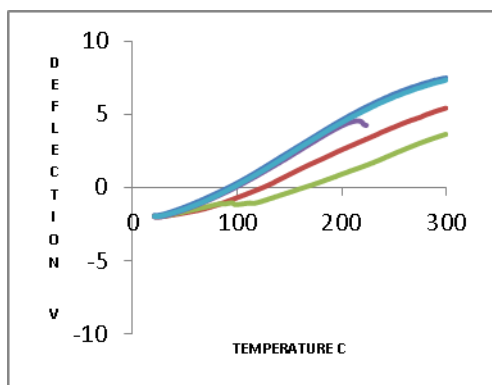
Ai)



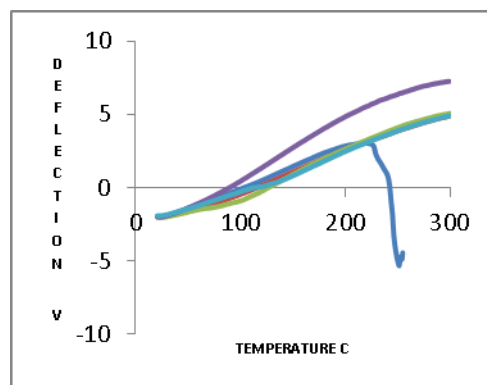
Aii)



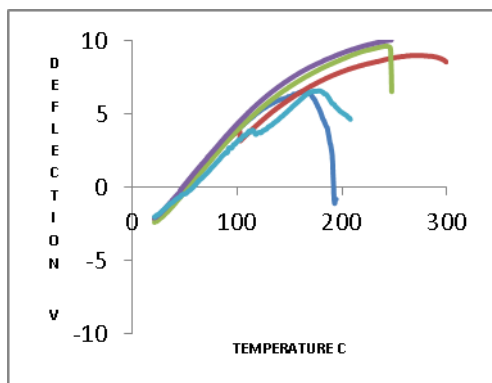
Bi)



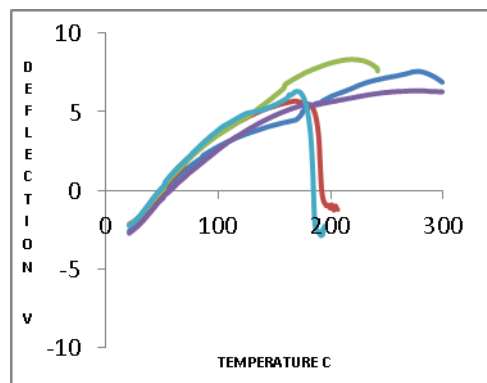
Bii)



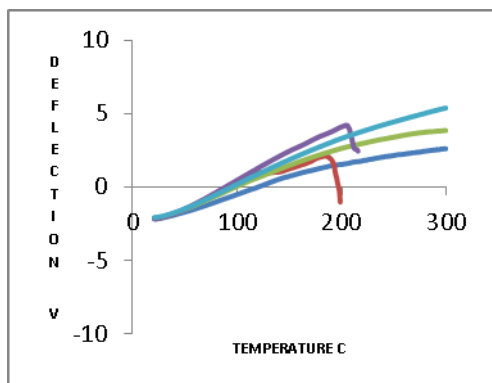
Ci)



Cii)



Di)



Dii)

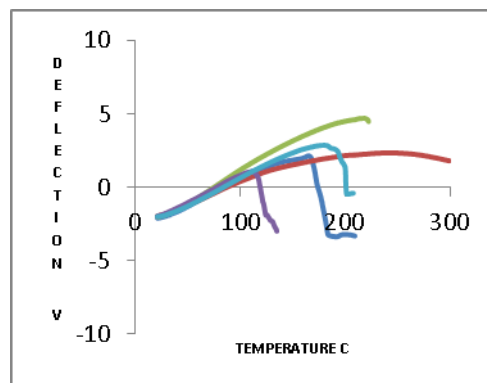


Figure 5.17: Nano-TA results for the 4-component compacts based on caffeine, using a nano probe. A) 33% CAF / 33% α -LM / 33% MCC / 1% MS. B) 33% CAF / 33% MCC / 33% PGS / 1% MS. C) 33% CAF / 33% α -LM / 33% PGS / 1% MS. D) 25% CAF / 25% α -LM / 25% PGS / 25% MCC. Position on the compact is given by i) centre, ii) outside. Five readings were taken at each position: dark blue - site 1, red - site 2, green - site 3, purple - site 4, light blue - site 5.

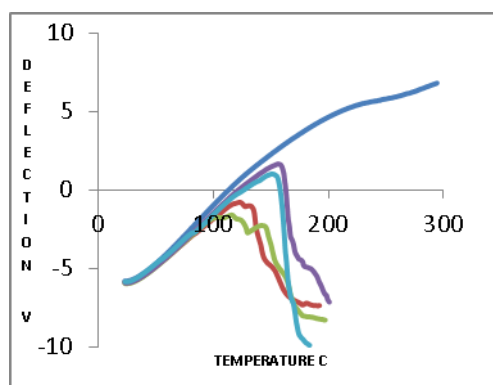
Formulation	Compact	Components identified (number of sites; maximum = 5)				
		CAF	α -LM	MS	MCC	PGS
33% CAF / 33% α -LM / 33% MCC / 1% MS	A i	3	1	0	1	X
	A ii	0	3	0	2	X
33% CAF / 33% MCC / 33% PGS / 1% MS	B i	0	X	0	4	1
	B ii	0	X	0	4	1
33% CAF / 33% α -LM / 33% PGS / 1% MS	C i	0	1 + 1*	0	X	3
	C ii	0	2	0	X	2 + 1**
25% CAF / 25% α -LM / 25% PGS / 25% MCC	D i	0	2	X	3	0
	D ii	1	2	X	1	1

Table 5.6: A summary of the most probable components identified from the nano-TA scans of the 4-component compacts based on caffeine shown in Figure 5.17. The number indicates the number of scans assigned to a particular component. X indicates that this component is not present in the compact.

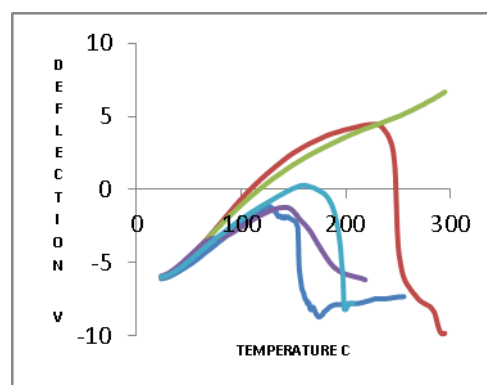
* This result suggests a thin layer of caffeine on top of a bulk layer of α -LM.

** This result suggests a thin layer of α -LM on top of a bulk layer of PGS.

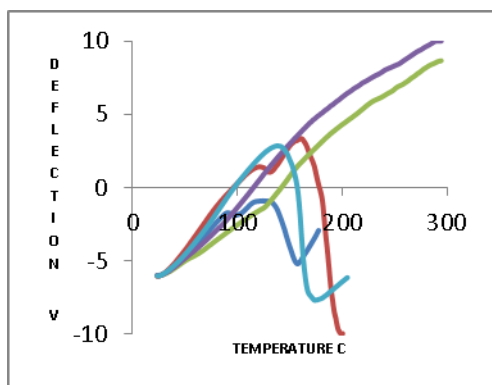
Ai)



Aii)



Bi)



Bii)

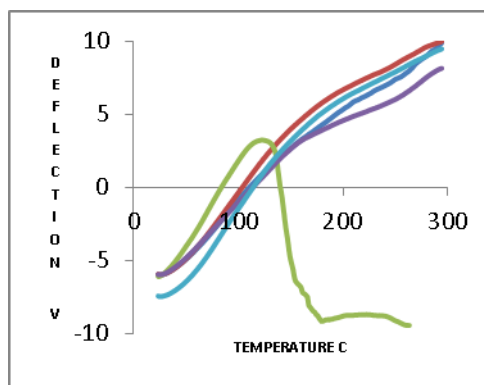


Figure 5.18: Nano-TA results for the 5-component compacts based on caffeine, using a nano probe. A) 24.75% CAF / 24.75% α -LM / 24.75% MCC / 24.75% PGS / 1% MS. B) 20% CAF / 20% α -LM / 20% MCC / 20% PGS / 20% MS. Position on the compact is given by i) centre, ii) outside. Five readings were taken at each position: dark blue - site 1, red - site 2, green - site 3, purple - site 4, light blue - site 5.

Formulation	Compact	Components identified (number of sites; maximum = 5)				
		CAF	α -LM	MS	MCC	PGS
24.75% CAF / 24.75% α -LM / 24.75% MCC / 24.75% PGS / 1% MS	A i	2	2	0	1	0
	A ii	2	1	0	1	1
20% CAF / 20% α -LM / 20% MCC / 20% PGS / 20% MS	B i	0	1 + 1*	1 **	0	2
	B ii	0	1	0	0	4

Table 5.7: A summary of the most probable components identified from the nano-TA scans of the 5-component compacts based on caffeine shown in Figure 5.18. The number indicates the number of scans assigned to a particular component. X indicates that this component is not present in the compact.

* This result suggests a thin layer of MS on top of a bulk layer of α -LM.

** This result suggests a thin layer of caffeine on top of a bulk layer of MS.

5.3.2.3 TTM

TTM was performed on the same compacts as AFM and nano-TA. The results are shown in Figures 5.19, 5.20, 5.21 and 5.22 for the two-, three-, four- and five- component compacts, respectively. The issues with interpretation discussed previously for the excipient compacts apply equally here.

The binary compacts with caffeine and MS showed some results at temperatures above what would be expected for either compound (Figure 5.19 A). The yellow colouration is where the end of the experiment (300°C) has been reached without an endpoint having been detected, which may be due to poor contact between the probe and the sample. As caffeine and MS show transitions in the same temperature range, they will both be assigned a blue colour by the software, so it is difficult to distinguish between them via TTM. However, as the concentration of MS is so low (1%), it may be presumed that the vast majority of the responses will be those of caffeine. It was easier to differentiate between caffeine and the other three excipients in the binary compacts, although there was some potential overlapping in the pink colouration between caffeine and α -LM.

In the three-, four- and five- component compacts containing caffeine, the technique had difficulty distinguishing between caffeine and MS, where both materials would be assigned a blue / purple colour, and between MCC and PGS, where both materials would be assigned a yellow colour. As seen previously, α -LM was the most easily identifiable material in the mixed compacts. Examination of the individual traces suggested that in a few cases, a thin layer of one material was formed on top of a thicker layer of another, as was discussed for the nano-TA results. In these cases, the result recorded by the software was variable, in that it was sometimes the lower temperature transition and sometimes the higher temperature transition, and it appeared to be dependent on the magnitude of the lower temperature transition.

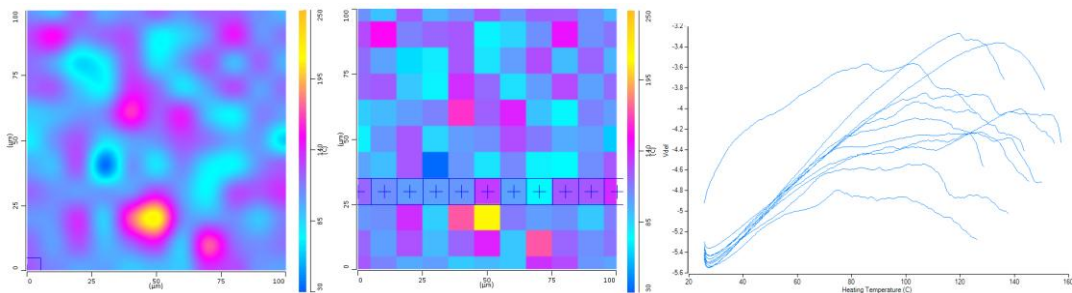
Some differences were observed between the outside and centre positions on the surface of the compact, but this is probably due to the distribution of material across the surface.

Column 1

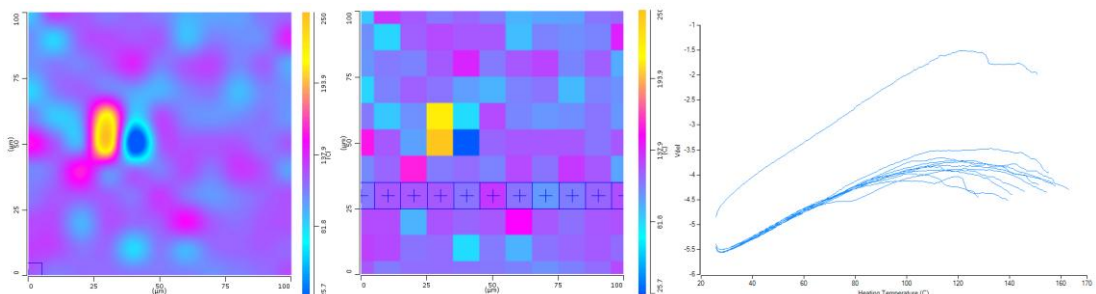
Column 2

Column 3

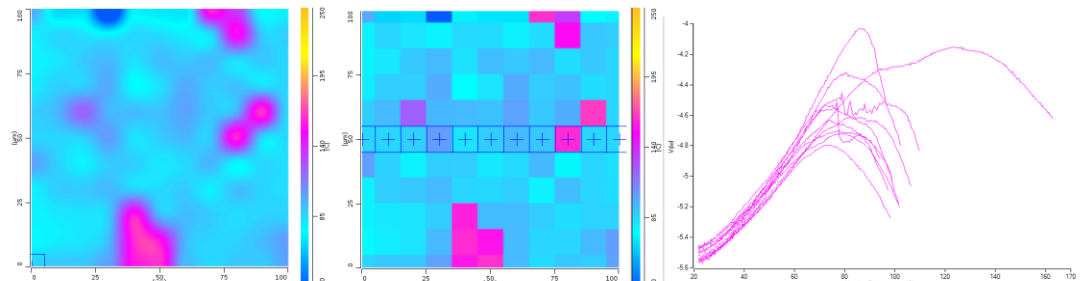
Ai)



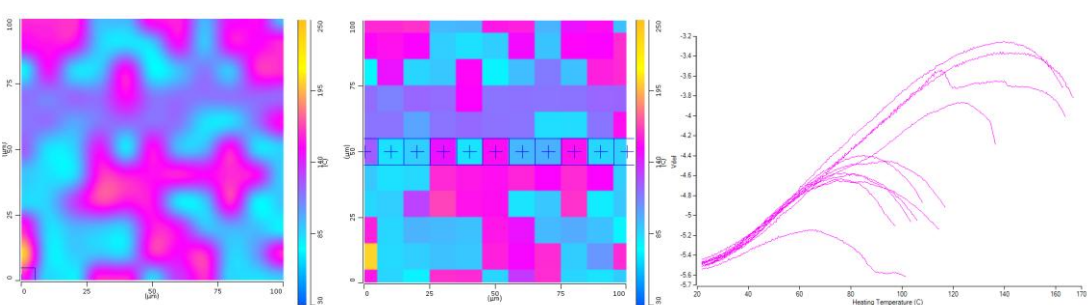
Aii)



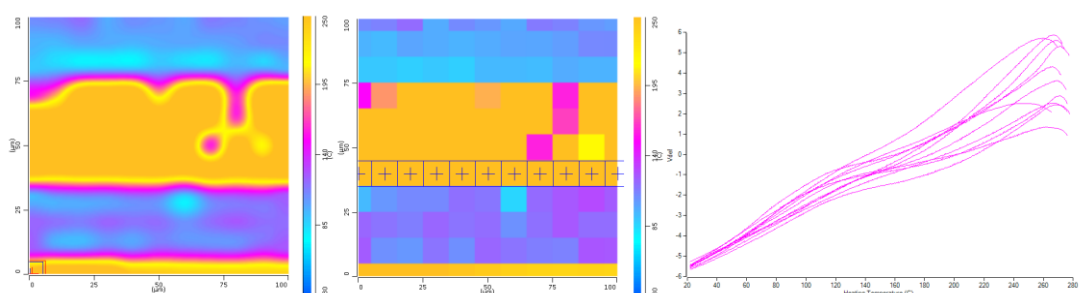
Bi)



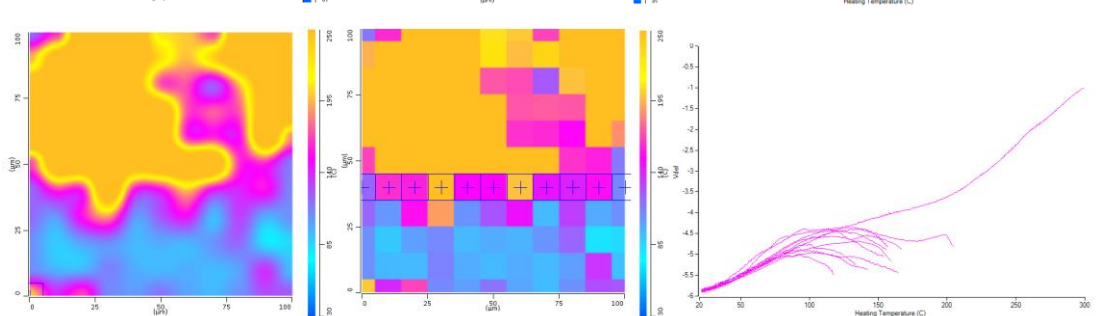
Bii)



Ci)



Cii)



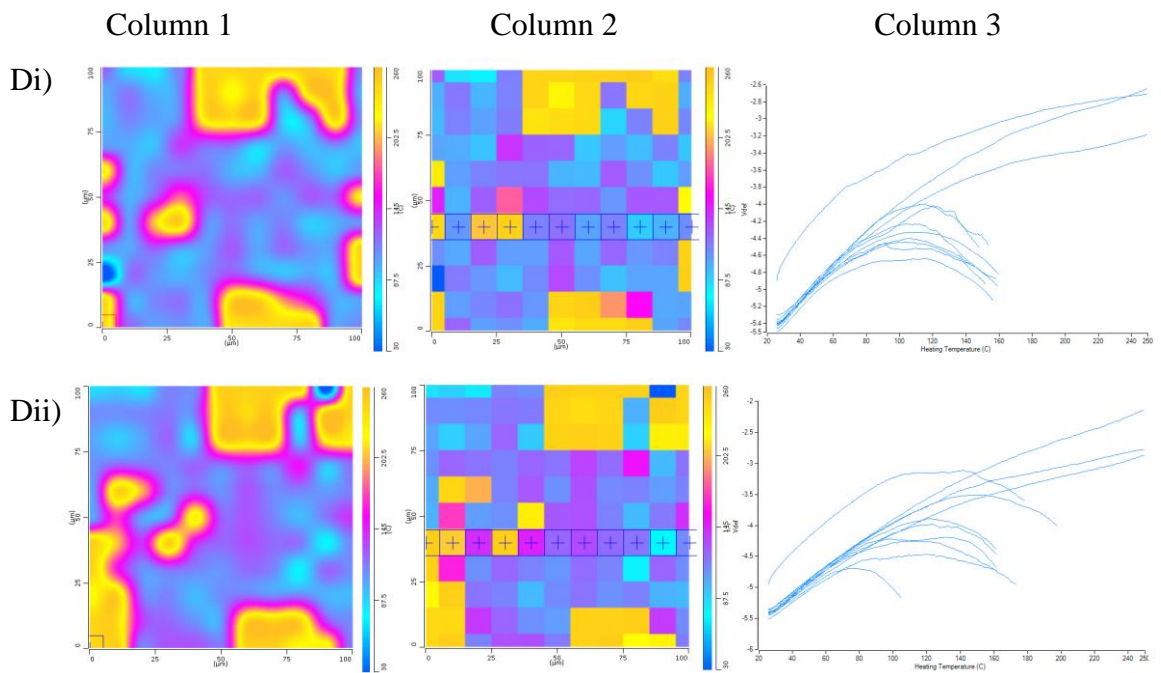
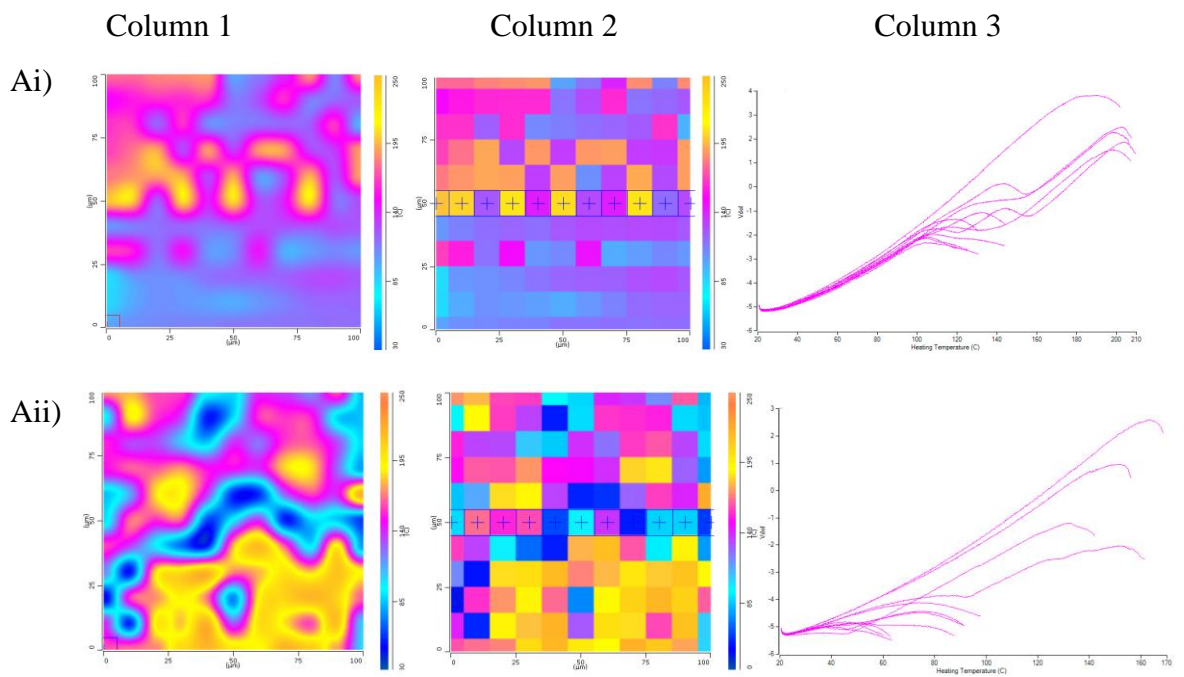


Figure 5.19: TTM maps for 2-component compacts based on caffeine, with representative colours. A) 99% CAF (blue / pink / purple) / 1% MS (not detected). B) 50% CAF (blue, pink / purple) / 50% α -LM (pink). C) 50% CAF (blue / pink / purple) / 50% MCC (yellow). D) 50% CAF (blue / pink / purple) / 50% PGS (yellow). Position on the compact is given by i) centre, ii) outside. Column 1 is the interpolated (smoothed) map, Column 2 is the discrete map, and Column 3 shows the individual nano-thermal results taken at the crossed points (+) on the discrete map.

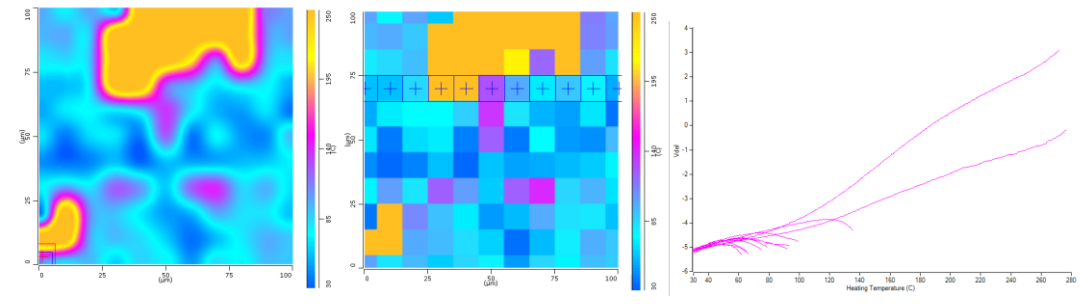


Column 1

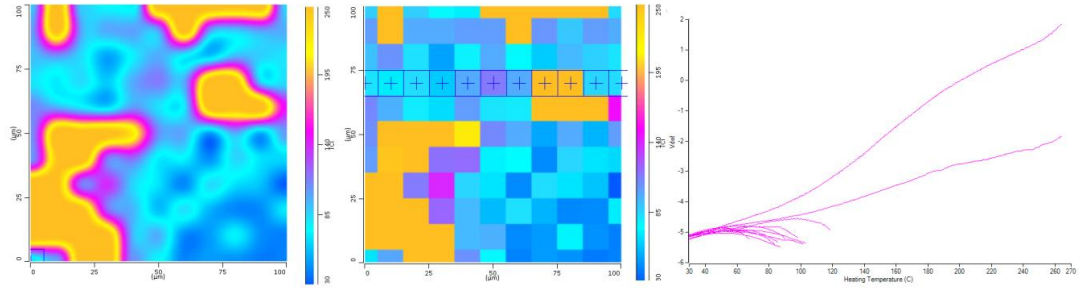
Column 2

Column 3

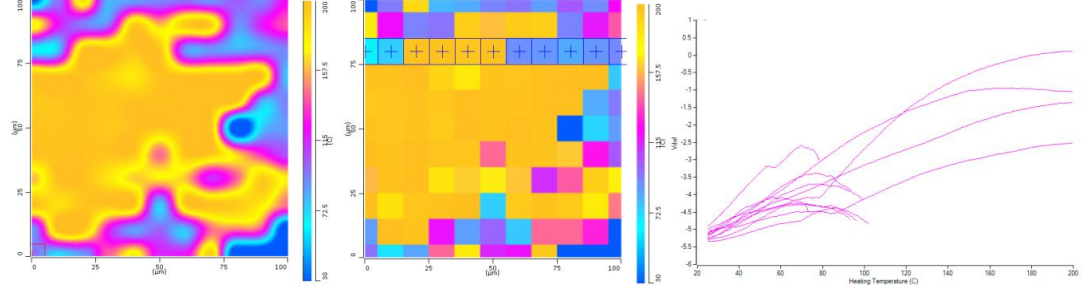
Bi)



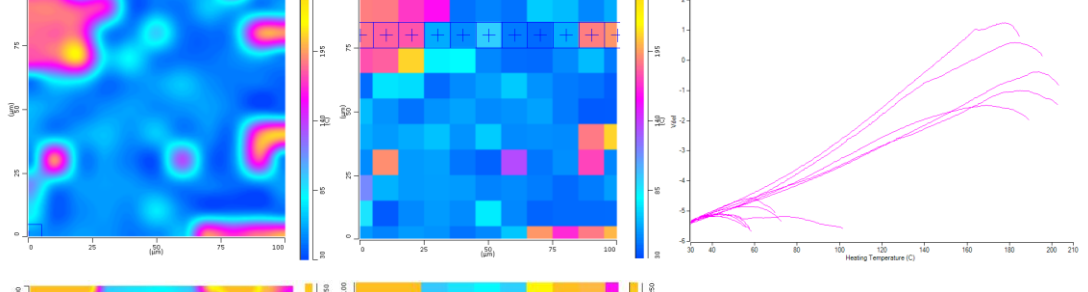
Bii)



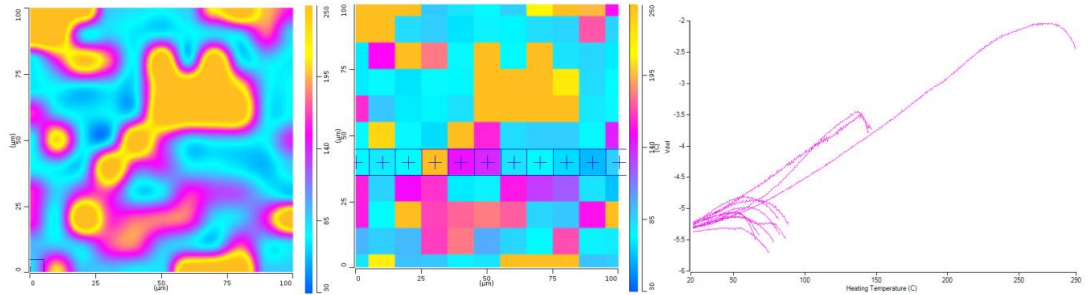
Ci)



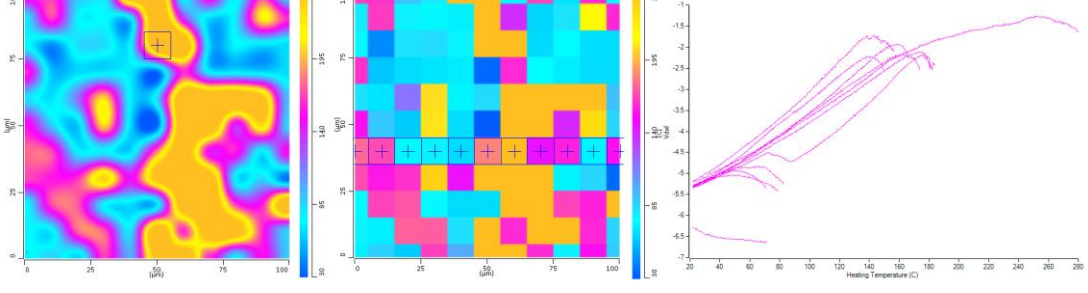
Cii)



Di)



Dii)



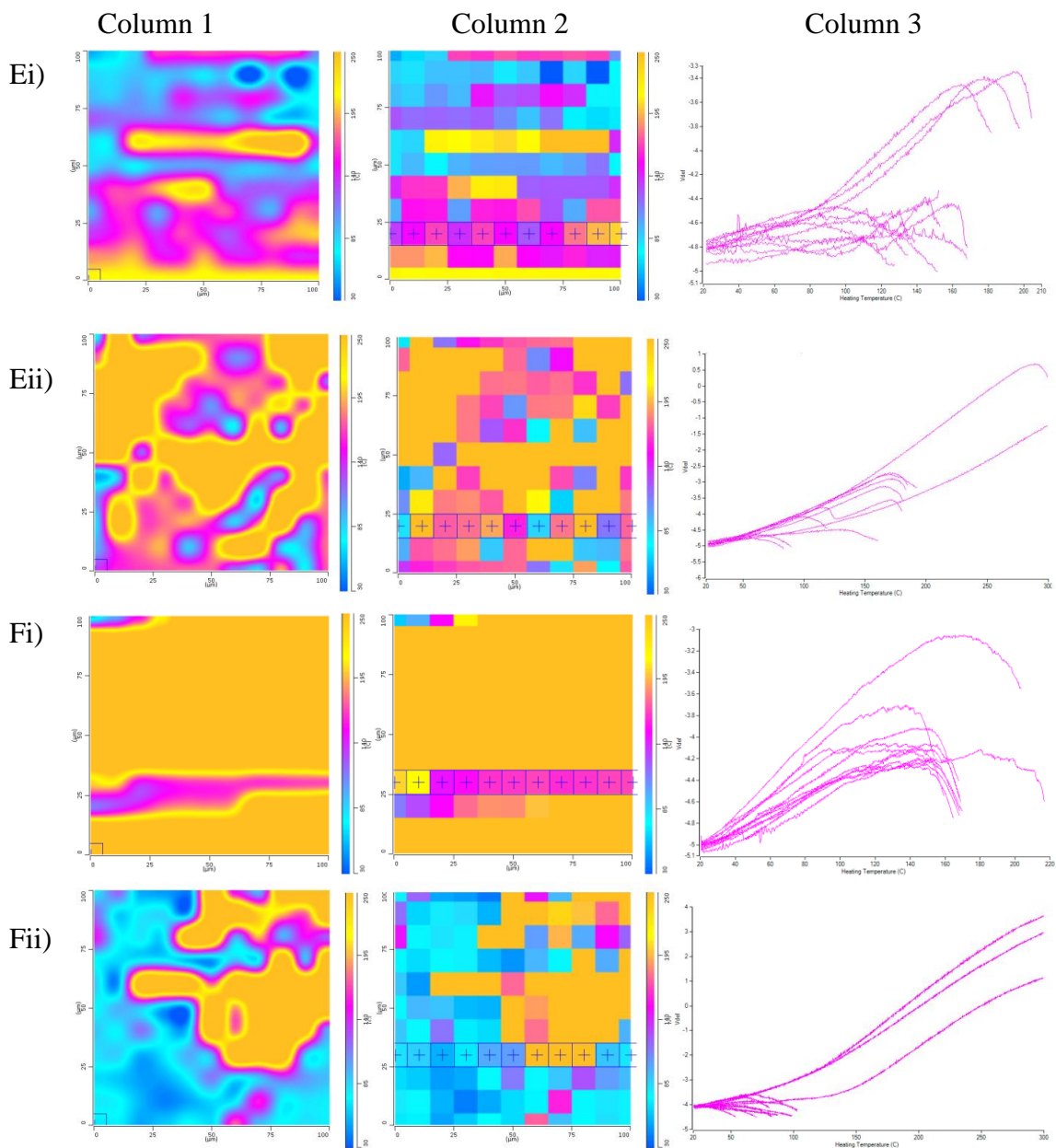


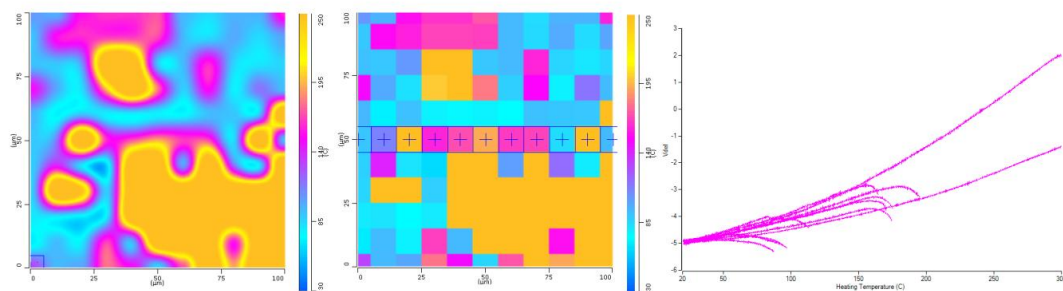
Figure 5.20: TTM maps for 3-component compacts based on caffeine, with representative colours. A) 49.5% CAF (blue) / 49.5% α -LM (pink / yellow) / 1% MS (not detected). B) 49.5% CAF (blue) / 49.5% MCC (yellow) / 1% MS (purple). C) 49.5% CAF (blue) / 49.5% PGS (yellow / pink) / 1% MS (not detected). D) 33.3% CAF (blue) / 33.3% α -LM (pink) / 33.3% PGS (yellow). E) 33.3% CAF (blue / purple) / 33.3% α -LM (pink) / 33.3% MCC (yellow). F) 33.3% CAF (blue) / 33.3% MCC (yellow) / 33.3% PGS (yellow / pink). Position on the compact is given by i) centre, ii) outside. Column 1 is the interpolated (smoothed) map, Column 2 is the discrete map, and Column 3 shows the individual nano-thermal results taken at the crossed points (+) on the discrete map.

Column 1

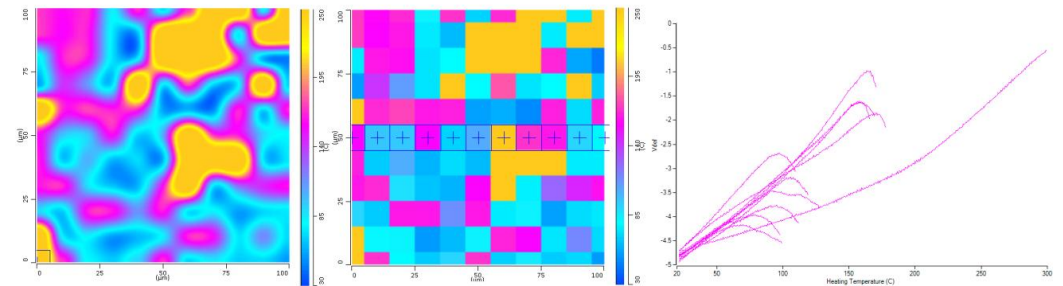
Column 2

Column 3

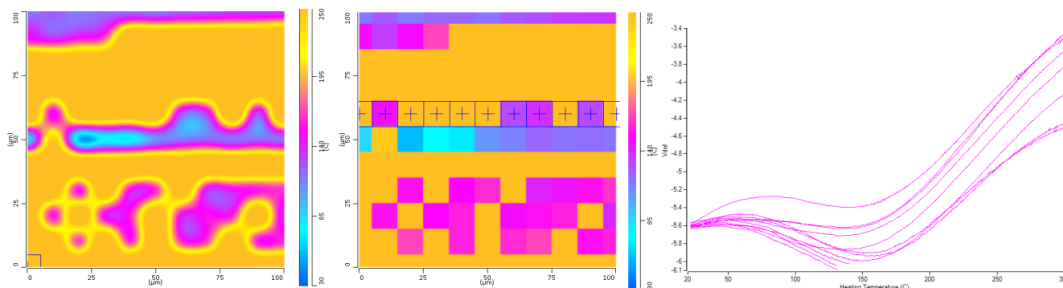
Ai)



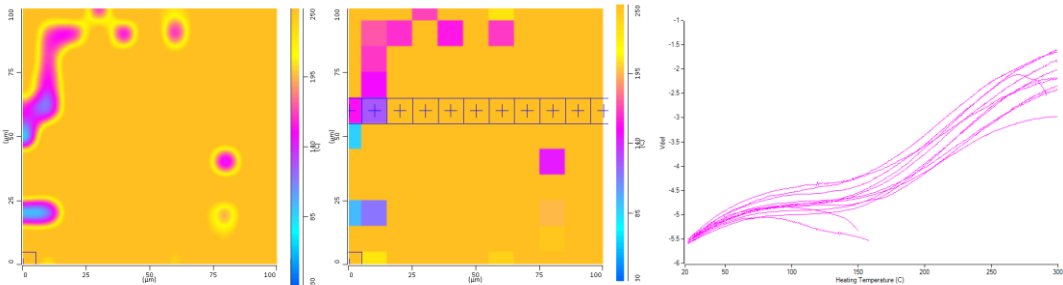
Aii)



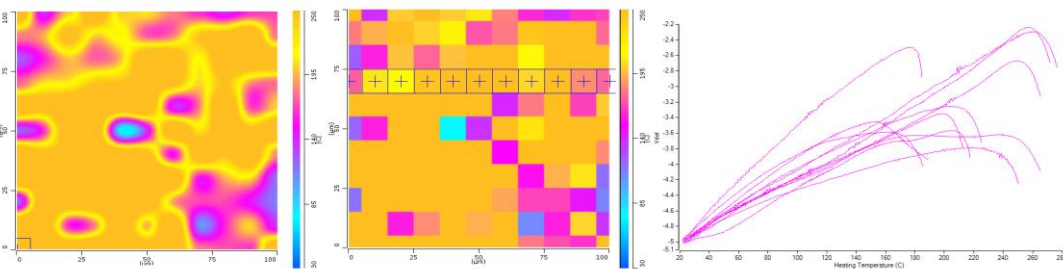
Bi)



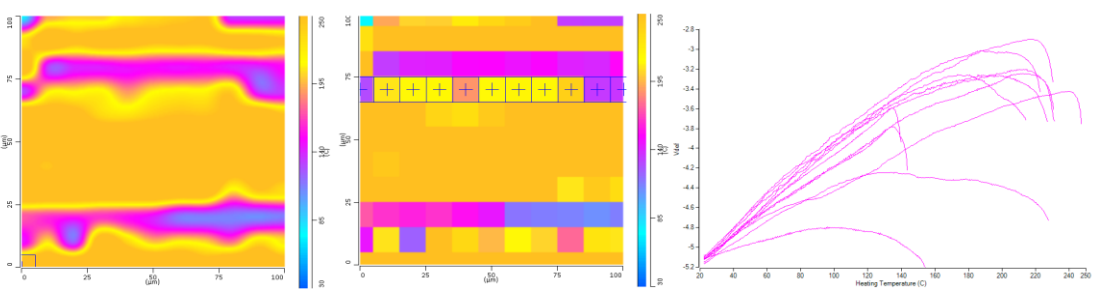
Bii)



Ci)



Cii)



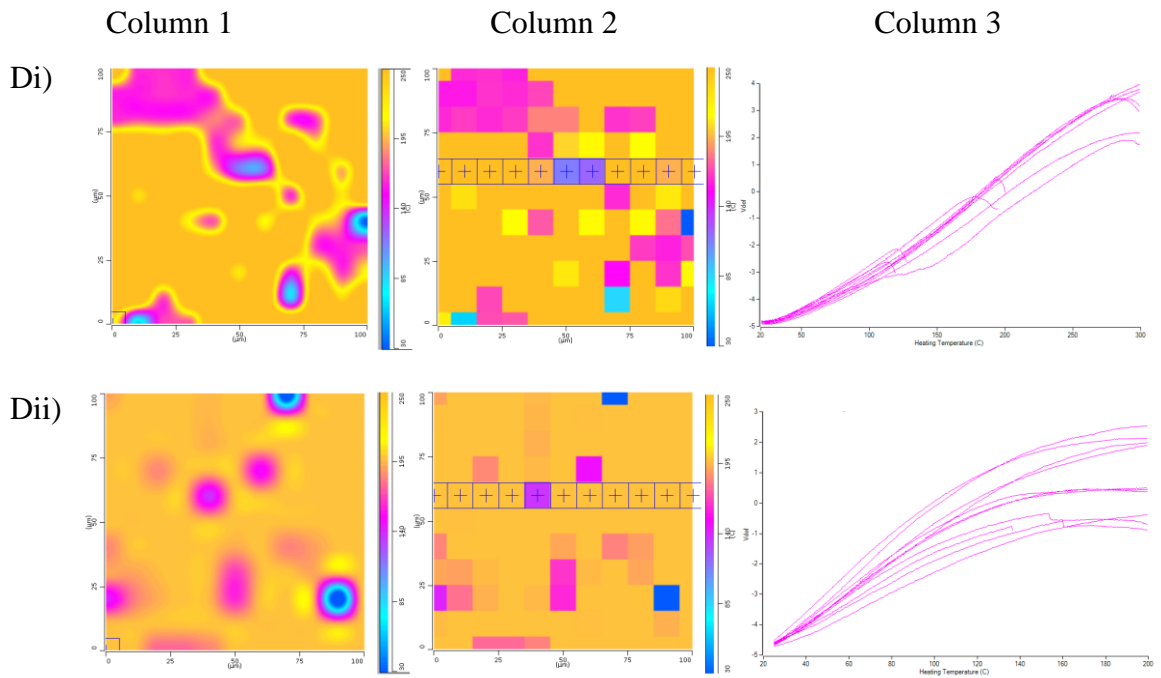
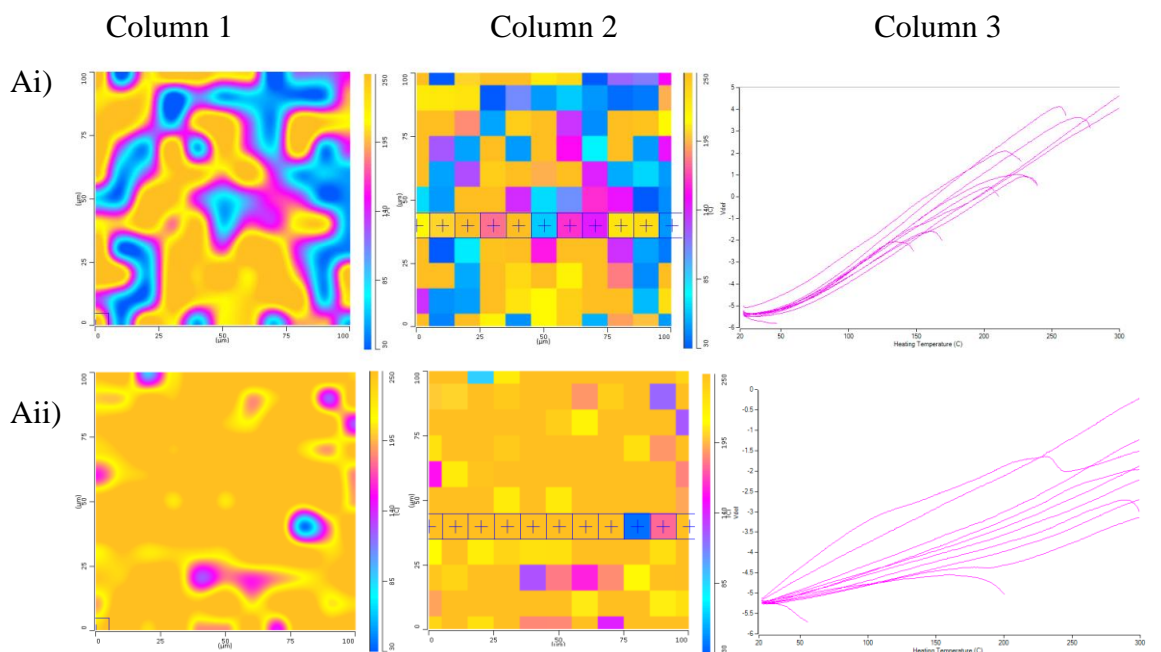


Figure 5.21: TTM maps for 4-component compacts based on caffeine, with representative colours. A) 33% CAF (blue) / 33% α -LM (pink) / 33% MCC (yellow) / 1% MS (purple). B) 33% CAF (blue / purple) / 33% MCC (yellow) / 33% PGS (yellow / pink) / 1% MS (not detected). C) 33% CAF (blue) / 33% α -LM (pink / purple) / 33% PGS (yellow) / 1% MS (not detected). D) 25% CAF (blue) / 25% α -LM (pink) / 25% PGS (yellow) / 25% MCC (yellow). Position on the compact is given by i) centre, ii) outside. Column 1 is the interpolated (smoothed) map, Column 2 is the discrete map, and Column 3 shows the individual nano-thermal results taken at the crossed points (+) on the discrete map.



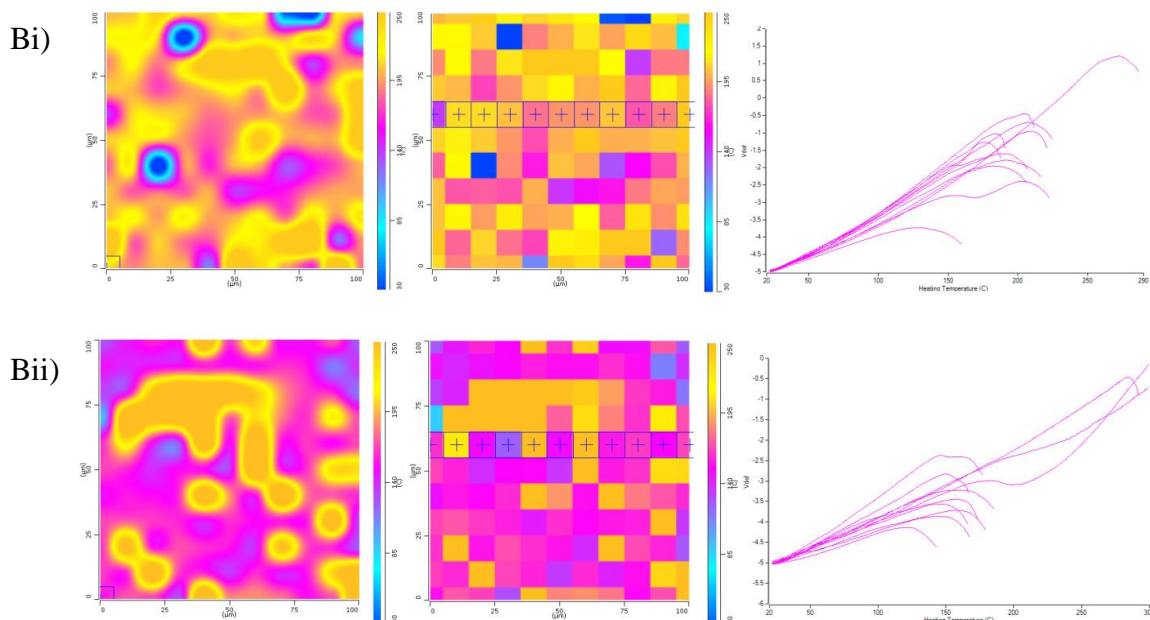


Figure 5.22: TTM maps for 5-component compacts based on caffeine, with representative colours. A) 24.75% CAF (blue) / 24.75% α -LM (pink) / 24.75% MCC (yellow) / 24.75% PGS (yellow) / 1% MS (purple). B) 20% CAF (blue) / 20% α -LM (pink) / 20% MCC (yellow) / 20% PGS (yellow) / 20% MS (purple). Position on the compact is given by i) centre, ii) outside. Column 1 is the interpolated (smoothed) map, Column 2 is the discrete map, and Column 3 shows the individual nano-thermal results taken at the crossed points (+) on the discrete map.

5.3.2.4 General discussion for the multi-component compacts containing caffeine

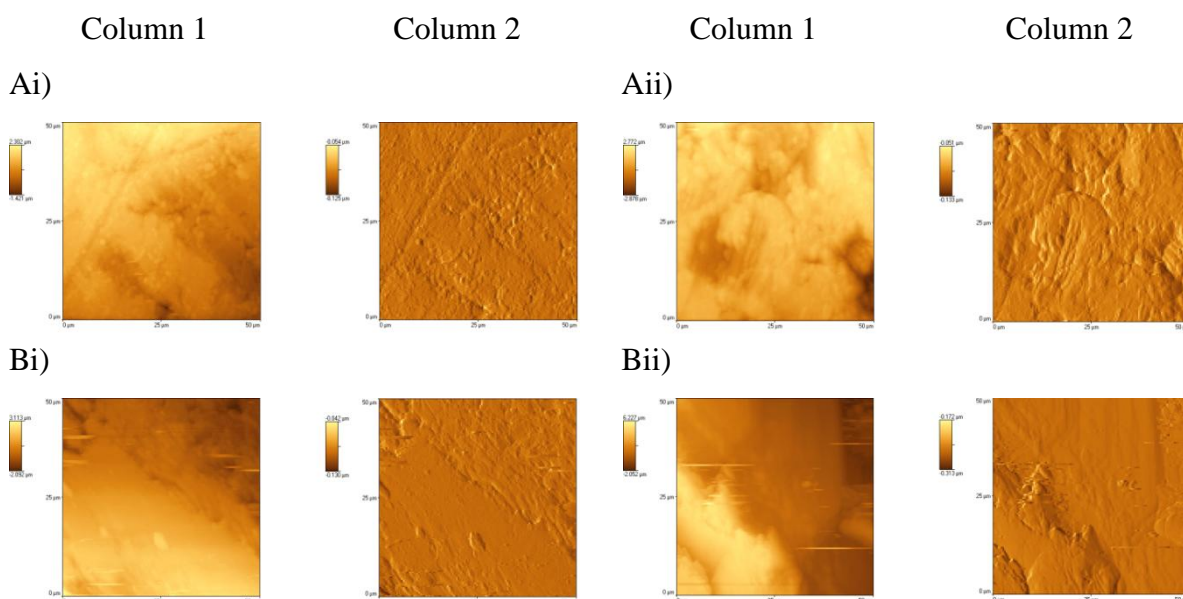
The results presented in this section confirm those of the excipient-only compacts, in that it is possible to detect the various components on the surface of the compact by their thermal profiles. However, in this case, it was difficult to distinguish between caffeine and MS as their observed thermal events occurred over a similar temperature range. Manual examination of the nano-TA traces allows the two components to be separated, but the automated data processing in the TTM software does not, as both materials will be assigned the same colour. An extra complication observed for the caffeine-loaded compacts that wasn't seen with the excipient-only compacts was the appearance of "double peaks", whereby a mini-endpoint was observed before the main endpoint. This was explained by the presence of a thin layer of one material with a lower temperature of transition on top of another with a higher temperature of transition.

5.3.3 Multi-component compacts containing ibuprofen

5.3.3.1 AFM

To mirror the analysis conducted with caffeine, compacts were made of all combinations of ibuprofen and one, two, three and four excipients. Representative AFM scans are shown in Figures 5.27, 5.28, 5.29 and 5.30 for the two-, three- four- and five- component compacts, respectively.

Generally, interpretation of the AFM images presented the same challenges as were discussed earlier. In some cases, materials could be identified from their AFM profile - PGS being the most obvious one. Ibuprofen and α -LM seem to be relatively easily distinguishable from each other by appearance on the AFM image. For example, Figure 5.27 Bi shows a diagonal strip running from the top left hand corner to the bottom right hand corner, which appears smoother than the rest of the image, suggesting the presence of two different materials. This was confirmed by the nano-TA results (Figure 5.31) whereby the three results representing this strip (light blue, dark blue and purple lines) are assigned to ibuprofen and the remaining two results (green and red) are assigned to α -LM. A similar interpretation can be made for Figure 5.17 Bii. In other cases, topographical variation was not due to the presence of different materials, but represented the variability within a single component. As was seen before with the excipient-only compacts and those based on caffeine, as the complexity of the formulation increased, the ease of identification by AFM imaging decreased.



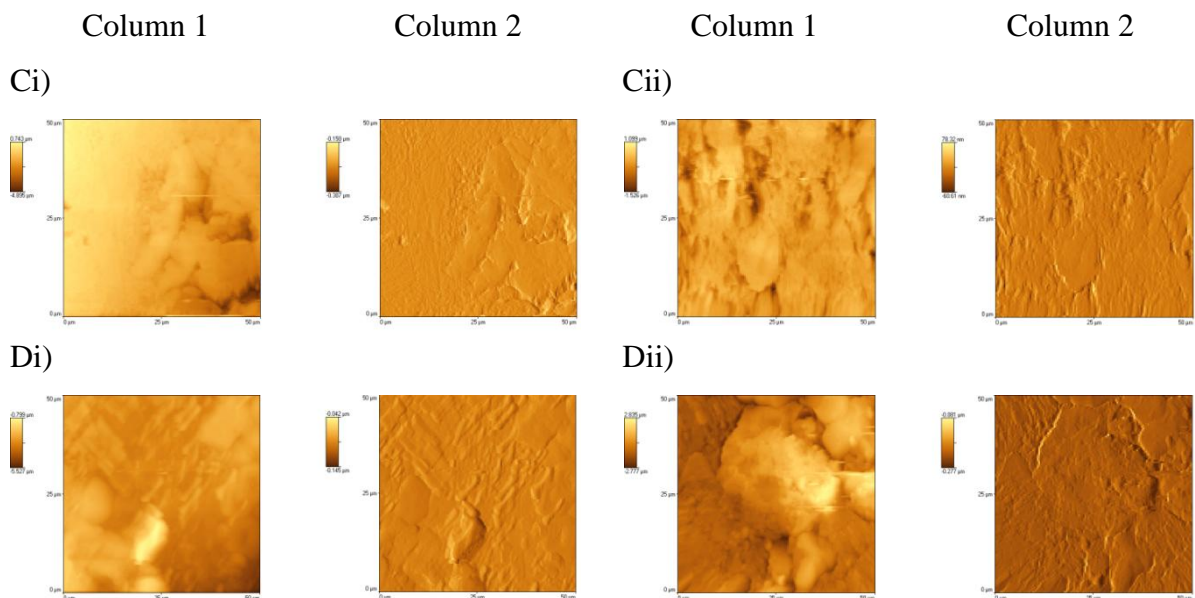
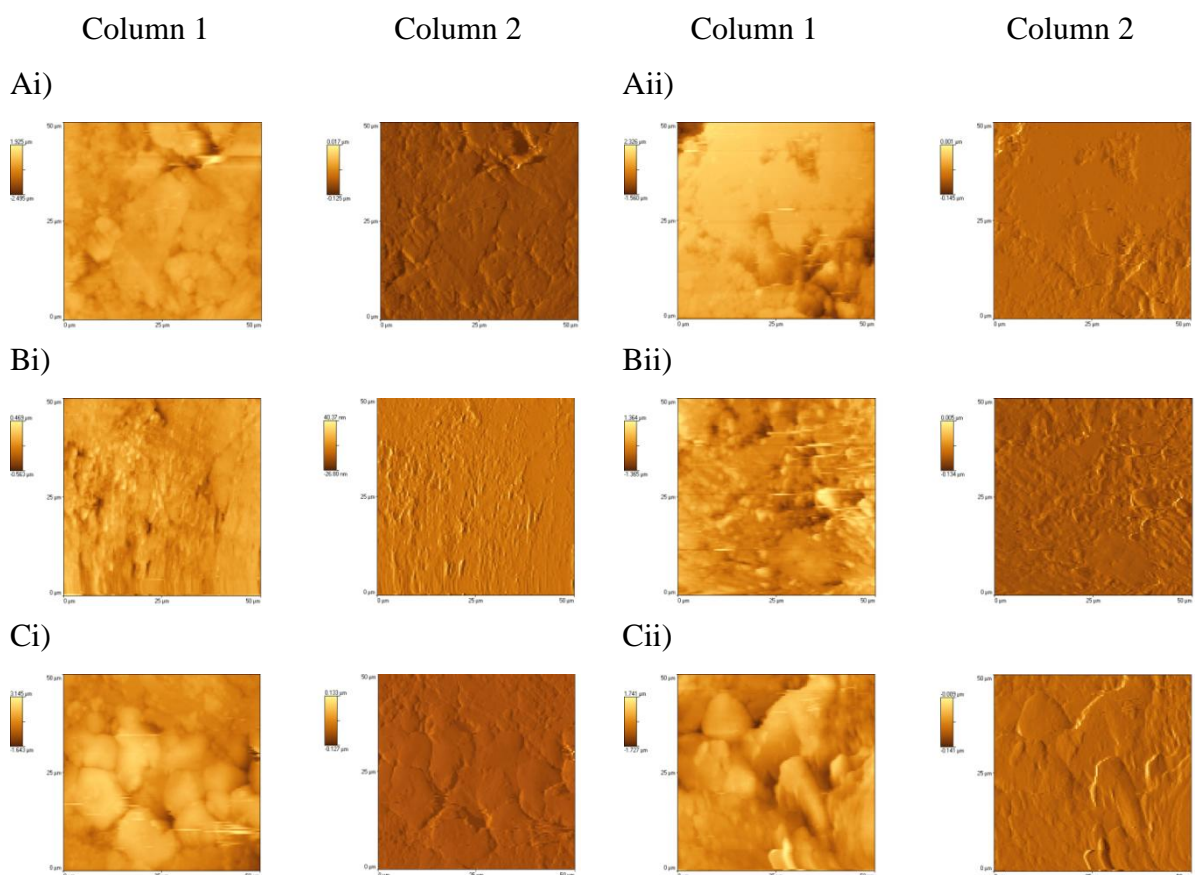


Figure 5.23: AFM images of the 2-component compacts based on ibuprofen, using a nano probe. A) 99% IBU / 1% MS. B) 50% IBU / 50% α -LM. C) 50% IBU / 50% MCC. D) 50% IBU / 50% PGS. Position on the compact is given by i) centre, ii) outside. Column 1 - height, Column 2 - deflection.



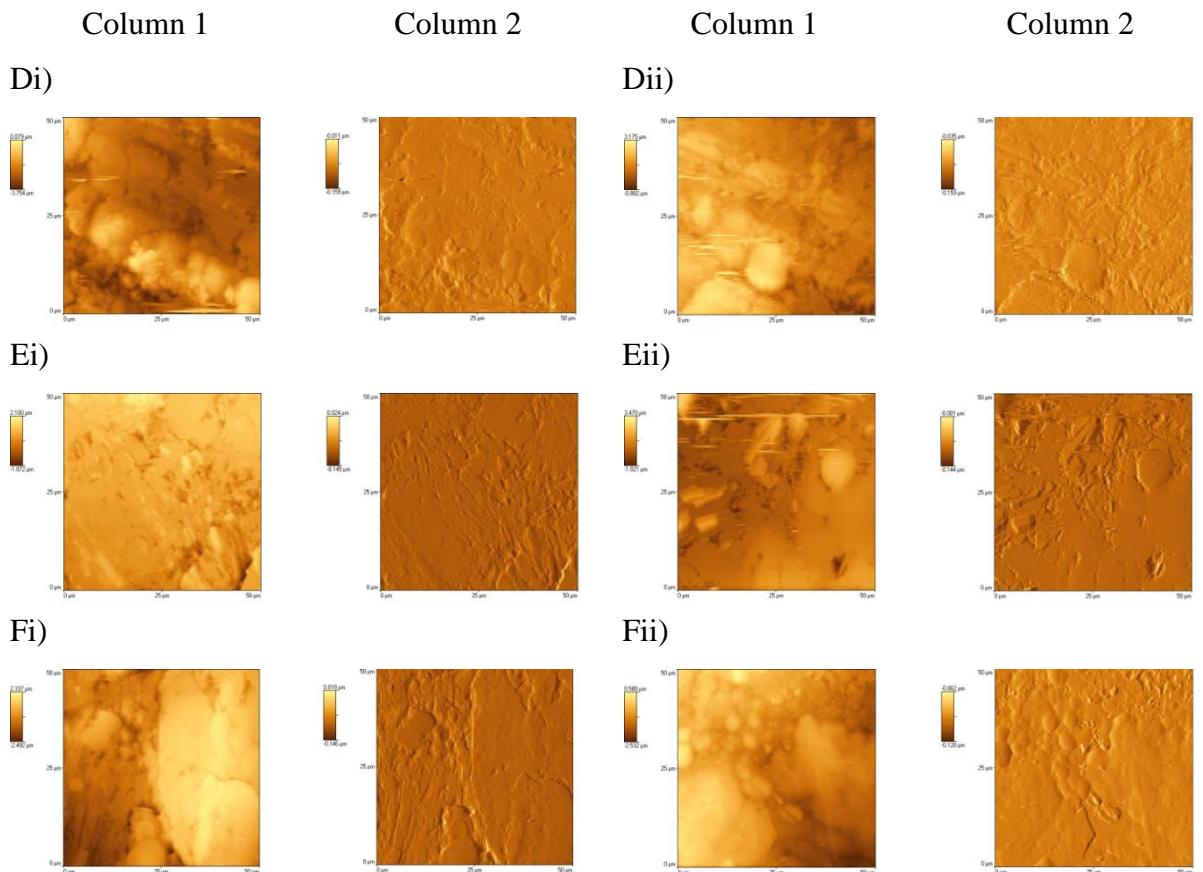
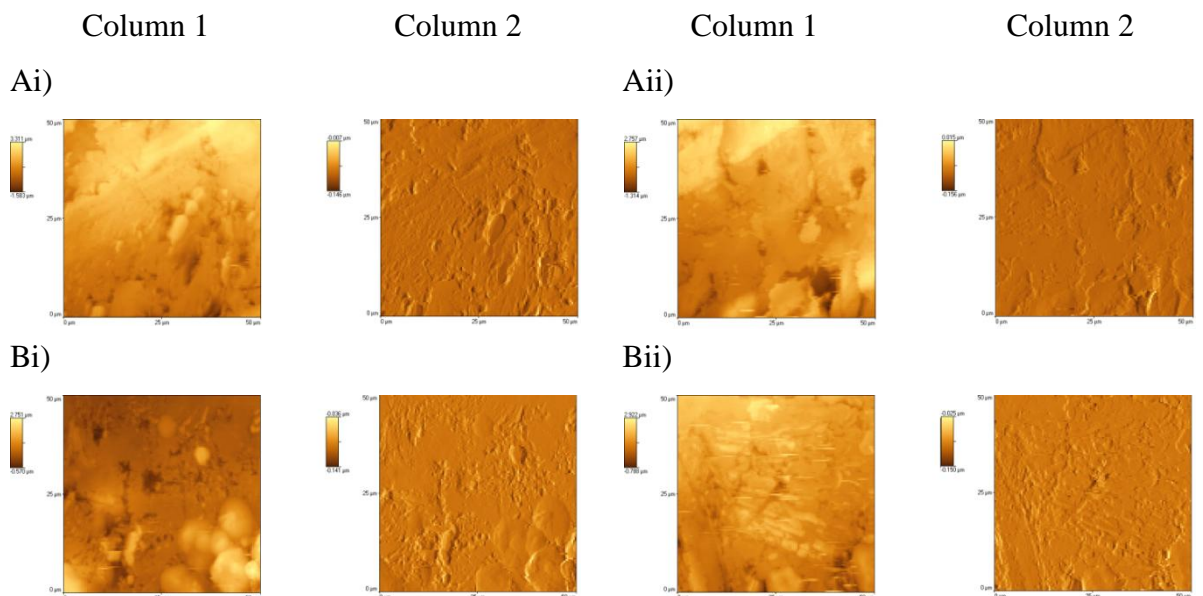


Figure 5.24: AFM images of the 3-component compacts based on ibuprofen, using a nano probe. A) 49.5% IBU / 49.5% α -LM / 1% MS. B) 49.5% IBU / 49.5% MCC / 1% MS. C) 49.5% IBU / 49.5% PGS / 1% MS. D) 33.3% IBU / 33.3% α -LM / 33.3% PGS. E) 33.3% IBU / 33.3% α -LM / 33.3% MCC. F) 33.3% IBU / 33.3% MCC / 33.3% PGS. Position on the compact is given by i) centre, ii) outside. Column 1 - height, Column 2 - deflection.



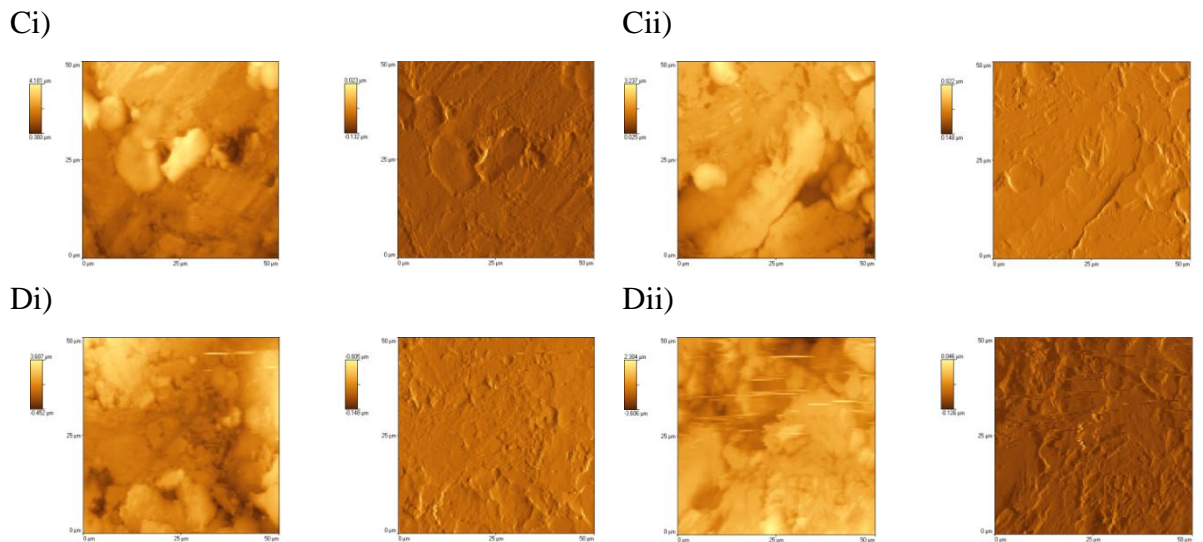


Figure 5.25: AFM images of the 4-component compacts based on ibuprofen, using a nano probe. A) 33% IBU / 33% α -LM / 33% MCC / 1% MS. B) 33% IBU / 33% MCC / 33% PGS / 1% MS. C) 33% IBU / 33% α -LM / 33% PGS / 1% MS. D) 25% IBU / 25% α -LM / 25% PGS / 25% MCC. Position on the compact is given by i) centre, ii) outside. Column 1 - height, Column 2 - deflection.

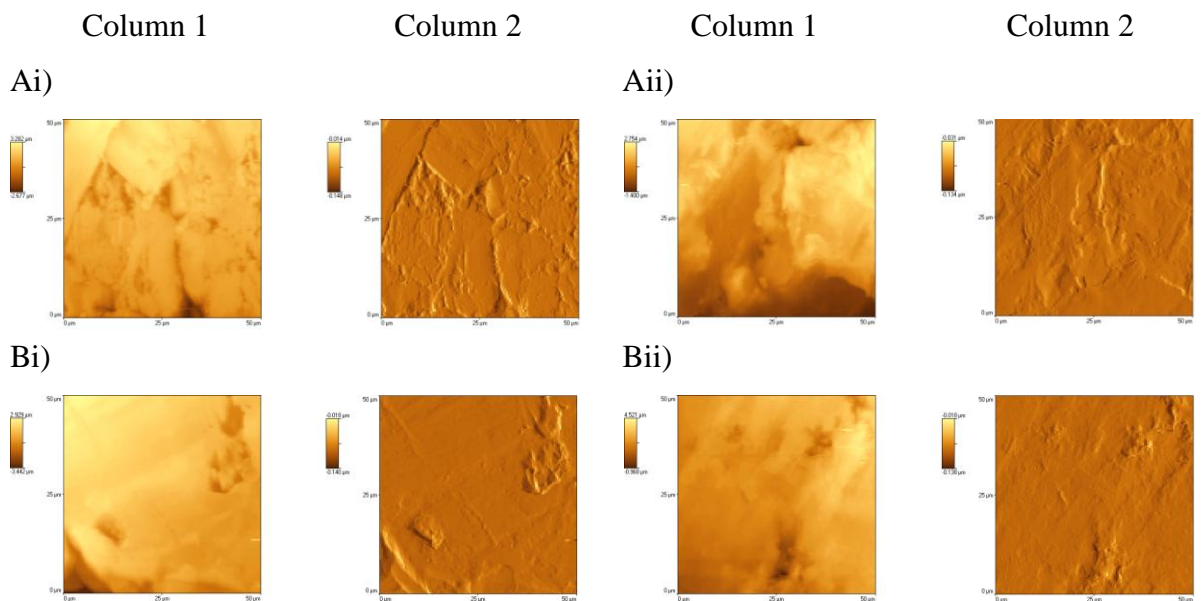


Figure 5.26: AFM images of the 5-component compacts based on ibuprofen, using a nano probe. A) 24.75% IBU / 24.75% α -LM / 24.75% MCC / 24.75% PGS / 1% MS. B) 20% IBU / 20% α -LM / 20% MCC / 20% PGS / 20% MS. Position on the compact is given by i) centre, ii) outside. Column 1 - height, Column 2 - deflection.

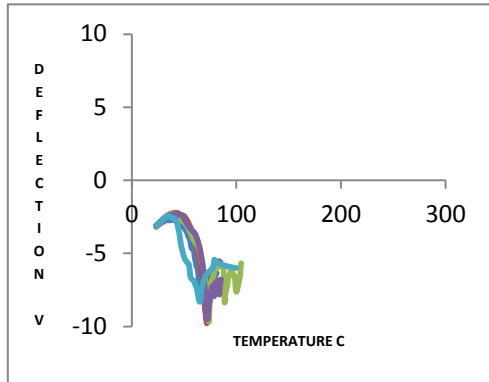
5.3.3.2 Nano-TA

Nano-TA was performed on each of the multi-component compacts based on ibuprofen after the AFM images were generated. Representative scans are shown in Figures 5.27, 5.28, 5.29 and 5.30 for the two-, three-, four- and five- component compacts, respectively. Comparison of these scans with those of the compacts of the individual components shown in Chapters 3 and 4 allowed identification of the most likely component(s) present. This is summarised in Tables 5.8, 5.9, 5.10 and 5.11, respectively. All five components could be identified by their thermal profiles, although as with the excipient-only or caffeine-based compacts, MS was identified the least frequently, reflecting its low concentration in the compacts.

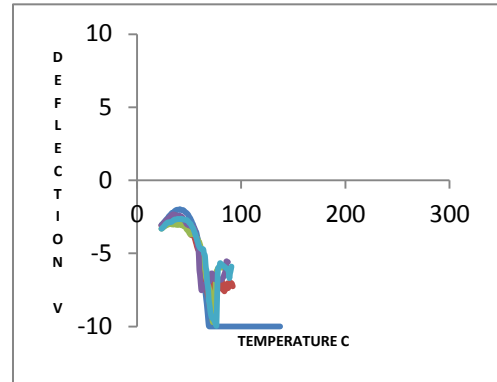
Occasionally, the thermal response for ibuprofen appears at a higher temperature than the circa 50°C generally associated with it, for example in Figure 5.27 B ii, but this was also sometimes seen with the pure substance, as discussed in Chapter 4. The thermal responses for ibuprofen and MS were in a similar temperature range, but were usually easily separable from each other by reference to their mono-component traces. For example, in Figure 5.28 Ai, the green line was assigned to MS rather than ibuprofen because it did not have the sharp V-shape minimum point seen in ibuprofen mono-component compacts and it also had a second peak which was occasionally seen when MS single component compacts were analysed.

In common with the observations on the caffeine-containing compacts, several of the nano-TA traces show evidence of two transitions. For example, in Figure 5.29 Ci the green line appears to show a dip at circa 180°C, then continue with no obvious thermal response until the end of the run, suggesting that at this position there was a thin layer of α -LM on the surface of MCC. As has been seen previously, it was difficult to distinguish between PGS and MCC in the mixed samples.

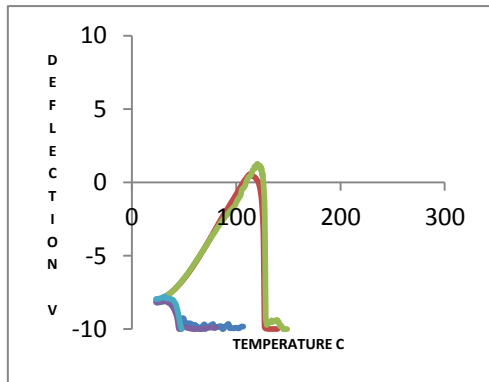
Ai)



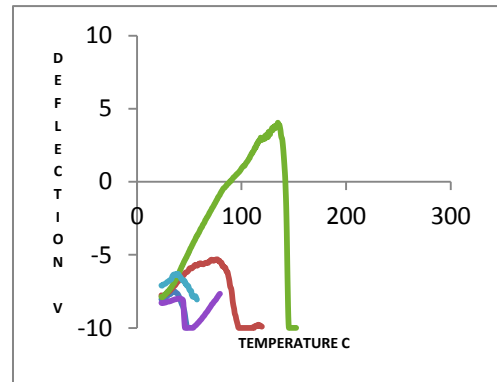
Aii)



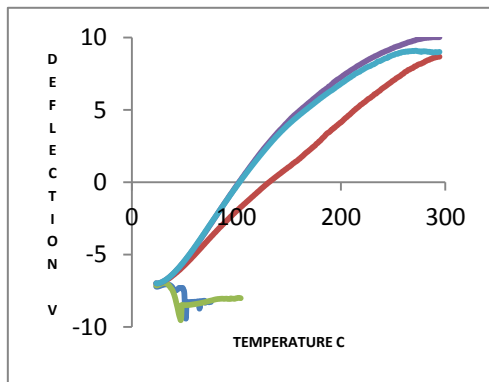
Bi)



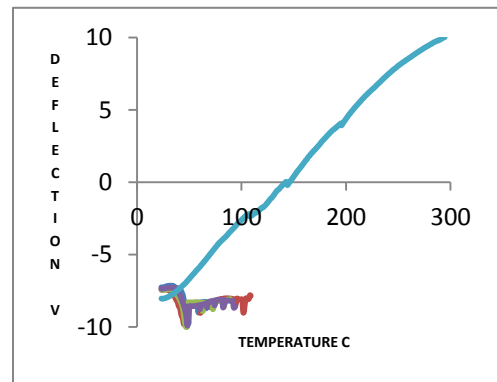
Bii)



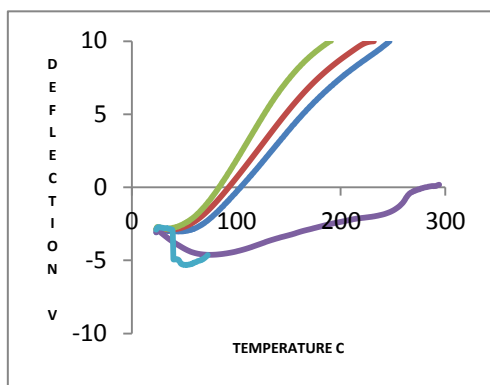
Ci)



Cii)



Di)



Dii)

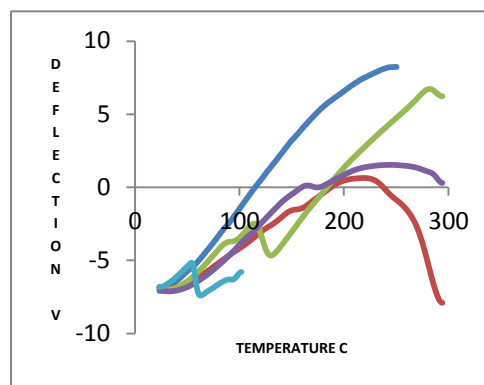
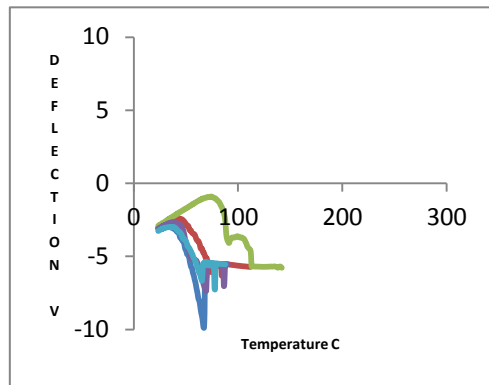


Figure 5.27: Nano-TA results for the 2-component compacts based on ibuprofen, using a nano probe. A) 99% IBU / 1% MS. B) 50% IBU / 50% α -LM. C) 50% IBU / 50% MCC. D) 50% IBU / 50% PGS. Position on the compact is given by i) centre, ii) outside. Five readings were taken at each position: dark blue - site 1, red - site 2, green - site 3, purple - site 4, light blue - site 5.

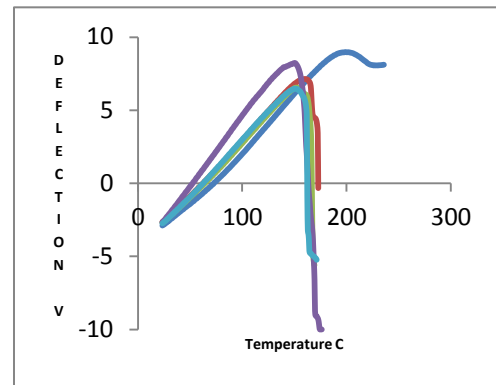
Formulation	Compact	Components identified (number of sites; maximum = 5)				
		IBU	α -LM	MS	MCC	PGS
99% IBU / 1% MS	A i	5	X	0	X	X
	A ii	5	X	0	X	X
50% IBU / 50% α -LM	B i	3	2	X	X	X
	B ii	4	1	X	X	X
50% IBU / 50% MCC	C i	2	X	X	3	X
	C ii	1	X	X	4	X
50% IBU / 50% PGS	D i	1	X	X	X	4
	D ii	1	X	X	X	4

Table 5.8: A summary of the most probable components identified from the nano-TA scans of the 2-component compacts based on ibuprofen shown in Figure 5.27. The number indicates the number of scans assigned to a particular component. X indicates that this component is not present in the compact.

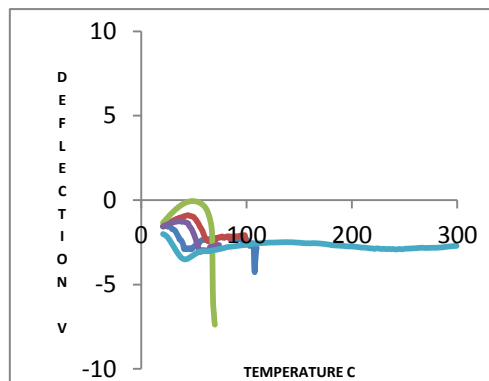
Ai)



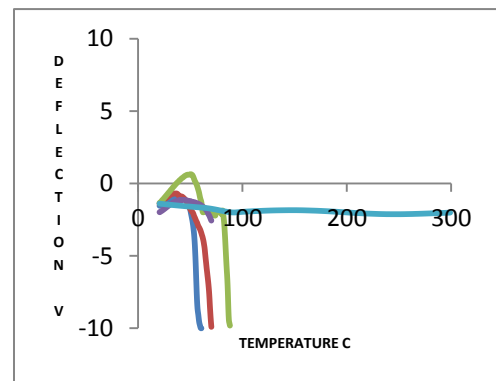
Aii)



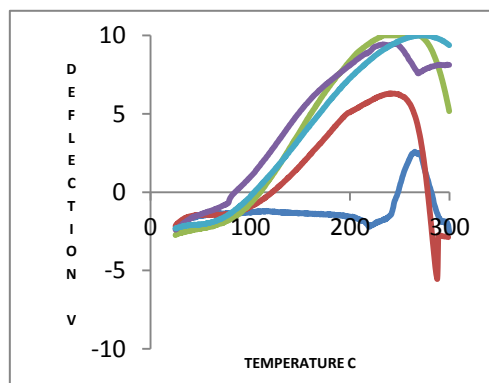
Bi)



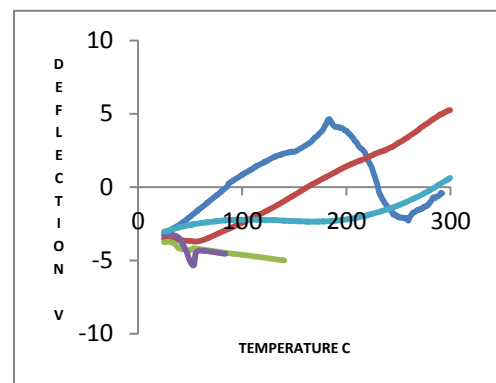
Bii)



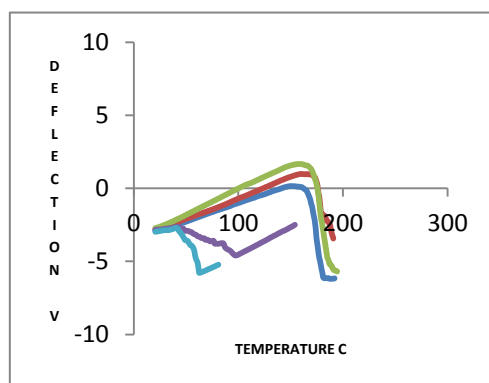
Ci)



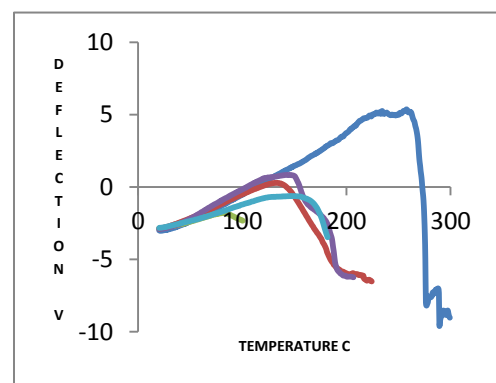
Cii)



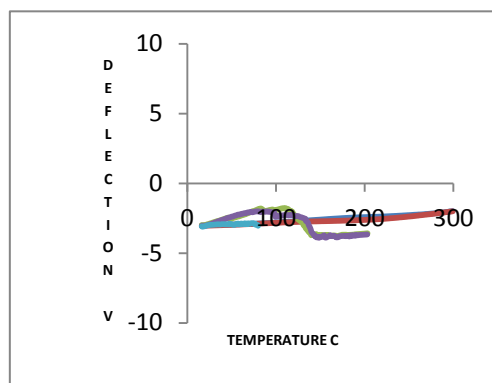
Di)



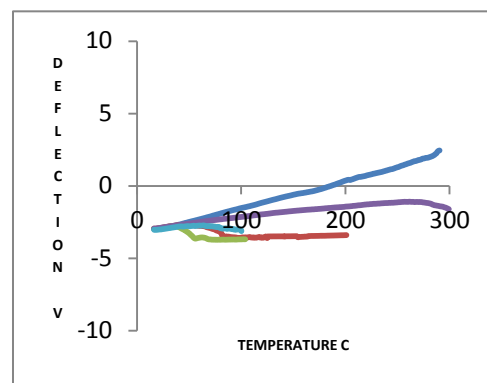
Dii)



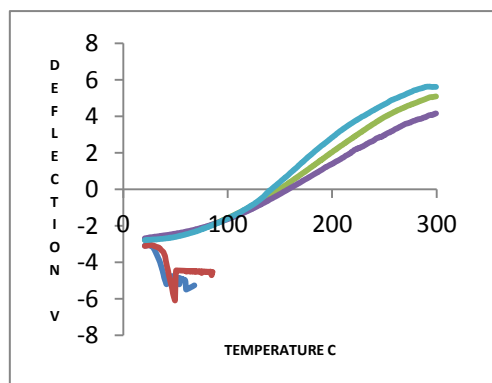
Ei)



Eii)



Fi)



Fii)

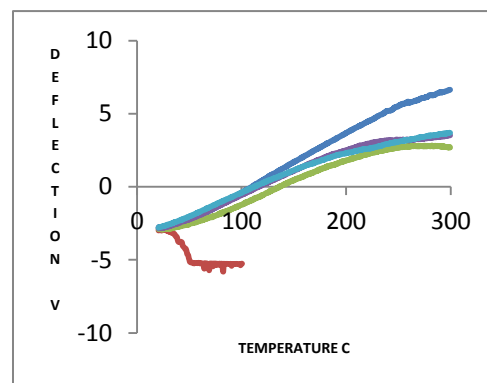
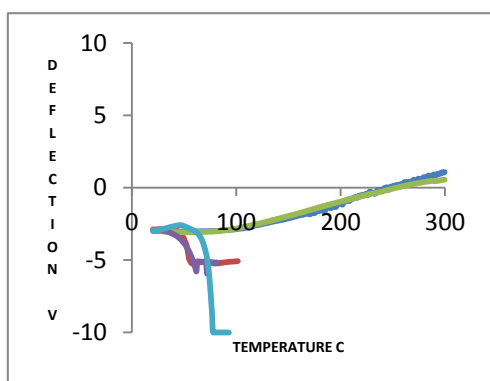


Figure 5.28: Nano-TA results for the 3-component compacts based on caffeine, using a nano probe. A) 49.5% IBU/ 49.5% α -LM / 1% MS. B) 49.5% IBU/ 49.5% MCC / 1% MS. C) 49.5% IBU/ 49.5% PGS / 1% MS. D) 33.3% IBU/ 33.3% α -LM / 33.3% PGS. E) 33.3% IBU/ 33.3% α -LM / 33.3% MCC. F) 33.3% IBU/ 33.3% MCC / 33.3% PGS. Position on the compact is given by i) centre, ii) outside. Five readings were taken at each position: dark blue - site 1, red - site 2, green - site 3, purple - site 4, light blue - site 5.

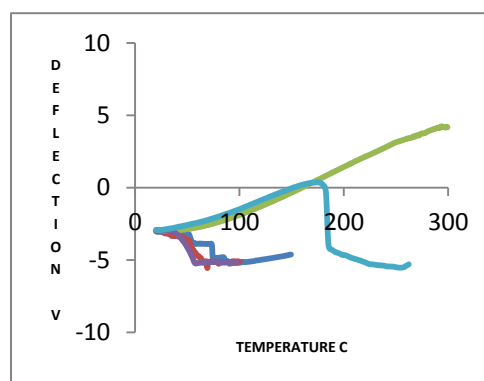
Formulation	Compact	Components identified (number of sites; maximum = 5)				
		IBU	α -LM	MS	MCC	PGS
49.5% IBU / 49.5% α -LM / 1% MS	A i	4	0	1	X	X
	A ii	0	5	0	X	X
49.5% IBU / 49.5% MCC / 1% MS	B i	4	X	0	1	X
	B ii	4	X	0	1	X
49.5% IBU / 49.5% PGS 1% MS	C i	0	X	0	X	5
	C ii	2	X	0	X	3
33.3% IBU / 33.3% α -LM / 33.3% PGS	D i	2	3	X	X	0
	D ii	1	3	X	X	1
33.3% IBU / 33.3% α -LM / 33.3% MCC	Ei	3	0	X	2	X
	Eii	1	0	X	4	X
33.3% IBU / 33.3% MCC / 33.3% PGS	Fi	2	X	X	3	0
	Fii	1	X	X	2	2

Table 5.9: A summary of the most probable components identified from the nano-TA scans of the 3-component compacts based on ibuprofen shown in Figure 5.28. The number indicates the number of scans assigned to a particular component. X indicates that this component is not present in the compact.

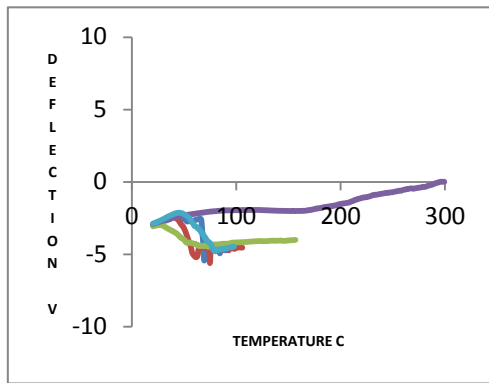
Ai)



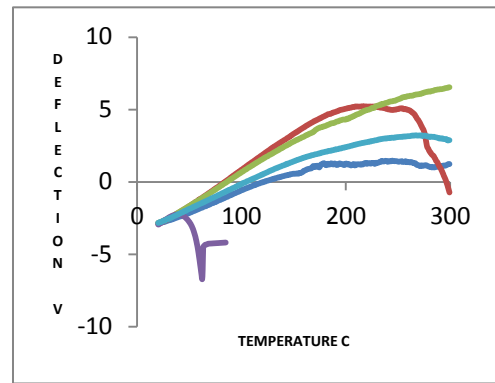
Aii)



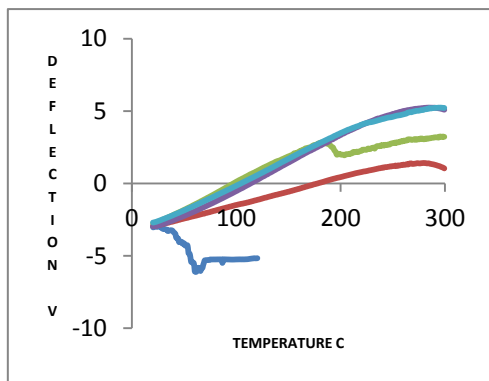
Bi)



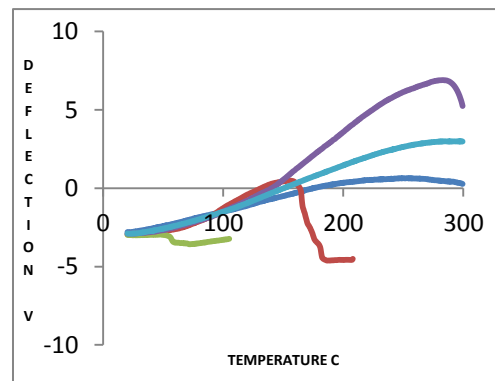
Bii)



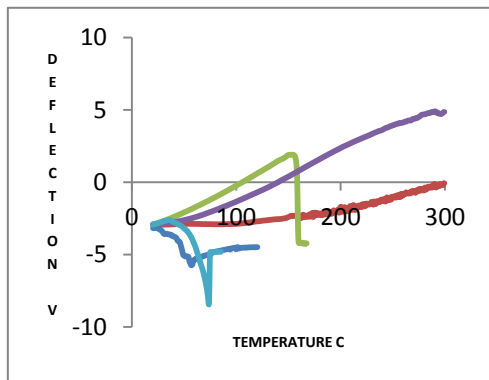
Ci)



Cii)



Di)



Dii)

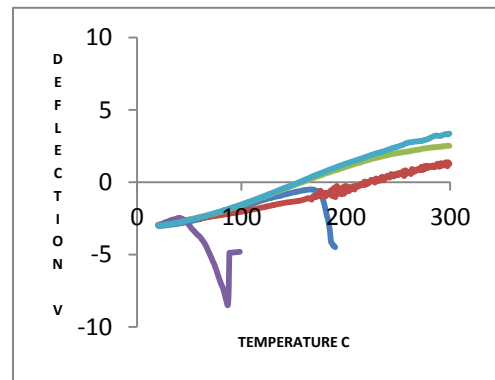


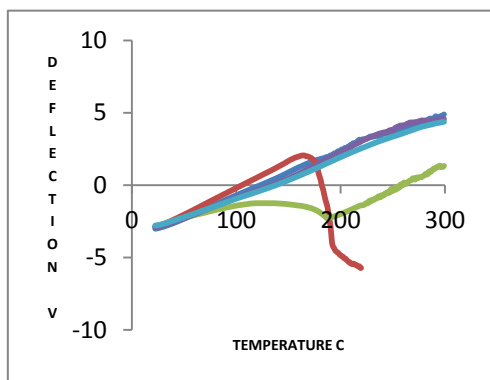
Figure 5.29: Nano-TA results for the 4-component compacts based on ibuprofen, using a nano probe. A) 33% IBU / 33% α -LM / 33% MCC / 1% MS. B) 33% IBU / 33% MCC / 33% PGS / 1% MS. C) 33% IBU / 33% α -LM / 33% PGS / 1% MS. D) 25% IBU / 25% α -LM / 25% PGS / 25% MCC. Position on the compact is given by i) centre, ii) outside. Five readings were taken at each position: dark blue - site 1, red - site 2, green - site 3, purple - site 4, light blue - site 5.

Formulation	Compact	Components identified (number of sites; maximum = 5)				
		IBU	α -LM	MS	MCC	PGS
33% IBU / 33% α -LM / 33% MCC / 1% MS	A i	3	0	0	2	X
	A ii	3	1	0	1	X
33% IBU / 33% MCC / 33% PGS / 1% MS	B i	4	X	0	1	0
	B ii	1	X	0	3	1
33% IBU / 33% α -LM / 33% PGS / 1% MS	C i	1	0	0	X	3 + 1*
	C ii	1	1	0	X	3
25% IBU / 25% α -LM / 25% PGS / 25% MCC	D i	2	1	X	1	1
	D ii	1	1	X	3	0

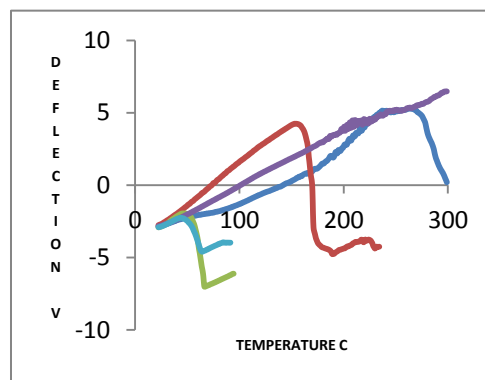
Table 5.10: A summary of the most probable components identified from the nano-TA scans of the 4-component compacts based on ibuprofen shown in Figure 5.29. The number indicates the number of scans assigned to a particular component. X indicates that this component is not present in the compact.

* This result suggests a thin layer of α -LM on top of a bulk layer of MCC.

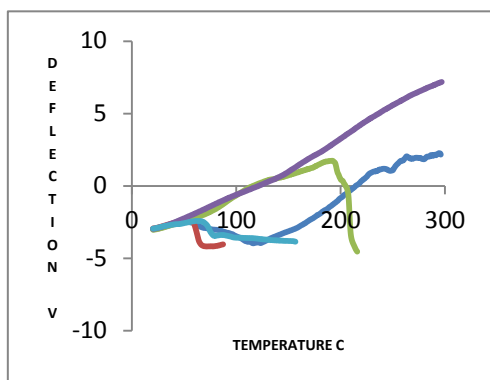
Ai)



Aii)



Bi)



Bii)

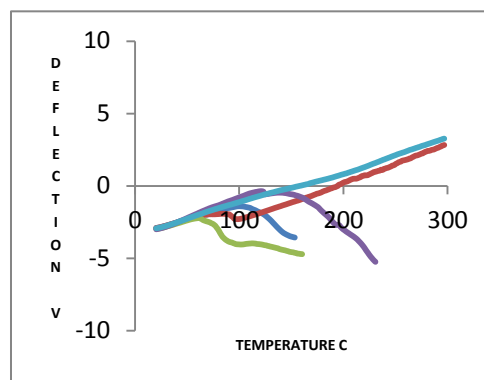


Figure 5.30: Nano-TA results for the 5-component compacts based on ibuprofen, using a nano probe. A) 24.75% IBU / 24.75% α -LM / 24.75% MCC / 24.75% PGS / 1% MS. B) 20% IBU / 20% α -LM / 20% MCC / 20% PGS / 20% MS. Position on the compact is given by i) centre, ii) outside. Five readings were taken at each position: dark blue - site 1, red - site 2, green - site 3, purple - site 4, light blue - site 5.

Formulation	Compact	Components identified (number of sites; maximum = 5)				
		IBU	α -LM	MS	MCC	PGS
24.75% IBU / 24.75% α -LM / 24.75% MCC / 24.75% PGS / 1% MS	A i	0	1	0	3 + 1*	0
	A ii	2	1	0	1	1
20% IBU / 20% α -LM / 20% MCC / 20% PGS / 20% MS	B i	2	1	0	1	1
	B ii	1	1	1	1 + 1**	0

Table 5.11: A summary of the most probable components identified from the nano-TA scans of the 5-component compacts based on ibuprofen shown in Figure 5.30. The number indicates the number of scans assigned to a particular component. X indicates that this component is not present in the compact.

* This result suggests a thin layer of α -LM on top of a bulk layer of MCC.

** This result suggests a thin layer of ibuprofen on top of a bulk layer of MCC.

5.3.3.3 TTM

TTM was performed on the same compacts as AFM and nano-TA. Representative scans are shown in Figures 5.31, 5.32, 5.33 and 5.34 for the two-, three-, four- and five-component compacts, respectively. The issues with interpretation discussed previously for the excipient-only and caffeine-containing compacts apply equally here. In addition, the low temperature "noise" discussed before, usually shown as a dark blue colouration, occurs in the same temperature (and hence colour) range as the thermal event for ibuprofen, so there is potentially some difficulty in definitively assigning a transition to ibuprofen.

In the binary compacts of ibuprofen and MS, most of the thermal events were recorded at circa 50°C, but occasionally some were noted at the slightly higher temperature of circa 75°C. This has been assigned to ibuprofen as it occurs at too low a temperature for MS and some variability was observed in the nano-TA response of ibuprofen, shown in Chapter 4. Ibuprofen was easily distinguished from the other three excipients in the binary compacts as the thermal events were well separated and hence the colouration was clearly different. MS was difficult to detect in the compacts containing only 1% MS, which is related to the chance of the probe landing on a region containing MS. This is illustrated in Figures 5.32 A and C, where the main responses are due to ibuprofen and α -LM or PGS, respectively, and a few squares with a purple colouration are assigned as MS. As noted before, TTM has difficulty separating MCC and PGS as neither has a clear transition, so are assigned the orange colour corresponding to the highest temperature studied.

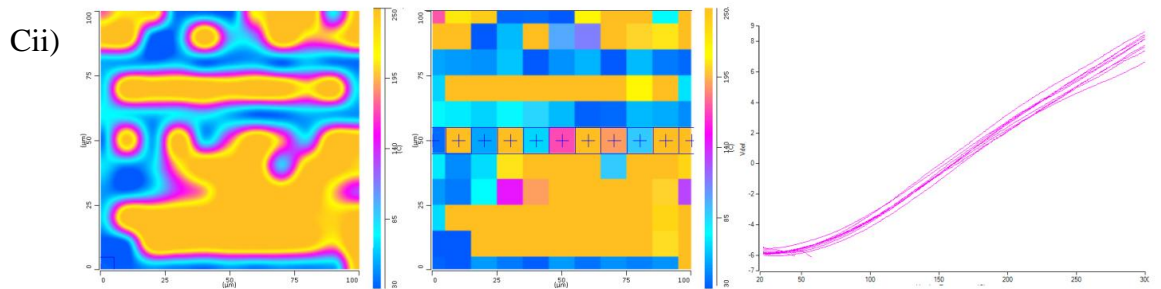
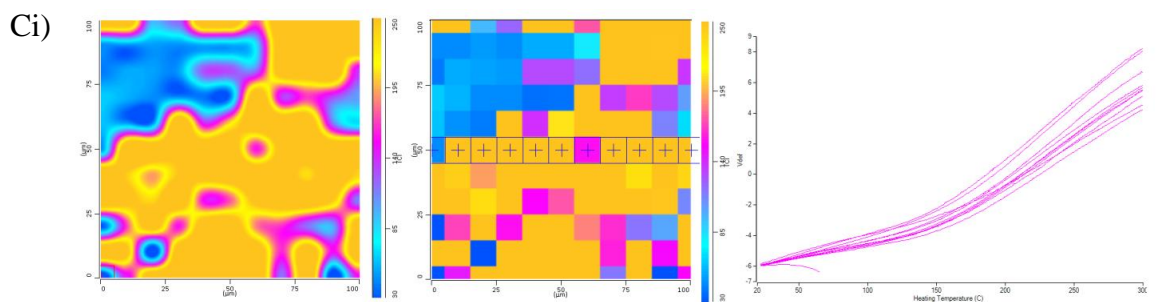
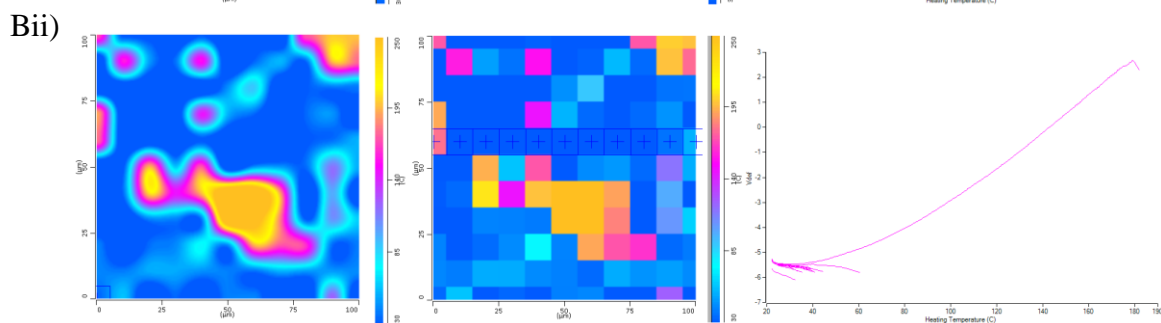
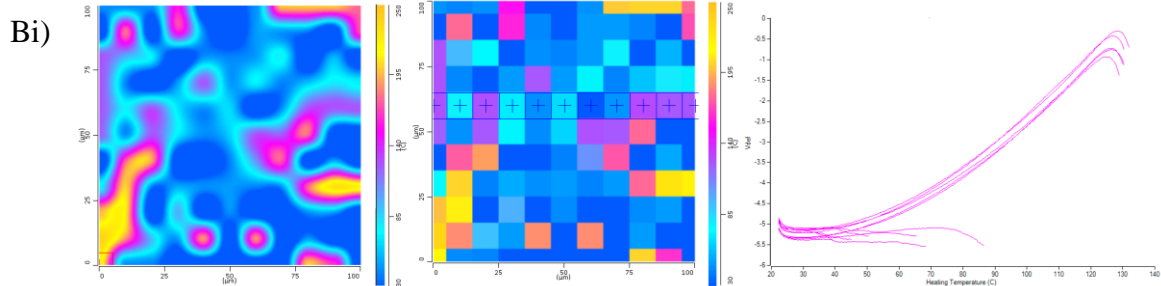
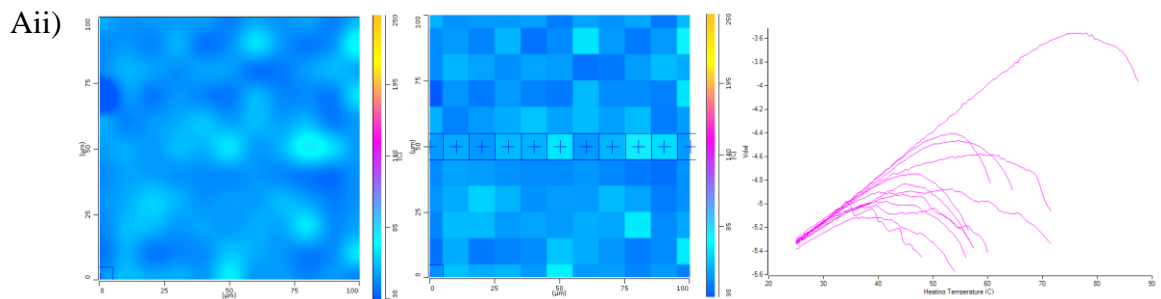
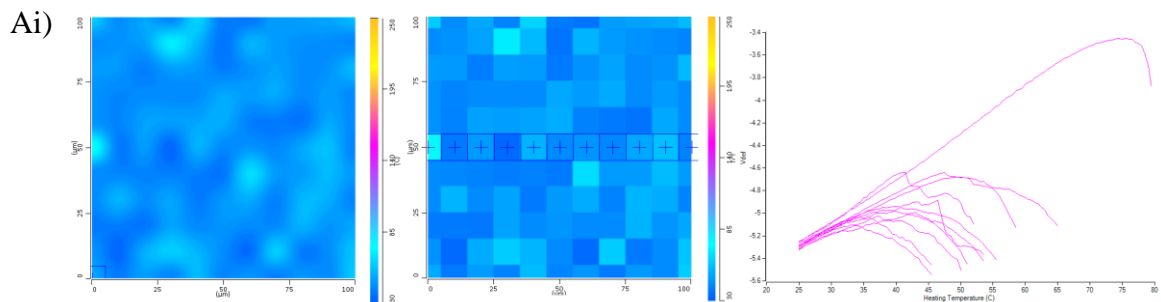
Some unusual results were also obtained, which may be related to instrument issues. For example, Figure 5.32 B shows the two colours expected for ibuprofen and MCC (blue and orange, respectively), but also a few pixels with a pink colouration. This would normally be assigned to α -LM but there is no α -LM in this formulation, and the third component, MS, would normally be expected to show a purple colouration because of the temperature of its thermal transition. It may be that the instrument has detected noise and therefore stopped the run too early, or has detected a slight curve in the result line and allotted this as the end point and coloured the pixel as such.

As before, some differences were noted between the outside and centre positions on the surface of the compact, but this is probably due to the distribution of material across the surface.

Column 1

Column 2

Column 3



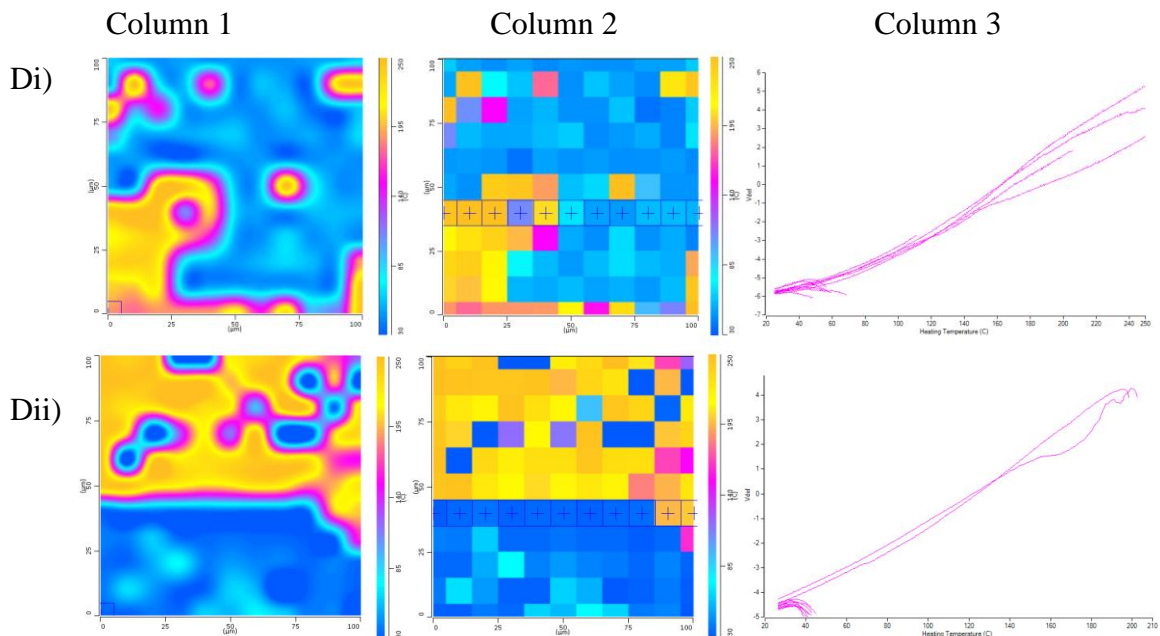
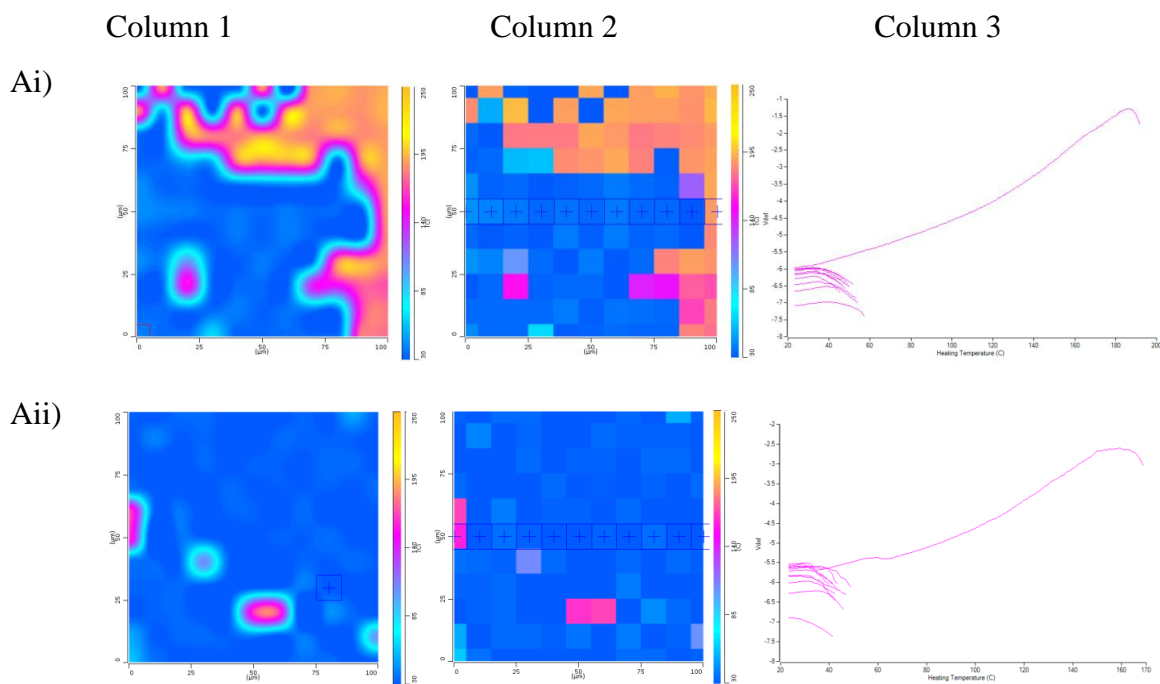


Figure 5.31: TTM maps for 2-component compacts based on ibuprofen, with representative colours. A) 99% IBU (blue) / 1% MS (not detected). B) 50% IBU (blue) / 50% α -LM (yellow / pink). C) 50% IBU (blue) / 50% MCC (yellow / pink). D) 50% IBU (blue) / 50% PGS (yellow / pink). Position on the compact is given by i) centre, ii) outside. Column 1 is the interpolated (smoothed) map, Column 2 is the discrete map, and Column 3 shows the individual nano-thermal results taken at the crossed points (+) on the discrete map.



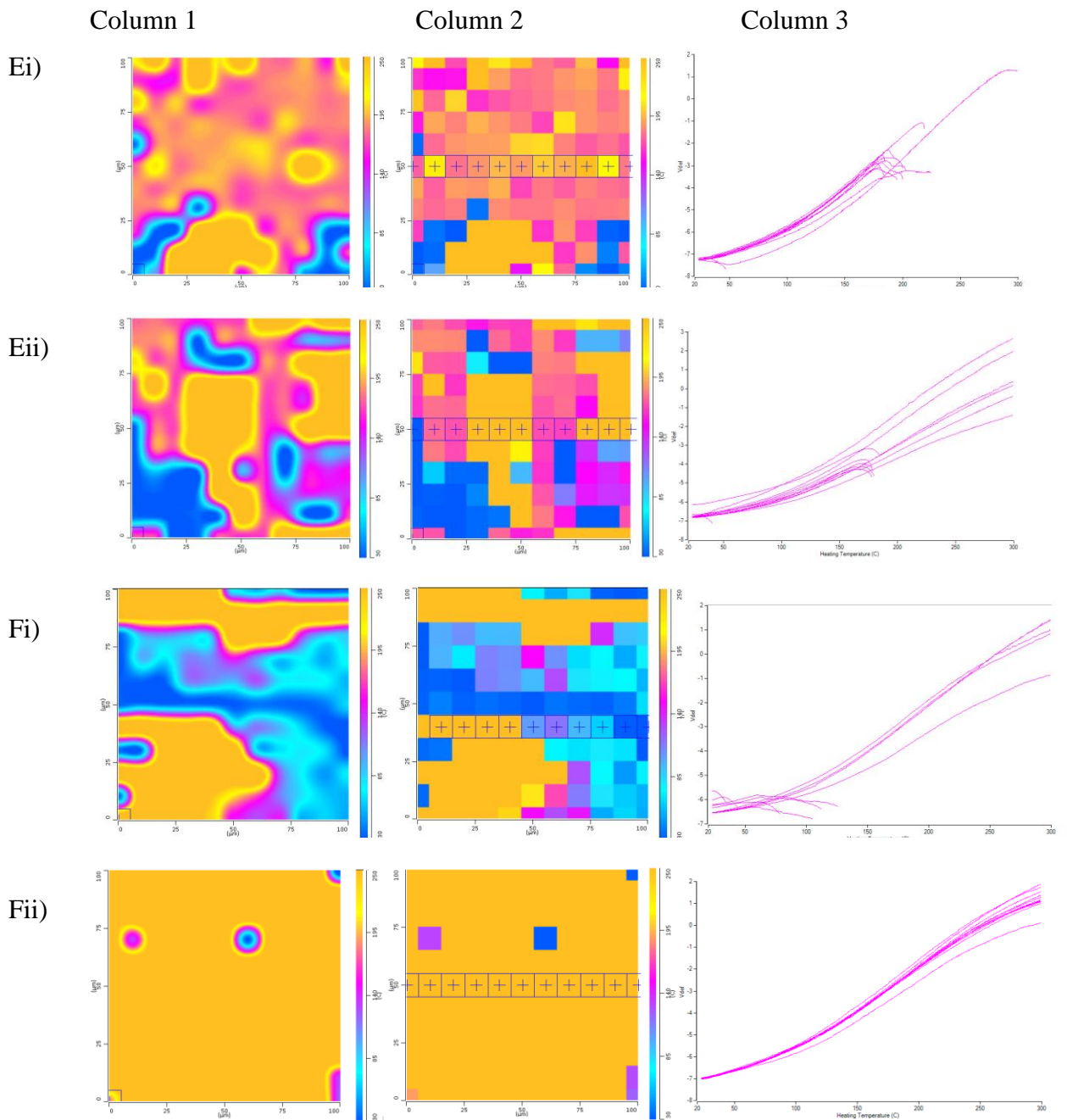


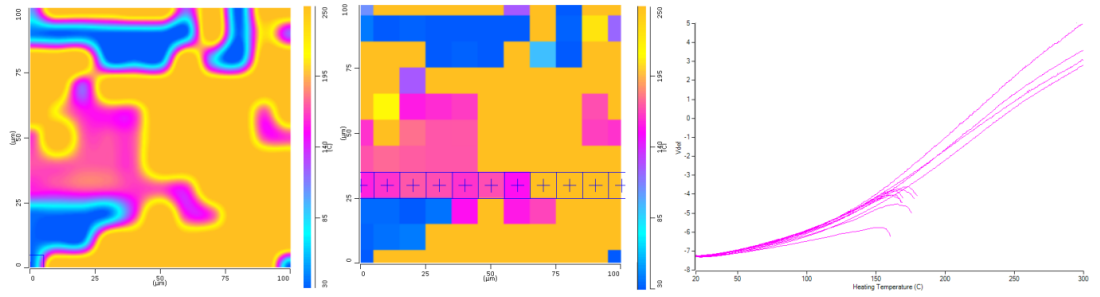
Figure 5.32: TTM maps for 3-component compacts based on ibuprofen, with representative colours. A) 49.5% IBU (blue) / 49.5% α -LM (pink / orange) / 1% MS (purple). B) 49.5% IBU (blue) / 49.5% MCC (yellow) / 1% MS (not detected). C) 49.5% IBU (blue) / 49.5% PGS (yellow) / 1% MS (purple). D) 33.3% IBU (blue) / 33.3% α -LM (pink) / 33.3% PGS (yellow). E) 33.3% IBU (blue) / 33.3% α -LM (pink) / 33.3% MCC (yellow). F) 33.3% IBU (blue) / 33.3% MCC (yellow) / 33.3% PGS (yellow). Position on the compact is given by i) centre, ii) outside. Column 1 is the interpolated (smoothed) map, Column 2 is the discrete map, and Column 3 shows the individual nano-thermal results taken at the crossed points (+) on the discrete map.

Column 1

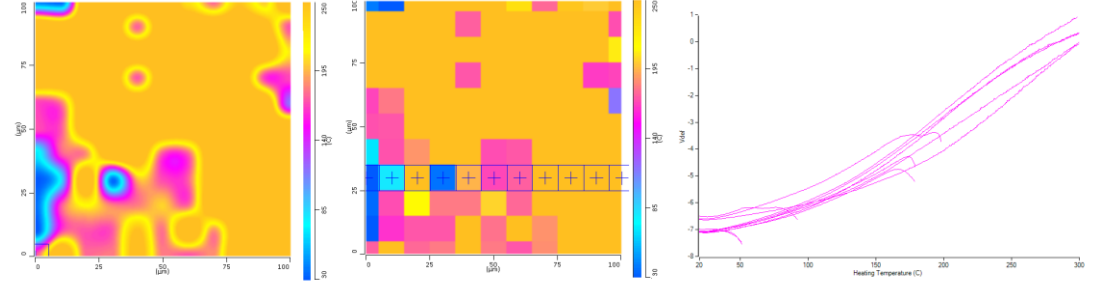
Column 2

Column 3

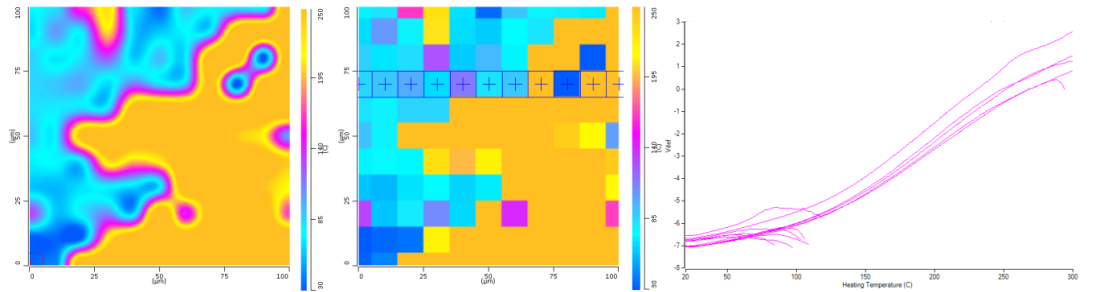
Ai)



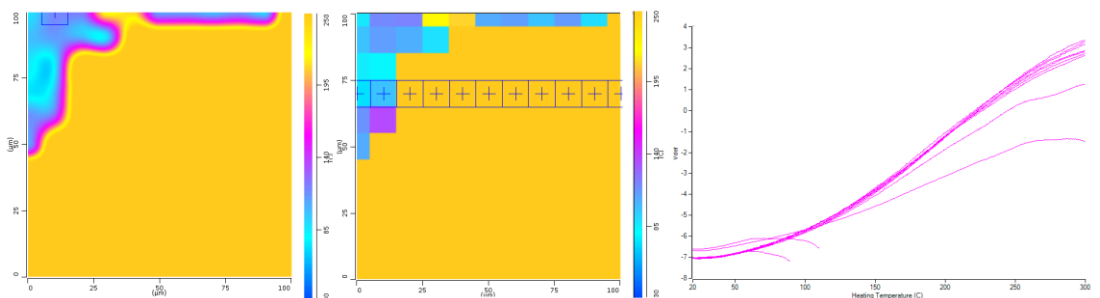
Aii)



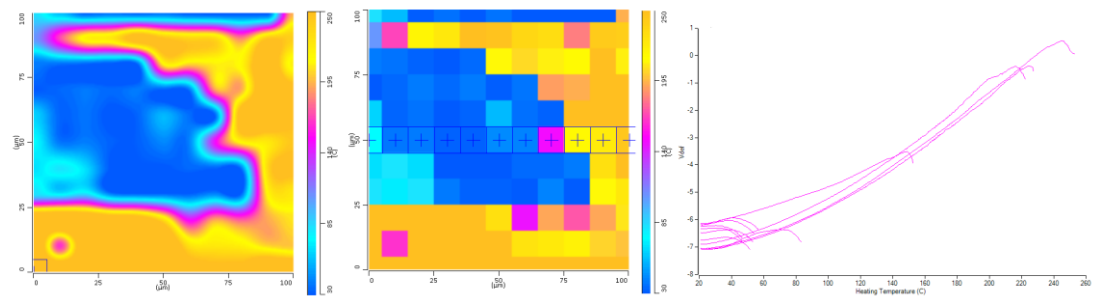
Bi)



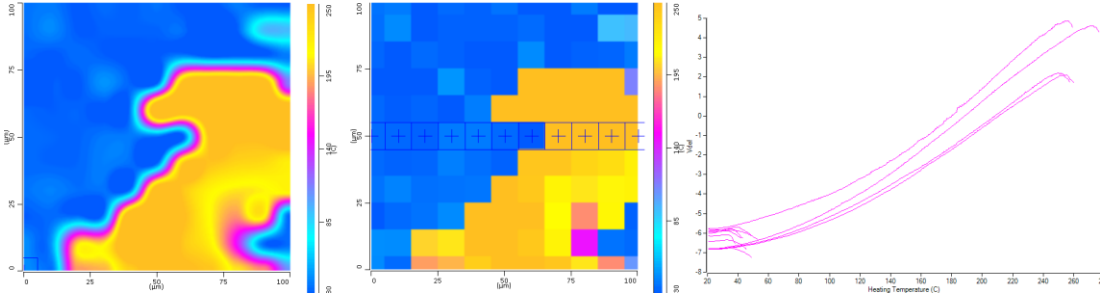
Bii)



Ci)



Cii)



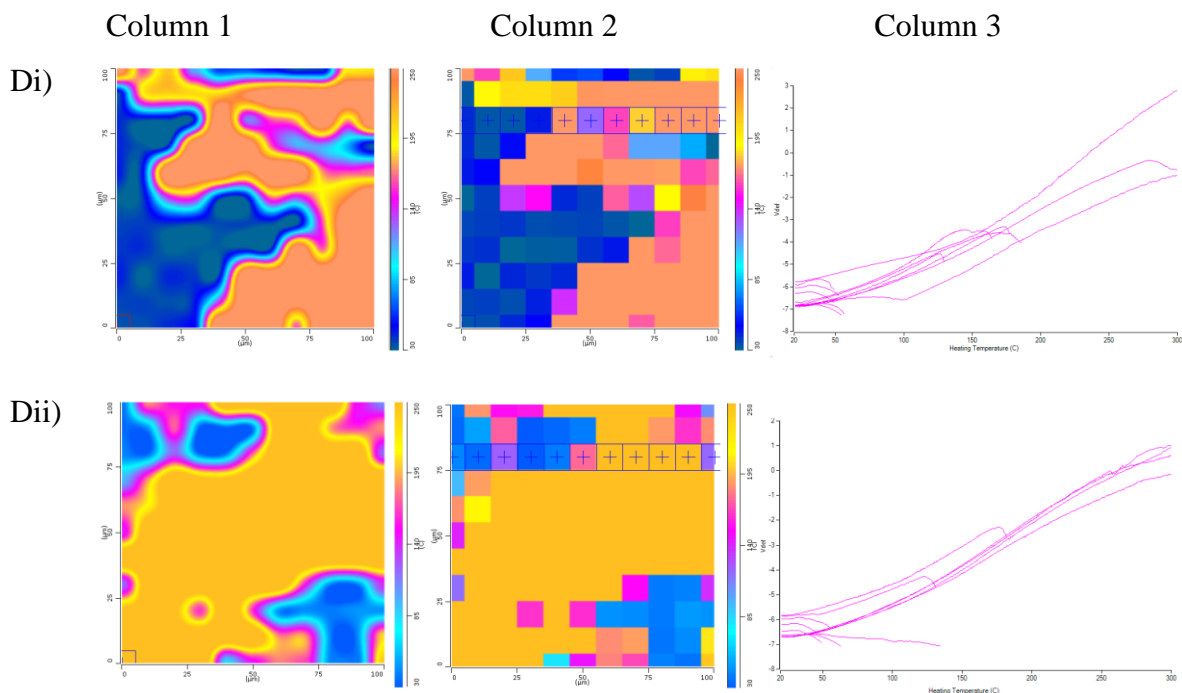
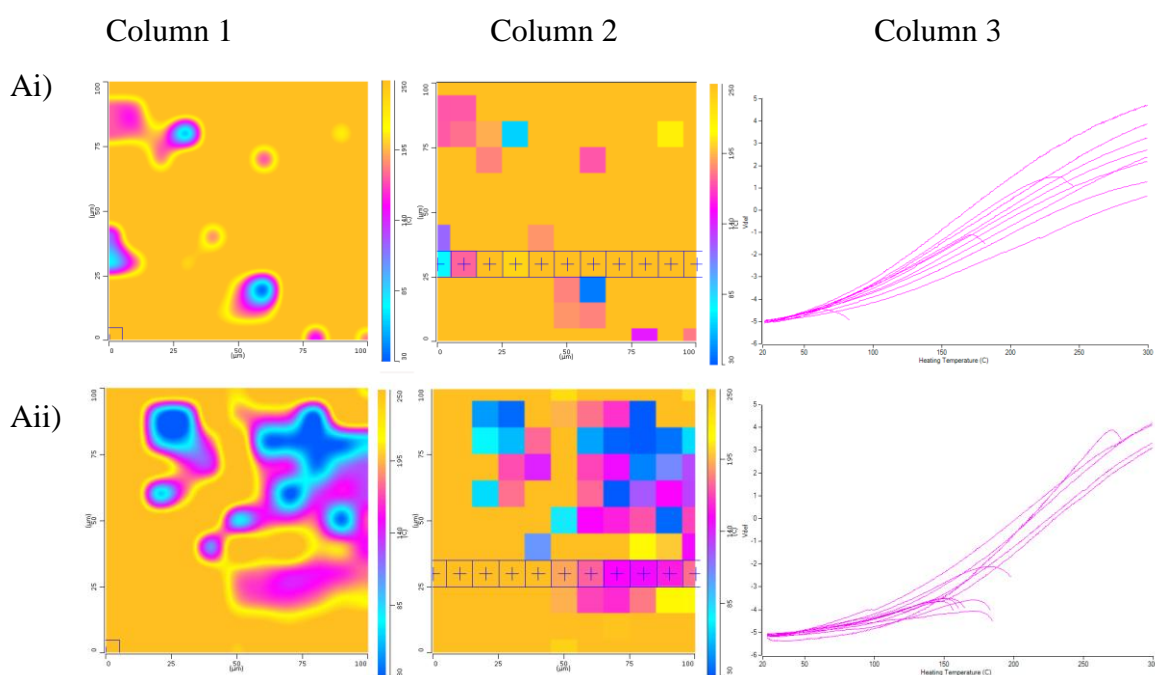


Figure 5.33: TTM maps for 4-component compacts based on ibuprofen, with representative colours. A) 33% IBU (blue) / 33% α -LM (pink) / 33% MCC (yellow) / 1% MS (purple). B) 33% IBU (blue) / 33% MCC (yellow) / 33% PGS (yellow) / 1% MS (purple). C) 33% IBU (blue) / 33% α -LM (pink) / 33% PGS (yellow) / 1% MS (purple). D) 25% IBU (blue) / 25% α -LM (pink) / 25% PGS (yellow) / 25% MCC (yellow). Position on the compact is given by i) centre, ii) outside. Column 1 is the interpolated (smoothed) map, Column 2 is the discrete map, and Column 3 shows the individual nano-thermal results taken at the crossed points (+) on the discrete map.



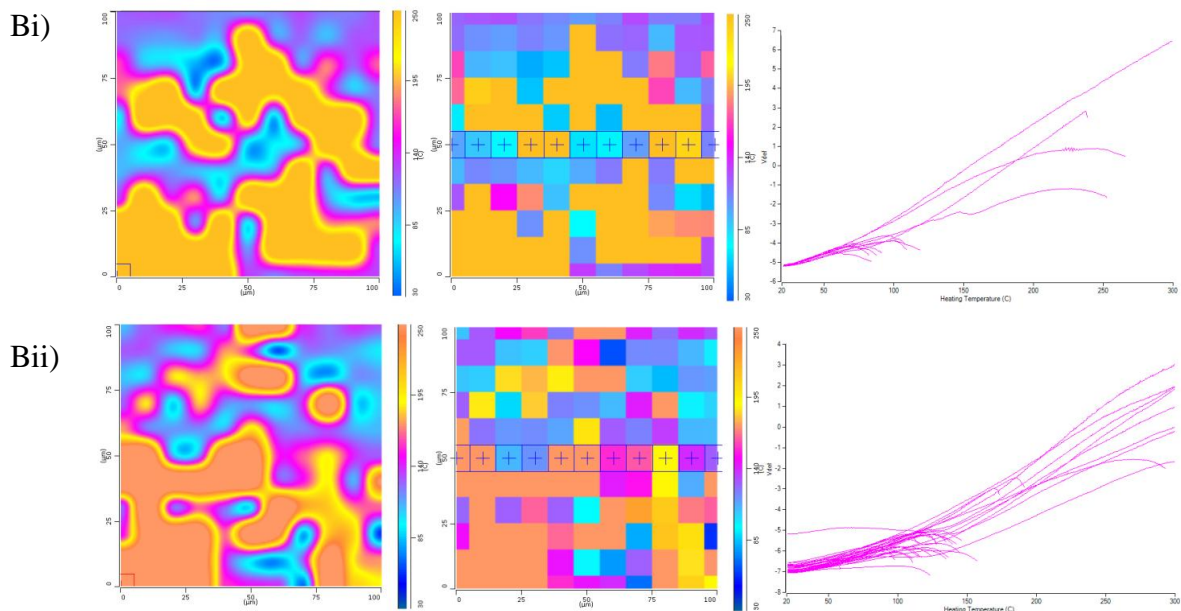


Figure 5.34: TTM maps for 5-component compacts based on ibuprofen, with representative colours. A) 24.75% IBU (blue) / 24.75% α -LM (pink) / 24.75% MCC (yellow) / 24.75% PGS (yellow) / 1% MS (purple). B) 20% IBU (blue) / 20% α -LM (pink) / 20% MCC (yellow) / 20% PGS (yellow) / 20% MS (purple). Position on the compact is given by i) centre, ii) outside. Column 1 is the interpolated (smoothed) map, Column 2 is the discrete map, and Column 3 shows the individual nano-thermal results taken at the crossed points (+) on the discrete map.

5.3.3.4 General discussion for the multi-component compacts containing ibuprofen

The conclusions to be drawn from the ibuprofen-containing compacts are the same as for the excipient-only and caffeine-containing compacts, with the same issues having been identified in terms of overlapping transitions and double endpoints.

5.4 Conclusions

This Chapter builds on the results presented in Chapters 3 and 4, with the intention of establishing the ability of the novel techniques of nano-TA and TTM to determine the distribution of materials across the surface of a multi-component compact. Data presented in Chapters 3 and 4 suggested that each of the excipients (α -LM, MCC, PGS and MS) and drugs (caffeine and ibuprofen) studied had a distinctive thermal profile, which should maximise the chance of the techniques being able to separate them in a mixed sample.

AFM, nano-TA and TTM were performed on all possible permutations of excipient-only, caffeine-based and ibuprofen-based compacts containing two, three, four or five components. In most cases, the materials were used in an even ratio, e.g. for a three-component compact the materials were each present in one-third quantities. Magnesium stearate was the exception to this, in that it was added to most formulations at 1 %w/w, reflecting its use in real tablet formulations, with the remaining ingredients being added equally. However, a four-excipient mixture was prepared using 25 %w/w of all ingredients and two five-component mixtures, one for each drug, were prepared with 20%w/w of each material, in order to determine whether MS could be identified in these formulations.

The results for the three parallel studies (excipient-only, caffeine-based and ibuprofen-based) were compatible with each other. AFM was conducted primarily run to detect any topographical features which could affect the nano-TA readings, but was also used to assess whether any regions of material could be identified simply by the texture of the surface. This was possible with mono-component or binary components, but proved unreliable as the number of components in the compact increased. If AFM is to be used to assess the distribution of materials across the surface of the compact, then a different mode of AFM could be used, e.g. tapping mode with a heated probe. This would have the advantage of (possible) improved detection as each material would be expected to respond according to its thermal profile. However, it would have the disadvantage of not permitting the nano-TA to be conducted on the same region of the compact, as once it is heated, the sample is effectively destroyed.

Nano-TA was performed on all the compacts, taking five readings at each location on the compact's surface. All materials could be identified using the nano-TA technique by reference to the nano-TA profiles of the single component compacts (Figure 5.1). In some cases, though, the difference between materials was subtle and required close examination of the nano-TA profiles for identification. For example, neither MCC nor PGS (e.g. Figure 5.6 C) showed a true thermal transition across the temperature range studied, but rather a change in the baseline, as a result of general thermal expansion to be expected of all samples. The change in the baseline was different for the two materials, so allowed assignment of a particular trace to one or other of the materials. Occasionally, a trace showed a mini-endpoint or a "dip" on the baseline before it demonstrated a true endpoint

(e.g. Figure 5.18 Bi). This was ascribed to the presence of a thin layer of one material on top of a material with a higher temperature thermal event. The probe would heat the top layer until it penetrated (moved downwards) and the deflection registered. When the probe encountered the underpinning layer it would stop moving and nothing further would be registered until the underpinning layer showed its transition, at which point the "true" endpoint would be registered and the experiment terminated. Detecting a thin layer of a material with a high temperature thermal event on top of a layer of material with a low temperature thermal event is more difficult, as the probe will not be expected to penetrate the top layer at a temperature below the transition point of the underpinning layer. However, if the top layer is thin enough, the heat from the probe may diffuse through the top layer to the bottom layer, allowing it to react, soften and possibly move. This may then give rise to an unsteady baseline or an apparent early start to the thermal event of the top layer. Some of the traces seen here may be explained by this mechanism (e.g. Figure 5.27 D ii).

TTM was used to generate maps across the surface of the compacts, showing the distribution of the various components. It is essentially an automated version of the nano-TA technique, in which grids of almost any size and number of points can be generated (allowing for limitations on experimental time). Here, 11 x 11 grids were generated, i.e. 121 points in total, over an area of 100 μm x 100 μm . The TTM software takes the measured transition endpoint and assigns a colour to it based on a temperature-colour scale. Thus a visual colour map is produced which will allow examination of the distribution of components across the surface, but will not actually identify individual materials. Two materials which show a similar transition temperature will show a similar colour (e.g. caffeine and the highest temperature MS (e.g. Figure 5.19 A)), which leads to problems in identifying which pixel relates to which material. Similarly, materials which do not show a thermal event within the temperature window studied (e.g. MCC and PGS (e.g. Figure 5.8 F) will all be assigned colour, again leading to issues with identification. These materials can be identified manually by examining the traces for each individual pixel and comparing them to the mono-component traces, but this is time consuming and negates the advantage of the automated technique. Alternatively, if more control could be given to the analyst on setting the colour-temperature boundaries based on knowledge of the materials under study, it may be possible to manipulate the scale, i.e. to stretch it in one temperature range and constrict it in another, so that all materials can be separated.

Experimental set-up issues, such as vibration in the lab may cause issues with endpoint detection (e.g. Figure 5.8 C ii dark blue regions are noise), as any probe movement will be registered and will potentially lead to erroneous results if it is due to vibration rather than actual sample behaviour. It is recommended that the equipment is used only in secure environments where traffic is kept to a minimum and it is used on an appropriate air table. Unlike the nano-TA technique, in which a topographical AFM image is taken before the nano-TA profiles are measured, the TTM is effectively a stand-alone technique. This is because it is based on an optical microscope, rather than an AFM as in the nano-TA technique, and an optical microscope will not have sufficient resolution to examine the surface of the sample in enough detail. Hence, any roughness which may affect the measurements will not be identified in TTM, unlike in the AFM-nano-TA system, and potentially spurious results may be obtained.

The most serious issue with the TTM technique is the smoothing process used to produce the interpolated (smooth, non-pixelated) maps. The software processes interfaces between two materials of different thermal characteristics (i.e. where a different colour has been assigned to each) as being composed of a third material of intermediate thermal behaviour and hence an intermediate colour. If the two materials are at opposite end of the temperature (and hence colour spectrum), then the interface will appear to be composed of multiple colours, suggesting it is composed of multiple materials. Serious mis-interpretation of the data may result as a consequence and it is therefore strongly recommended that only the pixelated images are used for analysis.

Even allowing for these issues, both nano-TA and TTM are useful techniques and will be used to study the "real" formulation mini-tablets in Chapter 6.

Chapter 6

The analysis of mini-tablets

CHAPTER 6

The analysis of mini-tablets

6.1 Introduction

In Chapters 3 and 4, the individual excipients and drugs were profiled by a range of analytical techniques and in Chapter 5 nano-TA and TTM were used to analyse complicated multi-component samples. The results from Chapter 5 suggested that all the components studied (α -LM, MCC, PGS, MS, CAF and IBU) can be identified in 2-, 3-, 4- and 5- component mixtures. In this Chapter, nano-TA and TTM were used to assess the spatial distribution of components across the surface of "real" mini- tablets.

Mini-tablets are a relatively new dosage form, so method development batches were produced and tested first, before the experimental batches were produced and analysed. The batches were characterised using standard physical and analytical techniques, before being subject to analysis by nano-TA and TTM.

6.2 Materials and Methods

Chapter 2 gives details of the analytical methods employed here. The excipients used here (α -LM, MCC, PGS, MS and PVP) were described in Chapter 2 in terms of their chemical and physical properties and were profiled analytically in Chapter 3. The drugs used here (caffeine and ibuprofen) were described in Chapter 2 in terms of their chemical and physical properties and were profiled analytically in Chapter 4.

6.2.1 Production of the mini-tablets

In total, five batches of mini-tablets were produced: two development batches and three experimental batches. The development batches were used to refine the manufacturing processes and analytical procedures, with the experimental batches being used to generate results. The formulations of all five batches are detailed in Table 6.1. Both development batches were excipients-only, one being a direct compression formulation and the other being a wet granulated formulation. PVP was used at 2 %w/w in the wet granulated

formulation, replacing 1 %w/w each of α -LM and MCC. All three experimental batches were wet granulated. The excipients-only batch had the same formulation as the development batch and the two drug-loaded batches were based on this formulation, replacing 5 %w/w each of α -LM and MCC with the drug.

Component	Development batches		Experimental batches		
	Direct compression	Wet granulated	Excipients only	Ibuprofen-based	Caffeine-based
Drug	0 %	0 %	0 %	10 %	10 %
α -LM	68 %	67 %	67 %	62 %	62 %
MCC	21 %	20 %	20 %	15 %	15 %
PGS	10 %	10 %	10 %	10 %	10 %
MS	1 %	1 %	1 %	1 %	1 %
PVP *	0 %	2 %	2 %	2 %	2 %
Water **	0%	q.s.	q.s.	q.s.	q.s.

Table 6.1: Formulation of the mini-tablets

* PVP was added as a 15 %w/v aqueous solution to the wet granulated batches.

** Water was added as required to form a good granule. The volume required was approximately 60 mL, but this varied between batches.

Mixing, granulation, drying and lubrication were performed as described in Chapter 2, at a batch scale of 750 g for the development batches and 100 g for the experimental batches. As it has previously been established within the research group that particle size control is extremely critical for successful production of mini-tablets, granules were wet sieved through a 500 μ m mesh prior to drying in order to remove particles larger than this. After drying but before lubrication the granules were again sieved through a 500 μ m mesh to remove larger particles, with any fine particles passing through a 125 μ m mesh also being discarded. Control of powder flow and particle size is essential for mini-tablet production to stop the die blocking (Flemming and Mielck (1995), Kachrimanis et al (2005)). The lubricated powder mix or granules was then compressed on an instrumented Piccola rotary tablet press (Riva, Argentina) using 2 mm diameter normal concave tooling. For the development batches, two stations were used and for the experimental batches, three stations were used.

6.2.2 Analysis of the mini-tablets

Each batch of mini-tablets was physically characterised in terms of weight uniformity, thickness, hardness (resistance to crushing) and friability. Content uniformity assays were carried out for the two drug-loaded batches. DSC was performed on both the powder mix / granule and the compressed mini-tablets. The surface of the mini-tablets was assessed for component distribution using AFM, nano-TA and TTM. All analytical procedures are described in Chapter 2.

6.3 Results and Discussion

6.3.1 Granules

Figure 6.1 shows the SEM images of the mixed powders used in the direct compression development batch and the granules produced from the wet granulated development batch. The SEM image of the direct compression powder mix (Figure 6.1 A) illustrates the different sizes and shapes of the various formulation components, as previously shown in Chapter 3. The SEM images of the granule (Figure 6.1 B and C) indicate that the granulation process was successful at incorporating the different components into a granule, increasing the particle size and generating a more reproducible product.

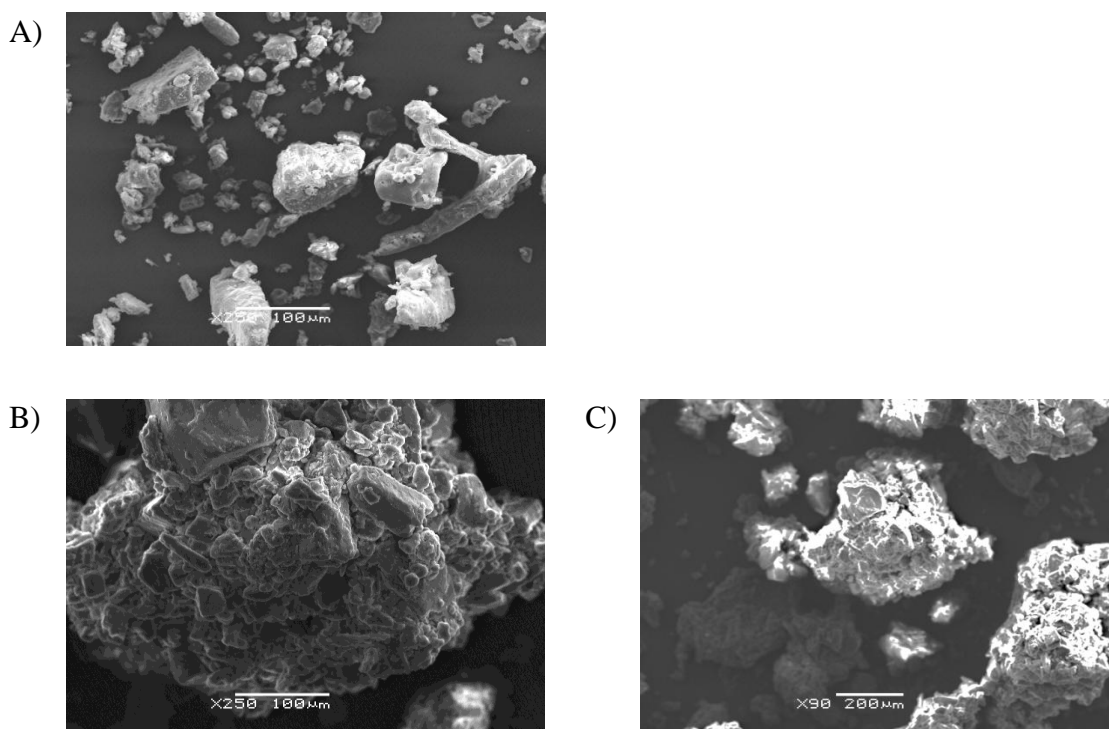


Figure 6.1: SEM images of powders and granules. A) Powder mix for the direct compression batch, magnification X250. B) Wet granulated granules, magnification X250. C) Wet granulated granules, magnification X90.

6.3.2 Tablet production

From the work presented in Chapter 3, it was seen that compacts made using the higher compaction pressure showed more reproducible surface analysis. Hence, the mini-tablets needed to be compressed to a similar or higher pressure in order to generate good images and to facilitate comparison with the results from the compacts.

In order to compare the different shaped compacts/tablets the applied pressure (force per unit area) needs to be calculated. The 13 mm compacts were compacted to 2 tons, which converts to a pressure of 148 MPa for these compacts. The development batches of mini-tablets were compressed at 383 MPa and the experimental batches were compressed at 404 MPa, 304 MPa and 428 MPa for the excipient batch, the ibuprofen-loaded batch and the caffeine-loaded batch, respectively.

The punch design for the mini-tablets includes a small "lip" area around the outside of the punch as well as the normal curved "dome" surface (normal concave for the punches, normal convex for the tablets). As a consequence, calculation of the surface area of the mini-tablets is slightly more complicated as both the lip and the dome areas need to be considered. Similarly, the compression force is not necessarily applied evenly across a flat and a curved surface, hence the pressure calculation results in an average value, which may not be exactly true at all points. However, it is sufficient for this first line analysis.

Calculation 6.1 Pressure used to prepare the compacts used in previous chapter

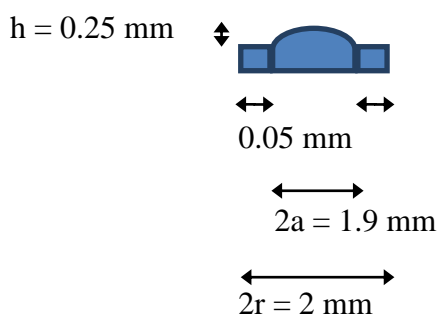
- Surface area (m²) = πr^2 (where r = radius)
 = $\pi \times (6.5 \times 10^{-3})^2 = 1.327 \times 10^{-4} \text{ m}^2$

- Force (kN) = Force (tonnes) x 9.806
 = 19.612 kN

- Pressure (MPa) = Force / area
 = 19.928 kN / $1.327 \times 10^{-4} \text{ m}^2$
 = 147792 kN/m²
 = 147792 kPa
 = 148 MPa

Calculation 6.2: Pressure used to prepare the mini-tablets

Dome part of tablet surface



Lip part of tablet surface



$$\begin{aligned}
\text{Surface area of dome (m}^2\text{)} &= \pi (a^2 + h^2) \\
&= \pi ((0.95 \times 10^{-3})^2 + (0.25 \times 10^{-3})^2) \\
&= 3.032 \times 10^{-6} \text{ m}^2
\end{aligned}$$

$$\begin{aligned}
\text{Surface area of larger circle (i) (m}^2\text{)} &= \pi r^2 \\
&= \pi \times (1 \times 10^{-3})^2 \\
&= 3.142 \times 10^{-6} \text{ m}^2
\end{aligned}$$

$$\begin{aligned}
\text{Surface area of smaller circle (ii) (m}^2\text{)} &= \pi r^2 \\
&= \pi \times (0.95 \times 10^{-3})^2 \\
&= 2.835 \times 10^{-6} \text{ m}^2
\end{aligned}$$

$$\begin{aligned}
\text{Surface area of lip (m}^2\text{)} &= \text{(i) - (ii)} \\
&= 3.07 \times 10^{-7} \text{ m}^2
\end{aligned}$$

$$\begin{aligned}
\text{Total surface area of mini-tablet} &= \text{surface area of dome} + \text{surface area of lip} \\
&= 3.032 \times 10^{-6} \text{ m}^2 + 3.07 \times 10^{-7} \text{ m}^2 \\
&= 3.339 \times 10^{-6} \text{ m}^2
\end{aligned}$$

Development batches

- Average force = 1.3 kN
- Pressure (MPa) = Force / area
 - = 1.3 kN / $3.339 \times 10^{-6} \text{ m}^2$
 - = 383480 kN/m²
 - = 383480 kPa
 - = 383 MPa

Experimental batch - excipient only

- Average force = 1.35 kN
- Pressure (MPa) = Force / area
 - = 1.35 kN / $3.339 \times 10^{-6} \text{ m}^2$
 - = 404313 kN/m²
 - = 404313 kPa
 - = 404 MPa

Experimental batch - ibuprofen-loaded

- Average force = 1.03 kN
- Pressure (MPa) = Force / area
= $1.03 \text{ kN} / 3.339 \times 10^{-6} \text{ m}^2$
= 303834 kN/m²
= 303834 kPa
= 304 MPa

Experimental batch - caffeine-loaded

- Average force = 1.43 kN
- Pressure (MPa) = Force / area
= $1.43 \text{ kN} / 3.339 \times 10^{-6} \text{ m}^2$
= 428272 kN/m²
= 428272 kPa
= 428 MPa

All five batches were compressed at forces which equated to pressures higher than those used in the preparation of the compacts, hence the surface should be sufficiently smooth to allow high-quality images to be obtained.

Compression was successful for all five batches. The compression parameters were kept largely the same for all batches, bearing in mind that each was a novel formulation and the parameters were adjusted slightly as necessary to achieve a suitable product. Two tooling stations were used for the development batches and three for the experimental batches. The number of mini-tablets compressed per batch was between 3500 and 5000. Figure 6.2 shows an example of the force exerted by the upper punch during a compression cycle, indicating the compression zone (sharp peak in the force at the start of the cycle), the time that the upper punch remains in contact with the granule after compression (the constant force zone) and the ejection zone (no force being applied by the upper punch). All compression profiles for all batches of mini-tablets were very similar.

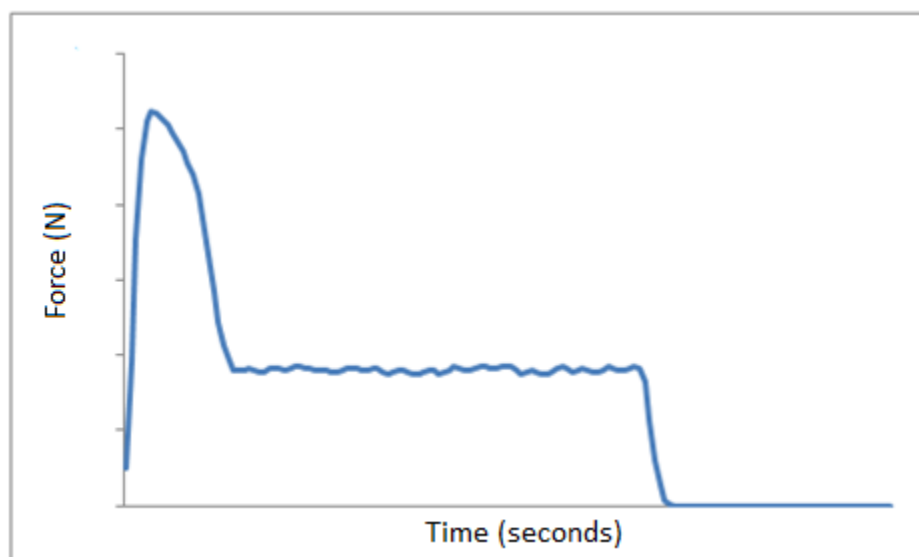


Figure 6.2: A typical example of the force exerted by the upper punch during a compression cycle for a mini-tablet. The profile was obtained from the tablet press during compression.

6.3.3 Tablet analysis

6.3.3.1 Physical characterisation of the development mini-tablet batches

In common with any tablet batch, the development batches produced here were characterised physically for weight uniformity, hardness (resistance to crushing), thickness and friability. However, there are issues in testing mini-tablets as the pharmacopoeial specifications and testing procedures are designed for standard size tablets (e.g. 7 mm in diameter) and may not apply particularly well to mini-tablets as these are so small (typically 2 mm in diameter). In this work, the British Pharmacopeia (BP) 2013 and previous published mini-tablet work was used as guidelines.

6.3.3.1.1 Weight uniformity

For the assessment of weight uniformity, 20 tablets were individually weighed. The BP 2013 states that for tablets of less than 40 mg weight, weight uniformity is not performed, but rather uniformity of content of the active material is assessed. However, as the development mini-tablet batches are placebo, i.e. they do not contain drug, weight

uniformity was performed. For uncoated tablets of less than 80 mg weight, the BP 2013 specification is that the weight of no more than two of the tablets deviates by more than 10 % of the mean value and none of the tablets deviate by more than 20 % of the mean weight. The results are shown in Table 6.2 and demonstrate that both development mini-tablet batches meet this requirement.

A slight difference in the mean weight and the weight uniformity was seen between the two batches. The wet granulated tablets were on average ~0.5 mg lighter than the direct compression tablets, but the weight uniformity was better, as can be seen from the RSD figures of 2.48 % and 3.18 % for the wet granulated and direct compression batches, respectively. The better uniformity of weight for the wet granulated batch could be explained by the granules having been designed to have greater uniformity and better flow properties compared to the simple powder mix used in the direct compressed batches. The lower mini-tablet weight for the wet granulated batch may be explained by the void spaces within and between the granules during filling reducing the total weight of material flowing into the die.

6.3.3.1.2 Hardness

Hardness (resistance to crushing) testing is difficult to perform on mini-tablets using the standard BP 2013 method of moving two flat jaws against the tablet and recording the force required to crush the tablet. Mini-tablets are so small and the force required to crush them so low that it is below the recording / detection limit of the standard equipment. Hence, a texture analyser was used to measure the crushing strength of the mini-tablets, following the general method described by Choonara et al (2006) and detailed in Chapter 2. The mini-tablets were placed on their side during the test in order to mimic as closely as possible the standard BP method of diametral compression. Table 6.2 records the resistance to crushing (as kN) for ten of the mini-tablets testing for weight.

The results suggested the wet granulated mini-tablets are approximately twice as resistant to crushing as the direct compressed mini-tablets and also show slightly less variability in this parameter. Granulation typically produces harder tablets than direct compression, which is attributed to a range of factors, such as the presence of the binder (PVP in this case) and better packing of the granules into the die allowing greater contact and hence stronger binding between neighbouring materials.

Figure 6.3 shows an example of the compression loading profile from the two batches. The probe makes contact with the tablet at 0 mm distance and then the tablet is crushed at ~0.1 mm, with the peak value of the force being recorded as the crushing strength of the tablet. The probe continues moving and crushes some of the tablet fragments at ~1 mm and onwards. It can clearly be seen that there is a difference in the compression loading between the wet granulated and direct compression tablets.

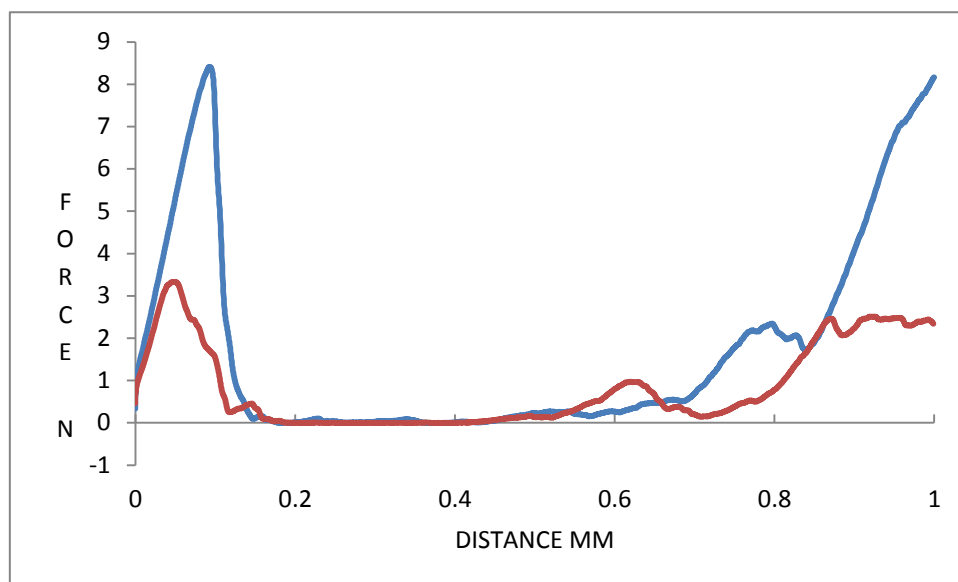


Figure 6.3: The compression loading profile for an example of the wet granulated tablets (red) and the direct compression tablets (blue).

	Wet granulated tablets		Direct compression tablets	
	Weight (mg)	Crushing strength (N)	Weight (mg)	Crushing strength (N)
Mean	8.83	7.54	9.27	3.02
SD	0.22	1.62	0.30	0.71
RSD	2.48 %	21.47 %	3.18 %	23.48 %
Mean + 10 %	9.71		10.20	
Mean - 10 %	7.95		8.34	
Lowest result	8.43	5.09	8.74	2.48
Highest result	9.17	10.03	9.84	4.20

Table 6.2: The weight and crushing strength results for the development batches (SD = standard deviation; RSD = relative standard deviation). (n = 20 tablets)

6.3.3.1.3 Thickness

The thickness of tablets is generally measured manually using callipers. However, due to the small size and handling issues of the mini-tablets, an optical microscopy process was used, whereby images of the mini-tablets were recorded and analysed via the inbuilt software. Figure 6.4 shows the optical micrographs of the two batches with the measured thickness values and Table 6.3 summarises these data. This measurement was performed on a different sub-set of mini-tablets from the weight uniformity and crushing strength testing. Tablets from the two batches showed a similar thickness but the wet granulation batch was slightly thicker and slightly more variable than the direct compression batch.

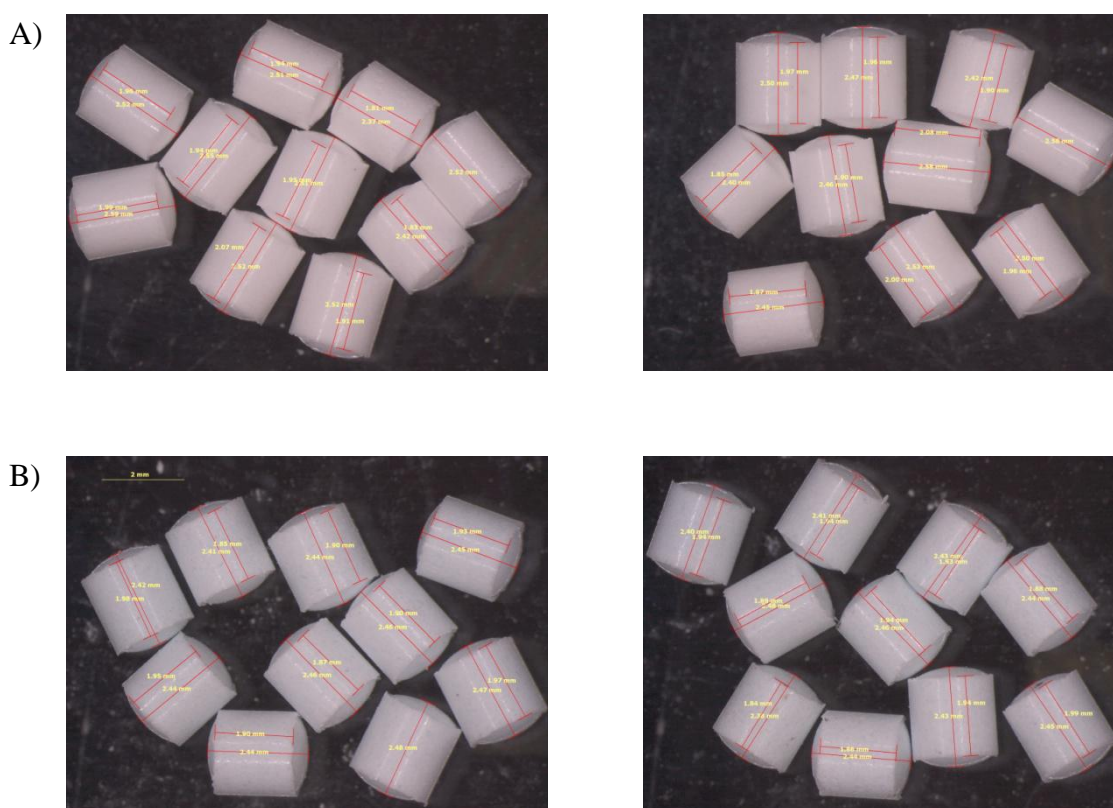


Figure 6.4: The optical microscopy image (magnification X10) of the development mini-tablets batches. A) Wet granulated mini-tablets. B) Direct compression mini-tablets.

	Wet granulated tablets	Direct compressed tablets
	Thickness (mm)	Thickness (mm)
Mean	2.50	2.44
SD	0.06	0.03
RSD	2.44 %	1.08 %
Lowest result	2.37	2.38
Higher result	2.59	2.48

Table 6.3: The thickness results for the development batches (SD = standard deviation; RSD = relative standard deviation) (n = 20 tablets)

6.3.3.1.4 Friability

The strength of the mini-tablets was also measured by the friability. A non-compendial method was used to reduce the number of mini-tablets required to be tested. In this case, 20 mini-tablets were de-dusted and weighed prior to being rotated in the BP apparatus (Erweka tarA friability instrument) 100 times at a speed of 25 revolutions per minute (rpm). The tablets were then de-dusted and weighed again and the weight loss calculated. A weight loss of less than 1 % will allow the tablets to pass the BP friability specification, although this value is quite large and ideally a much lower friability is required.

This method was followed for the two development mini-tablet batches and the results are shown in Table 6.4. Both batches failed this friability test, but the wet granulated batch was slightly better than the direct compression batch. No tablets were seen to be cracked, split or broken, indicating resilience. However, the BP friability equipment is not designed to deal with tablets so small and the BP test method used for granules and spheroids, which more closely resemble the size of mini-tablets, is completely different. It can be argued that a small number of tiny tablets in a large drum will be subject to more damage than the same number of larger tablets, but equally it could be argued that the mini-tablets have to undergo the same mechanical shock and attrition as larger tablets, so should be equally robust. Some authors (e.g. De Brabander et al (2000a) have added glass beads to a small number of mini-tablets in an effort to improve the reliability of the friability testing method. It is obvious that friability testing of mini-tablets needs some refinement before a generally applicable test is available.

Mini-tablet batch	Friability result
Wet granulated	1.42 % weight loss
Direct compression	1.90 % weight loss

Table 6.4: The friability results for the development batches.

6.3.3.1.5 DSC

DSC was performed on whole mini-tablets and the constituent granules / powder in order to assess whether any change in the physical state of the ingredients had occurred on compression.

Figure 6.5 A shows the results for the wet granulated mini-tablet and granules. Overall, the two plots for the wet granulated mini-tablet and the granule are very similar. α -LM dominates both scans, clearly showing both the dehydration endotherm and the melting / decomposition endotherm. The dehydration appears at a slightly higher temperature than was seen when α -LM was analysed as a single-component mini-tablet. Conversely, the melting/decomposition peak occurs at a slightly lower temperature than was seen with the α -LM mini-tablet. This may be caused by the presence of several different materials in the granule/mini-tablet compared to the single-component situation. A very broad endotherm is seen centred around 100°C, which is assumed to be the remaining moisture left in the granules/tablets after the wet granulation and drying processes. A small peak can be seen in both plots (too small to integrate for the tablet plot), which is probably due to the melting of the MS. A separate dehydration peak for MS is not seen, partly because it is present at only a very low level (1 % w/w) but also because it would probably be subsumed into the general water loss peak.

Figure 6.5 B shows the corresponding scans for the direct compression mini-tablets and the powder mix. α -LM dominates the scans, but as it is present in the highest concentration in the formulation this is to be expected. As seen with the wet granulated granules / tablets, the temperature for the dehydration of α -LM is slightly higher and the temperature for the melting / decomposition slightly lower than observed for the pure substance. In these scans, the behaviour of MS is much more obvious than in the scan of the wet granulated formulation, with both the dehydration and melting peaks being clearly seen.

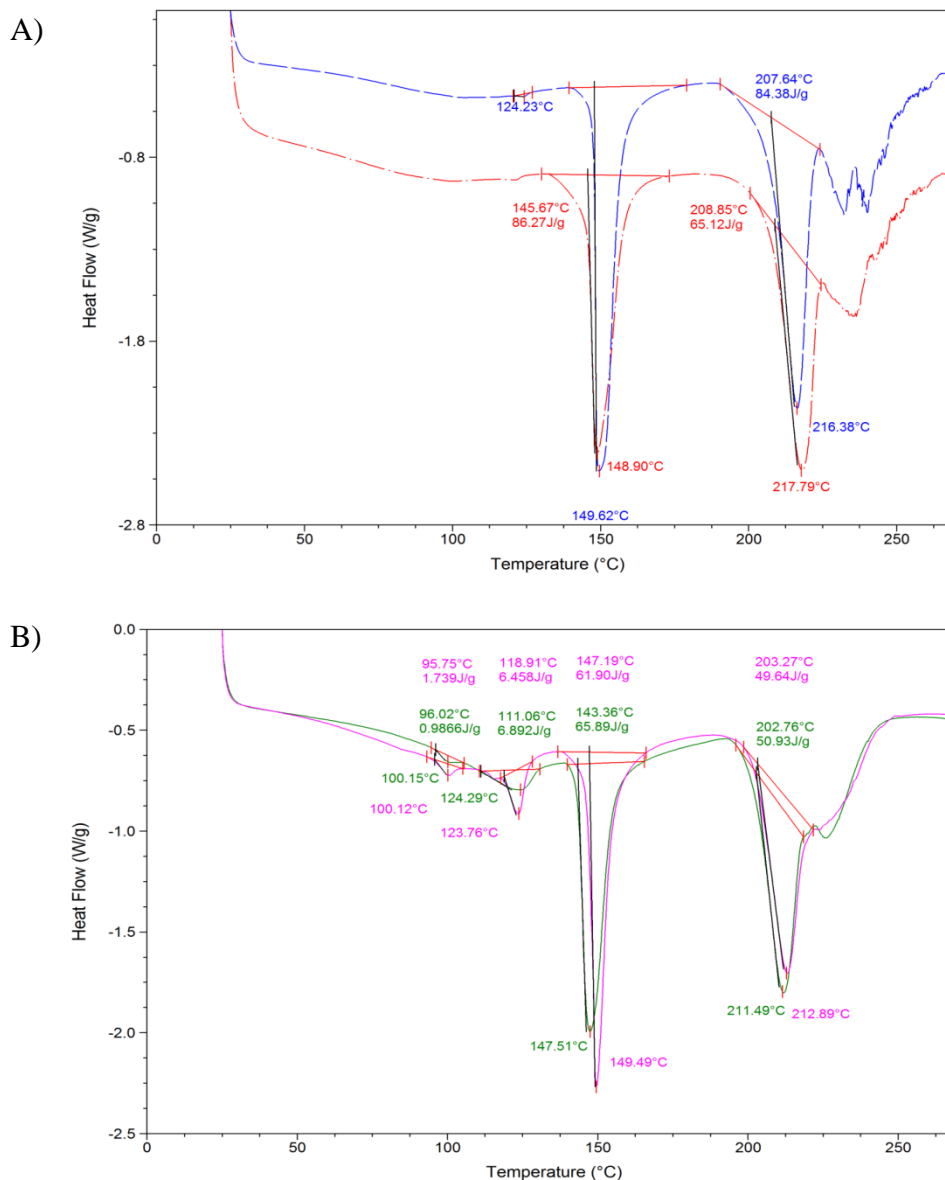


Figure 6.5: DSC scans for the development batches. A) Wet granulated mini-tablets (red), wet granulated granules (blue). B) Direct compression mini-tablets (green), direct compression mixed powders (pink).

6.3.3.1.6 Recommendation

Based on the evidence presented in this section, the wet granulated mini-tablet batch produced more consistent and stronger mini-tablets, so wet granulation was chosen for the experimental batches. However, this necessitated the use of PVP as a wet binder, which raised potential issues with the analysis of PVP in the final product, as discussed in Chapter 3.

6.3.3.2 Physical characterisation of the experimental mini-tablet batches

The three experimental batches were characterised physically in the same manner as the development batches, unless otherwise stated below.

6.3.3.2.1 Weight uniformity

The weight uniformity data are shown in Tables 6.5, 6.6 and 6.7 for the excipients-only batch, ibuprofen-loaded batch and caffeine-loaded batch, respectively. All three batches of tablets meet the requirements of the BP 2013 for weight uniformity, although the variation in weight in the ibuprofen-loaded batches was more than twice that of the other two batches: the RSD values for weight were 2.45 %, 2.02 % and 5.48 % for the excipient-only, caffeine-loaded and ibuprofen-loaded batches, respectively. The ibuprofen-loaded batch passed the BP 2013 specifications and was acceptable for this project as the main focus is surface analysis, but if it was required for clinical use, processing for the batch would be adjusted in order to reduce the variability.

6.3.3.2.2 Thickness

The thickness was measured on each of the tablets used for the weight uniformity test. Figure 6.6 shows the optical micrographs of the three batches with the measured thickness values and Tables 6.5, 6.6 and 6.7 summarises these data for the excipients-only batch, ibuprofen-loaded batch and caffeine-loaded batch, respectively. Ibuprofen-loaded tablets were slightly thicker than the other two batches and more variable: the RSD values for thickness were 1.58 %, 1.36 % and 2.45 % for the excipient-only, caffeine-loaded and ibuprofen-loaded batches, respectively.

6.3.3.2.3 Hardness

The crushing force was measured for each of the tablets used for the weight uniformity and thickness testing. Tables 6.5, 6.6 and 6.7 summarises these data for the excipients-only batch, ibuprofen-loaded batch and caffeine-loaded batch, respectively. Figure 6.7 shows an example of the compression loading profile from the three batches.

As noted above for the weight uniformity and thickness testing, the ibuprofen-loaded mini-tablets were the most variable. The mean values of crushing strength and the RSD were very similar for the excipients-only mini-tablets and the caffeine-loaded mini-tablets (8.66 N and 18.88 %, and 8.92 N and 18.95 %, respectively). The mean value of the crushing strength for the ibuprofen-loaded tablets was similar at 9.37 N, but the range of values was much greater (1.26 to 15.87 N), leading to an RSD value of 44.57 %. There was no obvious relationship between crushing strength thickness and weight for these mini-tablets. For a batch of mini-tablets intended for clinical use, this variation seen here would be inappropriate, but for the surface analytical work in this project, it was acceptable.

Although the crushing force is useful in comparing tablets within a batch, or between batches produced using the same tooling, it does not easily enable comparison between differently-sized or shaped tablets, as the force required to break a tablet (or any material) will vary with size and shape. Hence, the tensile strength of the mini-tablets was calculated using the standard tensile strength equation (Fell and Newton (1970)) and the Pitt equation (Pitt et al (1988)), which use the dimensions of the tablet as well as the crushing strength in order to calculate the tensile strength of the material. The standard tensile strength equation assumes that the surface of the tablet is completely flat and the Pitt equation assumes that the surface of the tablet has a uniform curvature. The challenge with the mini-tablets that were produced here is that there is a small (0.05 mm wide) flat lip around the outside of the tablet as well as a convex dome on the top and bottom faces. Neither equation deals specifically with this shape of tablet, so both were used. Firstly, the tablet was visualised mathematically as a completely flat compact with the thickness of the cylinder section (waist of the tablet) being calculated as the full measured thickness minus twice the dome height, and the standard tensile strength equation being applied. Secondly, the tablet was assumed to have uniform curvature, i.e. the dome section covered the entire face of the tablet, and the Pitt equation was applied. The "true" value of the tensile strength is probably somewhere between the values calculated from these equations, possibly nearer to the value calculated from the Pitt equation as the dome covers the majority of the tablet surface. The calculations are shown below and the results are detailed in Tables 6.5, 6.6 and 6.7 for the excipients-only mini-tablets, the ibuprofen-loaded mini-tablets and the caffeine-loaded mini-tablets, respectively. As would be expected from the crushing strength results, the ibuprofen-loaded batch was most variable, with an RSD of 43.52 % for the Pitt calculation, compared to RSD values of 18.68 % and 19.02 % for the excipient-only and caffeine-loaded mini-tablets, respectively. All three

batches showed a similar value of the tensile strength (circa 1.30 MPa), which probably reflects that fact that the formulations were very similar.

Calculation 6.3: The tensile strength calculation using the standard tensile strength equation

$$\sigma = \frac{2P}{\pi DT}$$

σ = Tensile strength

P = Fractural loading (crushing force)

D = Diameter

T = Thickness of cylinder, i.e. waist dimension of the tablet

= (measured total thickness – (2 x height of dome of tablet))

= (measured total thickness – (2 x 0.25 x 10⁻³ m))

Calculation 6.4: The tensile strength calculation using the Pitt equation

$$\sigma = \frac{10P}{\pi D^2 F}$$

σ = Tensile strength

P = Fractural loading (crushing force)

D = Diameter

F = Comparative factor = $\frac{2.84t}{D} - \frac{0.126t}{W} + \frac{3.15T}{D} + 0.01$

t = Overall thickness of the tablet

T = Thickness of cylinder, i.e. waist dimension of the tablet

= (measured total thickness – (2 x height of dome of tablet))

= (measured total thickness – (2 x 0.25 x 10⁻³ m))

	Weight (mg)	Thickness (mm)	Crushing strength (N)	Tensile strength (MPa)	
				Bi-convex	Flat
Mean	10.25	2.63	8.66	0.99	1.30
SD	0.25	0.04	1.63	0.19	0.24
RSD	2.45 %	1.58 %	18.88 %	18.69 %	18.68 %
Mean + 10%	11.28				
Mean - 10%	9.23				
Highest result	10.68	2.69	11.52	1.30	1.69
Lowest result	9.72	2.53	5.38	0.71	0.79

Table 6.5: The weight, thickness and crushing strength results and the calculated tensile strength for the excipients-only experimental mini-tablet batch (SD = standard deviation; RSD = relative standard deviation) (n = 20 tablets).

	Weight (mg)	Thickness (mm)	Crushing strength (N)	Tensile strength (MPa)	
				Bi-convex	Flat
Mean	10.44	2.82	9.37	0.99	1.28
SD	0.57	0.07	4.18	0.43	0.56
RSD	5.48 %	2.45 %	44.57 %	43.59 %	43.52 %
Mean + 10%	11.48				
Mean - 10%	9.39				
Highest result	11.34	2.95	15.57	1.66	2.15
Lowest result	9.51	2.72	1.26	0.14	0.18

Table 6.6: The weight, thickness and crushing strength results and the calculated tensile strength for the ibuprofen-loaded experimental mini-tablet batch (SD = standard deviation; RSD = relative standard deviation) (n = 20 tablets).

	Weight (mg)	Thickness (mg)	Crushing strength (N)	Tensile strength (MPa)	
				Bi-convex	Flat
Mean	10.01	2.62	8.92	1.03	1.34
SD	0.20	0.04	1.69	0.19	0.25
RSD	2.02 %	1.34 %	18.95 %	19.00 %	19.02 %
Mean + 10%	11.01				
Mean - 10%	9.01				
Highest result	10.44	2.69	11.84	1.37	1.79
Lowest result	9.66	2.55	6.51	0.76	0.99

Table 6.7: The weight, thickness and crushing strength results and the calculated tensile strength for the excipients-only experimental mini-tablet batch (SD = standard deviation; RSD = relative standard deviation) (n = 20 tablets).

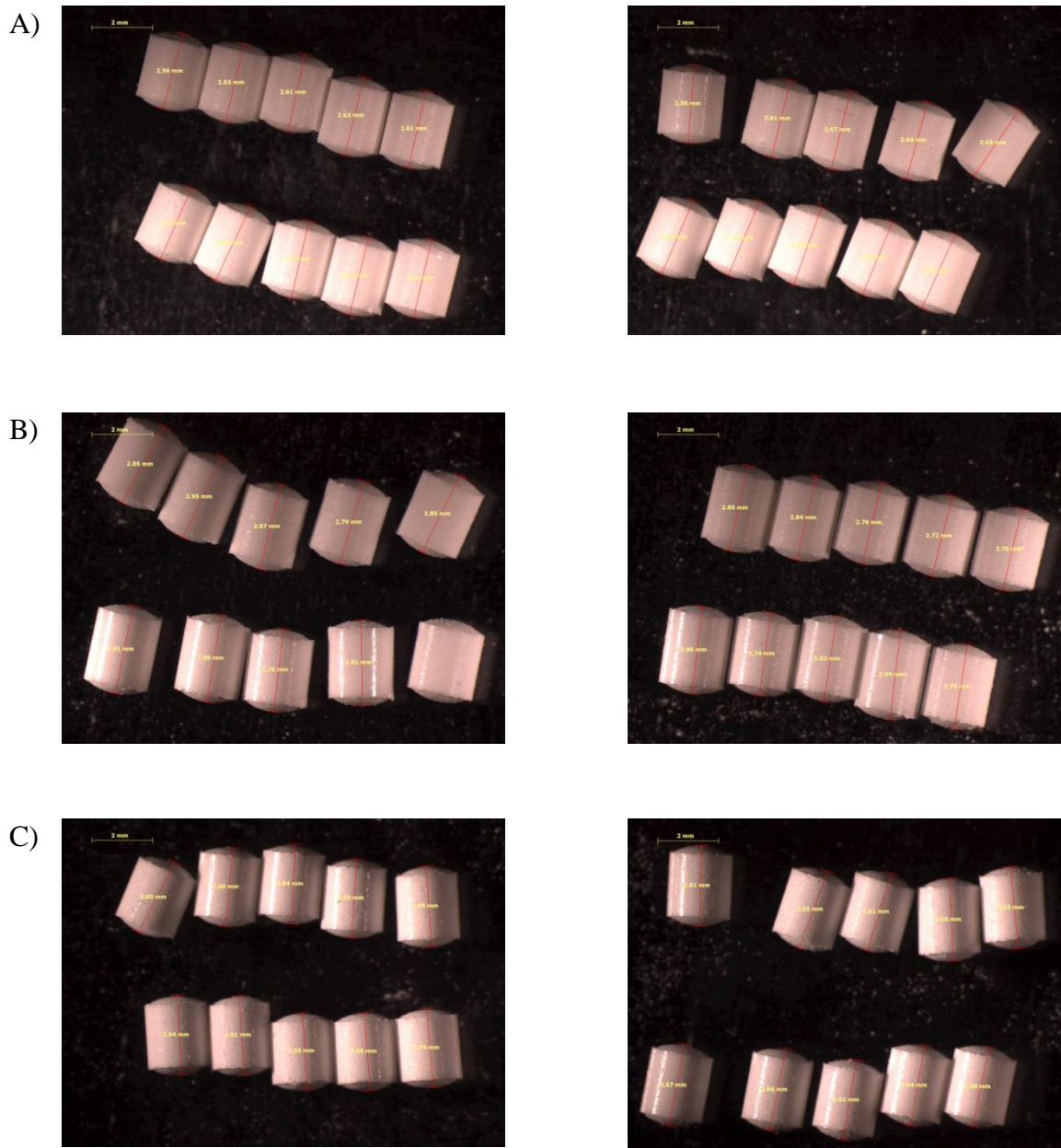


Figure 6.6: The optical microscopy image (magnification X10) of the experimental mini-tablets batches. A) Excipient-only mini-tablets. B) Ibuprofen-loaded. C) Caffeine-loaded mini-tablets.

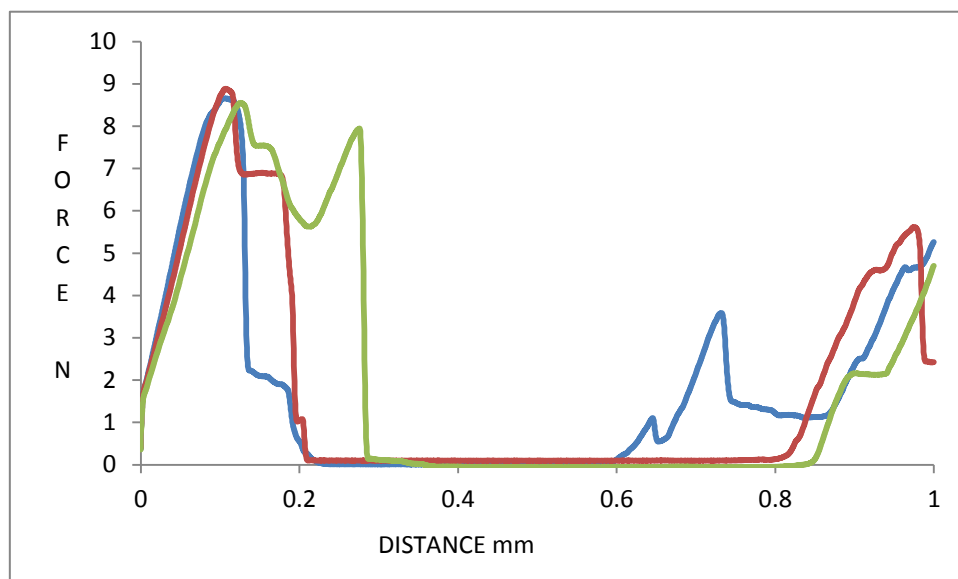


Figure 6.7: The compression loading profile for an example of the excipients-only mini-tablets (blue), ibuprofen-loaded mini-tablets (green) and caffeine-loaded mini-tablets (red).

6.3.3.2.4 Friability

The friability of the three experimental batches was assessed by two different methods, both based on the process described earlier in that the friability tester, the speed of revolution and the length of the test were all the same. The first method used 50 mini-tablets, rather than 20 as was used earlier, as it was felt that the lower number of tablets resulted in a too-vigorous assessment of tablet behaviour. The second method used a total of approximately 6.5 g of whole mini-tablets, reflecting the actual BP 2013 requirements for the friability test. A weight of 6.5 g equates to approximately 650 mini-tablets.

The results are shown in Table 6.8. All three mini-tablet batches passed the BP 2013 specification of no more than 1 % weight loss. However, the weight loss recorded with the lower number of mini-tablets (50) is noticeably higher than observed in the experiment using 6.5 g of mini-tablets (approximately 650 mini-tablets). No tablets were seen to be cracked, split or broken by the naked eye, although when the tablets were examined under an optical microscope there were signs of chipping around the outside edge. These results highlight the difficulties of performing friability testing on mini-tablets and what to consider as a "true" result. The values for the 6.5 g experiment are much more in line with the results expected from these formulations when compressed to standard tablet weights (internal research group data).

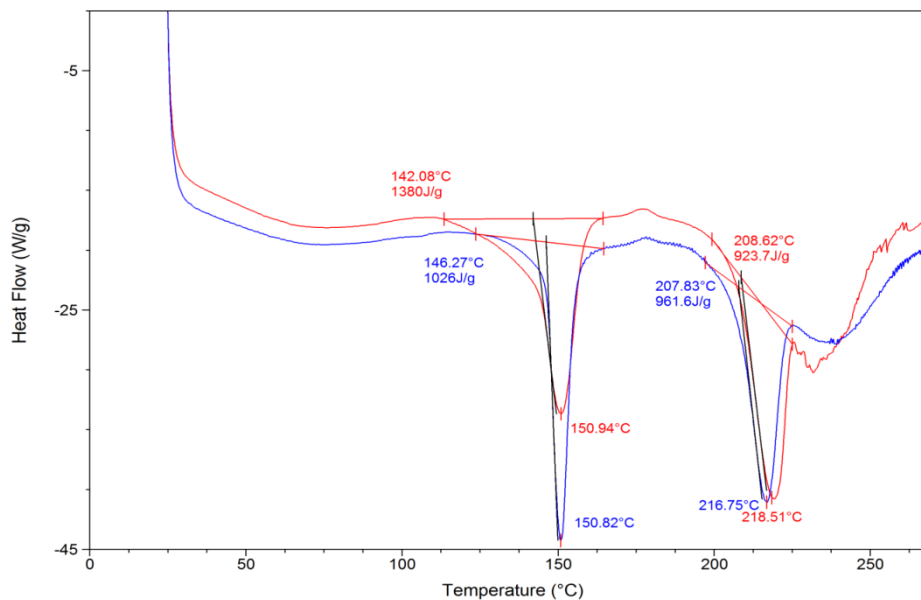
	Excipient-only		Ibuprofen-loaded		Caffeine-loaded	
	50 mini-tablets	6.5 g mini-tablets	50 mini-tablets	6.5 g mini-tablets	50 mini-tablets	6.5 g mini-tablets
Initial weight (g)	0.5090	6.5129	0.5196	6.5051	0.5040	6.5140
Final weight (g)	0.5060	6.5043	0.5151	6.4918	0.4996	6.4908
Weight loss (%)	0.59	0.13	0.87	0.20	0.87	0.36

Table 6.8: The friability results for the experimental batches, using both methods (50 mini-tablets and 6.5 g of mini-tablets).

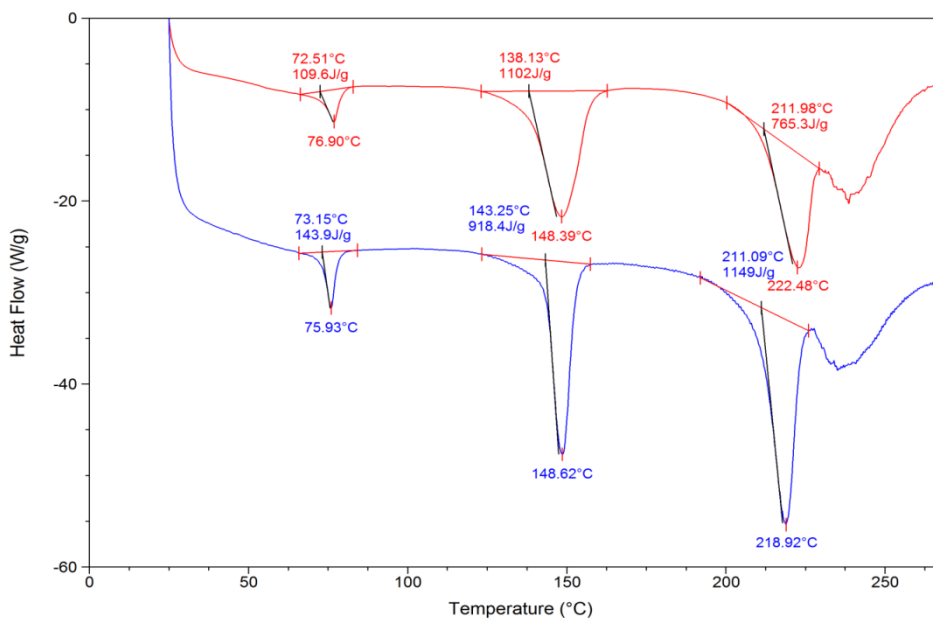
6.3.3.2.5 DSC

Figure 6.8 shows the DSC scans for the granules and mini-tablets for all three experimental batches. As observed with the development batches, the granules and tablets showed very similar responses. α -LM dominates the scans as was seen with the development batches. Dehydration of α -LM is observed at a slightly higher temperature and the onset of the melting/decomposition peak for α -LM is observed at a lower temperature (except for ibuprofen mini-tablets where the peak is broader) than observed when the single compound was analysed. For all scans there is a broad peak centred at circa 80°C which is attributed to evaporation of the remaining moisture after the wet granulation process. The one very obvious difference in the scans for the three batches is the peak attributable to ibuprofen, seen in Figure 6.8 B but not in Figure 6.8 A and C. The onset temperature for this peak is slightly lower than that for the individual component. No peak is seen for the melting of caffeine in the caffeine-loaded granules or mini-tablets (Figure 6.8 C), but its melting point (234°C) is in the region where α -LM is showing degradation, so is probably not detected as the baseline is noisy and it is present in a relatively small proportion, hence a separate, clear endotherm is not visible.

A)



B)



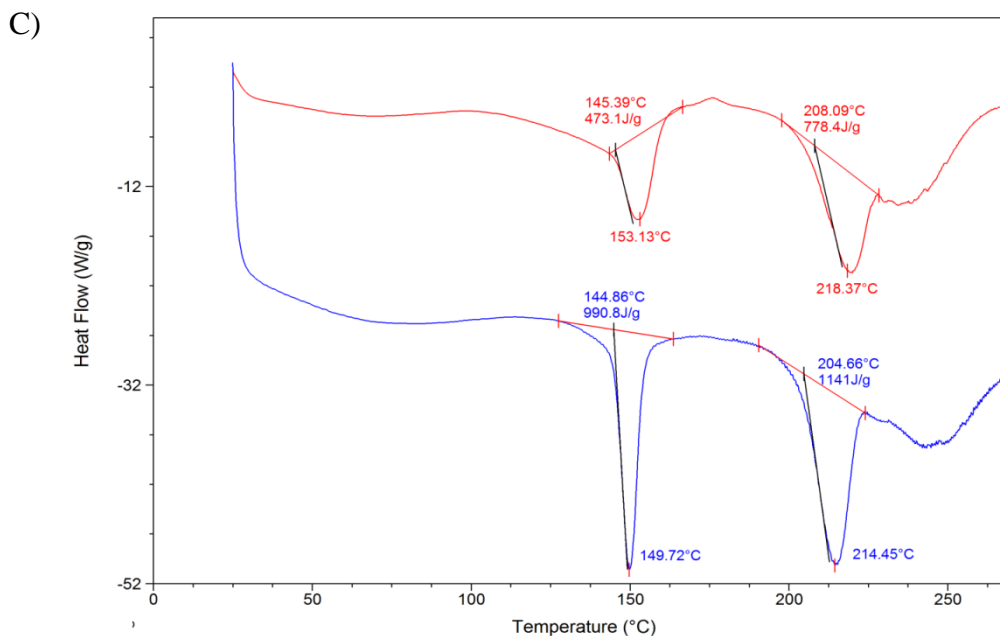


Figure 6.8: DSC scan for the experimental batches. A) Excipient-only granules (blue) and mini-tablets (red). B) Ibuprofen-loaded granules (blue) and mini-tablets (red). C) Caffeine-loaded granules (blue) and mini-tablets (red).

6.3.3.3 Content uniformity assessment of the drug-loaded experimental mini-tablet batches

Content uniformity assessment should be performed for all batches of tablets as good practice, but specifically for tablets less than 40 mg in weight, the BP 2013 states that content uniformity assessment is required rather than weight uniformity assessment. As the prime focus of this project was to look at the mini-tablet surface, content uniformity assessment was performed simply to ascertain that there was drug in each tablet. Hence, a straightforward spectrophotometric method was employed. A similar approach was taken by Deepali and Elvis (2010) who used lamivudine in their study.

The analytical method was as follows. Ten individual mini-tablets from each drug-loaded batch were tested. Each tablet was dispersed in the relevant solvent to extract the drug (0.1 M NaOH for ibuprofen and 0.1 M HCl for caffeine). The sample was filtered, made up to a 200 mL and then assayed in duplicate at $\lambda = 224$ nm for ibuprofen and $\lambda = 272$ nm for caffeine. For each drug, two standard solutions were prepared at the target concentration of the drug in the test solutions. During the analysis, the standard solution bracketed every

five test solutions. Test solutions from two excipients-only mini-tablets were prepared and tested to ascertain whether there was any interference from the excipients in the assay.

Tables 6.9 and 6.11 displays the analytical data for the standard solutions for each drug indicating that the standard solutions are reproducible and accurate. Tables 6.10 and 6.12 shows the assay results of the two batches of mini-tablets. The absorbance value for both standards drifted throughout the analysis but as the standards are bracketing the test solutions, the effect of this should be minimal. A low absorbance was detected from the excipients-only mini-tablets of 0.014 at $\lambda = 224$ nm (for the ibuprofen assay), but for the purposes of this analysis, it may be disregarded as there is such a large difference between this value and that of the test solutions. No absorbance was detected at $\lambda = 272$ nm for the excipients-only mini-tablets (for the caffeine assay).

The results from the two batches of mini-tablets were very similar, but within a batch the results were variable, with the ibuprofen-loaded mini-tablets showing content values ranging from 88.1 % to 113.5 % and the caffeine-loaded batches values of 87.2 % to 108.6 %, calculated by reference to the theoretical content of 10 %w/w drug in the mini-tablet. Both batches of mini-tablets met the BP 2013 content uniformity specification of all tablets being within 85 % and 115 % of the mean value.

Ideally, the drug content of the mini-tablets would be much closer to the target value of 100 %, so if the product was going to be developed for clinical use, it would need a bit of development work in the granulation stage to ensure that there was adequate mixing of the various components and probably some work in the screening / milling stage to ensure that the granule particle size was appropriate for filling of the die during the compression run. As mini-tablets are so small (10 mg), the effect of any minor variation in mixing efficiency or particle size distribution will be magnified compared to standard sized tablets (e.g. 200 mg or larger). However, as the tablets are to be used for analytical method development, and have passed the BP 2013 specification, they are suitable for use in this study.

Standard solution	Weight of ibuprofen (mg)	Concentration of standard solution (mg/L)	Absorbance at $\lambda = 244$ nm		
			Result 1	Result 2	Mean
A	11.3	5.65	0.215	0.216	0.2155
B	10.5	5.25	0.199	0.196	0.1975
			AGREEMENT = 98.63%		

Table 6.9: Analytical data for the ibuprofen standard solutions. Diluent used = 0.1 M NaOH, $\lambda = 224$ nm.

	Ibuprofen content (% theory by weight)
Mean	99.65
Highest test result	113.50
Lowest test result	88.06
85 % of mean	84.70
115 % of mean	114.60

Table 6.10: The content uniformity results for the ibuprofen-loaded mini-tablets (n = 10 tablets).

Standard solution	Weight of caffeine (mg)	Concentration of standard solution (mg/L)	Absorbance at $\lambda = 244$ nm		
			Result 1	Result 2	Mean
A	10.9	5.45	0.254	0.256	0.2550
B	10.1	5.05	0.242	0.237	0.2395
			AGREEMENT = 101.36%		

Table 6.11: Analytical data for the caffeine standard solutions. Diluent used = 0.1 M HCl, $\lambda = 272$ nm.

	Caffeine content (% theory by weight)
Mean	98.46
Highest test result	108.55
Lowest test result	87.23
85 % of mean	83.69
115 % of mean	113.23

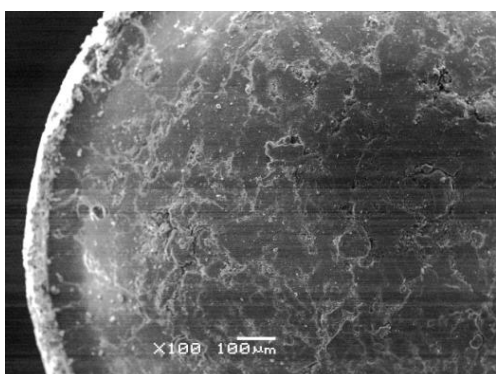
Table 6.12: The content uniformity results for the caffeine-loaded mini- tablets. (n = 10 tablets)

6.3.3.4 Surface characterisation of the development mini-tablet batches

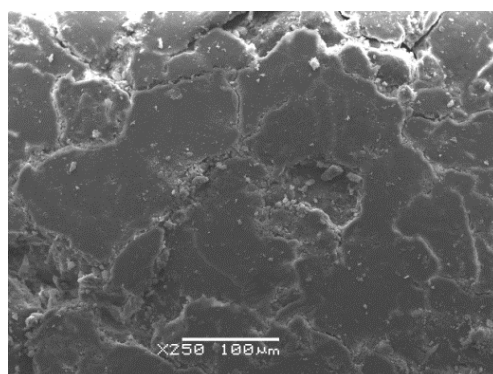
6.3.3.4.1 SEM

Figure 6.9 shows the SEM images of the surfaces of representative mini-tablets from the development batches at two levels of magnification. The surface of the direct compression mini-tablet is rough, with the crown of the tablet appearing to be the smoothest part. There appears to be some cracking and irregularities on the surface of the tablet, which probably just represent the junction of particles within the formulation. In contrast, the wet granulated mini-tablet shows a smoother surface, although the irregularities are still visible under higher magnification. The smoother appearance of the wet granulated mini-tablet is probably due to the more uniform nature of the granules compared to the powder mix used for the direct compression batch.

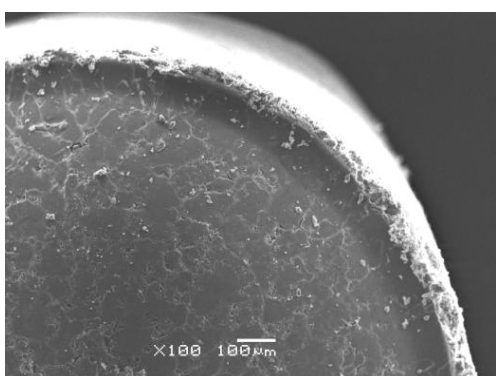
Ai)



Aii)



Bi



Bii)

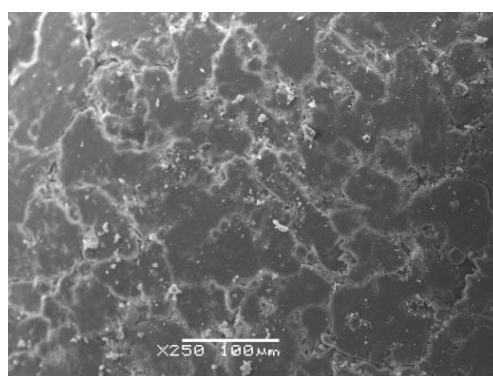
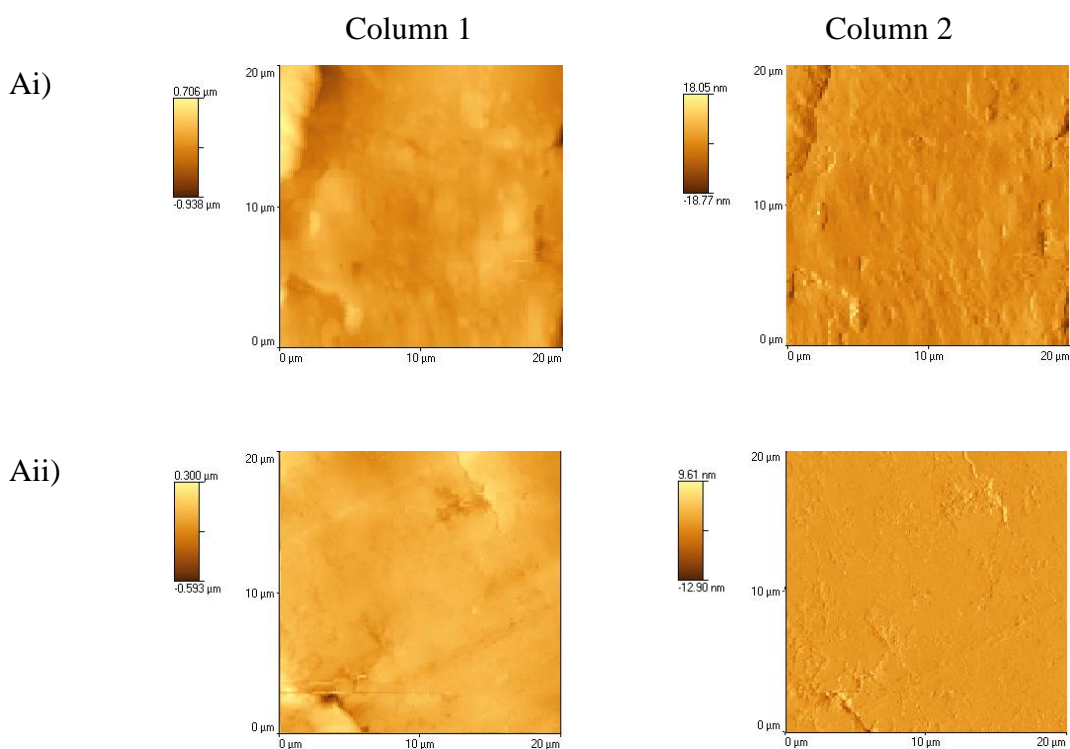


Figure 6.9: SEM images of the development batches of mini-tablets. A) Direct compression batch. B) Wet granulated batch. i) Magnification X100. ii) Magnification X250.

6.3.3.4.2 AFM

AFM images were taken of the region on the surface of the mini-tablets where the nano-TA was to be performed and are shown in Figure 6.10. All scans showed a very smooth surface, which is probably a result of the high pressures used to compress the powder/granule into tablets. The AFM images show very little evidence of the irregularities seen in the SEM images, but the area being scanned here is $20\ \mu\text{m} \times 20\ \mu\text{m}$ which is very small compared to the area of the SEM image (approximate $500\ \mu\text{m} \times 500\ \mu\text{m}$), and hence the irregularities would not be expected to be seen, unless the probe happened to land on the junction of neighbouring particles. A small area was studied under AFM and nano-TA to facilitate the experiments - as the surface of the mini-tablet is curved, it is more difficult for the probe to maintain contact during the experiment and hence a smaller area of study will give better results. Similarly, regions on the far edge of the mini-tablet were not studied as it was difficult for the probe to make and maintain good contact with the surface. From the areas scanned with AFM, the direct compression mini-tablets seemed to have a smoother surface than the wet granulation mini-tablets, but this is probably just a chance occurrence of the probe landing on a smooth particle, as the SEM images taken over a larger area suggested otherwise. For both mini-tablet batches, the surface was too compressed to distinguish areas of specific component materials.



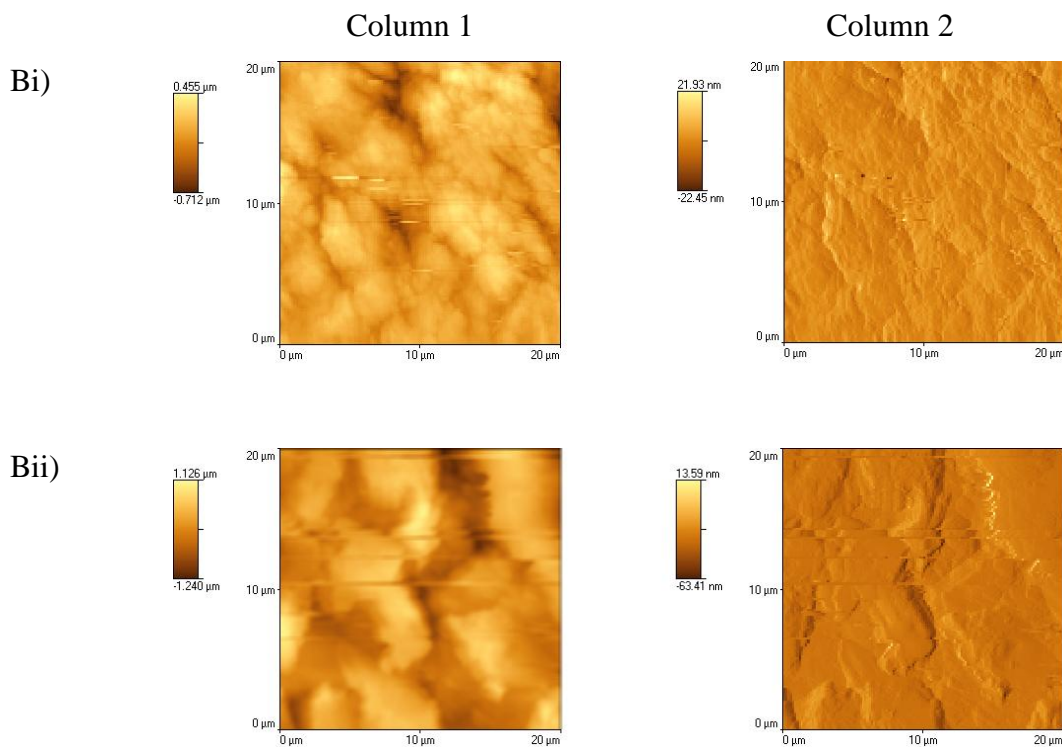


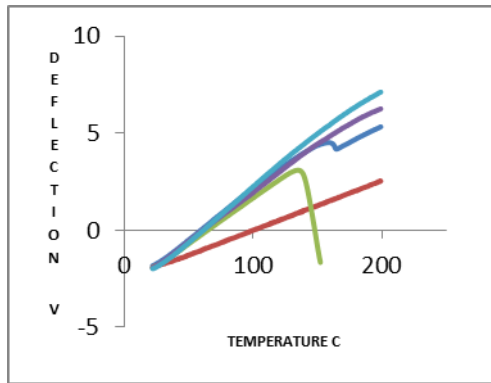
Figure 6.10: AFM scan of the development batches of mini-tablets using a nano probe. A) Direct compression batch. B) Wet granulated batch. Column 1 - height, Column 2 - deflection. Position on the radius of the compact is given by i) centre and ii) outside.

6.3.3.4.3 Nano-TA

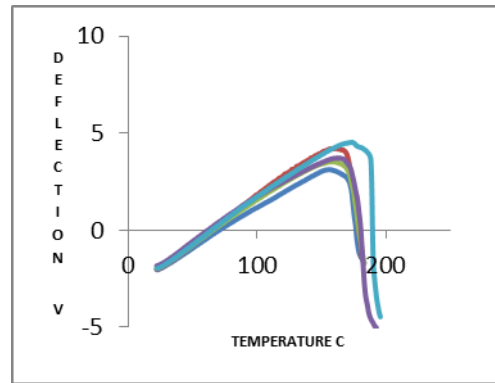
Nano-TA was performed on both development batches of the mini-tablets after the AFM images were generated and representative scans are shown in Figure 6.11. Comparison of these scans with those of the compacts of the individual components shown in Chapter 3 allowed identification of the most likely component(s) present. This is summarised in Table 6.13.

All components were detectable, although MS was detected only once (out of 20 scans), reflecting its low concentration in the formulation (1 %w/w). Conversely, α -LM was detected eight times (out of 20 scans) as a pure material and twice as a layer on top of MCC, commensurate with its higher concentration in the formulation (68 and 67 %w/w for the direct compression batch and the wet granulation batch, respectively). This thin layer effect is shown in Figure 6.11 Ai dark blue line and Bi red line and has been seen previously in Chapter 5 with the mixed compacts.

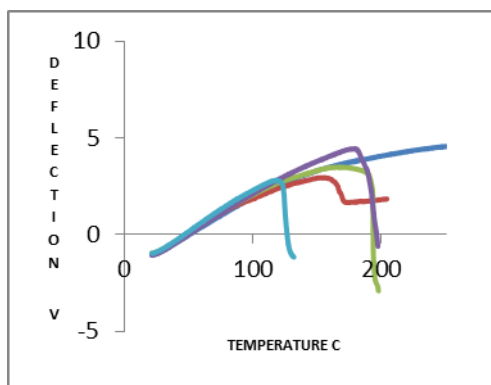
Ai)



Aii)



Bi)



Bii)

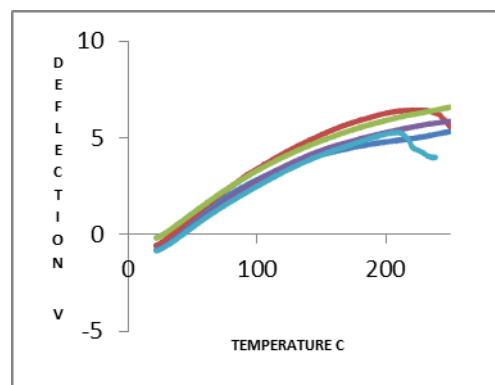


Figure 6.11 Nano-TA results of the development batches of mini-tablets using a nano probe. A) Direct compression mini-tablets. B) Wet granulated mini-tablets. Position on the radius of the compact is given by i) centre and ii) outside. Five nano-TA readings were taken at each position: dark blue - site 1, red - site 2, green - site 3, purple - site 4, light blue - site 5.

Formulation	Compact	Components identified (number of sites; maximum = 5)			
		α -LM	MS	MCC	PGS
Direct compression	A i	1	0	3 + 1*	0
	A ii	5	0	0	0
Wet granulation	B i	2	1	1 + 1*	0
	B ii	0	0	3	2

Table 6.13: A summary of the most probable components identified from the nano-TA scans of the development batches of mini-tablets shown in Figure 6.11. The number indicates the number of scans assigned to a particular component.

* This result suggests a thin layer of α -LM on top of a bulk layer of MCC.

6.3.3.4.4 TTM

TTM was performed on both development batches, with representative maps being shown in Figure 6.12. In this case, the scans were performed on regions of 20 μm x 20 μm rather than 50 μm x 50 μm as used with the flat compacts in Chapters 3, 4 and 5, due to concerns that the probe would lose contact with the curved surface of the mini-tablet during the run.

MCC seemed to predominate in the areas scanned on the surface of the direct compression mini-tablet, with α -LM and PGS dominating the surface of the wet granulated tablets. However, all four components were detected in both batches, and some of the pixels attributed to MCC may in fact have been due to PGS, as the technique does have problems distinguishing between these two components. Examination of the individual thermal scans (column 3) helps in identifying these two materials and may also allow help to identify areas where there is a thin layer of one material on top of another. In this latter case, a small deflection is seen in the individual trace before the endpoint of the underlying material is seen, whereas the map shows only the colour associated with the underpinning material.

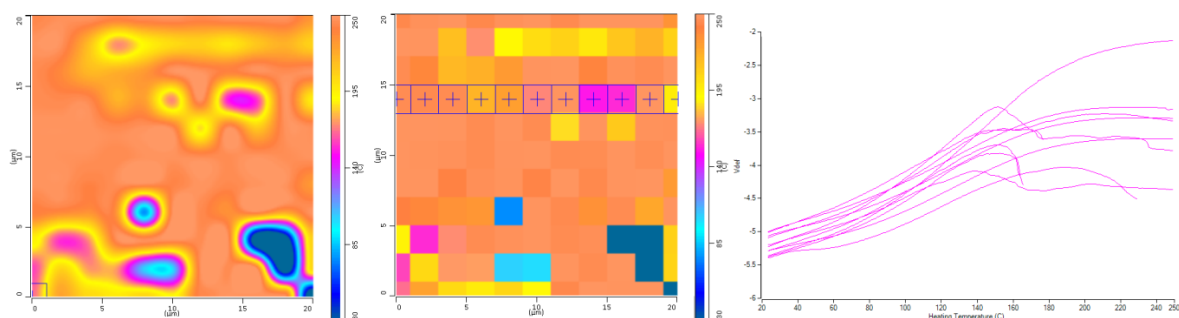
Differences observed between the two batches of mini-tablets and the positions on the tablets are thought to be real differences in the distribution of materials at the specific sites studied. The slightly rougher surface of the direct compression tablet did not seem to affect the surface analysis and there was no significant difference in baseline noise between the two batches.

Column 1

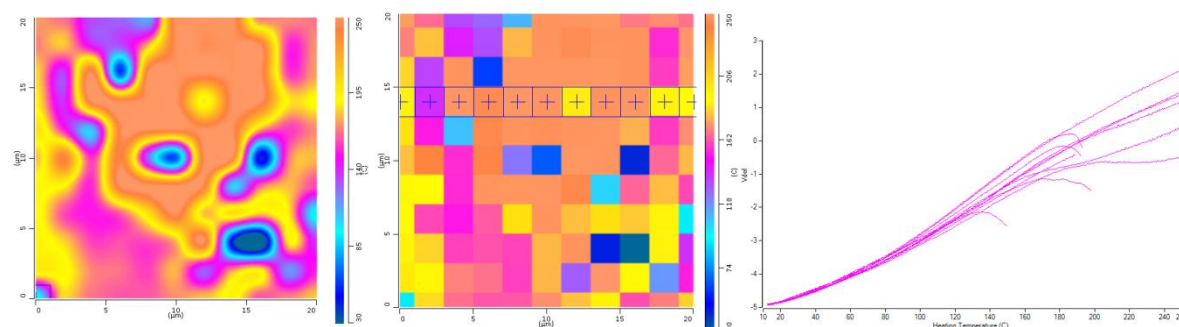
Column 2

Column 3

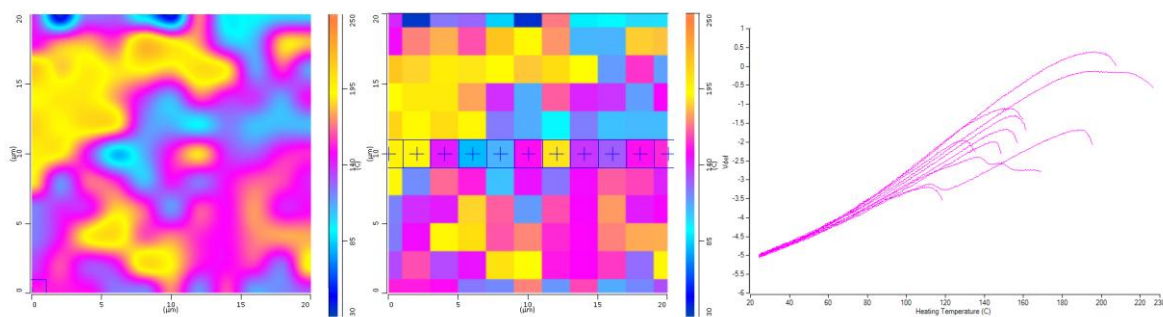
Ai)



Aii)



Bi)



Bii)

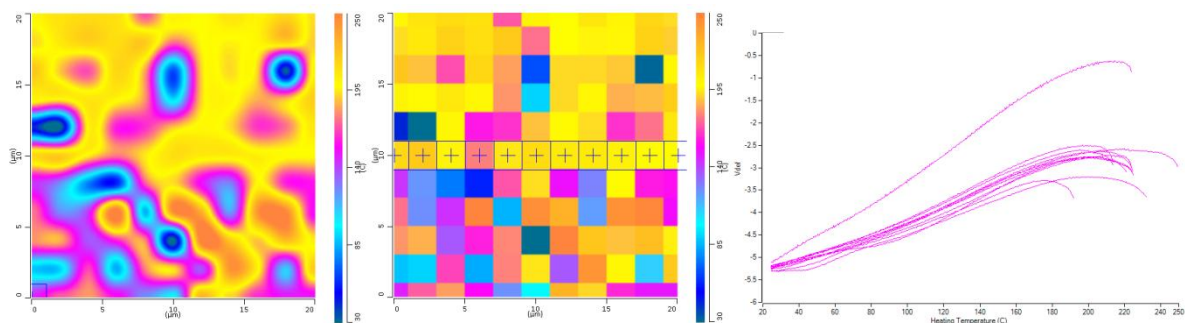
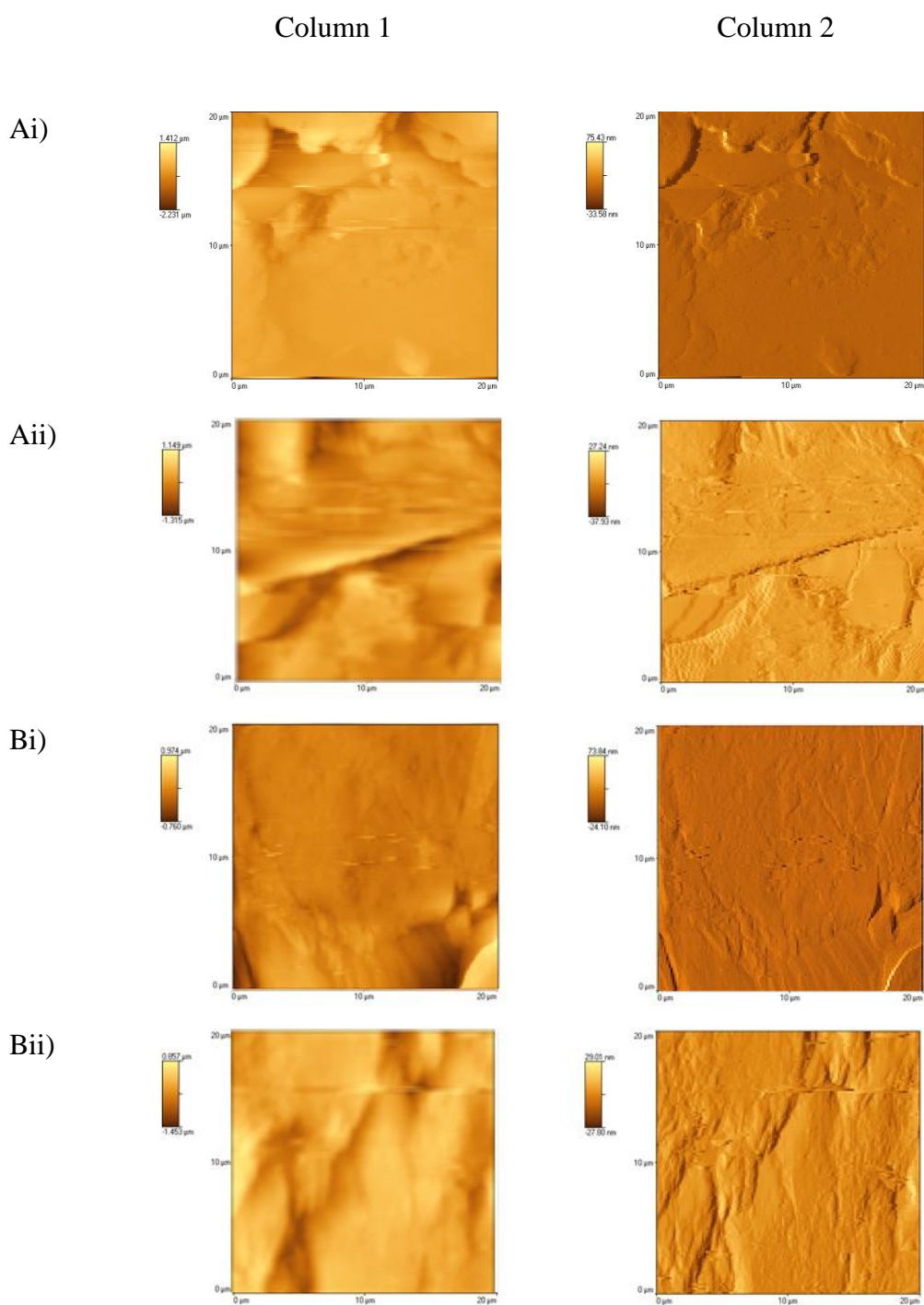


Figure 6.12: TTM maps for the development batches of mini-tablets. A) Direct compression mini-tablets. B) Wet granulated mini-tablets. Position on the radius of the compact is given by i) centre and ii) outside. Column 1 is the interpolated (smoothed) map, Column 2 is the discrete map, and Column 3 shows the individual nano-thermal results taken at the crossed points (+) on the discrete map. The colours represent the components: MCC (orange), PGS (orange/yellow), α -LM (pink/yellow), MS (blue/purple); the dark blue colour is noise.

6.3.3.5 Surface characterisation of the experimental mini-tablet batches

6.3.3.5.1 AFM

Figure 6.13 shows the AFM scans of the surface of mini-tablets from all three experimental batches. As seen with the development batches, the surface is too smooth to permit identification of individual components from the AFM images. There is no distinct difference between the three batches of mini-tablets and no evidence of large differences between the centre and outside of the mini-tablets.



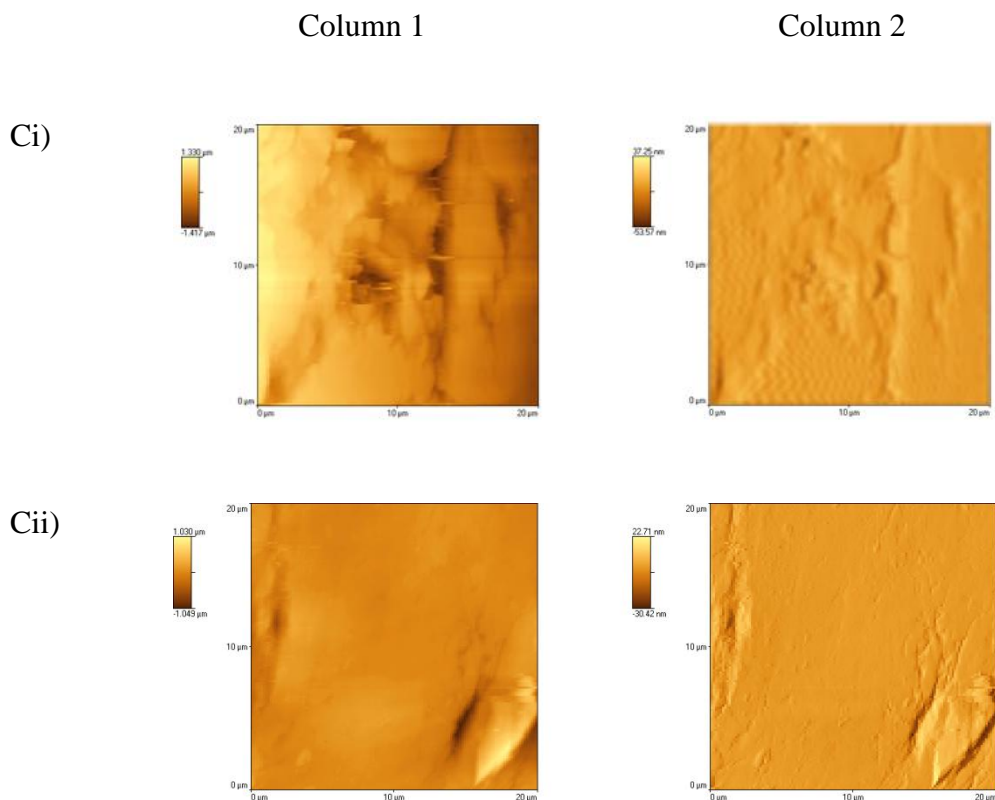


Figure 6.13: AFM scan of the experimental batches of mini-tablets using a nano probe. A) Excipients-only batch. B) Ibuprofen-loaded batch. C) Caffeine-loaded batch. Column 1 - height, Column 2 - deflection. Position on the radius of the compact is given by i) centre and ii) outside.

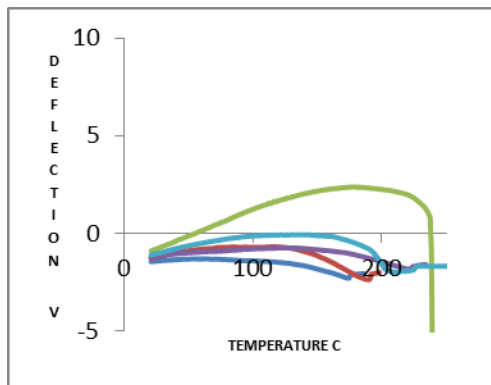
6.3.3.5.2 Nano-TA

Nano-TA was performed on all three experimental batches of mini-tablets after the AFM images were generated and representative scans are shown in Figure 6.14. Comparison of these scans with those of the compacts of the individual components shown in Chapters 3 and 4 allowed identification of the most likely component(s) present. This is summarised in Table 6.14. As with the development batches, all the major components were detectable, but MS was not detected in these scans, probably due to its low concentration.

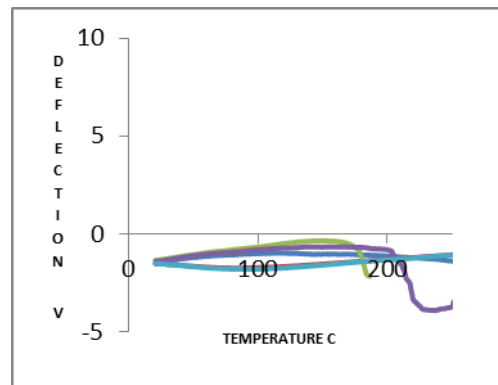
Caffeine did not show the same thermal behaviour here as in previous Chapters, as it did not show any thermal expansion at the start of the run, but instead a decreasing baseline right from the start of the experiment until the V-shaped minimum was observed at circa

180°C (Figure X Ci, red and purple lines). These runs have been assigned to caffeine based on this.

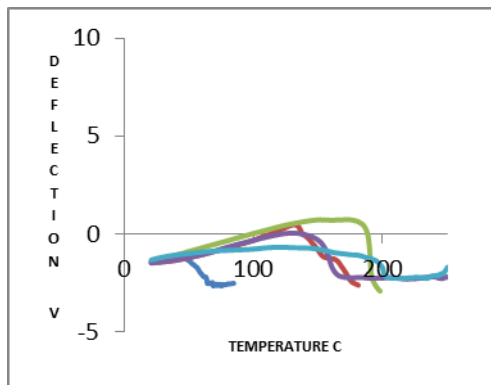
Ai)



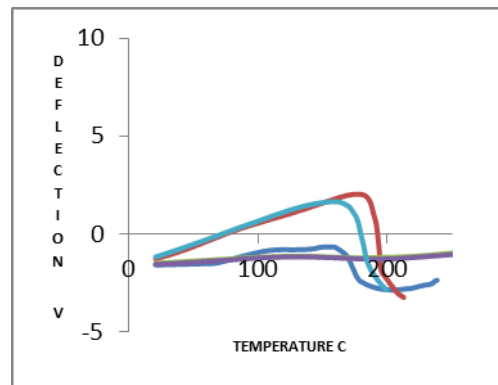
Aii)



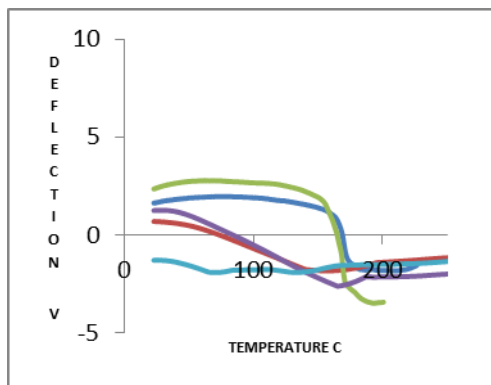
Bi)



Bii)



Ci)



Cii)

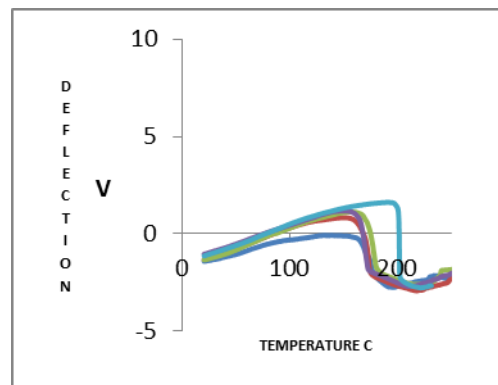


Figure 6.14: Nano-TA results of the experimental batches of mini-tablets using a nano probe. A) Excipients-only batch. B) Ibuprofen-loaded batch C) Caffeine-loaded batch. Position on the radius of the compact is given by i) centre and ii) outside. Five nano-TA readings were taken at each position: dark blue - site 1, red - site 2, green - site 3, purple - site 4, light blue - site 5.

Formulation	Compact	Components identified (number of sites; maximum = 5)					
		α -LM	MS	MCC	PGS	CAF	IBU
Excipients only	A i	4 *	0	0	1	X	X
	A ii	1	0	3	1	X	X
Ibuprofen- loaded	B i	3	0	0	1	X	1
	B ii	3	0	2	0	X	0
Caffeine- loaded	Ci	2	0	1	0	2	X
	Cii	5	0	0	0	0	X

Table 6.14: A summary of the most probable components identified from the nano-TA scans of the experimental batches of mini-tablets shown in Figure 6.14. The number indicates the number of scans assigned to a particular component. X indicates that this component is not present in the mini-tablet.

* The transition observed here is more clearly visible when the scale is expanded. However, the graph was kept at the same dimensions for comparison with the other scans.

6.3.3.5.3 TTM

TTM was performed on all three experimental batches, with representative maps being shown in Figure 6.15.

Prior to the analysis of the development batches of mini-tablets, there was concern that the nano probe would have difficulty making and maintaining contact with the curved surface of the mini-tablet and hence smaller areas were studied, i.e. 20 μm x 20 μm . In practice, it was hard but not impossible to maintain the probe in contact with the mini-tablet surface, so using a very small study area was probably not necessary. However, there are still concerns about moving the probe from one location on the tablet surface without damaging it, so for this study, one larger area of 100 μm x 100 μm in the centre of the tablet surface was chosen to be examined, rather than three smaller ones.

In the scan of the excipients-only mini-tablet, all components were identified, although there is probably some overlap in the assignment of MCC and PGS. MCC seemed to predominate in the scan of the caffeine-loaded mini-tablet and little caffeine was detected. However, the endpoints for MS and α -LM are in a similar temperature range to that of caffeine, so there may be issues with automatic assignment of colours to pixels. Examination of the individual traces for the line shown suggests that four components are present in that area, with caffeine probably being the purple/blue pixels and α -LM, PGS and MCC also being present. MS is probably represented by the bright blue colour in the line immediately below this line, being of a slightly lower temperature.

All four excipients were seen in the scan of the ibuprofen-loaded mini-tablet, although only a few pixels could be assigned to ibuprofen. For the line highlighted, ibuprofen, α -LM, PGS and MCC were detected, with MS being seen elsewhere on the map.

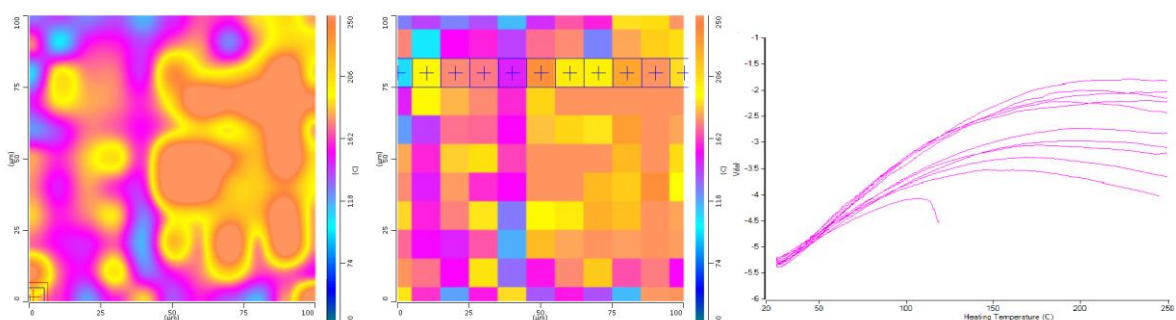
In addition to these TTM scans, where readings were taken every 10 μm in a grid pattern, a more detailed image was generated where scans were taken every 2 μm in a grid pattern. This was performed in order to assess whether more information could be gathered with the extra scans and also to enable comparison with the Raman microscopy high resolution scans discussed in Chapter 7. In this case, the total area covered was 75 μm x 75 μm , as a compromise between quantity of data collected and time of collection - this run took approximately 17 hours. Figure 6.16 shows the detailed TTM maps for the mini-tablets from all three experimental batches. All materials could be detected on the surface of the mini-tablets and the maps were more detailed than the previous TTM maps.

Column 1

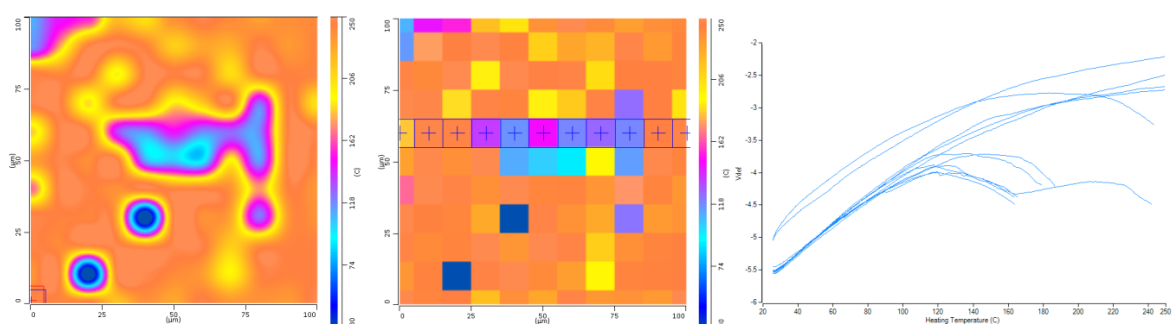
Column 2

Column 3

A)



B)



C)

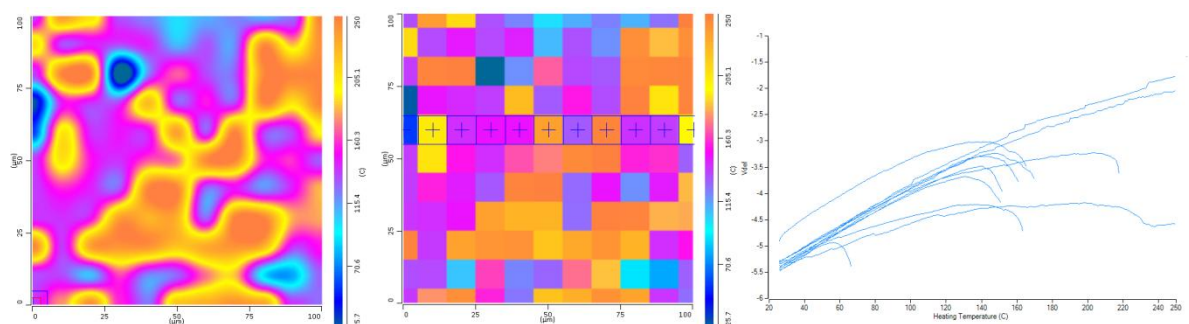


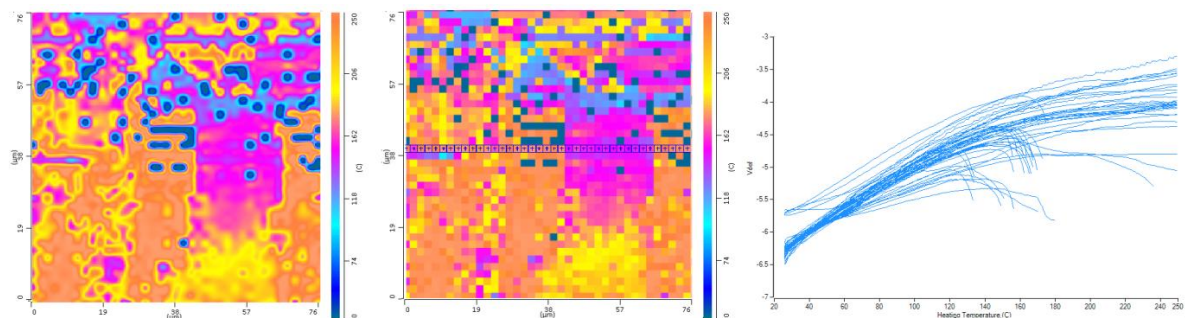
Figure 6.15: TTM maps for the experimental batches of mini-tablets. A) Excipients-only batch. B) Caffeine-loaded batch. C) Ibuprofen-loaded batch. Column 1 is the interpolated (smoothed) map, Column 2 is the discrete map, and Column 3 shows the individual nano-thermal results taken at the crossed points (+) on the discrete map. The colours represent the components: MCC (orange), PGS (orange/yellow), α -LM (pink/purple), MS (light blue), Ibuprofen (blue), Caffeine (pink/blue); the dark blue colour is noise.

Column 1

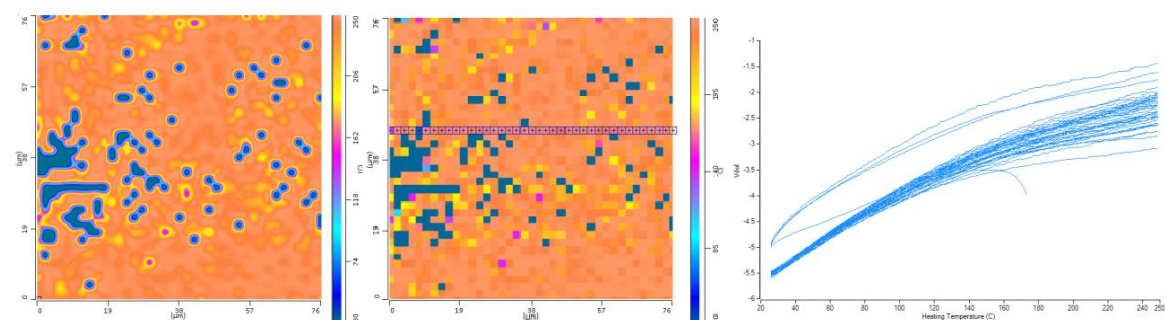
Column 2

Column 3

A)



B)



C)

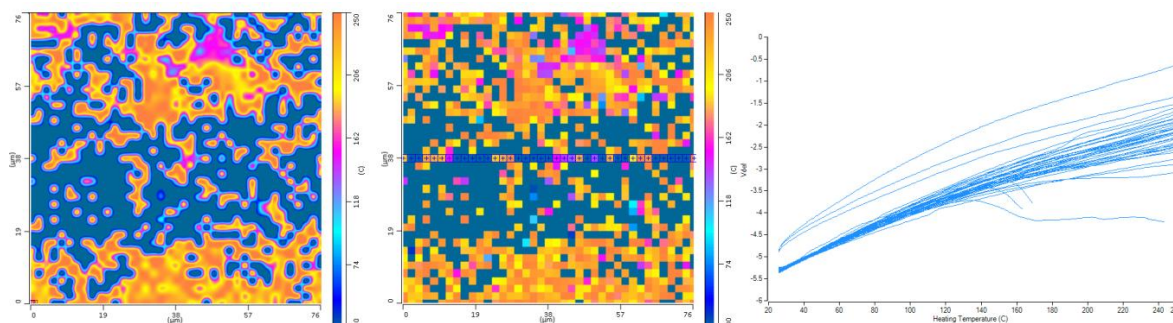


Figure 6.16: Detailed TTM maps for the experimental batches of mini-tablets. A) Excipients-only batch. B) Caffeine-loaded batch. C) Ibuprofen-loaded batch. Column 1 is the interpolated (smoothed) map, Column 2 is the discrete map, and Column 3 shows the individual nano-thermal results taken at the crossed points (+) on the discrete map. The colours represent the components: MCC (orange), PGS (orange/yellow), α -LM (pink/purple), MS (light blue), Ibuprofen (blue), Caffeine (pink/blue); the dark blue colour is noise.

One potential concern about performing the individual nano-TA experiments so close together (2 μm spacing rather than 10 μm spacing) was the extent of surface and sub-surface damage that will be caused by the testing. By its very nature, nano-TA (and by extension, TTM) heats the surface and melts the material immediately under the tip, so this precise location is damaged after the run. The concern is how far the heat will penetrate across the surface of the sample to the next testing site and whether this would have any deleterious effects on the next measurement. This is taken into account by the instrument manufacturer in terms of the recommended high heating rate, which should minimise the extent of heat diffusion across the sample. However, it is still a concern for the larger probes as visible holes are seen in the sample after micro-TA experiments, indicating a reasonable level of heat diffusion through the sample. There are no reported investigations in the literature as to the size of the hole and the heat penetration profile after a nano-TA experiment, but this is an area which could usefully be explored further. From the data shown here in the detailed maps, this would seem not to be a problem with the nano probe, as across the scan all materials could be detected.

MCC and PGS seemed to be detected to a greater extent than their concentrations in the formulations would suggest, which is particularly obvious here in the detailed scan of the caffeine-loaded mini-tablet. By examination of the other nano-TA and TTM results on this formulation in this Chapter and on the compacts shown in Chapter 5, this would seem to be a chance result of the probe landing on an area with a high concentration of MCC and/or PGS. However, this was investigated further as MCC and PGS are usually assigned the highest temperature colour (orange) if no transition has been observed by the time the experiment is terminated: this could possibly also have been the case if the probe had never made contact with the surface of the sample. Figure 6.17 shows a TTM map of a mini-tablet where the probe was deliberately not allowed to make contact with the surface, so is just moving through air as it performs the scan. This gives a distinct and reproducible S shape result, which has not been observed in any of the nano-TA or TTM scans seen in this work. Therefore, the high concentrations of MCC and PGS detected in the detailed TTM maps of the caffeine-loaded tablets (Figure 6.16 B) may be presumed to be a true result, rather than a machine artefact.

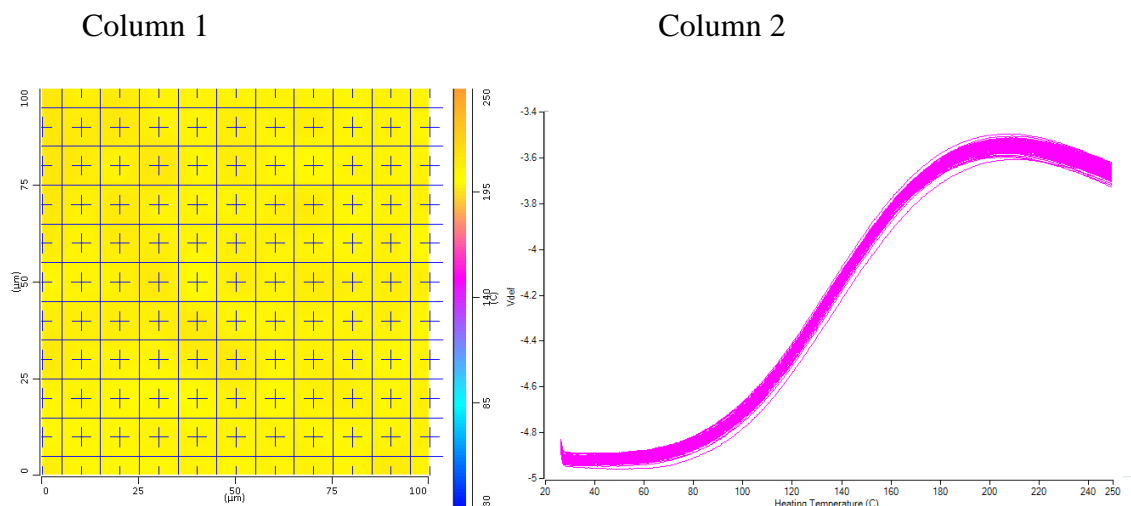


Figure 6.17: A TTM map of a mini-tablet where the probe has not made contact with the surface (column 1) and the individual nano-TA traces generated for the whole area (column 2).

A third issue identified with the detailed TTM scan is the number of pixels coloured as "noise", which was particularly noticeable in the scans of the ibuprofen-loaded mini-tablets. Using the TTM map shown in Figure 6.16 A for the excipients-only batch as an example, the individual nano-TA traces for the blue pixels were extracted and plotted manually. This is shown in Figure 6.18. It can be seen that these nano-TA traces do indeed match those of the individual components, so it is unclear why these traces were not included automatically by the software in its analysis. The assignment of these nano-TA traces to specific components was then done manually and then the TTM maps were updated manually. The final, corrected TTM maps for the three experimental mini-tablet batches are shown in Figure 6.19.

The extent of the noise seen in the TTM throughout this work is a serious issue if the technique is going to gain widespread acceptance. Although it is feasible to perform manual correction, this essentially defeats the object of having an automated system. It is a disadvantage of the current instrument software that this correction is not made automatically or at least with operator input.

Column 1

Column 2

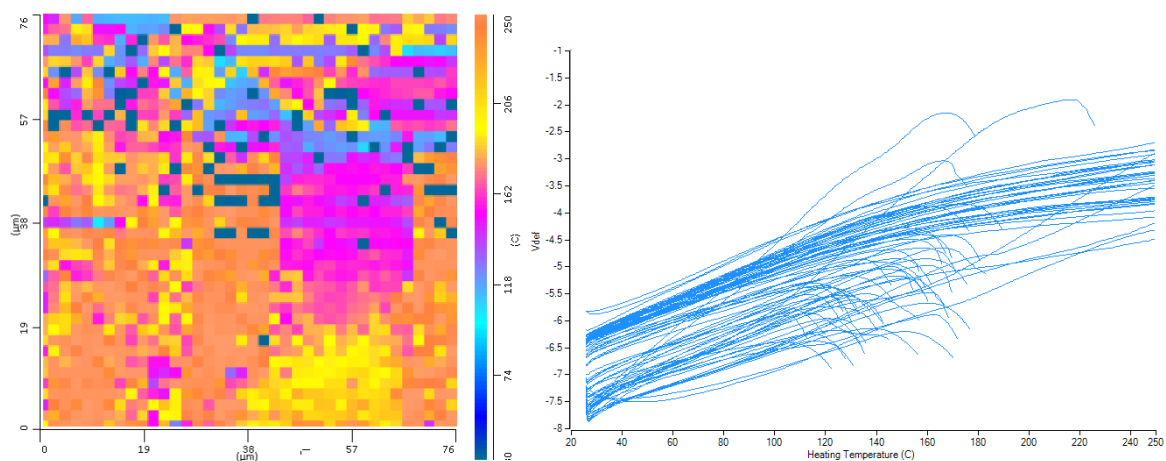


Figure 6.18: The TTM map of an excipient-only mini-tablet shown in Figure 6.16 A (column 1) and the individual nano-TA traces for the blue (noise) squares (column 2).

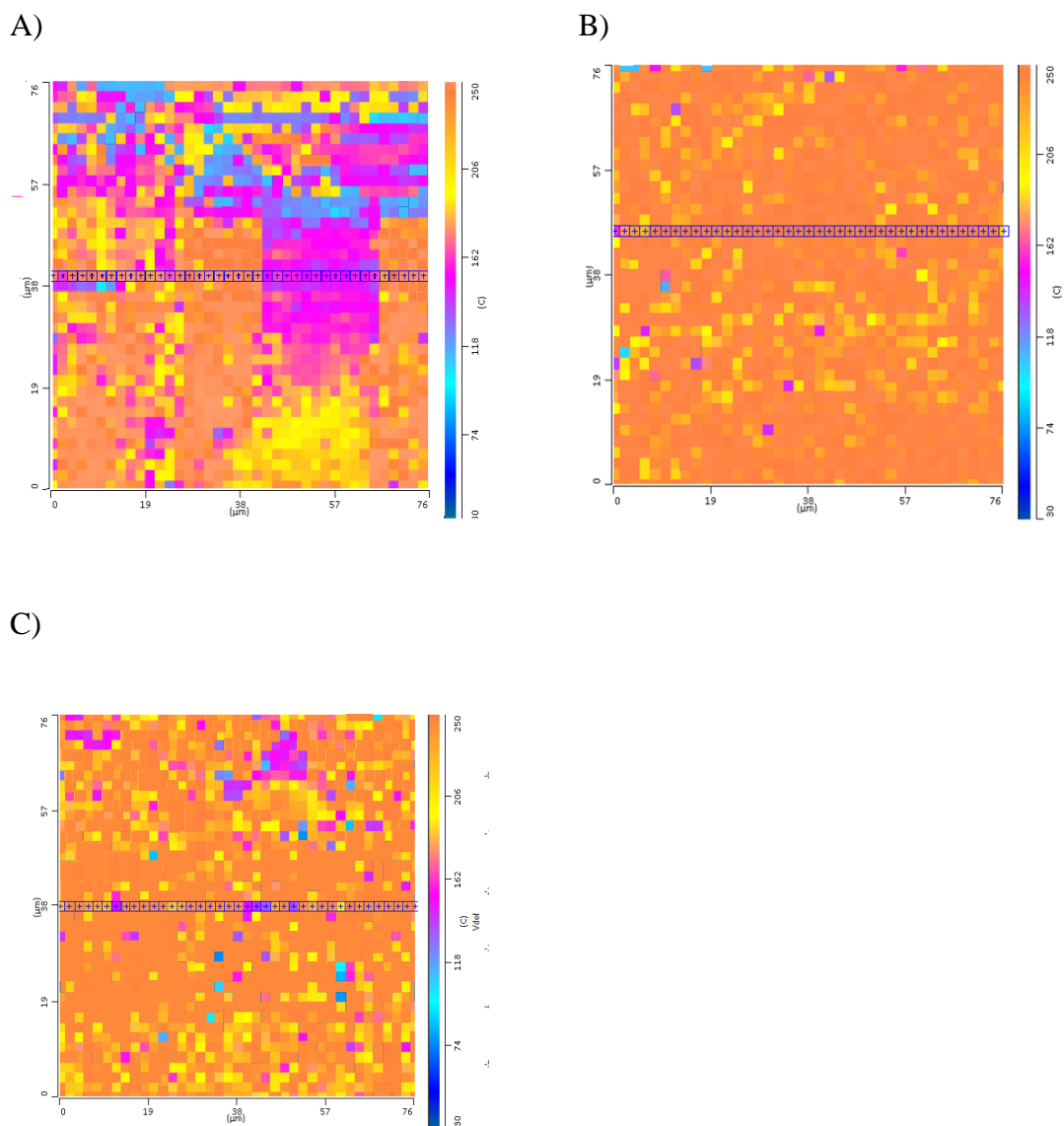


Figure 6.19: The corrected detailed TTM maps for the experimental batches of mini-tablets. A) Excipients-only batch. B) Caffeine-loaded batch. C) Ibuprofen-loaded batch. The colours represent the components: MCC (orange), PGS (orange/yellow), α -LM (pink/purple), MS (light blue), Ibuprofen (blue), Caffeine (pink/blue).

6.4 Conclusions

This Chapter builds on the results presented in Chapter 5, in which the ability of the novel techniques of nano-TA and TTM to determine the distribution of materials across the surface of a multi-component compact was confirmed. In this Chapter, more realistic mini-tablet formulations were investigated using these techniques.

The basic mini-tablet formulation was composed of the four excipients characterised in chapter 3 - α -LM, MCC, PGS and MS - all commonly used in pharmaceutical tablets (Crowley and Martini (2001)). Two batches of the same formulation were initially produced (the development batches) - one by direct compression and one by wet granulation with the addition of a wet binder (PVP) and minor adjustment of the quantities of α -LM and MCC. The tablets were compressed on a rotary tablet press to simulate a real-life production environment. Care was taken to control the particle size of the granule to between 125 μ m and 500 μ m, in order to ensure correct filling of the granule into the 2 mm die. Wet granulation produced more consistent and stronger tablets than direct compression, so was chosen as the method of preparation for the experimental batches.

Three experimental mini-tablet batches were produced: an excipients-only (placebo) batch with the same formulation as the wet granulated development batch; and two 10 %w/v drug-loaded formulations, whereby 5 %w/w of each of α -LM and MCC were replaced by the drug. The two drugs used were caffeine and ibuprofen, as studied in Chapter 4. Neither drug is sensitive to the presence of water or heat used in the granulation and drying processes. The relatively low level of drug in these formulations was a deliberate choice: it allowed good quality mini-tablets to be produced easily and it would challenge the technique in terms of detection limit.

The five mini-tablet batches were assessed by a range of standard pharmacopoeial tests, such as weight uniformity, content uniformity, hardness and friability. Modifications of the normal pharmacopoeial testing procedure for friability were made and it is still unclear which particular method is most suitable for mini-tablets. The experimental batches all passed all pharmacopoeial specifications and were suitable for use.

AFM, nano-TA and TTM were performed on all five batches, with the development batches being used to refine the analytical procedures before the experimental batches

were tested. The main reason for conducting AFM testing on the surface of the mini-tablets was to identify any topographical features which could affect the nano-TA readings, as the work in Chapter 5 had already established that it is unable to reliably identify materials in a complex mix such as is in the mini-tablets. The surface of the mini-tablets was smooth, due to the high pressures used during mini-tablet manufacture (Podczeck et al (1999)).

Nano-TA was successful in identifying the various components on the surface of the mini-tablets. However, the mini-tablets studied here are bi-convex, whereas the compacts studied in Chapter 5 are flat, and contact between the probe and the surface is more of an issue with the mini-tablets. From the perspective of the probe landing on the mini-tablet from above, the central crown area of the tablet is the flattest and presents the best chance of the probe making and maintaining good contact with the mini-tablet surface. Regions to the side of the tablet appear more steeply curved and there is danger that the cantilever will make contact with the surface and the probe will be suspended in air. Hence, care is needed to ensure good contact is made and to protect the delicate (and expensive) probes.

For the development batches, the nano-TA was conducted in small areas of 20 μm x 20 μm at the edges and the centre of the tablet because of concerns over contact as discussed above. For the experimental batches, a single area of 100 μm x 100 μm in the centre of the mini-tablet surface was used. As before, careful examination of the individual nano-TA trace was required to distinguish between MCC and PGS. Occasionally there was evidence in the nano-TA trace of a thin layer of one material on top of another.

TTM mapping was performed on mini-tablets from each of the five batches and was successful in detecting the full range of materials in the formulations. As with the nano-TA, it was performed over a small area for the development batches and a larger area for the experimental batches. The same issues were identified as described in Chapter 5 - two materials with similar transition temperatures will be assigned the same colour for the map and the interpolation software leads to confusion and possible misinterpretation of the location of the various components. A more detailed map was also generated, taking images every 2 μm over a 75 μm x 75 μm square, rather than every 10 μm over a 100 μm x 100 μm square. These more detailed maps gave a better overview of the distribution of material but took much longer to create, hence there is a balance to be struck between quantity of data and speed of generation. The more detailed maps also raised a few other issues: there appeared to be more "noise" pixels, whereby a very low temperature of

transition was recorded by the TTM software even though the nano-TA trace showed a real transition that could be assigned to a component. By manually extracting the individual nano-TA traces for these pixels and performing the assignment, a full map could be produced. However, this reduces the utility of the TTM software and the advantages of automated processing, so this issue needs some development work before the technique can be fully exploited. By performing the individual nano-TA scans so close (2 μm apart), there was a risk that heat from the probe at one location could penetrate through the sample and affect the reading at the next. The results shown here indicate that, at least with the nano probe, this does not occur and that the results are valid.

In conclusion, nano-TA and TTM have been shown to be useful techniques in assessing the distribution of component materials across the surface of mini-tablets. However, there are still some developmental challenges with these techniques, particularly relating to the software used for the TTM.

Chapter 7

Raman microspectroscopic mapping

CHAPTER 7

Raman microspectroscopic mapping

7.1 Introduction

AFM, nano-TA and TTM have been used successfully in Chapters 3, 4, 5 and 6 to determine the distribution of materials across the surface of mono-component and multi-component compacts and mini-tablets. The results indicated that all the materials used could be identified in multi-component systems. In this Chapter, these novel techniques will be supplemented by a more established technique, that of Raman microspectroscopic mapping.

7.2 Materials and methods

The excipients (α -LM, MCC, PGS, MS and PVP) and drugs (caffeine and ibuprofen) used here were described in Chapter 2 in terms of their chemical and physical properties. Flat, 13 mm diameter mono-component compacts and compacts composed of 25 %w/w of each of α -LM, MCC, PGS and MS were produced as described in Chapter 2. The "development" batches of granule (excipient-only) and the powders (excipient-only) were compressed into 2 mm diameter mini-tablets as described in Chapters 2 and 6, and used as received. However, the "experimental" batches of granule (excipient-only, caffeine-based and ibuprofen-based) were compacted into 3 mm diameter flat compacts to 0.4 MPa pressure using a hydraulic hand press. Chapter 2 gives details of the analytical methods employed here.

7.3 Results and Discussion

7.3.1 Mono-component excipient compacts

Each of the four excipients (α -LM, MCC, PGS and MS) were compacted as described previously. Reference Raman spectra were generated for each excipient by probing an area of 100 μ m x 100 μ m on the surface of the compacts in a 4 x 4 grid pattern. Two scans

were performed in each region. A total of 32 Raman scans were taken and averaged to give a representative profile for each material. These are shown in Figure 7.1.

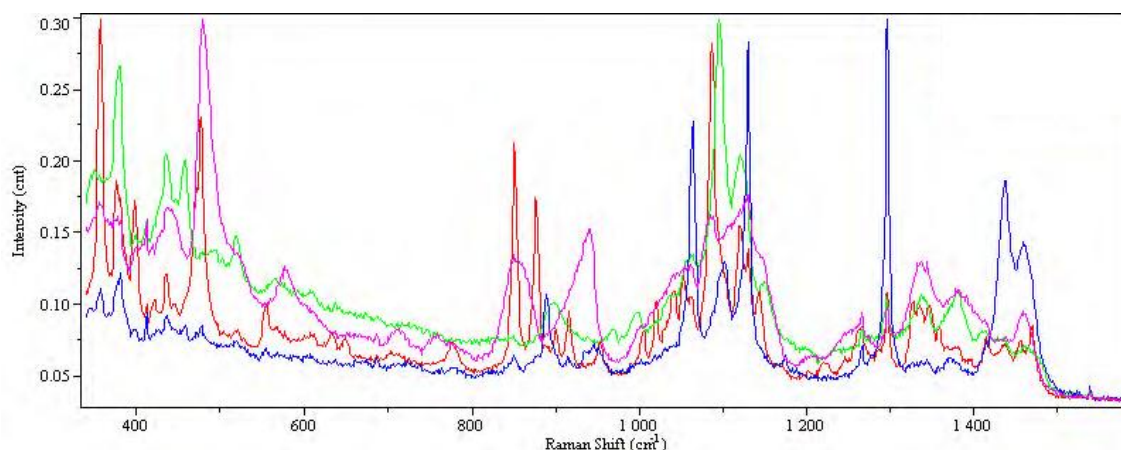


Figure 7.1: The reference Raman spectra for the finger print region for the excipients used in the formulation. α -LM (red), MCC (green), MS (blue) and PGS (pink).

As the Raman spectroscopic data were to be used to identify different materials in a mixture, a detailed assignment of peaks to bonds and functional groups was not conducted. However, as Raman spectroscopy results from the same electronic basis as IR spectroscopy, the positioning of the peaks will be the same as in the IR data discussed in Chapter 3. In order to facilitate further analysis and modelling, i.e. to be able to identify the individual components in a mixture, characteristic peaks were identified for all materials. These peaks are presented in Table 7.1 with their interpretation.

Compound	Raman shift value of the representative peak	Bond assignment
α -LM	840-865 cm^{-1}	C-O (bending) (coupled with other vibrations) (Murphy et al (2005))
MCC	1086-1112 cm^{-1}	C-O-C (deformation), C-C (stretch) (Wiley and Atalla (1987))
PGS	455-500 cm^{-1}	C-O-C (ring mode) C-C-O (deformation) (Labanowska et al (2013))
MS	1278-1310 cm^{-1}	CH (twist)

Table 7.1: The Raman shift value and bond assignment of the representative peak used in the modelling.

7.3.2 Multi-component excipient compacts

A compact composed of 25 %w/w of the four excipients was then analysed in a similar fashion to the mono-component systems. Duplicate scans were taken at 5 μm intervals across and down an area of 100 μm x 100 μm on the surface of the scan, giving a total of 441 point readings.

Figure 7.2 shows the initial data output. The instrument software takes all the readings and co-adds them to generate a global Raman spectrum. The lower line in Figure 7.2 represents the first spectrum taken and the higher line represents the total co-added spectrum.

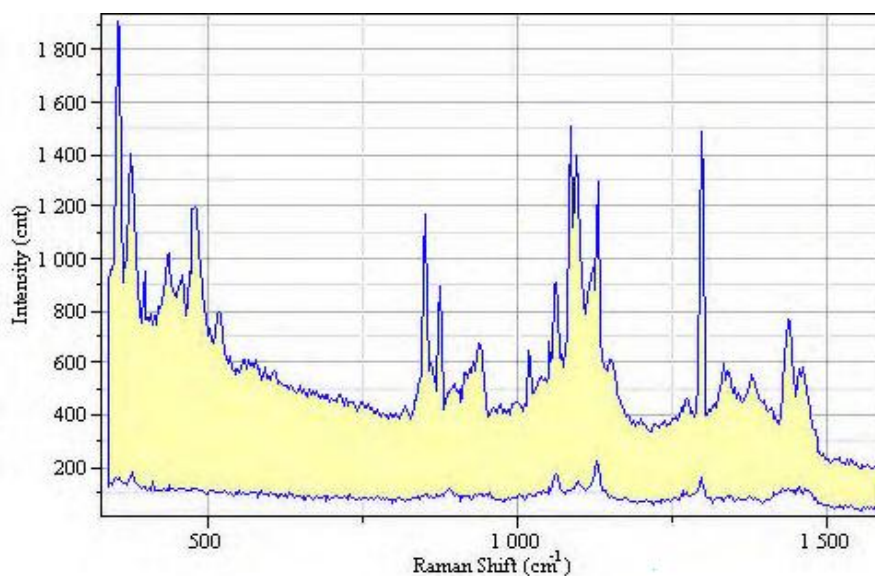


Figure 7.2: The raw Raman spectral data (the "global spectrum") for the multi-excipient compact (25 %w/w each of α -LM, MCC, PGS and MS).

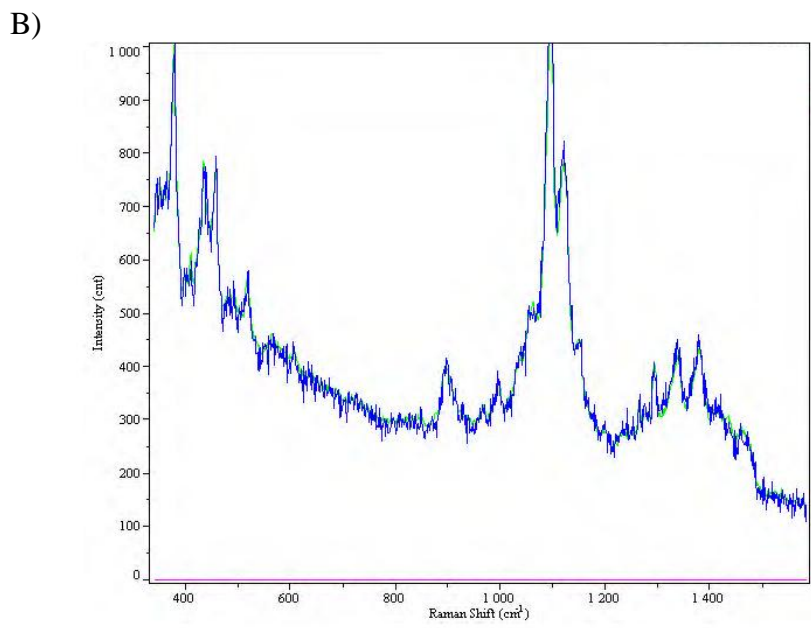
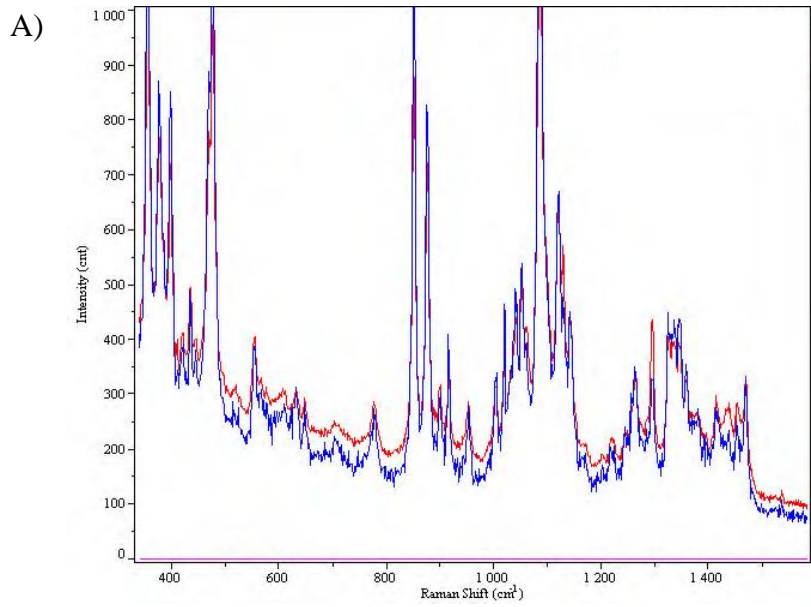
Obviously, Figure 7.2 is not particularly helpful when attempting to study the distribution of components across a surface, so the individual spectra across the grid are then compared to the reference spectra to generate a more detailed map. Using the representative peaks for each material described above as a starting point, the instrument software compares the test spectrum at a specific location to each of the reference spectra in turn, determining the one which fits the best. So if the strongest peak in the sample spectrum matches that of α -LM, the spectrum of α -LM is used as the starting point. This first reference spectrum is

scaled until the main peak intensities of the sample and reference spectra have been matched, then the whole spectra are compared. If there are any peaks in the sample spectrum that haven't been matched, then the process continues with the software identifying the strongest peak not yet fully matched and deciding which of the remaining reference spectra will be the best match to this peak. This iterative process continues until the sample spectrum has been completely matched.

This process is shown in Figure 7.3 for manually selected areas where the four individual components could be seen clearly. In Figure 7.3 A to D, the sample spectrum is shown in dark blue and the reference spectra are shown in the alternate colour: red for α -LM, green for MCC, green for MS and pink for PGS. A good match was seen for all four components, with a low error rating in most cases. The error was calculated by comparing the actual test spectrum with the reference spectrum and estimating the difference across the whole spectral region. The assignment and error for these spectra are shown in Table 7.2.

Scan in Figure 7.2	% of primary component	% of secondary component	% Error
A	106.5 % α -LM		6.5 %
B	100.5 % MCC		0.5 %
C	97.3 % MS	4 % α -LM	1.3 %
D	100.9 % PGS	0.3 % MS	1.2 %

Table 7.2: Calculation of the % components in the scans shown in Figure 7.2



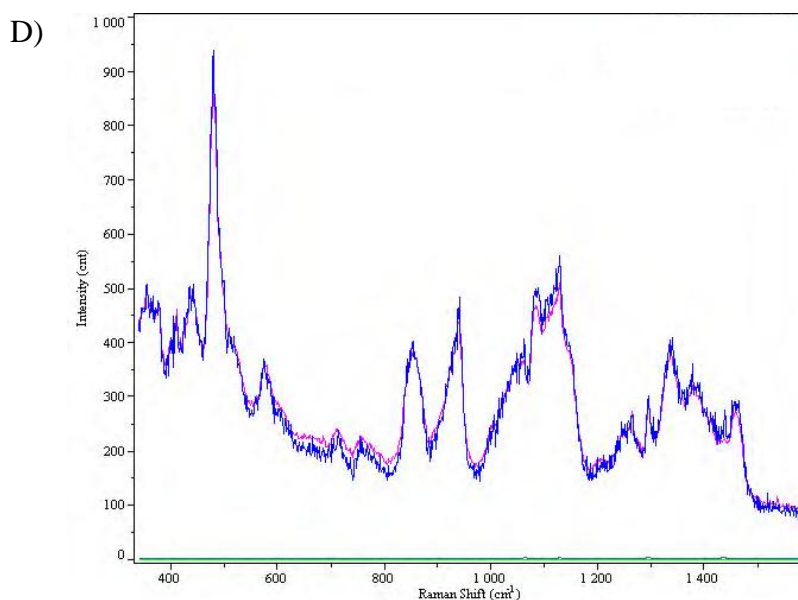
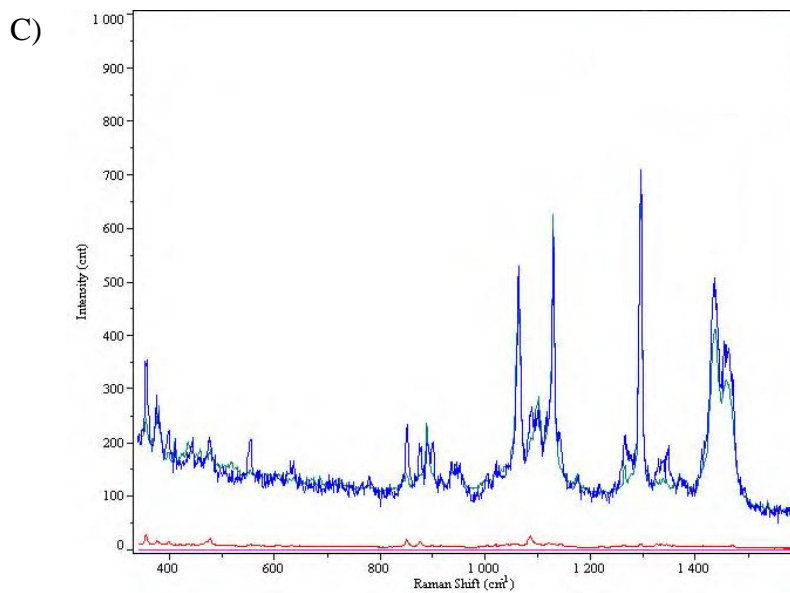


Figure 7.3: Examples of the analysis of the individual spectra and assignment of components. The test sample is the multi-excipient compact (25 %w/w each of α -LM, MCC, PGS and MS). For each location (A to D), the sample spectrum is dark blue and the reference spectrum is the alternate colour. A) α -LM (red). B) MCC (green). C) MS (green). D) PGS (pink).

Once the assignment has been made for each of the 441 individual spectra, two forms of a coloured map are then generated. The first is a single multi-component map showing the distribution of all components; the second consists of four individual maps each showing the distribution of a single component. Merging the four separate maps will generate the combined map. These are shown in Figure 7.4. The single component maps appear as areas of bright colour on a darker background of the same colour. It is the bright colouration which denotes the presence of the specific material: the darker background is an artefact of the software's data processing. It would be better, and less misleading, if the software processed the data to give a black background where no material was detected. The top line in maps such as Figure 7.4 is thought to be an artefact of the data processing, as it appears as a block of constant colour in many scans.

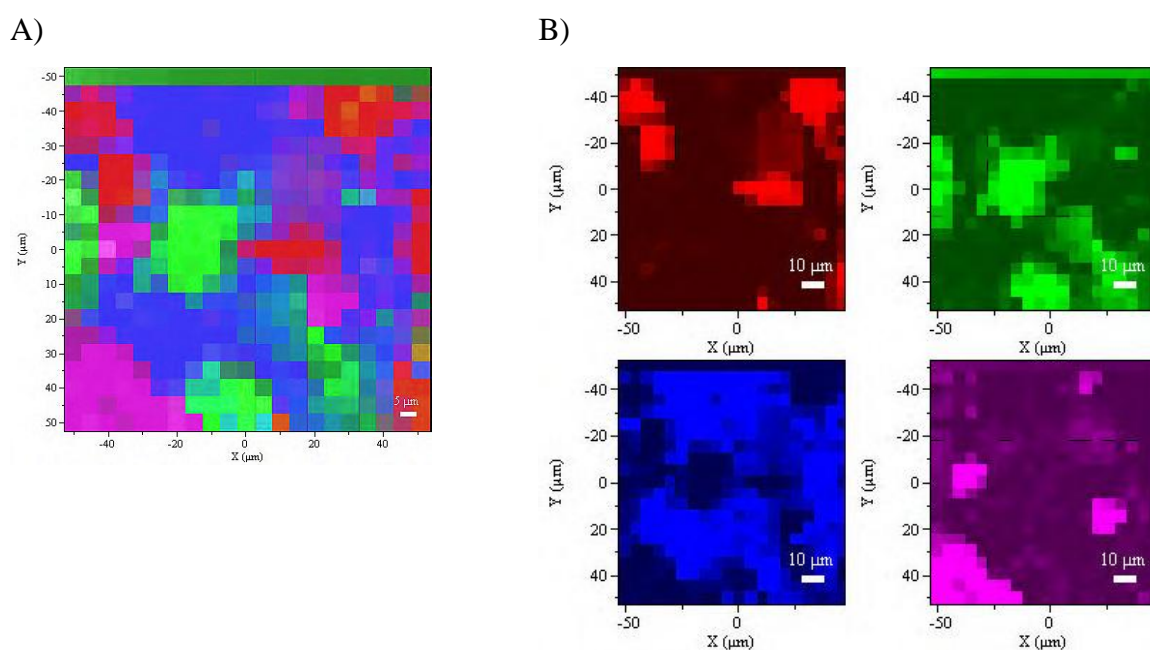
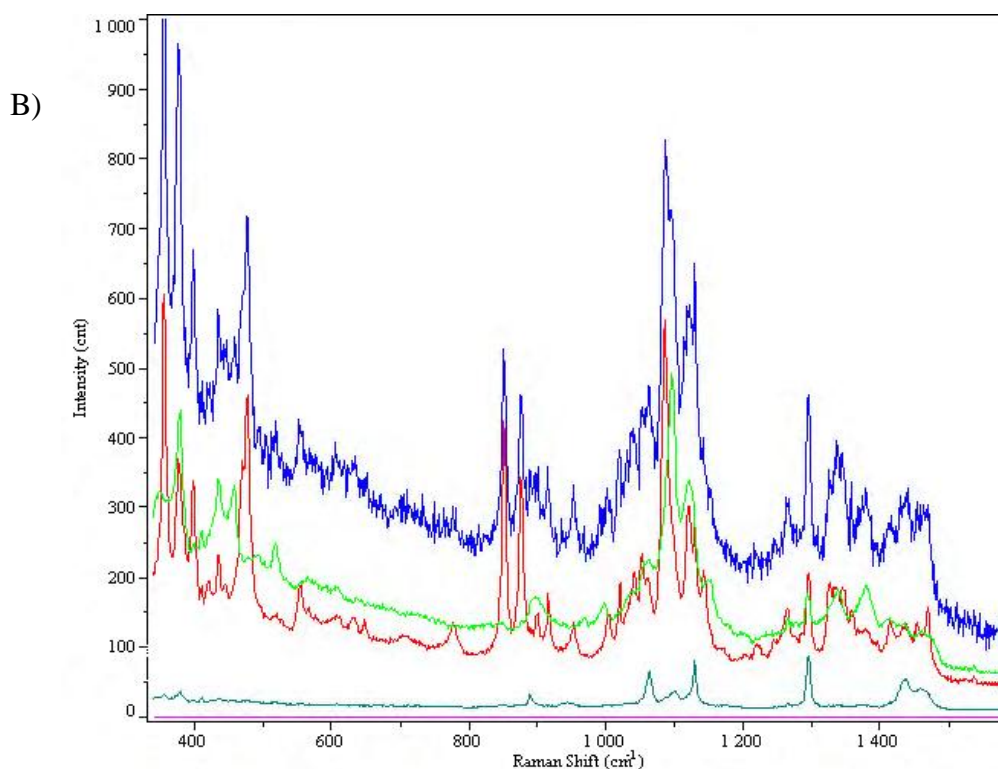
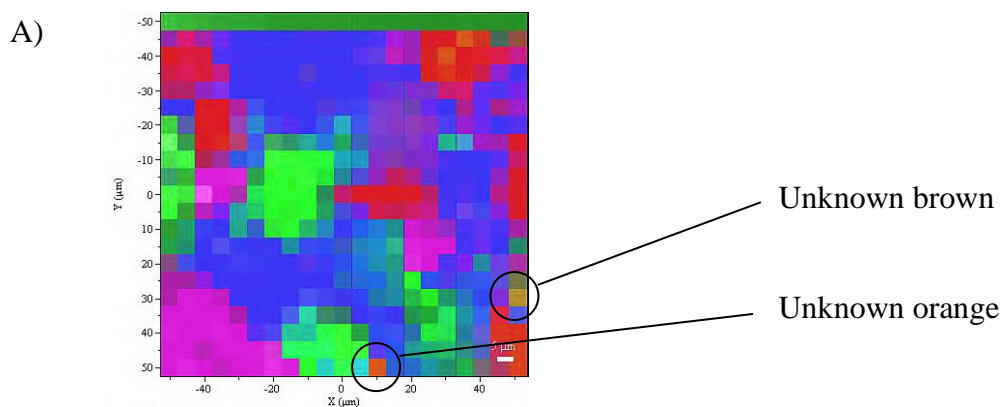


Figure 7.4: An example of the data processing and map generation. The test sample is the multi-excipient compact (25 %w/w each of α -LM, MCC, PGS and MS). A) The processed multi-component map. B) The processed maps of the individual components. The components are shown in the colours allocated in Figure 7.1: α -LM (red), MCC (green), MS (light blue), PGS (pink).

As can be seen from Figure 7.4, all four excipients were detected in this particular scan, giving confidence in the technique. In this scan, the major component was MS. However,

on the multi-component map (Figure 7.4 A), there are a few pixels which are not represented by one of the reference colours assigned to the individual excipients, but have been assigned alternative colours. Two of these pixels are highlighted in Figure 7.5 A and are denoted "unknown orange" and "unknown brown". These pixels correspond to a complex mixture of materials and by examination of the fitted spectra in Figure 7.5 B and C it can be seen that "unknown brown" is composed of 42.9 % α -LM, 50.6 % MCC and 6.0 % MS (in this scan there is an error of 0.5 %) and "unknown orange" consists of 77.2 % α -LM, 15.9 % MCC and 8.4 % MS (the error is 1.5% in this scan).

The colour assignment for these multi-component pixels is made automatically by the software and does not necessarily give any clues as to the actual composition of the sample at that point. For example, it would be expected that "unknown brown" showed a purple colouration, as its two main components are α -LM (assigned red) and MCC (assigned blue), rather than the brown colour it has actually been given.



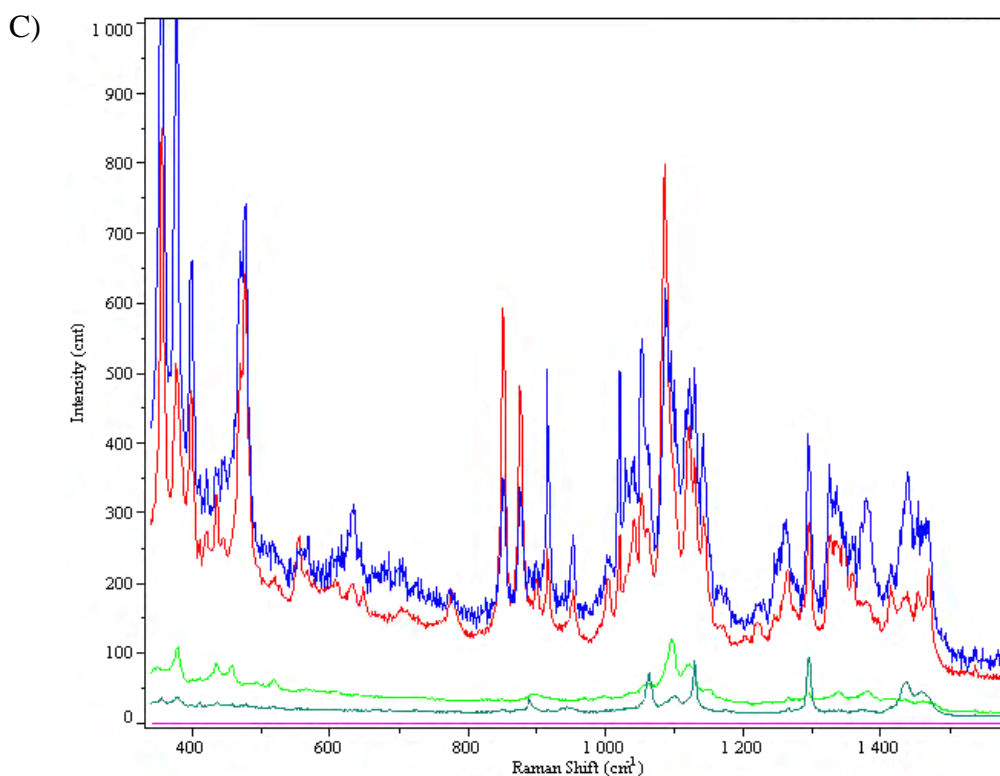


Figure 7.5: The multi-component map from Figure 7.4 of the multi-excipient compact (25 %w/w each of α -LM, MCC, PGS and MS). A) The "unknown" areas are highlighted. B) The assigned spectra for "unknown brown". C) The assigned spectra for "unknown orange". For each location (B and C), the sample spectrum is dark blue and the reference spectra are as follows: α -LM - red, MCC - bright green, MS - dark green, PGS - pink.

7.3.3 Mini-tablets - "development" batches

The work conducted on the mono-component and multi-component excipient compacts indicated that Raman microspectroscopy was sufficiently sensitive to individually detect the presence of the four excipients in a mixed system. The "development" batches of the mini-tablets were then tested in the same manner as the excipient compacts, i.e. an area of 100 μm x 100 μm was analysed, with readings being taken every 5 μm across and down the grid. Generally, it is recommended that a flat surface gives best results with Raman microspectroscopy, as the surface has to be brought into focus by the microscope before the spectra can be generated, which is more difficult for curved surfaces than flat ones. However, the development batches of mini-tablets had been compressed using normal concave punches, so had a curved surface. In this case, a reasonably flat area on the crown

of the mini-tablet was scanned. An example of the results for the direct compression mini-tablet batch is shown in Figure 7.6, illustrating the unprocessed "global" spectrum across the entire scanned area (A), the processed multi-component map (B) and the processed individual component maps (C). All four excipients were detected individually, although MCC and α -LM seem to dominate the response, with PGS and MS being seen in lower quantities. As seen for the compacts earlier, the first line in the scan appears to be anomalous.

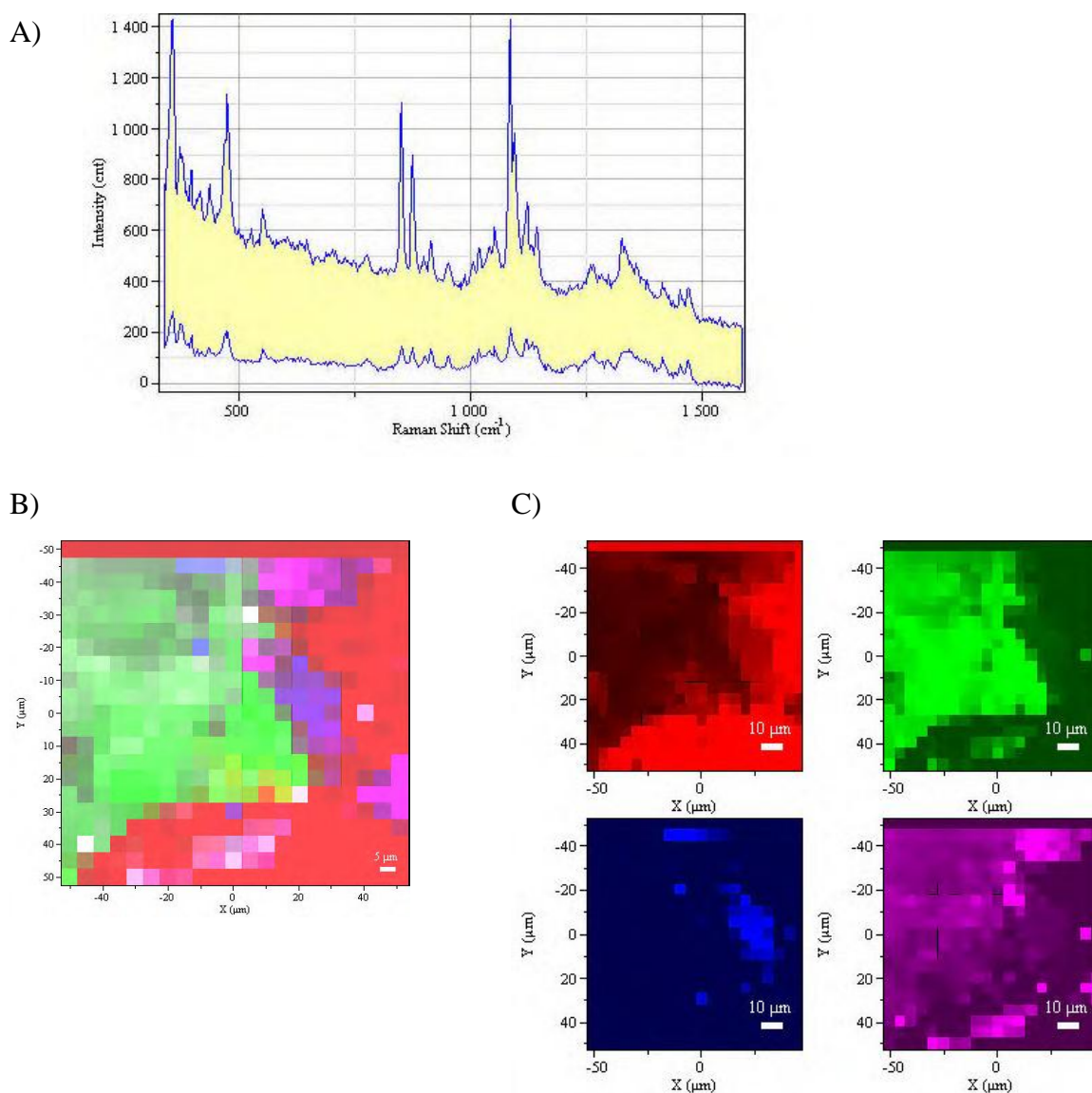


Figure 7.6: An example of the Raman microspectroscopy results for the direct compression mini-tablet development batch. A) The global spectrum of the scanned area. B) The processed multi-component map. C) The processed maps of the individual components. The components are shown in the following colours: α -LM - red, MCC - green, MS - blue, PGS - pink.

Figure 7.7 shows the equivalent results for the wet granulated development batch of mini-tablets. Again, the instrument did not seem to scan the first line correctly. In this case, MS was the predominant component, which was surprising because of its low concentration in the overall mix (1 %w/w). Most of the rest of the surface area examined was made up of MCC, with small amounts only being attributable to α -LM and PGS.

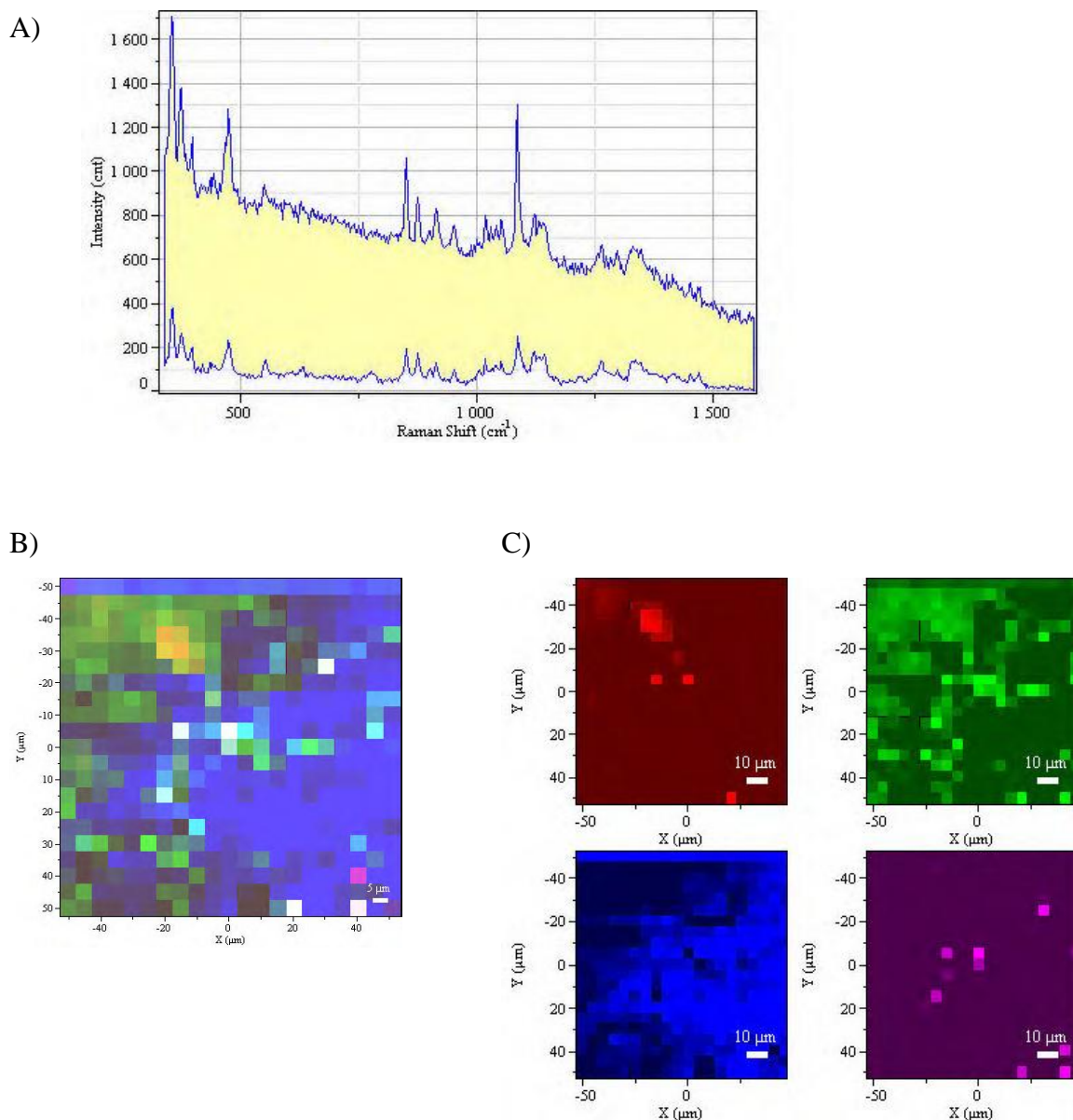


Figure 7.7: An example of the Raman microspectroscopy results for the wet granulated mini-tablet development batch. A) The global spectrum of the scanned area. B) The processed multi-component map. C) The processed maps of the individual components. The components are shown in the following colours: α -LM - red, MCC -green, MS - blue, PGS - pink.

7.3.4 Mini-tablets - "experimental" batches

The experimental batches of granule were compressed into 3 mm diameter compacts to give a flat surface, so as to maximise the efficiency of the Raman microspectroscopy experiments. This was in contrast to the thermal analytical work conducted in Chapter 6, whereby the granule was compressed into normal convex tablets. A similar protocol to that used previously for the development batches of mini-tablets was used here for the excipient-only experimental batch of tablets, but with a reduced scanning area (50 μm x 50 μm rather than 100 μm x 100 μm), as the formulation was so similar to that of the development batches and to maximise the equipment time for the drug-loaded batches. In addition, a higher-resolution scan was performed, taking readings every 2 μm across the full 100 μm x 100 μm area - in this case, the run took approximately 8 hours. The spectra were processed as described above using Figure 7.1 as the reference for the individual components.

Figure 7.8 shows an example of the "normal" Raman microspectroscopy results generated at 5 μm intervals on the wet granulated excipient-only experimental batch. Figure 7.9 illustrates the "high resolution" results, generated at 2 μm intervals. These images were taken across the surface of the same mini-tablet, but at different locations. All four excipients were detected in the "low resolution scans", roughly reflecting their concentrations in the formulation. MS predominated in the high resolution scan, covering approximately 50 % of the surface, with the other excipients being present in roughly their formulation proportions. The higher resolution image shows more information, but this has to be considered alongside the increased data acquisition time.

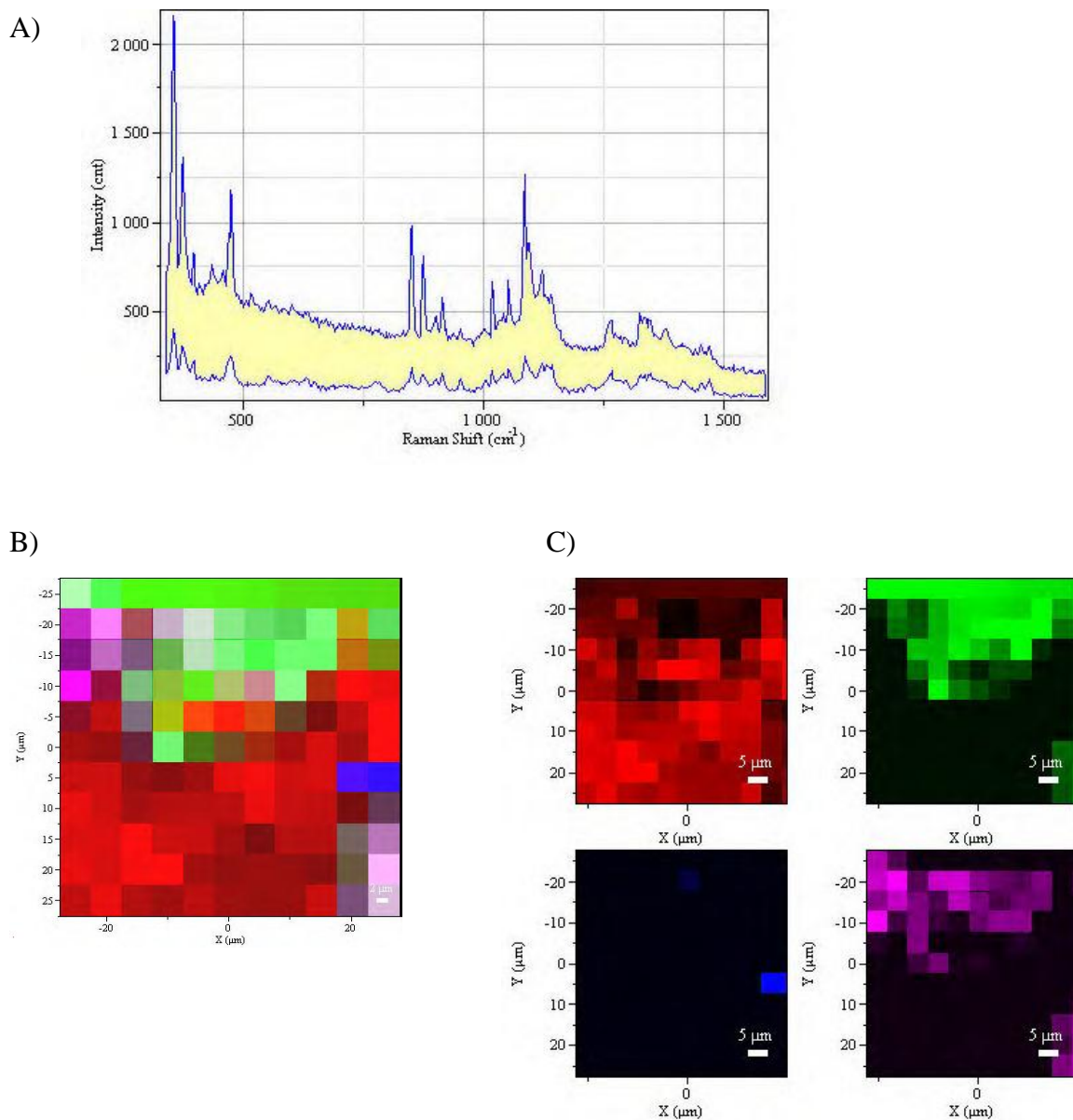


Figure 7.8: An example of the Raman microspectroscopy results for the excipient-only experimental batch of mini-tablets. A) The global spectrum of the scanned area. B) The processed multi-component map. C) The processed maps of the individual components. The components are shown in the following colours: α -LM - red, MCC -green, MS - blue, PGS - pink.

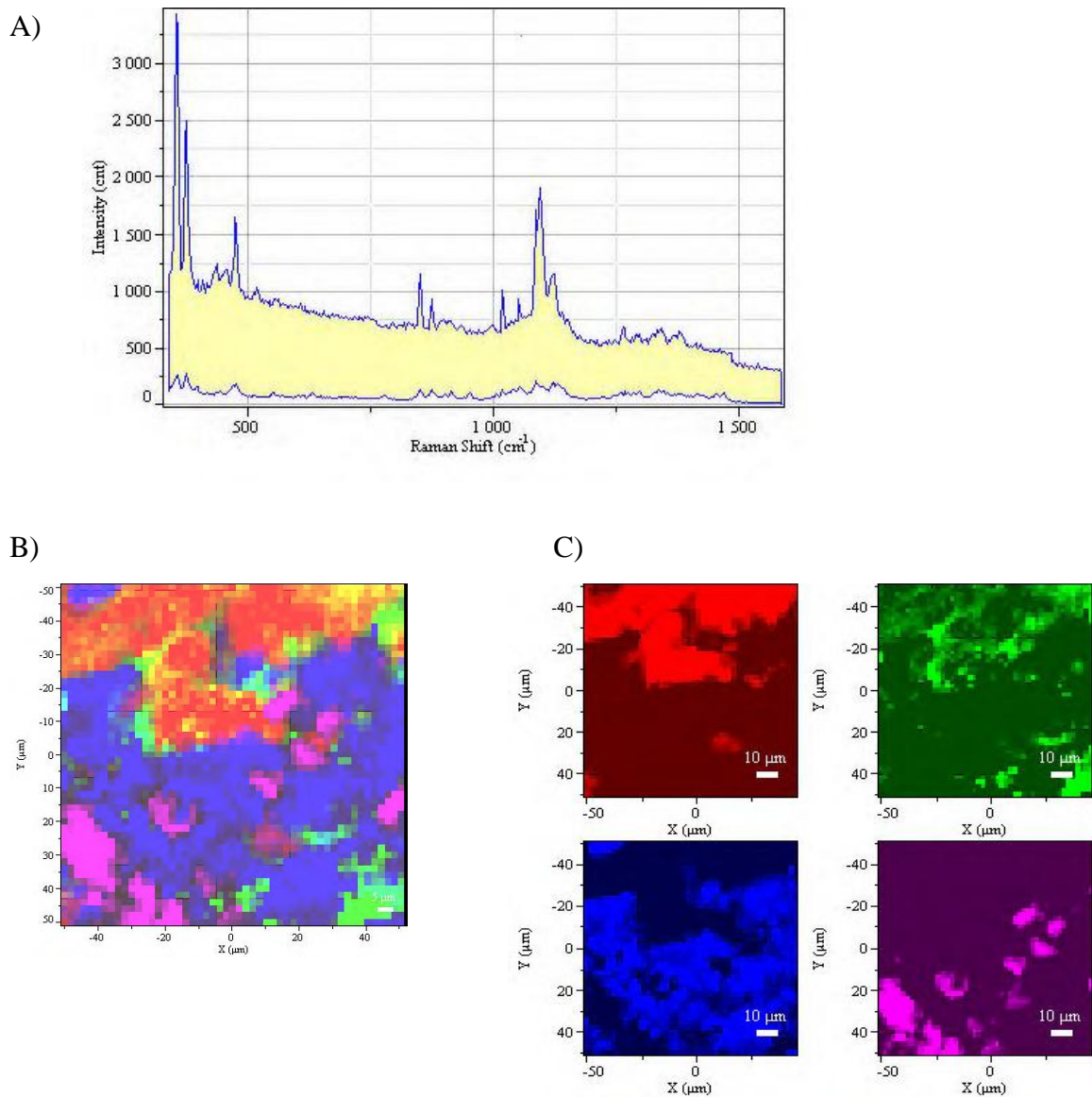


Figure 7.9: An example of the high resolution Raman microspectroscopy results for the excipient-only experimental batch of mini-tablets. A) The global spectrum of the scanned area. B) The processed multi-component map. C) The processed maps of the individual components. The components are shown in the following colours: α -LM - red, MCC - green, MS - blue, PGS - pink.

A similar data set was generated for the caffeine-loaded mini-tablets: a "normal" resolution image taking measurements every 5 μm and a higher resolution image taking measurements every 2 μm . Prior to the mini-tablets being scanned, a reference spectrum of caffeine was generated using the same process as for the excipients, and is shown in Figure 7.10 along with those of the excipients, taken from Figure 7.1. The peak at 530 to 585 cm^{-1} was taken to be the representative peak for caffeine and is ascribed to C-N-CH₃ deformation (Gunasekaran et al (2005)).

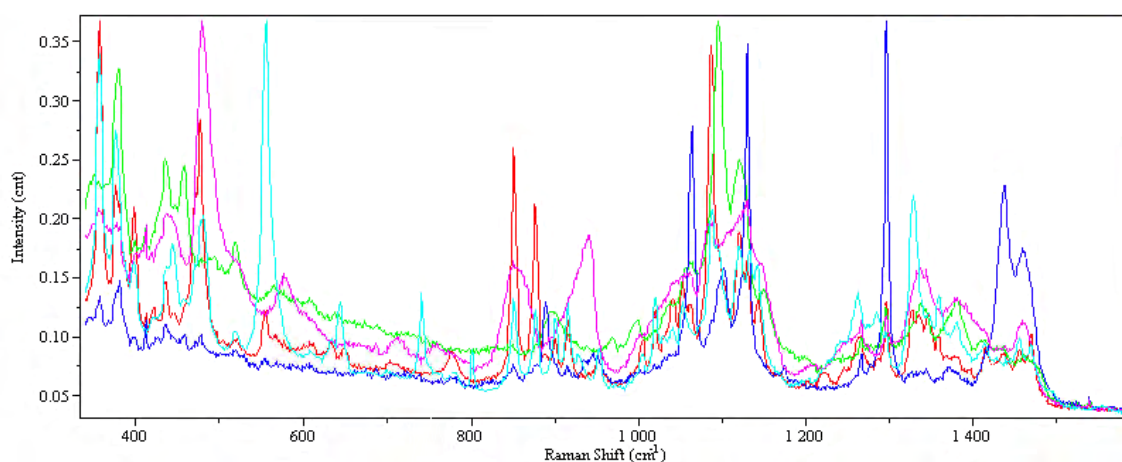


Figure 7.10: The reference Raman spectra for the excipients used in the formulation and caffeine. α -LM (red), MCC (green), MS (dark blue), PGS (pink) and caffeine (pale blue).

Figure 7.11 illustrates the assignment of the spectrum of a caffeine-rich region of the scan of the caffeine-loaded mini-tablets. The component assignment in this case was 96.1 % caffeine and 1 % PGS, with an error rating of 2.9 %.

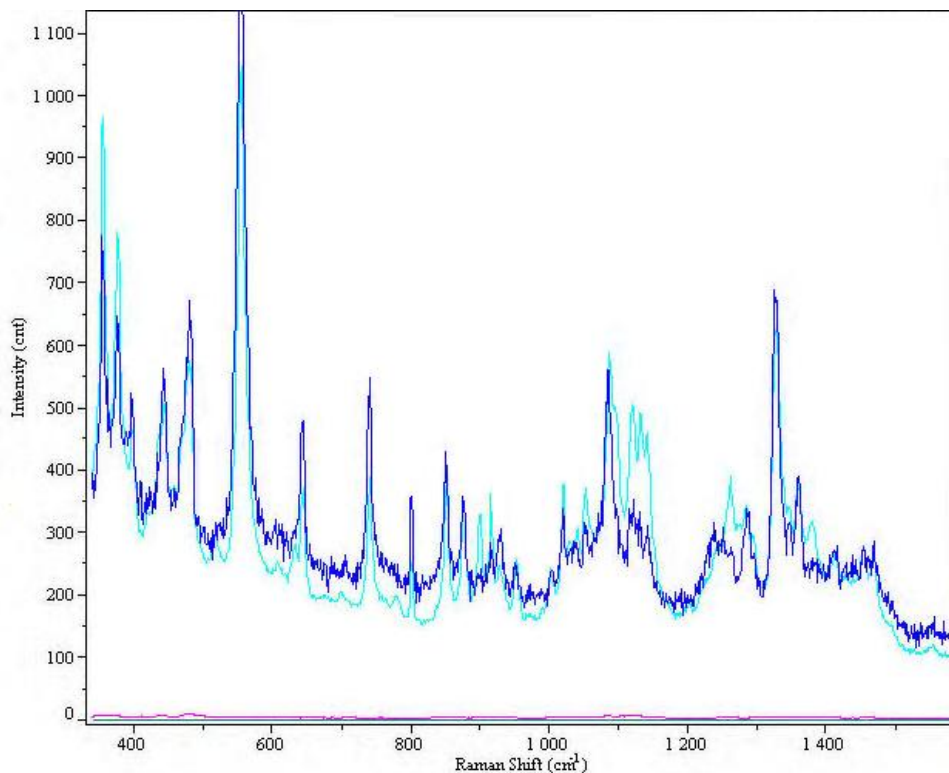


Figure 7.11: A sample spectrum of a caffeine-rich region on a caffeine-loaded compact. The sample spectrum is dark blue, caffeine's reference spectrum is pale blue and PGS is show in pink.

As with the excipient-only batch, both normal and higher resolution images were generated on the caffeine-containing mini-tablets, and the results are shown in Figures 7.12 and 7.13, respectively. In the lower resolution scan, the surface was composed mainly of α -LM with some MCC and caffeine, and very little of the two other components. The higher resolution scan showed similar results, with α -LM and caffeine predominating, but all materials being detected. Also as noted with the excipient-only compacts and mini-tablets, the first line of the scan appeared to be noise, with the instrument requiring this time to "settle down". The reason for this is unknown, but it seems to happen with all runs.

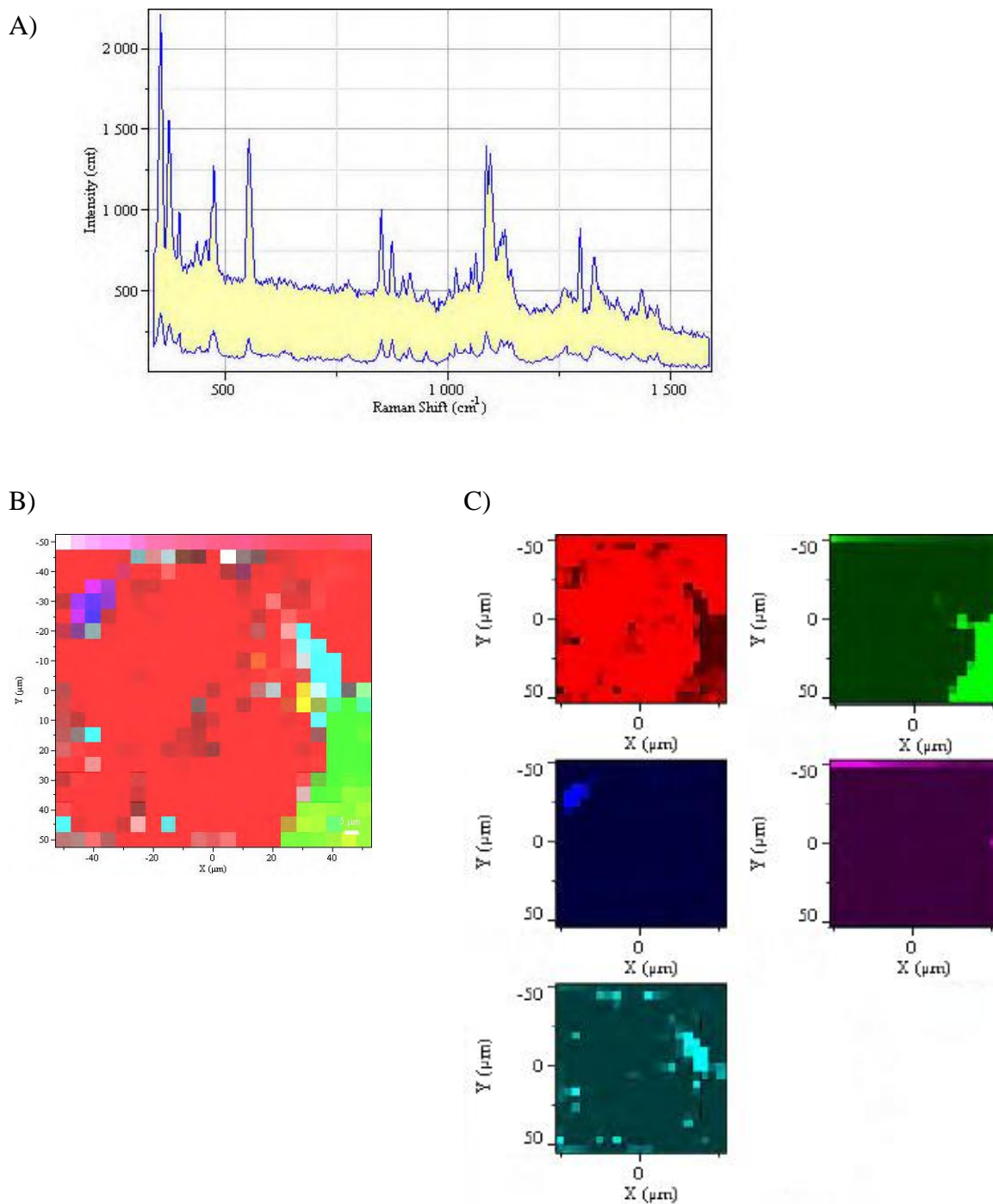


Figure 7.12: An example of the Raman microspectroscopy results for the caffeine-loaded experimental batch of mini-tablets. A) The global spectrum of the scanned area. B) The processed multi-component map. C) The processed maps of the individual components. The components are shown in the following colours: α -LM - red, MCC -green, MS - blue, PGS - pink, caffeine - pale blue.

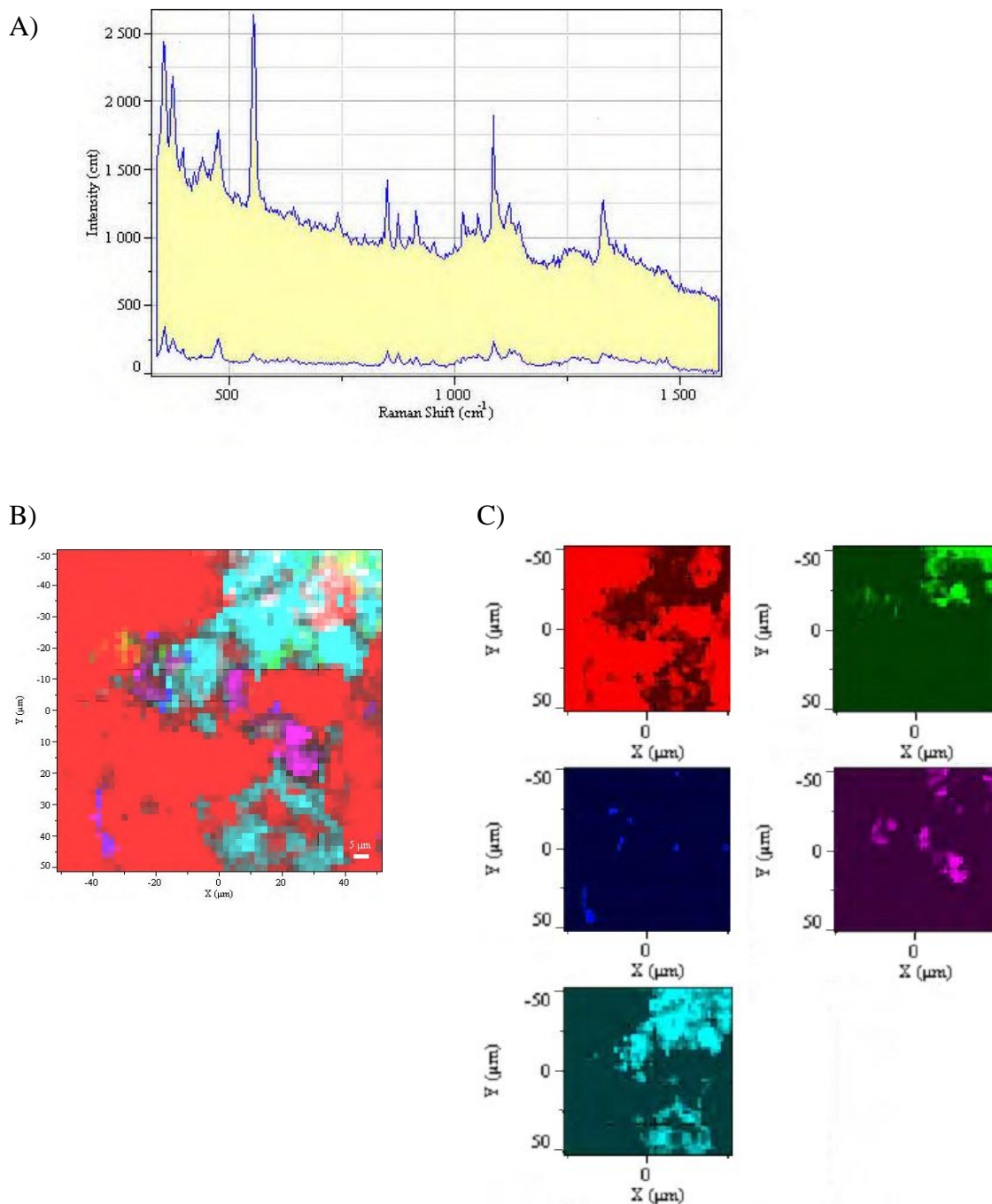


Figure 7.13: An example of the high resolution Raman microspectroscopy results for the caffeine-loaded experimental batch of mini-tablets. A) The global spectrum of the scanned area. B) The processed multi-component map. C) The processed maps of the individual components. The components are shown in the following colours: α -LM - red, MCC - green, MS - blue, PGS - pink, caffeine - pale blue.

The final data set was generated on the ibuprofen-loaded mini-tablets, with the experimental parameters being as described above for the caffeine-loaded mini-tablets. Both normal and high resolution images were generated. Prior to the mini-tablets being scanned, a reference spectrum of ibuprofen was generated using the same process as for the excipients, and is shown in Figure 7.14 along with those of the excipients, taken from Figure 7.1. The peak at 750 to 790 cm^{-1} was taken to be the representative peak for ibuprofen and is ascribed to out of plane bending, CH_3 rocking and C-O out of plane wagging (Vuebu et al (2008)).

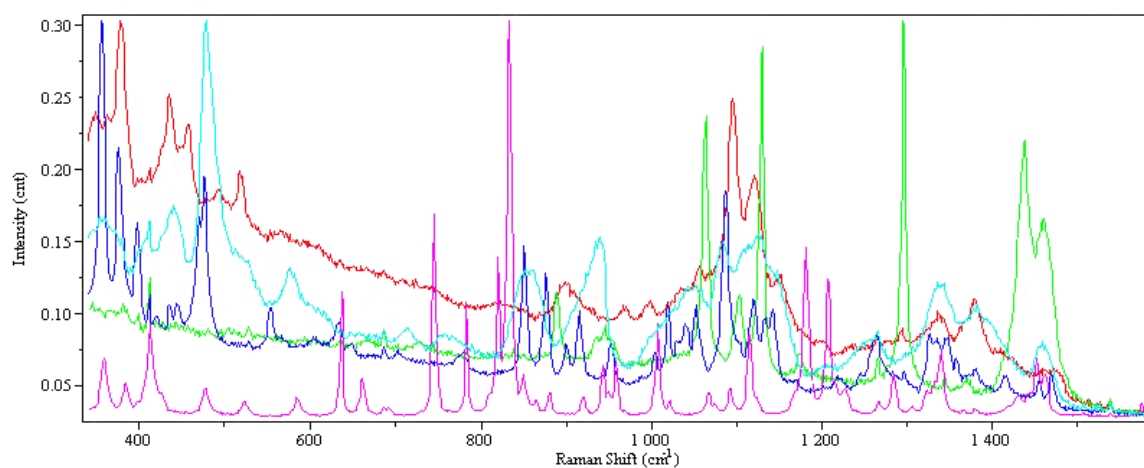


Figure 7.14: The reference Raman spectra for the excipients used in the formulation and ibuprofen. α -LM (dark blue), MCC (red), MS (green), PGS (light blue) and IBU (pink).

Figure 7.15 illustrates the assignment of the spectrum of an ibuprofen-rich region of the scan of the ibuprofen-loaded mini-tablets. The component assignment in this case was 48.6 % ibuprofen and 16.8 % PGS, 28.1 % α -LM, 5.5 % MS with an error rating of 1.0 %.

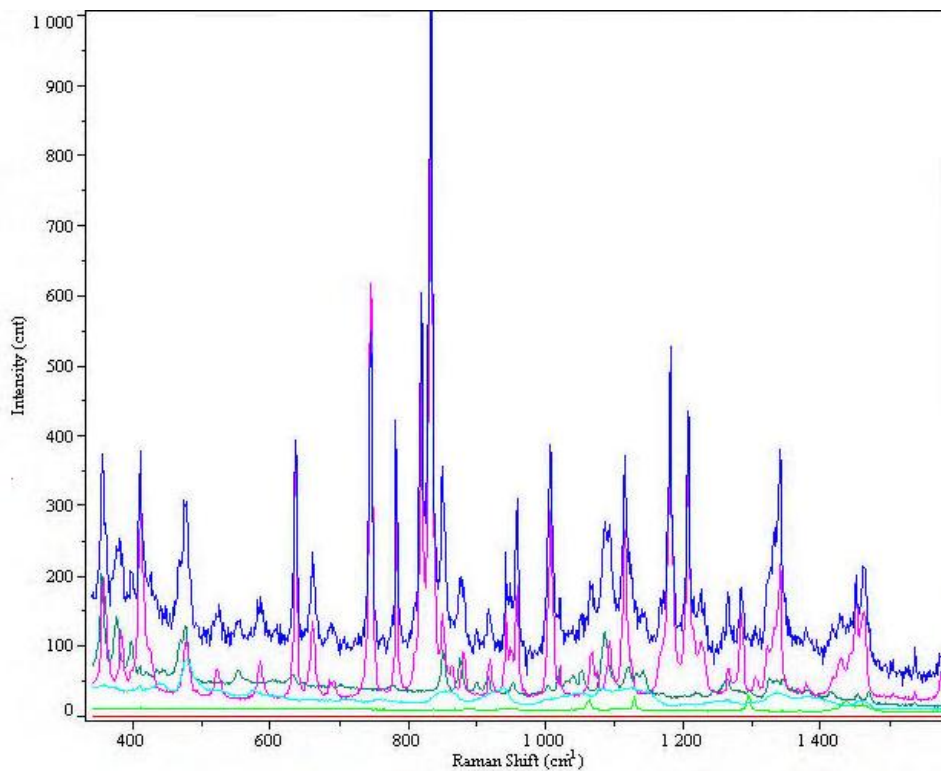


Figure 7.15: A sample spectrum of an ibuprofen-rich region on an ibuprofen-loaded compact. The sample spectrum is dark blue, ibuprofen's reference spectrum is pink, α -LM is shown in blue, MCC is shown in red, MS is shown in green and PGS is shown in pale blue.

Figures 7.16 and 7.17 show the normal and higher resolution images for the ibuprofen-loaded mini-tablets. All five components could be detected in both scans. α -LM was observed in high concentrations in both scans, reflecting its high concentration in the formulation. Ibuprofen was detected in higher amounts in the higher resolution scan.

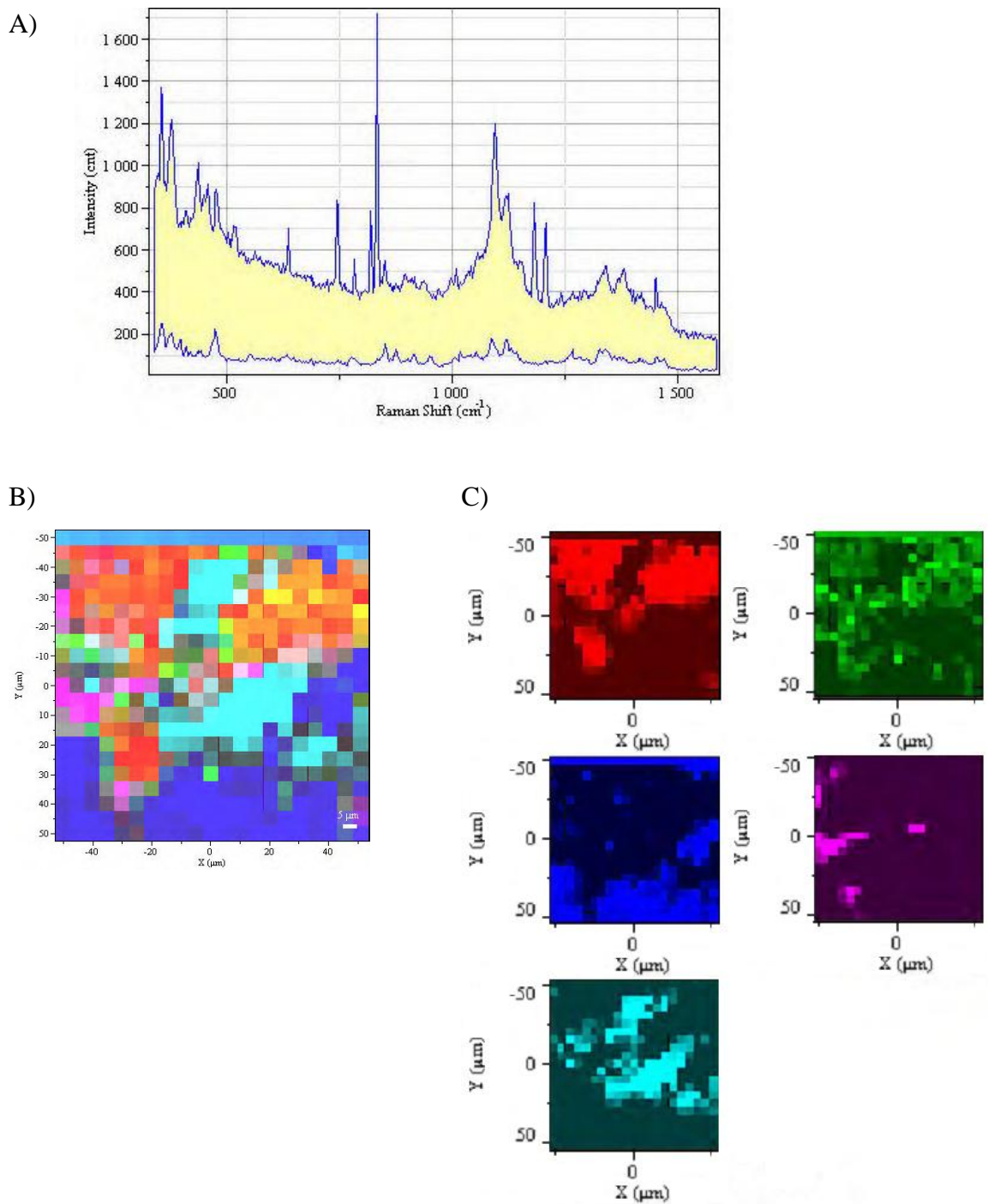


Figure 7.16: An example of the Raman microspectroscopy results for the ibuprofen-loaded experimental batch of mini-tablets. A) The global spectrum of the scanned area. B) The processed multi-component map. C) The processed maps of the individual components. The components are shown in the following colours: α -LM (blue), MCC (red), MS (green), PGS (light blue) and ibuprofen (pink).

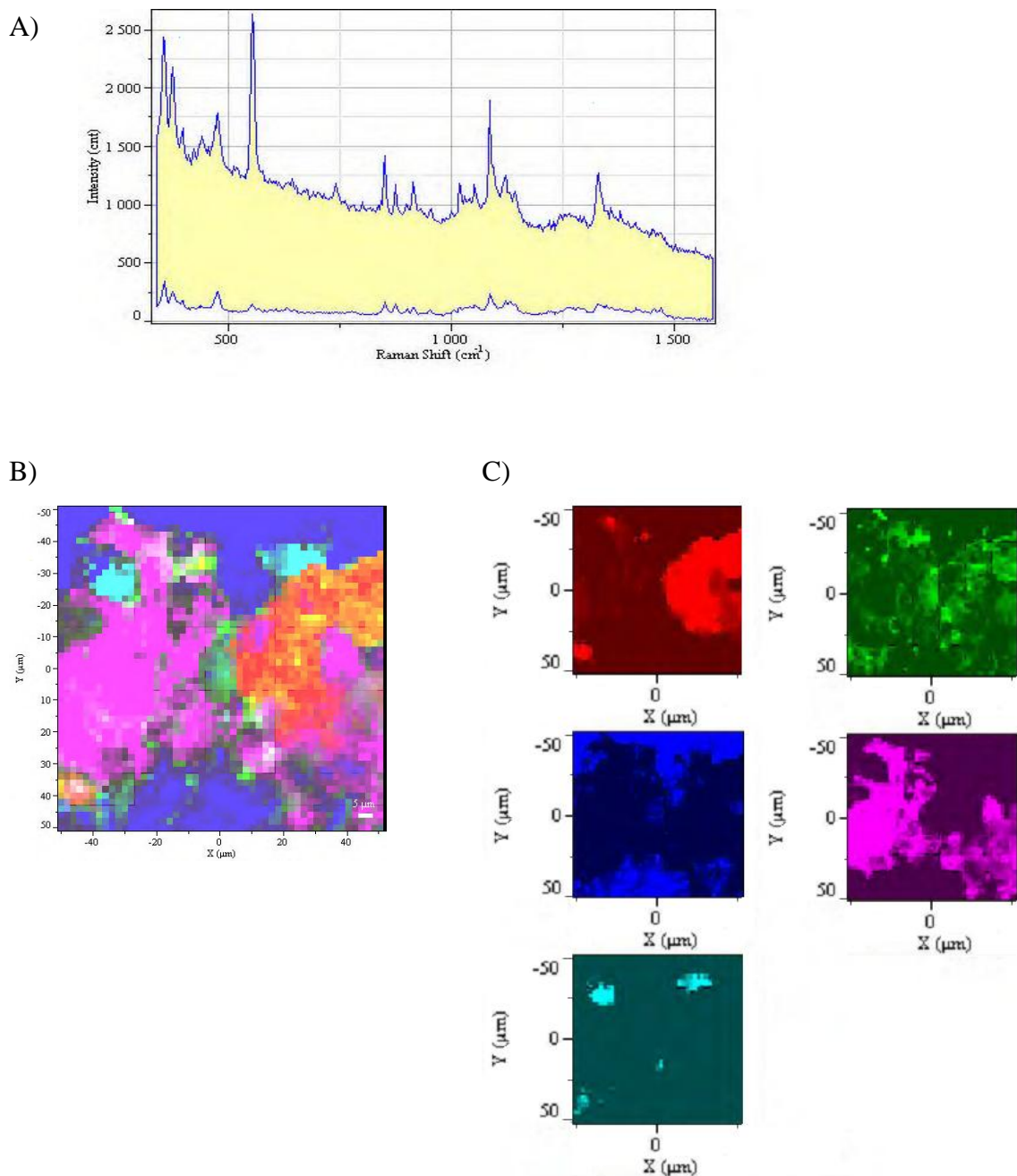


Figure 7.17: An example of the high resolution Raman microspectroscopy results for the ibuprofen-loaded experimental batch of mini-tablets. A) The global spectrum of the scanned area. B) The processed multi-component map. C) The processed maps of the individual components. The components are shown in the following colours: α -LM (blue), MCC (red), MS (green), PGS (light blue) and ibuprofen (pink).

7.4 Conclusions

The purpose of performing the Raman micro-spectroscopy work conducted in this Chapter was to allow a comparison between the novel surface analytical techniques studied in the previous Chapters (nano-TA and TTM) with a surface analytical technique originating from a different physical phenomenon. Nano-TA and TTM are based on the response of the sample to a thermal stimulus, i.e. how it responds to applied heat. In Raman spectroscopy, the sample responds to the application of light of a particular wavelength. Hence, the two sets of techniques should be complementary as they are probing different elements of a sample's behaviour.

As the Raman spectroscopic technique is more established, a shortened version of the development process was used, compared to that undertaken with the nano-TA and TTM. Here, the individual components were studied as mono-component compacts, but rather than the full 2-, 3-, 4- and 5- component exercise undertaken with the thermal analytical techniques, only the 4-excipient mixtures and the mini-tablet formulations were tested.

Raman microspectroscopic mapping works by generating a Raman profile at each point in a grid, co-adding these to give a global spectrum, then comparing the spectrum at each point to reference spectra previously generated. A map is then produced, with colours relating to the individual components. For all the multi-component samples tested here, each individual material could be observed individually. However, this separation obviously relies on the individual components being distinct enough in their Raman profiles to allow this to happen. Two materials with bands in too close proximity may be confused for each other during the deconvolution process. The more components in a mixture, the more difficult it will be to perform the deconvolution process, as obtaining a clear reference peak for each component will become more challenging the more the components are present. Similarly, the equipment must be stable as any "drift" in the spectra during the acquisition time will also affect the deconvolution process.

A more subtle issue arises with the intensity of the Raman response. The individual point spectra are co-added to give the global spectrum prior to deconvolution. Hence, a balance has to be struck between having a strong enough response to allow confidence in the results and a detailed enough response to allow the deconvolution process to occur. Adding more and more point spectra to a map will effectively overload the system and not

allow proper interpretation. Similarly, if the material under test shows fluorescence, this will be registered as a high intensity response, which can distort the analysis. In this work, this was seen once and the raw data are shown in Figure 7.18. The high intensity (almost 4000 counts, whereas other similar spectra showed about 2500 counts) was associated with one particular point reading which was abnormally high. From knowledge of the sample under test, this was ascribed to contamination and the response from this pixel was removed from the raw data before the data processing began. Of all the techniques studied here, only Raman microspectroscopic mapping allowed this removal process to occur. However, as fluorescence is a commonly observed phenomenon, it could be a potential problem with this technique and needs to be borne in mind when considering the results from a Raman microspectroscopic mapping exercise.

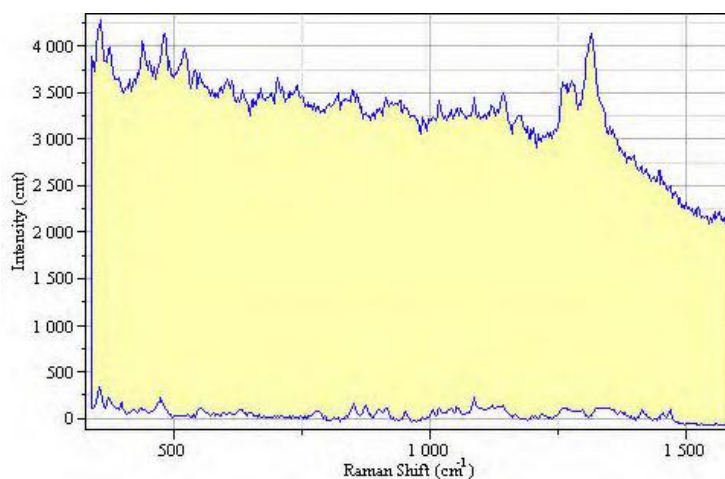


Figure 7.18: The raw results for a high resolution scan of a wet granulated mini-tablet (100 μm x 100 μm area and readings taken every 2 μm).

The final output of the Raman microspectroscopic mapping exercise is a multi-component pixellated map, which can then be split into maps of the individual materials. This splitting enables visual analysis and allows patterns of material distribution to be seen clearly. Raman microspectroscopic mapping was the only one of all the techniques examined which had this feature, so is a definite advantage to this technique. However, a slight issue relates to the colours assigned to an "unknown", when a point spectrum is due to a mixture of components rather than a single component. The software works from a red, blue and green palette and composes mixed colours from these, rather than from the normal, everyday colour mixing that people are familiar with. It is therefore not always

obvious what a mixed point might be composed of, so all unknown squares need to be examined individually to determine their composition.

Both "low" and "high" resolution images were taken in this work. The higher resolution image gave more detail, but required more time to obtain the images. On the other hand, the lower resolution image took less time to acquire, but the detail was not as great. A compromise is therefore required between acquisition time and information detail. A sensible compromise would probably be to obtain several "low" resolution images across the sample surface to examine the distribution of materials at different points.

During this work, there was a concern that the curved surfaces of the mini-tablets would prove too difficult to scan using Raman microspectroscopic mapping and so the experimental batches were compressed as flat 3 mm diameter compacts, rather than normal convex mini-tablets. Only the development batches of mini-tablets were studied with curved surfaces. The curvature of the surface proved not to be a problem, as the area scanned is relatively small (100 μm x 100 μm), so appears reasonably flat to the microscope. Hence, in future work, mini-tablets rather than flat compacts could be studied.

In conclusion, Raman microspectroscopy mapping has been shown to be a useful technique for the assessment of the distribution of component materials across the surface of mini-tablets. As it originates from a different physical phenomenon and is non-destructive, it can be used as a companion technique to the thermal analytical techniques discussed in previous Chapters.

Chapter 8

Overall discussion and conclusions

CHAPTER 8

Overall discussion and conclusions

8.1 Summary of work performed

The aim of this project was to investigate the surface distribution of materials in mini-tablets using a range of novel techniques. These techniques were micro-TA, nano-TA and TTM. Raman microspectroscopy was also performed on a range of samples for a comparison between these novel techniques and a more well-established surface technique based on a different physical phenomenon (response to light rather than response to heat).

8.1.1 Individual components

Initially, four excipients commonly used in tablet formulations (α -LM, MCC, PGS and MS) and two model drugs (caffeine and ibuprofen) were profiled using a range of analytical techniques (the results are presented and discussed in Chapter 3 and Chapter 4). Flat compacts or powder (as appropriate) of each individual component were produced and tested using SEM, VT-IR, DSC, AFM, micro-TA, nano-TA and TTM. The information gained from this initial profiling was used to interpret the more complicated multi-component products studied later.

SEM was conducted to gauge the general physical appearance of the surface of the powders and to give a measure of particle size and shape. The various materials were all quite different in their particle morphology.

DSC was conducted on both powder and mini-tablet compressed forms of each material. Pin-holed pans were used throughout to allow removal of loosely-adhered water or water of crystallisation of the excipients. The DSC traces of the loose powder and compressed mini-tablets were very similar for each excipient, with the main difference being the rate and temperature of removal of water from the sample. Generally, the mini-tablet form showed a slower rate of removal of water, which is thought to be due to the slower rate of transport of evaporated water from the centre of the mini-tablet than from the surface of the loose powder. MCC and PGS (Figure 3.3 and Figure 3.14 respectively) were

essentially un-reactive over the temperature range studied, showing only removal of loosely-adhered water, whilst MS showed dehydration and melting behaviour. α -LM showed complex behaviour with dehydration, muta-rotation to β -lactose, melting and decomposition all being seen (Figure 3.32). Caffeine demonstrated a polymorphic transition before melting (Figure 4.4), whereas ibuprofen showed only a melting transition, at the lowest temperature of any material studied here (Figure 4.18). DSC was performed to help interpret the data from the other techniques, although it must be remembered that DSC is an averaging technique, i.e. it measures the response of the whole sample, rather than just that of the surface as the other techniques do. The ability of DSC to examine the whole mini-tablet without further processing is useful in cases where compression of a powder into a tablet, or grinding of a tablet into powder for analysis, may cause polymorphic change (e.g. caffeine (Mazel et al (2011)), amorphisation (e.g. indometacin (Priemel et al (2013)) or re-crystallisation (cephalothin sodium (Otsuka and Kaneniwa (1990))), as it will allow the in-situ analysis of the form of the drug.

VT-IR was performed on all the individual materials in the powder form. It is possible to conduct the experiment on the compacts, but it was found that the powder gave better contact once the sample is clamped in place. The thermal limit of the experiment was dictated by the instrument used, which could only run between room temperature and 200°C. A higher endpoint of approximately 300°C would have been beneficial for studying PGS, MCC and caffeine. FT-IR scans were collected isothermally at 10°C intervals, following a 2 minute equilibration period at each testing temperature. A general observation was made that the thermal events seen with the VT-IR seemed to occur at slightly higher temperatures than the DSC experiment suggested. It is possible that this is due to a slight thermal lag in the experiment: the sample is sitting on a heated stage and it is the temperature of the stage that is recorded and controlled, rather than that of the sample itself. It would be useful to quantify this and it may be necessary to extend the equilibration period beyond that which was used in these experiments.

Another source of error in the VT-IR experiments is that a blank run could not be performed before each scan at the different temperatures. This is because the blank run needs to be performed on the empty cell and it is not possible to open the sample cell, remove the sample, close the sample cell, perform a blank run and replace the sample whilst keeping the temperature constant. As a compromise, a complete blank run was performed taking readings at each temperature with no sample present. These blank

readings were then subtracted from the test results to give the final spectra for analysis. However, it is appreciated that potentially not all instrument noise or drift related to temperature changes may be accounted for.

With the exception of α -LM (Figure 3.28), the materials studied appeared to be stable to heat when studied by VT-IR, with only dehydration and increased molecular movement within the sample being observed in the FT-IR scans as the temperature was increased. Most of the materials have the potential to form hydrogen bonds, which will be affected by temperature and in particular dehydration. α -LM gave the most unexpected result on VT-IR, with evidence that β -lactose was formed. Further investigation demonstrated that both evaporated water and pressure are required for this muta-rotation process to occur, as it did not take place for anhydrous α -lactose (Figure 3.30). The polymorphic transition for caffeine was clearly observed on DSC, but only minor changes were observed here on the VT-IR scans of the two polymorphs (Figure 4.3). Although the crystal habit is very different for the two forms of caffeine (Form I has a long needle-like crystals and Form II is more granular in appearance), the unit cells are very similar and hence do not show any appreciable difference on FT-IR.

AFM was performed to investigate the surface topography of the sample. Its main role was to assist with the micro-TA and nano-TA measurements, because it is important that the probe makes good contact with the surface and does not fall down a crack or off a local peak. Either of these occurrences would greatly affect the micro-TA or nano-TA results and give a false reading, so AFM is used to assess the positioning of the probe before the thermal measurements are taken. While no distinguishing feature for any of the materials which allows it to be identified visually, except for PGS (Figure 3.15) which showed a distinctive circular pattern.

Both micro-TA and nano-TA were conducted on separate compacts of all materials. Figures 8.1 and 8.2 show summaries of the micro-TA and nano-TA results, respectively. Each component gave a different micro-TA profile, which should enable identification in mixed systems, although some differences were relatively subtle. For example, PGS and MCC showed no distinct thermal response, such as melting, over the temperature range studied, but their baseline changes were sufficiently dissimilar to allow differentiation visually. α -LM occasionally showed a two-step micro-TA profile, which was more often seen when the compacts were made under higher pressure. It is thought the first step in

this process is dehydration of the α -LM to anhydrous α -lactose, as a deflection at this temperature was not observed when either anhydrous α -lactose or β -lactose were tested (Figure 3.43). A general trend was observed that the transition temperatures measured by either micro-TA or nano-TA are different to those observed by DSC, so some interpretation is required by the operator when examining data from these techniques. For the excipients, the transition temperatures measured by the nano-TA are similar to those observed using the micro-TA data. However, the drugs studied showed a different behaviour, in that the micro-TA and nano-TA results were not superimposable and the nano-TA results showed greater deviation from the DSC results in terms of observed transition temperatures. This observation was probed in more depth by the analysis of a range of other drugs and is thought to be related to the differences in surface and bulk behaviour of materials, and to the precise positioning of the nano-probe. This is discussed further in section 8.2.2, but the profiles generated are sufficient to allow the development of the TTM process.

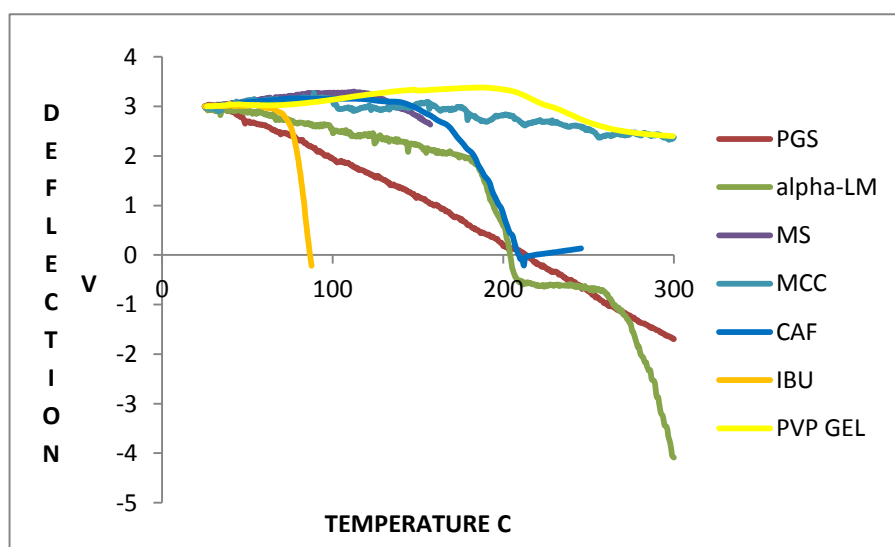


Figure 8.1: A summary of the micro-TA profiles of the excipients (α -LM, MCC, PGS, MS and PVP in the gel form) and drugs (caffeine and ibuprofen) used in this study.

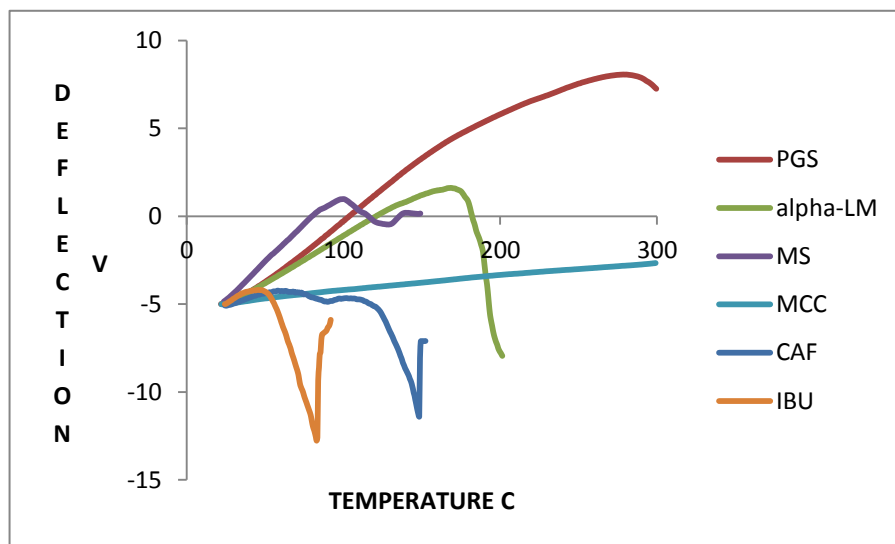


Figure 8.2: A summary of the nano-TA profiles of the excipients (α -LM, MCC, PGS and MS) and drugs (caffeine and ibuprofen) used in this study.

8.1.2 Mixed systems

Compacts of all possible permutations of 2, 3 and 4 excipients were prepared and tested using AFM, nano-TA and TTM, with the results being presented and discussed in Chapter 5. In most cases, MS was present at 1 %w/w to reflect its concentration in standard pharmaceutical tablet formulations, but for the 4-component system, it was also tested at a higher concentration (25 %w/w) to ensure that it could be detected in mixed systems. A parallel set of experiments was performed with the caffeine-loaded and ibuprofen-loaded compacts, in this case examining all possible combinations of 2, 3, 4 and 5 component systems. It proved to be difficult to identify components via AFM only, especially as the complexity of the sample increased.

Nano-TA was successful in identifying the individual components within a compact, using the data generated in Chapters 3 and 4 as a guide for interpretation and assignment of the profiles. Five individual nano-TA readings were taken at each location across the surface of the compact. The materials were identified in roughly the proportions that they were present at within the compact and even MS at a level of 1 %w/w was detected. Occasionally, a nano-TA profile which appeared to have two endpoints was observed and this was ascribed to a thin layer of one material (with a lower temperature of transition) on top of a layer of another material (with a higher temperature of transition). Visual assessment of the nano-TA profiles allowed assignment of the two materials involved.

TTM gave mixed results. Experimentally, a grid of 121 readings (11 x 11) was generated across a 100 μm x 100 μm square on the surface of the compact. A coloured map was produced automatically by the equipment software by reference to the temperature of the observed thermal event at each point in the grid, allowing a visual assessment of the distribution of material across the surface of the compact. In general, TTM was successful in separating all the component materials of the compacts. However, some issues were identified. Firstly, two materials which show similar temperatures of transition will be assigned the same colour by the software, hence making separation difficult. Secondly, a thin layer of one material on top of another will be recorded as the higher temperature material. Thirdly, the equipment did produce some "false negative" results, whereby the mapping software did not incorporate all the actual data, even though a full set of nano-TA profiles were available. These issues are discussed further in section 8.2.3.

Five batches of mini-tablets were produced: two development excipient-only batches and three experimental batches, which were excipient-only, caffeine-based and ibuprofen-based as discussed in Chapter 6. Each batch was tested by AFM, nano-TA and TTM, with the development batches being used to refine the techniques used for the experimental batches. As with the 4- or 5- component compacts, AFM was unsuccessful in identifying individual components. The nano-TA and TTM results were commensurate with those observed for the mixed compacts. α -LM dominated the nano-TA and TTM responses of the mini-tablets, which was not surprising as it was present in the largest quantity (circa 60 %w/w). However, MS was detected, even though it was present only at 1 %w/w, as well as all other components.

A slightly different approach was taken for the Raman microspectroscopy, as the technique is rather more established than nano-TA or TTM. Hence, only reference spectra for the individual components were generated before the mini-tablets were tested. The results indicated that all components were detected on the surface of the mini-tablets and that a curved surface did not pose the problems that were initially envisaged. Raman microspectroscopy showed that the individual components gave sufficiently different profiles to allow the development of the mapping technique for mixed systems (Figure 7.1, Figure 7.10 and Figure 7.14).

8.2 General discussion on the techniques used

8.2.1 AFM

AFM is a useful technique to assess the topography of a sample, in terms of surface roughness or smoothness and has found applications in several fields of science (Zhang and Murphy (2011)). It has generally been used to examine samples with relatively simple compositions. Its use in the analysis of the distribution of materials throughout a sample depends on those materials having a different topography or roughness. Unfortunately, of the components studied here only PGS (Figure 3.15) showed a distinctive topography, but even this could not be seen once the complexity of the samples increased beyond three components. Good contact between the sample and the probe is obviously required to obtain decent images and this usually requires the samples to be flat (Seitavuopio et al (2003)). The AFM images seen here were clearer when the compacts were compressed at a higher pressure, i.e. giving a smoother surface. Related to this, is an experimental issue in that there is only a limited amount of surface roughness that can be detected without the probe suffering damage

Surface roughness of tablets has been linked to tablet porosity, which in turn is a determining factor for the rate of dissolution of the drug from the tablet (Podczek et al (1999)). Surface roughness has also linked to the tablet friability, in that rougher samples tend to be more friable because the rough (effectively protruding) parts of the tablet surface are damaged by attrition (Riippi et al (1998)). It would be interesting to study this aspect in more detail and to determine the relationship between surface roughness and friability for the mini-tablets produced here.

During this project, AFM was always used in contact mode because its main function was to provide assurance that the micro-TA and nano-TA data are collected at suitable sites and not from local crevices or peaks, which could produce spurious results. It was important that the AFM scanning did not cause damage to the surface of the sample before the thermal scans were made.

However, "heating-tapping mode" could possibly be used to improve detection of different materials. In this mode, the probe is heated up to just below the temperature of a thermal event of one of the materials and then the area of interest scanned at this temperature.

Materials with thermal responses below this temperature will soften and become "tacky", so the force required to move the probe will change. This could form the basis of a distribution map as shown by Harding et al (2007) who mapped forms of indometacin and Dai et al (2009) who examined amorphous and crystalline lactose by this method. However, there are a few issues with this approach. The major (and most obvious) one is that the "heat-tapping mode" technique requires the application of heat, so is not non-destructive, but importantly will not allow further testing on the same site by another technique also uses heat as the probe, such as nano-TA or TTM. It is likely that this approach will struggle with separating materials with similar thermal profiles, or in a complex multi-component system such as the mini-tablets studied here. Finally, there is an issue with surface roughness as the probe need to oscillate and the smoother the surface the better. In a brief investigation here, the compacts were too rough for this mode, and as it was not the main focus of the study, it was not studied further. However, it would be interesting to investigate the potential of the heat-tapping mode for the analysis of the surface distribution of materials in complex systems.

"Temperature conductivity maps" may provide an alternative method of analysing the systems. This technique works on the basis that different materials show different thermal conductivity. Once the probe has been heated to a particular temperature (dependent on the material being studied) it is placed at a specific location on the sample surface and the heat flow required to keep the probe at that temperature is then measured. The probe is then moved to a new location and the process repeated. This approach has been used by Royall et al (2001) to examine ibuprofen and HPMC systems, Price et al (1999) to analyse paracetamol tablets and Zhang et al (2009) to investigate carbamazepine and HPMC systems. These examples were all simple systems of one or two components, rather than a complex mini-tablet as studies here. The technique may have some issue in discriminating between so many components and the similar type of materials used in the tablets.

8.2.2 Micro-TA and nano-TA

Both micro-TA and nano-TA were successful in discriminating between materials in this study. However, there are some concerns which remain to be overcome. Neither technique is a "fingerprint" technique which could be used to identify an unknown material in the same way that NMR or mass spectrometry could be used. Thus, reference spectra of single components are required to allow identification of individual components in a mixed system. However, it is possible to develop a library of spectra to aid identification of unknowns, but care must be taken to ensure that all spectra were acquired using the same equipment, probe type and experimental protocol. It was shown here that the micro-TA and nano-TA gave different results for the low molecular weight drugs, so data acquired on one system are not necessarily equivalent to data acquired on another.

Micro-TA and nano-TA rely on the materials within the system under test having different thermal profiles. Generally, melting points are the most common endpoint (e.g. Hardy et al (2007) and Hardy et al (2006)), but other transitions such as polymorphic transitions (e.g. Yonemochi et al (2005)), glass transitions (e.g. Fisher (2009)), and dehydration may also be detected. If materials have similar thermal profiles, they will not be easily distinguished from each other. An example of this is the various forms of lactose tested in Chapter 3, where the results were very similar. Interpretation issues also arise when materials show very limited thermal response, as was seen here with PGS and MCC, which could be distinguished only by visual examination of their baseline changes.

Surface roughness can be an issue as the probe needs to make good contact with the surface of the sample. Of the samples tested here, those compressed at higher forces showed smoother surfaces and gave more reproducible results. Hence, the compression force required to make the compacts or mini-tablets should be sufficiently high to ensure that the surface is smooth and maximise the quality of the results. This would not be expected to be a problem for real tablets but may be an issue for the simple compacts.

Micro-TA has a few advantages over nano-TA, even though it may be thought of as a "coarser" technique. The experimental set-up of the micro-TA and the use of a Wollaston wire micro-probe or a nano-probe allows AFM to be conducted prior to the thermal analysis in both modes. As mentioned before, an AFM scan will allow interpretation of the micro-TA or nano-TA results in the event that unexpected results are obtained - it

may be that the probe has landed on a local trough or peak, which would affect the thermal results. However, the Wollaston wire probe is much more resilient to handling and use than the nano-probe, which, considering the price of the probes, is a great advantage. Being larger, it has a poorer resolution, being in the order of 1 μm rather than the 20 nm seen with the nano-probe (Anasys Instruments literature) and has a tendency to leave visible "holes" in the surface of the material after testing, which is not seen with the nano-probe. The production of holes with micro-TA is related to heat being dispersed from the probe into the sample, but the exact mechanisms of heat transfer from the probe to the sample and through the sample are not fully understood (Craig et al (2002)). A consequence of this is that it is not clear how far apart repeat measurement should be to ensure that the site of the second reading has not been influenced by heat dissipating from the site of the first reading. Nano-TA has the advantage of greater resolution. Both techniques, but especially the nano-TA as it is more sensitive, are subject to noise and vibration from its environment, which may lead to spurious results. It is recommended that the equipment is sited in a quiet room, on an anti-vibration platform.

Micro-TA and nano-TA both show some variability in the measured transition temperatures for the same material and also the thermal transitions in micro-TA and nano-TA tend to occur at lower temperatures than seen with DSC, with the nano-TA showing the greater discrepancy. This effect was seen predominantly with the low molecular weight drugs, rather than the larger molecular weight polymeric excipients. When the nano-TA experiment was allowed to continue past the initial deflection, usually regarded as the endpoint for these techniques, a "V-shaped" profile was obtained, and the temperature at the minimum point was more closely related to the DSC transition temperature than the temperature at the onset of deflection. A number of explanations were considered for this.

The "topographical" hypothesis reflects the very small size of the nano probe and postulates that the probe, in some cases, is landing at the junction between two particles. As the temperature of the system is increased, the surface of the sample will expand and allow the probe to slip down further between the particles. The technique regards probe movement as the endpoint, hence an artefactual result is recorded. Variability in the nano-TA results could then be explained by the positioning of the probe: if it is at a junction between particles, a lower transition temperature is likely to be recorded and be a false reading, whereas if it is on the true surface of the particle, then a higher transition

temperature would be expected and is more likely to be a "true" result. As mentioned above, the nano-probe does not allow AFM images to be collected before the thermal profiles are collected, so the precise location of the probe is unknown. The larger size of the micro-TA probe will reduce this effect as it is less likely to be able to slip down between two neighbouring particles.

The "surface disorder" hypothesis regards the surface of a material as being a crystal with severe defects. These defects then allow heat to be propagated through the surface more easily than through a perfect 3-dimensional crystal, leading to a lower melting point of the surface material. Effectively, a thin film of molten liquid is created on the surface of bulk material and the probe sinks into this thin film, with the temperature at which this happens being recorded as the endpoint. The discrepancy between the nano-TA data and the DSC data is because the DSC is recording the thermal data for the bulk material, whereas nano-TA is determining the surface response.

A further consideration for both micro-TA and nano-TA is the temperature calibration protocol used. Generally, calibration is performed with discs of polymer supplied by the manufacturer (Anasys Instruments), which show reproducible behaviour. Calibration is conducted daily before the start of experiments. Here, the calibration discs were also tested after the unusual nano-TA results were obtained for the drug samples and showed the same results as in the calibration runs, indicating that the equipment was performing correctly. Polymer discs would be expected to have a smoother surface than compressed powders, so are more likely to give reproducible results. An alternative calibration method for compressed powder samples may be worth considering. Hardy et al (2007) investigated paracetamol and also found a discrepancy in the DSC melting value and micro-TA results. These results were attributed to the temperature calibration methods used and the authors suggested using different calibration standards for different test material types.

An issue of interpretation arose if the probe landed on an interface between two different materials or if there was a thin layer of one material on top of another. At an interface, the results are likely to be variable, as the material with the lower temperature of response will soften first, allowing some probe movement, which may be recorded as an endpoint or an unsteady baseline. Conversely, the material with the higher temperature of response will remain rigid for longer, giving the surface some mechanical stability and resulting in a

higher transition temperature being measured. There was no evidence in the results generated here that this had occurred. In the case of multi-layered samples, a small lower-temperature endpoint was seen before the trace stabilised and a higher-temperature main endpoint was seen, which was attributed to a thin layer of the material with the lower temperature response on top of a bulk layer of the material with the higher temperature response. There was no evidence in the results observed here for the opposite case, i.e. a thin layer of the material with the higher temperature response on top of a bulk layer of the material with the lower temperature response. In this case, the probe would move only when the top layer had softened sufficiently, which would be above the temperature of transition of the underlying material. A sharp downwards movement of the probe may be seen once the probe has penetrated through the upper layer and reached the underpinning layer, as this would now be expected to react quickly as it would be above its own transition temperature, resulting in fast movement of the probe. However, the software stops the experiment once a main endpoint has been reached, so this event may not be seen experimentally. If the top layer is very thin, then the heat dissipation downwards through the sample may be sufficient to allow the underpinning layer to soften and move, which will result in the probe moving and a spurious endpoint being registered. Interpretation of these events must be made by visual examination of the traces. Further work is required to investigate these issues.

One important consideration for the interpretation of the AFM, micro-TA and nano-TA results is the scale of scrutiny of these techniques compared to the particle size of the materials under consideration. The particle size of each of the materials studied here was estimated to be between 10 μm and 250 μm from the SEM data. The area scanned by Wollaston wire micro-probe was 100 x 100 μm and 50 x 50 μm for the nano probe, hence it is possible that the probe will land on the central surface of one particle or over the junction of two particles. In these situations, the results would be expected to represent a single component or show elements of the response of the two components. Utilising the AFM imaging before the LTA would ensure that the probe was located on the central surface of a particle, rather than at the junction between particles. This is possible for micro-TA but not for nano-TA, as the latter is based on an optical microscope, not an AFM. Specifically considering the granules used to produce the mini-tablets, the probe and sampling area is much smaller than an individual granule and in most cases smaller than individual particles as described above. It would be expected that the AFM, micro-TA and nano-TA results would be examining the sample at the sub-granular level, i.e. the

individual particles within the granule. Some of the AFM images showed "cracks" across the surface, and this is thought to be due to neighbouring particles / granules contacting each other during compression, with the "crack" effectively being the contact point between particles / granules. This may also provide a means of assessing the bonding between particles / granules during compression.

8.2.3 TTM

TTM is an automated version of the nano-TA technique, taking multiple nano-TA measurements in a pre-determined grid pattern across the surface of the sample. From the measured temperature of transition at each point, a coloured map can be generated, allowing the distribution of materials to be assessed. The major advantage of TTM is that it is automated, can run overnight and can generate detailed distribution maps, so has clear advantages over the manual nano-TA technique where the operator has to position the probe prior to each reading. It is therefore a useful technique and has many potential applications in pharmaceutical science. However, as it is based on the nano-TA technique, it suffers from the disadvantages discussed earlier, many of them related to the automatic data processing software.

The TTM software uses the onset of the probe movement as the endpoint for the transition. From the results presented in Chapter 4, the onset of probe movement is not always related to the DSC transition temperatures, but it can be considered to be characteristic of each material, so is a valid parameter to use for the generation of the distribution maps. Care must be taken therefore to ensure that there is a bank of nano-TA / TTM calibration data for reference, as the technique would not be able to identify any unknown material simply by its transition behaviour.

To construct the distribution maps, the TTM software takes the measured transition endpoint and assigns a colour to it based on a temperature-colour scale. The final coloured map is by definition a "transition" map, rather than a component map and the analyst is required to interpret the colours and assign them to individual components. Hence, materials which show a similar transition temperature will show a similar colour (e.g. caffeine and MS), which then leads to problems in identifying which pixel relates to which material. A further issue was identified in that materials which do not show a thermal event within the temperature window studied (e.g. MCC and PGS) will all be assigned the

highest temperature colour, again leading to issues with identification. It is possible to manually identify these materials by comparison to the mono-component traces, but this is time-consuming and negates the advantage of the automated technique.

It would be very useful if more control could be given to the analyst on setting the colour-temperature boundaries based on knowledge of the materials under study, so that all materials can be separated in the map. Figure 8.3 shows an example of how this might be accomplished, based on the materials studied in this project, i.e. the four excipients and two drugs. Instead of a continuous colour change with temperature as is used presently, a temperature range associated with a specific component would be given one definite colour. The bands could be wider or narrower depending on the material studied and the variability in the data expected from the nano-TA calibration work. The first advantage would be a much clearer distribution map would be generated and the second advantage is that each component could be lifted from the combined map to give an individual component map, as is seen with Raman microspectroscopy.

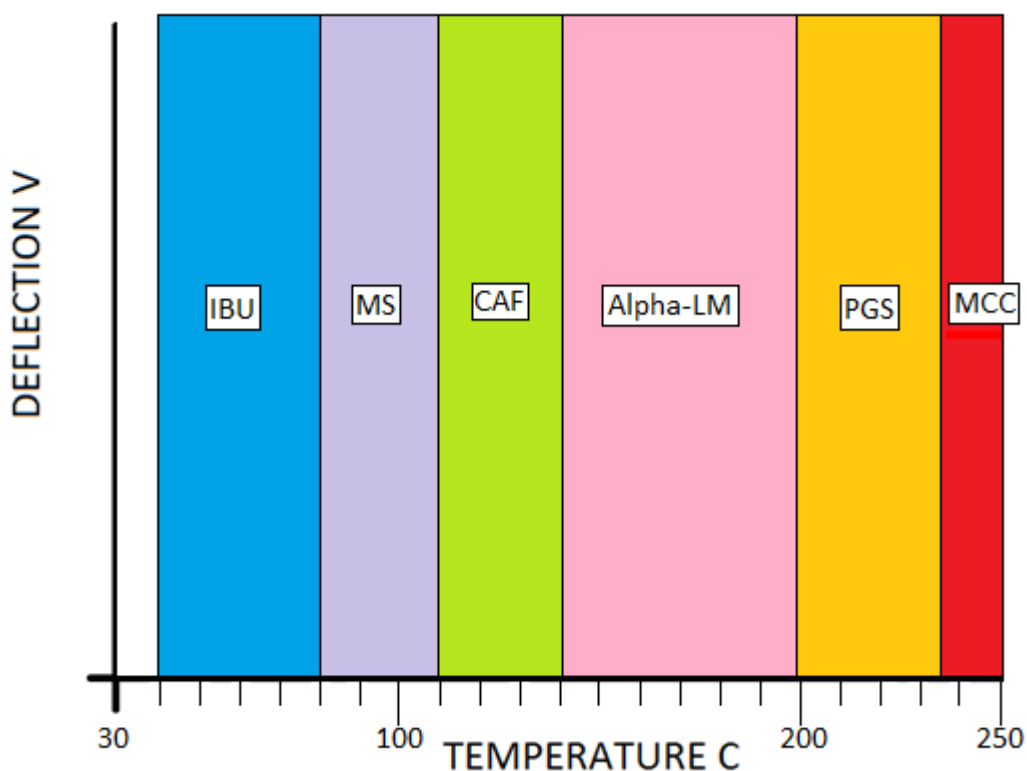


Figure 8.3: An example of the thermal colour banding which would be ideal for this study.

A further alteration to the current software would be to identify "noise" pixels automatically and to re-run those sites. The technique is prone to noise, due to lab vibrations, sample topography, etc, and the fact that the nano-probe is so small and delicate. Generally speaking, the noise endpoints occur at the low end of the temperature profile, before any true transitions have occurred, so there is no risk of thermal damage to the surface of the sample and so a repeated measurement on the same site should be valid.

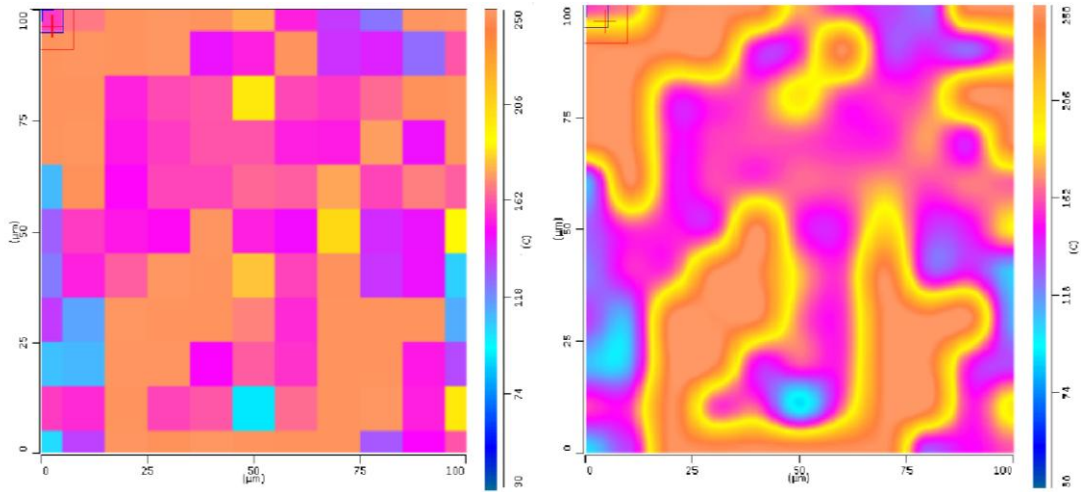
A serious issue with the TTM technique is the smoothing process used to produce the interpolated (smooth, non-pixelated) maps. The non-pixelated map is visually easier to read as the colours are smooth, but it does not necessarily give a true representation of what is happening in the sample on a nano-scale. Where there are neighbouring particles of different materials with different transition temperatures and hence assigned colours, the software moves from one to the other through the temperature-colour scale, assigning the border region an intermediate colour and hence giving the impression that there is a third material between the two materials actually detected. This was observed for samples composed of two materials only, where a third material was not present, so it is an artefact of the processing software. Hence, the smoothed maps need approaching with care to avoid mis-interpretation of the data and it is therefore strongly recommended that only the pixelated images are used for analysis.

Figure 8.4a shows an example of the discrete and interpolated TTM maps generated automatically by the software for a compact composed of 50 %w/w each of MCC and α -LM. The blue pixels are noise. As can be seen, the interpolated map gives multiple colours at the interfaces. It is known in this case that there are only two components, but for an unknown sample, this would lead to the false interpretation that there are multiple components present. In Figure 8.4b the initial results have been processed manually and the most likely component assigned by reference to the calibration results. Here, one colour only has been used for each component, as suggested above, which results in a much more simplified map. The interpolated map was produced using commercial photo-manipulation software. In this case, no spurious information is generated in the smoothing process. Unfortunately, this manual processing of the data is prohibitively expensive in terms of time, so amendment of the instrument software would be best.

Column 1

Column 2

A)



B)

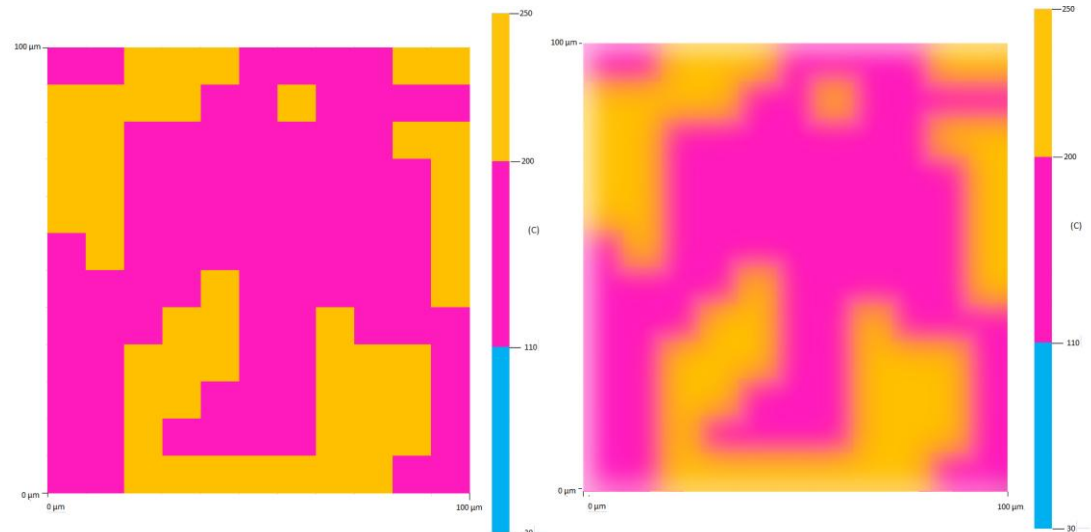


Figure 8.4: TTM maps for a compact of 50:50 %w/w MCC and α -LM compact. A) The maps generated automatically by the instrument software. B) The maps generated by manual processing. Column 1 is the discrete map and Column 2 is the interpolated (smoothed) map. The colours represent the components: MCC (orange), α -LM (pink); the blue colour is noise.

Experimentally, TTM is easy to use and has the advantage of automation. There is a balance to be struck between quantity of data acquired and the time required. For example, in this work 11 x 11 grids were generated, i.e. 121 points in total, over an area of 100 μm x 100 μm , taking approximately 1.5 hours per grid. More detailed scans, whereby more individual point readings are generated would take correspondingly longer. Generating multiple grids at different points across the sample surface would take much more time, with manual re-positioning of the probe at the new site between readings being necessary. An experimental disadvantage of the current TTM instrument is that it is based on an optical microscope rather than an AFM, so topographical images are not possible as they are with micro-TA. Sample surface roughness, which may affect the measurements, will therefore not be identified in TTM, and potentially spurious results may be obtained. Apparently, the new generation of TTM equipment will be based on an AFM, so hopefully this disadvantage will be removed in time. A further disadvantage of TTM, and nano-TA generally, is that it is so subject to noise. This is in part due to the sensitivity of the technique, but does require some analytical review of the data generated, so it cannot be used as a "black box" technique by untrained operators. Finally, the probes are very delicate, so easily broken, and very expensive!

8.2.4 Raman microspectroscopy mapping

Raman microspectroscopy was used here as a confirmatory technique to the thermally-based surface analytical techniques. The technique is an established one and has widely been used to map a drug in the solid state (e.g. Taylor and Langkilde (2000), Vajna et al (2010), Gamberini et al (2006) and Windberg et al (2009)). As it is based on the response of a material to light, it is non-destructive, unlike the thermal techniques. This non-destructive nature allows repeated measurements to be made on the same point on the surface of the sample, so a clearer spectrum can be obtained, with the effect of noise much reduced (Vajna et al (2012) compared to nano-TA and TTM). The fundamental processing of the acquired Raman spectral data is to look for peaks which can be uniquely associated with one particular component, hence materials which show similar responses may not be easily separated. It may be possible to perform this separation using more complex multi-variate data processing techniques, but here only a uni-variate data processing technique was used (Scoutaris et al (2014) and Zhang et al (2005)). MCC and PGS showed quite similar spectral behaviour, with consequent difficulty in separating them. This is because non-aromatic compounds have a σ -electron structure which does not result in strong Raman scattering as they are not so easily polarised. Conversely, most drugs are based on an aromatic chemical structure with a π -electron structure, which is more easily polarised and hence a stronger Raman response is produced (Gordon and Mcgoverin (2011)).

Using the spectral data for the individual components as a reference, the Raman microspectroscopy software will process the acquired spectral data into component parts, thus allowing a complex spectrum to be split into individual materials with an estimation of the relative proportion of each (Johansson et al (2005)). This is the only technique of those studied here which allowed one spectrum to be split into component parts - the thermally-based techniques will assign a single material to each data point. Raman spectra are then acquired at each point across the grid studied and processed as above. Each component is assigned a colour and a pixellated map generated showing the distribution of material. This multi-component pixellated map can then be split into individual component pixellated maps, making it easier to see the distribution of materials in the grid studied. As the data processing will split one spectrum into more than one component (if appropriate), it automatically solves the problem of the probe landing at an interface between materials, as both materials in that pixel will be identified. The issue of a thin layer of one material on top of another may also be overcome, at least in part, but this will depend on the

penetration distance of the light on the surface of the sample and how thick the thin top layer actually is. If the top layer is too thick, then the underpinning layer will not be analysed. There is some debate in the literature as to the penetration depth during the Raman experiment, but it is thought to be approximately 1 μm (Gordon and McGovern (2011)). A limited amount of operator input is required to ascertain the actual composition of mixed pixels, as the colour mixing performed by the software is not always obvious.

As the software performs a subtraction routine based on comparator spectra, Raman microspectroscopy mapping can be used only for samples whose composition is known. In that respect, it has the same issues as nano-TA and TTM, in that it could not be used for identification of an unknown. However, as discussed for the other techniques, a library of spectra could be generated, which could be used for reference, so in future this may not be such a disadvantage (Widjaja and Seah (2008)).

In this work, Raman microspectroscopy mapping was conducted on both compacts and mini-tablets, as initially there was a concern that the curved surface of the mini-tablets would not be conducive to good measurements. In practice, there was no problem with assessing mini-tablets by this technique. Although the results can not be compared directly to those generated using the thermal techniques, as the surface curvature and compression pressures are different, there are similarities in the results indicating that the various techniques are all measuring the same type of distribution of material.

8.2.5 General discussion

All the surface analytical techniques used here require comparison of the test results with calibration data on the components expected to be present in the test sample. Although this in itself is not a problem, it does mean that the techniques can not be used to determine the identity of an unknown material in a sample, but rather should be used to assess the behaviour of a sample of known composition. Ideally, therefore, a second technique, based on a different physical process, should be used to confirm the identity of material at a particular location. Unfortunately, this would be extremely hard to achieve, as only small areas across the surface of the sample are probed at any one time and it would be difficult to identify the precise location for study if the sample was moved between pieces of equipment. Additionally, the second technique would have to be totally non-destructive and would need to be run first before the thermal analytical techniques are run. As Raman

spectroscopy works from a different underpinning process and is non-destructive, if the TTM probe could be altered to include a Raman sensor, this would be ideal to allow two complementary but different techniques to be performed on the same location.

For all techniques used, the areas scanned were very small compared to the total surface area of the sample. The 2 mm diameter mini-tablets had a surface area of $1.26 \times 10^{-5} \text{ m}^2$ and the 13 mm compacts had a surface area of $5.31 \times 10^{-4} \text{ m}^2$, whereas the areas scanned were generally $1.0 \times 10^{-8} \text{ m}^2$, i.e. less than 0.1 % of the total surface area was being examined. Even when multiple locations across a tablet surface were examined, it would still be a very small fraction of the total. To scan the total surface area of a mini-tablet or compact would be prohibitively expensive in terms of experimental time required. A first line calculation would be to take the surface area of the mini-tablet, divide it by the surface area of the scan and multiply the result by the time it takes to generate one scan. For TTM, this would be in the order of 130 days to scan the mini-tablet surface. Thus, this limitation needs to be taken into account when reviewing the experimental results and would form a good area for future study.

However, the similarity between the results from the different techniques for these samples and the matching of the results from the mixed samples to those of the mono-component samples, gives confidence that the results are genuine and not the result of artefacts. All experimental data sets indicated that there was no difference in the behaviour of the individual components at different locations across the compact / tablet surface, i.e. top compared to bottom or across the diameter, giving confidence that the interpretation of the distribution of material in the sample was correct. As with any new technique, the more data sets that are generated, the better the analysis would be, so further work would be required to fully establish this. All techniques were able to separate all materials, although for some this required manual data processing, for example, to distinguish between PGS and MCC in the nano-TA and TTM data.

One positive result from this investigation is that all the surface analytical techniques were able to cope with the curvature of the mini-tablets. This was initially forecast to be a problem, because a flat surface is considered better for the probe to make contact with and for the microscopes to focus on. However, over the areas studied ($100 \mu\text{m} \times 100 \mu\text{m}$), the effect of the curvature is relatively modest and scanning was successful. If a larger area is to be scanned, then this might result in issues relating to probe movement and positioning,

so it remains to be borne in mind, especially if considering tablets which have a deep convex curvature. None of the mini-tablet or compact samples tested here were engraved and it would be expected that engraving on the surface of tablets would lead to severe problems with the positioning and movement of the probe.

The following three tables (Tables 8.1, 8.2 and 8.3) summarise the advantages and disadvantages of the AFM, micro-TA and nano-TA, and TTM for this work.

Advantages	Disadvantages
No vacuum required.	A clear visual difference is required between the various components. This was not possible here, except for PGS.
No complicated sample preparation required.	In contact mode, good contact between the probe and sample surface is essential. Very rough surfaces would affect the quality of the results.
Measures the topography of the sample to generate 2D maps and 3D maps.	Flat surfaces are best for imaging. The technique struggles with curved surfaces, which could be an issue with tablets.
Generally little or no damage to the surface of sample. This is dependent on the mode used and the sample, as contact mode could damage delicate samples.	The probe is affected by large cracks in the surface which knock the probe out of alignment. This may be a problem for engraved or embossed tablets
Allows a higher level of magnification compared to other techniques such as SEM and light microscopy.	The area scanned is very small, so the relevance to the entire sample surface may be questioned, unless repeat measurements are made.
A wide range of different modes may be used, so it is a flexible technique.	Scans can take a long time. It is a balancing act between resolution and times.
	If scanning a whole tablet it would take days and hard to find specific location of the tablet.

Table 8.1: A summary of the advantages and disadvantages of AFM.

Advantages	Disadvantages
Identifies components based on their thermal behaviour. Most other techniques use spectroscopic methods, so provides an alternative strategy for analysis.	Difficult to distinguish between compounds with similar thermal responses, e.g. MCC and PGS.
All thermal transitions detected, which allows for polymorphic determination.	Destructive technique.
Measures the surface properties rather than bulk properties.	Is not a fingerprint technique. Reference scans of the components required
A range of properties can be measured using same thermal probes in different modes e.g. thermal conductivity, pull off forces.	Generally gives different results to bulk DSC (especially for low molecular weight compounds) and between micro and nano probes.
Not affected by strong or weak response of the compound like Raman or IR.	Can give variable results because affected by the sample topography and probe contact.
Can be used in conjunction with AFM for greater surface information.	Curved tablets could be an issue, due to the requirement for contact between the sample and the probe.
	Calibration is performed on polymer disc but how representative is this of low molecular weight drug molecules?
	New and developing technique for this purpose (needs to be validated for this use).
	Further research is required to fully understand the response of multi-layered samples.

Table 8.2: A summary of the advantages and disadvantages of micro/nano TA

Advantages	Disadvantages
Automated.	Results are affected by the sample topography.
It can run overnight to produce high resolution maps of the surface.	Is based on an optical microscope (latest models have an AFM base).
Technique is a step towards scanning the whole tablet.	High resolution maps require a lot of time to generate.
Accurate positioning of the probe is achieved automatically so each reading is a selected distance from the next reading.	Analyst does not have overriding control of data processing which can cause problems.
Automated data processing, so is quick.	Subject to noise and vibration.
Is able to detect the individual components.	Cannot repeat results when the instrument has stopped.
Very sensitive technique.	The blending (unpixellated maps) process the software performs can be misleading.
	The area scanned is very small, so the relevance to the entire sample surface may be questioned, unless repeat measurements are made.
	Is not a quantitative technique (needs further development).

Table 8.3: A summary of the advantages and disadvantages of TTM.

8.3 Discussion on the mini-tablet formulations and results

The tablet formulations studied here were based on a standard tablet formulation used within the research group, as it was known to perform well when used to make larger tablets and is fairly robust to the addition of drug. Direct compression was the first processing technique assessed, but as particle size control is so critical for powders to be compressed into mini-tablets, it was abandoned in favour of a wet granulated process, which allows greater control of particle size distribution. Additionally, the wet granulated tablets were significantly harder than the direct compression tablets, due to the presence of the wet binder (PVP) and the other binding mechanisms (e.g. deposition of lactose bridges) which result from the wet granulation process (Iveson et al (2001)).

PVP presented an issue in terms of identification. It is present in the final tablet at 2 %w/w, but is added as an aqueous solution, and is likely to be present in the final tablet formulation in an amorphous phase and as a thin layer around the component parts of the granule, including in the centre of the granule having had the same initial distribution as the granulation fluid it was dissolved in. The amount of PVP on the surface of the tablet is likely to be limited and to be less than the 2 %w/w nominal content. PVP was tested here in three different formats, but could not be conclusively identified by the thermal techniques. PVP was not specifically considered during the acquisition of the Raman spectra (but is available in the literature (Fini et al (2008)) as a general reference), which is a potential limitation of the work, but could possibly be part of the explanation of the errors in the assignment calculations for mixed pixels (albeit that they are small).

A relatively low drug concentration (10 %w/w) was deliberately used in the tablets here, to ensure that good quality tablets could be made and to test the techniques using a mixed system. Typically, mini-tablets may be expected to have higher concentrations of drug and lower concentrations of excipients, to maximise the benefits of the small size. Different formulations were not studied here as the focus of the work was to examine the utility of the analytical techniques, rather than the challenges of mini-tablet formulation. As has been noted before, the pharmacopoeial specifications for tablets are designed for larger, conventionally-sized tablets, rather than mini-tablets, so there are still some challenges to be overcome in the testing procedures and specifications for friability and hardness, in particular. All the mini-tablet batches prepared here met the pharmacopoeial specifications, but were still more variable than would be ideally desired, so if the work

were to be extended, then the mixing, granulation and sizing processes would be refined to ensure that the tablets were as reproducible as possible.

8.4 Further work

Further work can be split into two sections: characterisation of tablet behaviour and analytical methodology development.

Mini-tablets will behave differently to larger tablets during compression, due to the greater surface area to volume ratio resulting in more contact between the powder and the compression tooling. This then results in differences in fragmentation behaviour at the point of contact between the particles and the tooling, and ultimately different force profiles through the different-sized tablets (Lennartz and Mielk (1998)). Where materials are known to undergo phase conversion on compression, it may be expected that this will occur to a greater extent with mini-tablets, but it would be useful to assess this using the thermal techniques studied here. Similarly, it would be useful to investigate more fully the effects of different compaction pressures on the behaviour of the materials. The physical distribution of materials within a mini-tablet compared to a standard sized tablet is generally assumed to be the same and dependent on the initial powder mixing and granulation processes, but it would be useful to compare the behaviour of various sized tablets in this regard.

Specifically for the formulations studied here, the granulation processes could be refined to ensure more reproducible tablets, although all batches met the BP specifications for content uniformity and weight uniformity. The direct compression formulation could probably be improved by narrowing the particle size distribution, allowing better powder mixing. Extending the range of the excipients used within the formulation would be of general benefit for all future users of this technique. Higher drug loadings would also be studied, although from an analytical technique point of view, it doesn't matter whether the drug is in a low concentration and the excipients in high concentration, or vice versa, as it is the separation of the responses of each that is important. What is necessary to understand is the limit of detection relating to the concentration of components in a formulation. If this formulation were to be used in future, a robust HPLC method could be developed for content uniformity assessment, rather than the spectrophotometric method used here. For example, El-Shahawi et al (2012) have developed a method for caffeine

and Ravisankar et al (1998) a method for ibuprofen). Understanding the extent and implications of lactose muta-rotation in formulations make an interesting study.

PVP posed a problem in this study. It is used in wet granulation formulations as a wet binder. It proved to be difficult to analyse by the surface techniques used here, especially when in a form that it likely to adopt in the final tablet formulation, i.e. the "gel" form. There was no evidence that it interfered with the detection of the other components within the formulation, but a further investigation into the behaviour of PVP is warranted, especially in relation to the Raman spectroscopy, where it wasn't studied specifically.

In terms of analytical method development, there are a number of additional studies which could be undertaken. Further work is required on the analysis and separation of materials with similar transition temperatures in the thermally-based techniques. In this study, separation of the responses of PGS and MCC was difficult for the automated TTM technique and required operator input. An improved software procedure for assignment of response to component is required, as described above, but will take some work. As described above, it would be interesting to develop a heated tapping probe AFM methodology to assess whether this could improve the resolution of compounds with similar thermal properties.

Further work is required to understand more fully the effects of surface melting and whether this can explain the difference seen between the DSC results and the thermal probe results. This discrepancy was more obvious with the small molecular weight drugs, but as these are the therapeutically active components within the tablet formulation, it is vital that their behaviour be understood. Hence, this would form a necessary part of any future study. More comparative studies examining the difference between the results generated with the micro and nano probes would be useful, to ascertain the benefits and disadvantages of each.

More studies are required into establishing exactly what occurs when a probe lands at an interface between particles of different materials, or when there is a thin layer of one material on top of another and how the software can separate the responses related to the different components. It may be possible to develop the technique to study film-coated tablets, whereby there is a deliberate thin layer of one material on top of another.

In this study, there appeared to be little or no difference in the response in the single component compacts at locations across the surface or on the top or bottom of the compact. However, more data is always useful to confirm this result, especially if there is any variation in the compaction pressure at different sites on the surface of the compact.

Finally, it would be useful to have a combination technique, so for example the probe could contain a Raman sensor as well as a thermal sensor. This would allow the same area to be scanned using two different analytical techniques, arising from two different physical processes, which would then provide an internal validation of the assignment of response to component from each technique. Currently it is virtually impossible to guarantee that the same area of the surface is scanned if the sample is moved between pieces of equipment between scanning runs.

Appendix

List of abbreviations

α -LM	Alpha- lactose monohydrate
AFM	Atomic force microscope
ATR	Attenuated total reflection
BNF	British National Formulary
BP	British Pharmacopoeia
CAF	Caffeine
CCD	Charge coupled device
CHMP	Committee for medicinal products for human use
DCP	Di Calcium Phosphate
DSC	Differential scanning calorimetry
EMA	European medical Agency
EU	European Union
FT-IR	Fourier transfer – Infrared spectroscopy
IBU	Ibuprofen
HPMC	Hydropropylmethylcellulose
HPLC	High performance liquid chromatography
LTA	Localise thermal analysis
MCC	Microcrystalline cellulose
Micro- TA	Micro- Thermal analysis
MS	Magnesium stearate
Nano- TA	Nano- Thermal analysis
N-IR	Near Infrared spectroscopy
NMR	Nuclear magnetic resonance
PGS	Pregelatinised Starch
PVP	Polyvinylpyrroindone
RSD	Relative Standard Deviation
SD	Standard Deviation

SEM	Scanning electron microscope
THE	Theophylline anhydrous
Tof – SIMS	Time of Flight Secondary Ion Mass Spectrometry
TTM	Transition temperature microscope
UV	Ultra-violet
VT-IR	Variable temperature – Infrared spectroscopy
WHO	World Health Organisation

References

Akins, P. W. (1996) "The elements of Physical chemistry second edition" Oxford University Press

Akseli, I., N. Ladyzhynsky, J. Katz, X. He (2013) "Development of predictive tools to assess capping tendency of tablets formulations" Powder Technology 236: 139- 148

Angyal, N., Á. Z. Dávid, G. Ujhelyi, A. Szabó, Gy. Marosi, I Klebovich, I. Antal (2007) "Combination of film coating and matrix forming effect of Eudragit[®] copolymers in controlled release minitables" European Journal of Pharmaceutical Sciences 32S: 42

Augsburger, L. L., S. W. Hoag (2008)"Pharmaceutical Dosage forms: Tablets Volume1: Unit operations and mechanical properties" Informa health care 3rd edition

Aulton, M. E. (2007) "Pharmaceuticals: The design and manufacture of medicines" Churchill Livingstone Elsevier

Barns, T. J., I. M. Kempson, C. A. Prestidge (2011) "Surface analysis for compositional, chemical and structural imaging in pharmaceuticals with mass spectrometry: A ToF-SIMS perspective" International Journal of Pharmaceutics 417: 61- 69

Becker, H., O. Bender, L. Bergmann, K. Rost, A. Zobel (1955) "Apparatus for measuring surface irregularities" United States Patent Office: 2,728,222

Belu, A., M. C. Davies, J. M. Newton, N. Patel (2000) "ToF-SIMS characterization and imaging of Controlled- Release Drug Delivery Systems" Analytical chemistry 72: 5625- 5638

Binnig, G., H. Rohrer, Ch. Gerber, E. Weibel (1982) "Surface Studies by Scanning Tunnelling Microscopy" Physical Review Letters 49: 57- 61

Binnig, G., C. F. Quate, Ch. Gerber (1986) "Atomic Force Microscope" Physical Review Letters 58: 930- 934

British National Formulary (BNF66) (September 2013- March 2014). BMJ group and Pharmaceutical press

Bracconia, P., C. Andres, A. N'diaye, Y. Pourcelet (2003) "Thermal analysis of commercial magnesium stearate pseudopolymorphs" *Thermochimica Acta* 429: 49- 51

British pharmacopeia (2010 with supplement to 2013) British Pharmacopoeia Commission

Bugay, D. E. (2001) "Characterization of the solid state: spectroscopic techniques." *Advanced Drug Delivery Reviews* 48: 43- 65

Buzin, A. I., P. Kamasa, M. Pyda, B. Wunderlich (2002) "Application of a Wollaston wire probe for quantitative thermal analysis" *Thermochimica Acta* 381: 9- 18

Chan, K. L. A., S. V. Hammond, S. G. Kazarian (2003) "Applications of Attenuated Total Reflection Infrared Spectroscopic Imaging to Pharmaceutical Formulations" *Analytical Chemistry* 75: 2140- 2146.

Chan, K. L. A., N. Elkhider, S. G. Kazarian (2005) "Spectroscopic imaging of compacted pharmaceutical tablets" *Chemical Engineering Research and Design* 83(A11): 1303- 1310

Cheng, W., S. Lin, S. Wang (2008) "Differential scanning calorimetry with curve-fitting program used to Quantitatively analyze the polymorphic transformation of Famotidine in the compressed compact" *Drug development and Industrial Pharmacy* 34: 1368- 1375

Choonara, Y., V. Pillay, T. Carmichael, M. Danckwerts (2006) "An in vitro study of the design and development of a novel doughnut- shaped minitabket for intraocular implantation" *International Journal of Pharmaceutics*, 310: 15-24

Clarke, F. C., M. J. Jamieson, D. A. Clark, S. V. Hammond, A. C. Moffat (2001) "Chemical Image Fusion. The Synergy of FT-NIR and Raman Mapping Microscopy to Enable a More Complete Visualization of Pharmaceutical Formulations" *Analytical Chemistry* 73: 2213- 2220

Craig, D. Q. M., M. Reading (2007) "Thermal Analysis of Pharmaceuticals" CRC Press

Craig, D. Q. M., V. L. Kett, C. S. Andrews, P. G. Royall (2002) "Mini review: Pharmaceutical Application of Micro-Thermal Analysis" *Journal of Pharmaceutical sciences* 91:1201- 1212

Crowley, P., L. G. Martini (2001) "Drug-Excipient interactions" Pharmaceutical Technology Europe March 2001

Cruz, J., M. Blanco (2011). "Content uniformity studies in tablet by NIR-CI" Journal of Pharmaceutical and Biomedical Analysts 56: 408-412

Dai, X., M. Reading, D. Q. M. Craig (2009) "Mapping Amorphous Material on a Partially Crystalline Surface: Nanothermal Analysis for Simultaneous Characterisation and Imaging of Lactose Compacts." Journal of Pharmaceutical Sciences, 98: 1499-1510

Dai, X., J. G. Moffat, J. Wood, M. Reading (2012) "Thermal scanning probe microscopy in the development of pharmaceuticals" Advanced Drug Delivery Reviews, 64: 449- 460.

Dash, J. G., A. W. Rempel, J. S. Wettlaufer (2006) "The physics of pre-melted ice and its geophysical consequences" Reviews of Modern Physics 78: 695-741

De Brabander, C., C. Vervaet, L. Fiermans, J.P. Remon (2000a) "Matrix mini-tablets based on Starch/microcrystalline wax mixtures" International Journal of Pharmaceutics 199: 195

De Brabander, C., C. Vervaet, J. P. Görtz, J.P. Remon, J. A. Berlo (2000b) "Bioavailability of ibuprofen from matrix mini-tablets based on a mixture of starch and microcrystalline wax" International Journal of Pharmaceutics 208: 81- 86

Deepali ,G., M. Elvis (2010) "UV Spectrophotometric Method for Assay of the Anti-Retroviral Agent Lamivudine in Active Pharmaceutical Ingredient and in its Tablet Formulation" Journal of Young Pharmacists 2: 417- 419

Edge, S., A. M. Belu, U. J. Potter, D. F. Steele, P.M. Young, J. N. Staniforth (2002) "Chemical Characterisation of sodium starch glycolate particles" International Journal of Pharmaceutics 240: 67- 78

Elkhider, N., K. L. A. Chan, S. G. Kazarian (2006) "Effect of Moisture and Pressure on Tablet Compaction Studied With FTIR Spectroscopic Imaging" Journal of Pharmaceutical Sciences 96: 351- 360

El-Shahawi , M. S., A. Hamza, S. O. Bahaffi, A. A. Al-Sibaai, T. N. Abduljabbar (2012) "Analysis of some selected catechins and caffeine in green tea by high performance liquid chromatography" Food Chemistry 134: 2268- 2275

Ernest, T. B., D. P. Elder, L. G. Martini, M. Roberts, J. L. Ford (2007) "Developing paediatric medicines: identifying the needs and recognizing the challenges" *Journal of Pharmacy and Pharmacology* 59: 1043- 1055

Ertel, K. D., J. T. Carstensen (1988) "An examination of the physical properties of pure magnesium stearate" *International Journal of Pharmaceutics* 42: 171- 180

Fell, J. T., J. M. Newton (1970) "Determination of tablet strength by the diametral-compression test" *Journal of Pharmaceutical Sciences* 59: 688- 691

Fernández-Hervás, M. J., J. T. Fell (1998) "Pectin /Chitosan mixtures as coating for colon-specific drug delivery: an in vitro evaluation" *International Journal of Pharmaceutics* 169: 115- 119

Fini, A., C. Cavallari, F. Ospitali (2008) "Raman and thermal analysis of indomethacin/ PVP solid dispersion enteric microparticles" *European Journal of Pharmaceutics and Biopharmaceutics* 70: 409- 420

Fisher, H. R. (2010) "Micro- thermal analysis of polyester coatings" *Applied Surface Science* 256: 3714- 3717

Flemming, J., J. B. Mielck (1995) "Requirements for the production of microtablets: Suitability of direct-compression excipients estimated from powder characteristics and flow rates" *Drug Development and Industrial Pharmacy* 21: 2239- 2251

Flemming, A., K. M. Picker-Freyer (2008) "Compaction of lactose drug mixtures: Quantification of the extent of incompatibility by FT-Raman spectroscopy" *European Journal of Pharmaceutics and Biopharmaceutics* 68: 802- 810

Gamberini, M. C., C. Baraldi, A. Tinti, C. Rustichelli, V. Ferioli, G. Gamberini (2006) "Solid state characterization of chloramphenicol palmitate. Raman spectroscopy applied to pharmaceutical polymorphs" *Journal of Molecular Structure* 785: 216- 224

Giuliodori, M. J., H. L. Lujan, W. S. Briggs, G. Palani, S. E. DiCarlo (2009) Hooke's law: - applications of a recurring principle" *Advances physiology Education* 33: 293- 296

Goole, J., F.Vanderbist, K.Amighi (2007) "Development and evaluation of new multiple-unit levodopa sustained-release floating dosage forms" *International Journal of Pharmaceutics* 334: 35-41

Gordon, K. C., C. M. McGovrin (2011) "Raman mapping of pharmaceuticals" *International Journal of Pharmaceutics* 417: 151-162

Grund, J., M. Koerber, M. Walther, R. Bodmeier (2014) "The effect of polymer properties on direct compression and drug release from water- insoluble controlled release matrix tablets" *International Journal of Pharmaceutics* 469: 94- 101

Gunasekaran, S., G. Sankari, S. Ponnusamy (2005) "Vibrational spectral investigation on Xanthine and its derivatives – theophylline, caffeine and theobromine." *Spectrochimica Acta part A* 61: 117-127

Haaf, F., A. Sanner, F. Straub (1985) "Polymers of N-Vinylpyrrolidone: Synthesis, Characterization and uses" *Polymer Journal* 17: 143- 152

Harding, L., W. P. King, X. Dai, D. Q. M. Craig, M. Reading (2007). "Nanoscale characterisation and imaging of partially amorphous materials using local thermomechanical analysis and heated tip AFM" *Pharmaceutical Research* 24: 2048-2054

Harding, L., M. Reading, D. Q. M. Craig (2008) "The Development of Heated Tip Force- Distance Measurements as a Novel Approach to Site- Specific Characterization of Pharmaceutical Materials" *Journal of Pharmaceutical Sciences*, 97: 2768-2779

Huang, M., H. Hsu, C. Wu, S. Lin, Y. Ma, T. Cheng, J. Shiea (2007) "Characterisation of the chemical components on the surface of different solids with electrospray-assisted laser desorption ionization mass spectrometry" *Rapid Communication in Mass spectrometry* 21: 1767- 1775.

Huang, W., Y. Shi, C. Wang, K. Yu, F. Sun, Y. Li (2013) "Using spray-dried lactose monohydrate in wet granulation method for a low-dose oral formulation of a paliperidone derivative" *Powder Technology* 246: 379- 394

Ishida, M., K. Abe, M. Hashizume, M. Kawamura (2008) "A novel approach to sustained pseudoephedrine release: Differentially coated minitables in HPMC capsules" *International Journal of Pharmaceutics* 359: 46-52.

Iveson, S. M., J. D. Lister, K. Hapgood, B. J. Ennis (2001) "Nucleation, growth and breakage phenomena in agitated wet granulation processes: a review" *Powder Technology* 117: 3- 39

Jackson, S., I. C. Sinka, A. C. F. Cocks (2007) "The effect of suction during die fill on a rotary tablet press" *European Journal of Pharmaceutics and Biopharmaceutics* 65: 253- 256

Jivraj, M., L. G. Martini, C. M. Thomson (2000) "An overview of the different excipients useful for the direct compression of tablets" *Pharmaceutical Science and Technology Today* 3: 58- 63

Johansson, J., S. Pettersson, S. Folestad (2005) "Characterization of different laser irradiation methods for quantitative Raman tablet assessment" *Journal of Pharmaceutical and Biomedical Analysis* 39: 510- 516.

Kachrimanis, K., M. Petrides, S. Malamataris (2005) "Flow rate of some pharmaceutical diluents through die-orifices relevant to mini-tableting" *International Journal of Pharmaceutics* 303: 72- 80

Karehill, P. G., M. Glazer, C. Nyström (1990) "Studies on direct compression of tablets. XXIII. The importance of surface roughness for the compactability of some directly compressible materials with different bonding and volume reduction properties" *International Journal of Pharmaceutics* 64: 35- 43

Kazarian, S. G., G. G. Martirosyan (2002) "Spectroscopy of polymer/drug formulation processed with supercritical fluids: in situ ATR- IR and Raman study of impregnation of ibuprofen into PVP" *International Journal of Pharmaceutics* 232: 81- 90

Kirk, J. H., S. E. Dann, C. G. Blatchford, (2007) "Lactose: A definitive guide to polymorph determination" *International Journal of Pharmaceutics* 334: 103-114

Kizill, R., J. Irudayaraj, K. Seetharaman, (2002) "Characterization of irradiated starches by using FT-Raman and FT-IR spectroscopy" *Journal of Agricultural and food chemistry* 50: 3912-3918

Klang, V., C. Valenta, N. B. Matsko (2013) "Electron microscopy of pharmaceutical systems" *Micron* 44: 45- 74

Labanowska, M., A. Weselucha-Birczyńska, M. Kurdziel, P. Puch, (2013) "Thermal effects on the structure of cereal starches. EPR and Raman spectroscopy studies" *Carbohydrate polymer* 92: 842-848

Lee, T., S. Lin (2005) "Microspectroscopic FT-IR mapping system as a tool to assess blend homogeneity of drug – excipient mixtures" *European Journal of Pharmaceutical Sciences* 23: 112- 117

Lei, Y., Q. Zhou, Y. Zhang, J. Chen, S. Sun, I. Noda (2010) "Analysis of crystallized lactose in milk powder by Fourier- Transform infrared spectroscopy combined with two- dimensional correlation infra red spectroscopy" *Journal of Molecular Structure* 974: 88- 93

Lemartz, P., J. B. Mielck (1998)"Minitabletting: improving the compactability of paracetamol powder mixtures" *International Journal of Pharmaceutics* 173: 75-85

Manduva, R., V. L. Kett, S.R. Banks, J. Wood, M. Reading, D.Q.M. Craig, (2008) "Calorimetric and spatial characterization of polymorphic transitions in caffeine using Quasi- isothermal MTDSC and localized thermomechanical analysis" *Journal of Pharmaceutical Science* 97: 1285-1300

Martinello, T., T. M. Kaneko, M. V. R. Velasco, M. E. S. Taqueda, V. O. Consiglieri (2006) "Optimization of poorly compactable drug tablets manufactured by direct compression using the mixture experimental design" *International Journal of Pharmaceutics* 322: 87- 95

Mazel, V., C. Delplace, V. Busignies, V. Faivre, P. Tchoreloff, N. Yagoubi (2011) "Polymorphic transformation of anhydrous caffeine under compression and grinding: a re-evaluation" *Drug Development and Industrial Pharmacy* 37: 882- 840

Mazurek, S., R. Szostak (2011) "Comparison of infrared attenuated total reflection and Raman spectroscopy in the quantitative analysis of diclofenac sodium in tablet" *Vibrational Spectroscopy* 57: 157- 162

McPhilips, H., D. Q. M. Craig, P. G. Royall, V. L. Hill (1999) "Characterisation of the glass transition of HPMC using modulated temperature differential scanning calorimetry" *International Journal of Pharmaceutics* 180: 83- 90

Meka, L., B. Kesavan, V. N. Kalamata, C. M. Eaga, S. Bandari, V. Vobalaboina, M. R. Yamsani(2009) "Design and evaluation of polymeric coated minitables as multiple unit gastroretentive floated drug delivery system for Furosemide" *Journal of Pharmaceutical Sciences* 98:2122- 2132

Miller, T. A., P. York (1988) "Pharmaceutical tablet lubrication" *International Journal of Pharmaceutics* 41: 1- 19

Mohamed, F. A. A., M. Roberts, L. Seton, J. L. Ford, M. Levina, A. R. Rajabi-Siahboom (2013) "Production of extended release mini-tablets using directly compressible grades of HPMC" *Drug Development and Industrial Pharmacy* 39: 1690-1697

Moreno-Pirajan, J. C., V. S. Garcia-Cuello, L. Giraldo-Gutierrez (2011) "Thermodynamic and Calorimetric Study of Acetylsalicylic Acid (Aspirin) and Ibuprofen" *E-Journal of Chemistry* 8: 1298- 1308

Munday, D. L. (1994) "A comparison of the dissolution characteristics of Theophylline from film coated granules and mini-tablets" *Drug Development and Industrial Pharmacy* 20: 2369- 2379

Murphy, B. M., S. W. Prescott, I. Larson (2005) "Measurement of lactose crystallinity using Raman spectroscopy" *Journal of Pharmaceutical and Biomedical Analysis* 38: 186-190.

Murray, A., T. Lever, M. Reading, D. Price (1998) "Not just a pretty small picture" *Materials world* 6: 615- 616

Nunn, T., J. Williams (2005) "Formulation of medicines for children" *British Journal of Clinical Pharmacology* 59: 674- 676

Nunn, A., R. Richey, U. Shah, C. Barker, J. Craig, M. Peak, J. Ford, M. Turner (2013) "Estimating the requirement for manipulation of medicines to provide accurate doses for children" *European Journal hospital pharmaceutical* 20: 3- 7

Oprea, A., M. Nistor, M. I. Popa, C. E. Lupusoru, C. Vasile (2012) "In vitro and in vivo theophylline release from cellulose/ chondroitin sulphate hydrogels" *Carbohydrate Polymers* 90: 127- 133

Otsuka, M., N. Kaneniwa (1990) "Effect of grinding on the crystallinity and chemical stability in the solid state of cephalothin sodium" *International Journal of Pharmaceutics* 62: 65- 73

Overgaard, A. B., J. Højsted, R. Hansen, J. Møller-sonnergaard, L. L. Christrup (2001) "Patients' evaluation of shape, size and colour of solid dosage forms" *pharmacy World and Science* 23: 185- 188

Park, H., J. Lee, S. Cho, H. Baek, S. Lee (2002) "Colon delivery of Prednisolone based on chitosan coated polysaccharide tablets" *Archives of Pharmacal Research* 25: 964-968

Pinto, S. S., H. Diogo (2006) "Thermochemical study of two anhydrous polymorphs of caffeine" *Journal of Chemical Thermodynamics* 38: 1515- 1522

Pitt, K. G., J. M. Newton, P. Stanley (1988) "Tensile fracture of doubly-convex cylindrical discs under diametral loading" *Journal of Materials Science* 23: 2723-2728

Pivonka, D. E., J. M. Chalmers, P. R. Griffiths (2007) "Applications of vibrational spectroscopy in pharmaceutical research and development" Wiley

Pluis, B., A. W. Denier van der Gon, J. F. van der Veen (1987) "Crystal-face dependence of surface melting" *Physical Review Letters* 59:2678- 2681

Podczec, F., S. Brown, J. M. Newton (1999) "The influence of powder properties and tableting conditions on the surface roughness of tablets" *Particle & Particle Systems Characterization* 16: 185- 190

Podczec, F., N. Course, J. M. Newton, M. B. Short (2007) "Gastrointestinal transit of model mini-tablet controlled release oral dosage forms in fasted human volunteers" *Journal of Pharmacy and Pharmacology* 59: 914- 945

Pollock, H. M., A. Hammiche (2001) "Micro-thermal analysis: techniques and applications" *Journal of Physics D: Applied Physics* 34: R23- R53

Price, D. M., M. Reading, A. Hammiche, H. M. Pollock (1999) "Micro-thermal analysis: scanning thermal microscopy and localised thermal analysis" *International Journal of Pharmaceutics* 192: 85- 96

Priemel, P. A., R. Laitinen, H. Grohgan, T. Rades, C. J. Strachan (2013) "In situ amorphisation of indomethacin with Eudragit[®] E during" *European Journal of Pharmaceutics and Biopharmaceutics* 85: 1259- 1265

Qi, S., J. G. Moffat, Z. Yang (2013) "Early stage phase separation in pharmaceutical solid dispersion thin films under high humidity: Improved spatial understanding using probe-based thermal and spectroscopic nanocharacterization methods" *Molecular pharmaceutics* 10: 918- 930

Rady, M. (2009) "Study of phase changing characteristics of granular composites using differential scanning calorimetry" *Energy conversion and management* 50: 1210-1217.

Raimi-Abraham, B. T., S. Mahalingam, M. Edirisinghe, D. Q. M. Craig (2014) "Generation of poly(N-vinylpyrrolidone) nanofibres using pressurised gyration" *Material Science and Engineering C* 39:168- 176

Raman, C. V., K. S. Krishnan (1928) "The Optical Analogue of the Compton Effect" *Nature* 121: 711- 711

Rasenack, N., B. W. Müller (2002) "Ibuprofen crystals with optimized properties" *International Journal of Pharmaceutics* 245: 9- 24

Ravisankar, S., M. Vasudevan, M. Gandhimathi, B. Suresh (1998) "Reversed-phase HPLC method for the estimation of acetaminophen, Ibuprofen and chlorzoxazone in formulation" *Talanta* 46: 1577- 1581

Ricci, C., C. Eliasson, N. A. Macleod, P. N. Newton, P. Matousek, S. G. Kazarian (2007) "Characterization of genuine and fake artesunate anti- malarial tablets using Fourier transform infrared imaging and spatially offset Raman spectroscopy through blister packs" *Analytical and Bioanalytical Chemistry* 389: 1525- 1532

Riippi, M., O. Antikainen, T. Niskanen, J. Yliruusi (1998) "The effect of compression force on surface structure, Crushing strength, friability and disintegration time of erythromycin acistrate tablets" *European Journal of Pharmaceutics and Biopharmaceutics* 46: 339- 345

Romero-Torres, S., J. D. Pérez- Ramos, K. R. Morris, E. R. Grant (2011) "Raman spectroscopic measurement of tablet-to-tablet coating variability" *Journal of Pharmaceutical and Biomedical Analysis* 38: 270- 274

Rowe, R. C., P. J. Sheskey, M. E. Quinn (2009) "Handbook of Pharmaceutical excipients" RPS publishing.

Royall, P. G., D. Q. M. Craig, D. B. Grandy (2001) "The use of micro-thermal analysis as a means of in situ characterisation of a pharmaceutical tablet coat" *Thermochimica Acta* 380: 165- 173

Royall, P. G., D. Q. M. Craig, D. M. Price, M. Reading, T. J. Lever (1999) "An investigation into the use of micro-thermal analysis for the solid state characterisation of an HPMC" *International Journal of Pharmaceutics* 192: 97-103

Saettone, M. F., P. Chetoni, L. Mariotti Bianchi, B. Giannaccini, U. Conte. M. E. Sangalli (1995) "Controlled release of timolo maleate from coated ophthalmic mini-tablets prepared by compression" *International Journal of Pharmaceutics* 126:79- 82

Šantl, M., I. Ilic, F. Vrečer, S. Baumgartner (2011) "A compressibility and compactibility study of real tableting mixtures: The impact of wet and dry granulation versus a direct tableting mixture" *International Journal of Pharmaceutics* 414: 131- 139

Saunders, G. H. W., C. J. Roberts, A. Danesh, A. J. Murray, D. M. Prices, M. C. Davies, S. J. B. Tendler, M. J. Wilkins (2000) "Discrimination of polymorphic forms of a drug product by localized thermal analysis" *Journal of Microscopy* 198: 77-81.

Schrim, E., H. Tobi, T. W. de Vreis, I. Choonara, L. T. W. De Jong-van den Berg (2003) "lack of appropriate formulations of medicines for children in the community" *Acta Paediatrica* 92:1483- 1489

Scoutaris, N., K. Vithani, I. Slipper, B. Chowdhry (2014) "SEM/EDX and confocal Raman microscopy as complementary tools for the characterization of pharmaceutical tablets" *International Journal of Pharmaceutics* 470: 88- 98

Seitavuopio, P., J. Rantanen, J. Yliruusi (2003) "Tablet surface characterisation by various imaging techniques" *International Journal of Pharmaceutics* 254: 281-28

Sharpe, S. A., M. Celik, A.W. Newman, H. G. Brittain, (1997) "Physical characterization of the polymorphic variations of magnesium stearate and magnesium palmitate hydrate species" *Structural Chemistry* 8: 73-84

Smith, G. D., R. J. H. Clark, (2004) "Raman microscopy in archaeological science" *Journal of Archaeological Science* 31: 1137-1160

Spooner, N., V. Klingmann, I. Stoltenberg, C. Lerch, T. Meissner, J. Breitkreutz (2012) "Acceptance of uncoated mini-tablets in young children: results from a prospective exploratory cross-over study" *Archives of Disease in Childhood* 97: 283-286

Succliffe, A. G.(1999) "Prescribing medicines for children" *BMJ* 319: 70- 71

Taylor, L. S., F. W. Langkide (2000) "Evaluation of solid-state forms present in tablets by Raman spectroscopy" *Journal of Pharmaceutical Science* 89: 1342-1353

Terinte, N., R. Ibbette, K. C. Schuster (2011) "Overview on native cellulose and microcrystalline cellulose I structure studied by X-ray diffraction (WAXD): comparison between measurement techniques" *Lanzinger Berichte* 89: 118-131

Thomason, M. J., W. Rhys- Williams, A. W. Lloyd, G. W. Hanlan, (1998) "The stereo inversion of 2- acyl propionic acid non-steroidal anti- inflammatory drugs and structurally related compounds by *verticillium lecanii*" *Journal of applied microbiology* 85: 155-163.

Thomson, S. A., C. Tuleu, I. C. Wong, S. Keady, K. G. Pitt, A. G. Sutcliffe (2009) "Minitablets : new modality to deliver medicines to preschool-aged Children" *Pediatrics* 123: 235-238

Tomuta, I., S. E. Leucuta (2007) "The influence of formulation factors on the kinetic release of Metoprolol tartrate from prolong release coated minitables" *Drug Development and Industrial Pharmacy* 33: 1070- 1077

Turrell, G., J. Corset (1996) "Raman Microscope: Developments and Applications" Academic Press

Uesu, N.Y., E. A. G. Pineda, A. A. W. Hechenleitner, (2000) "Microcrystalline cellulose from soy bean husk: effects of solvent treatments on its properties as acetylsalicylic acid carrier" *International journal of pharmaceutics* 206: 85-96

Vajna, B., I. Farkas, A. Szabó, Z. Zsigmond, G. Marosi,(2010) "Raman microscope evaluation of technology dependent structural differences in tablets contain imipramine model drug" *Journal of Pharmaceutical and Biomedical Analysis* 51: 30-38

Vajna, B., A. Farkas, H. Pataki, Z.Zsigmond, T. Igricz, G. Marosi (2012) " Testing the performance of pure spectrum resolution from Raman hyperspectral images of differently manufactured pharmaceutical tablets" *Analytica Chimica Acta* 712: 45- 55

van Soest, J. J. G., H. Tournois, D. de Wit, J. F. G. Vliegthart (1995) "Short-range structure in (partially) crystalline potato starch determined with attenuated total reflectance Fourier-transform IR spectroscopy" *Carbohydrate Research* 279: 201- 214

Vankeirsbilck , T., A. Vercauteren, W. Baeyens, G. Van der Weken, F. Verpoort, G. Vergote, J. P. Remon (2002) "Applications of Raman spectroscopy in pharmaceutical analysis" *Trends in Analytical Chemistry* 21: 869- 877

- Vueba, M. L., M. E. Pina, L. A. E. Batista De Carvalho (2008) "Conformational Stability of ibuprofen: Assessed by DFT calculation and optical vibrational spectroscopy" *Journal of Pharmaceutical Sciences* 97: 845-859
- Wallace, J. M. (2012) "Application of atomic force microscopy for the assessment of nanoscale morphological and mechanical properties of bone" *Bone* 50: 420- 427
- Ward, S., M. Perkins, J. Zhang, C. J. Roberts, C. E. Madden, S. Y. Luk, N. Patel, S. J. Ebbens (2005) "Identifying and mapping surface amorphous domains" *Pharmaceutical Research* 22 (7): 1195-1202
- Weyenberg, W., A. Vermeire, E. D'Haese, G. Vanhaelewyn, P. Kestelyn, F. Callens, H. J. Nelis, J. P. Remon, A. Ludwig (2004) "Ocular Bioerodible mini-tablets as Strategy for the management of Microbial Keratitis" *Investigative Ophthalmology and Visual Science* 45: 3229- 3233
- Weyenberg, W., A. Vermeire, J. Vandervoort, J. P. Remon, A. Ludwig (2005) "Effects of roller compaction settings on the preparation of bioadhesive granules and ocular minitables" *European Journal of Pharmaceutics and Biopharmaceutics* 59: 527- 536
- Widjaja, E., R. K. H. Seah (2008) "Application of Raman microscopy and band-target entropy minimization to identify minor components in model pharmaceutical tablets" *Journal of Pharmaceutical and Biomedical Analysis* 46: 274- 281
- Wiley, J. H, R. H. Atalla (1987) "Band assignment in the Raman spectra of celluloses" *Carbohydrate Research* 160: 113-129
- Williams, D. H., I. Fleming (1997) "Spectroscopic Methods in Organic Chemistry fifth edition" McGraw- Hill
- Windberg, M., M. Jurna, H. L. Offerhaus, J. L. Herek, P. Kleinebudde, C. J. Strachan (2009) "Chemical imaging of oral solid dosage forms and changes upon dissolution using coherent anti-Stokes Raman scattering microscopy" *Analytical Chemistry* 81: 2085- 2091
- Xie , X., Q. Liu, S. W. Cui (2006) Studies on the granular structure of resistant starches (type 4) from normal, high amylose and waxy corn starch citrates" *Food Research International* 39: 332-341

Yonemochi, E., T. Hoshino, Y. Yoshihashi, K. Terada (2005) "Evaluation of physical stability and local crystallization of amorphous terfenadin using XRD-DSC and micro-TA" *Thermochimica Acta* 432: 70- 75

Young, R., J. Ward, F. Scire (1972) " Topografiner : An Instrument for Measuring Surface Microtopography" *A Review of Scientific Instruments* 43: 999 -1011

Zhang, Y., K. D. Murphy (2011) "Multi-modal analysis on the intermitten contact dynamics of atomic force microscope" *Journal of Sound and Vibration* 330: 5569-5582

Zhang, L., M. J. Henson, S. S. Sekulic (2005) "Multivariate data analysis for Raman imaging of a model pharmaceutical tablet" *Analytica Chimica Acta* 545: 262- 278

Zhang, J., M. Bunker, X. Chen, A. P. Parker, N. Patel, C. Roberts (2009) " Nanoscale thermal analysis of pharmaceutical solid dispersions" *International Journal of Pharmaceutics* 380: 170-173

Zhao, N. A. Zidan, M. Tawakkul, V. A. Sayeed, M. Khan (2010) " Tablet splitting: Product quality assessment of metoprolol succinate etended release tablets" *International Journal of Pharmaceutics* 401: 25-31